THE UNIVERSITY
of EDINBURGH

An Investigation of Diamagnetic Bearings & Electrical Machine Materials for Flywheel Energy Storage Applications

Siraj Sabihuddin

Submitted in satisfaction of the requirements

for the degree of Doctor of Philosophy in

THE UNIVERSITY OF EDINBURGH

2016

Lay Summary

Renewable energy solutions offer more sustainable methods of energy production. Unfortunately, such energy production is also intermittent and not always available when it's needed. To make use of this energy during periods of demand some form of energy storage is required. A range of energy storage options exist; however, most are not suitable for the large scales necessary for serving a large community of people.

Among potential storage solutions is Flywheel Energy Storage (FES). FES involves spinning a wheel (called a flywheel) and storing energy as kinetic energy. FES has one key problem: the wheel eventually stops and all the energy stored in it is lost. If the spinning of the flywheel can be maintained for hours and days rather than minutes, FES has significant advantages as a large scale and long duration storage approach.

This study looks at reducing friction in the spinning flywheel to achieve this end. The study first notes that significant friction occurs in the flywheel via a mechanical bearing or because of the air environment. This friction can be reduced by shifting to electromagnetic bearings that levitate the wheel and by applying a hard vacuum to the FES environment. Energy continues to be lost even with these two measures. This study looks at reducing this lost energy in electromagnetic bearings.

Typical approaches to levitation use energy input to levitate objects, however, making use of diamagnetic materials (such as graphite) it is possible to levitate without energy input. This suggests an avenue of reducing losses in the bearing significantly. Unfortunately, the forces associated with current diamagnetic materials are tiny and of little practical value. This study proposes a method of multiplying this

tiny force to levitate heavier objects and specifically to levitate the flywheel in an FES device.

Conversations about such diamagnetic bearings, because of stiffness issues, must be accompanied by conversations about electrical machines (motors / generators). Such machines are used to input and remove energy from the flywheel assembly. If air friction is neglected, two kinds of electromagnetic effects cause energy loss in such an electrical machine and diamagnetic bearing system: Eddy current and hysteresis losses. This study tries to determine how much energy is lost from each of these and then attempts to reduce this energy loss further.

Of the two losses, hysteresis related loss tends to dominate. This loss is a result of the magnetization of the motor or generator material. Even when this electrical machine is inactive, some magnetization remains in the materials. This magnetization produces a dragging force on the flywheel-rotor assembly and slows it down. To reduce this energy loss, this study introduces and analyses a method to manufacture electrical machine materials using magnetic nano-materials (specifically magnetite). Magnetite nano-materials become superparamagnetic below a certain size range. Their superparamagnetic nature prevents them from maintaining magnetization and removes hysteresis related losses. This study demonstrates that such nano-materials can help reduce power loss in a diamagnetic bearing further.

Abstract

Recent trends in energy production have led to a renewed interest in improving grid level energy storage solutions. Flywheel energy storage is an attractive option for grid level storage, however, it suffers from high parasitic loss. This study investigates the extent to which passive diamagnetic bearings, a form of electromagnetic bearing, can help reduce this parasitic loss.

Such bearings require three main components: a weight compensation mechanism (lifter-floater), a stabilizing mechanism and an electrical machine. This study makes use of a new radial modification of an existing linear multi-plattered diamagnetic bearing. Here a prototype is built and analytical expressions derived for each of the three main components. These expressions provide a method of estimating displacements, fields, forces, energy and stiffness in the radial diamagnetic bearing. The built prototype solution is found to lift a 30 [g] mass using six diamagnetic platters for stabilization (between ring magnets) with a disc lifter and spherical floater for weight compensation. The relationship between mass and number of platters was found to be linear, suggesting that, up to a point, increases in mass are likely possible and indicating that significant potential exists for these bearings where high stiffness is not needed – for instance in flywheel energy storage.

The study examines methods of reducing bearing (parasitic) losses and demonstrates that losses occur in three main forms during idling: air-friction losses, electrical machine losses, stabilizing machine losses. Low speed (158 [rpm]) air-friction losses are found to be the dominant loss at 0.1 [$\mathrm{W/m^3}$]. The focus of this study, however, is on loss contributions resulting from the bearing's electrical machine and stabilizing machine. Stabilizing machine losses are found to be very low at: 1×10^{-6} [$\mathrm{W/m^3}$] – this leaves electrical machine losses as the dominant loss.

Such electrical machine losses are analysed and divided into eddy current loss and hysteresis loss. Two components of hysteresis loss are remanent field related cogging loss and remagetization loss. Eddy current losses in silicon steel laminations in an electrical machine are quite high, especially at high speeds, with losses in the order of 1×10^5 [$\mathrm{W/m^3}$]. Noting the further high cost of producing single unit quantities of custom lamination-based electrical machine prototypes, this high loss prompts a look at potentially lower cost ferrite materials for building these machines. A commercial sample of soft magnetite ferrite is shown to have equivalent eddy current losses of roughly 1×10^{-13} [$\mathrm{W/m^3}$]. The study notes that micro-structured magnetite has significant hysteresis loss. Such loss is in the order of 1×10^{-3} [$\mathrm{W/m^3}$] when referring to both remanence related cogging and remagnetization.

This study, thus, extends its examination of loss to nano-structured magnetite. Magnetite nano-particles have shown superparamagnetic (no hysteresis) behaviour that promises the elimination of hysteresis losses. A co-precipitation route to the synthesis of these nano-particles is examined. A detailed examination involving a series of 31 experiments is shown to demonstrate only two pathways providing close-to-superparamagnetic behaviour. After characterization by Scanning Electron Microscope (SEM), X-Ray Diffractometer (XRD), Superconducting Quantum Interference Device (SQUID) and crude colorimetry, the lowest coercivity and remanence found in any given sample falls at -0.17 [Oe] (below error) and 0.00165 [emu/g] respectively. These critical points can be used to estimate hysteresis related power loss, however, to produce bulk ferrite a method of sintering or bonding synthesized powder is needed. A microwave sintering solution promises to preserve nano-structure when taking synthesized powders to bulk material. A set of proof-of-concept experiments provide the ground work for proposing a future microwave sintering approach to such bulk material production.

The study uses critical points measured by way of SEM, XRD, SQUID characterization (e.g. remanence and coercivity) to implement a modified Jiles-

Atherton model for hysteresis curve fitting. The critical points and curve fitting model allow estimation of power loss resulting from remanent related cogging and remagnetization effects in nano-structured magnetite. Such nano-structured magnetite is shown to exhibit hysteresis losses in the order of 1×10^{-4} [W/m^3] from remagnetization and 1×10^{-7}[W/m^3] from remanence related cogging drag. These losses are lower than those of micro-structured samples, suggesting that nano-structured materials have a significant positive effect in reducing electrical machine losses for the proposed radial multi-plattered diamagnetic bearing solution. The lower parasitic loss in these bearings suggests excellent compatibility with flywheel energy storage applications.

Acknowledgements

Without the kindness and support of a number of people, the particular direction of this study would not have been possible. First and foremost, I'd like to thank Sue Simpson, a former postgraduate secretary, whose kind responses and helpfulness by email and in-person were the reason for my final decision to come to the University of Edinburgh. I'd also like to extend this thanks to Hieu Thanh Ngo, fellow Ph.D. student, who inspired my work on nano-materials during a random conversation on the street.

I'm deeply deeply appreciative of Roger Watson, then Postdoc in the Carbon Capture and Storage group here in the School of Engineering who took the role of informal co-supervisor and helped me work through some of the early synthesis chemistry and provided advice on experimental and safety procedures. I'm also deeply thankful for the incredible support provided by Nicholas Odling, the Senior Technical Officer at the Geosciences X-Ray laboratory whose openness and enthusiasm were key to completing my work. He also graciously allowed free access to XRD equipment without which much of my synthesis work would have been in vain. I must, of-course, extend a thank you to Nicola Cayzer, Senior Research Fellow at the Geosciences SEM laboratory for kindly showing me how to use the facilities and providing me with access to the sample preparation room.

I'd also like to further thank: Konstantin Kamenev for approving access to SQUID facilities; Xiao Wang for arranging a schedule for me to use these facilities and for topping up the Helium in the machine; Bill Buschle for allowing me access to his fume cupboard while it wasn't being used; the Carbon Capture group for allowing me to store some of my equipment and chemicals in their lab for a short period; Dimitri Mignard, who kindly read over, suggested modifications and verified my risk

assessments for early synthesis experiments and provided some nano-material samples as well.

A final thank you to Aristides Kiprakis, my primary supervisor, who purchased a license of COMSOL Multiphysics, read through my thesis and papers, provided me with access to money for attending a conference, helped purchase a gas dispersion tube and purchase an additional limited access journal paper. Further thanks to Aristides for making the case for extending my submission deadline by a critical month. Without this added month, I wouldn't have been able to complete the writing of this thesis. A further final thank you to Markus Mueller, my second-supervisor, for providing some small funding for me to characterize my work using Geoscience SEM facilities and for approving an unrelated grant application that allowed me an additional two month salary to help finish my work here. I appreciate the three year stipend, office space, computer access and access to journal databases and library facilities provided by the University of Edinburgh – all of which helped me complete my research.

Declaration

I declare that this thesis was composed by myself, that the work contained herein is my own except where explicitly stated otherwise in the text, and that this work has not been submitted for any other degree or professional qualification except as specified.

Siraj Sabihuddin

Table of Contents

Table of Figures

Table of Tables

Nomenclature

When considering a discussion of magnetic materials, it is worth noting that literature is rife with misunderstanding, confusion and unstated assumptions about the variables describing magnetic properties [1], [2]. It is with this understanding that the following clarifications are provided. Note that for a more detailed discussion of units in electromagnetics, please refer to [3].

- Significant confusion has been noted with regards to units. It is not uncommon to see mixing of CGS and SI unit systems – often this occurs without explicit definition. It is for this reason that distinct superscripts, namely, $\blacksquare^{cgs}$, $\blacksquare^{si}$ will be used to distinguish variables in a particular unit system. For instance, mass magnetization, $\acute{M}^{cgs}$ has unit: [emu/g] while $\acute{M}^{si}$ has unit: [Am^2/Kg]. Furthermore, where the superscript is omitted, the unit is assumed to be in SI.

- Magnetic properties for materials can be normalized by mass or volume. To avoid errors a distinction is made such that: $\breve{\blacksquare}$ is for volumetrically normalized forms and: $\acute{\blacksquare}$ is for mass normalized forms. For example: Mass magnetization, $\acute{M}^{cgs}$ is in CGS units of [emu/g] while volume magnetization, $\breve{M}^{cgs}$ is in CGS units of [emu/cm^3]. Where no accent is given, the normalization is assumed to be by volume.

- When referring to magnetic hysteresis, there is some confusion over the interpretation of M-H and B-H curves. This is a result of ambiguity and unstated assumptions regarding the definition of the B-field. In particular, it is noted that most commonly, for B-H curves, the B-field is represented as approximately equivalent to the magnetic polarization [4] field, namely, $\breve{B}^{si} \approx \breve{J}^{si} = \mu_0^{si}\breve{M}^{si}$ or $\breve{B}^{cgs} \approx \breve{J}^{cgs} = \breve{M}^{cgs}$. However, this approximation only holds when the relative permeability (μ_r^{si}, μ_r^{cgs}) is high enough that the H-field can be ignored – note that this may not hold true for hard magnetic materials. For the purposes of this study, given the topic of soft magnetic materials, this approximation is valid.

- The B-H curve does not reach a zero slope at saturation and will continue to increase indefinitely. Ambiguity, thus, exists as to the definition of the magnetic saturation field, B_s. The M-H curve arrives to zero slope at saturation, M_s and so any use of B_s within this paper will assume that it represents the flux density at saturation of the M-H curve.

- The B-H and M-H curve definitions of coercivity, namely H_c and H_{ci} (intrinsic coercivity) are treated as equivalent and in some cases distinctions between the two are not made. Given that $\breve{B} \approx \breve{J}$ (i.e. for soft high permeability materials) these two values are equivalent. This is not the case for hard materials. This paper will assume that H_c always refers to the coercivity of the M-H curve (intrinsic) and that no other definition of coercivity is valid.

- In the CGS unit system, the unit $[\mathrm{emu}]$ can take multiple distinct meanings [5]–[9] causing significant confusion. In the case of magnetic moments and volume or mass magnetization, M, for instance, the equivalency is given by: $[\mathrm{emu}] = [\mathrm{erg/G}]$. Occasionally, however, magnetic moment may also be defined as: $[\mathrm{emu}] = [\mathrm{erg/Oe}]$. When referring to molar, mass or volume susceptibility, $\breve{\chi}$, the definition is given as $[\mathrm{emu}] = [\mathrm{cm}^3]$. A further difficulty arises when EMU (combined with ESU) is used to indicate a general unit system within CGS – i.e. electromagnetic units (EMU) and electrostatic units (ESU). In such a scenario, the Gaussian unit system may be defined as a combination of EMU and ESU systems. Occasionally, in such scenarios, rather than specifying the exact unit, for instance EMU $[\mathrm{Bi}]$ for current, the general unit $[\mathrm{emu}]$ may be used to express that unit. To avoid such confusions, it should be noted that this text exclusively uses the definition: $[\mathrm{emu}] = [\mathrm{erg/G}]$.

- It is also assumed that the use of constants, such as μ_0^{si}, are free of any error. Likewise, with theoretical densities or other externally obtained quantities where errors have not been quantified.

- Finally, estimators resulting from optimization and similar process will be denoted by the accent $\widehat{\blacksquare}$.

A. List of Variables

Given these assumptions and the defined clarifying nomenclature the following sets of variables and constants will be used during computations in this study. Variables are listed in pseudo alphabetical order. Those variables not from the traditional English alphabet are grouped with Greek and script letters that are similar in appearance.

Variable	**Description**	**Units SI**
α	Deceleration of rotor assembly or Weiss coefficient	$[m/s^2]$
α_f	Deceleration of rotor from air friction	$[m/s^2]$
α_m	Deceleration of rotor from electromagnetic effects	$[m/s^2]$
a_g	Acceleration (gravitational)	$[m/s^2]$
Å	Lattice parameter	[m]
A	Vector potential	$[(V \cdot s)/m]$
A	Area of object surface	$[m^2]$
A_s	Area of side surfaces of object	$[m^2]$
A_{tb}	Area of top and bottom surfaces of object	$[m^2]$
β	Tuning parameter for penalty cost computation	[]
$\mathcal{B}$	Broadness of peaks resulting from XRD counts	[rad]
B	Magnetic flux density	[T]
B_d	Magnetic flux density (levitating diamagnet)	[T]
B_l	Magnetic flux density (lifter magnet)	[T]
B_{lr}	Magnetic flux density (lifter magnet remanence)	[T]
B_{lx}	Magnetic flux density (lifter magnet x-directional)	[T]
B_m	Magnetic flux density (stabilizer magnet)	[T]
B_{mr}	Magnetic flux density (stabilizer magnet remanence)	[T]
B_{mz}	Magnetic flux density (stabilizer magnet z-field)	[T]

B_{peak}	Peak magnetic field	[T]
B_{rem}	Magnetic flux density (general remanence)	[T]
B_r	Remanent flux density	[T]
B_s	Magnetic flux density (stator pole), or saturation flux	[T]
B_{sh}	Field produced by stator remanence at rotor position	[T]
B_{shr}	Remanent field generated by stator hysteresis effects	[T]
B_{sr}	Magnetic flux density (stator pole remanence)	[T]
B_{sx}	Magnetic flux density (stator coil x-directional)	[T]
c	Coefficient (anhysteretic & irreversible field fraction)	[]
C	Loss coefficient (steinmetz)	[]
C	Cost function	[]
C	Circumference of stator pole	[m]
C_d	Coefficient of drag	[]
C_{dd}	Coefficient of drag over a thin cylindrical disc	[]
C_{df}	Coefficient of drag for floater	[]
C_{dr}	Coefficient of drag over a cube	[]
C_{dsh}	Coefficient of drag for shaft	[]
C_p	Heat capacity of material	[J/°K]
d	d-spacing in XRD measurements or depth/thickness	[m]
$dd = dd_o$	Outer diameter of stabilizer diamagnetic discs	[m]
$dd_i = shd$	Inner diameter of stabilizer diamagnetic discs	[m]
dg	Air gap from centre of diamagnetic disc to magnet	[m]
dm	Mass of diamagnetic disc	[Kg]
dp	Centre distance b/w neighbouring diamagnetic discs	[m]
dt	Thickness of stabilizer graphite diamagnetic discs	[m]
$\mathbb{D}$	Electric displacement field	$[C/m^2]$
D	Grain or particle diameter	[m]
ε	Voltage (electric potential)	[V]

ϵ_0	Permittivity of free space	$[C/(V \cdot m)]$
ϵ_π	Energy required to move magnetic moment 180 deg.	[J]
ε_d	Induced voltage across diamagnetic disc	[V]
e	Electron charge	[C]
$\mathbb{E}$	Electric field	[V/m]
E	Total combined energy	[J]
E_a	Energy and work as a result of air friction	[J]
E_{an}	Anisotropy energy	[J]
E_d	Potential energy (levitating diamagnet)	[J]
E_g	Potential energy (gravitational)	[J]
E_P	Potential energy	[J]
E_{pe}	Potential energy (electric field)	[J]
E_{pin}	Pinning energy	[J]
E_{pm}	Potential energy (magnetic field)	[J]
E_{rh}	Energy loss in rotor from hysteresis	[J]
E_t	Thermal energy	[J]
E_z	Zeeman free energy	[J]
f	Frequency of input current	[Hz]
f_L	Larmor frequency	[Hz]
f_N	Neel frequency	[Hz]
fd	Diameter of floater (assume spherical)	[m]
fg	Centre of floater to lifter magnet surface airgap	[m]
fm	Mass of floater	[Kg]
fx	Floater x-position	[m]
$\mathcal{F}$	Magnetomotive force	$[A \cdot turn]$
F	Force	[N]
F_{al}	Frictional drag force (linear) from air flow	[N]
F_{dz}	Force (z-directional for levitating diamagnet)	[N]

F_f	Force (on floater from lifter)	[N]
F_{fx}	Force (x-directional on floater)	[N]
F_{fz}	Force (z-directional for floater)	[N]
F_r	Force (on rotor)	[N]
F_{rx}	Force (x-directional on rotor)	[N]
F_{sh}	Force (on shaft from gravity)	[N]
F_x	Force (x-directional)	[N]
F_z	Force (z-directional)	[N]
g	G-factor	[]
G_{eq}	Equality constraint function	$[A^2/m^2]$
G_{neq}	Inequality constraint function	$[A^2/m^2]$
$\hbar$	Reduced plank's constant (Dirac constant)	$[J \cdot s]$
h	Height of cylinder or disc	[m]
H	Magnetic field strength	$[A/m]$
H_C	Coercive field strength	$[A/m]$
H_d	Magnetic field strength (levitating diamagnet)	$[A/m]$
H_{eff}	Effective applied field	$[A/m]$
H_{ex}	Exchange bias field strength of a material	$[A/m]$
H_s	Applied field at saturation	$[A/m]$
I	The moment of inertia of the rotor	$[Kg \cdot m^2]$
I_d	Moment of inertia of diamagnetic discs	$[Kg \cdot m^2]$
I_f	Moment of inertia of the floater	$[Kg \cdot m^2]$
I_r	Moment of inertia of the rotor	$[Kg \cdot m^2]$
I_{sh}	Moment of inertia of the shaft	$[Kg \cdot m^2]$
κ	Coercivity parameter	$[A/m]$
k_b	Boltzmann's constant	[J/°K]
$\mathfrak{K}$	Magnetic anisotropy	$[J/m^3]$
$\mathfrak{K}_{eff}$	Effective anisotropy	$[J/m^3]$

$\mathcal{K}$	Shape factor of crystalline structure (XRD)	[]
K	Total stiffness	[N/m]
$\mathrm{K_d}$	Total levitating diamagnet stiffness	[N/m]
$\mathrm{K_{dz}}$	Levitating diamagnet, z-directional stiffness	[N/m]
$\mathrm{K_f}$	Total floater stiffness	[N/m]
$\mathrm{K_{fz}}$	Levitating floater, z-directional stiffness	[N/m]
$\mathrm{K_x}$	Total x-directional stiffness	[N/m]
$\mathrm{K_z}$	Total z-directional stiffness	[N/m]
λ	Wavelength of X-Ray emissions in XRD	[m]
λ	Learning rate	[]
λ_S	Saturation magnetostriction	[ppm]
ℓ	Number of laminations	[]
l	Distance between magnetic charges in Gilbert Model	[m]
$\mathrm{ld} = \mathrm{ld_o}$	Lifter magnet outer diameter	[m]
$\mathrm{ld_i}$	Lifter magnet inner diameter	[m]
lt	Lifter magnet thickness	[m]
$\mathcal{L}$	Langevin function	[]
m	Magnetic dipole moment	[J/T]
$\mathrm{m_B}$	Bohr magneton	[J/T]
$\mathrm{m_d}$	Magnetic dipole moment (levitating diamagnet)	[J/T]
$\mathrm{m_f}$	Magnetic dipole moment (floater)	[J/T]
$\mathrm{m_{rh}}$	Magnetic moment of rotor from hysteresis effects	[J/T]
$\mathrm{m_{rhr}}$	Magnetic moment of the rotor from rotor hysteresis	[J/T]
$\mathrm{m_{rhs}}$	Magnetic moment of the stator pole from rotor effects	[J/T]
$\mathrm{m_{uc}}$	Uncompensated magnetic moment	[J/T]
$\mathrm{md} = \mathrm{md_o}$	Outer diameter of stabilizer permanent magnets	[m]
$\mathrm{md_i}$	Inner diameter of stabilizer permanent magnets	[m]
mg	Air gap between stabilizer permanent magnets	[m]
mt	Thickness of stabilizer permanent magnets	[m]

$\mathcal{M}_{\mathrm{sin}}$	Sintering sample mass	[Kg]
$\mathcal{M}_{\mathrm{d}}$	Mass (levitating diamagnet)	[Kg]
$\mathcal{M}_{\mathrm{sh}}$	Mass (of shaft)	[Kg]
$\mathcal{M}_{\mathrm{f}}$	Mass (of floater)	[Kg]
$\mathcal{M}_{\mathrm{W}}$	Molecular weight	[Kg/mol]
$\mathcal{M}_{\mathrm{e}}$	Mass of electron	[Kg]
M	Magnetization	[A/m]
M_{an}	Anhysteretic magnetization	[A/m]
$\mathrm{M}_{\mathrm{an}_{\mathrm{c}}}$	Anhysteretic magnetization at coercive field point	[A/m]
$\mathrm{M}_{\mathrm{an}_{\mathrm{init\ tip}}}$	Anhysteretic loop tip initial magnetization	[A/m]
$\mathrm{M}_{\mathrm{an}_{\mathrm{r}}}$	Anhysteretic magnetization at remanence point	[A/m]
M_{d}	Magnetization (levitating diamagnet)	[A/m]
M_{fc}	Magnetization value for FC curve	[A/m]
$\mathrm{M}_{\mathrm{init\ tip}}$	Initial loop tip magnetization	[A/m]
$\mathrm{M}_{\mathrm{irr}}$	Irreversible magnetization	[A/m]
M_{l}	Magnetization (lifter magnet)	[A/m]
M_{m}	Magnetization (stabilizer magnet)	[A/m]
M_{r}	Remanent magnetization of a material	[A/m]
$\mathrm{M}_{\mathrm{rev}}$	Reversible magnetization	[A/m]
$\mathrm{M}_{\mathrm{rhr}}$	Remanent magnetization of the rotor from hysteresis	[A/m]
M_{s}	Saturation magnetization of a material	[A/m]
$\mathrm{M}_{\mathrm{shr}}$	Remanent magnetization of the stator from hysteresis	[A/m]
$\mathrm{M}_{\mathrm{zfc}}$	Magnetization value for ZFC curve	[A/m]
η_{an}	Anomolous loss term for eddy currents in laminations	[]
n	Number of turns in motor coil	[]
$\bar{\mathrm{n}}$	Number of pinning sites	[]
n	Iteration number for optimization, number of dipoles	[]
n_{fu}	Number of formula units in a unit cell	[]
n_{X}	Measured counts via XRD	[]

N_A	Avagadro's constant	$[mol^{-1}]$
N_M	Number of measured magnetization values	[]
N_{mc}	Number of Monte Carlo datasets	[]
N_t	Number of temperature-magnetization data points	[]
θ_i	The ith parameter estimate	–
θ	Orientation/angle w.r.t. to z-axis, or fitting parameters	[rad]
φ	Orientation/angle w.r.t. to x-axis	[rad]
ρ	Tuning parameter for penalty cost computation	[]
ρ_d	Density of material	$[Kg/m^3]$
ρ_e	Electric charge density	$[C/m^2]$
ρ_r	Resistivity of material	$[\Omega \cdot m]$
p	Number of equality constraint functions	[]
p	Number of platters	[]
P	Power input into sample or power lost by rotor	[W]
P_a	Power loss from air-friction effects	[W]
P_{ad}	Power loss of diamagnetic disc from air friction	[W]
P_{af}	Power loss of floater from air friction	[W]
P_{ar}	Power loss of rotor from air friction	[W]
P_{ash}	Power loss of shaft from air friction	[W]
P_{eq}	Equality penalty function	$[A^2/m^2]$
P_f	Floater rotational power loss	[W]
P_m	Power loss from electromagnetic effects	[W]
P_{neq}	Inequality penalty function	$[A^2/m^2]$
P_r	Rotor power loss	[W]
P_{re}	Eddy current loss in the electrical machine rotor	[W]
P_{rh}	Hysteresis loss in the electrical machine rotor	[W]
q	Charge	[C]
q	Number of inequality constraint functions	[]
q_e	Electric charge	[C]

q_m	Magnetic “charge”	$[A \cdot m]$
Q	Heat energy of the sample	$[J]$
$\mathscr{r}$	Per meter resistance of coil wire	$[\Omega/m]$
$\mathfrak{r}$	Number of rotor poles	[]
r	Distance from Gilbert Model dipole	$[m]$
r_i	Residual error for ith parameter	$[A/m]$
rd	Rotor pole to pole outer diameter	$[m]$
rg	Rotor centre to stator pole air gap	$[m]$
rm	Rotor mass	$[Kg]$
rp	Rotor pole height	$[m]$
rt	Rotor pole diameter or width	$[m]$
R	Radius to edge of disc	$[m]$
R	Total coil resistance of stator pole	$[\Omega]$
δ	Sign adjustment parameter	[]
$\bar{\delta}$	Loop shape parameter	[]
$\mathscr{s}$	Number of stator poles	[]
s	Swept arc length	$[m]$
sd	Stator pole width or diameter	$[m]$
sd_o	Stator outer diameter	$[m]$
sg	Stator inner diameter (pole to pole airgap)	$[m]$
$shd = shd_o$	Outer diameter of shaft	$[m]$
shd_i	Inner diameter of shaft	$[m]$
shl	Length of shaft	$[m]$
shm	Mass of shaft	$[Kg]$
sI	Stator pole current total	$[A]$
sp	Stator pole height or stator height	$[m]$
st	Stator pole thickness or length	$[m]$
S	SSD cost function	$[A^2/m^2]$

τ	Torque on rotor assembly	$[N \cdot m]$
τ_0	Attempt time	$[s]$
τ_m	Measurement time	$[s]$
τ_N	Neel relaxation time	$[s]$
τ_{rh}	Torque on the rotor as a result of remanence	$[N \cdot m]$
t	Time of measurement	$[s]$
T	Temperature of sample	$[°K]$
T_b	Blocking temperature`	$[°K]$
T_c	Curie Temperature of material	$[°K]$
T_{irr}	Temperature of irreversibility	$[°K]$
T_N	Neel temperature	$[°K]$
T_p	Peak temperature	$[°K]$
μ	Permeability	$[(T \cdot m)/A]$
μ_0	Permeability of free space	$[(T \cdot m)/A]$
μ_r	Relative permeability	[]
μ_{ri}	Initial relative permeability of material	[]
v	Linear/tangential velocity of moving object	$[m/s]$
V	Volume of material	$[m^3]$
V_d	Volume of material (levitating diamagnet)	$[m^3]$
V_l	Volume of the lifter magnet	$[m^3]$
V_r	Volume of the rotor	$[m^3]$
ω	Angular velocity of the rotor assembly	$[rad/s]$
χ	Susceptibility	[]
χ_{AF}	Antiferromagnetic susceptibility	[]
X_{an_c}	Anhysteretic coercive point susceptibility	[]
$\chi_{an_{dec\ tip}}$	Decreasing anhysteretic loop tip susceptibility	[]
$\chi_{an_{inc\ tip}}$	Increasing anhysteretic loop tip susceptibility	[]
$X_{an_{init}}$	Initial anhysteretic susceptibility	[]
X_c	Hysteretic coercive point susceptibility	[]

χ_d	Susceptibility (levitating diamagnet)	[]
$\chi_{dec\ tip}$	Decreasing hysteretic loop tip susceptibility	[]
χ_f	Susceptibility of floater material	[]
$\chi_{inc\ tip}$	Increasing hysteretic loop tip susceptibility	[]
χ_{init}	Initial hysteretic susceptibility	[]
$\chi_{init\ tip}$	Initial loop tip susceptibility	[]
χ_{irr}	Susceptibility of irreversible curve	[]
χ_r	Susceptibility of rotor material	[]
χ_{rev}	Susceptibility of reversible curve	[]
χ_s	Susceptibility of stator pole material	[]
x	Position in the x-direction	[m]
γ	Gyromagnetic ratio	[]
y	Position in the y-direction	[m]
z	Position in the z-direction	[m]
z	Langevin function constant	[]

B. List of Abbreviations

In addition to the variables, the following abbreviations will be used throughout this study as well. Abbreviations are listed in alphabetical order

Abbreviation	**Description**
3D	Three Dimensional
ABS	Acrylonitrile Butadiene Styrene
AC	Alternating Current
AFM	Antiferromagnetic
BMG	Bulk Metallic Glass
CIE	Commission Internationale de l'Eclairage

CMYK	Cyan, Magenta, Yellow, Key
DC	Direct Current
DEG	Diethylene Glycol
DOF	Degrees of Freedom
FC	Field Cooling
FDM	Fused Deposition Modelling
FES	Flywheel Energy Storage
FM	Ferrimagnetic
GTO	Gate Turn-Off
HTS	High Temperature Superconductor
IGBT	Insulated Gate Bipolar Transistor
IL	In Lens
LAB	Lightness, A and B
LHS	Left Hand Side
MEA	Monoethanol Amine
MNP	Magnetic Nano-Particle
MRI	Magnetic Resonance Imaging
OA	Oleic Acid
PAA	Polyacrylic Acid
PEG	Polyethylene Glycol
PID	Proportional Integral Derivative
PVA	Polyvinyl Alcohol
RGB	Red, Green, Brown
RHS	Right Hand Side
SE	Secondary Electron
SEM	Scanning Electron Microscope (or Microscopy)
SP	Superparamagnetic
SQUID	Superconducting Quantum Interference Device
TEAOH	Tetraethylammonium Hydroxide

TEG	Triethylene Glycol
UMP	Unbalanced Magnetic Pull
XRD	X-Ray Diffractometer (or Diffractometry)
ZFC	Zero Field Cooling

1 Introduction

The accelerated growth of the modern energy economy is highly dependent on potentially dwindling fossil fuel resources (Figure 1-1). Some predictions indicate that depletion of known reserves are expected within 34-40 years for oil, 106-200 years for coal and 36-70 years for natural gas [10]. These predictions have spurred a renewed interest in renewable generation technologies. This increase in interest is, in some sense, similar to that experienced during the 1970s U.S. peak oil crisis. Technologies range from our traditional wind turbines, solar panels, hydroelectric, biomass and geothermal systems to emerging tidal and wave energy generators. Improvements in renewables have become a driving force for improved energy storage and have highlighted the necessity for storage even for non-renewables. Energy storage may, in-fact, be essential for a transition to sustainable energy production. A full review of energy storage technologies is provided in an earlier work by the author of this study in [11].

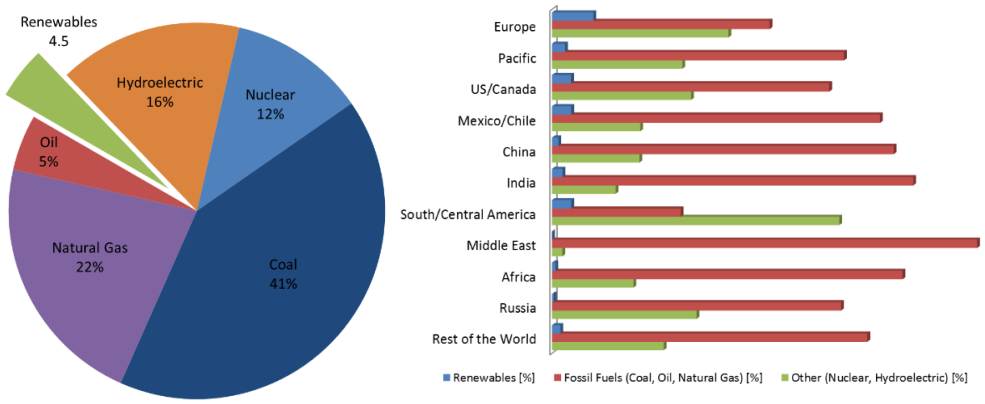

Figure 1-1: On the left, worldwide distribution of electricity production in 2011. On the right, national reliance for electricity production as of 2010. Data extracted from [12], [13].

While a wide variety of solutions exist (Figure 1-2), flywheel energy solutions provide an attractive avenue for further study. Flywheel energy storage (FES) systems store energy in a rotating mass. Such solutions are characterized by a reasonably high energy density, very high power density, very high energy efficiency, long lifespans at low maintenance, very long cycle life, reasonably wide operating temperatures, very low environmental impact and, potentially, high scalability [11].

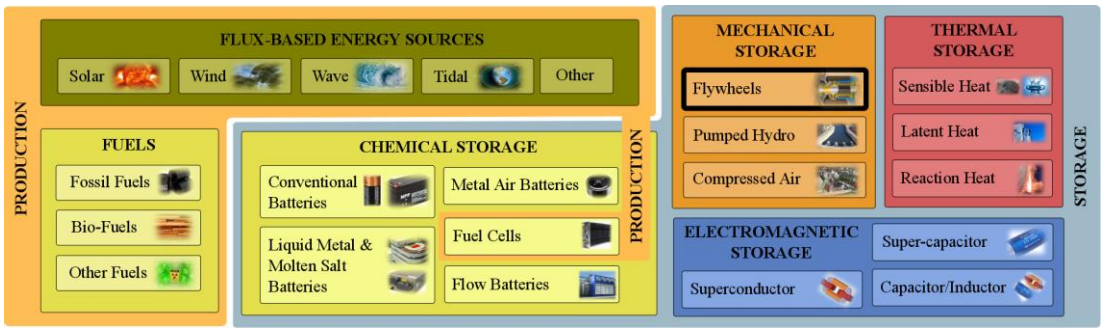

Figure 1-2: The landscape of energy/electricity generation and storage solutions representative sample) - figure modified from [11]. Note that flywheel energy storage applications are focus of this study.

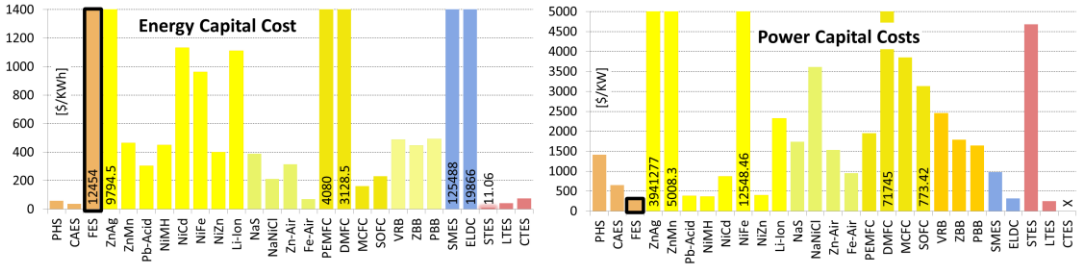

Figure 1-3: A cost comparison of energy storage solutions. Note the currently high average energy capital cost of 12,454 [$/KWh] for flywheel (FES) solutions. Figure modified from [11].

The main theme of this study is thus aimed at flywheel energy storage applications. In particular, we note that flywheels suffer from two major shortfalls: high cost and high self-discharge rates [11]. While cost related issues are beyond the scope of this study, some effort has been made by the author of this study to evaluate and compare costs associated with flywheel solutions (Figure 1-3). Abbreviations shown in the figure are described in Table 1-1.

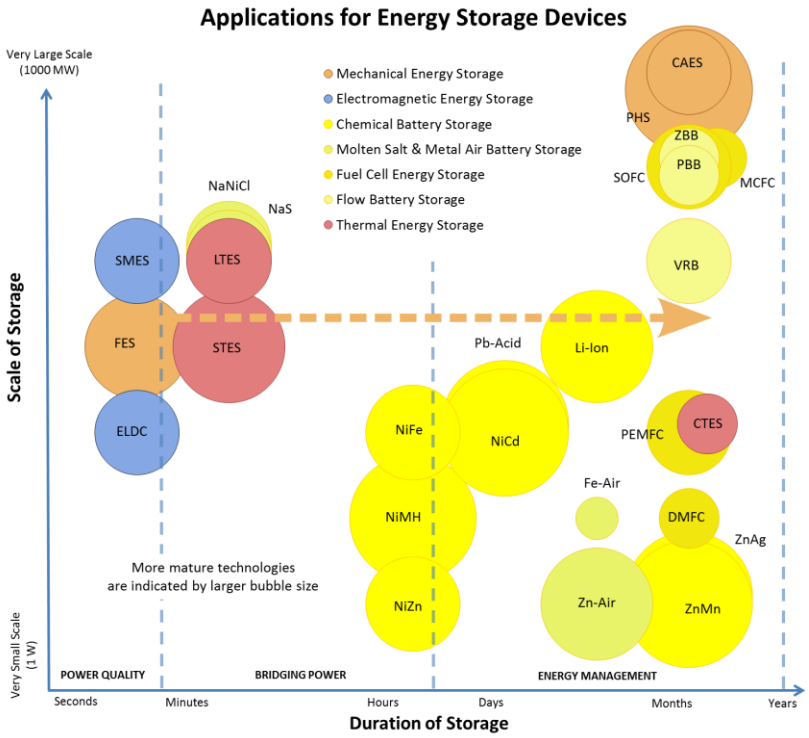

Figure 1-4: A rough breakdown of the specific applications for which storage technologies are suited. Figure from [11]. Note the FES indicates flywheel energy storage. A full explanation of abbreviations and graph is provided in [11].

Table 1-1: Abbreviations for various energy storage devices.

PHS	Pumped Hydro.
CAES	Compressed Air
FES	Flywheel
NiFe	Nickel Iron
NiMH	Nickel Metal Hyd.
NiZn	Nickel Zinc
NiCd	Nickel Cadmium
Pb-Acid	Lead Acid
Li-Ion	Lithium Ion
ZnMn	Zinc Manganese Diox.
ZnAg	Zinc Silver Oxide
NaNiCl	Sodium Nickel Chlor.
NaS	Sodium Sulfur
VRB	Vanadium Redox Flow
PBB	Polysulphide Bromine
ZBB	Zinc Bromine Flow Bat
MCFC	Molten Carbonate
SOFC	Solid Oxide Fuel Cell
PEMFC	Polymer Ex. Fuel Cell
DMFC	Methanol Fuel Cell
STES	Sensible Thermal
LTES	Latent Thermal

Fe-Air	Iron Air
Zn-Air	Zinc Air

CTES	Chemical Thermal
SMES	Super Conductor
ELDC	Super Capacitor

The focus of this study, rather than on cost, will be on reducing the losses that result in high discharge rates. The hope being that improvements in flywheel technologies can make them more attractive contenders as large scale and medium duration storage solutions. In particular, this study looks at a solution that aims to push the flywheel bubble in Figure 1-4 to the right side of the graph. To facilitate this some work will also be done on analyzing and estimating displacements, fields, forces, energy and stiffness associated with design variables for a prototype machine.

1.1 Main Focus

So, how can losses be reduced in a flywheel system to achieve low self-discharge and extend storage duration? To answer this question, we can look more closely at the subsystems that form the basis of FES solutions, namely: the flywheel, the bearing, the electrical machine, the controller and the containment chamber. Figure 1-5 provides a diagrammatic overview of these elements.

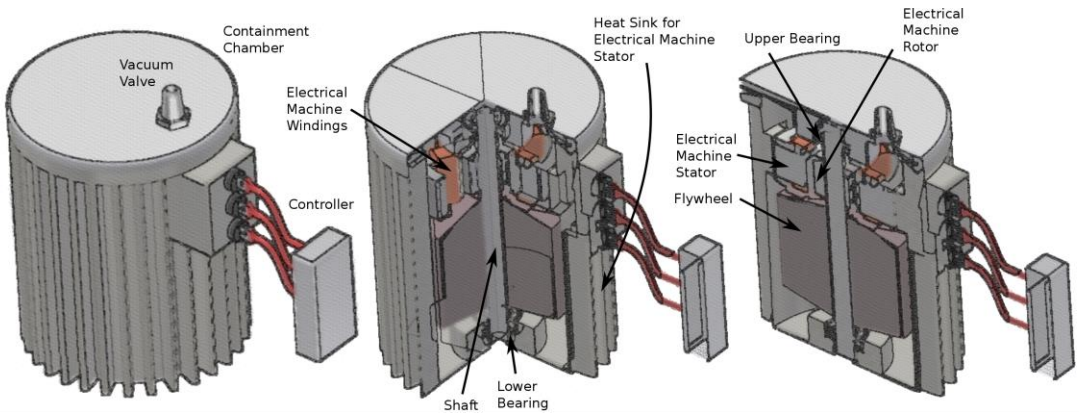

Figure 1-5: Sectioned views for the main subsystems of a generic flywheel energy storage device. The main components are the flywheel, the bearings, the electrical machine, the controller and the containment chamber.

The most visible source of loss is a result of air friction and bearing friction [14]. Further losses may occur as a result of gyroscopic precession - particularly in mobile and portable applications. Finally, losses are also likely to occur in the electrical machine through core losses and in the power converter (controller) as a result of high switching frequencies.

This study will focus on the losses from two particular subsystems, namely, the bearings and the electrical machine. Typical FES development decouples design of these subsystems. This approach is flexible but non-optimal and so recent efforts have attempted more holistic design methodologies. It is with this in mind that these two particular subsystems are considered together in this study. This study will look at the feasibility of passive magnetic bearing systems for FES applications with an additional deep focus on the foundational magnetic materials that can be used to minimize loss in electrical machines used with such a passive bearing.

This study notes that the use of diamagnetically stabilized passive magnetic bearings combined with the use of nano-structured magnetic ferrites offers potential reductions in losses. Diamagnetic materials can stabilize otherwise unstable magnetic levitation without the power loss typically exhibited by actively controlled magnetic bearings. Likewise, magnetic nano-materials, specifically magnetite, have the potential to significantly reduce iron losses resulting from both eddy currents and hysteresis.

1.1.1 Thesis and Contribution to Knowledge

The main question of this study is, thus, to answer the following: “Is the combined use of diamagnetic bearings and nano-structured ferrite-cored electrical machines sufficient to take FES from power quality applications to longer duration bridging power/energy management applications?” This question leads to the main thesis. This study proposes that the use of diamagnetic bearings and nano-structured cores

will reduce parasitic power loss over conventional bearings, laminated cores and ferrites. A further tertiary discussion on the practical stability conditions and frequency behaviour of the combined systems is also needed to determine the extent to which diamagnetic bearings can be used in practical systems.

To verify this thesis the following contributions to knowledge will be made over the course of this document:

1. **A concise survey of existing literature on magnetic bearings with special emphasis on diamagnetic bearings.** Such machines are divided into three distinct components: lifter-floater, stabilizing machine and electrical machine. For the first time, literature is structured into a taxonomy based on these categorizations.

2. **A design and implementation for a new prototype radial multi-plattered diamagnetic bearing.** The design expands on an existing linear machine patent and makes use of multiple layered platters of diamagnetic material sandwiched between permanent magnets to stiffen the stability zone (stabilizing machine) for the bearing. This is combined with weight compensation (lifter-floater) and a reluctance (electrical) machine for power transfer.

3. **Derived analytical expressions for understanding how the dimensions, fields, forces, energy and stiffness of the diamagnetic bearing implementation are impacted by each of the three components in the bearing**. These derived expressions are used to evaluate the scalability of diamagnetic bearings to higher mass.

4. **A first quantitative look at attributing electromagnetic rotational losses in multi-plattered diamagnetic bearings.** Excluding air-friction, these losses are categorized and divided into contributions from eddy currents in the stabilizing machine and eddy currents along with hysteresis (during idling conditions) in the electrical machine. A combined approach involving derived analytical estimation, simulations and velocity measurements is used for power loss estimation across these different categories.

5. **An approach to combining antiferromagnetic effects into the Jiles-Atherton model for hysteresis modelling of core electrical machine material.** This approach allowed for modelling of losses from both minor and major loops using sparse measurement data. Such sparse data allowed for lower cost and more rapid measurement of hysteresis curves.

6. **An approach to estimating operational frequency of core electrical machine material.** Such estimation is done by making use of field cooling (FC) and zero field cooling (ZFC) measurements.

7. **A concise survey of synthesis and sintering approaches relevant to magnetite Magnetic Nano-Particles (MNPs).** These surveys provide deeper comparative look at existing soft magnetic materials.

8. **A first attempt at evaluating the benefits of using magnetite Magnetic Nano-Particles (MNPs) synthesized via reverse co-precipitation for electrical machine cores.** A detailed study (involving 31 experiments) of the effect of MNP synthesis pathways. Pathways use relatively unused techniques (for MNPs) involving some combinations of surfactant Polyethylene Glycol (PEG) and bases Sodium Hydroxide (NaOH) (as well as Ammonium Hydroxide (NH_4OH)). These pathways are compared to micro-structured ferrite material. The losses in the MNPs are juxtaposed with other losses in a multi-plattered diamagnetic bearing design.

9. **An early proof-of-concept experimental examination of the potential of producing bulk electrical machine cores from magnetite MNPs via microwave sintering.** A proposed design for an improved microwaving sintering furnace for experimentation with magnetite MNPs is presented. A series of 7 experiments provide initial characterization of thermal profiles in microwave setups to set the stage for future MNP sintering and characterization.

It should be noted that the bearing design presented in this study is based on prior work by Pelrine et al. [15]–[18] along with Geim et al. [19]–[22], Cazacu et al. [23]–[25], Kustler et al. [26]–[28] and Bleuler et al. [29]. The study focuses on a modification of this prior art by implementing a radial bearing and contributing additional analysis, simulation and experimental data for engineering diamagnetic bearing designs. This is, arguably, the first quantitative look at power loss contributors in low loss bearings and a first link between low loss electrical machines and the superparamagnetic nature of magnetite nano-particles.

1.1.2 Thesis Structure

This study will answer the main question over the course of the next ten chapters. Chapter 2 begins with a survey of existing literature and prior art as it pertains to flywheel energy storage and diamagnetic bearings. This is accompanied by an introduction to a radial multi-plattered diamagnetic bearing design. Analytical expressions aimed at calculating displacements, fields, forces, energy and stiffness for this bearing design are introduced in Chapter 3. A more detailed look at the synthesis process for the MNPs that may be used as base material for low hysteresis loss electrical machines is provided in Chapter 4. This is followed closely in Chapter 5 by an introduction to a proof-of-concept microwave sintering furnace implementation. The aim being to take synthesized magnetite MNPs to bulk material while preserving nano-structure. Here, a design proposal for a next generation microwave sintering furnace is also provided. Both synthesis and sintering approaches are pulled together with a discussion of nano-material characterization, thermal measurement and bearing speed measurements in Chapter 6. At this point a discussion of rotational loss contributors (plus measurement/simulation approaches) is provided in Chapter 7 and extended into Chapter 8 by looking at hysteresis modelling for the diamagnetic bearing's electrical machine core material. This discussion of hysteresis loss also touches upon blocking temperature and frequency of operation estimates. The final results, from the various sections, are presented collectively in Chapter 9 and concluding remarks provided in Chapter 10.

2 Diamagnetic Bearings

Earlier, we noted that a typical FES system is composed of five key subsystems. Of these, the containment chamber, the control & power converter and the flywheel are largely neglected for this study. There is, however, extensive work being done on these systems as well. In the interest of completeness, a very brief overview of this work is provided in the next sub-section.

The remaining two sub-systems, i.e. the bearing and electrical machine, are the focus of this study. The goal here is to reduce the self-discharge rates towards which these two subsystems may contribute. After a discussion of literature on flywheels, containment chambers and control, this chapter will continue by taking a closer look at existing literature on magnetic bearings, diamagnetic levitation and electrical machines.

Considering that comparatively little work has been undertaken on the practical uses of diamagnetic stabilization, this chapter will end by introducing an implementation for a new radial diamagnetic bearing for FES applications. This bearing design will form the basis of future analysis in later chapters. The key features of the proposed design are a homopolar axial thrust bearing with multiple diamagnetic platter based stabilization. A permanent disc magnet is combined with a floater to provide weight compensation while power transfer is provided via a reluctance machine.

2.1 Advances in Flywheel Design, Containment & Control

Briefly digressing from our conversation on diamagnetic bearings and associated electrical machines, we note that significant advances have been made in other flywheel sub-systems. For instance, advances in materials have led to a transition from low speed (6,000 [rpm]) steel flywheels to much higher speed, safer and more energy dense composite and alloy materials. While costs of high speed systems are almost five times as high as lower speed equivalents [30], the gains associated with the higher speeds have resulted in trends showing a shift to lower density and higher tensile strength materials. Among these materials are: aluminium alloys and graphite/carbon/glass fibre composites with added polymer (epoxy) resin support matrices [31], [32]. Speeds of these higher speed flywheels range from 10,000 to 110,000 [rpm] [30], [31]. These higher speeds exploit the quadratic improvements resulting from increases in speed rather than increases in mass. In an effort to improve safety, epoxy supported filament wound multi-ring flywheels showed significant improvements [32], [33]. Generally, such modern materials can support tangential speeds of 1000 [m/s] [34]. Recent trends in carbon nanotubes have seen the emergence of biscrolling techniques to produce yarns for use in fibre composite flywheels [35]. These nanotubes could increase maximum speeds and subsequent storage densities quite significantly.

However, increases in speed must be matched with improved and bulkier containment vessels which may eventually put an upper limit on storage capacities [32]. Most high speed FES systems operate under high vacuum to minimize the effects of friction. The high costs associated with pumping machinery and the poor heat dissipation characteristics have, however, prompted the use of low friction helium-air or other gas mixtures in containment vessels [31]. As safety is often a significant concern, the design of flywheels is aimed at producing high safety margin, non-bursting, incrementally failing flywheels. These types of flywheels reduce the requirements for containment from containing the full kinetic energy of the flywheel to simply retaining the failure within the chamber. The disintegration of composite flywheels, however, can still produce high energy, high impulse abrasive

particulate fluid. Free floating containment vessels have been used to contain this resulting fluid [36] more effectively.

Typically transferring power to and from the flywheel has occurred through electrical machines via bi-directional variable frequency power converters [30]. The development of high power semiconductor switches has been critical to improvements in control. The low cost, compact, reliable and highly efficient design of GTO thyristors have traditionally made them the choice switch for power conversion. However, the added convenience and higher switching frequencies of IGBTs have resulted in greater adoption for variable frequency power converters in recent years [14].

2.2 A Review of Magnetic Bearings

Moving on to the remaining two subsystems we note that a range of bearing options exist. Bearings usually take the form of one or more of the following combination: mechanical, fluid, active electromagnetic, superconducting, permanent magnet, ferrofluid, electrodynamic, gyroscopic or diamagnetic. Recent advances in materials have led to better quality mechanical bearings that reduce losses and are suitable for lower speed FES systems (20,000 to 40,000 [rpm]) [30], [31]. These bearings have short life at the upper end of this low speed range [14]. As a slightly better replacement, fluid bearings may be used. At higher speeds, frictional losses make both mechanical and fluid bearings inappropriate, however. Instead electromagnetic variants can present more efficient and longer life alternatives.

Of these, the following are classes of magnetic bearings that tend to have relevance when talking about diamagnetic systems: active electromagnetic bearings, superconducting bearings, permanent magnet bearings, ferrofluid bearings, electro-dynamic bearings and gyroscopic bearings. Generally, magnetic bearing solutions are a combination of one or more of these types and advances in one approach can often be seen carried over to another. This sub-section introduces work done in the study

of these bearings to help determine which elements are most pertinent in being carried over to developments in diamagnetic bearings.

2.2.1 Active Bearings

In practice, as demonstrated by Earnshaw, purely permanent magnet solutions have been demonstrated to be unstable [37]. For stability, the potential energy surface generated from the levitating rotor (in such bearings) must form some local minima in the region of levitation. For considerable time this led to a research focus on active electromagnetic bearings of which superconductors may, in some sense, be considered a sub-set. To provide some examples, active bearings have been used for military combat and mobile applications where flywheels systems providing high power density and continuous operation under high shock conditions are required [38]. These bearings can have high stiffness of around $6.3 - 12.3$ [KN/mm] of air gap. Generally, they are supported via two axial bearings and four radial bearings (Figure 2-1, *left*) providing stiffness in 5 degrees of freedom (DOF) with only one free rotational DOF. The resultant position can be accurate to within 15 [μm] of perfectly centric rotation [39]. When high stiffness isn't a major concern permanent magnets can be used to support a few degrees of freedom as long as at least one degree of freedom is supported by some other means [40]. In FES, such permanent magnets may also be used as a lifter while the active control only provides stabilization.

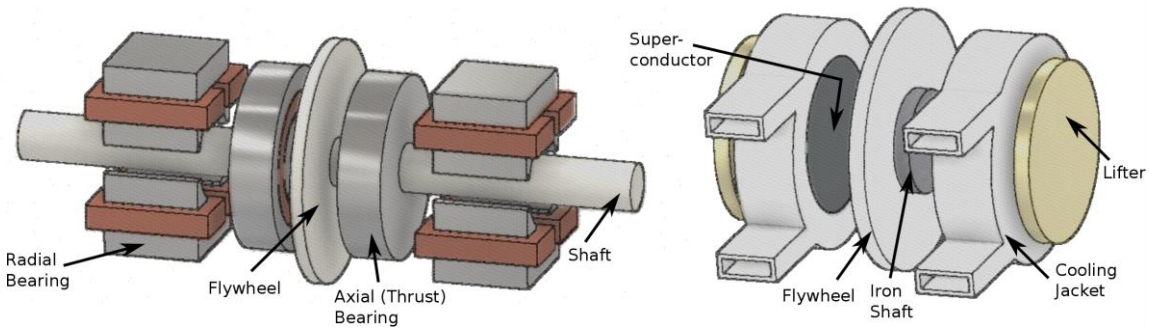

Figure 2-1: Active electromagnetic bearing (left) and a hybrid super conducting bearing (right).

Mechanical bearings typically result in parasitic losses of about 5% capacity or more per hour. This can be lowered to about 1% via active electromagnetic bearings [41]. Unfortunately, electromagnetic variations suffer from iron losses related to stator and rotor eddy currents and material hysteresis. The use of better materials, thus, becomes important – a bulk of this study will focus on such materials.

2.2.2 Superconducting Bearings

Superconductors do somewhat more poorly than active bearings and remain much more in the early stages of development. Active bearings can provide levitation pressures of around 1 [MPa] whereas superconducting bearings, in comparison, provide around only 0.28 [MPa]. These forces are small compared to mechanical bearings which can provide much more than 10 [MPa] pressure [34]. Despite this, superconductors of the bulk high temperature superconductor (HTS) variety have been popular especially where speeds are in the order of 100,000 [rpm]. Recent advances in high temperature superconductors reduce rotor idling losses down to 0.1% of total capacity per hour [31].

Unfortunately, reducing the costs and size of cryogenic systems has proven difficult [14], [31]. Further, it should be noted that HTS materials tend to be fragile and can limit maximum operating speeds in some configurations. Furthermore, the maximum effective bulk HTS size (roughly 100 [mm] diameter) means that larger bearing configurations can experience additional eddy current losses – something that can further limit their effectiveness.

Two particular approaches, to HTS use involve field cooling (FC) or zero field cooling (ZFC) techniques of which ZFC produces less stable levitation at high force and FC produces greater stability via flux pinning, at the expense of levitation force [34]. Note that both FC and ZFC curves will be discussed and clarified in relation to magnetic nano-materials (i.e. magnetite) later in Chapter 6 of this study. There have

been further explorations with HTS configurations similar to those used with active bearings and diamagnetic bearings – i.e. with a lifter magnet providing the bulk of force and with an HTS used as stabilizing material. Figure 2-1 *(right)* provides one example of this kind of stabilization that also reduces the need for rotating permanent magnets or rotating bulk HTS material (called mixed-μ configuration). These configurations (e.g. HTS stabilization and nested ring lifters) are discussed further in the context of diamagnetism in the next few sections below – and as shall be seen, are used in existing prototype diamagnetic bearing devices.

2.2.3 Permanent Magnet Bearings

At this point we should note that extensive work has been done with permanent magnet topologies in an attempt to achieve better stability as well as higher lifting forces. The use of modern day permanent magnets can allow for up to $573\ [\mathrm{KN/m^2}]$ of levitation pressure [42]. While permanent magnet bearings cannot exist in isolation of stabilizing methods, the advantages of these large forces have motivated some studies examining their effects – see Figure 2-2 for examples. For instance, some topologies have looked at the use of radially magnetized rings [43]. This approach is inherently unstable in the axial direction and requires the use of a touch bearing, however losses are low at $0.1 - 2$ [W] for 2500 [rpm] angular speed [43]. Alternative approaches have made use of conical rings to achieve axial stability at the expense of radial stability [44]. Air gaps for these bearings are typically in the order of about 4 [mm]. Such conical magnets are difficult to manufacture and can be substituted for a series of stacked ring or embedded ring/disc structures [42] – this is a discussion very relevant to diamagnetic lifter magnets as will be seen later in this study. The use of radially magnetized magnets is complicated by the limited range of manufacturing options as well.

Normally, as noted, permanent magnet bearings provide weight compensation and are combined with constant energy input electromagnetic control (active bearing) [14] or partially-passive electrodynamic stabilization (e.g. as in Maglev trains) [45].

There is one notable exception to this that uses gyroscopic precession (i.e. levitron) that simply requires a spinning rotor for stability [46].

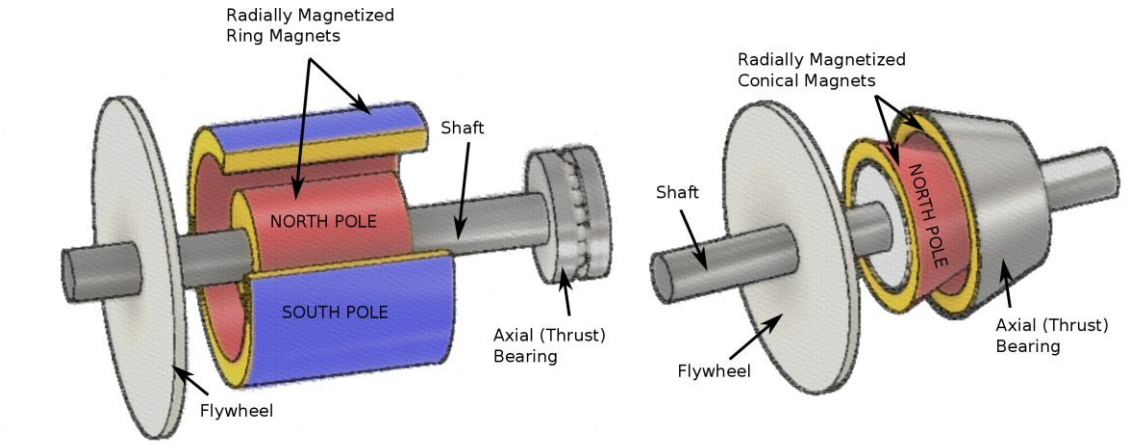

Figure 2-2: Radially magnetized rings accompanied by a touch bearing (left) – an example of a homopolar radial machine. A conic ring to provide thrust bearing functionality (right).

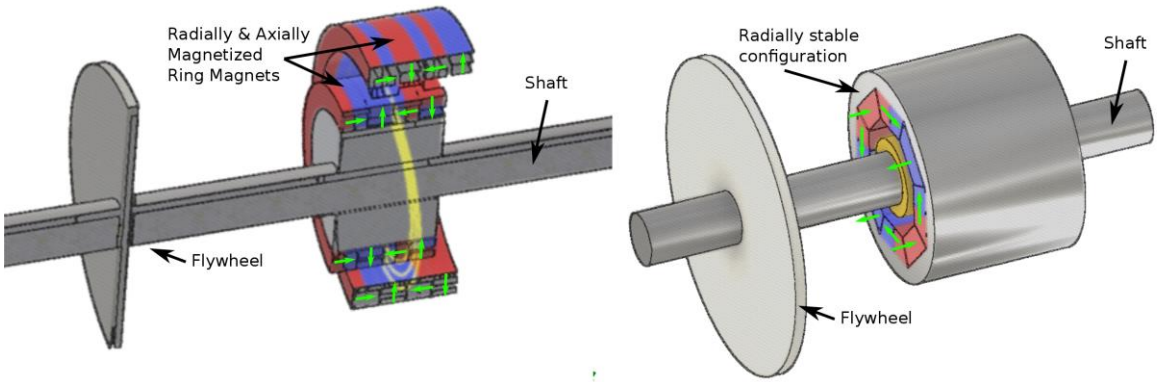

Figure 2-3: Various configurations for halbach arrays. On the left, a thrust bearing for axial stability. On the right, a journal bearing for radial stability – an example of a hetropolar radial machine.

Despite manufacturing challenges, Halbach arrays have also been used to good effect. Such arrays combine multiple magnets of varying magnetization directions to provide a "one sided" field. They offer the greatest benefits in terms of space efficiency allowing up to 27 [%] reduction in magnet volume [45] compared to other configurations. The permanent magnet topologies in Figure 2-2 can be replaced by even more complex variations of halbach arrays (Figure 2-3). The results are stiffness increases from 100 [N/m] to potentially 1440 [N/m] [47] and levitation forces of around 2700 [N] for roughly 136 [mm] diameter rotors [48]. As a point of reference, a standard reluctance actuator of similar scale may produce stiffness in the order of $10^4 - 10^5$ [N/m].

2.2.4 Electrodynamically Stabilized Bearings

The recent (and not so recent) work with Maglev technologies offers a clear demonstrator for the use of permanent magnets combined with electrodynamic stabilization [45]. Permanent magnet approaches coupled with electrodynamic stabilization show low power consumptions – one source [49] has indicated 0.8 [W] for levitating a 1.3 [Kg] mass at 4800 [rpm].

Such approaches can also allow for, potentially, 10 [mm] airgaps making variations in loading conditions more tolerable in Maglev systems. It is here, thus, that conversations of electrical machines become more pertinent. Typically, electrodynamic stabilization takes place via either homopolar or heterpolar machine variants. Homopolar machines typically present no inversions in the magnetic field across the rotor (Figure 2-2, *left radial bearing*), while heterpolar machines do (Figure 2-3, *right radial bearing*).

The traditional AC heterpolar machines have fallen out of favour as a result of high eddy currents and resulting heat loss generated in the rotor [50] – a situation somewhat similar to that which can occur with active bearings. One significant concern with these bearings has been rotordynamic stability issues which have

limited their use in industry [50]. Rotating versions of the halbach configurations shown in Figure 2-3 (right radial bearing) have instead been combined with the use of stationary litz wire. The focus of such wiring being to reduce the contributions of skin effect while also reducing eddy current generation during centric rotation. Of course, wire wound rotor configurations with stationary halbach arrays can also be used in null flux coil configurations.

The use of null flux coils (originally designed for Maglev suspension), in axial flux bearings for instance (Figure 2-1, *left*), introduces a method to eliminate eddy current losses for centric rotation by inducing oppositely circulating eddy currents in a heteropolar configuration of a rotating disk [51]. With appropriate geometric configurations, these coils provide damping during off-centric rotation. Some studies showed stiffnesses of around $1000 - 2000$ [N/m] from passive coils [42]. At low frequencies ($32 - 48$ [Hz]), power losses are low at $1.2 - 2.4$ [W] [42]. Unfortunately, off-centric damping losses at higher frequencies, resulting from the use of null flux coils, were found to be too high [50] and may have prompted further exploration of homopolar machines in recent years.

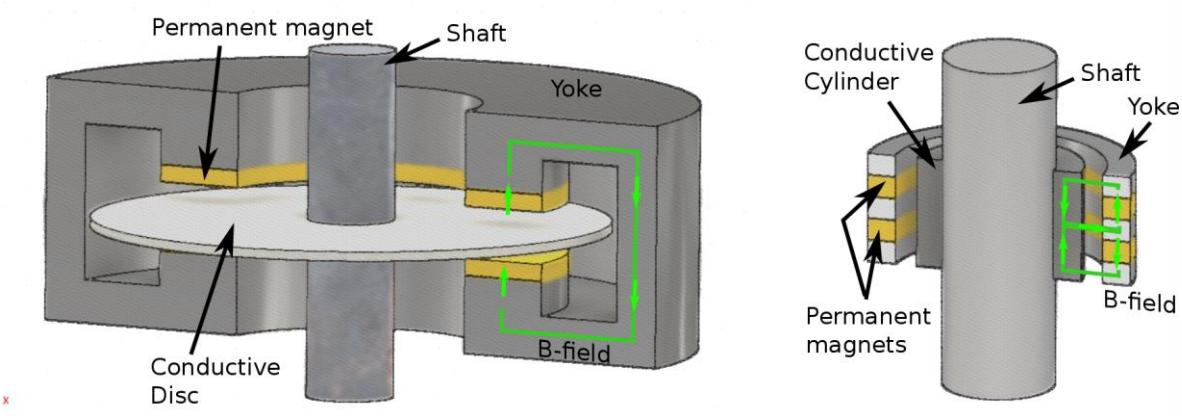

Figure 2-4: Axial and radial flux homopolar machines. Note that axial flux machines present a constant non-inverting magnetic field across a conducting disc. A similar field is presented across a conducting cylinder for radial flux machines.

The diamagnetic bearings presented in this study act largely in homopolar configurations (rather than heteropolar). They are used as thrust bearings and, consequently, can face similar challenges to other machines that involve electrodynamic effects – a discussion will follow in later sub-sections. The homopolar configurations, however, introduce virtually no drag or torque when the rotor is centric relative to the magnetic field's axis of symmetry [50], [51]. As such, it can be considered very similar to the centric null coil configurations of a heteropolar system but with lower off-centre losses. Homopolar machines are generally variants of one of two types (axial or radial) as shown in Figure 2-4. Such machines, while introduced over a 180 years prior, remain a point of considerable discussion, disagreement and analysis [52]. Homopolar machines were largely supplanted from popular use as generators in favour of coiled systems. This was a result of their poor efficiencies (from current flows in non-uniform field regions) and low voltage outputs. This may partially explain present day theory-related disagreements [52]. A point of note related to electrodynamic systems is the possibility of what the author of this study will label "magnetodynamic stabilization".

2.2.5 Ferrofluid Stabilized Bearings

Studies by NASA showed that permanent magnet rotation in flywheel systems may also be stabilized by the use of ferrofluids [53], [54]. These systems showed roughly 200-500 [N/m] stiffness values and hold significant promise. An examination of ferrofluids is well outside the purview of this study except from the context that this study produces base low hysteresis magnetic nano-particles (MNPs).

2.2.6 Gyroscopically Stabilized Bearings

One final technique of importance with regards to stability in permanent magnet flywheel systems is gyroscopic stabilization. Perhaps the most well-known example of gyroscopically stabilized permanent magnet bearings, has been a toy called the Levitron (Figure 2-5) patented in 1983 [55].

The foundational theory explaining the stability induced via gyroscopic precession has been explained extensively in literature [46], [56]–[60], however very few practical studies with regards to real bearing systems exist. Around the equilibrium point, studies have, however, noted that the stability zone/window for such bearings is generally quite small at around $3-3.2$ [mm] in the vertical direction and 2 [mm] in the radial direction. Mass must be selected carefully to within 1% tolerance at between $20-25$ [g] for stable suspension [46], [56]. This is for systems with stators around 134 [mm] and rotors of around 30 [mm] diameters spinning at roughly 1380 [rpm].

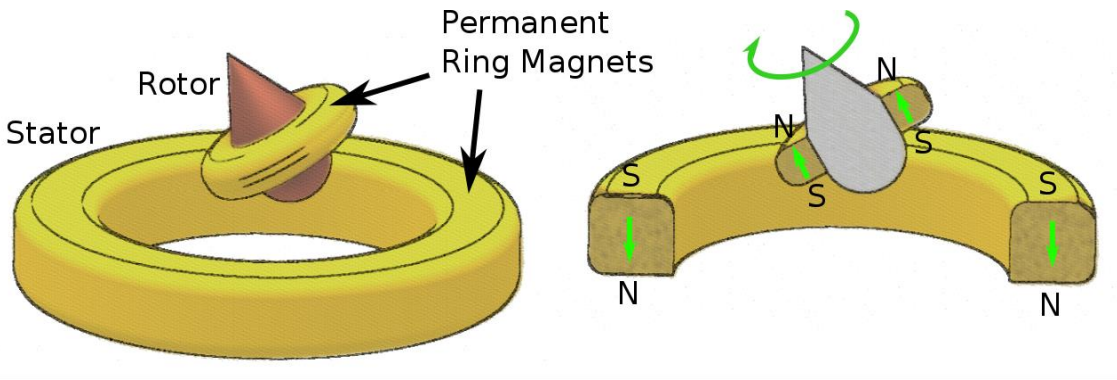

Figure 2-5: Levitron, a toy example of a gyroscopically stabilized bearing.

2.2.7 Diamagnetically Stabilized Bearings

Recently, with the advent of stronger neodymium magnets and the improved availability of ultra-pure diamagnetic graphite, the potential of diamagnetically stabilized magnetic bearings is becoming evident. These materials allow passive levitation and can potentially reduce losses below the 0.1 [%] of superconducting solutions [61]. It is with this understanding that diamagnetic bearings will be considered in this study. It must, however, be noted that the large scale feasibility and economic viability of diamagnetically stabilized bearings remains in question and such bearings remain more in the realm of theory and small scale prototypes as opposed to practical application. This study will present a solution for a potential implementation of these bearings and use analytical and experimental approaches to discuss their feasibility as low loss subsystems for longer duration (bridging and energy management) applications.

We note that, for diamagnetic bearings, a number of relevant points come across from a study of the wider arena of magnetic bearings. Namely, we note for one, that there is a plurality of approaches for their stability, with all approaches making use of permanent magnets to achieve stability in some or most degrees of freedom. Secondly, we note that most approaches, where possible, make use of permanent magnet lifters or stabilizers in a variety of configurations. Some of these configurations establish Halbach arrays and conical structures as an optimal for stability, levitation force and stiffness. Thirdly, we note that the theoretical foundation of all approaches is somewhat similar in that the goal of stabilization is to take a saddle shaped potential energy surface for a levitating rotor and convert it into one with a local minima. The stabilizing approach provides the greatest gains when producing the local minima in the final DOF only – all other DOFs being stabilized by other means. Finally, we note that a major point of focus on such bearings has been on the elimination of eddy current losses during centric rotation and the reduction of unnecessary eddy current losses in off-centric rotation. A significant focus has been given to the homopolar machine for this purpose. We note that the design of a diamagnetic bearing can use a variety of elements from these existing

stabilizing methods – in particular there is some relevance to stacked and concentric ring magnets as a means of maximizing stability of the floater portion of a levitating rotor. Further, we found that homopolar approaches are a particularly useful approach to reducing unnecessary losses and that the use of permanent magnet stabilizers would best be served by the use of Halbach configurations.

2.3 A Review of Electrical Machines & Relevance to FES

Energy transfer to and from a flywheel must occur via some form of electrical machine. Permanent magnet (PM), induction and reluctance machines are the most common choice of electrical machines for FES [30] – see Figure 2-6. Such machines generally avoid the use of high wear components such as slip rings, commutators or brushes. In some cases, electrostatic machines have also been used. These electrostatic machines however are beyond the scope of this study.

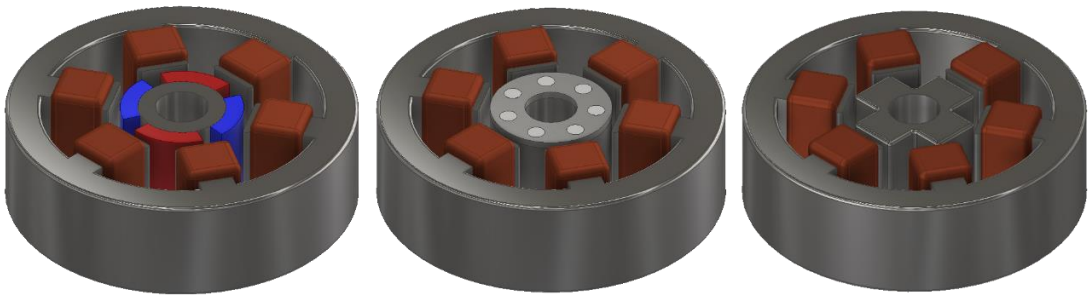

Figure 2-6: The three different kinds of electrical machines typically used in FES. From left to right are the permanent magnet machine, induction machine and reluctance machine. The most significant differences among these three machines generally pertain to the topology of the rotor. The PM machine has magnets forming the rotor poles, the induction machine makes use of short circuited rotor bars in a squirrel cage formation and the reluctance machine uses physical asymmetry in the magnetic material on the rotor.

The power dense PM machines have traditionally been chosen for high speed FES. These PM machines eliminate copper losses in the rotor and so mitigate heat dissipation problems in the high vacuum environments of FES devices. They can, however, pose a problem not only in cost, but also with regards to demagnetization risk and low magnet tensile strength (at high speeds). Add to this cogging issues and associated idling losses and they quickly become less attractive [14], [30]. Cogging issues can be reduced or eliminated with slotless stator designs but at the expense of performance.

Asynchronous induction machines have, thus, also been proposed as rugged, low cost alternatives. Unfortunately, complex rotor geometries, variable speed control methods and heat dissipation concerns remain something of an issue and generally at very high speeds these machines cannot be used [40].

The simpler reluctance machines have thus gained more popularity as an alternative for FES [62]. Despite being less energy dense than PM machines and requiring more complex controls, these machines are particularly suited for diamagnetic bearings – a discussion will follow in subsequent chapters. Issues such as torque ripple and acoustic noise that are prevalent in reluctance machines, fortunately, are less of a problem for flywheel systems than for other applications. Likewise, while heat dissipation issues also remain, they are less pronounced than those of induction machines [14]. The use of materials synthesized in this study can make these overheating issues even less of a concern. It is bearing this point in mind that this study will focus on the use of reluctance machines for FES.

In both, electromagnetically controlled active bearings and diamagnetically stabilized passive bearings, core magnetic materials for our reluctance machine play a significant role. In-fact, this statement could be extended to induction machines and to a much wider arena of transformers and inductors as well. Traditionally, the approach to building electrical machines involves steel laminations. At the very high speeds of FES systems, even with laminations, the switching magnetic fields generated across the core material can increase iron losses. These iron losses

originate from both eddy currents and magnetic hysteresis. The resultant heating of a flywheel rotor from such a process, can further cause significant magnetization and efficiency problems in the FES vacuum environment. A large chunk of this study focuses on the feasibility of using ferrites in place of traditional electrical steel. The high electrical resistance resulting from the use of ferrites holds a distinct advantage in reducing eddy current losses. More recent work further demonstrates that ferrite nano-materials exhibit much lower hysteresis loss. In-fact, such materials exhibit zero coercivity suggesting that iron losses can be virtually eliminated – a discussion will follow in later chapters.

This study will confine itself to looking at a commonly used ceramic ferrite called magnetite. Magnetite has seen considerable applications in bulk ferrite material. It, thus, provides an excellent starting point for a study of the feasibility of taking nano-materials into bulk materials for FES-based electrical machine applications.

2.4 A More Detailed Review of Diamagnetic Bearings

As noted in the previous section, the exploration of diamagnetic bearings is largely a result of improvements in magnet technologies in the last 50 years whereby the remanent flux density of new materials has risen from 0.46 [T] to values as high as 1.46 [T] [63]. We noted some key features in existing bearings that are of value in discussions of diamagnetic bearings as well. These features can roughly be divided into the following key elements: the lifter, the rotor assembly, the electrical machine and the stabilizing machine.

Generally, the arrangement of these elements in diamagnetic bearings can be schematically represented in the form shown in Figure 2-7. Within the rotor assembly, a floater interacts with the lifter such that the levitating portion is very close to the equilibrium point – the point where gravitation and magnetic forces balance. A levitating stabilized material, combined with some fixed stabilizer is used to change the local potential energy of the rotor such that there is a stabilizing

window or zone. Under normal magnetostatic conditions, the potential energy of the levitating body would form a saddle surface with no stable equilibrium point. The rotor in the rotor assembly is arranged either axially or radially with respect to a fixed stator to provide energy input and output to and from the system and impart a rotational velocity.

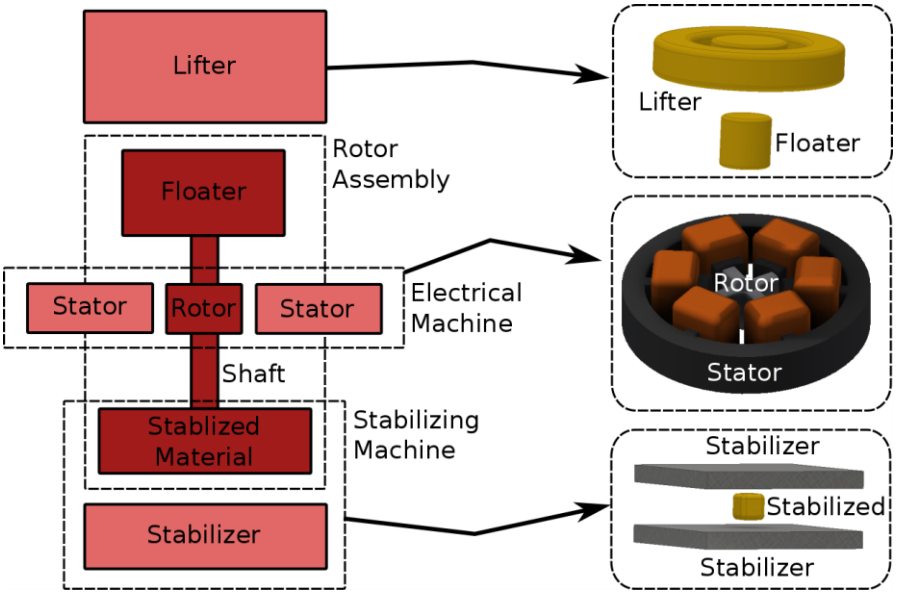

Figure 2-7: Left, an arrangement of elements making up a diamagnetic bearing system. Right, examples of potential forms that the lifter-floater, electrical machine and stabilizing machine may take.

This section will discuss each of the diamagnetic bearing elements in Figure 2-7 individually from the perspective of existing literature. The discussion will be followed by a look at Earnshaw's theory and the corresponding theory of diamagnetism and associated concepts.

2.4.1 The Lifter & Floater

The lifter is typically composed of either coils or permanent magnets. While being power consuming elements, the coils are a useful approach for the testing of passive configurations [23], [64], [65]. Only a few lifter configurations have been attempted across literature as shown in Figure 2-8. For instance, Bleuler et al. [29] have made use of a disc magnet to provide weight compensation to levitate an 80-92 [g] mass by 300 [μm]. Bachovchin et al. [66], [67] employ ring magnets for the same purpose and suggest the use of concentrically magnetized and radially magnetized Halbach arrays for higher lifting forces. However, no detailed study of shape related performance of such lifters has been attempted.

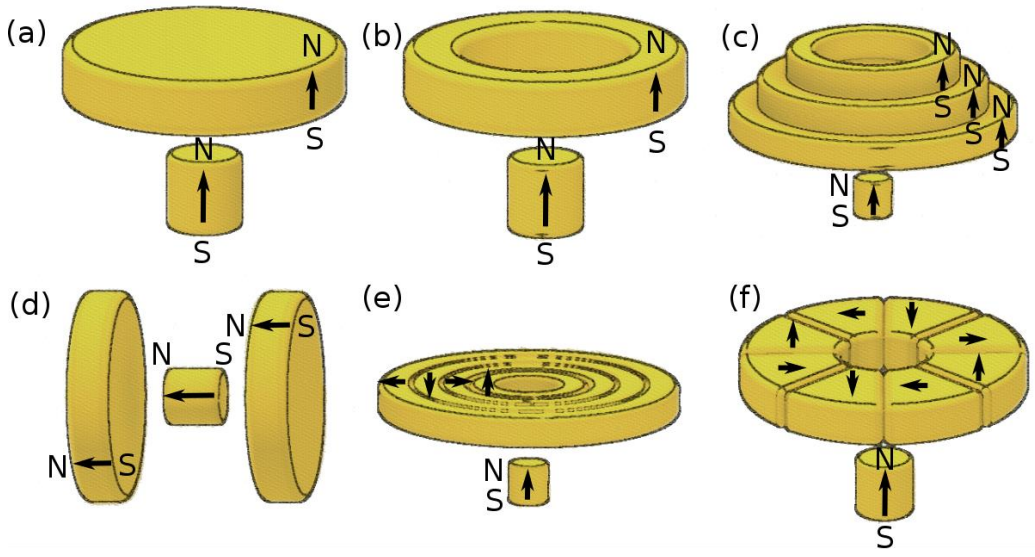

Figure 2-8: Various configurations for diamagnetic bearing lifters. (a) Disc magnet lifter [172]. (b) Ring lifter [66], [67]. (c) Ascending conical lifter [23], [64], [65]. (d) Horizontal disc lifter [25], [68]. (e) Concentric Halbach lifter [66], [67]. (f) Radial Halbach lifter [66], [67]. It should be noted that the floater can be replaced by a ferromagnetic material.

Chow et al. [64], [65] go a little further and make an initial attempt to understand lifter configurations by making use of ascending (conical), descending (inverted conical) and centre diverging (barrel) shaped coils and permanent magnets. In the study, a small stabilized cubic magnet (weighing 0.79 [g]) was levitated between fixed graphite stabilizers and used to demonstrate that an ascending (conical) lifter stacking showed the highest increases in the maximum allowable stabilizer gap (by 7 to 8 [%]). The best results appeared to be produced from individual lifter elements (magnets/coils) having uniform specific energy.

Cazacu et al. noted similar results with a two layer conical coil configuration [23]. It was noted that the high magnetic field curvature provided by such configurations is important in enlarging stability zone. All these configurations involve vertical lifting, however, some work has looked at horizontal lifters as well, with permanent magnets and coils used on either end to hold a levitating permanent magnet stiff between two stabilizer plates [68]. Virtually all approaches make use of a permanent magnet floater. Though in some cases the possibility of using a ferromagnetic sphere has also been considered [69].

2.4.2 Stabilizing Machine

The lifters, with the help of gravity, at best can stabilize the levitating rotor assembly in 4 DOFs. One DOF allows for free rotation while the remaining vertical direction (for a vertically lifted bearing) must be stabilized with the help of a diamagnetic stabilizer system.

The first such stabilizer with practical application was proposed in the 1966 by Waldron [70], [71] based on earlier work by Braunbek whereby a piece of pyrolytic graphite was levitated very close to the poles of a permanent magnet (Figure 2-9a). Waldron's work led to a patent [72] that covered a wide series of configurations aimed at levitating diamagnetic spheres, rings and plates to produce linear and thrust bearings. At his best, Waldron was able to demonstrate the levitation of a 4.49 [g]

ring magnet with embedded diamagnetic material [26], [71]. In and around the same time, Emeslie et al. [73] also filed a patent for radial bearings utilizing pyrolytic graphite as the diamagnet. Perhaps as a result of the immaturity of the magnet technologies of the time, these patents did not lead to any practical applications. Prior to Waldron's work, another researcher, Steingroever, had also independently patented a thrust bearing design [26].

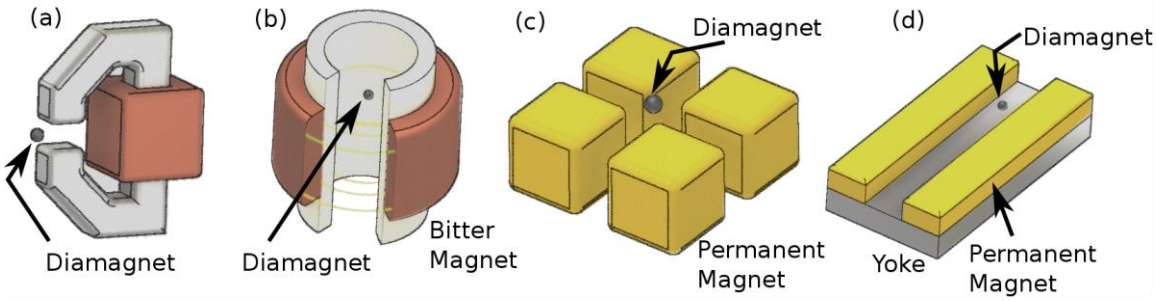

Figure 2-9: Various configurations for diamagnetic bearing stabilizers – simplified representations. (a) Approach by Waldron using non-linear regions of poles [70]. (b) Approach by Geim et al. using a bitter magnet for levitating small objects [19]. (c, d) Approach by Chetouani et al. [74], [75] for micro-droplet levitation.

It was not until the 1990s and early 2000s that the next steps took place. Patents and papers by Pelrine et al. demonstrated the possibility of frictionless multi-plattered stabilization for linear transport systems [15]–[18]. As no characterization work appears to have been done for these patented systems and given the reports of high levitation mass in the order of 13.6 [Kg], it is the work done by Pelrine et al., adapted for radial bearing applications, that will form the basis of the diamagnetic bearing design in this study.

Around this same time frame, Geim et al. [19]–[22] and Austin [76] produced a series of publications to explain the theoretical foundations of diamagnetic levitation and stabilization above a disk magnet and within a solenoid field (Figure 2-9b). This

early work looked, largely, at stabilization of a diamagnetic material in a bitter magnet solenoid field with the aim of studying fluid behaviour. Additional treatment was given to the levitation of a magnet inside the stabilizing zone produced by an open-ended bismuth cylinder embedded in this field (Figure 2-10a). This framework has been used by more recent research looking at various diamagnetically stabilized configurations.

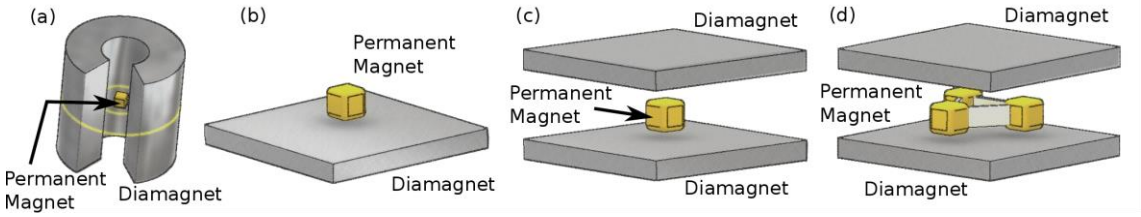

Figure 2-10: Various configurations for diamagnetic bearing stabilizers – simplified representations. (a) Approach by Geim et al. using bismuth cylinder [20], [21]. (b) Approach by Cazacu et al. [23], [25], [77], [78]. (c) Approach by Cazacu et al. [24] and Boukallel et al [68], [79]. (d) Approach by Ho et al. [80], [81].

At present day, work has been extended further to the field of microfluidics by Chetouani et al. [74], [75]. Their work makes use of magnetic microarrays to levitate diamagnetic microdroplets and transport them along pre-determined fluid channels (Figure 2-9c *and* Figure 2-9d). They also make use of strongly paramagnetic mediums to enhance the levitation effects of weakly diamagnetic latex beads. Noting that weak diamagnetism of most materials can be a concern, some researchers such as Economou et al. [82] have looked at the study of metamaterials that demonstrate enhanced diamagnetic response of split ring resonators.

More relevant work in the macro scale has been done by Bleuler et al. [29], [69] who make use of a diamagnetic graphite plate levitated above a flat and checkerboard planer Halbach array configuration for motor bearing applications (Figure 2-11c).

Boukallel et al. [68], [79] make use of a magnet levitated between two graphite plates or above/below a single plate for applications in nano-force sensing

(Figure 2-10b and Figure 2-10c). They showed the levitation of a mass 11 to 30 [mg] for this purpose. Cazacu et al. [23]–[25], [77], [78] likewise use a similar configuration as Boukallel et al. but also characterize stability zones for horizontal as well as vertical stabilization of the magnet between the fixed plates. They have reported lifting of masses of between $0.39 - 0.79$ [g] with weight compensation. Some attempts are also made to understand the impact of plate thickness on stability zones.

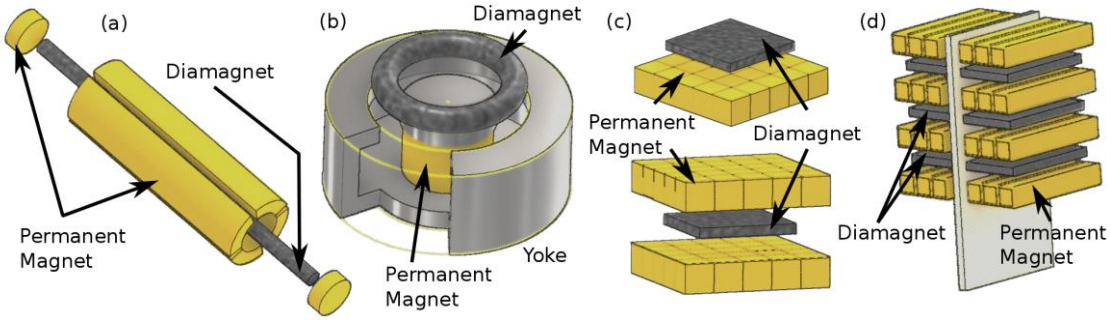

Figure 2-11: Various configurations for diamagnetic bearing stabilizers – simplified representations. (a) Approach by Emslie et al. [73] for rotary machine. (b) Approach by Steingroever [26] for a thrust bearing. (c) Approach by Liu, Kustler, Suzuki, Moser et al. [27], [28], [83]–[88]. (d) Approach by Pelrine et al. [15]–[18] for linear bearings.

This work, like that of Blueler et al., has focused on motor bearing applications. Following this trend, Ho et al. [80], [81] take things further by looking at the levitation of a triangular assembly of three permanent magnets (weighing a total of 2.8 [g]) between these plates, again for similar motor applications (Figure 2-10d).

Liu et al. [83], [89] have focused on micro-gyroscopes in their work by levitating the graphite plate above permanent magnets (Figure 2-11c). Their work utilized a variety of configurations for the permanent magnets ranging from single directional fields to linear and radial alternating fields.

Following considerations by Liu et al., both Kustler et al. [26]–[28] and Moser et al. [69], [84], [86] have focused more on the effects of more varied configurations of fixed permanent magnet arrays for levitating graphite. Kustler et al. have reported levitating rotor masses of 70 [g] and 90 [g]. Focus has been given to linear and radial alternating and halbach field configurations.

Suzuki et al. [87], [88] have focused on the effect of edge angle of levitating graphite plates with fixed halbach arrays. They have also introduced permanent magnet topologies that utilize stacking of alternating field permanent magnets and iron yokes – the effect of this configuration is unclear.

Moser et al. have also filed patents for the use of stabilized diamagnetic levitation for improved low friction inertial sensing. Pelrine et al., to date, are the only group that have extended work to multi-plattered approaches where a series of stacked graphite layers are levitated and act as stabilizers between interleaved and fixed alternating field permanent magnets (Figure 2-11d). Their work has applied to linear machines and, considering that little characterization work has been done, their work will be further characterized in the radial regime in this study.

2.4.3 Electrical Machine

In comparison to work on the stabilizing machinery, only a few studies have given rigorous treatment to the electrical machine used with diamagnetic bearings. For instance, Bleuler et al. [69] have looked at the use of an electrostatic machine whereby a glass coating is used as charge carrier (Figure 2-12a). The charged glass surface is driven by a three phase electrode assembly.

Liu et al. [89][83] took a similar electrostatic approach by driving a gear shaped pyrolytic graphite rotor and exploiting variable capacitance effects (Figure 2-12b). Unlike these approaches, Ho et al. [80], [81] used their levitated triangular permanent magnet configuration in combination with axially and radially oriented three phase

coils to drive the system with a more traditional magnetic flux based machine (Figure 2-12c and Figure 2-12d).

This study will examine the effects of a variable reluctance approach to driving a diamagnetically stabilized bearing.

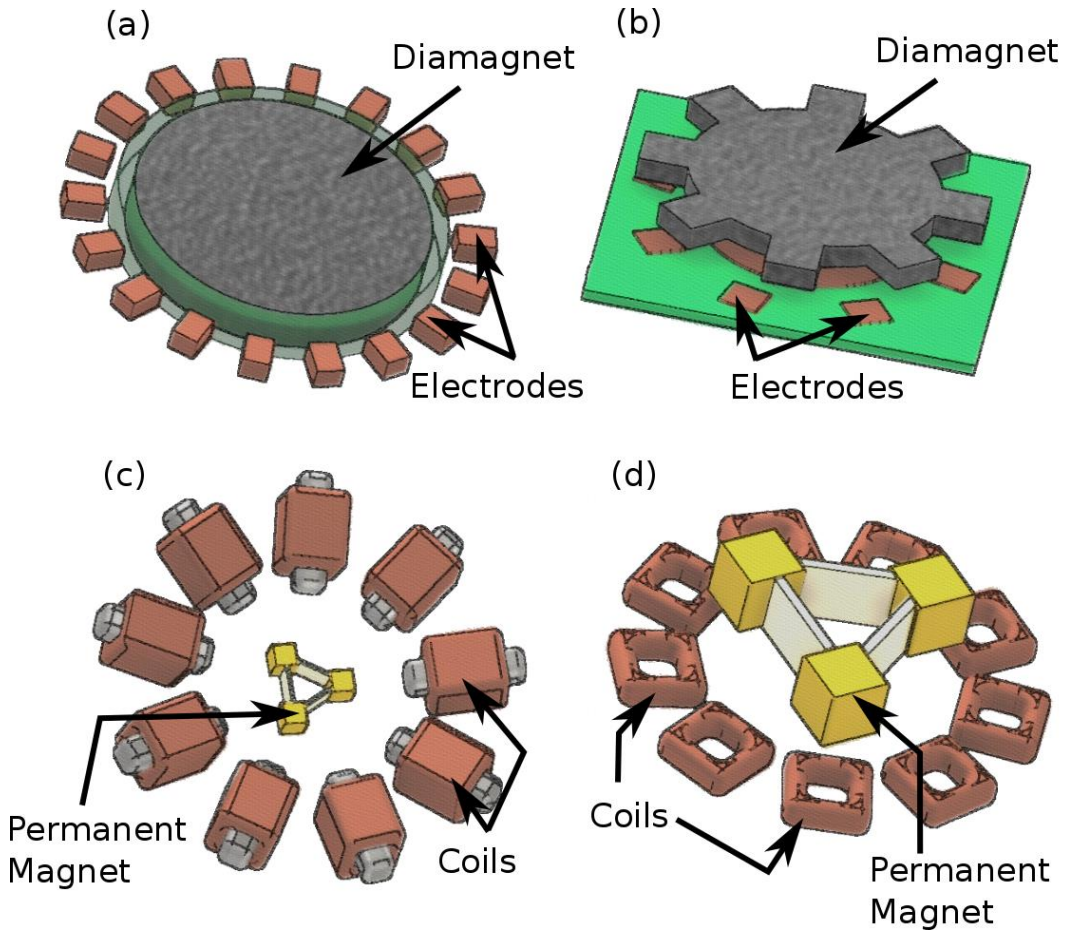

Figure 2-12: Various configurations for electrical machines used in diamagnetic bearings – simplified representations. (a) Electrostatic glass motor as attempted by Bleuler et al. [192]. (b) Variable capacitance motor used by Liu et al. [83], [89]. (c,d) Radial and axial flux permanent magnet machine used by Ho et al. [80], [81].

2.5 A Radial Multi-plattered Diamagnetic Bearing Design

The multi-plattered approach taken by Pelrine et. al. [15]–[18] in their patent for linear bearings holds significant promise. As was seen in the previous section, existing literature has focused to some extent on studying the contributions of various components making up such a bearing. However, the extent to which the machines can be applied to engineering problems in energy storage remains uncertain and further modelling work is needed to determine the specific design parameters for building and testing a prototype machine.

This study proposes a radial rotating modification of the linear machine shown by Pelrine as a possible method of implementing flywheel energy storage. A general design, for a proposed solution, including enclosure and flywheel as well as bearings and electrical machine is shown in Figure 2-13.

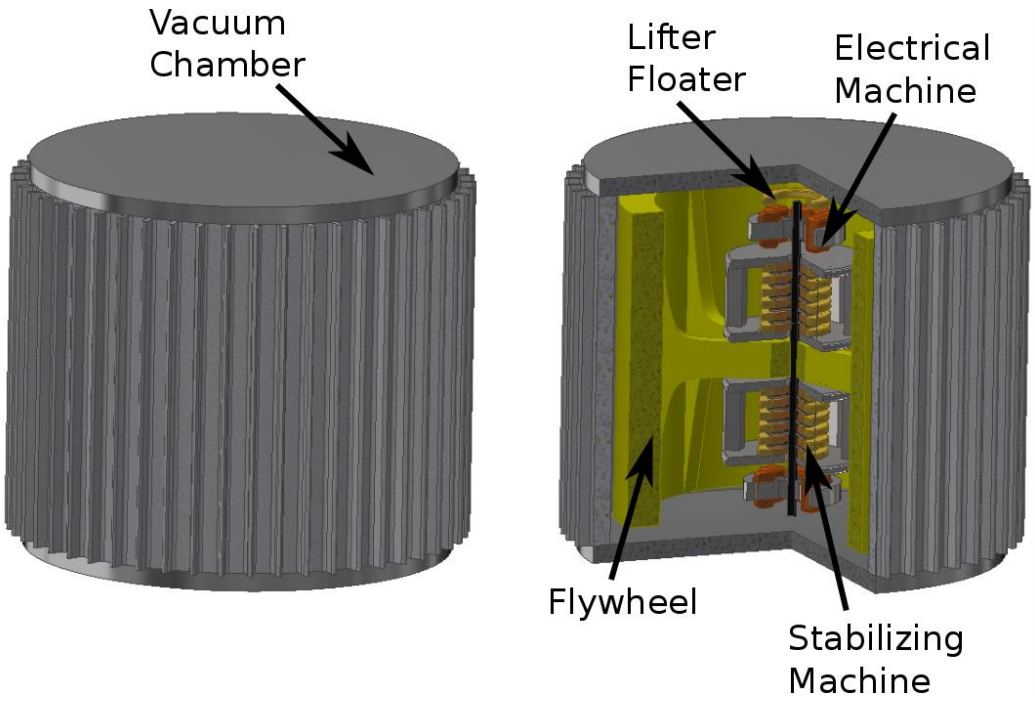

Figure 2-13: A design for a flywheel system. While the flywheel, and enclosure as well as the control electronics are neglected in this study, focus is given to the lifter-floater, electrical machine and stabilizing machine combination.

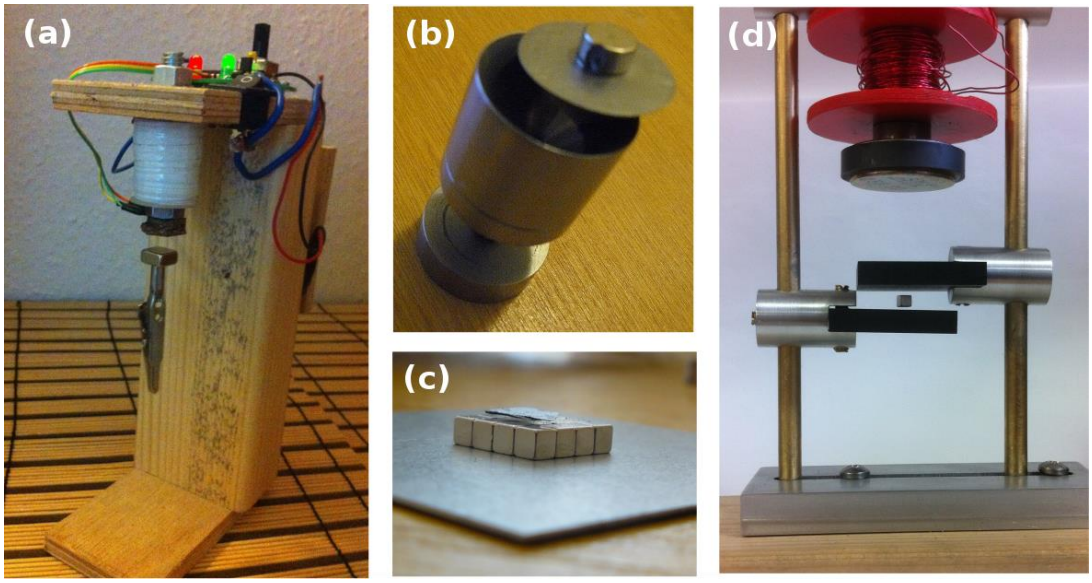

Figure 2-14: Qualitative test configurations for (a) an active bearing system, (b) a static permanent magnet bearing system, and (c, d) a simple diamagnetic bearing system.

Prior to developing the design shown in Figure 2-13, some proof-of-concept designs were built based on existing literature (e.g. Figure 2-9, Figure 2-10, Figure 2-11) – see Figure 2-14c and Figure 2-14d. An active approach and a permanent magnet approach was also tested (see Figure 2-14a and Figure 2-14b).

The complexity of designing such a machine can be simplified, somewhat, for practical first iteration implementation. We can focus on the inner stabilizing machine, electrical machine and lifter/floater while eliminating the flywheel and surrounding vacuum chamber. This simpler design is shown in Figure 2-15.

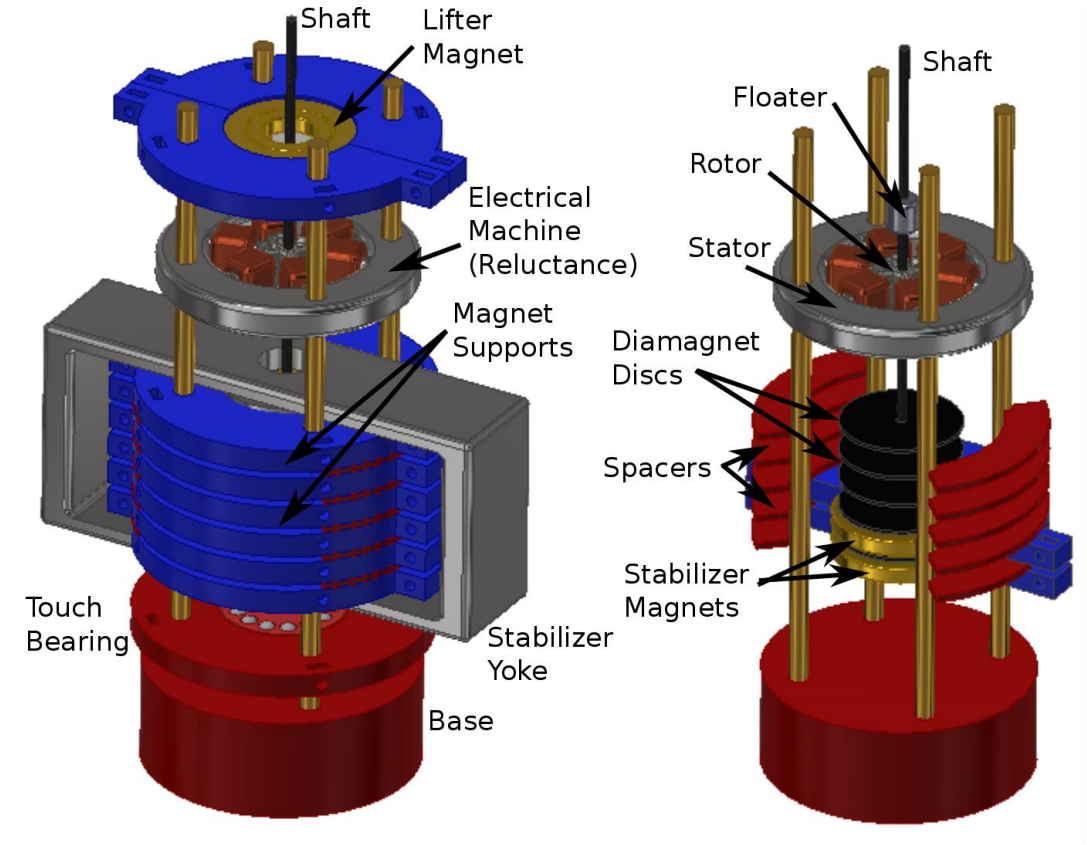

Figure 2-15: A simplified version of the Figure 2-13 design. On the left, a complete design for a proof of concept prototype. On the right, removing the outer supports to show the stabilizing machinery. Note that the floater used in the actual system was spherical.

Implementing this design is relatively straight forward. Notice that the cylindrical floater, shown in earlier discussions (i.e. Section 2.4.1), can be replaced with a large spherical ball bearing. The floater may also be completely removed such that the reluctance machine rotor acts as the weight compensation mechanism. As will be seen in later chapters, the reluctance machine can be manufactured as a ferrite material utilizing nano-materials thus reducing iron losses.

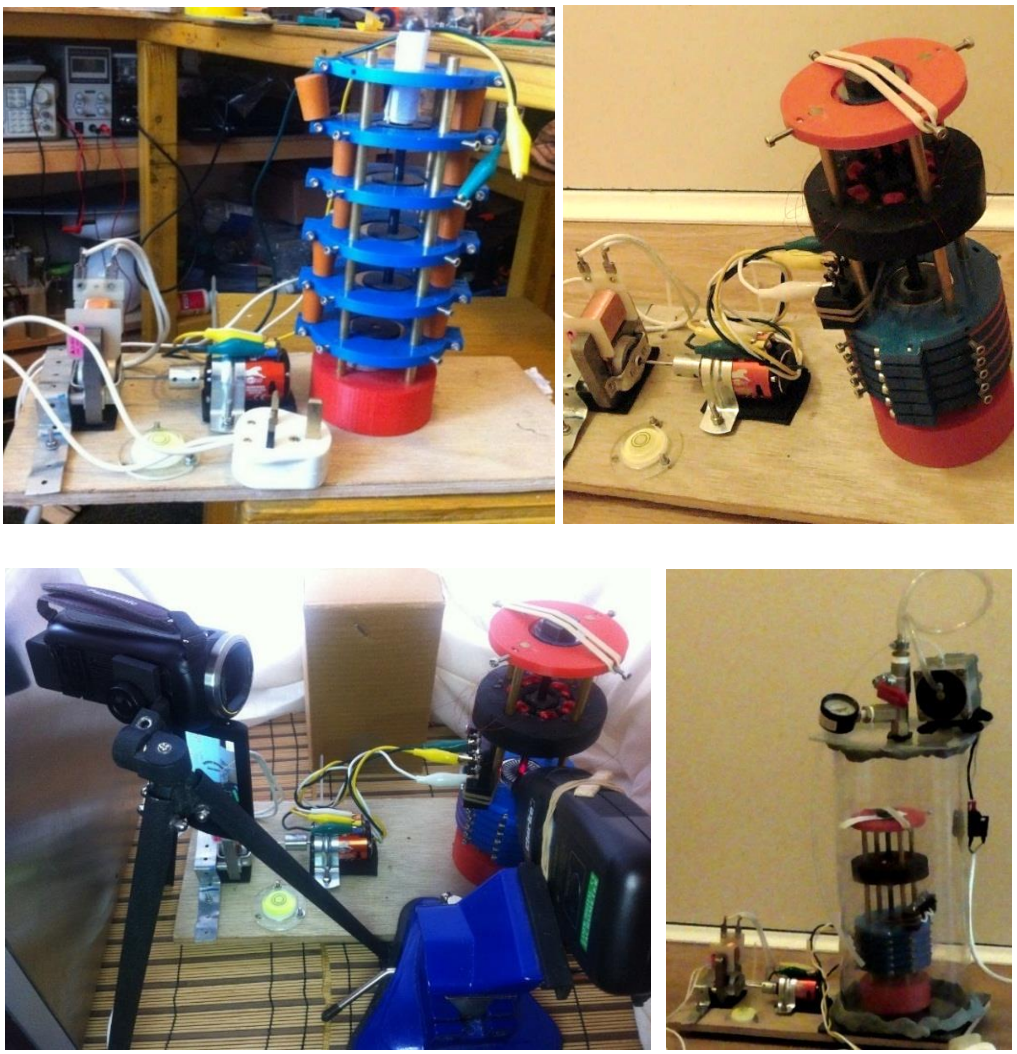

Figure 2-16: The prototype diamagnetic bearing for a flywheel system. A shaded pole induction motor drives a 3 phase DC brushless motor. This motor generates a three-phase supply and drives a very low power 6-4 reluctance machine. The machine drives a rotor and spins a shaft. The shaft is interconnected with 6 pyrolytic graphite diamagnetic platters and a spherical floater. The entire bearing assembly is placed inside a transparent vacuum chamber for testing. Typical vacuum pressures used were at low vacuum at around -60 [KPa].

The same can be said for the stabilizer yoke material – however, given the absence of a changing magnetic field in this material, losses resulting from eddy current and hysteresis are likely to be negligible. The blue and red parts shown in Figure 2-15 are

3D printed and used to hold the stationary lifter and stabilizer magnets in place, with spacers providing the specific airgap for a diamagnetic material (pyrolytic graphite).

The completed prototype is shown in Figure 2-16. In order to produce the necessary three-phase supply for the reluctance machine, a three-phase DC brushless motor was coupled to and driven by a single phase shaded pole induction machine. Multiple discs (6 discs) of pyrolytic graphite were sandwiched between concentrically embedded neodymium magnets to provide stabilizing machinery. To compensate for the mass of the levitating rotor, shaft and diamagnetic discs a permanent magnet (disc) lifter was used with a spherical floater. The rotor and stator of a reluctance machine were manufactured as a cast magnetite (Fe_3O_4) ferrite and wired for control to the three-phase power supply as shown in Figure 2-17.

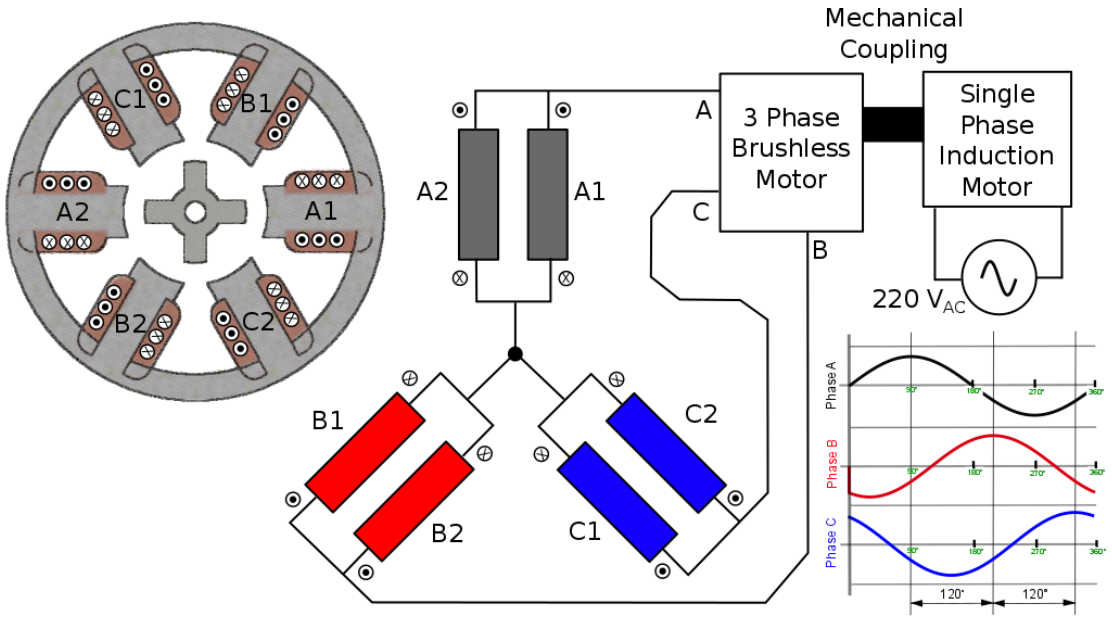

Figure 2-17: Star configuration wiring for the reluctance machine stator windings.

There are significant problems with this approach to open loop control and in the end it wasn't sufficient to drive the rotor. It was hoped that the higher inertia of the

induction machine and 3 phase motor supply would be sufficient to allow the rotor assembly of the bearing to keep up with the changing three phase frequency. While no slow-down was noted in the three-phase machine, the power output is likely to have been too low for driving across the large stator-rotor airgap. For prototyping purposes the rotor and stator ferrite was made using a resin binder combined with magnetite. This is likely to have reduced the permeability of the electrical machine and will have contributed to the lower driving torque available through the three-phase supply. While in the instance of the prototype, a resin binder was used, a more novel method of manufacture using the synthesis and sintering of nanoparticles is discussed in future chapters (i.e. Chapters 4 and 5) of this study. As an improved future approach, a controllable speed DC-motor can provide a simple in place replacement to the induction motor driving the three-phase supply and thus provide a variable frequency drive. If available, however, a switched reluctance control used with hall sensors is ideal.

For the prototype setup shown in Figure 2-18, Table 2-1 provides details of the key dimensional parameters. These dimensions will be used in subsequent analysis to allow calculation of the effect of critical design considerations for any geometrical variation of the proposed diamagnetic bearing solution.

The diamagnetic bearing was successfully shown to levitate a considerable mass of approximately 29.3 [g]. This is an improvement over some literature (about 13 papers) which indicated levitated masses of $0.39 - 4.49$ [g]. This mass is in the same order of magnitude as works by a few authors (about 4 papers) who have reported results of $70 - 92$ [g] of levitated mass. As will be seen in the results chapter, there is no reason that this result can't be extended to larger masses. This study, as a result of limited resourcing, was, unfortunately, unable to extend lifted mass to the 13.6 [Kg] mass reported by Pelrine et al.

Using the dimensional variables shown in Figure 2-18 and Table 2-1, the system can be broken down and analysed separately by first looking at a single diamagnetic disc levitating above a single stabilizing permanent magnet. This can then be expanded to

the same diamagnet sandwiched between two disc magnets. An examination of the effect of multiple platters logically follows from this.

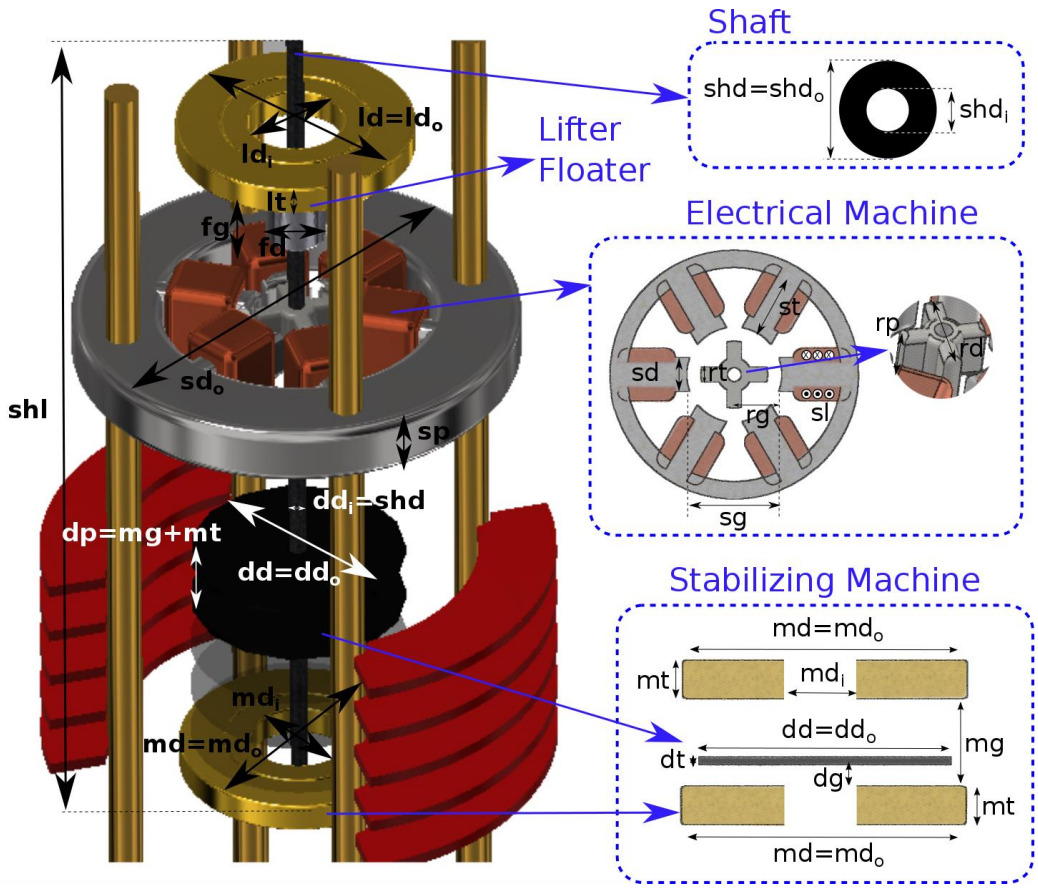

Figure 2-18: Dimensional parameters for the prototype diamagnetic bearing setup – CAD representation.

The combined force of the lifter and floater and the platters provides a measure of the stability and stiffness of our levitating assembly. The radial forces generated reluctance motor can be evaluated to ensure that they fall below a desired stiffness. Losses from rotating as a result of this reluctance machine and induced eddy currents in the homopolar machine making up the stabilizing elements can also be considered. The next section takes a detailed look at each of these elements step by step and derives analytical expressions for diamagnetic bearing design where reasonable.

Table 2-1: Dimensional parameters for the prototype diamagnetic bearing setup. Items marked as "tuned" are a result of rotor levitation and will vary during operation of the bearing based on stiffness.

Parameter	Description	Value	Unit
mg	Air gap between stabilizer permanent magnets	4	[mm]
$md=md_o$	Outer diameter of stabilizer permanent magnets	40	[mm]
md_i	Inner diameter of stabilizer permanent magnets (assumed zero for analysis)	16	[mm]
mt	Thickness of stabilizer permanent magnets	5	[mm]
$dd=dd_o$	Outer diameter of stabilizer graphite diamagnetic discs	36	[mm]
dd_i=shd	Inner diameter of stabilizer graphite diamagnetic discs (assumed zero for analysis)	6	[mm]
dt	Thickness of stabilizer graphite diamagnetic discs	1.5	[mm]
dg	Air gap from centre of diamagnetic disc to surface of permanent magnet	*tuned*	[mm]
dp	Centre distance between neighbouring diamagnetic discs (mg+mt)	9	[mm]
dm	Mass of diamagnetic disc	1.8	[g]
p	Number of diamagnetic disc platters	6	[]
$shd=shd_o$	Outer diameter of shaft	6	[mm]
shd_i	Inner diameter of shaft	4	[mm]
shl	Length of shaft	160	[mm]
shm	Mass of shaft	1	[g]
fd	Diameter of floater (assume spherical)	8	[mm]
fm	Mass of floater	11	[g]
fg	Centre of floater to lifter magnet surface airgap	*tuned*	[mm]
rd	Rotor pole to pole outer diameter	21	[mm]
rt	Rotor pole diameter or width (assume cylindrical pole for analysis, rt=rp)	6	[mm]
rp	Rotor pole height (assume cylindrical for analysis, rp=rt)	10	[mm]
rm	Rotor mass	6.5	[g]
rg	Rotor centre to stator pole air gap (in aligned position)	*tuned*	[mm]
sd	Stator pole width or diameter (assume cylindrical stator pole for analysis, sd=sp)	10	[mm]
sp	Stator pole height or stator height (assume cylindrical pole for analysis, sp=sd)	10	[mm]
sg	Stator inner diameter (pole to pole airgap)	27	[mm]
st	Stator pole thickness or length	9	[mm]
sd_o	Stator outer diameter	85	[mm]
n	Number of turns	200	[]
r	Per metre resistance of wire (32 AWG)	0.5383	[Ω/m]
sI	Stator pole current ($sI = nI$) – tuned by desired rotor displacement, I=0.30 [A] for tests	*tuned*	[A]
$ld=ld_o$	Lifter magnet outer diameter (magnet changed to tune B-field in real setup)	40	[mm]
ld_i	Lifter magnet inner diameter (magnet changed to tune B-field in real setup)	16	[mm]
lt	Lifter magnet thickness (magnet changed to tune B-field in real setup)	5	[mm]

2.6 Summary and Final Remarks

This chapter took a detailed look at flywheel energy storage devices and narrowed in on two key intertwined components, the bearing and the electrical machine. A range of such bearing options exist and discussions included prior art pertaining to active electromagnetic bearings, superconducting bearings, permanent magnet bearings, ferrofluid bearings, electro-dynamic bearings, gyroscopic bearings and diamagnetic bearings. Further discussions explored the electrical machine options including permanent magnet machines, induction machines and reluctance machines. Considering the thesis of this study, as a promising avenue of reduced loss, literature on diamagnetic systems, was given in-depth attention. Such systems can be broken down into three main sub-systems: the stabilizing machine, the lifter-floater and the electrical machine. Diamagnetism as a physical property for exploitation in bearings remains a relatively young field of study. This study, was prompted by this opportunity towards further exploration. A modification on existing diamagnetic bearings was proposed and a prototype presented. The resulting implementation demonstrated levitation of an approximate 30 [g] rotor assembly. This prototype will be the subject of further analysis in subsequent chapters and focus will be given to rotor assembly displacements, forces, energy and stiffness as well as rotational power loss.

3 Modelling and Analysis of Diamagnetic Bearing Solution

As noted in Chapter 2, a purely permanent magnet approach to levitation is unstable. As a result, permanent magnet bearings must be combined with some method of stabilization. In the previous chapter we discussed various methods, of which, electrodynamic, gyroscopic and diamagnetic effects are particularly relevant for this study. The focus of this study, however, will be on just diamagnetic effects, with electrodynamic effects discussed in the context of eddy currents.

This chapter begins with a look at Earnshaw's theorem and demonstrates how stable levitation isn't possible by a purely magnetostatic (or electrostatic) system. It follows with a discussion of potential energy and then with a closer look at magnetic fields produced in the region of a levitating diamagnetic dipole. This is then expanded to a discussion of forces generated by a diamagnetic material or platters of diamagnetic material in the presence of permanent magnets. The combination of these materials under rotation form a homopolar machine. A brief introduction to losses resulting from this machine is presented. This sub-section concludes after a discussion of fields and forces resulting from lifter magnets and the relationship between potential energy and stiffness.

3.1 Earnshaw's Theorem, Stability & Potential Energy

In a 1839 paper [37], it was noted by Samuel Earnshaw that any combination of static charges (and by corollary magnetic dipoles) cannot exist in stable equilibrium without some additional method of stabilization. Since a modernized proof of Earnshaw's theorem isn't often discussed in existing literature, a quick reminder has been provided here.

To begin, we note that in order for stable levitation of our rotor to occur, its potential energy, E_P, must be at some local minima. This implies that the laplacian (∇^2) of this energy must be greater than zero ($\nabla^2 E_P > 0$) in all spatial dimensions in and around the levitation point as shown in Equation (3-1).

$$\nabla^2 E_P > 0 \tag{3-1}$$

$$\frac{\partial^2 E_P}{\partial x^2} + \frac{\partial^2 E_P}{\partial y^2} + \frac{\partial^2 E_P}{\partial z^2} > 0$$

$$\mathbf{\frac{\partial^2 E_P}{\partial x^2} > 0, \frac{\partial^2 E_P}{\partial y^2} > 0, \frac{\partial^2 E_P}{\partial z^2} > 0}$$

Looking at the electrostatic case we note that the potential energy of the system is proportional to the voltage, ε, at the location of a test charge, q_e, such that the potential energy from electrostatic considerations is given as $E_{pe} = q_e \varepsilon$. For this generic case we note that the Laplacian is less than or equal to zero (see Equation (3-2)) for any test charge q_e and equivalent charge density ρ_e. Note that $\vec{\mathbb{D}} = \epsilon_0 \vec{\mathbb{E}}$ with the value $\vec{\mathbb{E}}$ representing the electric field and $\nabla \cdot \vec{\mathbb{D}} = \rho_e$ (where ϵ_0 is the permittivity of free space and $\vec{\mathbb{D}}$ is the electric displacement field.

$$E_{pe} = q_e \varepsilon = q_e(-\oint_C \vec{\mathbb{E}} \cdot d\vec{l}) \tag{3-2}$$

$$\frac{\partial E_{pe}}{\partial \vec{l}} = -q_e \vec{\mathbb{E}} = -q_e \frac{\vec{\mathbb{D}}}{\epsilon_0}$$

$$\nabla \cdot \nabla E_P = \nabla^2 E_P = -\frac{q_e}{\epsilon_0} \cdot \nabla \cdot \vec{\mathbb{D}} = -\frac{q_e \rho_e}{\epsilon_0}$$

$$\boldsymbol{\nabla^2 E_P \leq 0}$$

As with the electrostatic systems we see a similar situation with magnetostatic systems as well. Equation (3-3) demonstrates this by noting that the potential energy of a test magnetic dipole, $\vec{m}$, in a magnetic field $\vec{B}$ is given as $E_{pm} = -\vec{m} \cdot \vec{B}$. Demonstrating a Laplacian of zero requires the use of Gauss' law ($\nabla \cdot \vec{B} = 0$) and an understanding that the magnetomotive force may be defined as $\mathcal{F} = \oint_C \vec{H} \cdot d\vec{l}$. Note that $\vec{H}$ is the applied or material independent magnetic field strength.

$$E_{pm} = -\vec{m} \cdot \vec{B} = -\vec{m} \cdot \frac{\partial(\oint_C \mu_0 \vec{H} \cdot d\vec{l})}{\partial \vec{l}} = -\vec{m} \cdot \mu_0 \nabla \mathcal{F} \tag{3-3}$$

$$\frac{\partial E_{pm}}{\partial \vec{l}} = -\vec{m} \cdot \mu_0 \frac{\partial(\nabla \mathcal{F})}{\partial \vec{l}}$$

$$\nabla E_{pm} = -\vec{m} \cdot \mu_0 \nabla(\nabla \mathcal{F}) \Rightarrow \nabla \cdot \nabla E_{pm} = -\vec{m} \cdot \mu_0 \nabla \cdot \nabla(\nabla \mathcal{F})$$

$$\nabla^2 E_{pm} = -\vec{m} \cdot \mu_0 \nabla^2(\nabla \mathcal{F}) \Rightarrow \nabla^2 E_{pm} = -\vec{m} \cdot \mu_0 \nabla(\nabla^2 \mathcal{F}) = -\vec{m} \cdot \mu_0 \nabla(\nabla \cdot \nabla \mathcal{F})$$

$$\nabla^2 E_{pm} = -\vec{m} \cdot \nabla(\nabla \cdot \vec{B}) \Rightarrow \nabla^2 E_{pm} = -\vec{m} \cdot \nabla(\nabla \cdot \vec{B})$$

$$\boldsymbol{\nabla^2 E_{pm} = 0}$$

A sample levitated dipole ($\vec{m}$) in a B-field must form a local minimum in order for stable levitation to occur. This potential energy of $\vec{m}$ as it is moved through every point and orientation in space can be computed via a derivation of the B-field for each point in space (Equation (3-4)). Note that Figure 3-2 later in this chapter elaborates.

$$E_P(x, y, z, \theta, \varphi) = -\vec{m} \cdot \vec{B} = -\vec{m}(x, y, z, \theta, \varphi) \cdot \vec{B}(x, y, z) \tag{3-4}$$

$$\mathbf{E_p} = -\frac{\boldsymbol{\mu_0}}{\mathbf{4\pi}} \cdot \frac{\vec{\mathbf{1}}}{\mathbf{r^3}}\, \vec{\mathbf{m}} \cdot (\mathbf{3}(\vec{\mathbf{m}} \cdot \hat{\mathbf{r}})\hat{\mathbf{r}} - \vec{\mathbf{m}})$$

Alternatively, the energy resulting from the collective contribution of individual dipoles within a materials (also represented as $\vec{m}$) can be computed over some volume, V, of the material and the magnetization, $\vec{M}$. The resulting Laplacian from this process is shown in Equation (3-5). To fully complete this computation, however, some method computing the B-field resulting from this dipole is needed.

$$\nabla^2 E_P = \nabla \cdot \nabla E_p = \frac{\partial^2 E_P}{\partial x^2} + \frac{\partial^2 E_P}{\partial y^2} + \frac{\partial^2 E_P}{\partial z^2} \tag{3-5}$$

$$\nabla^2 E_P = \nabla \cdot \left(\frac{\partial E_p}{\partial x}\hat{x} + \frac{\partial E_p}{\partial y}\hat{y} + \frac{\partial E_p}{\partial z}\hat{z} \right)$$

$$\nabla^2 E_P = \nabla \cdot \left(\frac{\partial(-\vec{m}_s \cdot \vec{B})}{\partial x}\hat{x} + \frac{\partial(-\vec{m}_s \cdot \vec{B})}{\partial y}\hat{y} + \frac{\partial(-\vec{m}_s \cdot \vec{B})}{\partial z}\hat{z} \right)$$

$$\nabla^2 \mathbf{E_P} = -\left[\left(\frac{\partial^2 \vec{\mathbf{m}}_\mathbf{s}}{\partial \mathbf{x}^2} \cdot \vec{\mathbf{B}} + \frac{\partial \vec{\mathbf{m}}_\mathbf{s}}{\partial \mathbf{x}} \cdot \frac{\partial \vec{\mathbf{B}}}{\partial \mathbf{x}}\right) + \left(\frac{\partial \vec{\mathbf{m}}_\mathbf{s}}{\partial \mathbf{x}} \cdot \frac{\partial \vec{\mathbf{B}}}{\partial \mathbf{x}} + \vec{\mathbf{m}}_\mathbf{s} \cdot \frac{\partial^2 \vec{\mathbf{B}}}{\partial \mathbf{x}^2}\right)\right]$$
$$-\left[\left(\frac{\partial^2 \vec{\mathbf{m}}_\mathbf{s}}{\partial \mathbf{y}^2} \cdot \vec{\mathbf{B}} + \frac{\partial \vec{\mathbf{m}}_\mathbf{s}}{\partial \mathbf{y}} \cdot \frac{\partial \vec{\mathbf{B}}}{\partial \mathbf{y}}\right) + \left(\frac{\partial \vec{\mathbf{m}}_\mathbf{s}}{\partial \mathbf{y}} \cdot \frac{\partial \vec{\mathbf{B}}}{\partial \mathbf{y}} + \vec{\mathbf{m}}_\mathbf{s} \cdot \frac{\partial^2 \vec{\mathbf{B}}}{\partial \mathbf{y}^2}\right)\right]$$
$$-\left[\left(\frac{\partial^2 \vec{\mathbf{m}}_\mathbf{s}}{\partial \mathbf{z}^2} \cdot \vec{\mathbf{B}} + \frac{\partial \vec{\mathbf{m}}_\mathbf{s}}{\partial \mathbf{z}} \cdot \frac{\partial \vec{\mathbf{B}}}{\partial \mathbf{z}}\right) + \left(\frac{\partial \vec{\mathbf{m}}_\mathbf{s}}{\partial \mathbf{z}} \cdot \frac{\partial \vec{\mathbf{B}}}{\partial \mathbf{z}} + \vec{\mathbf{m}}_\mathbf{s} \cdot \frac{\partial^2 \vec{\mathbf{B}}}{\partial \mathbf{z}^2}\right)\right]$$

Table 3-1: Early "virtual" (simulated) experiments to verify Earnshaw's theorem and determine the effect of various magnet topologies on potential energy surface.

	Description	**Sam. Label**
2D	Point Dipole Geometries	D.1
	Dipole Ring Geometries	D.2
	Dipole Rings & Rotation Effects	D.3
3D	Monopole Ring Geometries	D.4
	Dipole Ring Geometries	D.5
	Monopole Cylinder Geometries	D.6
	Dipole Cylinder Geometries	D.7
	Monopole Disc Geometries	D.8
	Monopole Sphere Geometries	D.9
	Complex Linear Machine Geometry	D.10

It is possible to visualize the potential energy surfaces resulting from various electrostatic and magnetostatic configurations and verify Earnshaw's theorem. Analytical expressions (derived later in this chapter) and simulations using a commericial finite element software called COMSOL were used to provide some intuition about the nature of magnetostatic and electrostatic systems. This intuition

was useful in understanding issues associated with potential diamagnetic bearing designs.

Simulations started with an initial investigation of stability in permanent magnet bearings. This study uses the Gilbert (magnetic charge) model as a basis of estimating the B-field and moment of the floater-lifter assembly briefly noted in discussions of permanent magnet (and other) bearings in the previous chapter. A simple hand-coded finite element modelling approach was taken to map out potential energy surfaces. A set of "virtual" experiments, shown in Table 3-1, were carried out. The detailed results from these experiments are shown in the results chapter.

Ultimately, as will be seen towards the end of this document, the results of these simulations demonstrate that no configuration of statically positioned electrostatic monopoles or magnetic dipoles could be used to produce potential energy minima in all degrees of freedom. Stability in one degree was often compromised by instability in another degree.

3.2 Magnetic Field Estimation

Considering that potential energy is strongly linked to the local magnetic field we can start by producing an expression that estimates this field. There are two general approaches [90] to this, one is to make use of the Gilbert model which approximates magnetic dipole fields using the "non-physical" assumption of magnetic monopoles (Figure 3-1b). The other is the more precise Amperian model which utilizes current loops (Figure 3-1a).

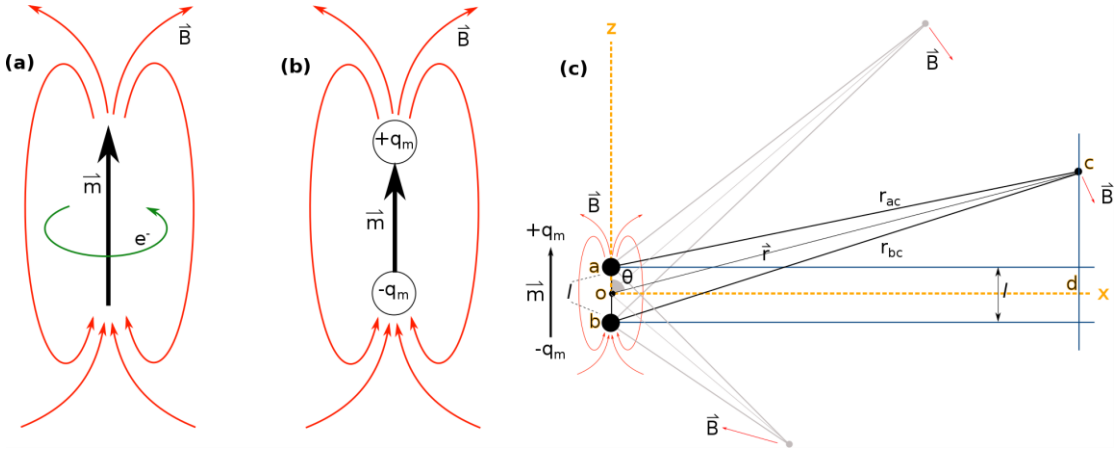

Figure 3-1: The Gilbert and Amperian model of a magnetic dipole. (a) The Amperian model makes use of more representative current loops. (b) The Gilbert model makes use of "non-physical" magnetic dipoles to approximate the dipole field, (c) Gilbert model geometry (radial).

This study uses the Gilbert model as a simple method aimed at initial exploration of Earnshaw's theorem and, subsequently, fields, forces and energy resulting from diamagnet and lifter configurations. Unfortunately, the model has a number of problems. Namely, that the approximation only holds under the assumption that the distance between the magnetic charges (l) is much smaller than that between dipole and field measurement location (r), that is, $r \ll l$ (Figure 3-1c). This can be regarded as a form of far field approximation.

Notice that, in the Gilbert model, the contributions to the B-field at a point c in Figure 3-1c are a result of the superposition of fields generated by $+q_m$ and $-q_m$ magnetic charges, respectively. The resultant magnetic moment from these charges is, thus, $m = q_m l$. In this paradigm, the B-field is directly analogous to the electric displacement field ($\overrightarrow{\mathbb{D}}$) in electrostatics.

This relationship allows us to estimate the B-field resulting from a single magnetic monopole (either $+q_m$ or $-q_m$) as shown in Equation (3-6) and Equation (3-7).

$$\vec{\mathbb{D}} = \boldsymbol{\epsilon_0}\vec{\mathbb{E}} = \frac{\mathbf{1}}{\mathbf{4\pi}} \cdot \frac{\mathbf{q_e}}{\mathbf{r^2}} \propto \frac{\mathbf{q_e}}{\mathbf{r^2}} \tag{3-6}$$

$$\vec{\mathbf{B}} = \boldsymbol{\mu_0}\vec{\mathbf{H}} = \frac{\boldsymbol{\mu_0}}{\mathbf{4\pi}} \cdot \frac{\mathbf{q_m}}{\mathbf{r^2}} \propto \frac{\mathbf{q_m}}{\mathbf{r^2}} \tag{3-7}$$

The superposition field from the monopoles can be represented as shown in Equations (3-8) and (3-9) for each component of $\vec{B}$ (i.e. B_x radial and B_z axial) using Equation (3-7) and the geometry shown in Figure 3-1c and Figure 3-2a.

$$B_x = \left(B_{x\,(+)} + B_{x\,(-)}\right) \tag{3-8}$$

$$B_x = \left(B_{(+)}\sin\theta_{(+)} + B_{(-)}\sin\theta_{(-)}\right)$$

$$B_x = \frac{\mu_0}{4\pi} \cdot \left(\frac{q_m}{r_{(+)}^2} \cdot \frac{x}{r_{(+)}} - \frac{q_m}{r_{(-)}^2} \cdot \frac{x}{r_{(-)}}\right)$$

$$\mathbf{B_x} = \frac{\boldsymbol{\mu_0 q_m x}}{\mathbf{4\pi}} \cdot \left(\frac{\mathbf{1}}{\mathbf{r_{(+)}^3}} - \frac{\mathbf{1}}{\mathbf{r_{(-)}^3}}\right)$$

$$B_z = \left(B_{z\,(+)} + B_{z\,(-)}\right) \tag{3-9}$$

$$B_z = \left(B_{(+)}\cos\theta_{(+)} + B_{(-)}\cos\theta_{(-)}\right)$$

$$B_z = \frac{\mu_0}{4\pi} \cdot \left(\frac{q_m}{r_{(+)}^2} \cdot \frac{z - \frac{l}{2}}{r_{(+)}} - \frac{q_m}{r_{(-)}^2} \cdot \frac{z + \frac{l}{2}}{r_{(-)}}\right)$$

$$\mathbf{B_z} = \frac{\boldsymbol{\mu_0 q_m}}{\mathbf{4\pi}} \cdot \left(\frac{\mathbf{z - \frac{l}{2}}}{\mathbf{r_{(+)}^3}} - \frac{\mathbf{z + \frac{l}{2}}}{\mathbf{r_{(-)}^3}}\right)$$

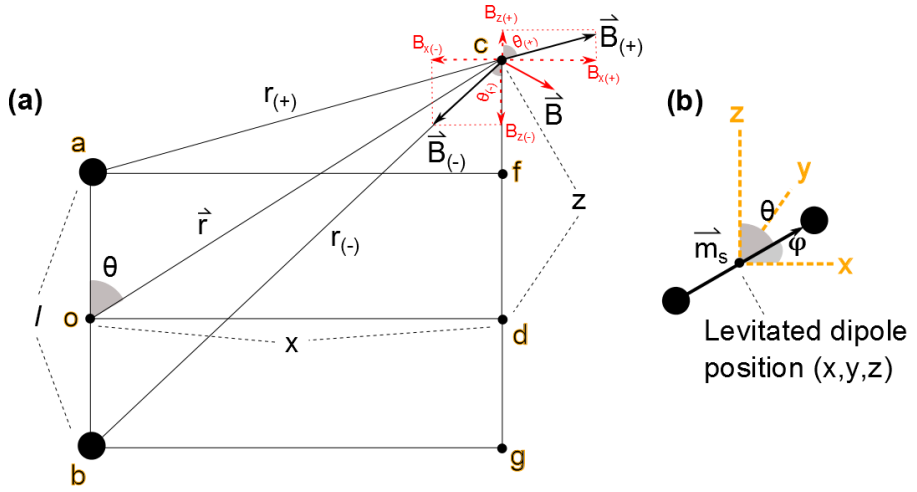

Figure 3-2: (a) Geometry for a far field approximation using the Gilbert model dipole as a starting point. (b) The orientation of a test dipole in space.

In both the x directional field and z directional field, we note that two terms repeat themselves, namely, $1/r_{(+)}^3$ and $1/r_{(-)}^3$. These terms are expanded in Equations (3-10) and (3-11).

$$\frac{1}{r_{(+)}^3} = \left[x^2 + \left(z - \frac{l}{2}\right)^2\right]^{-\frac{3}{2}} = \left[x^2 + z^2 - zl + \frac{l}{4}^2\right]^{-\frac{3}{2}} = \left[r^2 - zl + \frac{l}{4}^2\right]^{-\frac{3}{2}} \tag{3-10}$$

$$\lim_{l\to 0} \frac{1}{r_{(+)}^3} = [r^2 - zl]^{-\frac{3}{2}} = \left[\frac{1}{r^3}\left(1 - \frac{zl}{r^2}\right)^{-\frac{3}{2}}\right] = \frac{1}{r^3}\left(1 + \frac{3}{2}\cdot\frac{zl}{r^2}\right)$$

$$\frac{1}{r_{(-)}^3} = \left[x^2 + \left(z + \frac{l}{2}\right)^2\right]^{-\frac{3}{2}} = \left[x^2 + z^2 + zl + \frac{l}{4}^2\right]^{-\frac{3}{2}} = \left[r^2 + zl + \frac{l}{4}^2\right]^{-\frac{3}{2}} \tag{3-11}$$

$$\lim_{l\to 0} \frac{1}{r_{(-)}^3} = [r^2 + zl]^{-\frac{3}{2}} = \left[\frac{1}{r^3}\left(1 + \frac{zl}{r^2}\right)^{-\frac{3}{2}}\right] = \frac{1}{r^3}\left(1 - \frac{3}{2}\cdot\frac{zl}{r^2}\right)$$

To produce a general model with respect to the definition of the magnetic dipole, $\vec{\mathrm{m}} = \mathrm{q_m} l$, the separating distance, l, between the dipoles must be extracted. This distance is made infinitesimally small such that $l \to 0$ (while $\vec{\mathrm{m}}$ is held constant) as shown in the equations.

Notice that taking the limit as $l \to 0$ we find that the term $\mathrm{r}^2 \pm \mathrm{z}l$ dominates over $l^2/4$. And so an approximation is possible where by our representations for the positive and negative charge terms can be simplified to: $[\mathrm{r}^2 \pm \mathrm{z}l]^{-3/2}$ without significant loss of precision. We also note that, in and around $l = 0$, both terms can be simplified further to eliminate the $-3/2$ exponent value. This is done by expanding our terms $\mathrm{f}(l) = 1/\mathrm{r}_{(\pm)}^3$ to produce a linear approximation by a first order Taylor series as shown in Equation (3-12). Figure 3-3 demonstrates that this approximation is valid around $l = 0$ for the function $\mathrm{f}(l)$ generated from the Taylor series representation.

$$\mathrm{f}(l) = \frac{1}{\mathrm{r}_{(\pm)}^3} = \mathrm{f}(0) + \frac{\mathrm{d}\big(\mathrm{f}(0)\big)}{\mathrm{d}l} \cdot \mathrm{l} = \frac{1}{\mathrm{r}^3}\left(1 \pm \frac{3}{2} \cdot \frac{\mathrm{z}l}{\mathrm{r}^2}\right) \tag{3-12}$$

A point of note about this approximation is that as $\mathrm{r} \to l$ the resulting field becomes less and less accurate at up to a factor of -2 times the actual value. The result of the $l \to 0$ limit is a final dipole B-field as shown in Equations (3-13) and (3-14).

$$\mathrm{B_x} = \lim_{l \to 0} \frac{\mu_0 \mathrm{q_m x}}{4\pi} \cdot \left(\frac{1}{\mathrm{r}_{(+)}^3} - \frac{1}{\mathrm{r}_{(-)}^3}\right) = \frac{\mu_0 \mathrm{q_m x}}{4\pi} \cdot \left(\lim_{l \to 0} \frac{1}{\mathrm{r}_{(+)}^3} - \lim_{l \to 0} \frac{1}{\mathrm{r}_{(-)}^3}\right) \tag{3-13}$$

$$\mathrm{B_x} = \frac{\mu_0 \mathrm{q_m x}}{4\pi} \cdot \left(\frac{1}{\mathrm{r}^3}\left(1 + \frac{3}{2} \cdot \frac{\mathrm{z}l}{r^2}\right) - \frac{1}{\mathrm{r}^3}\left(1 - \frac{3}{2} \cdot \frac{\mathrm{z}l}{r^2}\right)\right)$$

$$\mathbf{B_x} = \frac{\boldsymbol{\mu_0}}{\boldsymbol{4\pi}} \cdot \frac{\vec{\mathbf{m}}}{\mathbf{r^3}} \mathbf{3}\left(\frac{\mathbf{x}}{\mathbf{r}} \cdot \frac{\mathbf{z}}{\mathbf{r}}\right) = \frac{\boldsymbol{\mu_0}}{\boldsymbol{4\pi}} \cdot \frac{\vec{\mathbf{m}}}{\mathbf{r^3}} \mathbf{3 sin\theta\, cos\theta}$$

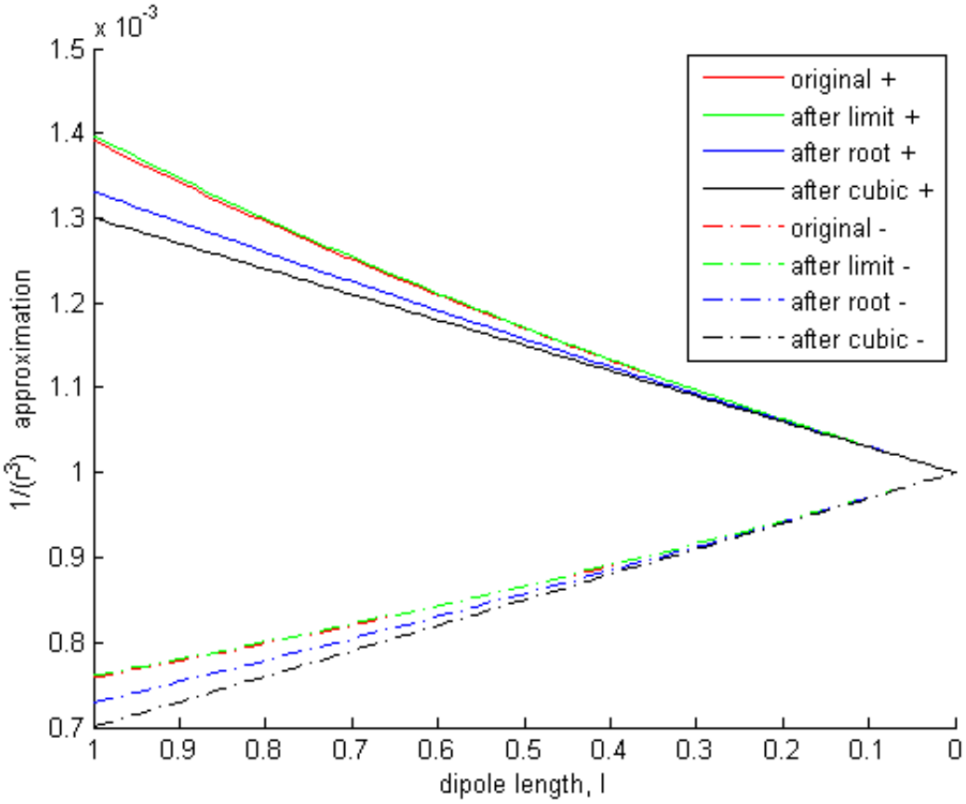

Figure 3-3: A demonstration of how a decreasing dipole length such that $\mathbf{l \to 0}$ can be used to remove cubic and square root exponents from our $\mathbf{1/r^3_{(\pm)}}$ approximation.

$$B_z = \lim_{l \to 0} \frac{\mu_0 q_m}{4\pi} \cdot \left(\frac{z - \frac{l}{2}}{r^3_{(+)}} - \frac{z + \frac{l}{2}}{r^3_{(-)}} \right) \tag{3-14}$$

$$B_z = \frac{\mu_0 q_m}{4\pi} \cdot \left(\left(z - \frac{l}{2} \right) \cdot \lim_{l \to 0} \frac{1}{r^3_{(+)}} - \left(z + \frac{l}{2} \right) \cdot \lim_{l \to 0} \frac{1}{r^3_{(-)}} \right)$$

$$B_z = \frac{\mu_0 q_m}{4\pi} \cdot \left(\left(z - \frac{l}{2} \right) \cdot \frac{1}{r^3} \left(1 + \frac{3}{2} \cdot \frac{zl}{r^2} \right) - \left(z + \frac{l}{2} \right) \cdot \frac{1}{r^3} \left(1 - \frac{3}{2} \cdot \frac{zl}{r^2} \right) \right)$$

$$\mathbf{B_z = \frac{\mu_0}{4\pi} \cdot \frac{\vec{m}}{r^3} \left(3 \frac{z}{r} \cdot \frac{z}{r} - 1 \right) = \frac{\mu_0}{4\pi} \cdot \frac{\vec{m}}{r^3} (3 \cos^2 \theta - 1)}$$

We can modify our representation for B_x and B_z for the spherical coordinate system that more closely represents the point source nature of the dipole. This is shown in Equation (3-15). The field is converted into cylindrical representation such that the x-directional field is taken as the radial direction and rotation (φ) of our arbitrary point c from Figure 3-2 is along the z axis.

With some careful manipulation, the B-field can be converted into a form independent of the coordinate system and purely based on the distance ($\vec{r}$) from the dipole and the magnetic moment ($\overrightarrow{m}$). This final form of the far field approximation of the magnetic field can also be derived from the Amperian model and the vector potential ($\overrightarrow{\mathbb{A}}$) via $\vec{B} = \nabla \times \overrightarrow{\mathbb{A}}$. The resultant field is a simple way to do a basic exploration of magnetostatics and the impact of diamagnetic materials and lifter topologies.

$$\vec{B}(r,z) = \frac{\mu_0}{4\pi}\cdot\frac{m}{r^3}3\sin\theta\cos\theta\,\hat{r} + \frac{\mu_0}{4\pi}\cdot\frac{\overrightarrow{m}}{r^3}(3\cos^2\theta - 1)\,\hat{z} \tag{3-15}$$

$$\vec{B}(x,y,z) = \frac{\mu_0}{4\pi}\cdot\frac{m}{r^3}3\sin\theta\cos\theta\,(\cos\varphi\,\hat{x} + \sin\varphi\,\hat{y}) + \frac{\mu_0}{4\pi}\cdot\frac{\overrightarrow{m}}{r^3}(3\cos^2\theta - 1)\,\hat{z}$$

$$\vec{B}(x,y,z) = \frac{\mu_0}{4\pi}\cdot\frac{m}{r^3}[3\sin\theta\cos\theta\,(\cos\varphi\,\hat{x} + \sin\varphi\,\hat{y}) + (3\cos^2\theta - 1)\hat{z}]$$

$$\begin{aligned}\vec{B}(r,\theta,\varphi) = \frac{\mu_0}{4\pi}\cdot\frac{m}{r^3}[&3\sin\theta\cos\theta\,(\cos\varphi\,(\sin\theta\cos\varphi\,\hat{r} + \cos\theta\cos\varphi\,\hat{\theta} - \sin\varphi\,\hat{\varphi})\\ &+ \sin\varphi\,(\sin\theta\sin\varphi\,\hat{r} + \cos\theta\sin\varphi\,\hat{\theta} + \cos\varphi\,\hat{\varphi}))\\ &+ (3\cos^2\theta - 1)(\cos\theta\,\hat{r} - \sin\theta\,\hat{\theta})]\end{aligned}$$

$$\vec{B}(r,\theta,\varphi) = \frac{\mu_0}{4\pi}\cdot\frac{m}{r^3}\,(2\cos\theta\,\hat{r} + \sin\theta\,\hat{\theta})$$

$$\vec{B}(r,\theta,\varphi) = \frac{\mu_0}{4\pi}\cdot\frac{m}{r^3}\left(2\cos\theta\,\hat{r} + \sin\theta\,\hat{\theta}\right) + \frac{\overrightarrow{m}}{r^3} - \frac{\overrightarrow{m}}{r^3}$$

$$\vec{B}(r,\theta,\varphi) = \frac{\mu_0}{4\pi}\cdot\frac{m}{r^3}\left(2\cos\theta\,\hat{r} + \sin\theta\,\hat{\theta}\right) + \frac{m\hat{z}}{r^3} - \frac{\overrightarrow{m}}{r^3}$$

$$\vec{B}(r,\theta,\varphi) = \frac{\mu_0}{4\pi}\cdot\frac{m}{r^3}\left(2\cos\theta\,\hat{r} + \sin\theta\,\hat{\theta}\right) + \frac{m(\cos\theta\,\hat{r} - \sin\theta\,\hat{\theta})}{r^3} - \frac{\vec{m}}{r^3}$$

$$\vec{B}(r,\theta,\varphi) = \frac{\mu_0}{4\pi}\cdot\frac{1}{r^3}\left(3m\cdot\cos\theta\,\hat{r} - \vec{m}\right)$$

$$\boldsymbol{\vec{B} = \frac{\mu_0}{4\pi}\cdot\frac{1}{r^3}\left(3(\vec{m}\cdot\hat{r})\hat{r} - \vec{m}\right)}$$

$$\boldsymbol{\vec{B} = \frac{\mu_0}{4\pi}\cdot\frac{1}{(x^2+y^2+z^2)^{\frac{3}{2}}}\left(3\left([m_x, m_y, m_z]\cdot[r_x, r_y, r_z]\right)[r_x, r_y, r_z] - [m_x, m_y, m_z]\right)}$$

To find a solution for the B-field at the relevant points in space, computational steps can be, and are discretized. The discretization approach, as an early exploration by the author, utilizes a rudimentary rectangular mesh by which the fields, forces, and potential energy can be roughly determined.

We note that insertion of a magnetic material can affect the field in all regions of space, the field approximation used in this section, must, thus, be used with great care to account for contributions from all dipoles in the space. A number of problems can, thus, occur from simplistic discretization approaches. In order to accommodate geometries and configurations with greater flexibility, this analytical exploration is only used as an early exploration tool and is taken further via further analysis for our specific diamagnetic bearing implementation and via a commercial finite element modelling software called COMSOL Multiphysics. A detailed discussion of the results of simulations from this simple formulation and the more complex formulations implemented with the aid of COMSOL Multiphysics are discussed in Chapter 9 of this study.

3.3 Diamagnetic Stabilizing Machinery Analysis

Given our understanding of Earnshaw's theorem along with discussions about potential energy and magnetic fields, attention can now be turned to the effect of diamagnetic stabilization in our specific bearing design. We noted that the Laplacian of our potential energy must be positive ($\nabla^2 E_p > 0$) for stable levitation.

The potential energy (E_p) of our diamagnetic stabilizing assembly has a contribution from gravitational potential energy (E_g) as well as the diamagnetic material (E_d). We can start from a simple system which involves the levitation of a diamagnetic disc of diameter, dd and thickness dt and with total magnetic moment, $\vec{m}_d$. This disc is floating above a permanent magnet of diameter md and thickness mt as shown in Figure 3-4.

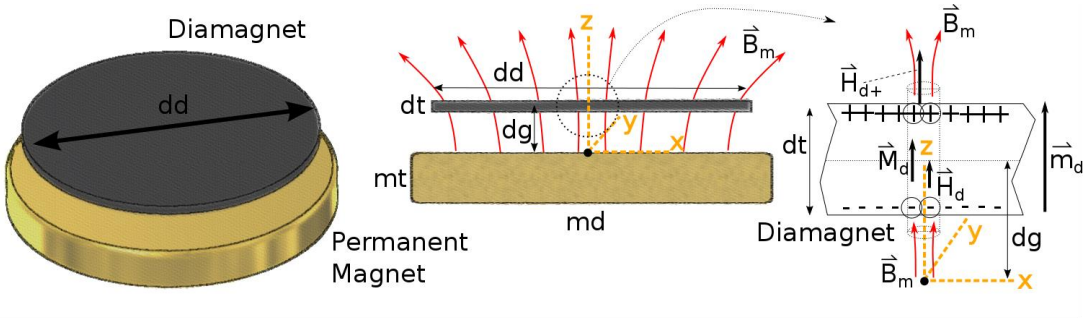

Figure 3-4: A simple base geometry for the analysis of diamagnetic configurations shown in the earlier Figure 2-11c. This basic configuration forms the basis of this study.

For comparison, we also consider another system with a diamagnetic sphere of diameter dd in our analysis as well. The analysis of both the sphere and the disc relates closely to configurations shown earlier in Figure 2-11 and will form the basis of the implementation presented later in this section. Note that this analysis is an extension of foundational ground work laid out by Austin et al. [76] as well as Geim

et al. [19]–[22] and a few other researchers whose primary focus was aimed at explaining the electrodynamic stability of the Levitron [56]–[59].

We can start the process off by noting that $\mathrm{md} \gg \mathrm{dd}$ and so the permanent magnet produces a uniform magnetic field, $\vec{B}_m$, in the xy plane over the entire diamagnetic sphere or disc region. The total net field at any point on the diamagnetic sphere or disc is then largely a function of z. The total field is given as: $\vec{B} = \vec{B}_m + \vec{B}_{d+}$. Given the uniform external field we can also say that the internal field within the levitating diamagnet is uniform as well. That is, the magnetization field, $\vec{M}_d$, of the sample is uniform over the volume of the sample V_d and the resultant field from this magnetization, $\vec{B}_d$ is also uniform.

The total field, $\vec{B}$, taking into account both the internal and external contributions can be used then to derive a general expression for the total magnetic moment ($\vec{m}_d$) of the diamagnetic disc as shown in Equation (3-16). This moment can then be used to evaluate our earlier expression for the energy of the diamagnet, E_p as shown in Equation (3-4).

Notice that to evaluate the internal field contribution of the diamagnetic sphere or disc, we start by noting that, within a Gaussian pillbox region, this contribution can be represented as a field ($\vec{H}_{d+}$) generated by our non-physical surface magnetic charges from the Gilbert model. This field would be a superposition of the internal magnetization ($\vec{M}_d = \vec{m}_d/V_d$) of the diamagnetic material and the internal diamagnetic field ($\vec{H}_d$). This is represented by the equation: $\vec{H}_{d+} = \vec{H}_d + \vec{M}_d$. The permeability and susceptibility of diamagnetic material are given by μ_r or alternatively $\chi_d = \mu_r - 1$ while $\mu = \mu_0\mu_r$ is the total permeability and μ_0 is the permeability of free space. For $\vec{H}_{d+}$ this permeability is $\mu_r = 1$ (air), while for $\vec{H}_d$ we have diamagnetic permeability $\mu_r < 1$ or $\chi_d < 0$.

$$\vec{B} = \vec{B}_m + \vec{B}_{d+} = \mu\vec{H} \tag{3-16}$$

$$\vec{B}_m + \vec{B}_{d+} = \mu(\vec{H}_m + \vec{H}_d)$$

$$\vec{B}_m + \vec{B}_{d+} = \mu\left(\frac{\vec{B}_m}{\mu_0} + \vec{H}_d\right) = \mu\left(\frac{\vec{B}_m}{\mu_0} + \vec{H}_{d+} - \vec{M}_d\right) = \mu\left(\frac{\vec{B}_m}{\mu_0} + \frac{\vec{B}_{d+}}{\mu_0} - \frac{\vec{m}_d}{V_d}\right)$$

$$\vec{B}_m + \vec{B}_{d+} - \mu\frac{\vec{B}_m}{\mu_0} - \mu\frac{\vec{B}_{d+}}{\mu_0} + \mu\frac{\vec{m}_d}{V_d} = 0$$

$$\vec{m}_d = \frac{V_d}{\mu}\left(-\vec{B}_m - \vec{B}_{d+} + \mu\frac{\vec{B}_m}{\mu_0} + \mu\frac{\vec{B}_{d+}}{\mu_0}\right)$$

$$\boldsymbol{\vec{m}_d = \frac{V_d}{\mu_0}\cdot\left(\frac{\chi_d}{\chi_d + 1}\right)\cdot\left(\vec{B}_m + \vec{B}_{d+}\right)}$$

Given the general representation of the diamagnetic dipole moment ($\vec{m}_d$), the $\vec{B}_{d+}$ field can be computed directly from the earlier derivation of the dipole B-field in Equation (3-15) with the understanding that it is dependent on the internal dipoles of the diamagnet itself rather than the external dipoles (leading to $\vec{B}_m$) of the permanent magnet.

Equations (3-17) and (3-18) demonstrate this for a diamagnetic sphere of diameter dd as shown in Figure 2-9c and for a diamagnetic disc from Figure 3-4. In both cases, as expected, when the material is diamagnetic ($\chi_d < 0$), the direction of the magnetic dipole is opposite that of the external field ($\vec{B}_m$).

$$\vec{m}_d = \frac{V_d}{\mu_0}\cdot\left(\frac{\chi_d}{\chi_d + 1}\right)\cdot\left(\vec{B}_m + \frac{\mu_0}{4\pi}\cdot\frac{1}{r^3}\,(3(\vec{m}_d\cdot\hat{r})\hat{r} - \vec{m}_d)\right) \tag{3-17}$$

$$\vec{m}_d = \frac{\frac{4}{3}\pi\left(\frac{dd}{2}\right)^3}{\mu_0}\left(\frac{\mu_r - 1}{\mu_r}\right)\left(\vec{B}_m + \frac{\mu_0}{4\pi}\frac{1}{\left(\frac{dd}{2}\right)^3}\,(3([0,0,m_d]\cdot[0,0,1])[0,0,1] - [0,0,m_d])\right)$$

$$\vec{m}_d = \frac{\pi\, dd^3}{6\mu_0} \cdot \left(\frac{\mu_r - 1}{\mu_r}\right) \cdot \left(\vec{B}_m + \frac{\mu_0}{\pi} \cdot \frac{4\vec{m}_d}{dd^3}\right)$$

$$\vec{m}_d = \frac{\frac{\pi\, dd^3}{6\mu_0} \cdot \left(\frac{\mu_r - 1}{\mu_r}\right) \cdot \vec{B}_m}{1 - \frac{\pi\, dd^3}{6\mu_0} \cdot \left(\frac{\mu_r - 1}{\mu_r}\right) \frac{4\mu_0}{\pi dd^3}}$$

$$\boldsymbol{\vec{m}_d = -\frac{\pi\, dd^3 \chi_d}{\mu_0(\chi_d + 3)} \cdot \vec{B}_m}$$

$$\vec{m}_d = \frac{V_d}{\mu_0} \cdot \left(\frac{\chi_d}{\chi_d + 1}\right) \cdot \left(\vec{B}_m + \frac{\mu_0}{4\pi} \cdot \frac{1}{r^3}\,(3(\vec{m}_d \cdot \hat{r})\hat{r} - \vec{m}_d)\right) \tag{3-18}$$

$$\vec{m}_d = \frac{\pi\left(\frac{dd}{2}\right)^2 dt}{\mu_0}\left(\frac{\mu_r - 1}{\mu_r}\right)\left(\vec{B}_m + \frac{\mu_0}{4\pi}\frac{1}{dt^3}\,(3([0,0,m_d] \cdot [0,0,1])[0,0,1] - [0,0,m_d])\right)$$

$$\vec{m}_d = \frac{\pi\, dd^2 dt}{4\mu_0} \cdot \left(\frac{\mu_r - 1}{\mu_r}\right) \cdot \left(\vec{B}_m + \frac{\mu_0}{2\pi} \cdot \frac{\vec{m}_d}{dt^3}\right)$$

$$\vec{m}_d = \frac{\frac{\pi\, dd^2 dt}{4\mu_0}\left(\frac{\mu_r - 1}{\mu_r}\right)}{1 - \frac{dd^2}{8dt^2} \cdot \left(\frac{\mu_r - 1}{\mu_r}\right)} \vec{B}_m = \vec{B}_m$$

$$\boldsymbol{\vec{m}_d = \frac{2\pi\, dd^2 dt^3 \chi_d}{\mu_0((8dt^2 - dd^2)(\chi_d + 1) + dd^2))} \vec{B}_m}$$

Given this moment, $\vec{m}_d$, the energy of the levitating sphere (Equation (3-19)) and disc (Equation (3-20)) can now be computed. The total potential energy of the system is given in Equation (3-21) by E_p for some mass, $\mathcal{M}_d$, for our levitating sphere or disc. Note that a_g is the acceleration due to gravity with z being the position relative to the origin point.

$$\mathbf{E_P = E_g + E_d = \mathcal{M}_d a_g z - \vec{m}_d \cdot \vec{B}_m} \tag{3-19}$$

$$\mathbf{E_P = \mathcal{M}_d a_g z - \frac{\pi\, dd^3(\chi_d)}{\mu_0(\chi_d + 3)} B_{mz}^2} \tag{3-20}$$

$$\mathbf{E_P = \mathcal{M}_d a_g z - \frac{2\pi\, dd^2 dt^3 \chi_d}{\mu_0((8dt^2 - dd^2)(\chi_d + 1) + dd^2))} B_{mz}^2} \tag{3-21}$$

An important point of note before continuing is that in the case of the disc, given that there is a uniform z-directional field present, stability in the xy plane must be achieved by some other means. For our purposes, we'll assume that the lifter magnet, along with gyroscopic and electrodynamic effects from our homopolar stabilizing machinery will provide this stability. To say that the diamagnetic material doesn't provide any stability in the xy-direction is somewhat incorrect. Some xy stability will be provided via the sphere and disc as a result of fringing (not z-directional) field contributions – these are neglected for this analysis.

Returning to our energy formulation from Equations (3-19) and (3-20), the focus is, thus, simply on the z-directional motion of the disc. From the energy, the force on the diamagnetic material in this z-direction can be computed directly as the gradient given as $F = -\nabla E_p$ as shown in Equations (3-22), (3-23) and (3-23).

Note that Equation (3-23) represents the force on a levitating sphere, while Equation (3-24) represents the force on a levitating diamagnetic disc.

$$F_z = -\frac{\partial}{\partial z}(\mathcal{M}_d a_g z) + \frac{\partial}{\partial z}(\vec{m}_d \cdot \vec{B}_m) = -\mathcal{M}_d a_g + \frac{\partial}{\partial z}(\vec{m}_d \cdot \vec{B}_m) \tag{3-22}$$

$$\mathbf{F_{dz} = -\mathcal{M}_d a_g + \frac{\pi\, dd^3 \chi_d}{\mu_0(\chi_d + 3)} \frac{\partial}{\partial z} B_{mz}^2} \tag{3-23}$$

$$\mathbf{F_{dz} = -\mathcal{M}_d a_g + \frac{2\pi\, dd^2 dt^3 \chi_d}{\mu_0((8dt^2 - dd^2)(\chi_d + 1) + dd^2))} \frac{\partial}{\partial z} B_{mz}^2} \tag{3-24}$$

At equilibrium the force on the sphere or disc must equal zero and so an airgap length, $z = dg$, for our diamagnet relative to the surface of our magnetic field source (our z origin) can be computed. The diamagnet is assumed to be close enough to the magnet that fringing effects can be discounted somewhat. The surface (remanent) magnetization of the magnet ($\overrightarrow{M_m}$) is generally a known quantity expressed as $\overrightarrow{B}_{mr} = \mu_0 \overrightarrow{M}_m$.

The magnet has thickness mt and diameter md such that the thickness is much smaller than the diameter: $mt \ll md$. The z component of the B-field (B_{mz}) resulting from the permanent magnet, given this assumption, is shown below in Equation (3-25).

$$\overrightarrow{B}_m = \frac{\mu_0}{4\pi} \cdot \frac{1}{r^3} \left(3(\overrightarrow{m} \cdot \hat{r})\hat{r} - \overrightarrow{m}\right) \tag{3-25}$$

$$\overrightarrow{B}_m = \frac{\mu_0}{4\pi} \cdot \frac{1}{\left(\sqrt{\left(\frac{md}{2}\right)^2 + z^2}\right)^3} \left(3\left(\overrightarrow{M}_m V_m \cdot \hat{r}\right)\hat{r} - \overrightarrow{M}_m V_m\right)$$

$$\overrightarrow{B}_m = \frac{1}{4\pi} \cdot \frac{1}{\left(\sqrt{\left(\frac{md}{2}\right)^2 + z^2}\right)^3} \pi \left(\frac{md}{2}\right)^2 mt \left(3\left(\overrightarrow{B}_{mr} \cdot \hat{r}\right)\hat{r} - \overrightarrow{B}_{mr}\right)$$

$$B_{mz} = \frac{md^2 mt}{8\left(\left(\frac{md}{2}\right)^2 + z^2\right)^{\frac{3}{2}}} B_{mr}$$

$$\mathbf{B_{mz} = \frac{md^2 mt}{(md^2 + 4z^2)^{\frac{3}{2}}} B_{mr}} \quad \mathbf{= \frac{md^2 mt}{(md^2 + 4\,dg^2)^{\frac{3}{2}}} B_{mr}}$$

The resulting derivative of this field is a useful computation for looking more closely at forces and distances involved and is shown in Equation (3-26).

$$\frac{\partial\, \mathrm{B_{mz}}}{\partial \mathrm{z}} = \frac{\partial}{\partial \mathrm{z}} \frac{\mathrm{md^2 mt}}{(\mathrm{md^2} + 4\,\mathrm{z^2})^{\frac{3}{2}}}\ \mathrm{B_{mr}} \tag{3-26}$$

$$\boldsymbol{\frac{\partial\, \mathrm{B_{mz}}}{\partial \mathrm{z}} = -\frac{12\,\mathrm{md^2 mt\,z}}{(\mathrm{md^2} + 4\mathrm{z^2})^{\frac{5}{2}}} \mathrm{B_{mr}} = -\frac{12\,\mathrm{md^2 mt\,dg}}{(\mathrm{md^2} + 4\,\mathrm{dg^2})^{\frac{5}{2}}} \mathrm{B_{mr}}}$$

An alternative approach to defining the B-field (and derivative) is to assume that the permanent magnet field is a result of virtual currents and use the Biot-Savart law. Regardless of the approach this expression can now be used to compute $\mathrm{z} = \mathrm{dg}$, the equilibrium height of the diamagnet – a quantity very useful for designing a real system.

However, we note a distinct problem on substituting into our force equations from Equations (3-23), (3-24) and (3-25) - namely that finding the value $\mathrm{z} = \mathrm{dg}$ would become a challenging factoring problem of the form: $\mathrm{z}/(4\mathrm{z}^2 + \mathrm{md}^2)^4$ or $\mathrm{dg}/(4\mathrm{dg}^2 + \mathrm{md}^2)^4$ when $\mathrm{F_{dz}} = 0$. See Equations (3-27) (diamagnetic sphere) and (3-28) (diamagnetic disc) for details and note that the resultant polynomial generated is unsolvable by analytical approaches. Numerical root finding approaches are a potential method to solving for our equilibrium z distance, $\mathrm{z} = \mathrm{dg}$. The approach used here will involve the use of Newton's method.

$$\mathrm{F_{dz}} = -\mathcal{M}_\mathrm{d} a_\mathrm{g} + \frac{\pi\, \mathrm{dd^3} \chi_\mathrm{d}}{\mu_0(\chi_\mathrm{d} + 3)} \frac{\partial}{\partial \mathrm{z}} \mathrm{B_{mz}^2} = -\mathcal{M}_\mathrm{d} a_\mathrm{g} + \frac{\pi\, \mathrm{dd^3}(\chi_\mathrm{d})}{\mu_0(\chi_\mathrm{d} + 3)} 2\mathrm{B_{mz}} \frac{\partial}{\partial \mathrm{z}} \mathrm{B_{mz}} \tag{3-27}$$

$$\mathrm{F_{dz}} = -\mathcal{M}_\mathrm{d} a_\mathrm{g} + \frac{\pi\, \mathrm{dd^3} \chi_\mathrm{d}}{\mu_0(\chi_\mathrm{d} + 3)} 2 \frac{\mathrm{md^2 mt}}{(\mathrm{md^2} + 4\,\mathrm{z^2})^{\frac{3}{2}}} \mathrm{B_{mr}} \frac{\partial}{\partial \mathrm{z}} \left(\frac{\mathrm{md^2 mt}}{(\mathrm{md^2} + 4\,\mathrm{z^2})^{\frac{3}{2}}}\ \mathrm{B_{mr}} \right)$$

$$F_{dz} = -\mathcal{M}_d a_g + \frac{\pi\, dd^3 \chi_d}{\mu_0(\chi_d + 3)} 2 \frac{md^4 mt^2}{(md^2 + 4\, z^2)^{\frac{3}{2}}} B_{mr}^2 \frac{\partial}{\partial z}\left(\frac{1}{(md^2 + 4\, z^2)^{\frac{3}{2}}}\right)$$

$$F_{dz} = -\mathcal{M}_d a_g + \frac{\pi\, dd^3 \chi_d}{\mu_0(\chi_d + 3)} 2 \frac{md^4 mt^2}{(md^2 + 4\, z^2)^{\frac{3}{2}}} B_{mr}^2 \left(-\frac{12z}{(md^2 + 4z^2)^{\frac{5}{2}}}\right)$$

$$\mathbf{F_{dz} = -\mathcal{M}_d a_g - \frac{24\pi\, dd^3 md^4 mt^2 \chi_d z\, B_{mr}^2}{\mu_0(\chi_d + 3)(md^2 + 4\, z^2)^4}}$$

$$\mathbf{F_{dz} = -\mathcal{M}_d a_g - \frac{24\pi\, dd^3 md^4 mt^2 \chi_d dg\, B_{mr}^2}{\mu_0(\chi_d + 3)(md^2 + 4\, dg^2)^4}}$$

$$F_{dz} = -\mathcal{M}_d a_g + \frac{2\pi\, dd^2 dt^3 \chi_d}{\mu_0((8dt^2 - dd^2)(\chi_d + 1) + dd^2))} \frac{\partial}{\partial z} B_{mz}^2 \tag{3-28}$$

$$F_{dz} = -\mathcal{M}_d a_g + \frac{2\pi\, dd^2 dt^3 \chi_d}{\mu_0((8dt^2 - dd^2)(\chi_d + 1) + dd^2))} 2 \frac{md^4 mt^2}{(md^2 + 4\, z^2)^{\frac{3}{2}}} B_{mr}^2 \left(-\frac{12z}{(md^2 + 4z^2)^{\frac{5}{2}}}\right)$$

$$\mathbf{F_{dz} = -\mathcal{M}_d a_g - \frac{48\pi\, dd^2 dt^3 md^4 mt^2 \chi_d z\, B_{mr}^2}{\mu_0((8dt^2 - dd^2)(\chi_d + 1) + dd^2))(md^2 + 4\, z^2)^4}}$$

$$\mathbf{F_{dz} = -\mathcal{M}_d a_g - \frac{48\pi\, dd^2 dt^3 md^4 mt^2 \chi_d dg\, B_{mr}^2}{\mu_0((8dt^2 - dd^2)(\chi_d + 1) + dd^2))(md^2 + 4\, dg^2)^4}}$$

Exploring the space of potential $z = dg$ values something to note is that two potential solutions are possible (see Figure 3-5) of which only the smaller dg value is physically valid. In this figure, the left hand side (LHS) and right hand side (RHS) of Equation (3-29) and (3-30) (for diamagnetic sphere and disc) with $F_z = 0$ is graphed over varying dg. Increasing the volume of our diamagnetic material (V_d) results in a linear increase in diamagnetic force and the potential for higher levitation height or greater support for a higher levitating mass ($\mathcal{M}_d$).

$$F_{dz} = 0 = -\mathcal{M}_d a_g - \frac{24\pi\, dd^3 md^4 mt^2 \chi_d z\, B_{mr}^2}{\mu_0(\chi_d + 3)(md^2 + 4\, z^2)^4} \tag{3-29}$$

$$LHS = \frac{z}{(md^2 + 4z^2)^4} \qquad RHS = \frac{-\mathcal{M}_d a_g u_0(\chi_d + 3)}{24\pi\, dd^3 \chi_d md^4 mt^2 B_{mr}^2}$$

$$F_{dz} = 0 = -\mathcal{M}_d a_g - \frac{48\pi\, dd^2 dt^3 \chi_d}{\mu_0((8dt^2 - dd^2)(\chi_d + 1) + dd^2))} \frac{z\, md^4 mt^2}{(md^2 + 4\, z^2)^4} B_{mr}^2 \tag{3-30}$$

$$LHS = \frac{z}{(md^2 + 4z^2)^4} \qquad RHS = -\frac{\mathcal{M}_d a_g u_0\left((8dt^2 - dd^2)(\mathcal{X}_d + 1) + dd^2\right)}{48\pi\, dd^2 dt^3 \chi_d md^4 mt^2 B_{mr}^2}$$

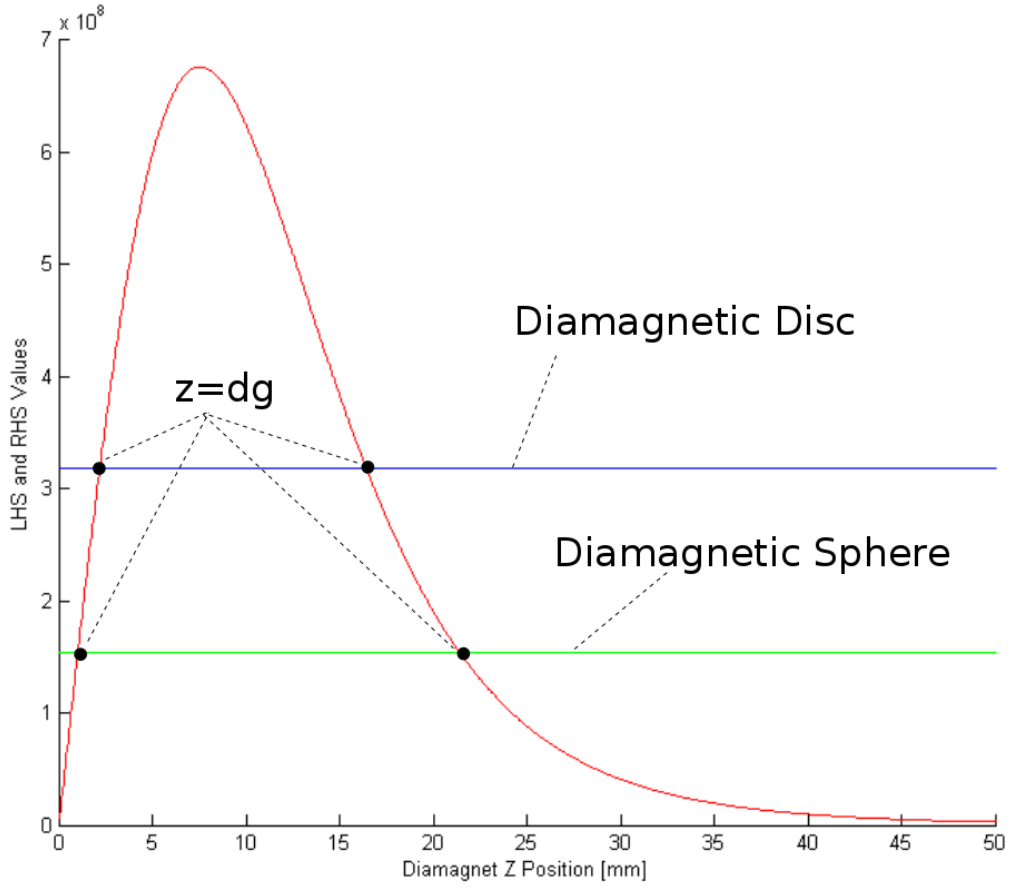

Figure 3-5: A graphical approach to finding a solution for the equilibrium position **z = dg**. Notice that two solutions exist of which only the lower **dg** value is valid.

It is useful to compute the derivatives of our force, F_{dz}. The derivative equations for the diamagnetic sphere and disc are shown in Equations (3-31) and (3-32) respectively.

$$\frac{\partial F_{dz}}{\partial z} = -\frac{24\pi\, dd^3 \chi_d md^4 mt^2 B_{mr}^2}{\mu_0(\chi_d + 3)(md^2 + 4\, z^2)^4} \cdot \frac{md^2 - 28z^2}{md^2 + 4z^2} \tag{3-31}$$

$$\frac{\partial F_{dz}}{\partial z} = -\frac{48\pi\, dd^2 dt^3 \chi_d md^4 mt^2 B_{mr}^2}{\mu_0((8dt^2 - dd^2)(\chi_d + 1) + dd^2))(md^2 + 4\, z^2)^4} \cdot \frac{md^2 - 28z^2}{md^2 + 4z^2} \tag{3-32}$$

An iterative approach to finding a solution for the equilibrium height produces a result $z_n = dg$ for some sufficient number of iterations, n. Equations (3-33)(3-33 (sphere) and (3-34) (disc) demonstrate using Newton's method starting from some initial guess, z_0 obtained via graphical means from Figure 3-5.

$$z_n = z_{n-1} + \frac{F_{dz}(z_{n-1})}{\partial F_z(z_{n-1})/\partial z} \tag{3-33}$$

$$z_n = z_{n-1} + \left(\mathcal{M}_d a_g - A\, z_{n-1}\right) / \left(- A \cdot \frac{md^2 - 28z_{n-1}^2}{md^2 + 4z_{n-1}^2} \right)$$

$$\text{where } A = \frac{24\pi\, dd^3 \chi_d md^4 mt^2 B_{mr}^2}{\mu_0(\chi_d + 3)(md^2 + 4\, z_{n-1}^2)^4}$$

$$z_n = z_{n-1} + \frac{F_{dz}(z_{n-1})}{\partial F_z(z_{n-1})/\partial z} \tag{3-34}$$

$$z_n = z_{n-1} + \left(\mathcal{M}_d a_g - A\, z_{n-1}\right) / \left(- A \cdot \frac{md^2 - 28z_{n-1}^2}{md^2 + 4z_{n-1}^2} \right)$$

$$\text{where } A = \frac{48\pi\, dd^2 dt^3 \chi_d md^4 mt^2 B_{mr}^2}{\mu_0((8dt^2 - dd^2)(\chi_d + 1) + dd^2))(md^2 + 4\, z^2)^4}$$

It is natural to take our sphere/disc plus magnet combination of stabilizing machine a little further. The addition of an additional magnet can provide greater uniformity in the magnetic field passing through our diamagnetic material while also increasing the total force. In our earlier presentation of Figure 2-11, an approach that uses multiple stacked diamagnet discs sandwiched between permanent magnets was noted.

The total forces resulting from this stacking in a radial machine is fairly easy to compute by modifying the topology presented in Figure 3-4 with the addition of an additional magnet as shown in Figure 3-6. The resultant force on the diamagnet would be that generated by a superposition of the two individual fields generated by each individual magnet. This superposition can be approximated as double that of the field from the single magnet. A more precise estimate, however, can be obtained by utilizing the formulation, $\vec{B}$, from Equation (3-15).

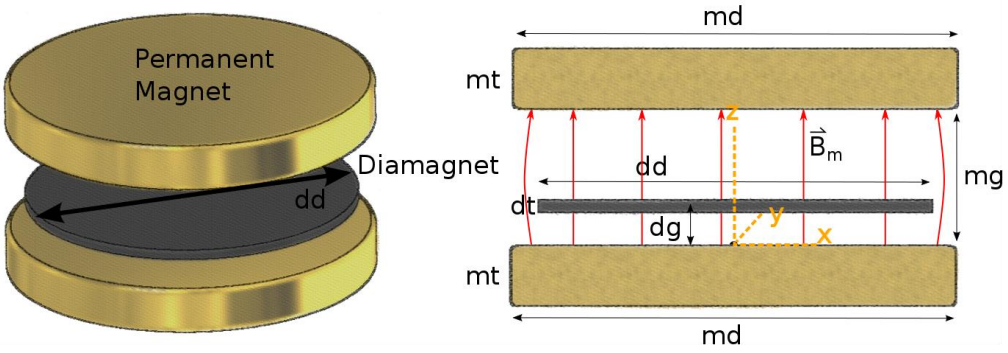

Figure 3-6: Extending the disc and magnet topology to multiple magnets and platters. Notice that the contribution from additional diamagnetic discs will be a linear combination of the contribution of the one disc above.

The new B-field passing through the diamagnetic material is given in Equation (3-35). This is a modification to our earlier estimate in Equation (3-25).

$$B_{mz} = \frac{md^2mt}{(md^2 + 4\,z^2)^{\frac{3}{2}}}\ B_{mr} + \frac{md^2mt}{(md^2 + 4\,(mg - z)^2)^{\frac{3}{2}}}\ B_{mr} \tag{3-35}$$

$$\mathbf{B_{mz} = \frac{md^2mt}{(md^2 + 4\,z^2)^{\frac{3}{2}}}\ B_{mr} + \frac{md^2mt}{(md^2 + 4\,(mg - z)^2)^{\frac{3}{2}}}\ B_{mr}}$$

$$\mathbf{B_{mz} = \frac{md^2mt}{(md^2 + 4\,dg^2)^{\frac{3}{2}}}\ B_{mr} + \frac{md^2mt}{(md^2 + 4\,(mg - dg)^2)^{\frac{3}{2}}}\ B_{mr}}$$

The resulting derivative of the field is useful for computing the force in our new configuration. This derivative is given by Equation (3-36).

$$\frac{\partial B_{mz}}{\partial z} = \frac{\partial}{\partial z}\left(\frac{md^2mt}{(md^2 + 4\,z^2)^{\frac{3}{2}}}\ B_{mr}\right) + \frac{\partial}{\partial z}\left(\frac{md^2mt}{(md^2 + 4\,(mg - z)^2)^{\frac{3}{2}}}\ B_{mr}\right) \tag{3-36}$$

$$\mathbf{\frac{\partial B_{mz}}{\partial z} = -\frac{12md^2mt\,z}{(md^2 + 4z^2)^{\frac{5}{2}}}B_{mr} + \frac{12md^2mt\,(mg - z)}{(md^2 + 4\,(mg - z)^2)^{\frac{5}{2}}}\ B_{mr}}$$

$$\mathbf{\frac{\partial B_{mz}}{\partial z} = -\frac{12md^2mt\,dg}{(md^2 + 4\,dg^2)^{\frac{5}{2}}}B_{mr} + \frac{12md^2mt\,(mg - dg)}{(md^2 + 4\,(mg - dg)^2)^{\frac{5}{2}}}\ B_{mr}}$$

From this B-field and derivative the z-directional force on the diamagnetic material resulting from the two magnets can be recomputed as shown in Equations (3-37) (sphere) and (3-38) (disc). The increased complexity of these new equations makes them difficult to simplify.

$$F_{dz} = -\mathcal{M}_d a_g + \frac{\pi\, dd^3 \chi_d}{\mu_0(\chi_d + 3)} \frac{\partial}{\partial z} B_{mz}^2 = -\mathcal{M}_d a_g + \frac{\pi\, dd^3 \chi_d}{\mu_0(\chi_d + 3)} 2B_{mz} \frac{\partial}{\partial z} B_{mz} \qquad (3\text{-}37)$$

$$\mathbf{F_{dz} = -\mathcal{M}_d a_g + \frac{\pi\, dd^3 \chi_d}{\mu_0(\chi_d + 3)} 2 \left(\frac{md^2 mt}{(md^2 + 4\, z^2)^{\frac{3}{2}}}\ B_{mr} + \frac{md^2 mt}{(md^2 + 4\,(mg - z)^2)^{\frac{3}{2}}}\ B_{mr} \right) \left(-\frac{12 md^2 mt\, z}{(md^2 + 4z^2)^{\frac{5}{2}}}\ B_{mr} + \frac{12 md^2 mt\,(mg - z)}{(md^2 + 4\,(mg - z)^2)^{\frac{5}{2}}}\ B_{mr} \right)}$$

$$F_{dz} = -\mathcal{M}_d a_g + \frac{2\pi\, dd^2 dt^3 \chi_d}{\mu_0((8dt^2 - dd^2)(\chi_d + 1) + dd^2))} 2B_{mz} \frac{\partial}{\partial z} B_{mz} \qquad (3\text{-}38)$$

$$\mathbf{F_{dz} = -\mathcal{M}_d a_g + \frac{4\pi\, dd^2 dt^3 \chi_d}{\mu_0((8dt^2 - dd^2)(\chi_d + 1) + dd^2))} \left(\frac{md^2 mt}{(md^2 + 4z^2)^{\frac{3}{2}}}\ B_{mr} + \frac{md^2 mt}{(md^2 + 4\,(mg - z)^2)^{\frac{3}{2}}}\ B_{mr} \right) \left(-\frac{12 md^2 mt\, z}{(md^2 + 4z^2)^{\frac{5}{2}}}\ B_{mr} + \frac{12 md^2 mt\,(mg - z)}{(md^2 + 4\,(mg - z)^2)^{\frac{5}{2}}}\ B_{mr} \right)}$$

From this we can construct a new formulation for Newton's method to iteratively compute the levitation position ($z = dg$) for a particular rotor mass ($\mathcal{M}_d$) with particular dimensions (mt, md, mg, dt, dd) and number of platters (p). First, however, the derivative of our force for a single platter, F_{dz}, is given in Equation (3-39) (sphere) and (3-40) (disc). Newton's method iteration steps can be computed from this derivative and from Equations (3-37) and (3-38) with our earlier method used in Equations (3-33) and (3-34). With p platters of diamagnetic material each

sandwiched between two permanent magnets the net force generated would be $F_d = pF_{dz}$.

$$\frac{\partial F_{dz}}{\partial z} = -\frac{24\pi\, dd^3 md^4 mt^2 \chi_d B_{mr}^2}{\mu_0(\chi_d + 3)} \cdot \left(\frac{1}{(md^2 + 4z^2)^{\frac{3}{2}}(md^2 + 4(mg - z)^2)^{\frac{5}{2}}} - \frac{1}{(md^2 + 4z^2)^{\frac{5}{2}}(md^2 + 4(mg - z)^2)^{\frac{3}{2}}} + \frac{1}{(md^2 + 4(mg - z)^2)^4} + \frac{1}{(md^2 + 4z^2)^4} - \frac{32z^2}{(md^2 + 4z^2)^5} - \frac{32(mg - z)^2}{(md^2 + 4(mg - z)^2)^5} + \frac{20z^2}{(md^2 + 4z^2)^{\frac{7}{2}}(md^2 + 4(mg - z)^2)^{\frac{3}{2}}} - \frac{20\,(mg - z)^2}{(md^2 + 4z^2)^{\frac{3}{2}}(md^2 + 4(mg - z)^2)^{\frac{7}{2}}} \right) \tag{3-39}$$

$$\frac{\partial F_{dz}}{\partial z} = -\frac{48\pi\, dd^2 dt^3 md^2 mt\, \chi_d\, B_{mr}}{\mu_0((8dt^2 - dd^2)(\chi_d + 1) + dd^2))} \cdot \left[\left(\frac{1}{(md^2 + 4z^2)^{\frac{3}{2}}} + \frac{1}{(md^2 + 4(mg - z)^2)^{\frac{3}{2}}} \right) \left(\frac{1}{(md^2 + 4z^2)^{\frac{5}{2}}} + \frac{1}{(md^2 + 4(mg - z)^2)^{\frac{5}{2}}} - \frac{20z^2}{(md^2 + 4z^2)^{\frac{7}{2}}} - \frac{20(mg - z)^2}{(md^2 + 4(mg - z)^2)^{\frac{7}{2}}} \right) + \left(\frac{12(mg - z)}{(md^2 + 4(mg - z)^2)^{\frac{5}{2}}} - \frac{12z}{(md^2 + 4z^2)^{\frac{5}{2}}} \right) \left(\frac{z}{(md^2 + 4z^2)^{\frac{5}{2}}} - \frac{mg - z}{(md^2 + 4(mg - z)^2)^{\frac{5}{2}}} \right) \right] \tag{3-40}$$

This implies that the additional platters have the effect of increasing the gradient of the potential energy surface in the z direction as shown in Figure 3-7 below. Notice that we have a local minima in the energy indicating stability in the z-direction. This energy is also a representation of stiffness for the disc in the same direction.

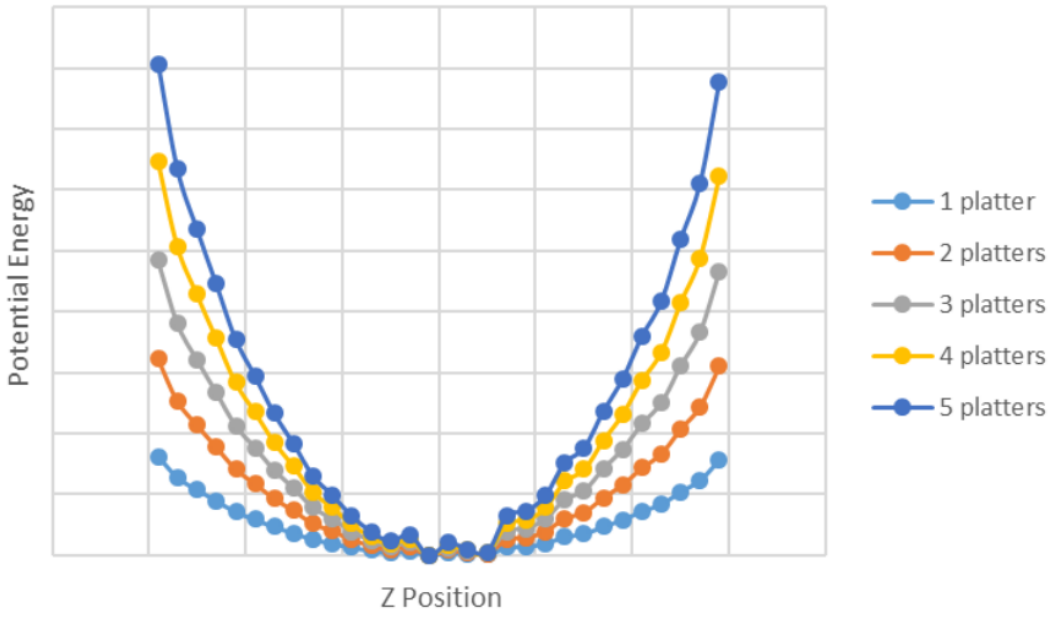

Figure 3-7: The effect of the multiple platters where $\mathbf{p = 1, 2, 3, 4}$ **and** $\mathbf{5}$. Simulation of platter energy effects – note that for demonstration only the relative difference in potential energy has been indicated.

With the equilibrium height as well as force now solved for, some attention needs to be given to the lifter assembly and stiffness, stability and electrodynamic loss considerations.

3.4 Lifter-Floater Weight Compensation Machinery Analysis

The lifter and floater combination from the earlier presentation in Figure 2-8 are an essential component needed to lift larger masses (weight compensation) than possible with the very weak diamagnetic susceptibilities ($\chi_d = -5 \times 10^{-5}$) of stabilizing machinery alone. We consider two topologies in this theoretical treatment. A spherical ferromagnetic floater is combined with either a disc or ring permanent magnet lifter. These configurations are shown in Figure 3-8.

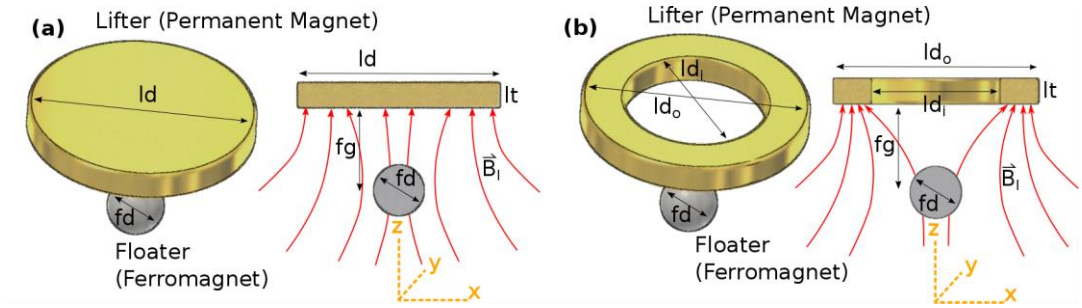

Figure 3-8: Two Lifter and floater combinations: (a) A disc magnet, (b) A ring magnet.

The floater is not pre-magnetized and non-magnetized initially. This is something not attempted previously in literature. The advantage of using a piece of ferromagnetic material here is the potential for shaping this floater as a rotor and using it directly in a reluctance machine.

We assume that the lifter/floater assembly does not interfere with the diamagnetic stabilizing machine. As with the study of diamagnetic forces, we can start by utilizing our formulation for the magnetic field from Equation (3-15). Here we note that the magnetic moment of our floater ($\vec{m}_f$) and our field from the lifter ($\vec{B}_l$) can be used to compute the potential energy (E_p) and hence the force on the floater ($\vec{F}_f = -\nabla E_p$). As with the diamagnetic sphere and disc we can start with the representation from *Equation (*3-16 and compute the moment from Equation (3-41).

$$\vec{B} = \vec{B}_l + \vec{B}_{f+} = \mu\vec{H} = \mu(\vec{H}_l + \vec{H}_f) \tag{3-41}$$

$$\vec{B}_l + \vec{B}_{f+} = \mu\left(\frac{\vec{B}_l}{\mu_0} + \vec{H}_f\right) = \mu\left(\frac{\vec{B}_l}{\mu_0} + \vec{H}_{f+} - \vec{M}_f\right) = \mu\left(\frac{\vec{B}_l}{\mu_0} + \frac{\vec{B}_{f+}}{\mu_0} - \frac{\vec{m}_f}{V_f}\right)$$

$$\vec{B}_l + \vec{B}_{f+} - \mu\frac{\vec{B}_l}{\mu_0} - \mu\frac{\vec{B}_{f+}}{\mu_0} + \mu\frac{\vec{m}_f}{V_f} = 0$$

$$\vec{m}_f = \frac{V_f}{\mu}\left(-\vec{B}_l - \vec{B}_{f+} + \mu\frac{\vec{B}_l}{\mu_0} + \mu\frac{\vec{B}_{f+}}{\mu_0}\right)$$

$$\boldsymbol{\vec{m}_f = \frac{V_f}{\mu_0}\cdot\left(\frac{\chi_f}{\chi_f + 1}\right)\cdot\left(\vec{B}_l + \vec{B}_{f+}\right)}$$

From here, Equation (3-42) defines our magnetic moment, $\vec{m}_f$ for the disc and ring lifters shown in Figure 3-8. This equation can be formulated in the same manner that the earlier equation (Equation (3-17)) was used to estimate the magnetic moment of a diamagnetic sphere. The main difference is that the susceptibility of a ferromagnetic material is in the order of $\chi_f = 400$.

$$\vec{m}_f = \frac{V_f}{\mu_0}\cdot\left(\frac{\chi_f}{\chi_f + 1}\right)\cdot\left(\vec{B}_l + \frac{\mu_0}{4\pi}\cdot\frac{1}{r^3}\,(3(\vec{m}_f\cdot\hat{r})\hat{r} - \vec{m}_f)\right) \qquad (3\text{-}42)$$

$$\boldsymbol{\vec{m}_f = -\frac{\pi f d^3 \chi_f}{\mu_0(\chi_f + 3)}\cdot\vec{B}_l}$$

The magnetic field, $\vec{B}_l$, generated by the lifter magnet can now be computed in a manner similar to that shown by Equation (3-25) earlier. The z directional field generated by a disc magnet is shown in Equation (3-43) while that generated by a ring magnet is shown in Equation (3-44) for a floater distance $z = fg$ from the magnet.

Again, we note that the lifter magnet has a remanent magnetization $\vec{M}_l$ and volume, V_l. Typically, we will have a known surface remanent B-field of $\vec{B}_{lr}$ reported for this magnet. A simple method of completing the computation for our ring lifter is simply to subtract the contributions of the central hollow region from our disc.

$$\vec{B}_l = \frac{\mu_0}{4\pi} \cdot \frac{1}{r^3} \left(3(\vec{m} \cdot \hat{r})\hat{r} - \vec{m}\right) = \frac{\mu_0}{4\pi} \cdot \frac{1}{\left(\sqrt{\left(\frac{ld}{2}\right)^2 + z^2}\right)^3} \left(3\left(\vec{M}_l V_l \cdot \hat{r}\right)\hat{r} - \vec{M}_l V_l\right) \quad (3\text{-}43)$$

$$\mathbf{B_{lz}} = \frac{\mathbf{ld^2 lt}}{(\mathbf{ld^2 + 4z^2})^{\frac{3}{2}}}\ \mathbf{B_{lr}} = \frac{\mathbf{ld^2 lt}}{\left(\mathbf{ld^2 + 4\ fg^2}\right)^{\frac{3}{2}}}\ \mathbf{B_{lr}}$$

$$\mathbf{B_{lz}} = \frac{\mathbf{ld_o^2 lt}}{\left(\mathbf{ld_o^2 + 4z^2}\right)^{\frac{3}{2}}}\ \mathbf{B_{lr}} - \frac{\mathbf{ld_i^2 lt}}{\left(\mathbf{ld_i^2 + 4z^2}\right)^{\frac{3}{2}}}\ \mathbf{B_{lr}} \quad (3\text{-}44)$$

$$\mathbf{B_{lz}} = \frac{\mathbf{ld_o^2 lt}}{\left(\mathbf{ld_o^2 + 4fg^2}\right)^{\frac{3}{2}}}\ \mathbf{B_{lr}} - \frac{\mathbf{ld_i^2 lt}}{\left(\mathbf{ld_i^2 + 4fg^2}\right)^{\frac{3}{2}}}\ \mathbf{B_{lr}}$$

The derivatives are once again a useful computation and are presented in *Equation (*3-45) and *(*3-46) for our disc and ring field respectively.

$$\frac{\partial B_{lz}}{\partial z} = \frac{\partial}{\partial z}\left(\frac{ld^2 lt}{(ld^2 + 4z^2)^{\frac{3}{2}}}\ B_{lr}\right) \quad (3\text{-}45)$$

$$\frac{\partial\ \mathbf{B_{lz}}}{\partial \mathbf{z}} = -\frac{\mathbf{12\ ld^2 lt\ z}}{(\mathbf{ld^2 + 4z^2})^{\frac{5}{2}}}\mathbf{B_{lr}} = -\frac{\mathbf{12\ ld^2 lt\ fg}}{(\mathbf{ld^2 + 4\ fg^2})^{\frac{5}{2}}}\mathbf{B_{lr}}$$

$$\frac{\partial B_{lz}}{\partial z} = \frac{\partial}{\partial z}\left(\frac{ld_o^2 lt}{(ld_o^2 + 4z^2)^{\frac{3}{2}}}\ B_{lr}\right) - \frac{\partial}{\partial z}\left(\frac{ld_i^2 lt}{(ld_i^2 + 4z^2)^{\frac{3}{2}}}\ B_{lr}\right) \quad (3\text{-}46)$$

$$\frac{\partial\ \mathbf{B_{lz}}}{\partial \mathbf{z}} = -\frac{\mathbf{12\ ld_o^2 lt\ z}}{\left(\mathbf{ld_o^2 + 4z^2}\right)^{\frac{5}{2}}}\mathbf{B_{lr}} + \frac{\mathbf{12\ ld_i^2 lt\ z}}{\left(\mathbf{ld_i^2 + 4z^2}\right)^{\frac{5}{2}}}\mathbf{B_{lr}}$$

The total energy of our floater system is given by Equation (3-47). Equation (3-48) demonstrates the resulting z directional force ($F_f = F_{fz}$) generated on the floater ($F_{fz} = -\nabla E_p$) by the disc lifter while Equation (3-49) provides the computation for the ring lifter.

$$E_P = E_g + E_f = \mathcal{M}_f a_g z - \vec{m}_f \cdot \vec{B}_l \tag{3-47}$$

$$F_{fz} = -\mathcal{M}_f a_g - \frac{\pi\, fd^3 \chi_f}{\mu_0(\chi_f + 3)} \cdot 2B_{lz} \frac{\partial}{\partial z} B_{lz} \tag{3-48}$$

$$\mathbf{F_{fz} = -\mathcal{M}_d a_g - \frac{24\pi\, fd^3 ld^4 lt^2 \chi_d\, z\, B_{lr}^2}{\mu_0(\chi_d + 3)(ld^2 + 4z^2)^4}}$$

$$\mathbf{F_{fz} = -\mathcal{M}_d a_g - \frac{24\pi\, fd^3 ld^4 lt^2 \chi_d\, fg\, B_{lr}^2}{\mu_0(\chi_d + 3)(ld^2 + 4fg^2)^4}}$$

$$F_{fz} = -\mathcal{M}_f a_g - \frac{\pi\, fd^3 \chi_f}{\mu_0(\chi_f + 3)} \cdot 2B_{lz} \frac{\partial}{\partial z} B_{lz} \tag{3-49}$$

$$\mathbf{F_{fz} = -\mathcal{M}_f a_g - \frac{24\pi\, fd^3 \chi_f lt^2 z\, B_{lr}^2}{\mu_0(\chi_f + 3)} \cdot \left(- \frac{ld_o^4}{\left(ld_o^2 + 4z^2\right)^4} + \frac{ld_i^2 ld_o^2}{\left(ld_o^2 + 4z^2\right)^{\frac{3}{2}} \left(ld_i^2 + 4z^2\right)^{\frac{5}{2}}} + \frac{ld_i^2 ld_o^2}{\left(ld_i^2 + 4z^2\right)^{\frac{3}{2}} \left(ld_o^2 + 4z^2\right)^{\frac{5}{2}}} - \frac{ld_i^4}{\left(ld_i^2 + 4z^2\right)^4} \right)}$$

The derivative of this computed force is shown in Equations (3-50) and (3-51) for the disc and ring lifter respectively. The derivative for our disc lifter and spherical floater looks very similar to that of the diamagnetic sphere & disc magnet from Equation (3-31).

$$\frac{\partial \mathbf{F_{fz}}}{\partial \mathbf{z}} = -\frac{\mathbf{24\pi\, fd^3 \chi_d ld^4 lt^2 B_{lr}^2}}{\mathbf{\mu_0(\chi_d + 3)(ld^2 + 4\, z^2)^4}} \cdot \frac{\mathbf{ld^2 - 28z^2}}{\mathbf{ld^2 + 4z^2}} \tag{3-50}$$

$$\begin{aligned}\frac{\partial \mathbf{F_{fz}}}{\partial \mathbf{z}} = -\frac{\mathbf{24\pi\, fd^3 \chi_f lt^2 B_{lr}^2}}{\mathbf{\mu_0(\chi_f + 3)}} \\ \cdot \left(\frac{\mathbf{32\, ld_i^4 z^2}}{\mathbf{(ld_i^2 + 4z^2)^5}} + \frac{\mathbf{32\, ld_o^4 z^2}}{\mathbf{(ld_o^2 + 4z^2)^5}} - \frac{\mathbf{ld_o^4}}{\mathbf{(ld_o^2 + 4z^2)^4}} - \frac{\mathbf{ld_i^4}}{\mathbf{(ld_i^2 + 4z^2)^4}} \right. \\ + \frac{\mathbf{ld_i^2 ld_o^2}}{\mathbf{(ld_i^2 + 4z^2)^{\frac{3}{2}} (ld_o^2 + 4z^2)^{\frac{5}{2}}}} + \frac{\mathbf{ld_i^2 ld_o^2}}{\mathbf{(ld_i^2 + 4z^2)^{\frac{5}{2}} (ld_o^2 + 4z^2)^{\frac{3}{2}}}} \\ - \frac{\mathbf{20\, ld_i^2 ld_o^2 z^2}}{\mathbf{(ld_i^2 + 4z^2)^{\frac{3}{2}} (ld_o^2 + 4z^2)^{\frac{7}{2}}}} - \frac{\mathbf{20\, ld_i^2 ld_o^2 z^2}}{\mathbf{(ld_i^2 + 4z^2)^{\frac{7}{2}} (ld_o^2 + 4z^2)^{\frac{3}{2}}}} \\ \left. - \frac{\mathbf{24\, ld_i^2 ld_o^2 z^2}}{\mathbf{(ld_i^2 + 4z^2)^{\frac{5}{2}} (ld_o^2 + 4z^2)^{\frac{5}{2}}}} \right)\end{aligned} \tag{3-51}$$

As with our diamagnetic material we can set $F_{fz} = 0$ and compute the $z = fg$ airgap value numerically using Newton's method. Together with our value dg for our diamagnet, this yields the optimal distance between the stationary and levitating elements of the diamagnetic bearing. For the sake of simplicity, the Newton's method formulation has not been shown – the formulation is, however, similar to that shown in Equations (3-37) and (3-38).

Ultimately, we see that the z-directional net force on the levitating rotor assembly of a diamagnetic bearing consisting of a stabilizing machine and a floater. Considering the combination of a multi-plattered stabilizer consisting of diamagnetic disc

levitated above a disc magnet and weight compensated with a spherical floater and ring magnet lifter, we can represent this force as shown in Equation (3-52). An additional contribution to the forces results from the shaft connecting the diamagnetic material to the floater – this force is represented as $F_{sh} = \mathcal{M}_{sh} a_g$. Note that we assume that the ring lifter magnet and the permanent magnets in the stabilizing machine have the same remanence such that $B_{rem} = B_{mr} = B_{lr}$. There is a problem combining the forces given that different points of reference are used for our z variable. In the case of our diamagnet, we define this z relative to the bottom stabilizing magnet while in the lifter we define it from the perspective of the top lifting magnet. To clarify we replace our z values with $z = dg$ and $z = fg$ for the stabilizer and lifter-floater respectively. The value dg represents the distance between the diamagnet and stabilizing magnet for each of the p platters.

$$F_z = F_d + F_f + F_{sh} \tag{3-52}$$

$$\mathbf{F_z} = \mathbf{p}\left[-\boldsymbol{\mathcal{M}_d a_g} + \frac{4\pi\, dd^2 dt^3 \chi_d}{\mu_0((8dt^2 - dd^2)(\chi_d + 1) + dd^2))} B_{rem}^2 \left(\frac{md^2 mt}{(md^2 + 4dg^2)^{\frac{3}{2}}} + \frac{md^2 mt}{(md^2 + 4\,(mg - dg)^2)^{\frac{3}{2}}}\right)\left(-\frac{12 md^2 mt\, dg}{(md^2 + 4dg^2)^{\frac{5}{2}}} + \frac{12 md^2 mt\,(mg - dg)}{(md^2 + 4\,(mg - dg)^2)^{\frac{5}{2}}}\right)\right] + \left[-\boldsymbol{\mathcal{M}_f a_g} - \frac{24\pi\, fd^3 \chi_f lt^2 fg}{\mu_0(\chi_f + 3)} B_{rem}^2 \cdot \left(-\frac{ld_o^4}{(ld_o^2 + 4fg^2)^4} + \frac{ld_i^2 ld_o^2}{(ld_o^2 + 4fg^2)^{\frac{3}{2}}(ld_i^2 + 4fg^2)^{\frac{5}{2}}} + \frac{ld_i^2 ld_o^2}{(ld_i^2 + 4fg^2)^{\frac{3}{2}}(ld_o^2 + 4fg^2)^{\frac{5}{2}}} - \frac{ld_i^4}{(ld_i^2 + 4fg^2)^4}\right)\right] - \boldsymbol{\mathcal{M}_{sh} a_g}$$

We noted in our earlier discussion of the diamagnetic stabilizing machinery that the diamagnet contributed largely to stability in the z direction and very little to stability in the xy plane. The primary method of providing stabilizing forces in this plane must thus be from the lifter magnet. We can compute the force applied in the radial x direction (F_x) in and around our z direction levitation point of $z = fg$. As with our previous computations we use the potential energy formulation: $F_x = -\nabla E_p$ where

there is no contributing component from the mass of our floater for E_p. This means that $F_x = \nabla(\vec{m}_f \cdot \vec{B}_l)$ with only the x component of $\vec{m}_f$ and $\vec{B}_l$ considered.

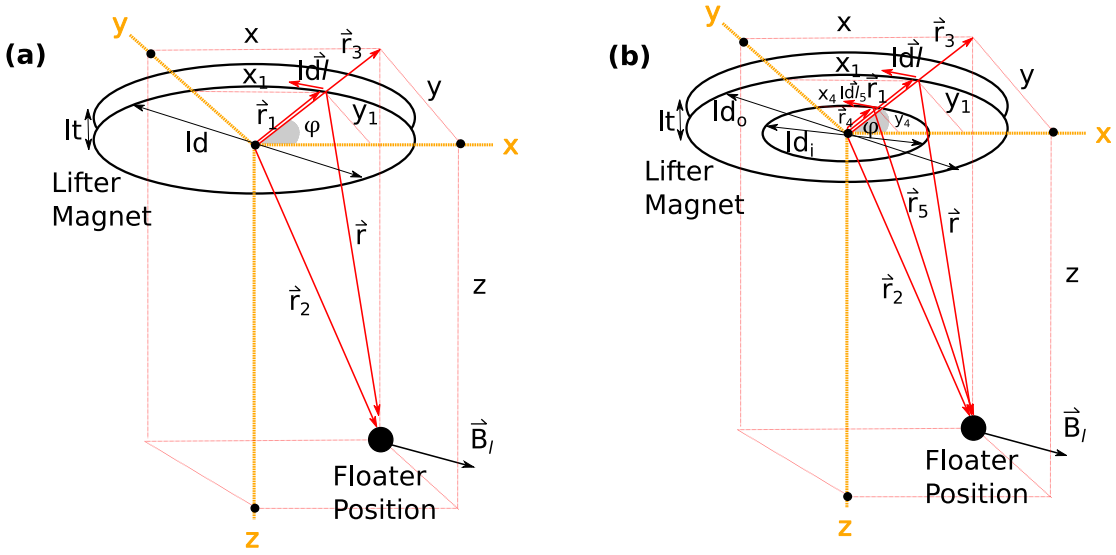

Figure 3-9: Determining the $\vec{r}$ for two lifter and floater combinations: (a) A disc magnet. (b) A ring magnet. The ring magnet can be regarded as a disc magnet with subtracted from a smaller disc magnet.

This xy direction calculation is somewhat more complicated than simply considering axial z directional fields and forces. However, given that the bearing will maintain its position roughly at a fixed z position and that radial symmetry exists implies that some simplification is not unreasonable. Figure 3-9 demonstrates some additional geometric considerations. To compute the B-field (and subsequently the force) the vector, $\vec{r} = r \cdot \hat{r}$ in this scenario becomes somewhat more complex and is given by $\vec{r} = \vec{r}_2 - \vec{r}_1$ for the disc in Figure 3-9a. For the ring two vectors are used for computations: $\vec{r} = \vec{r}_2 - \vec{r}_1$ and $\vec{r}_5 = \vec{r}_2 - \vec{r}_4$.

Using this understanding we can compute the B-field for both geometries as shown in Equation (3-53) (disc) and (3-54) (ring). We assume that the floater is hovering below the lifter at some airgap $z = fg$ and rotating off-centric at some position $x = fx$. Be aware that the equation presented changes from a vector form to an x directional field by dropping the y and z components of the field. As with our z directional field for the ring magnet, a superposition can be used to eliminate the contributions of the central region of the ring. As with our previous z direction calculations, the remanence of the magnet is given by B_{lr}.

$$\vec{B}_l = \frac{\mu_0}{4\pi} \cdot \frac{1}{r^3} \left(3(\vec{m} \cdot \hat{r})\hat{r} - \vec{m}\right) = \frac{\mu_0}{4\pi} \cdot \frac{1}{(\|\vec{r}_2 - \vec{r}_1\|)^3} \left(3\left(\vec{M}_l V_l \cdot \hat{r}\right)\hat{r} - \vec{M}_l V_l\right) \tag{3-53}$$

$$\vec{B}_l = \frac{1}{4\pi} \cdot \frac{V_l}{((r_3 - r_1)^2 + z^2)^{\frac{3}{2}}} \left\{3\left([0,0,B_{lr}] \cdot \left[\frac{(r_3 - r_1)\cos\varphi}{r}, 0, \frac{z}{r}\right]\right)\left[\frac{(r_3 - r_1)\cos\varphi}{r}, 0, \frac{z}{r}\right] - [0,0,B_{lr}]\right\}$$

$$B_{lx} = \frac{1}{4\pi} \cdot \frac{\pi r_1^2 lt}{((r_3 - r_1)^2 + z^2)^{\frac{3}{2}}} \left(\left[\frac{3B_{lr} z(r_3 - r_1)\cos\varphi}{r^2}, 0, \frac{3B_{lr} z^2}{r^2} - B_{lr}\right]\right)$$

$$B_{lx} = \frac{3B_{lr} z(r_3 - r_1) r_1^2 lt}{4((r_3 - r_1)^2 + z^2)^{\frac{5}{2}}} = \frac{3z\left(x - \frac{ld}{2}\right)\left(\frac{ld}{2}\right)^2 lt}{4\left(\left(x - \frac{ld}{2}\right)^2 + z^2\right)^{\frac{5}{2}}} B_{lr} = \frac{3z(2x - ld)ld^2 lt}{((2x - ld)^2 + z^2)^{\frac{5}{2}}} B_{lr}$$

$$\mathbf{B_{lx} = \frac{3z(2x - ld)ld^2 lt}{((2x - ld)^2 + z^2)^{\frac{5}{2}}} B_{lr} = \frac{3\,fg\,(2fx - ld)ld^2 lt}{((2fx - ld)^2 + fg^2)^{\frac{5}{2}}} B_{lr}}$$

$$B_{lx} = B_{lx_o} - B_{lx_i} \tag{3-54}$$

$$\mathbf{B_{lx}} = \frac{\mathbf{3z(2x - ld_o)ld_o^2 lt}}{((\mathbf{2x - ld_i})^2 + \mathbf{z^2})^{\frac{5}{2}}}\mathbf{B_{lr}} - \frac{\mathbf{3z(2x - ld_i)ld_i^2 lt}}{((\mathbf{2x - ld_i})^2 + \mathbf{z^2})^{\frac{5}{2}}}\mathbf{B_{lr}}$$

$$\mathbf{B_{lx}} = \frac{\mathbf{3fg(2fx - ld_o)ld_o^2 lt}}{((\mathbf{2fx - ld_i})^2 + \mathbf{fg^2})^{\frac{5}{2}}}\mathbf{B_{lr}} - \frac{\mathbf{3fg(2fx - ld_i)ld_i^2 lt}}{((\mathbf{2fx - ld_i})^2 + \mathbf{fg^2})^{\frac{5}{2}}}\mathbf{B_{lr}}$$

Now that the B-field (B_{lx}) as well as the magnetic moment ($\vec{m}_f$) of the lifter-floater is known in the xy plane, the force can also be computed as shown in Equation (3-55) and (3-56) for the disc and ring lifter respectively.

$$F_{fx} = \nabla(\vec{m}_f \cdot \vec{B}_l) = \frac{\pi\, fd^3 \chi_f}{\mu_0(\chi_f + 3)} \cdot \frac{\partial B_{lx}^2}{\partial x} = \frac{2\pi\, fd^3 \chi_f}{\mu_0(\chi_f + 3)} \cdot B_{lx} \frac{\partial B_{lx}}{\partial x} \tag{3-55}$$

$$F_{fx} = \frac{2\pi\, fd^3 \chi_f}{\mu_0(\chi_f + 3)} \cdot \frac{3z(2x - ld)ld^2 lt}{((2x - ld)^2 + z^2)^{\frac{5}{2}}} B_{lr} \frac{\partial}{\partial x}\left(\frac{3z(2x - ld)ld^2 lt}{((2x - ld)^2 + z^2)^{\frac{5}{2}}} B_{lr} \right)$$

$$F_{fx} = \frac{18\pi\, fd^3 \chi_f\, z^2 (2x - ld)ld^4 lt^2}{\mu_0(\chi_f + 3)((2x - ld)^2 + z^2)^{\frac{5}{2}}} B_{lr}^2 \frac{\partial}{\partial x}\left(\frac{(2x - ld)}{((2x - ld)^2 + z^2)^{\frac{5}{2}}} \right)$$

$$\mathbf{F_{fx}} = -\frac{\mathbf{36\pi\, fd^3 \chi_f\, ld^4 lt^2 (4z^2 (2x - ld)^3 + z^4 (2x - ld))}}{\mathbf{\mu_0(\chi_f + 3)((2x - ld)^2 + z^2)^6}} \mathbf{B_{lr}^2}$$

$$\mathbf{F_{fx}} = -\frac{\mathbf{36\pi\, fd^3 \chi_f\, ld^4 lt^2 (4fg^2 (2fx - ld)^3 + fg^4 (2fx - ld))}}{\mathbf{\mu_0(\chi_f + 3)((2fx - ld)^2 + fg^2)^6}} \mathbf{B_{lr}^2}$$

$$F_{fx} = F_{fx\,(outer)} - F_{fx\,(inner)} \tag{3-56}$$

$$\mathbf{F_{fx} = -\frac{36\pi\, fd^3 \chi_f lt^2}{\mu_0(\chi_f + 3)} B_{lr}^2 \left(\frac{ld_o^4 \left(4z^2(2x - ld_o)^3 + z^4(2x - ld_o)\right)}{((2x - ld_o)^2 + z^2)^6} - \frac{ld_i^4 \left(4z^2(2x - ld_i)^3 + z^4(2x - ld_i)\right)}{((2x - ld_i)^2 + z^2)^6} \right)}$$

$$\mathbf{F_{fx} = -\frac{36\pi\, fd^3 \chi_f lt^2}{\mu_0(\chi_f + 3)} B_{lr}^2 \left(\frac{ld_o^4 \left(4fg^2(2fx - ld_o)^3 + fg^4(2fx - ld_o)\right)}{((2fx - ld_o)^2 + fg^2)^6} - \frac{ld_i^4 \left(4fg^2(2fx - ld_i)^3 + fg^4(2fx - ld_i)\right)}{((2fx - ld_i)^2 + fg^2)^6} \right)}$$

As with our earlier computations, it is useful to compute the derivative of the force as well. These derivatives are shown in Equations (3-57) and (3-58) for the disc and ring lifter acting on the spherical floater respectively.

$$\frac{\partial F_{fx}}{\partial x} = -\frac{36\pi\, fd^3 \chi_f lt^2}{\mu_0(\chi_f + 3)} B_{lr}^2 \frac{\partial}{\partial x} \left(\frac{ld^4 \left(4z^2(2x - ld)^3 + z^4(2x - ld)\right)}{((2x - ld)^2 + z^2)^6} \right) \tag{3-57}$$

$$\mathbf{\frac{\partial F_{fx}}{\partial x} = -\frac{36\pi\, fd^3 \chi_f lt^2}{\mu_0(\chi_f + 3)} B_{lr}^2 \left[\frac{ld^4(24z^2(ld - 2x)^2 + 2z^4)}{((ld - 2x)^2 + z^2)^6} - \frac{6ld^4(4ld - 8x)\left(4z^2(ld - 2x)^3 + z^4(ld - 2x)\right)}{((ld - 2x)^2 + z^2)^7} \right]}$$

$$\mathbf{\frac{\partial F_{fx}}{\partial x} = -\frac{36\pi\, fd^3 \chi_f lt^2}{\mu_0(\chi_f + 3)} B_{lr}^2 \left[\frac{ld^4(24fg^2(ld - 2fx)^2 + 2fg^4)}{((ld - 2fx)^2 + fg^2)^6} - \frac{6ld^4(4ld - 8fx)\left(4fg^2(ld - 2fx)^3 + fg^4(ld - 2fx)\right)}{((ld - 2fx)^2 + zfg^2)^7} \right]}$$

$$\frac{\partial F_{fx}}{\partial x} = -\frac{36\pi\, fd^3 \chi_f lt^2}{\mu_0(\chi_f + 3)} B_{lr}^2 \frac{\partial}{\partial x}\left(\frac{ld_o^4\left(4z^2(2x - ld_o)^3 + z^4(2x - ld_o)\right)}{((2x - ld_o)^2 + z^2)^6} - \frac{ld_i^4\left(4z^2(2x - ld_i)^3 + z^4(2x - ld_i)\right)}{((2x - ld_i)^2 + z^2)^6}\right) \tag{3-58}$$

$$\frac{\partial \mathbf{F_{fx}}}{\partial \mathbf{x}} = -\frac{\mathbf{36\pi\, fd^3 \chi_f lt^2}}{\mathbf{\mu_0(\chi_f + 3)}} \mathbf{B_{lr}^2}\left(\frac{\mathbf{ld_o^4(24z^2(ld_o - 2x)^2 + 2z^4)}}{\mathbf{((ld_o - 2x)^2 + z^2)^6}} - \frac{\mathbf{ld_i^4(24z^2(ld_i - 2x)^2 + 2z^4)}}{\mathbf{((ld_i - 2x)^2 + z^2)^6}} + \frac{\mathbf{6ld_i^4(4ld_i - 8x)\left(4z^2(ld_i - 2x)^3 + z^4(ld_i - 2x)\right)}}{\mathbf{((ld_i - 2x)^2 + z^2)^7}} - \frac{\mathbf{6ld_o^4(4ld_o - 8x)\left(4z^2(ld_o - 2x)^3 + z^4(ld_o - 2x)\right)}}{\mathbf{((ld_o - 2x)^2 + z^2)^7}}\right)$$

$$\frac{\partial \mathbf{F_{fx}}}{\partial \mathbf{x}} = -\frac{\mathbf{36\pi\, fd^3 \chi_f lt^2}}{\mathbf{\mu_0(\chi_f + 3)}} \mathbf{B_{lr}^2}\left(\frac{\mathbf{ld_o^4(24fg^2(ld_o - 2fx)^2 + 2fg^4)}}{\mathbf{((ld_o - 2fx)^2 + fg^2)^6}} - \frac{\mathbf{ld_i^4(24fg^2(ld_i - 2fx)^2 + 2fg^4)}}{\mathbf{((ld_i - 2fx)^2 + fg^2)^6}} + \frac{\mathbf{6ld_i^4(4ld_i - 8fx)\left(4fg^2(ld_i - 2fx)^3 + fg^4(ld_i - 2fx)\right)}}{\mathbf{((ld_i - 2fx)^2 + fg^2)^7}} - \frac{\mathbf{6ld_o^4(4ld_o - 8fx)\left(4fg^2(ld_o - 2fx)^3 + fg^4(ld_o - 2fx)\right)}}{\mathbf{((ld_o - 2fx)^2 + fg^2)^7}}\right)$$

With z-directional forces and x directional forces computed for our bearing, the next step is the computation of stiffness. This stiffness will tell us the force that can be applied by the reluctance machine to the rotor assembly in the x direction and the extent of free z-directional forces as well.

3.5 Stiffness and Stability Analysis

The rate at which our z-directional force changes is an indication of the extent of stability in our bearing assembly and provides a measure for stiffness. With a solution available for the diamagnetic stabilizing force, $\vec{\mathrm{F}}_\mathrm{d}$, and the lifter force, $\vec{\mathrm{F}}_\mathrm{f}$, this stiffness can be represented as a combined contribution, $\vec{\mathrm{K}} = \vec{\mathrm{K}}_\mathrm{d} + \vec{\mathrm{K}}_\mathrm{f}$. Interestingly, this relates very closely to our Laplacian which is given as the following: $\nabla^2\mathrm{E}_\mathrm{p} = \nabla \cdot \nabla\mathrm{E}_\mathrm{p} = -\nabla \cdot \left(-\nabla\mathrm{E}_\mathrm{p}\right) = -\nabla \cdot \mathrm{F}$.

In our earlier treatment of levitation forces, we focused on the z-directional contributions. The z-directional stiffness can be represented by the following formulation: $\mathrm{K}_\mathrm{z} = -\nabla \cdot \mathrm{F}_\mathrm{z} = -\partial\mathrm{F}_\mathrm{z}/\,\partial\mathrm{z}$. These derivative values have been computed in the previous section and so a final equation for our total stiffness is presented in Equation (3-59). Note that we assume that the remanent magnetization of both the lifter magnet and the stabilizer magnets is the same ($\mathrm{B}_\mathrm{rem} = \mathrm{B}_\mathrm{mr} = \mathrm{B}_\mathrm{lr}$).

$$\mathrm{K}_\mathrm{z} = \nabla^2\mathrm{E}_\mathrm{p} = \mathrm{K}_\mathrm{dz} + \mathrm{K}_\mathrm{fz} = -\nabla \cdot \mathrm{F}_\mathrm{dz} - \nabla \cdot \mathrm{F}_\mathrm{fz} \tag{3-59}$$

$$\mathrm{K}_\mathrm{z} = -\frac{\partial \mathrm{F}_\mathrm{dz}}{\partial \mathrm{z}} - \frac{\partial \mathrm{F}_\mathrm{fz}}{\partial \mathrm{z}}$$

$$\mathbf{K_z} = -\left\{-\frac{48\pi\,\mathbf{dd^2dt^3md^2mt}\,\chi_\mathrm{d}}{\mu_0((8\mathbf{dt^2}-\mathbf{dd^2})(\chi_\mathrm{d}+1)+\mathbf{dd^2}))}\mathbf{B_{rem}}\left[\left(\frac{1}{(\mathbf{md^2}+4\mathbf{dg^2})^{\frac{3}{2}}}+\frac{1}{(\mathbf{md^2}+4(\mathbf{mg}-\mathbf{dg})^2)^{\frac{3}{2}}}\right)\left(\frac{1}{(\mathbf{md^2}+4\mathbf{dg^2})^{\frac{5}{2}}}+\right.\right.\right.$$
$$\left.\frac{1}{(\mathbf{md^2}+4(\mathbf{mg}-\mathbf{dg})^2)^{\frac{5}{2}}}-\frac{20\mathbf{dg^2}}{(\mathbf{md^2}+4\mathbf{dg^2})^{\frac{7}{2}}}-\frac{20(\mathbf{mg}-\mathbf{dg})^2}{(\mathbf{md^2}+4(\mathbf{mg}-\mathbf{dg})^2)^{\frac{7}{2}}}\right)+$$
$$\left.\left.\left(\frac{12(\mathbf{mg}-\mathbf{dg})}{(\mathbf{md^2}+4(\mathbf{mg}-\mathbf{dg})^2)^{\frac{5}{2}}}-\frac{12\mathbf{dg}}{(\mathbf{md^2}+4\mathbf{dg^2})^{\frac{5}{2}}}\right)\left(\frac{\mathbf{dg}}{(\mathbf{md^2}+4\mathbf{dg^2})^{\frac{5}{2}}}-\frac{\mathbf{mg}-\mathbf{dg}}{(\mathbf{md^2}+4(\mathbf{mg}-\mathbf{dg})^2)^{\frac{5}{2}}}\right)\right]\right\}-\left\{-\frac{24\pi\,\mathbf{fd^3}\chi_\mathrm{f}\mathbf{lt^2}}{\mu_0(\chi_\mathrm{f}+3)}\mathbf{B_{rem}^2}\cdot\right.$$
$$\left(\frac{32\,\mathbf{ld_i^4fg^2}}{(\mathbf{ld_i^2}+4\mathbf{fg^2})^5}+\frac{32\,\mathbf{ld_o^4fg^2}}{(\mathbf{ld_o^2}+4\mathbf{fg^2})^5}-\frac{\mathbf{ld_o^4}}{(\mathbf{ld_o^2}+4\mathbf{fg^2})^4}-\frac{\mathbf{ld_i^4}}{(\mathbf{ld_i^2}+4\mathbf{fg^2})^4}+\frac{\mathbf{ld_i^2ld_o^2}}{(\mathbf{ld_i^2}+4\mathbf{fg^2})^{\frac{3}{2}}(\mathbf{ld_o^2}+4\mathbf{fg^2})^{\frac{5}{2}}}+\right.$$
$$\left.\left.\frac{\mathbf{ld_i^2ld_o^2}}{(\mathbf{ld_i^2}+4\mathbf{fg^2})^{\frac{5}{2}}(\mathbf{ld_o^2}+4\mathbf{fg^2})^{\frac{3}{2}}}-\frac{20\,\mathbf{ld_i^2ld_o^2fg^2}}{(\mathbf{ld_i^2}+4\mathbf{fg^2})^{\frac{3}{2}}(\mathbf{ld_o^2}+4\mathbf{fg^2})^{\frac{7}{2}}}-\frac{20\,\mathbf{ld_i^2ld_o^2fg^2}}{(\mathbf{ld_i^2}+4\mathbf{fg^2})^{\frac{7}{2}}(\mathbf{ld_o^2}+4\mathbf{fg^2})^{\frac{3}{2}}}-\frac{24\,\mathbf{ld_i^2ld_o^2fg^2}}{(\mathbf{ld_i^2}+4\mathbf{fg^2})^{\frac{5}{2}}(\mathbf{ld_o^2}+4\mathbf{fg^2})^{\frac{5}{2}}}\right)\right\}$$

As mentioned earlier, stiffness in the radial direction is dominated by the force of our lifter with little contribution from the stabilizing machine. This stiffness is thus given by the expression: $K_x = -\nabla \cdot F_x = -\partial F_x / \partial x$. Equation (3-60) provides an expanded expression.

$$K_x = \nabla^2 E_p = K_{fx} = -\nabla \cdot F_{fx} = -\frac{\partial F_{fx}}{\partial x} \tag{3-60}$$

$$\mathbf{K_x = -\frac{\partial F_{fx}}{\partial x} = \frac{36\pi\, fd^3 \chi_f lt^2}{\mu_0(\chi_f + 3)} B_{lr}^2 \left(\frac{ld_o^4(24fg^2(ld_o - 2fx)^2 + 2fg^4)}{((ld_o - 2fx)^2 + fg^2)^6} - \frac{ld_i^4(24fg^2(ld_i - 2fx)^2 + 2fg^4)}{((ld_i - 2fx)^2 + fg^2)^6} + \frac{6ld_i^4(4ld_i - 8fx)\left(4fg^2(ld_i - 2fx)^3 + fg^4(ld_i - 2fx)\right)}{((ld_i - 2fx)^2 + fg^2)^7} - \frac{6ld_o^4(4ld_o - 8fx)\left(4fg^2(ld_o - 2fx)^3 + fg^4(ld_o - 2fx)\right)}{((ld_o - 2fx)^2 + fg^2)^7} \right)}$$

The x directional stiffness can be used to estimate the current and voltage applied to a driving reluctance machine. We note that the radial force generated by a particular pole of the reluctance machine can be tuned to the maximum allowable x displacement of the rotor. This displacement is closely linked to the unbalanced magnetic pull (UMP).

3.6 Electrical Machine Analysis

From our computation of stiffness, K_x, we can, thus, estimate the machine driving current for a single pole pair under stall conditions where the rotor is fully aligned with the pole. This would likely be the maximum applied radial force on the rotor. For this we consider the geometry shown in Figure 3-10. Upon displacement, a spherical floater is likely to produce the least wobble inducing torque (rotation about the radial axis as opposed to the z axis) on the machine. However, this spherical floater can potentially be replaced completely by the rotor of the reluctance machine. For the purposes of this analysis we assume that this is the case and that the rotor

poles are small enough that the effective pull applied by the lifter is equivalent to that applied to a sphere.

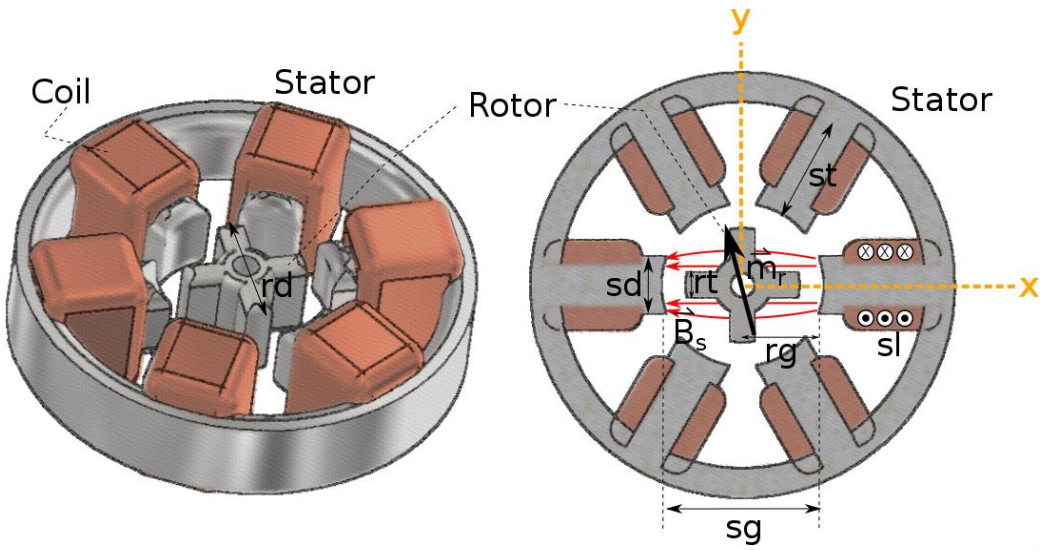

Figure 3-10: The geometry of a 6 stator pole 4 rotor pole reluctance machine. The operating assumption is that the applied force on the rotor from the stator is acting such that the entire rotor assembly translates along the radial direction (rather than twisting), i.e. the rotor also take the role of the floater.

Once again we can follow a similar procedure as was done for the floater and lifter combination. With the spherical assumption and using the prior formulation from Equation (3-42), the magnetic moment, $\vec{m}_r$ of the 4 pole rotor may be described as shown in Equation (3-61). In truth, a spherical representation for the rotor will not experience a torque from the reluctance machine. In this representation we assume a rotor diameter, rd, an airgap between rotor and stator pole of rg, a field generated by the stator pole of $\vec{B}_s$ and a rotor magnetic susceptibility of χ_r.

$$\vec{\mathbf{m}}_\mathbf{r} = -\frac{\boldsymbol{\pi}\,\mathbf{rd}^3\boldsymbol{\chi}_\mathbf{r}}{\boldsymbol{\mu}_\mathbf{0}(\boldsymbol{\chi}_\mathbf{r}+\mathbf{3})}\cdot\vec{\mathbf{B}}_\mathbf{s} \tag{3-61}$$

Two field contributors will be present in the x-direction, one from the lifter (B_{lx}) and one from the motor stator pole pair (B_{sx}). The combined x-directional field is a superposition of these fields. Since B_{lx} has already been computed, focus is given to B_{sx} in Equation (3-62). Unlike the lifter and stabilizing machine, the field source here is a stator coil current, sI. It is, however, a simple matter to tailor our earlier computation of two magnet stabilizer field (Equation (3-35)) to a radial field from a coil. The remnant field can be represented as a solenoid field given by the following equation: $B_{sr} = \mu_0(\chi_s + 1)sI/st$. The stator poles have diameter sd, are separated by a distance sg and a pole length st. The material making up the pole has susceptibility χ_s. Note that we assume some displacement of the rotor $x = rg$ and that the z position of the rotor is aligned with that of the stator. This z alignment is a reasonable assumption considering that the stator is likely to force alignment towards minimum reluctance and add stiffness in the z direction when energized.

$$B_{sx} = \frac{sd^2 st}{(sd^2 + 4x^2)^{\frac{3}{2}}} B_{sr} + \frac{sd^2 st}{(sd^2 + 4\,(sg - x)^2)^{\frac{3}{2}}} B_{sr} \tag{3-62}$$

$$\mathbf{B_{sx} = \mu_0(\chi_s + 1)sd^2 sI\left(\frac{1}{(sd^2 + 4x^2)^{\frac{3}{2}}} + \frac{1}{(sd^2 + 4\,(sg - x)^2)^{\frac{3}{2}}}\right)}$$

$$\mathbf{B_{sx} = \mu_0(\chi_s + 1)sd^2 sI\left(\frac{1}{(sd^2 + 4rg^2)^{\frac{3}{2}}} + \frac{1}{(sd^2 + 4\,(sg - rg)^2)^{\frac{3}{2}}}\right)}$$

From this field the added x directional force, $F_r = F_{rx}$ follows as shown in Equation (3-63). Once again, since the x position, $x = rg$ (rotor equation) and $x = fx$ (lifter equation) are relative to different reference points some care must be taken to take this force equation and unify it.

$$F_{rx} = \nabla\left(\vec{m}_r \cdot \vec{B}_s\right) = \frac{\pi\, rd^3 \chi_r}{\mu_0(\chi_r + 3)} \frac{\partial B_{sx}^2}{\partial x} = \frac{\pi\, rd^3 \chi_r}{\mu_0(\chi_r + 3)} 2B_{sx} \frac{\partial B_{sx}}{\partial x} \tag{3-63}$$

$$\mathbf{F_{rx} = -\frac{2\pi\, rd^3 \chi_r(\chi_s + 1) sd^2 sI}{(\chi_r + 3)}\left(\frac{1}{(sd^2 + 4x^2)^{\frac{3}{2}}} + \frac{1}{(sd^2 + 4\,(sg - x)^2)^{\frac{3}{2}}}\right)\left(\frac{12x}{(sd^2 + 4x^2)^{\frac{5}{2}}}\right)}$$

$$\mathbf{F_{rx} = -\frac{2\pi\, rd^3 \chi_r(\chi_s + 1) sd^2 sI}{(\chi_r + 3)}\left(\frac{1}{(sd^2 + 4rg^2)^{\frac{3}{2}}} + \frac{1}{(sd^2 + 4\,(sg - rg)^2)^{\frac{3}{2}}}\right)\left(\frac{12rg}{(sd^2 + 4rg^2)^{\frac{5}{2}}}\right)}$$

The maximum current, sI, should be chosen to meet some maximum tolerance in radially directed position change. For instance, supposing that our maximum displacement in the radial direction is given by some value $x = fx$, the force (F_{fx}) resulting from x directional stiffness (K_x) must be balanced by the force applied through the stator poles (F_{rx}) such that: $F_{rx} = F_{fx}$. The maximum displacement is governed by the geometry and possibility of collision. Equation (3-64) demonstrates a solution for sI given this understanding. The reference point of displacement fx is taken relative to the static equilibrium position in the xy plane. This means that our position $x = rg$ must be adjusted from a stator reference to $x = rg - fx$. Only the forces associated with the ring shaped lifter are considered for F_{fx}.

$$\mathbf{sI = \frac{3\, fd^3 lt^2 \chi_f(\chi_r+3)}{2\mu_0\, rd^3 sd^2 \chi_r(\chi_f+3)(\chi_s+1)} B_{lr}^2 \left(\frac{ld_o^4\left(4fg^2(2fx-ld_o)^3+fg^4(2fx-ld_o)\right)}{((2fx-ld_o)^2+fg^2)^6} - \frac{ld_i^4\left(4fg^2(2fx-ld_i)^3+fg^4(2fx-ld_i)\right)}{((2fx-ld_i)^2+fg^2)^6}\right)\left(\frac{(sd^2+4rg^2)^4(sd^2+4\,(sg-rg)^2)^{\frac{3}{2}}}{rg(sd^2+4\,(sg-rg)^2)^{\frac{3}{2}}+rg(sd^2+4rg^2)^{\frac{3}{2}}}\right)} \tag{3-64}$$

With this stator current known, one final computation is needed. We note that, in practice, to achieve the indicated stator current requires stator windings such that $sI = n \cdot I$, where n is the number of turns and I is the current sinked from our power

supply. While typically, a three-phase supply is generally available, a simple way to generate such a supply is to drive a 3 phase brushless motor from a single phase machine – this technique has been employed in this study. In small scale, the voltage and current generated by such a setup can be quite low so care must be taken to ensure that the coil resistance (R) of the system is sufficiently low as well for some given voltage, ε. Given the voltage output and current sourcing capacity of the system is known and the per meter resistance (r) of the wire also known, it is possible to compute the number of turns (n) required in our setup to achieve the current sI as shown in the Equation (3-65). Note that the circumference of the pole is given as C.

$$\varepsilon = IR \quad \Rightarrow \varepsilon = I\,(n\,r\,C) \quad \Rightarrow \varepsilon = I\left(n\,r\,2\pi\left(\frac{sd}{2}\right)\right) \tag{3-65}$$

$$\boldsymbol{n = \frac{\varepsilon}{\pi\, sd\, I\, r}}$$

At this stage, it is worth mentioning that one particular stabilizing force has not been considered thus far in terms of stiffness, namely gyroscopic stabilization. We note that such stabilization has some considerations similar to the Levitron problem mentioned earlier in this study (see Section 2.2.6). The primary contribution of stiffness here would be to reduce the effect of disc wobble (rotation along radial axis). Given that some distance must exist between the floater and the diamagnetic stabilizing machinery, the stabilizing force can significantly improve stiffness of a levitating rotor assembly and hold it parallel to the z-directional axis of rotation. For the purposes of this study, gyroscopically induced stiffness has been neglected.

There is one final consideration beyond the magnetic moment, B-field, force, stiffness and current that has yet to be addressed, namely, the loss resulting from rotor assembly rotation. These will be addressed further into this study.

3.7 Summary and Final Remarks

This chapter discussed theoretical considerations of the diamagnetic bearing prototype introduced by this study in the prior chapter. The chapter began with discussion and implications of Earnshaw's theory. An approach to calculating magnetic fields was used to form an analytical frame work for analysing the role of the different diamagnetic bearing components. Under a range of simplifying assumptions, including uniform fields and axial symmetries, expressions for stabilizing machinery, lifter-floater and electrical machine parameters were derived. These provide a first step towards examining and evaluating diamagnetic bearing parameters with somewhat greater ease. Subsequent chapters aim to elaborate on this foundation and introduce a method of reducing power loss further by way of low loss nano-materials. These materials will be used for the electrical machine. Rotational losses, in the three diamagnetic bearing components will be analysed and compared with other bearing types and electrical machine core materials. Eddy currents and hysteresis effects will be examined and used as a means of determining if the thesis presented in this study holds.

4 Nano-material Synthesis for Low Loss Electrical Machines

Iron (II, III) oxide, more commonly known as magnetite (Fe_3O_4) is a highly magnetic, naturally occurring mineral. Magnetite particles along with a wider class of magnetic (ferromagnetic or ferrimagnetic) particles in the nanometre scale range begin to exhibit superparamagnetic (SP) properties [91]. In this chapter, we look at a co-precipitation route to the synthesis of superparamagnetic Fe_3O_4 magnetic nano-particles (MNPs) and explore their potential value as a material for producing high quality geometrically unconstrained bulk ferrites via microwave sintering. The goal here is to develop a low loss ferrite for use in the reluctance machine of our previously discussed diamagnetic bearing. Furthermore, the ability to manufacture customized motors using potentially low cost casting and microwave sintering techniques is an extremely attractive small scale rapid prototyping approach for a wide range of ceramic and metal nano-scale powder experiments. The typical cost of the 85 [mm] diameter (10 [mm] thick) motor shown in our previous diamagnetic bearing assembly, built custom from laminations, has been quoted by UK manufactures to fall between £517 − £613 [92], [93] for a single item. Thus, there is significant advantage for the small-scale experimentalist working with electrical machines to make use of sintering as an alternative. The author of this study noted that the cost of building an entire experimental setup (and associated materials) to complete the sintering process is roughly only twice the cost of a single custom manufactured motor.

This chapter begins with a general overview of MNPs and their applications. This is followed by a more detailed look at and overview of existing work with soft magnetic materials and ferrites. The reason for the use of nano-particles and ferrites will be elaborated and the requirements that the synthesis approach must fulfil for bulk ferrite production provided. These requirements will be used to eliminate a range of the existing synthesis techniques. Ultimately, it will be noted that co-precipitation approaches are amicable to the purpose of ferrite production. A discussion of the specific control variables (e.g. temperature, base, pH, stoichiometry, mixing rates, etc.) and properties of the produced magnetite (Fe_3O_4) MNPs will follow. This chapter will provide a description of the specific experimental synthesis technique used during this study. While not fully implemented, a microwave sintering approach to taking these synthesized particles from powdered MNPs into bulk nano-structured ferrite material will be presented in the subsequent chapter. A later chapter will continue and discuss measurement and analysis of the produced MNPs. The study will return to our diamagnetic prototype bearing to discuss the implications of nano-structured ferrites as well as other component elements towards rotational power loss as well at this later stage.

4.1 The Big Picture: MNPs and Soft Magnetic Materials

Traditionally, MNPs have seen use mostly in biomedical applications [94]. These uses range from contrast enhancement in magnetic resonance imaging (MRI), targeted drug delivery, cell labelling, cell probing, magnetic separation and targeted therapeutic heating. The low toxicity of Fe_3O_4 has made them particularly attractive MNPs for biological applications. Outside the biomedical paradigm, focus has been on data storage applications [95]. Utilization of MNPs remains somewhat less well researched in other areas. Despite this, a wide range of alternative applications have been explored [5], [53], [96], [97]. These applications include the use of ferrofluids. Ferrofluids have been used for dynamic sealing of rotating shafts, heat dissipation (e.g. in loud speakers), passive magnetic bearings, magnetic doping for liquid crystal

displays, tuneable optical devices (e.g. filters, switches, gratings, limiters), microfluidics, micro-robotics and micromechanical sensors.

4.1.1 Soft Magnetic Materials and MNPs

High quality soft magnetic materials are characterized by low iron losses, namely, low hysteresis and eddy current losses. It is the presence of these properties that makes the use of Fe_3O_4 MNPs for the development of soft magnetic materials [98] another alternative application – this is particularly true considering the previous discussion of a high speed reluctance machine utilized in earlier presented diamagnetic bearing (Section 2.5). Fe_3O_4 MNPs have seen less exploration as a bulk ferrite material. The general utilization of MNPs for magnetic materials have partly focused on alternative nano-materials for the production of hard magnetic materials – one such example is the nanocomposite exchange-spring magnet [98], [99]. Among soft materials work has mostly focused on micro-structured silicon, nickel and cobalt steels [100] and similarly structured iron oxide based ceramics (e.g. Mn-Zn, Ni-Zn ferrites) – obviously none of these exhibit intentional nano-structure. More recently, focus has shifted to the use of amorphous (bulk metallic glass - BMG) materials (i.e. materials that having no long range crystalline ordering) – Metglas is one such amorphous material. While amorphous materials aren't nano-structured, a number of BMG nano-materials have also been developed [101]. This has been primarily to affect an increase in saturation magnetization [95]. Among these are metallic glass systems such as Finemet [102], Nanoperm [103], Hitperm and Vitroperm [104] alloys. In addition to Iron (Fe), most such nano-structured alloys utilize some two phase (nanocrystal, amorphous) combination of the following typical alloying materials: Silicon (Si), Boron (B), Niobium (Nb), Copper (Cu), Hafnium (Hf), Zirconium (Zr) – see [95].

Generally, both micro-structured steels and amorphous/nano-crystalline BMG alloys come with a range of excellent properties and are in some respects superior to existing composite iron-oxide based ceramic ferrites (e.g. iron oxide + Mn-Zn, Ni-

Zn). Recently, this has motivated an increasing interest in nano-structured ferrites as well [105], [106]. And a range of composite oxide forms have been explored. Often these ferrites are categorized by crystalline structure, i.e. spinels, garnets and hexaferrites, with spinel structures being the most stable choice for soft ferrite production and hence the focus of this chapter.

Table 4-1: Properties of soft magnetic materials averaged across select literature. The following sources were used for this table: [4], [5], [100], [102], [103], [107]–[144]. The variables in the column headings are defined as follows: Resistivity (ρ_r), Initial Relative Permeability (μ_{ri}), Coercivity ($\boldsymbol{H_C}$), Saturation Flux Density ($\boldsymbol{B_s}$), Remanent Flux Density ($\boldsymbol{B_r}$), Saturation Magnetostriction (λ_S), Grain Size (D), Density (ρ_d), Curie Temperature (T_C). Note that where initial permeabilities aren't known the maximum permeability is divided by a factor of 5 to provide a rough estimate. Also note that grain size would not be a relevant parameter for amorphous metglas as such materials are unlikely to have crystalline structure.

Material	ρ_r [Ω·m]	μ_{ri} []	H_C [A/m]	B_s [T]	B_r [T]	λ_S [ppm]	D [nm]	ρ_d^{cgs} [g/cm^3]	T_C [°C]	Typical Form	Cost
Iron Powder *(Fe)*	100	56.5	488.7	1.10	0.30	High	4000	7.20	770	Resin + Powder	Very Low
Electrical Steel *(Si-Fe)*	2.60 x 10^{-7}	1825	33.51	1.76	1.31	0.91	2500	7.62	745	Laminate 100-350 [μm]	Low – Medium
Supermendur *(Co-Fe-V)*	5.73 x 10^{-7}	1284	44.97	2.19	2.10	51.7	35000	8.04	918	Laminate 100-350 [μm]	Very High
Permalloy (Ni-Fe)	6.08 x 10^{-7}	18714	3.935	1.15	0.73	6.25	120000	8.56	455	Laminate/Tape 100-350 [μm]	High
Finemet/Nanoperm *(Fe-Si-B-Cu-Nb)*	1.13 x 10^{-6}	38833	2.000	1.23	0.81	0.97	10	7.38	585	Ribbon/Tape 18-25 [μm]	High – Very High
Metglas *(Cr-Fe-Si-C-B-Ni)*	1.30 x 10^{-6}	19883	8.489	1.39	1.08	27.0	???	7.36	392	Ribbon/Tape 25-30 [μm]	High – Very High
Ferrite *(Mn-Zn)*	4.83	2140	21.86	0.39	0.15	1.93	9000	4.69	203	Sintered Powder	Low
Ferrite *(Ni-Zn)*	35.3 x 10^3	490.6	125.3	0.25	0.15	9.27	7850	4.84	308	Sintered Powder	Low
Magnetite *(Fe_3O_4)*	10^{-2}	5.7	7243	0.22	0.13	15.9	109	5.19	585	Sintered Powder	Low

Despite these recent efforts, BMG and iron alloys remain at the forefront of commercial development. We see a clear demonstration of their superiority over

standard commercial ferrites in Table 4-1. The table provides a baseline study of existing materials and their magnetic properties to establish a metric for comparing and evaluating the applicability of bulk Fe_3O_4 MNPs as a soft magnetic material. We note that both steels and BMG's exhibit superior magnetic saturation performance. Likewise, BMG's have much lower coercivities, high Curie temperatures and in some cases, very low magnetostriction as well. The natural question then arises: Given their inferiority, what value is there in returning to an investigation of ceramics such as Fe_3O_4? And what benefit is gained from the use of Fe_3O_4 MNPs?

4.1.1 Why Ferrites and Fe_3O_4 MNPs?

A number of problems exist with non-ferrites. For instance, the utilization of steels (Si-Fe, Co-Fe, Ni-Fe) is typically limited to laminations ($100 - 350$ [μm] thick) designed to reduce eddy currents – these eddy currents are a result of low resistivity ($\sim 10^{-8} - 10^{-7}$ [$\Omega \cdot$ m]). With a lower bound on lamination thickness, excessive core losses can result at operating frequencies too much beyond the typical $50/60$ [Hz] of grid level power systems. As we see, the production of ribbons/tapes, especially with BMGs (finemet, nanoperm, metglas), provide a much thinner ($18 - 30$ [μm]) laminating layer and lower coercive fields resulting in much lower loss, but at much higher expense.

Both, laminated steels and ribbons, in addition to their low resistivities, also have strong topological restrictions limiting their uses primarily to stacked or wound magnetic cores. These topological restrictions in laminations are a result of hot/cold rolling techniques required for cost effectiveness [109]. For magnetic BMGs these limitations are a result of the very rapid cooling [101] rates ($104 - 106$ [°K/s]) required to produce an amorphous starting material. Such cooling rates are achievable by melt-spinning and similar techniques, however, these technique have challenges in the manufacture of anything but thin magnetic materials [145].

It is, thus, in applications involving greater topological freedom, high resistivity, low eddy current loss, flat frequency response and low cost manufacture that ferrites (and powders) become truly attractive [5]. Furthermore, ferrites offer high hardness, corrosion resistance, machinability and excellent chemical stability compared to metals [5], [95], [105], [109]. The controllable composition of ferrites with the flexibility of sintering [146] processes allows for tuneable properties and the potential for multi-layer fabrication [106] – something that would likely be cost prohibitive for novel topologies utilizing laminations or tapes.

The nano-structure of some BMG's, however, has proven to be critical in reducing the coercivity and hysteresis loss of magnetic materials. Reductions in hysteresis loss, similar to those observed in BMG's have also been evidenced by a range of iron-oxide based MNPs [105], [106]. It is this evidenced observation, along with the other advantages (e.g. low eddy current loss) of ferrites, that motivates another look at soft MNPs. But the question arises as to the choice of MNP. Most commercial soft ferrites are sintered mixtures of iron oxide plus some combination of Manganese (Mn), Zinc (Zn) or Nickel (Ni). Given that iron-oxide powders form a key component of these ferrites they are likely to be an essential contributor to bulk material properties of any MNP-based material. It is with this in mind that an exploration of Fe_3O_4 (iron (II, II) oxide), as a bulk ferrite, forms an important step towards understanding other ferrite mixtures. Furthermore, it is noted that a key approach to producing bulk ferrites from powders relies on sintering [146], [147]. Traditional sintering approach can lead to grain growth when heating rates are slow. The utilization of newer approaches involving rapid microwave sintering can preserve the nano-crystalline structure of MNPs [146]–[148]. It is noted that Fe_3O_4 is a good susceptor for microwaves utilized in such sintering approaches. Furthermore, in a reducing environment resulting undesirable oxide states (e.g. maghemite) can be converted to magnetite with relative ease, making the need to preserve purity a lesser concern during synthesis. It is these considerations that add further value to the investigation of Fe_3O_4 as a bulk ferrite material.

4.2 Requirements for Synthesized MNPs

In order to test the viability of Fe_3O_4 MNPs as potential low loss materials for ferrites requires selection of synthesis method. There are a number of approaches available for the synthesis of Fe_3O_4 soft MNPs. Of these, top-down approaches take a large material and break it down into smaller nano-structured components. Photolithography and high energy milling are two examples [95]. Unlike top-down approaches, bottom-up synthesis techniques start at small scales and exploit self-assembly. As a result of their lower cost, bottom-up approaches have been, and are, the preferred option for this study. They include [95], [149]–[151]: colloidal synthesis (e.g. organometallic, sol-gel, polyols), high temperature synthesis (e.g. solvothermal, thermal decomposition/thermolysis, aerosol/vapour), bacterial synthesis, hydrolysis & co-precipitation synthesis techniques. In addition, modifications can be made to some of these synthesis methods utilizing: sonochemical synthesis, flow injection synthesis and surface/surfactant mediated synthesis techniques.

Selecting the appropriate synthesis approach is based on a need to produce particles with reasonable magnetic saturation and very low hysteresis losses. The choice of synthesis method should be scalable and cheap, produce small particles and pure oxides that lead to ultra-low coercivity. Elaborating on this, the discussion below considers these criteria in greater depth.

4.2.1 Be fast, easy, cheap and scalable

For the purposes of this study, the synthesis technique selected should allow for a large number of repeat trials and case studies (> 30) at low cost - the goal being to facilitate the trial and testing of a variety of control parameters and their effect on hysteresis loss. Further the potential for high volume production must exist – this is needed for any conversation about bulk ferrite applications – a potential high volume industrial solution is presented at the end of this chapter. A production quantity of between 12 [g] and 50 [g] per trial is desirable for laboratory scale investigations.

Techniques involving multi-step, high temperature and pressure processes must be avoided so as to make safe use of existing equipment and to reduce expenses.

4.2.2 Be able to produce well controlled & small particles

Below a certain critical size range, Fe_3O_4 MNPs exhibit superparamagnetic (SP) behaviour of which zero coercivity is symptomatic – low coercivity is a trait that's highly desirable in the soft magnetic materials produced in this study. Both experiment and theory suggest that magnetite particles exhibit single domain (SD) behaviour below the size range of $27 - 76$ [nm] and SP behaviour below a 25 [nm] size [152]–[154]. It is thus essential that the synthesis procedure produce particles that have a size range that falls below this limit. As sintering techniques needed for the production of bulk materials can enlarge grain size, a smaller particle diameter averaged at 10 [nm] is desirable. A narrow size distribution would be ideal as well, however, such a narrow distribution is not necessary as long as particle size is bounded sufficiently below the SP size limit - in this study, within 2.5 [nm] standard deviation from our average desired diameter would be sufficient. This is based on an understanding that the sintering approach (microwave sintering) has been shown to enlarge grain size by about 2 times [155] – a particle of size 12.5 [nm] could thus undergo growth to the edge of the SP size limit of 25 [nm]. A discussion of the specific sintering technique will follow in later chapters.

4.2.3 Produce particles with low agglomeration & oxidation

The agglomeration of particles resulting from Van Der Waals attractions leads to increased crystal growth at nucleation sites [95], [149]. Nucleation sites are those locations where a state change to solid first occurs. Nucleation sites close together can lead to agglomeration of particles. Agglomeration, in turn, can lead to poor shape control and result in higher anisotropy as well as increased particle sizes. While a great deal of shape control is not needed, agglomeration should be limited during synthesis, to some degree, to restrict particle size and shape related anisotropy. One

thing to note with relation to agglomeration is that smaller particles are likely to produce agglomerations that are mesoporous in nature [156]. The higher surface area of these mesoporous particles will be accompanied by higher oxidation effects than particles of more spherical shapes even in the presence of protective coatings (depending on the nature of the protective coating, of-course). Small particles will also exhibit core shell structures where by different oxides will form shells around a central core of magnetite – these shells will normally take the form of maghemite (γ-Fe_2O_3) and hematite (α-Fe_2O_3). This core-shell formation should be limited, if possible. However, this is not critical as reversal of this oxidation is possible in the correct sintering environment.

4.2.4 Produce particles with high saturation, low coercivity and remanence

Significant evidence has shown that amorphous materials exhibit lower anisotropy than crystalline structures [5], [95]. And amorphous materials are typically characterized by lower coercivity. Thus, synthesis approaches that favour such production are more desirable. However, crystallinity is associated with increasing magnetic saturation values [157]. Thus, in practice, a balance must exist between the high crystallinity/anisotropy (high permeability) and high isotropy (lower coercivity). As such, a two phase controlled synthesis is the most desirable for soft-materials. The presence of crystalline formations also makes the material amicable to X-Ray Diffraction (XRD) based analysis at the same time as increasing magnetic saturation. One thing to note is that the resultant oxide shell formations can lead to a shift in the hysteresis curve and result in coercivity values dependant on the direction of change of the applied field (i.e. exchange bias).

Given these requirements, it should be noted that for the particularly large number of case studies performed, the need for size distribution, shape and oxidation effects take a back seat to scalability, cost and particle size. Furthermore, as noted earlier,

oxidation effects can be reversed during subsequent sintering during bulk ferrite production.

4.3 Comparing and Selecting Synthesis Route

Synthesis approaches have focused on the production of Fe_3O_4 MNPs with uniform dispersion (monodisperse) and narrow size distributions. Some synthesis routes produce a precursor oxide (e.g. maghemite (γ-Fe_2O_3), hematite (α-Fe_2O_3)) that then undergoes treatment to form the desired Fe_3O_4 particles. Furthermore, synthesis routes may utilize other iron pre-cursors as a starting step for magnetite synthesis. Regardless of the nature of the precursor, controllability of particle size and shape has been a significant concern and point of focus in the community. Higher controllability involves greater separation and rate control of crystal nucleation and crystal growth – short nucleation duration and slow growth being ideal for monodispersion (uniform size) and large crystal formation.

Among colloidal approaches, organometallic synthesis routes [158] focus precisely on this separation and are known for their production of highly regularized monodispersed crystals at low temperatures (via decomposition of organometallic precursors) – particles fall in a size range of $5 - 13$ [nm]. Unfortunately, due to the air-sensitive nature of their reactants, reactions must be performed in carefully controlled environments. These reactions also produce very small amounts of material thus limiting scalability [95]. Within this same group, sol-gel techniques utilize a colloidal solution that evolves into gels that then undergo long duration heat treatment (annealing) to produce Fe_3O_4 dense ceramics (size: $18 - 25$ [nm]) from, for instance, maghemite (γ-Fe_2O_3). Like organometallic synthesis, high purity, uniform particles can be produced, but only at high cost in small quantities [95], [150], [159]. Polyols offer alternative (not water) solvents for reactions at higher temperatures and serve as a reducing agent (low oxidation) while also preventing agglomeration to produce narrow size distributions. The higher reaction temperature

is also likely to encourage crystal growth and increased magnetic saturation [150]. While an excellent technique ($6-7$ [nm] particle size) for synthesis [160], the higher temperature reaction combined with the use of toxic ethylene-based organic compounds is the primary reason why this technique is undesirable.

Alternative to colloidal approaches, are high temperature processes. For instance, solvothermal techniques rely on high pressure and high temperature (boiling point) solvent reactions [95] to control the relative rate of nucleation v.s. crystal growth [150]. The resulting high temperatures lead to accelerated crystal growth at narrow size distributions [95] with the added benefit of shape control [149], [151] and with particle sizes [161] of roughly $8-11$ [nm]. Unfortunately, the requirement for closed system autoclaves are likely accompanied with higher costs and scalability issues. Consequently other high temperature routes such as thermal decomposition or thermolysis have similar benefits with similar size [162] distributions (roughly $11-13$ [nm]). Thermal decomposition can also provide a more scalable route to large scale production. Unfortunately, the high temperature requirements and the need for non-polar solvents make this approach more challenging [149]. Aerosol and vapour approaches such as laser pyrolysis (thermolysis) may, in some cases, also be classed as high temperature processes. Laser pyrolysis aims at producing narrow size distributions of small non-aggregated particles in a continuous one-step process involving laser heating and resulting in a gaseous phase reaction of iron precursors. The production method is suited to high volume production and very small nano-particles ($2-9$ [nm]) with low anisotropy. The compromise being high initial cost at laboratory scale production volumes and a potential additional step requiring the conversion of precursor oxide, Maghemite (γ-Fe_2O_3) [150], [163] to Fe_3O_4.

A newer approach to magnetite synthesis utilizes bacteria or other micro-organisms. Such approaches [164] showed production of $35-120$ [nm] particles, however, these particles are well beyond the SP limit and scalability remains a significant concern.

Hydrolysis techniques of which co-precipitation may be considered one, are, by far, the most common, easiest, most flexible, scalable and cheapest routes to synthesis of Fe_3O_4 MNPs. Unfortunately, methods such as co-precipitation come with problems relating to size control and agglomeration effects. Oxidation can also make the production of pure Fe_3O_4 difficult. Despite this, these approaches lend themselves to a number of enhancements via sonochemical, flow injection and surface/surfactant mediated techniques. Furthermore, co-precipitation style reactions are often accompanied by large numbers of nucleation sites [165] and corresponding preferential production of amorphous materials. After enhancements, the result is well controlled, low agglomeration, low oxidation/pure particles in the $6 - 12$ [nm] size range [156]. Furthermore, co-precipitation techniques, unlike many other approaches are amicable to industrial scale production, relatively easy to implement and benign from an ecological perspective [166].

Sonochemical approaches are technically high temperature processes that utilize high energy acoustic cavitation [95], [149]–[151] to produce high temperature reactions. They are normally combined with existing wet-chemical synthesis approaches such as co-precipitation. These sonochemical routes are very promising and relatively easy to implement, yielding particle size reductions of up to 53 [%] of the original synthesis route [167]. Flow injection techniques alternatively attempt to convert batch synthesis to continuous processes [150], [151] without a compromise to (and in some cases improvement in) the characteristics of synthesized particles [168]. The utilization of surface and surfactant mediation can improve performance of synthesis procedures as well. Microemulsions do this by performing synthesis by a surfactant mediated boundary layer between water and oil. Other techniques utilize polymer in-reaction coatings.

With an understanding of the range of approaches, the question of which approach is most appropriate for bulk ferrites comes to the forefront. We note that most techniques can achieve the < 25 [nm] particle size range required by earlier mentioned criteria. Taking into account cost, complexity and scalability; organometallic, sol-gel, solvothermal and thermolysis techniques can be eliminated.

Polyols, while markedly simple, still require a level of complexity that increases base costs to produce powder material. This leaves the utilization of co-precipitation routes as the most likely candidates. This method is more likely to provide a multi-phase crystalline and amorphous material. Some augmentation, most likely surfactant coating, can be used to reduce agglomeration. Surfactant coating has been shown to enhance the very characteristics needed for our purposes and does so at a very small increase in complexity relative to other augmentation approaches (e.g. sonochemical, flow injection and microemulsion). Furthermore, in terms of cost and scalability co-precipitation approaches seem to be the most amicable candidates as well.

4.4 Synthesis by Co-precipitation

Having identified co-precipitation as the most suitable candidate for the particular needs of our soft ferrite, we can start to look at the theoretical and practical aspects of such an approach. The hallmark of the reaction lies in the use of Fe^{2+} and Fe^{3+} salts to precipitate out cubic inverse-spinal [169] structured Fe_3O_4 in the presence of a base. Formulas (**A**), (**B**), (**C**), (**D**), (**E**) and (**F**) below demonstrate one reaction pathway leading to the formation of magnetite via goethite (α-$Fe^{3+}O(OH)$) intermediary. However, reaction pathways for co-precipitation are quite complex and alternative pathways also exist – some of these have been discussed in more detail in [166].

It's notable that the iron ion stoichiometry is particularly important with an ideal molar ratio (Fe^{2+}/Fe^{3+}) of $a = 0.5$ for optimal yield – we note, however, that stoichiometry of OH^- ions is more flexible and ions can exist in concentrations at or in excess of stoichiometric values.

Ferric hydroxide formation $$Fe^{3+} + 3 \cdot H_2O \rightarrow Fe(OH)_3 + 3 \cdot H^+ \quad \text{(A)}$$

Transformation to goethite	$\mathrm{Fe(OH)_3 \rightarrow FeO(OH)\ + H_2O}$	(B)
Ferrous hydroxide formation	$\mathrm{Fe^{2+} + \ 2 \cdot H_2O \ \rightarrow Fe(OH)_2 + 2 \cdot H^+}$	(C)
Growth of ferrous hydroxide on geothite	$\mathrm{Fe(OH)_2 + 2 \cdot FeO(OH) \rightarrow Fe(OH)_2 + (FeO(OH))_2}$	(D)
Transformation to magnetite	$\mathrm{Fe(OH)_2 + (FeO(OH))_2 \rightarrow Fe_3O_4\ + \ 2 \cdot H_2O}$	(E)
Co-precipitation Reaction	$\mathbf{Fe^{2+} + 2 \cdot Fe^{3+} + 8 \cdot OH^- \rightarrow Fe_3O_4\ + \ 4 \cdot H_2O}$	(F)

Formula (**F**) is the typical formulation seen for the co-precipitation reaction. An alternative way to present this reaction was provided by [120] and can be used to explain the precipitation of Fe^{2+}, Fe^{3+} in terms of the formation of ferric (dark brown) and ferrous (reddish brown) hydroxides precipitates as shown in Formula (**G**).

Co-precipitation Reaction	$\mathbf{Fe(OH)_2 + 2 \cdot Fe(OH)_3 \rightarrow Fe_3O_4\ + \ 4 \cdot H_2O}$	(G)

We note that the typical approach to synthesizing magnetite nano-particles is to perform standard co-precipitation whereby the Fe^{2+} and Fe^{3+} salts are mixed in solution and the base (OH^-) added at some fixed rate. A less often used alternative that will be utilized in this study does the reverse, i.e. adds the salts to the base. Consequently, this approach is called reverse co-precipitation. The benefits of this reverse approach will become clear further on in this chapter.

4.5 Co-precipitation Control Variables

There are a number of control variables that can be adjusted during reverse co-precipitation based synthesis to produce small particles with good shape morphologies, reasonably narrow size distributions, high magnetic saturation, low remanence, low coercivity, small exchange bias values and relatively pure oxide compositions as per the requirements from Section 4.2. Below follows a discussion of the variables and control measures needed to achieve these desirable characteristics for soft ferrite production.

4.5.1 Type of Base Used and pH

Returning to our reverse co-precipitation formulas (Formulas (**F**) & (**G**)) we note that an excess of OH^- ions is preferred during reactions. The role of OH^- concentration is essential for the precipitation of the Fe^{2+} and Fe^{3+}. In particular, some literature has indicated that iron (III) ferric hydroxide $Fe(OH)_3$ is likely to precipitate out at roughly 2-4 pH, while iron (II) ferrous hydroxide $Fe(OH)_2$ at 7-9 pH [170], [171]. Control of the pH over the course of the reaction can thus determine the critical reaction path leading to the formation of magnetite. A drop in the local pH below the thresholds required by $Fe(OH)_2$ can lead to a shift from the ideal molar ratio of $a = 0.5$ with potentially excess Fe^{3+} left over. Using the reaction pathway above as an example, the result of this local shift in molar ratio would be a reduced growth of magnetite and increased growth of the left over goethite (or other equivalent FeO(OH) oxide forms) leading to the potential formation of needle like low density weakly-magnetic structures. This in itself is likely to reduce magnetic saturation of any resultant ferrite produced via the products of the reverse co-precipitation reaction [172]. Furthermore the presence of the undesirable oxide form may lead to added pinning sites that prevent the free spinning of magnetic moments in the final sintered ferrite. The likely result: an increased coercivity and increased power loss.

By adding the iron salts to the much larger quantity of base, the use of the reverse co-precipitation process ensures that the local pH environment of the iron hydroxides

remains higher [173] and that the molar ratios remain close to the desired value ($a = 0.5$). Of-course to maintain the high pH, depending on the base used, large excess quantities (high concentration) of OH^- ions and good mixing is required. Figure 4-1 demonstrates the difference between the co-precipitation and the reverse co-precipitation approaches.

Given this understanding of high local pH, the choice of base becomes important. A relatively small selection of bases have been used in literature. Among these are the following: Ammonium Hydroxide (NH_4OH) [165], Sodium Hydroxide (NaOH) [156], [173]–[175], Tetraethylammonium Hydroxide ($(C_2H_5)_4NOH$ or TEAOH) [156], [169], Potassium Hydroxide (KOH) [156], Lithium Hydroxide (LiOH) [172]. Of these, NaOH, TEAOH, KOH and LiOH are strong bases, while NH_4OH is a weak base. The use of strong bases can encourage the formation of weakly magnetic or non-magnetic iron oxides such as goethite – this is a result of the longer incubation periods at increased pH values [172]. Furthermore, strong bases disassociate fully in solution and pH is likely to drop over the course of the reaction. It has been noted that larger quantities of NaOH, however, can be used to alleviate this effect and have shown a corresponding drop in particle size [156].

Likewise the use of the less common TEAOH has shown smaller particle sizes than NaOH at around 6.5 [nm] – in this case, TEAOH actively acts as an inhibitor to agglomeration [156]. A reverse co-precipitation approach utilizing a weak base with a pH above 9 (at around 11) has been shown to produce small (8 [nm]) particles [176]. Weak bases act as buffered sources of OH^- ions and don't fully disassociate in solution. As OH^- is consumed by the co-precipitation reaction further OH^- disassociates and enters solution. This study focusses on the use of two bases, NH_4OH and NaOH (with pH values above 9 ranging from $11.63 - 15.18$) as routes to magnetite production and evaluates the effectiveness of each. An additional base, Monoethanolamine (MEA) provides a higher pH (of 12) than NH_4OH along with buffering and so was also briefly considered in this study.

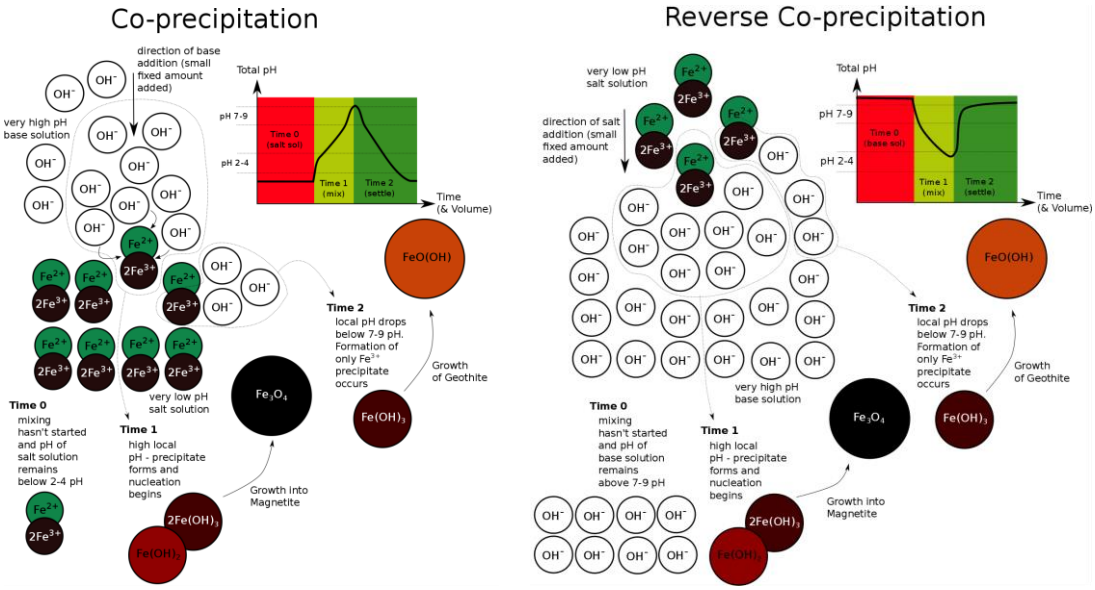

Figure 4-1: Differences between co-precipitation and reverse co-precipitation based approaches using a strong base. Note that [171] provides a more concrete curve for a co-precipitation approach. During co-precipitation very rapid addition of a large quantity base is required to maintain a high pH. While for reverse co-precipitation, slower addition of a iron salt solution in a large excess quantity of base will maintain higher pH during reaction.

One further point of note is that in addition to the pH of the base, the initial pH of the iron salt solution is also important. A starting pH below 4.7 for this solution has been shown to significantly reduce the production of goethite [172]. Because of reduced goethite production, a low pH would thus also be accompanied by an increase in magnetic saturation. In fact, increases in starting pH from 0.7 to 4.7 also resulted in particle size increases from 6.5 [nm] to 9.9 [nm] indicating that a lower starting iron salt pH reduces the interfacial tension (and inhibits the mechanisms of Ostwald ripening) leading to slower crystal growth and smaller particle sizes [172], [177]. Accompanying this, the lower pH reduces oxygen intake and prevents ferrous hydroxide changes to ferric hydroxide, within the iron salt solution, prior to reaction [172] resulting in a molar ratio $a < 0.5$. The final pH at the end of the reaction, however, should remain high to produce smaller particles. This study attempts to maintain a low pH by mixing hydrated ferrous sulphate ($FeSO_4 \cdot 7H_2O$) directly into

concentrated 40% ferric chloride solution ($FeCl_3$) without dilution to achieve a measured pH as low as -0.30.

4.5.2 Stoichiometric Ratio

We noted earlier that the stoichiometric ratio for our iron ions Fe^{2+}/Fe^{3+} should be $a = 0.5$. Further, as mentioned in discussions of pH, this ratio can be modified by oxidation effects taking place in our iron salt solution or by drops in local pH such that $a < 0.5$. It was thus that our bases were selected to provide sufficiently high pH. Ideally, the reaction pH window of between 10 and 13 (sufficiently above 9) provides the potential for maintaining the stoichiometric ratio at 0.5 [156].

Both these cases look at the ratio with respect to an increase in Fe^{3+}, however, the molar ratio may also be in favour of excess Fe^{2+}. Stoichiometric ratios with $a > 0.5$ can increase the rate of reaction of the co-precipitation process [178]. The presence of a small surplus of $Fe(OH)_2$ has demonstrated production of more uniform and smaller particle sizes [179] as well. Some have indicated that in-fact a ratio of $a > 0.66$ would could help account for losses in Fe^{2+} during open air reactions [172]. There seems to be some contradictory results however that indicate an increase in particle size resulting from increases in molar ratio [178] – these are likely a result of very large excesses at $a > 1$. This study takes the existing findings into account by maintaining a molar ratio of $a = 0.5$ while erring on the side of slight excess in ferrous ions during initial reactant mass measurements.

4.5.3 Rate and Method of Mixing

Both with standard co-precipitation and reverse co-precipitation the rate of mixing is critical. Poor mixing can result in local drops in pH well below that required for the reaction. Furthermore, local temperature can rise drastically. Improvements in mixing have been shown to increase reaction rates and result in smaller particles [165], [176], [178], [180]. This is of-course limited up-to some maximum. When

mechanical stirring was involved this could range from a few hundred rpm [156], [167], [176], [181], [182] to 10,000-25,000 [rpm] [180]. Generally, an increase in mixing rate was shown to result in a decrease in particle size and greater uniformity as long as the mixing rate wasn't accompanied by a temperature rise. For the purposes of this study achieving mixing rates in the tens of thousands of rpms wasn't practical and generally improvements from such high speeds beyond 900 [rpm] were demonstrated in literature to be marginal [176]. As a result mixing rate was maintained at a fixed rate at the lower regime of around 800-900 [rpm]. Various sources have used mixing durations of between 60 [min] [176] to 3 [hrs] [156] to ensure complete crystal formation however, in practice 10-20 [min] was found to be sufficient in this study. Prior to mixing the rate of addition of base to iron salt (co-precipitation) or iron salt to base (reverse co-precipitation) is significant. With co-precipitation approaches, as shown in Figure 4-1, very fast addition followed by rigorous mixing will maintain the high local pH needed for the reaction to proceed fully towards magnetite production – this has been demonstrated by [156]. Sources rarely indicate this addition time, but some have mentioned a time of 20 [s] [172]. In order to increase the number of nucleation sites rapid addition followed by mixing should occur in the time scale of milliseconds [157]. The relative rate of addition of iron ions to base in reverse co-precipitation would however be more relaxed and, as shown in Figure 4-1, a slower rate would be beneficial to maintain the local pH environment as long as base quantity is in large excess and sufficient mixing is maintained after addition. This study takes advantage of this by adding the iron salts to base at a slow rate of $10\ [\mathrm{g/s}]$ or $12\ [\mathrm{mL/s}]$.

4.5.4 The Temperature of Reaction

A number of studies have looked at temperature effects on co-precipitation approaches. For instance, in relation to temperature, both Mizutani [178] and Hieu [165] noted that an increased and sustained temperature of reaction led to increases both in particle size and crystallinity. The reaction temperature should not be greater than $50\ [°\mathrm{C}]$. Deviations in either direction around this mark lead to larger particles.

However, considering that oxidation effects can change molar ratios, a start from room temperature reactants (from 20 to 30 [°C]) is a common approach for synthesis [156] and will be used in this study. Considering that co-precipitation reactions producing magnetite are exothermic, despite this lower starting temperature a likely occurrence will be an increase in local temperature.

If this increase is sufficiently above 50 [°C], chemical sintering of agglomerations during nucleation can occur. This is particularly true given that co-precipitation reactions tend to produce many nucleation sites. The end result of the agglomeration is larger particle size and mesoporous structures. An increased rate of crystal growth also occurs at a particular temperature range above that of nucleation resulting from a process that can be described by Ostwald ripening [157], [177]. This process energetically favours growth to larger particles with lower surface energy. Combined with agglomeration effects, the result is increased anisotropy (and coercivity) of the particles in question. Finally, higher temperatures (e.g. above 50 [°C]) during reaction can increase goethite production and decrease magnetic saturation to values as low as 2.5 [emu/g] = 13.1 [KA/m] [172]. Prior to reaction, a high initial temperature for iron salt solution can also lead to increased goethite production. As large particle sizes, high anisotropy (and potentially, coercivity) and low magnetic saturation are undesirable properties, the use of re-circulating water bath-based cooling and increased solution volume can help to reduce temperature rise during reaction. Both of these approaches are used in this study. Alternatively, the use of smaller, higher surface area vessels can help with faster heat dissipation during reaction – a discussion of this follows later in this chapter when looking at an example industrial processing solution.

4.5.5 Surfactant Additive

Maintaining an environment that limits agglomeration plus crystal growth and increases nucleation sites while also preventing the formation of undesirable oxides is challenging via standard routes to co-precipitation. While a number of

modifications can be made to the co-precipitation process, one particularly simple approach is the use of surface active agents. In addition to their use as stabilizing agents, these surfactants may also be used in other synthesis methods as solvents (e.g. polyols) [160]. A wide variety of surface active agents, usually in the form of organic/polymer coatings, have been used to modify particle surfaces. They act as dispersants while also preventing agglomeration by mechanisms of electrostatic repulsion [95], [149], [183]. Some synthetic examples include Polyethylene Glycol (PEG) [149], [174], [182], [184]–[186], Diethylene Glycol (DEG) [173], Triethylene Glycol (TEG) [187], Polyvinyl Alcohol (PVA) [149], [186], Polyacrylic Acid (PAA) [40, 124], Sodium Oleate [170], [176] and Oleic Acid (OA) [172], [188]. The use of surfactants such as PEG, DEG and OA have shown decreases in particle sizes with resultant sizes in the range of $7 - 8.5$ [nm] and coercivities as low as 0.6 [Oe] [173], [176]. Coated nanoparticles have also shown some evidence of higher magnetic saturation with saturation decreasing with molecular weight increases [174], [184].

Of the surfactants mentioned, the benign nature and solubility of PEG ($H(OCH_2CH_2)_nOH$) in both polar and non-polar solvents makes it an attractive choice for this study. MNPs will typically have hydrophobic surfaces that will cause them to preferentially agglomerate together in aqueous reaction media [149]. The use of surfactant acts to reduce the surface or interfacial tension and establish itself as a boundary between the nucleating magnetite and the aqueous solution. This results in the balancing of Van der Waal forces normally responsible for agglomeration during particle thermal motion [95], [149]. Figure 4-2 demonstrates this action whereby PEG attaches itself to magnetite particles via adsorption mechanism of the PEG hydroxyl group [189], [190]. In normal conditions without PEG, magnetite is able to react both with base (OH^-) and acid (H^+) and as a result considered amphoteric. The surface charge of magnetite in the high pH environment of the co-precipitation process is positive and so the Fe^{2+} magnetite surface attaches itself oxygen to produce a maghemite shell (γ-Fe_2O_3). The PEG adsorbs to the magnetite surface limiting this oxidation reaction (steric hindrance).

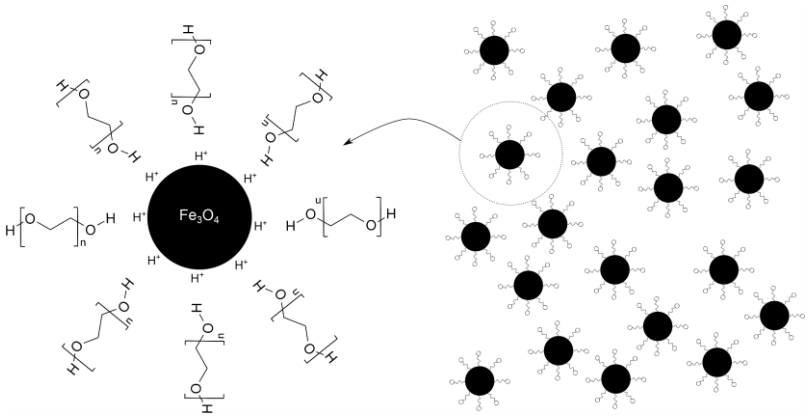

De-protonation of Magnetite surface in the presence of a base:

$$Fe(OH) \rightarrow FeO + H^+$$

Charge develops on surface that attracts and encourages the adsorption of OH^- ions from basic environment

Figure 4-2: PEG hydroxyl group attaches itself to magnetite nano-particle during nucleation and reduces crystal growth while also limiting oxidation through steric hindrance. Note that this attachment occurs as a result of positive surface charge from de-protonation process..

The molecular weight of PEG signified by script variable n can have an effect on particle size and coercivity. The hydrodynamic size will increase with molecular weight as a result of the longer PEG chain [182] however the exact effect on magnetite itself remains unclear. Some literature suggests that an optimal but low molecular weight PEG surfactant may lead to smaller magnetite particle sizes [174], [185]. Low molecular weight PEG has shown some evidence of particle size in the 7 [nm] range [173], [176] with increases in size to $12 - 18$ [nm] for high molecular weights (e.g. 20000 [da]) [184]. Existing studies have looked at weights ranging from $1500 - 20000$ [da] [174], [176], [184]. This study clarifies the effect of PEG molecular weight by looking at a variety of PEG molecular weights and their effect on various particle properties – a discussion of particle properties will follow further along in this chapter. It should be noted that traditional studies have favoured the use of Sodium Oleate over PEG as a result of the lower surfactant efficiency whereby larger quantities of PEG are required for the same interfacial tension reduction [176]. In this study, the efficiency isn't considered a critical parameter and so the more easily accessible PEG was used. Despite indications of poor efficiency though, some sources have indicated that a concentration as low as 0.1 [mg/L] of PEG [175] is

sufficient. Note that this study adds PEG to the base during the reverse co-precipitation reaction.

The addition of PEG encourages greater dispersion of magnetite meaning that magnetic separation of particles becomes more important [174]. Furthermore, organic surfactants such as PEG are more likely to react in the presence of high pH bases – in-fact as will be seen later in this study, just such a reaction occurs both with the NaOH and MEA used.

4.5.6 Type of Atmosphere Present during Reaction

As an alternative or addition to the use of surface active agent has been better control of the atmosphere in which reactions take place. Nitrogen (N_2) degassing has been the most common approach to removing oxygen from reactants [156], [165], [178], [191]. A less common approach has been the use of Argon (especially where high temperature reactions are being attempted) [178]. As mentioned earlier, the oxidation process can shift the reaction away from the ideal molar ratio and so in air atmosphere some have suggested a move to a ratio of $a > 0.66$. A shift back to $a = 0.5$, can be reliably affected with careful control of atmosphere. This study will make use of nitrogen as a purging gas and evaluate its effectiveness relative to an open air synthesis approach.

4.5.7 Strength of Magnetic Field

A magnetic field in the order of $0.1 - 0.22$ [T] is used as a means of magnetic separation in the past. However, the presence of a magnetic field during synthesis can have a profound effect on the co-precipitation reaction. In particular, sources have noted that the result is an increase in particle size and improved and regularized crystal growth [181]. The use of magnetic stirrers during reaction can have similar effects – at present the rotating nature of the magnetic field makes this effect

unpredictable. This study will attempt to evaluate the effect of magnetic field on particle properties.

4.5.8 Washing, Drying & Storage

In most cases subsequent to reaction a standard washing procedure usually involving either deionized/degassed water or ethanol is followed [178]. Washed particles are rinsed repeatedly between 3 to 5 times and occasionally re-dispersed in surfactant subsequent to washing [172], [174], [176]. Supernatant is removed via decanting or centrifugation and magnetite is dried at temperatures of 70 [°C] and up. The use of ethanol as a washing solvent can also help capture and dilute water content for a higher resulting vapour pressure. This process allows faster and more complete drying. This study will follow similar procedures for washing and drying making use of decanting and controlled siphoning to remove excess supernatant. A key point of note is that storage of magnetite especially at small size ranges is subject to oxidation to maghemite and so low temperature and air tight storage is the preferred method. Samples stored for over 6 months can see significant oxidation if care is not taken during storage [172]. For this purposes of this study, considering that samples are designed to undergo sintering in reduced atmosphere, this is not a particularly significant problem.

4.6 Properties of Particles Produced by Reverse Co-precipitation

Looking at existing literature we can delve further into some of the typical properties (and characterizations) for magnetite MNPs produced by the co-precipitation and reverse co-precipitation routes. The list below discusses some of these properties and their implication towards the development of soft ferrites with the requirements discussed in Section 4.2.

4.6.1 Particle Size (D), Distribution and Shape

The size of nano-particles produced through co-precipitation, while roughly falling in the 6-12 [nm] range [156], vary considerably between synthesis approaches. For instance, using a few examples from literature, we see the following size ranges: $5-20$ [nm] [191], $10-30$ [nm] [165], 11 [nm] [156], $8-20$ [nm] [176], $6.5-9.9$ [nm] [172] and 10 [nm] [173], [180]. These examples clearly show that co-precipitation produces magnetite MNPs in a range where superparamagnetism (SP) takes hold. For co-precipitation based techniques, this points in the direction of suitability as a synthesis method. Furthermore, understanding that the method produces particles that fall well below the superparamagnetic limit suggest that the resultant product is amicable to sintering approaches. One thing to note, however, is that there are challenges in achieving narrow particle size distributions – a consequence of this is wider distributions with a relatively wide range of blocking temperatures [192]. Blocking temperature determines the transition from and to SP behaviour – particles below the blocking temperature begin to exhibit non-SP behaviour. The blocking temperature is also linked to relaxation time – a parameter that can determine the maximum operating frequency at which particles remain in the SP window. This suggests that a wider distribution may in-fact diminish the quality of the material in some cases. Particle shape and morphology (e.g. resulting from agglomeration), as well, can play a role in determining anisotropy and have an effect on the material quality from the perspective of soft magnetic ferrites – however, this is not a parameter that is often characterized fully in literature. While typically not reported, some standard deviations resulting from size distributions are given in literature as: 2 [nm] [177], $2.4-4.7$ [nm] [180], $1.0-2.2$ [nm] [157]. Combined X-Ray Diffraction, Electron Microscopy and Magnetometric measurements can aid in determining, not only size distribution, but anisotropy, shape, blocking temperatures and particle sizes.

4.6.2 Magnetic Saturation (M_s)

One of the results of decreasing particle size is a corresponding decrease in magnetic saturation [156], [165], [178], [183]. Given that co-precipitation is likely to have more amorphous material than crystalline, an additional decrease in magnetic saturation [173] is likely to result. The typical bulk (non-MNP) magnetization of magnetite [174], [176], [191] falls at roughly a value of $\acute{M}_s^{cgs} = 90\ [emu/g]$ (between $88 - 92\ [emu/g]$ specifically). This is an SI mass equivalent of $\acute{M}_s^{si} = 90\ [Am^2/Kg]$ or, given a typical bulk magnetite density of $5.15\ [g/cm^3]$, an SI volume equivalent of $\breve{M}_s^{si} = 10^3 \rho_d \acute{M}_s^{cgs} = 463.5\ [KA/m]$. Converting to B-field, a value of $\breve{B}_s^{si} = \mu_0 \breve{M}_s^{si} = 0.58\ [T]$ would be a volumetric equivalent. Using examples from literature, this value drops at nano-particle scales – some representative values are: $43 - 50\ [emu/g]$ (or $\breve{M}_s^{si} = 225.9 - 262.7\ [KA/m]$, $\breve{B}_s^{si} = 0.28 - 0.33\ [T]$) [174], $60 - 80\ [emu/g]$ (or $\breve{M}_s^{si} = 315.3 - 420.4\ [KA/m]$, $\breve{B}_s^{si} = 0.40 - 0.53\ [T]$) [165], $30 - 70\ [emu/g]$ (or $\breve{M}_s^{si}$=157.6 - 367.8 [KA/m], $\breve{B}_s^{si} = 0.20 - 0.46\ [T]$) [157] and $17 - 59\ [emu/g]$ (or $\breve{M}_s^{si} = 89.3 - 310.0\ [KA/m]$, $\breve{B}_s^{si} = 0.11 - 0.39\ [T]$) [172]. Considering that reports of density are relatively rare in literature, an average density of $\rho_d = 5.25\ [g/cm^3]$ was used for unit conversion purposes and has been obtained from the author's own experimental data on co-precipitation based MNP synthesis. A discussion of the full data will follow in Section 4.7 and in Chapter 9. Interestingly, a decreasing particle size may result in increased density which would have a positive effect on volumetric saturation. Likewise, as noted earlier, both increases in particle size and higher crystallinity results in higher magnetic saturation values. Increased crystallinity is dependent on a variety of environmental factors including temperature, mixing rates and magnetic field presence – these will be discussed further on in Section 4.5. One further point to note is that saturation magnetization can help distinguish between iron oxides (magnetite and maghemite) that would normally be difficult to distinguish through traditional X-Ray diffraction measurements. In particular maghemite has lower room temperature saturation than magnetite [157] and so lower values (once particle size has been accounted for) are likely indication of greater maghemite presence.

4.6.3 Remanence (M_r), Coercivity (H_c) and Exchange Bias (H_{ex})

The remanent magnetization remains less reported in literature and is sometimes stated as immeasurably small. One source that does report this value indicates a result of $0.92 - 1.91$ [emu/g] (or $\breve{M}_s^{si} = 4834 - 10{,}036$ [A/m], $\breve{B}_s^{si} = 6.07 - 12.6$ [mT]) [172] while another reports roughly 5 [emu/g] (or $\breve{M}_s^{si} = 26{,}274$ [A/m], $\breve{B}_s^{si} = 33.0$ [mT]) [177]. In comparison, coercivity has been reported at a range of values from 42-650 [Oe] (or $H_c^{si} = 3{,}342 - 51{,}725$ [A/m]) [174], 50 [Oe] (or $H_c^{si} = 3{,}979$ [A/m]) [177] to $0.15 - 10.46$ [Oe] ($12 - 832$ [A/m]) [157] and $0.6 - 7$ [Oe] (or $H_c^{si} = 47.7 - 557$ [A/m]) [173]. As with remanence, in some cases, coercivity is also reported as being zero, indeterminate or immeasurably small [156], [176], [180]. Both remanence and coercivity are linked to mechanisms that pin magnetic moments within a material. A more detailed discussion will follow in Chapter 6, 8 and 9. A further related property sometimes discussed but rarely characterized is exchange bias. The resultant large surface area of the particles in question produces oxide shell structures which can cause further pinning of magnetic moments leading to shifts in the hysteresis curve. A detailed discussion of this phenomenon will follow in Chapter 8.

4.6.4 Colour, Composition and Oxides

Speaking of iron oxide forms, we noted earlier that magnetite may undergo oxidation. Typically this would happen during or after the synthesis process to produce one of maghemite (γ-Fe_2O_3) or hematite (α-Fe_2O_3). Under certain conditions the reaction pathway may also produce goethite (α-FeOOH), Akaganeite (β-FeOOH), Lepidocrocite (γ-FeOOH) or Feroxyhyte (δ'-FeOOH) [166], [193] – for example where the Fe^{2+}, Fe^{3+} reactants aren't fully consumed as a result of non-optimal synthesis conditions [166]. In addition, molar ratios may also change within the iron salt solution prior to reaction as a result of oxidation [172].

Distinguishing between maghemite, magnetite and hematite is difficult from traditional X-Ray diffraction based approaches at the nano-scale. Therefore, combined with diffraction data, magnetic saturation data and electron microscopy data; observations of sample colour can help determine the presence of oxides. Colour observations, however, are rarely done for magnetic minerals [194]. These observations are best done in the LAB colour space to allow for quantification. In practice, the use of colourimeters and spectrophotometers is ideal for such quantification [195], [196], however sometimes digital cameras can be used for this purpose [197].

Matters are complicated by changes in optical properties between solid bulk materials and powders of differing micro and nano-structures. Normally, goethite tends towards yellow (roughly parallel to the b axis of LAB) [198], hematite towards red (roughly parallel to the a axis of LAB) [198], while magnetite tends towards black and maghemite towards brown. Maghemite is less stable than hematite, however, at nano-scale, maghemite stability approaches that of hematite [166] resulting in an increasing presence [156] and complicating other approaches (such as X-Ray diffraction) for determining composition [157] and resulting magnetic properties. Given that maghemite is itself an MNP, its presence would not negatively affect this study since sintering in a reducing environment can convert it back to magnetite.

4.7 Experimental Method for Reverse Co-precipitation

With an understanding of the control variables required for co-precipitation based approaches we can develop a set of experimental procedures for this study. We noted key variables for managing and controlling the synthesis process, namely:

- Type of base
- Base pH
- Type of iron salts
- Iron salt solution pH
- Stiochiometry of salt solution
- Stiochiometry of base
- Rate of addition of iron salt solution to base
- Rate of mixing of reactants
- Initial Temperature
- Surfactant type
- Surfactant quantity
- Surfactant molecular weight
- Type of purging gas
- Flow rate of purging gas
- Magnetic field strength
- Washing solvent
- Number of washes
- Drying temperature
- Drying duration
- Storage method

Two weak bases: Aqueous (35 [%]) NH_4OH and liquid MEA with pH of 11.63 and 12 respectively, were used. In addition, one strong pelletized base, NaOH, with pH selectively varying between 14.03 and 15.18 was also used. Quantities of base were varied between stoichiometric values to upto an excess of about 15 times required values. Hydrated solid $FeSO_4$ ($FeSO_4 \cdot 7H_2O$) and aqueous (40 [%]) $FeCl_3$ were used as precursor salts to provide Fe^{2+} and Fe^{3+} ions. Starting iron salt molar ratio was maintained at the traditional value of 0.5. The rate of addition of iron salt solution to base was kept at a constant of roughly 12 [mL/s] with a mix rate kept largely constant at 800 [rpm] for $10 - 20$ [min] – some exceptions apply and will be discussed in Chapter 9. Where added, surfactant PEG was added to the base in quantities well in excess of 20 [%] of the total solution volume at between $40 - 50$ [%]. The average molecular weight was varied for surfactant between 300 [da] and 20000 [da]. Reactions were carried out both without a purging gas in air and in a more controlled setting with N_2 at a flow rate of approximately $0.5 - 1$ [L/min] for degassing. The reaction was attempted both under condition of a magnetic field and without. Where used, permanent magnets of surface magnetic field strength of $0.1 - 0.22$ [T] were used both during reaction and for magnetic separation of

produced magnetite from supernatant. Deionized water and ethanol were used as wash solvent (4 washes total) and combined with decanting and siphoning to remove excess supernatant. Left over solvent was dried in a low temperature furnace at 70 [°C] for a period of between 11.5 to 44 [hrs] - some exceptions involving air drying and drying on an electric hob should be noted. A total of 31 successful batch runs of the synthesis were completed under varying base type, base pH, surfactant concentrations and molecular weights, purging gas and magnetic field conditions. Table 4-2 provides a detailed set of conditions for these batch runs. Given the added information about base, the formula for our co-precipitation reaction (Formula (**F**)) can be rewritten as a set of three formulas – one for each base used. These are shown in Formulas (**H**), (**I**) and (**J**) below.

NH_4OH $\mathrm{Fe(OH)_2 + 2 \cdot Fe(OH)_3 \rightarrow Fe_3O_4 \ + \ 4 \cdot H_2O}$ (H)

MEA $\mathrm{FeSO_4 + 2 \cdot FeCl_3 \ + 8 \cdot H_2NCH_2CH_2OH_{(aq)} \rightarrow Fe_3O_4 + 4 \cdot H_2O + other}$ (I)

NaOH $\mathrm{FeSO_4 + 2 \cdot FeCl_3 \ + 8 \cdot NaOH_{(aq)} \rightarrow Fe_3O_4 + 4 \cdot H_2O + other}$ (J)

In addition to the main products of the reactions, "other" products will form as well. These consist of the unused components of our base and iron salts. For instance, in the case of our NH_4OH reaction, this would include SO_4^{2-}, $3Cl^-$ and $8NH_4^+$ ionic species. The resultant supernatant products are likely to be relatively benign combinations of water soluble Ammonium Hydroxide (NH_4OH), Ammonium Sulfate ($(NH_4)_2SO_4$) or Ammonium Chloride (NH_4Cl). Likewise, supernatants of NaOH reactions will take the form of Sodium Hydroxide (NaOH), Sodium Sulfate (Na_2SO_4) and Sodium Chloride (NaCl). These products are also water soluble and can easily be washed by water and subsequently ethanol. With MEA the supernatant is somewhat more complex - the reaction failed to produce the desired co-precipitation products and thus is neglected for the remainder of this study.

Table 4-2: A list of batch runs for the reverse co-precipitation procedure. Tests are conducted to determine the effect of a number of synthesis routes on the end magnetic properties.

Impact of changes in	Sample Label	Present	$FeCl_3$ Qty. [g]	$FeSO_4$ Qty. [g]	α	Base					PEG		Wash Qty. [g]
						Type	pH	Qty. [g]	H_2O Qty. [g]	Excess	MW [da]	Qty. [g]	
Magnetic Field	S.1	Yes	175.1	60	0.5	NH_4OH	11.63	211.2	400	1.02x	n/a	0	400
	S.2	No	175.1	60	0.5	NH_4OH	11.63	220.0	400	1.06x	n/a	0	500
	S.17.1	No	44.68	15.1	0.5	NaOH	14.03	19.45	447.33	1.12x	n/a	0	425.87
	S.17.2	Yes	43.93	15.90	0.5	NaOH	14.03	19.36	447.86	1.12x	n/a	0	477.26
Nitrogen Purge	S.2	No	175.1	60	0.5	NH_4OH	11.63	220	400	1.06x	n/a	0	500
	S.4	Yes	176	60.11	0.5	NH_4OH	11.63	352	325	1.70x	n/a	0	600
Water Bath	S.9.5	No	44.11	15.10	0.5	NH_4OH	11.63	88.3	0	2.00x	n/a	0	86.5
	S.9	Yes	43.69	15.13	0.5	NH_4OH	11.63	88.70	0	2.00x	n/a	0	86.5
Base Type	S.9.5	n/a	44.11	15.10	0.5	NH_4OH	11.63	88.3	0	2.00x	n/a	0	86.5
	S.16.3	n/a	44.08	15.16	0.5	NaOH	14.40	35.38	334.81	2.03x	n/a	0	356.56
Base pH	S.11.1	n/a	43.81	15.23	0.5	NaOH	15.073	272.46	447.93	15.76x	n/a	0	450.9
	S.11.2	n/a	43.80	15.04	0.5	NaOH	14.80	113.45	397.32	6.57x	n/a	0	436.32
	S.11.3	n/a	49.29	16.77	0.5	NaOH	14.40	45.79	430.77	2.62x	n/a	0	431.32
	S.11.4	n/a	44.68	15.1	0.5	NaOH	14.03	19.45	447.33	1.12x	n/a	0	425.87
Base Volume	S.12.1	n/a	44.49	15.63	0.5	NaOH	14.40	20.13	190.94	1.16x	n/a	0	201.25
	S.12.2	n/a	43.93	15.39	0.5	NaOH	14.40	30.48	285.98	1.74x	n/a	0	313.84
	S.12.3	n/a	44.14	15.49	0.5	NaOH	14.40	40.27	381.49	2.33x	n/a	0	388
PEG Quantity	S.18.1	No	44.68	15.1	0.5	NaOH	14.03	19.45	447.33	1.12x	n/a	0	425.87
	S.18.2	Yes	44.13	15.44	0.5	NaOH	14.03	19.34	441.14	1.12x	300	12.91	554.15
	S.18.3	Yes	44.14	15.53	0.5	NaOH	14.03	19.41	441.25	1.12x	300	25.98	478.13
	S.18.4	Yes	43.92	15.91	0.5	NaOH	14.03	19.39	441.19	1.12x	300	43.24	409.15
	S.10	Yes	43.92	15.03	0.5	NH_4OH	11.63	86.86	0	2.00x	300	6.18	92.75
	S.10.1	Yes	44.02	15.52	0.5	NH_4OH	11.63	87.06	0	2.00x	300	12.37	99
	S.10.2	Yes	43.93	15.30	0.5	NH_4OH	11.63	86.52	0	2.00x	300	25.39	111.5
	S.10.3	Yes	43.96	15.09	0.5	NH_4OH	11.63	86.55	0	2.00x	300	25.93	86.19
	S.7	No	44.34	15.33	0.5	NaOH	15.18	34.85	42.11	2.00x	n/a	0	76.96
	S.7.2	Yes	44.14	15.03	0.5	NaOH	15.18	35.34	41.25	2.00x	300	6.47	81.35
	S.7.3	Yes	44.51	15.03	0.5	NaOH	15.18	34.06	40.69	2.00x	300	12.92	87.60
	S.7.4	Yes	44.34	15.17	0.5	NaOH	15.18	34.15	40.56	2.00x	300	26.61	100.1
PEG Molecular Weight	S.13.1	-	44.13	15.44	0.5	NaOH	14.03	19.34	441.14	1.12x	300	12.91	554.15
	S.13.2	-	44.56	15.85	0.5	NaOH	14.03	19.32	440.98	1.12x	400	13.04	459.22
	S.13.3	-	44.48	15.82	0.5	NaOH	14.03	19.51	441.22	1.12x	8000	12.82	511.78
	S.13.4	-	43.97	15.80	0.5	NaOH	14.03	19.39	441.25	1.12x	20000	12.96	463.20

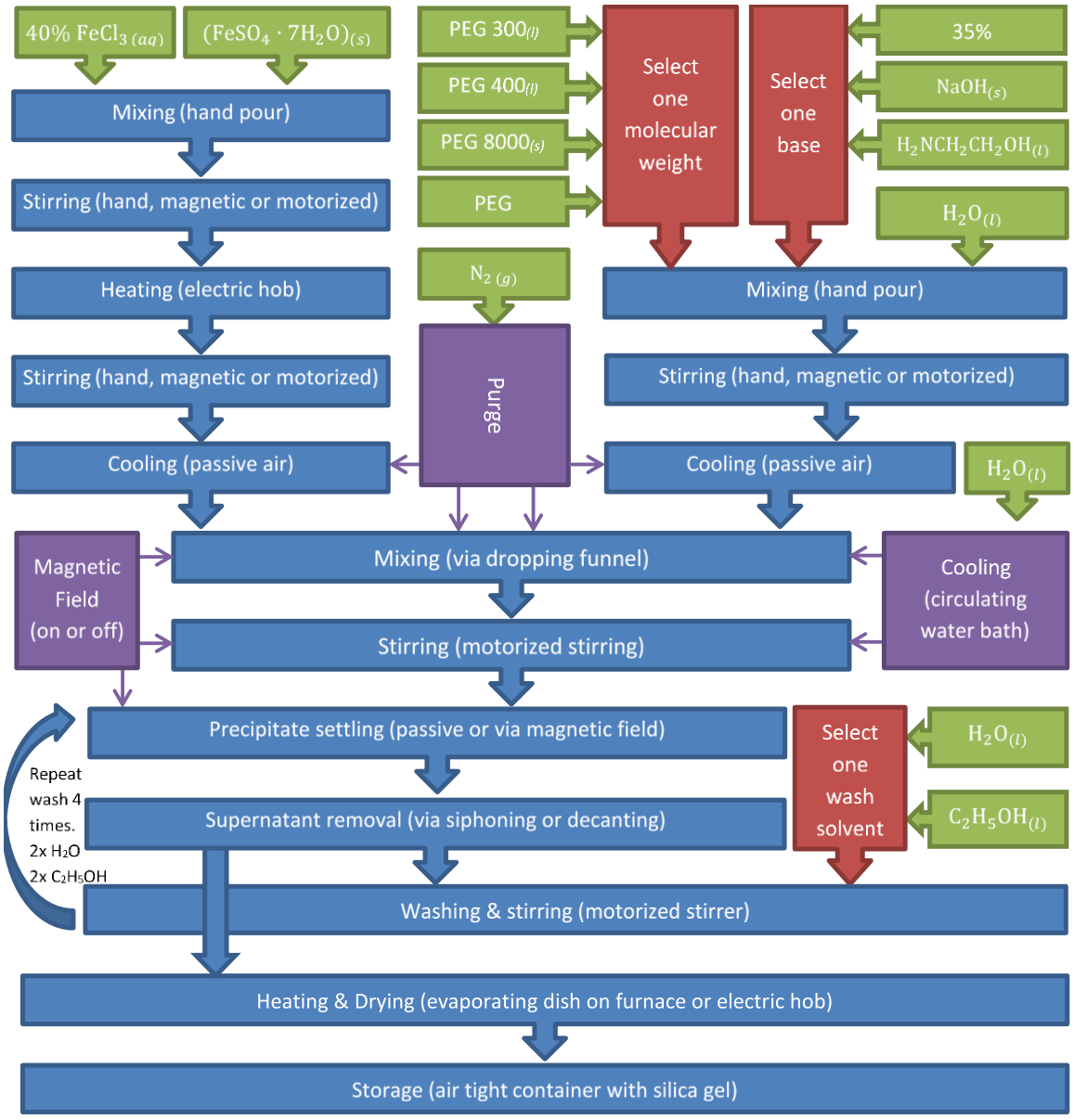

Figure 4-3: Procedural flowchart for reverse co-precipitation. The base solution and salt solution can be prepared in parallel. Green indicates reactants used, red indicates selection choice for chemicals, blue indicates the main tasks and purple indicates parallel processes running at the same time as the particular main task. Note that mixing refers to the addition of one reactant (or intermediary) into another while stirring refers to the process of agitating the solution for more consistent dispersion.

The flowchart presented in Figure 4-3 provides an overview of the experimental procedure, Figure 4-4 follows with a full experimental setup for a batch reactor and

Figure 4-5 with photograph of the "real life" setup used. Note that a number of apparatus elements were designed and built with the aid of a FDM (Fused Deposition Modelling) 3D printer to reduce cost.

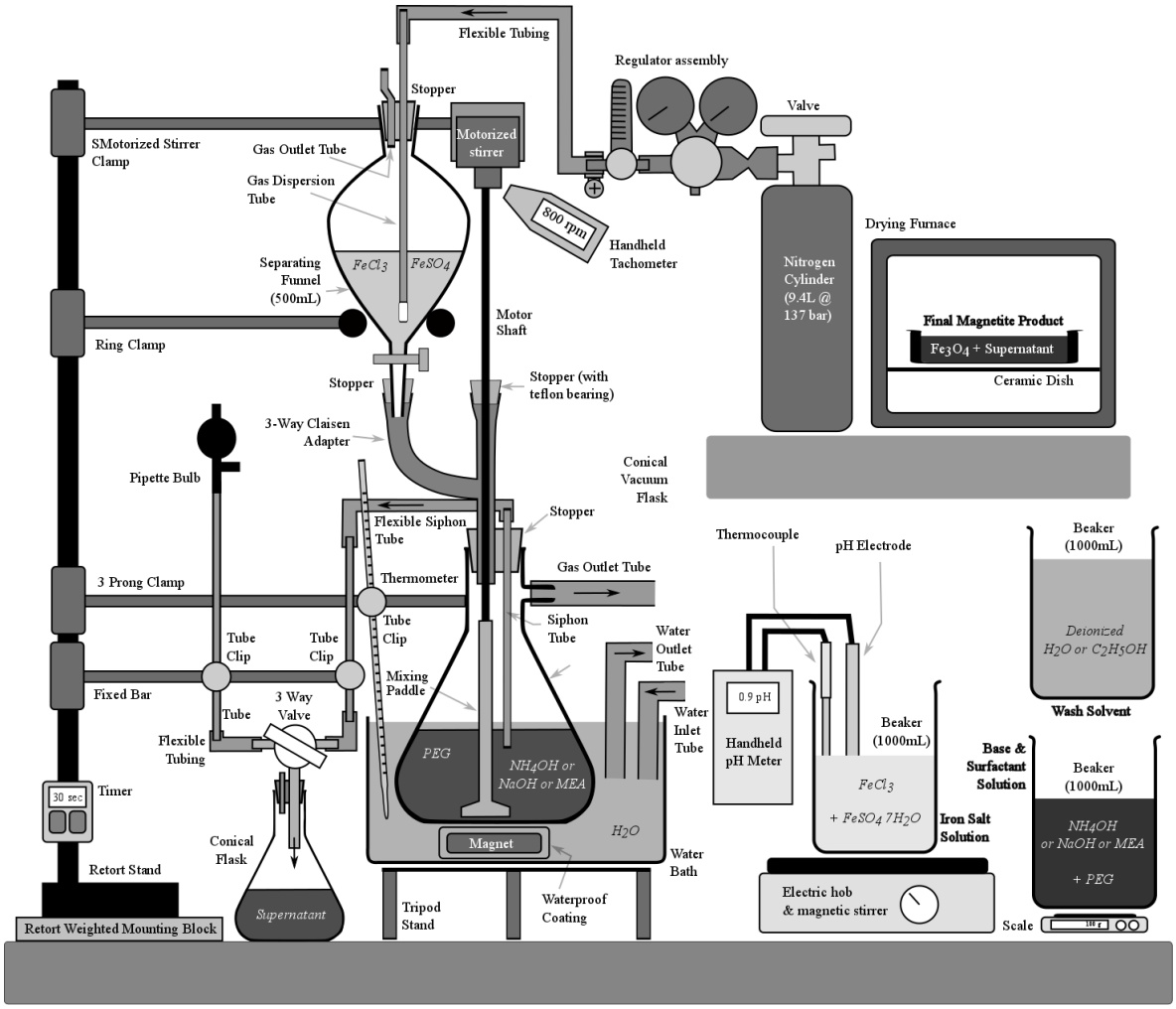

Figure 4-4: The apparatus used for experiments. Base and surfactant are measured and mixed and transferred to the dropping/separating funnel and after purging with nitrogen transferred to the vacuum conical flask. After heating, mixing the salt solution is likewise transferred to the dropping funnel where it is cooled and purged with nitrogen. The salt solution is then mixed with the base solution while being stirred by the motorized stirrer. Once complete the end solution is allowed to settle and the supernatant siphoned off. This process is repeated and the remaining contents of the vacuum flask are transferred to a ceramic dish for heating.

To begin, a precision scale is used to measure out quantities of the starting base (NH_4OH, NaOH or MEA) which is then mixed with deionized water and PEG up to the desired concentration. The solution is stirred magnetically or by hand depending on the particular sample being produced. Likewise, $FeCl_3$ and hydrated $FeSO_4$ are measured, mixed, heated and stirred. Quantities of washing solvent are measured out after the main reverse co-precipitation reaction has taken place. These wash solvent quantities are not critical but have been roughly aimed at equalling the total mass of our collective reactants. After four washes the process should dilute any supernatant to at least 25% of its original concentration – though it is likely that dilution will be much higher even given that some supernatants are insoluble in ethanol.

We noted earlier that Table 4-2 provides a complete listing of the specific quantities for each batch run – a total of 31 runs of this synthesis process were carried out and compared with two commercial samples herein labelled S.-1 (magnetite). A further commercial sample of iron was also used during the sintering stage – this sample is labelled S.0 for future reference. Sample S.-1 was obtained from Inoxia Ltd. while the S.0 was obtained from MB Fibreglass UK.

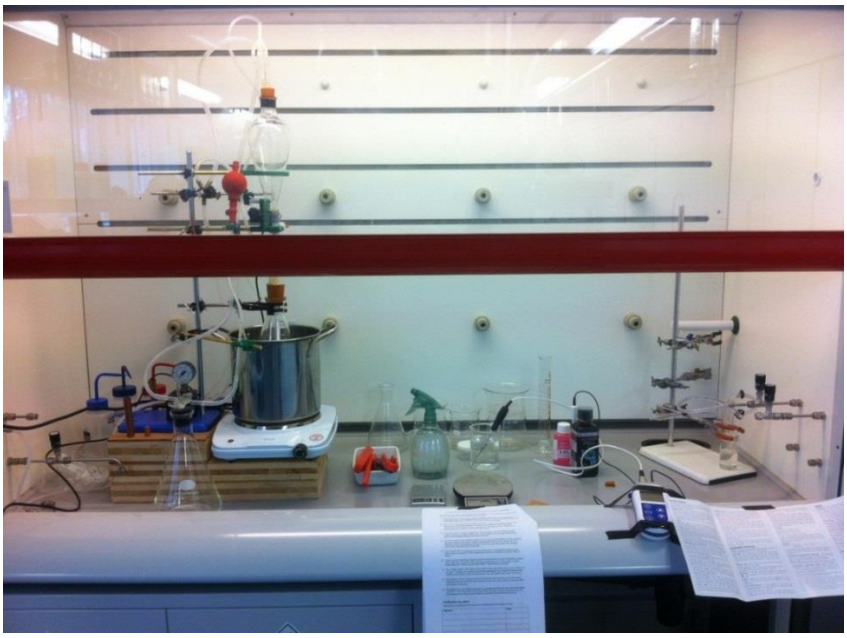

Figure 4-5: The actual experimental apparatus under a fumehood.

At this stage we should note that the mixing process involves pouring or transferring one reactant into the same container as another. Stirring involves the agitation of the contents of this container either by hand or by a magnetic or motorized stirrer. The process of mixing and stirring base quantities and PEG can be strongly exothermic, especially in the case of pelletized NaOH being dissolved in water. As a result, the solutions must be mixed and stirred slowly and with care and subsequently be allowed to cool back to room temperature to control reaction pathways better. In some batches the addition of PEG to high pH bases (MEA and NaOH) can result in side reactions that consume the surfactant and produce unwanted by-products. This was the case in some batch runs.

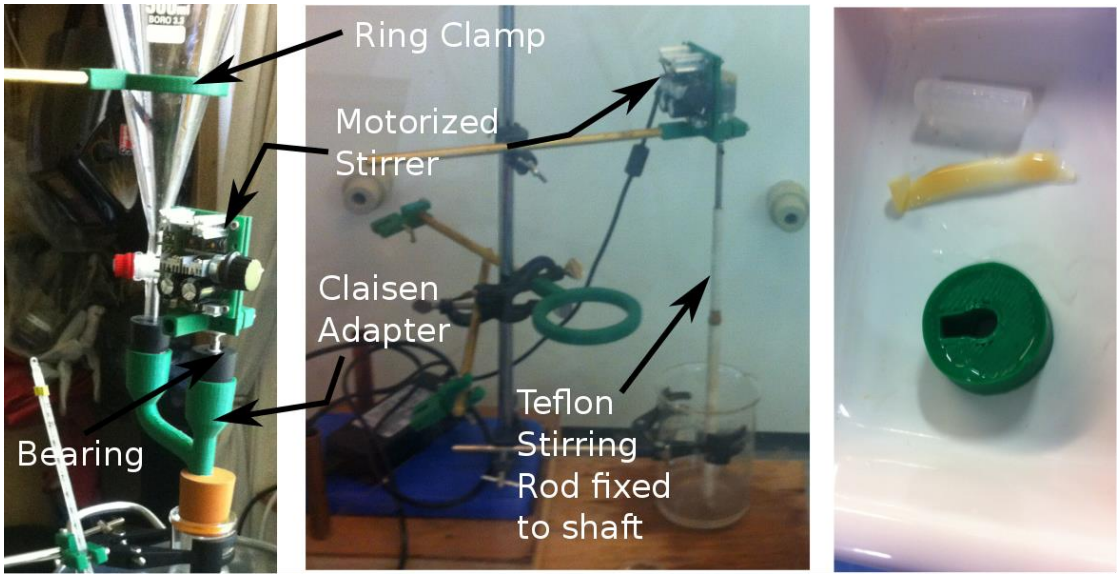

Figure 4-6: A close up of the mechanical stirring device, 3D printed ring clamp and 3D printed claisen adapter. Right image shows testing of various 3D printed and resin/latex/plastic materials used in the apparatus in the volatile ammonium hydroxide base over a 24 hr period.

Likewise, with reference to the salt solution, dissolving solid hydrated $FeSO_4$ into $FeCl_3$ at room temperature is somewhat difficult at the given concentrations. Slight heating of this mixture can improve solubility and speed up the mixing process. The

use of a combined magnetic stirrer and heating hob is ideal for this purpose. As with our base solution, the resultant salt solutions should be cooled back to room temperature before proceeding with the final stage of the reverse co-precipitation reaction. At this stage a handheld pH meter was used to measure the pH and temperature of the base and salt solutions.

In order to transfer the base solution into the lower conical vacuum flask shown in Figure 4-4 and Figure 4-7, the base is first transferred to the dropping/separating funnel where it undergoes nitrogen purging to reduce oxygen content. This will reduce the subsequent potential for oxidation occurring during the reaction. The base is then transferred onto the bottom conical flask. The gas outlet in the bottom flask can be closed off at this stage to allow some level of protection from further oxygen intake. After transfer of the base, the salt solution is transferred to the top flask and undergoes nitrogen purging as well. The gas outlet tube in the top separating funnel allows venting of nitrogen after purging. As shall be seen in the discussion chapter (i.e. Chapter 9) of this study, it is critical that the nitrogen flow be stopped prior to final mixing of the salt solution into the base solution.

The motorized stirrer, consisting of a DC motor, H-bridge control and a Teflon paddle is started at a rate of roughly 800 [rpm] as measured by a hand-held tachometer – this setup had to be custom designed and built by the author as a result of the dimensional restrictions needed to insert a mixer into the conical flask – this stirrer is shown in Figure 4-6.

The dropping funnel (secured via a custom ring clamp) is fully opened and the iron salt solution is allowed to mix into the base at a controlled and known rate while stirring occurs. A custom 3-Way Claisen adapter is used to simultaneously allow stirring while mixing the two solutions – an ABS 3D printed adapter proved to be sufficient and inert for the chemicals involved in the reaction (see Figure 4-6). This rate is measured with a timer by performing repeat test drops using an iron salt solution and water. The resultant mixture is stirred continuously for at least 10 [min]. During the reaction, a circulating water bath is connected to the mains tap

with excess water siphoned off into a drain. The bath helps keep the reaction at a stable temperature for the stirring duration.

After stirring is complete a large diameter strong neodymium magnet is fixed to the bottom of the conical flask and the precipitated magnetite allowed to settle. Note that this magnet may be inserted and fixed to the bottom of the conical flask during the reaction to apply a weak field as well. The precipitate can take from 6-60 [min] to settle. A picture of this precipitate solution is provided in Figure 4-7a. A pipette bulb (combined with a 3-Way glass valve) is used to create a vacuum and siphon off any excess supernatant into a waste flask (see Figure 4-7b). In some scenarios, the siphon may become clogged and so a larger bulb with a wider siphon diameter may be needed to ensure faster and easier siphoning.

Figure 4-7: (a) The precipitate solution, (b) the siphoned supernatant and (c) settled magnetite after the last washing is complete.

After the first quantity of supernatant has been removed, washing proceeds (Figure 4-7c). Two washes using deionized water and two washes using ethanol are completed – the aim being to minimize the ionic species present in the supernatant. The magnet is removed and the motorized stirrer is run at 800 [rpm] while nitrogen purged wash solvent is added through the top separating funnel and into the bottom conical flask. At the end of the last siphoning the remaining supernatant is vigorously

mixed, the motorized stirrer and siphon removed and the bottom conical flask contents are dumped into a ceramic dish.

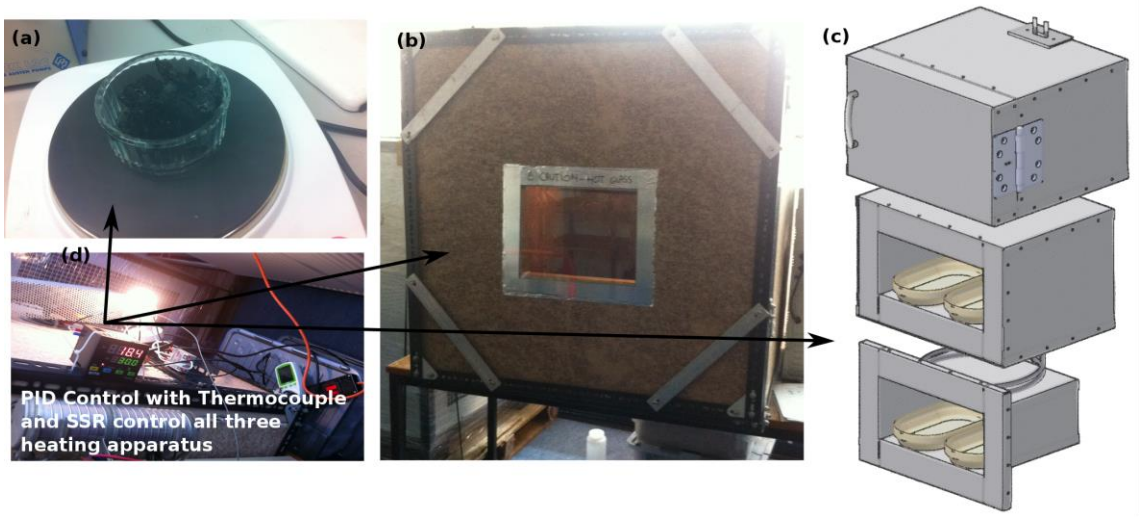

Figure 4-8: Different approaches to heating all with PID control. (a) An electric hob; (b) A low temperature furnace with a fireboard refractory; (c) A high alumina refractory lined furnace design that protects against contamination; (d) A PID control and power monitor.

The dish is placed in a ventilated low temperature furnace and baked at 70 [°C] to remove the remaining ethanol and leave behind powdered magnetite (see Figure 4-8b). Unfortunately, a risk of contamination is possible in such ovens as a result of flaking fibrous or brittle refractory linings – it is important to place the samples for drying in a more appropriate furnace, a design of which is shown in Figure 4-8c. Another approach to drying is the use of an electric hob (Figure 4-8a). Such an approach, however, was found to produce uneven heating. A simple PID controller is used in all approaches (Figure 4-8d). The method of heating and washing both were noted to have an impact on the oxidation of the magnetite into less desirable oxides – proper wash and storage is essential.

Figure 4-9: Air tight sample containers for small quantities of magnetite**.**

The magnetite is placed in an air tight containers along with packaged silica gel for analysis (see Figure 4-9). Samples, despite these measures, were found to undergo oxidation while awaiting the next characterization stage and so, in some cases colour changes were noted.

Subsequent chapters will continue with a look at the characterization and subsequent modelling and analysis of the produced nano-particles. However, prior to that it is worth pointing out a technique for taking synthesized nano-particles to bulk material via sintering. The next chapter will provide a discussion of sintering.

4.8 Summary and Final Remarks

In earlier discussions of our prototype diamagnetic bearing, a reluctance machine was used for power transfer (see Section 2.5). Such machines are not easily available on the market and the cost of custom built machines, even on the small scales required for this study, proved to be excessive. Given this high cost, and considering that this study is aimed at reducing parasitic losses in our diamagnetic bearing

implementation, some emphasis was given in this chapter on low loss electrical machine core materials.

The two main forms of core loss are a result of eddy currents and hysteresis. The use of ferrite materials over traditional laminations is far superior when operating frequencies for the electrical machine is beyond the typical $50/60$ [Hz]. Unlike, eddy current losses, hysteresis loss occurs because of the magnetization of the rotor. This remanent magnetization persists and can lead to a dragging force on the rotor as a result of the stationary stator. Magnetic nano-particles have shown super-paramagnetic properties that eliminate loss from hysteresis. The combination of reduced hysteresis, reduced eddy current loss and the lower cost of producing prototype machines in unconstrained geometries has led to an investigation of magnetite nano-particles for making core materials.

Magnetic nano-particles have shown super-paramagnetic properties that eliminate loss as a result of hysteresis. The combination of reduced hysteresis, reduced eddy current loss and the ability to produce geometrically unconstrained prototype machines has led to this chapter's investigation of magnetite nano-particles for making core materials.

While a range of approaches for synthesis of these materials were noted, a particularly simple and well used approach was used. This approach utilizes co-precipitation of magnetite from a combination of base and iron salts. The approach has shown promise in producing magnetite nano-particles in the 10 [nm] scale range needed for superparamagnetic and low loss behaviour. An experimental apparatus aimed at providing limited control to a range of control variables was used to synthesize several batches of MNPs. Among the experiments, a somewhat novel approach, involving the use PEG was introduced. This added PEG can help reduce agglomeration effects, oxidation effects and further help generate smaller particle sizes. The characterization approaches used to evaluate the effectiveness of these batch synthesis runs are introduced later in this study. Results of characterization

presented towards the end of this study also lend credence that PEG has some benefit during the reverse co-precipitation process.

Powder synthesis of magnetite nano-particles in the superparamagnetic regime isn't sufficient to reach the goal of producing a low loss reluctance machine however. Powder most be converted into bulk material. The following chapter outlines a proof-of-concept approach to sintering the synthesized nano-scale powders into bulk material via microwave sintering.

5 Nano-material Sintering

Sintering techniques can take powdered material produced via our earlier synthesis method (Section 4.7), and fuse it into a bulk material. The production of ferrites of low loss characteristics for use in our diamagnetic bearing reluctance machine is the ultimate goal of this final sintering process. Before proceeding, however, it would be prudent to remember that in our earlier discussion of the synthesis process (Chapter 4) an observation was made: namely, that the overall saturation magnetization drops with shrinking particle size. In practice, this means a trade-off must occur. The use of our sintered nano-structured ferrite will mean lower permeability and, hence, lower resulting flux density (and energy density) than a motor built with steel laminations. However, in case of experimental work, a large number of motor topologies and designs may need to be tested. Some of these may not be partial to the geometric limitations of traditional punched lamination manufacture. Furthermore, the costs associated with typical custom manufacture of these laminated versions was noted to be excessive. This provides significant justification for a lower cost sintering solution.

The particular technique for sintering discussed in this section will be microwave sintering. After a review of sintering approaches, a proof-of-concept approach to sintering is demonstrated here and followed with a design proposal for a sintering furnace suitable for the nano-particles discussed in this study.

5.1 Introduction to Sintering

Producing bulk material can be done by melting and casting or by sintering. Sintering fuses powders by controlled heating well below that required for the traditional casting process. The approach has been most widely used for the production of ceramic objects. It is only recently that the use of sintering techniques has extended beyond the narrow confines of traditional ceramic materials, however. The main reason for transitioning to sintering techniques can be roughly categorized as follows [199]:

- Higher purity of bulk materials and relatively simple process to achieve purity.
- Easily controlled and repeatable. Ability to create materials of uniform porosity.
- Higher mechanical strength and greater ductility of end product.
- Relatively easy to produce dimensional products with low shrinkage/expansion.
- Operation at lower temperatures than required for melting.
- Lower costs (both environmental and monetary) than alternative techniques.

The sintering process is generally a result of two competing forces: densification and coarsening. These processes are driven by a combination of local or global driving forces and associated energetics. Particles in the sintering process are always trying to minimize global surface energy through a localized atomic scale diffusion process [199]. The densification process causes inter-particle gaps to shrink leading to reduced porosity. The coarsening process, conversely, encourages diffusion, starting with necking behaviour and then through surface and volume mass transport mechanisms. The result of this process is the formation of grain boundaries and potential enlargement of the grain size. Occasionally the addition of impurities or surface oxide states can restrict the motion of grain boundaries and limit grain growth.

Where our magnetite nano-particles are concerned, in order to preserve the superparamagnetic properties, the end product of sintering must be nano-structured. This means that coarsening mechanisms and grain boundary expansion must be inhibited over densification.

There are two sets of variables that can have an impact on controlling the nano-structure of the final bulk product. The first of these have already been covered in the treatment given to the magnetite synthesis process. They pertain to the effect of left over impurities from reaction pre-cursors. They also pertain to the resultant agglomeration of particles, their size and shape distributions and their surface oxidation states [200]. As with our prior discussion, agglomerations and associated Van der Waal forces (and more strongly bound aggregations) must be minimized. Likewise, shape morphology should aim at amorphous material in order to provide favourable structure preserving conditions for the sintering process. A presence of some variation in size distribution (or poly dispersion) is somewhat useful during sintering as it allows for optimal packing of particles during processing [199].

The second of these variables is related to the actual process control variables during sintering and includes: added impurities, temperature, pressure, time, heating and cooling rates and atmospheric conditions [200]. It is these variables that become important when building a sintering furnace. Of the variables mentioned, time and temperature are the easiest to control.

In general, the operating temperatures of sintering typical micrometre scale powders is roughly $50 - 80$ [%] of the melting point temperature of the material. For nano-materials this temperature can be much lower, as much as $20 - 30$ [%] of the melting temperature [199]. Unfortunately, the heating and cooling rates play a significant part in preserving nano-structure. We noted this with our discussion of bulk metallic glasses (Section 4.1), wherein the rapid cooling of the material led to the production of an amorphous material. Some observers have noted similar effects from rapid heating during sintering. Conventional “free” sintering via an electric furnace faces challenges in achieving the high heating rates needed to preserve

nanostructure easily. The typical heating rates used in these furnaces are in the range of around $5 - 50$ [°C/min] [199], [200], with most operating at the lower range. If heating rates can be increased to the range of 300 [°C/min] (or more) and dwell (or soak) times at high temperatures reduced, a significant improvement in density without corresponding grain growth is seen [199]. As such an alternative approach is needed.

A range of alternatives exist [199] – to name a few: Selective laser sintering, microwave sintering, spark plasma sintering, pulse current sintering and pressure assisted sintering. The costs and complexity of the apparatus needed for a bulk of these approaches does not easily lend itself to proof-of-concept style implementation, and subsequently, experimental production of various topologies of our reluctance machine. It is here that microwave sintering starts to look promising. The technique provides a highly efficient method of sintering nano-particle via rapid heating mechanisms.

5.2 A Survey of Microwave Sintering

The efficiencies of microwave sintering are well in excess to those of conventional electric sintering technologies and can reach as high as $80 - 90$ [%] efficiency [201] – of-course it should be noted that comparison to fossil fuel based furnaces (efficiency of 40 [%]) are not as favourable (microwave sintering falling to 12 [%] efficiency) once intermediate energy conversion steps leading up to electricity generation are taken into consideration [201]. At the laboratory scale for rapid prototyping purposes such lower efficiency isn't a concern however.

In addition to the high heating rates, and higher efficiency, microwave sintering offers an additional cost advantage. This cost advantage is firstly a result of the high reliability ($80{,}000$ [hr] lifespans [200]) of typical magnetrons. A range of frequency options exist for these magnetrons [201], [202], namely: $28, 60, 140, 500,$ 915 [MHz] and $2.45, 30, 83$ [GHz]. While most frequencies come at high cost, the

extensive and almost ubiquitous use of commercial microwave ovens has driven the cost of 2.45 [GHz] devices down to a value that is very cost effective. It turns out that for our magnetite samples this proves to be an ideal range in that the permeability and permittivity of the powdered material is high enough and the conductivity low enough to allow it to fall within the high-power loss region of our 2.45 [GHz] source signal (see Figure 5-1).

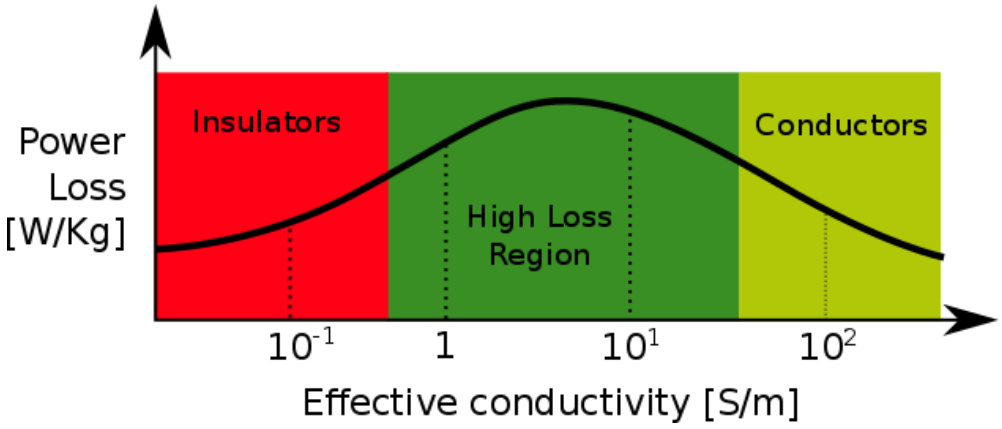

Figure 5-1: Microwave power loss as a measure of conductivity for the 2.45 [GHz] range. Note that graph is a demonstration only & not accurate representation of real data. Figure modified from [216].

It should be noted that a high conductivity means that issues of induced currents and penetration depth (skin depth) become a concern. By taking some materials with high permeability and permittivity, but high conductivities as well, and creating powdered materials, it's possible to artificially reduce this conductivity and increase power loss – this was discovered and demonstrated relatively recently by some researchers [202]–[205]. For magnetite, which typically has quite low conductivity ($10^{-3} - 10^{-2}$ [S/m] [170]) well in the range of an insulator, it is important to note that reasonably high initial relative permeability (72 [140]) and relative permittivity (33.7 [206]) allow for rapid heating mechanisms. Materials, like magnetite, that absorb microwave radiation well are sometimes known as susceptors [146].

There are a number of problems associated with direct microwave heating of magnetite. Both the permittivity and the permeability are dependent on temperature. There is a significant shortage of data on the effects of this temperature on permittivity (or equivalently on the dielectric constant) [146], especially where high temperature conditions are of relevance. This problem becomes compounded further by the fact that a frequency dependence must also be considered in microwave systems. Looking through literature, the same appears to be true with regards to permeability with only one study found on the subject [207]. It is clear, however, that the magnetic component of magnetite plays an insignificant role above the Curie temperature of roughly 575 [°C] regardless of frequency [207].

In this study, our proof-of-concept implementation demonstrated an inflection point in heating as a result of a drop in microwave absorption suggesting that both the permittivity and permeability appear to fall beyond an approximate temperature of around 400 [°C].

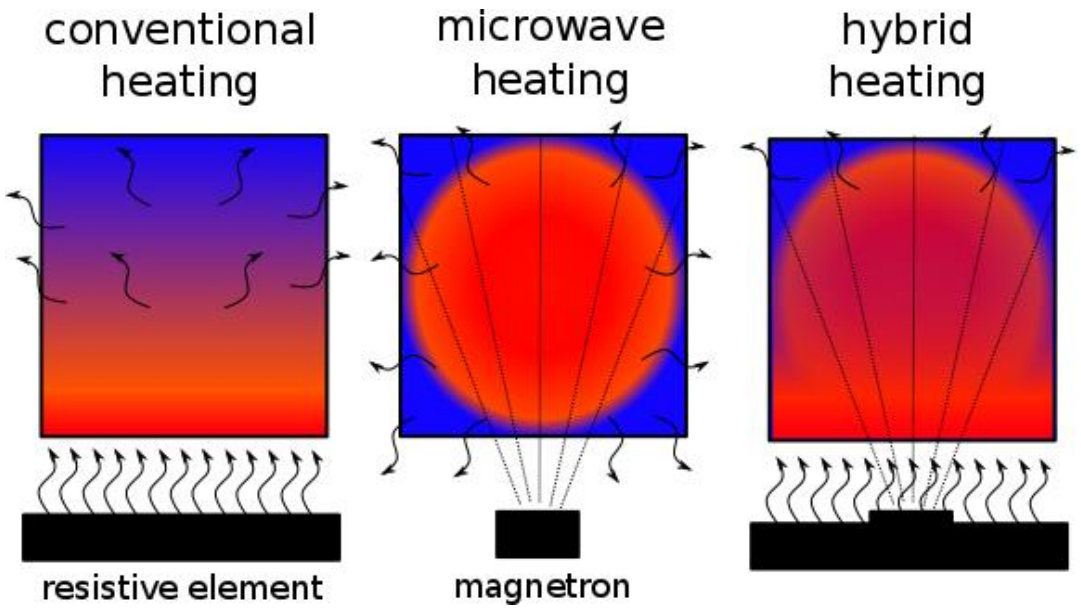

Figure 5-2: Convention to microwave based approaches to heating. The most effective approaches combine the two to generate heating from the interior and exterior of the material. Red regions are hot, while blue regions are cool. Images are for demonstration only and not obtained from real data.

This reduced loss at microwave frequencies means that in order to maintain the high heating rates a mix of direct microwave heating and indirect convective (conventional) heating is needed. Figure 5-2 demonstrates. A commonly used approach to achieving this hybrid approach is to make use of the microwave absorption characteristics of other susceptor materials tuned to the particular temperature range. Both Silicon Carbide (SiC) and Carbon (C) as well as magnetite (itself) are susceptors that have commonly been used for hybrid heating purposes [146], [199]–[205], [208]. An alternative more easily controlled approach (than the use of susceptors) is the use of resistive heating elements.

Practical considerations must also be taken into account when making use of microwave sintering. For instance, the nature and dimensionality of the cavity can have a significant influence. Cavities (also known as applicators) can be multimodal or single modal depending on dimensional factors. The wave length of the microwave frequency input can lead to 3D standing or traveling wave pattern leading to these modalities. Tuning the applicator dimensions and the use of physically movable partitions can provide adjustment towards greater harmonic oscillation and greater power transfer.

However, this is not the only consideration. Appropriate insulation is also required. The use of high alumina (Aluminium Dioxide - Al_2O_3) content ($47.5 - 85$ [%]) and high silica (Silcon Dioxide - SiO_2) refractory linings seems the way forward in terms of quality of insulation. Such refractory has been used extensively in heating considerations [209]. Unfortunately, from our proof-of-concept experimental setup, the choice is challenging. Such refractories are typically designed for use in conventional electric or gas fired kilns and thus can contain high concentrations of microwave absorbing materials.

For instance, the most common combination of additives, in addition to Al_2O_3, include one or more of the following: Hematite (Fe_2O_3), Silicon Dioxide (SiO_2), Chromium Oxide (Cr_2O_3), Aluminium Phosphate ($AlPO_4$), Graphite (C) and

Zirconium Dioxide (ZrO_2). From the author's own prior experiences in glass working and melting, the use of expanded perlite tends to be a simple approach used for some refractories. Perlite is a composite of one or more of the above additives with SiO_2 being the most abundant, followed by Al_2O_3 and fractional components of the remainder. As seen from Table 5-1, the relative permittivity (at room temperature) for these materials can be high and lead to high losses at higher temperatures as well. It should be noted that high temperature data for microwave frequencies are quite sparsely available in the literature and so it is difficult to draw firm conclusions.

Table 5-1: Relative permittivity, permeability along with thermal and electrical conductivity for typical materials used during the microwave sintering process. Note that RT indicates room temperature, UT label indicates unknown temperature and UF, unknown frequency conditions. Where the phrase "assumed" is used, no data is available, however value is expected to be close to the indicated value. Further note that all data is for standard pressure conditions. Data for this table is collected from multiple sources [140], [206], [207], [210]–[233].

Material	Relative Permittivity	Initial Relative Permeability	Thermal Conductivity [W/m · K]	Electrical Conductivity [S/m]
Fe_3O_4	33.7-81 @ RT, 60 [Hz] 7-9 @ RT, 2 [GHz]	72 @ UT, UF	3.8 @ RT 4-6.25 @ RT-800 [°C]	10^{-3}-10^{-2} @ UT, UF
Fe_2O_3	1.4 @ RT, 1 [KHz] 1.3 @ RT, 1 [MHz] 4.7-5.1 @ RT, 2.45 [GHz]	~1 @ RT, 2.45 [GHz]	7.6 @ RT 4-15 @ RT-800 [°C]	10^{-9}-10^{-4} @ 150-500 [°C], UF
SiC	5-20 @ RT, 2.45 [GHz]	*Assumed* ~1	120 @ RT	0.03-0.06 @RT-1300[°C], 2.14[GHz]
C	10-15 @ UT, UF	0.999984 @ RT, UF	25-470 @ RT	$1.6x10^3$-$3.3x10^4$ @ RT, UF $3.3x10^4$-$2x10^5$@ RT, UF
Al_2O_3	3.06 @ RT, High freq. 8.9 @ RT, low freq.	0.99999976 @ UT, UF	12-38.5 @ UT, UF	10^{-24}-10^{-18} @ UT, UF
SiO_2	3.9 @ UT, UF 3.8-5.4 @ RT, 1 [MHz]	*Assumed* ~1	1.3 @ UT	10^{-16}-10^{-12} @ RT, 1 [MHz] $7.5x10^{17}$ @ RT, UF
Cr_2O_3	11.8-13 @ RT, 2 [MHz] 11.9-13.3 @ RT, 1 [KHz]	*Assumed* ~1	9.99-32.94 @ UT	10^{-4} @ RT, 20 [KHz]
$AlPO_4$	6.05 @ RT, 1 [KHz]	*Assumed* ~1	UV @ UT, UF	???
ZrO_2	18-24 @ 275-375 [°C], 1 [KHz] 8-13 @ 275-375 [°C], 1 [MHz]	*Assumed* ~1	1.8-2.2 @ RT	10^{-12}-10^{-3} @ RT-1000 [°C], UF

Noting this difficulty, we can see that the use of SiO_2 and Al_2O_3 is justified by their low permittivities. However, unlike the indications by some sources, the lower thermal conductivity of Silica (SiO_2) suggests a preference for its use. Furthermore, a low conductivity is also desired for not only the sample being sintered but also the insulating and hybrid heating susceptor material. The consequence of higher conductivity is insufficient loss and potential reflected power (because of high Q-factor) back in to the magneton. The result of this potential increase in temperature of the magnetron is a shortened life. While not generally required at low powers (< 2 [KW]), at higher output powers ($2 - 6$ [KW]), a dummy load connected to a circulator (sometimes called an isolator) is needed to dissipate reflected microwave power and to maximize power transfer [234].

While the study of magnetite (and nano-material variants) at high temperatures is very much incomplete in existing literature, some general trends can be evaluated from studies of existing iron based ferrite materials. For instance, one study [235] looking at Mn-Zn nano-ferrite materials noted a slow increase in permittivity with temperature (for frequencies of $0.1 - 30$ [MHz]) followed by relatively sharp decline from roughly $460 - 500$ [°C]. Another study [236] looked at copper doped magnetite (of unknown particle size) and noted a similar dip between roughly $400 - 500$ [°C] followed by a sharp increase and an asymptotic levelling off at $600 - 800$ [°C] and for frequencies between 10^{-4} to 1 [MHz]. The only study directly relevant to magnetite nano-particles that could be found was one by Takayama et al. [148] who used the 2.45 [GHz] frequency range to sinter magnetite nano-particles (10 [nm] particle size) successfully at 1000 [°C] without significant grain growth. This work by Takayama was inspired by seminal work in the early 2000's by Agarwal et al. [202]–[204]. While the study lacks certain important details, it, along with Agarwal's work, has inspired a look at microwave sintering as a potential avenue for bulk ferrite production from MNPs for our low loss reluctance machine in this study.

5.3 Proof-of-Concept Implementation of Microwave Sintering

Given the understanding of the microwave sintering process, we can now build our proof-of-concept sintering system. This system modifies an existing microwave oven. Figure 5-3 shows the layout of the different components of the setup.

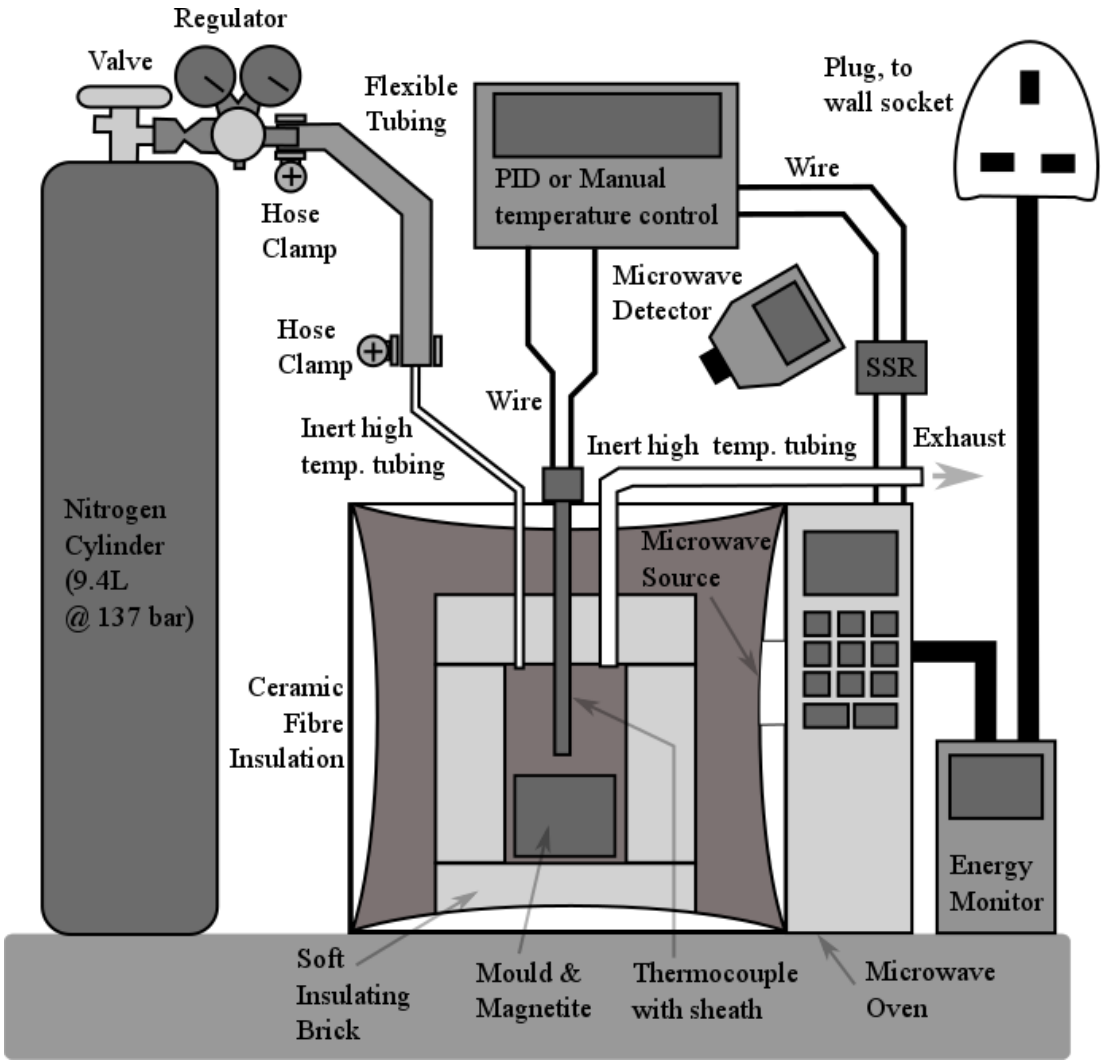

Figure 5-3: A simple proof-of-concept setup for a microwave sintering furnace.

The real system is shown in Figure 5-4. A tuneable PID temperature control is connected to the internal microwave transformer circuit to provide basic on-off style control of the current going to the magnetron. This controller can be operated in either for manual control of the magnetron or for more precise temperature control. The microwave heating process is highly dependent on the materials absorbing the radiation. As a result, PID tuning is a challenging task that requires repeated tuning for each new type of material or combination of materials added to the insulating cavity. Given the time and effort needed to synthesize magnetite nano-particles, this meant that some less valuable and more easily obtained micro-scale commercial magnetite sample was needed for testing tuning parameters.

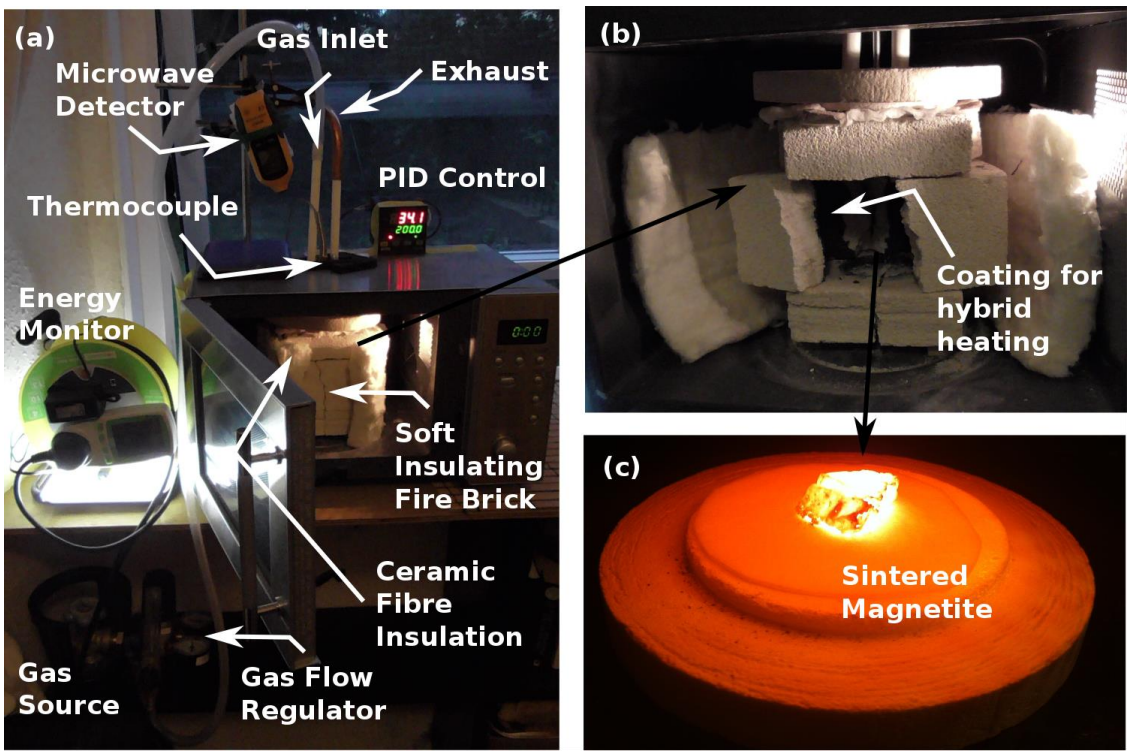

Figure 5-4: Images of simple experiments in Microwave sintering: (a) A simple proof-of-concept setup for a microwave sintering furnace. (b) A high alumina refractory insulation coated with some combination of magnetite, carbon and silicon carbide for hybrid heating. (c) A sintered magnetite sample cooling rapidly in air.

During the heating and cooling process, a shielding gas, in this case nitrogen (N_2) is pumped into the insulated region of the applicator at a controllable flow rate. With the positive flow rate, exhaust from the sintering process flows through the exhaust outlet. This exhaust will be a result of burn-off of binding material or other impurities in the sample. Both the inlet and the exhaust are made from a high alumina cast refractory tubes. An energy and power monitor along with a temperature display provides data which can be recorded on a minute by minute basis. A microwave detector provides an alarm in the event that microwave leakage is detected above the commercial standard safe level of $5\ [\mathrm{mW/cm^2}]$.

To achieve hybrid heating, a combination of magnetite, silicon carbide and graphite are mixed together with a small quantity of water and methyl cellulose or sugar. The methyl cellulose and sugar act as binding agents. These are mixed to a consistency of thick paint and applied to disposable layer of fine ceramic fibre, ceramic block or directly to the inside walls of the insulating chamber. Baking the insulating chamber at low temperature allows the binder to burn off or carbonize leaving a susceptor that provides additional microwave absorption and convective heating of the sample.

The insulating chamber has an internal cylindrical cavity of 43 [mm] diameter and 75 [mm] depth. This cavity is carved into a high alumina refractory block with a square base of 115 [mm] and height of 145 [mm]. The entire insulating chamber is wrapped on the outside with an insulating high alumina content refractory fibre.
Unfortunately, this chamber is too small for sintering of the reluctance machine from our diamagnetic bearing assembly directly. As such, it is used as a method of testing various sintering regimes on magnetite samples generated during the synthesis process. This study was unable to take sintered samples and perform detailed characterization on them using XRD, SEM and SQUID instrumentations. However, the proof-of-concept implementation was used to collect initial data on determining the feasibility of sintering synthesized magnetite nano-particles using microwave approaches. A clear demonstration on one early nano-particle sample (shown in Figure 5-4c) demonstrated that sintering is very much possible.

Unfortunately, because of time and monetary considerations final evidence of whether this sintering process can preserve nano-structure in our magnetite samples could not be obtained and is left to future study. The upcoming chapters will focus, thus, on characterization of the base synthesized powdered material and its potential as a material for low loss in our diamagnetic bearing assembly's reluctance machine.

It is important to note that preparation of samples, prior to sintering, can have a significant effect on the final output material. For instance, addition of small quantities of carbon into the sample material can pull away oxygen from the magnetite sample to produce iron. These additives can also have the effect of producing heating in our magnetite beyond the Curie point of the material. Likewise, careful control of the reducing environment via nitrogen or argon can take the unstable maghemite core-shell structure present on some of the magnetite samples and can energetically favour conversion to magnetite as opposed to hematite. Figure 5-5 demonstrates the steps taken for preparing synthesized powder for sintering.

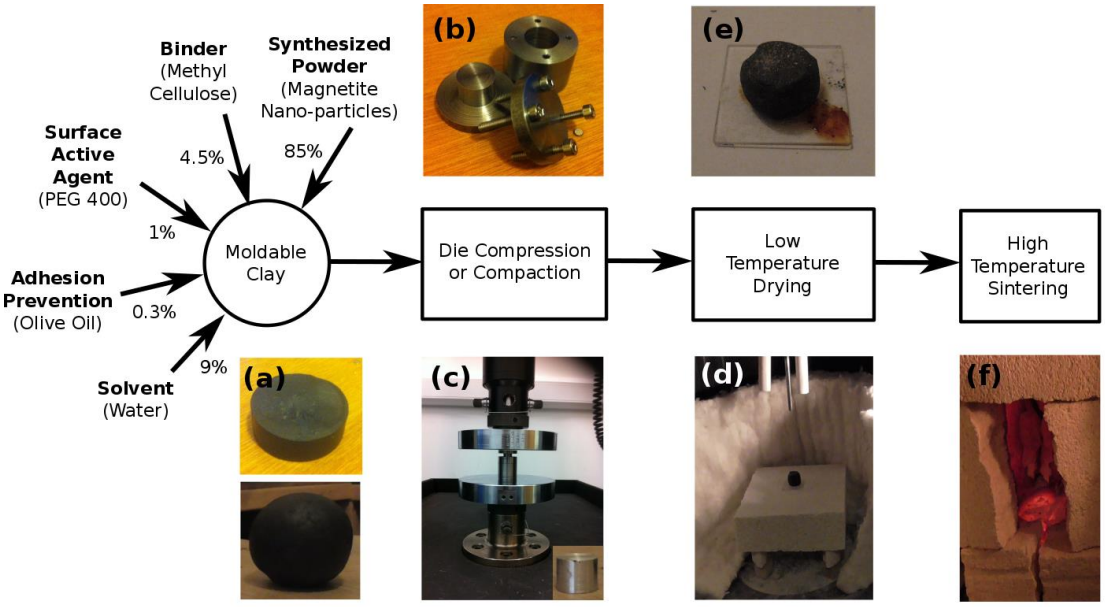

Figure 5-5: After powder synthesis for magnetite is complete it goes through a process by which it is formed into (a) metal clay, (b) using a die. The clay is put under (c) compression and (d) dried. The resulting (e) pre-sinter is then (f) sintered under microwave field.

The production of the clay was based on existing patents for silver clay production filed by Hirasawa et al. [237]. These clays are a relatively recent development and have undergone a number of improvements from the 1990's up to 2006. The use of Methyl Cellulose as binder is beneficial in that the heating process causes gelling sufficient to hold the powder material together until sintering is underway. Compression of the produced clay material was done with the use of Instron machine and then via simpler approaches using an Arbor Press and by hand.

As a result of the dimensionality of the applicator cavity, placement of the sample can be a concern. If the sample is placed in an anti-node location within the cavity, heating can be negatively affected. Damp thermal paper (often used in cash registers) wrapped around inside the furnace was used to determine the optimal height of the sample such that it fell within a region of changing microwave field (an antinode).

Table 5-2: Sintering experiments executed. Note that the sample numbers S.-1 and S.0 are calibration samples that were used to compare co-precipitation based synthesized nano-particles. All samples are powdered materials, except in the case of refractories where materials are cast prior to tests.

Type of Experiment	Sam. Label	Material Used	Mass [g]
Refractory Test	M.13	High Alumina Brick	1394
Pellet (Bulk) Material Tests	M.4	Silicon Carbide	26.7
	M.8	Carbon	17.4
	M.5	Iron (synthesis sample # S.0)	39.5
	M.3	Magnetite (synthesis sample # S.-1)	30.6
	M.11	Fe_3O_4 (S.-1) + C + SiC	16.5
Thin film test	M.14	Fe_3O_4 (S.-1) + C + SiC	36.36

Table 5-2 lists select experiments attempted in the furnace. As mentioned, only one sample of nano-scale magnetite was tested. The range of samples produced via co-precipitation synthesis route were of limited quantity (12.5 [g] per sample) and

considering the time and access needed to prepare these initial samples, it was important that characterization of a sintered test sample occurred so that adjustments to the sintering regime could take place. While, constraints prevented final XRD, SEM, SQUID characterization. The resultant thermal profile of the heating process is a first (for the materials used) under microwave heating regimes.

The samples, indicated in Table 5-2, were tested by making temperature and power measurements per unit time to produce thermal profiles. From the resultant temperature rise information (ΔT), power input (P) and the mass ($\mathcal{M}_{sin}$) of the material inside the microwave cavity, it is possible to estimate the heat capacity (C_p) of the object as shown in Equation (5-1) below over a time interval $[t_i, t_f]$. Note that the value Q represents the quantity of heat energy.

$$Q = C_p \cdot \mathcal{M}_{sin} \cdot \Delta T = \int P \, \partial t \tag{5-1}$$

$$\mathbf{C_p} = \frac{\int \mathbf{P \partial t}}{\boldsymbol{\mathcal{M}_{sin}} \mathbf{\Delta T}}$$

A discussion of the thermal heating results of the sintering process will follow in the results chapter of this study.

5.4 Design Proposal for an Improved Sintering Furnace

Several problems were encountered with the setup shown in Figure 5-4. While testing, it was noted that the structure made it difficult to test sufficiently large samples and, particularly, to construct a completed reluctance machine. The nature of the physical setup made it difficult to extract and insert samples as well.

Some researchers have additionally pointed out that the use of thermocouples in microwave fields can bias temperature readings [237]. Furthermore, distortions and reflections in the microwave field resulting from the presence of thermocouples can be a problem in lower loss materials. A similar situation can occur even without the thermocouple where the Q-factor of the applicator remains high. Overheating of the magnetron in the earlier proof-of-concept setup was noted in a few instances when testing refractory materials. The installation of a thermal cut off switch and more complex control electronics can help limit resulting damage. On to this can be added the difficulties of manually recording temperature, energy, power and microwave leakage readings on a minute by minute basis.

Positioning the sample at an optimal nodal position was also a considerable challenge. And further the application of hybrid heating of susceptor material and the testing of various combinations of susceptor material proved tricky in the setup.

Improvements to account for these factors can be made as shown in the design in Figure 5-6. The addition of an infrared sensor combined with a movable germanium lense can be used to determine the extent to which thermocouple measurements interfere with temperature measurements (Figure 5-7). Such a lense is transparent to infrared radiation and can withstand temperatures in excess of 1000 [°C] easily. The larger cavity and the horizontal orientation of the cavity can allow for easy positioning of larger samples. At the same time a moveable microwave source allows repositioning of nodal positions along the length of the cavity. The wave guide can easily be combined with a circulator containing a dummy load and thereby reducing reflected power and damage to the magnetron. A cylindrical sheet metal sheath that can be inserted into the oven cavity provides a method of converting the furnace from a multimode to single mode type (Figure 5-8). The sheath can also be easily coated with susceptor material to provide an easy method to remove and test different susceptor combinations. A more flexible control (Figure 5-9) with computer interface and customizable display also allows for automated data collection and more fine-tuned temperature controls where heating rate, hold and soak time and sintering temperature can be controlled easily.

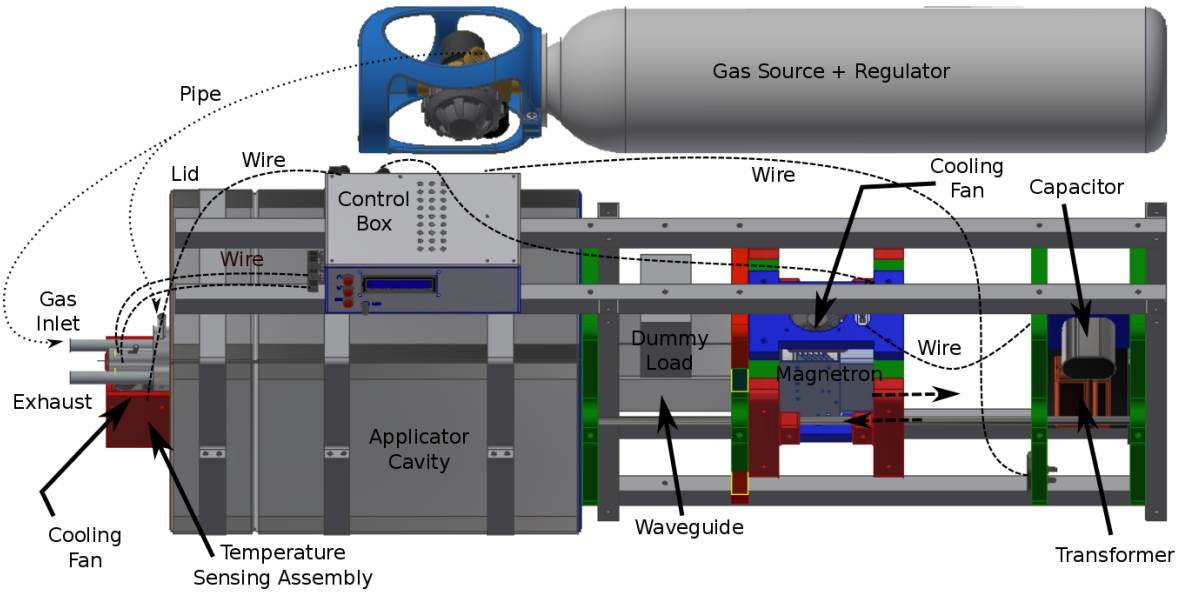

Figure 5-6: An overview of an improved design for a sintering furnace.

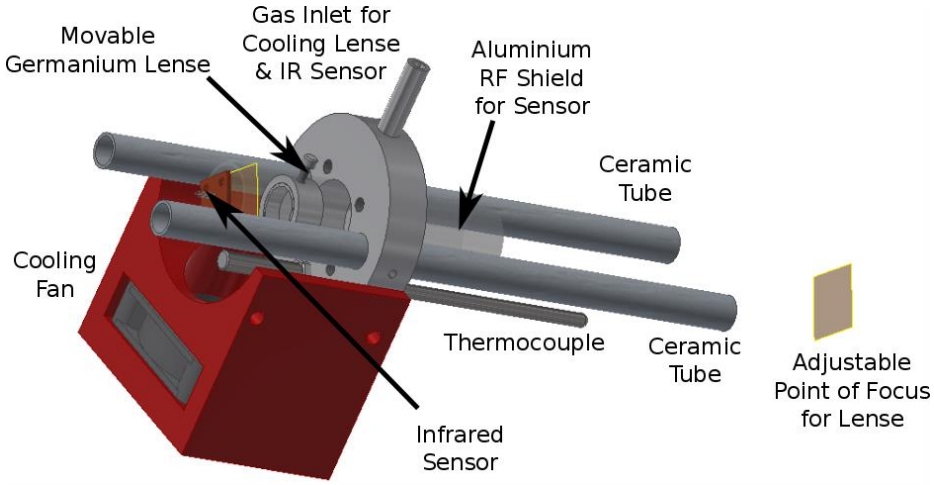

Figure 5-7: A closer look at the temperature sensing assembly – a combination of thermocouple and optical IR temperature sensor.

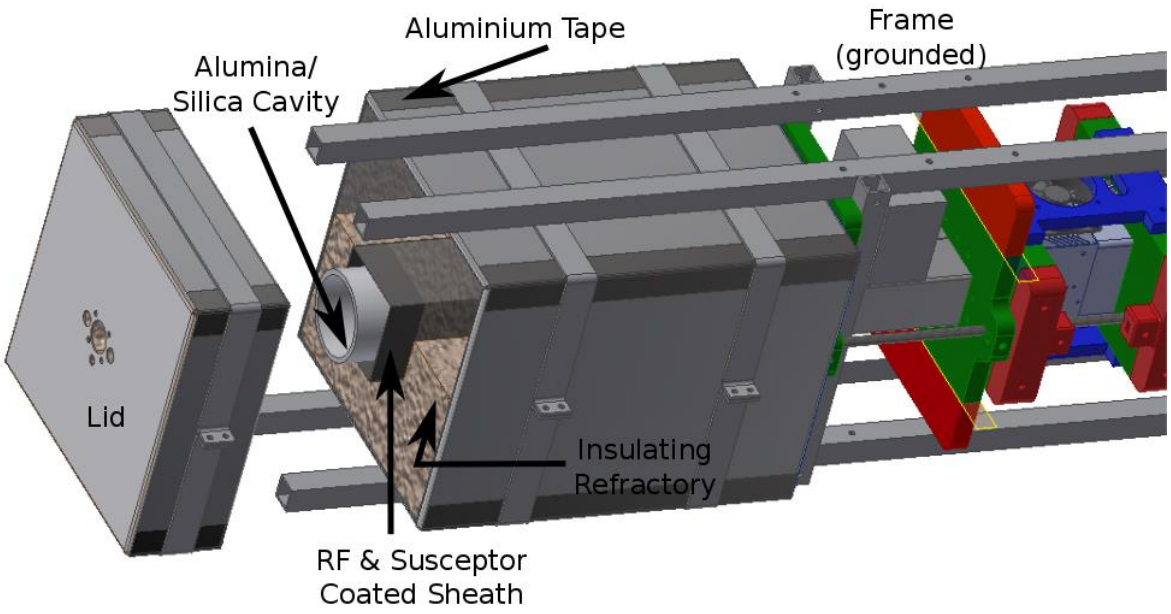

Figure 5-8: A view inside the applicator. A steel sheath can be coated with susceptor material for hybrid heating while still allowing absorption by the sample being sintered. Applicator, lid and frame are grounded to prevent high charge build-up.

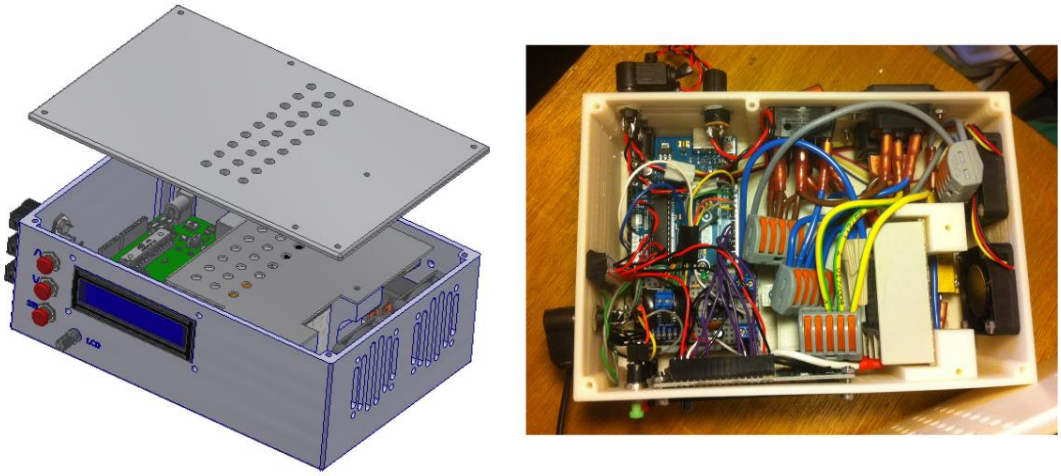

Figure 5-9: A control box with high voltage and low voltage sections. High voltage is ground shielded to prevent RF interference. Low voltage side uses an Arduino to provide sensor interface to IR sensor and thermocouples. Output to cooling fans is also provided via the control box.

The control circuit for the control box is shown in Figure 5-10. Note that the original PID box used for the proof-of-concept sintering furnace continues to provide the control. The control box converts data from both the thermocouple and the IR sensor and uses both signals to recreate a K-Type thermocouple output for PID box. The advantage of taking this approach is that it eliminates the need for programming PID and related autotuning features from scratch in the Arduino. At the same time the Arduino provides current, voltage sensing interface display interface and data logging and computer interfacing necessary for larger scale controlled tests.

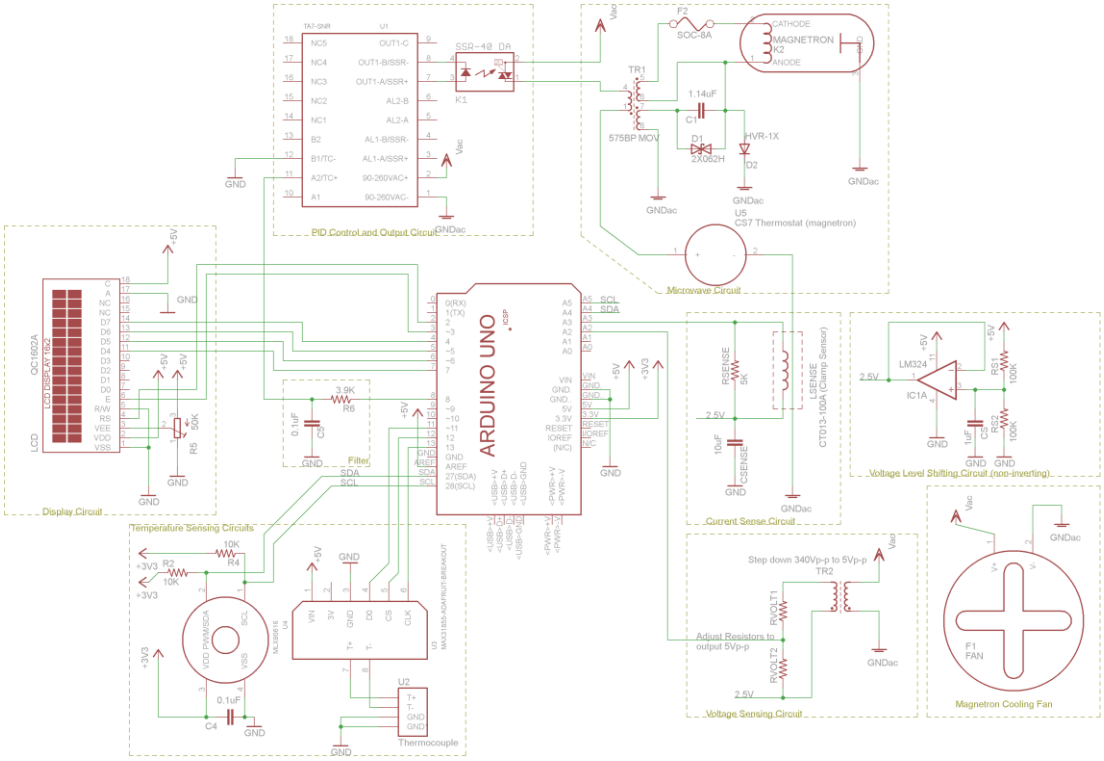

Figure 5-10: A control circuit for the control box in Figure 5-9. The PID control box from the original proof-of-concept furnace provides the necessary output control signals using an artificially generated K-Type Thermocouple output from the Arduino.

5.5 Summary and Final Remarks

This chapter outlined a proof-of-concept approach to sintering synthesized nano-scale powders into bulk material. It was noted that a significant challenge to producing bulk material while maintaining superparamagnetic properties lies in preserving nano-structure in the sintered product. This nano-structure should be preserved in order to reduce parasitic loss via hysteresis effects in the diamagnetic bearing's electrical machine.

Rapid heating and rapid cooling appear to help preserve this structure. The typical approaches to sintering using electric furnaces, cannot easily achieve this rapid sintering. Some literature has suggested an alternative approach using microwave sintering may be the way forward. It is this that motivated the modification of an existing microwave oven to attempt magnetite nano-particle sintering.

A series of test runs were attempted using an oven modified to allow thermocouple based temperature sensing and PID control in a reducing environment. These test runs were used to demonstrate the microwave absorption characteristics of insulation material, suceptor material and both commercial and nano-scale magnetite samples. Thermal curves associated with these tests are presented in a subsequent results chapter. Unfortunately, while sintering was shown to be successful, the necessary characterization steps could not be carried out to verify and compare the nano-structure of the sintered material to the nano-structure of the original powder synthesis. There appears to be promise in this area, but the final characterization has been left as future work.

As a concluding point, an upgraded and modified design for an improved sintering furnace has been presented. This furnace attempts to address many of the challenges associated with collecting data on the sintering process. While some design work has attempted to work out details of this new furnace, a complete implementation is left as future work.

The process of characterization for sintered samples when compared to characterization of the original synthesized powdered MNPs remains largely unchanged. The next chapter provides an overview of the methods used to characterize and understand the physical properties of nano-stuctured magnetite samples. The chapter further looks at measurement techniques for understanding loss in the diamagnetic bearing as a whole as well.

6 Measurements and Characterization

Thus far, we have noted that it is when it pertains to discussions of absence of hysteresis that nano-particles hold significant promise. The low (zero) coercivities and low (zero) remanence associated with particles entering the superparamagnetic regime can potentially remove all contributions to loss resulting from cogging related remanent field drag in the rotor-stator of our diamagnetic bearing reluctance machine. This chapter will discuss briefly the technique used for measuring rotor speed and drag before drilling down into a detailed discussion of nano-particle characterization.

It is worth remembering the reasons for choosing magnetite in this study. While magnetite is not the ideal choice of material, it proved to be a convenient one for the purposes of synthesis within the tight time constraints, limited control measures available and the economic challenges of the study. The reason for this non-ideal nature is largely associated with the low magnetic saturation of the material compared to silicon steel. However, there are several advantage to its use in terms of simplicity and stability (along with low power loss). Magnetite forms a good starting pre-cursor for other ferrite formulations as well. Furthermore, it is relatively easy to reverse unstable oxidation states (e.g. maghemite) with control of sintering environment. With strict measures, some initial sintering experiments in the proof-of-concept microwave setup of this study demonstrated (via the production of what appeared to be pig iron) that conversion to iron may also be possible. This offers the potential of producing nano-particle iron by an alternative synthesis route that does

not appear to be explored in literature. It should be noted that, barring one existing study, studies of magnetite nano-particle sintering via this approach (or indeed any other) have never been done either – at least to the knowledge of the author.

To evaluate whether superparamagnetism indeed does occur and to determine under what conditions the property can be preserved, a total of 31 experiments were completed. These experiments produced magnetite samples under varying synthesis conditions with the aim of determining an optimal route towards superparamagnetic material. Four avenues were taken to provide characterization of the base synthesized particles, namely: Scanning Electron Microscopy (SEM), X-Ray Diffractometry (XRD), Magnetometry (SQUID) and basic camera-based colorimetry. These same characterization methods can be largely used for the sintering process as well. During sintering thermocouple based temperature characterization can also be added to the list. This chapter provides an overview and discussion of each of these measurement techniques used for MNP characterization in this study. Further to this the chapter expands on electromagnetic simulations that were used to support experimental work.

A point of note regarding characterization needs to be made. A significant amount of time was needed to complete the synthesis and characterization process for each magnetite sample, with each sample taking roughly 2 weeks to synthesize, dry, prepare, calibrate and characterize. Of the experiments run (roughly 1 year of continuous effort), only 2 samples demonstrated some limited promise of superparamagnetic properties below the margin of error of the particular characterization approach. Only these 2 samples demonstrated a coercivity and remanence falling below the measurement error – only these samples could reasonably be given the label of zero coercivity and remanence necessary to indicate superparamagnetism. Given this understanding, some shortcuts were used to reduce the time & cost of characterization.

6.1 Bearing Measurements

There are a number of challenges in making measurements for our diamagnetic bearing system. The small displacements and the low stiffness of the prototype setup shown and analysed earlier (Chapter 3), meant that contact force sensors would significantly bias results. Furthermore, the high precision required to make such measurements of particularly small displacements (< 1 [mm]) and forces (< 1 [N]) meant that high quality non-contact sensors would be required.

Figure 6-1: Encoder, tachometer and reluctance drive for testing diamagnetic bearing loss. Encoder lines separated by 11.25 [deg].

Obtaining such sensors wasn't possible. As such a simpler and cruder approach to loss measurement was taken and then supplemented by finite element and other

analytical modelling. Some correlation was found between the real built bearing and analytical results via crude measurements. These measurements demonstrated a stable levitating rest position of approximately $dg = 1$ [mm] for $p = 6$ [platters]. This was measured using a marked piece of paper, though an improved method using laser pointer angle displacement was also attempted. Unfortunately, poor reflective quality of foil and poor precision of alignment made this a challenging task. Constructing a Michelson–Morley style interferometer was also considered and abandoned. The theoretical prediction of levitated mass (as computed by earlier analytical expressions – Section 3.4) proved to be off by roughly a factor of two, predicting liftable mass at 16 [g] while the real system lifted roughly 30 [g].

A simple method of measuring changes in rotational velocity used a handheld digital tachometer and encoder wheel to measure rotational velocity. Figure 6-1 demonstrates this setup. The encoder wheel was pasted on to the top diamagnetic stabilization disk in the bearing setup.

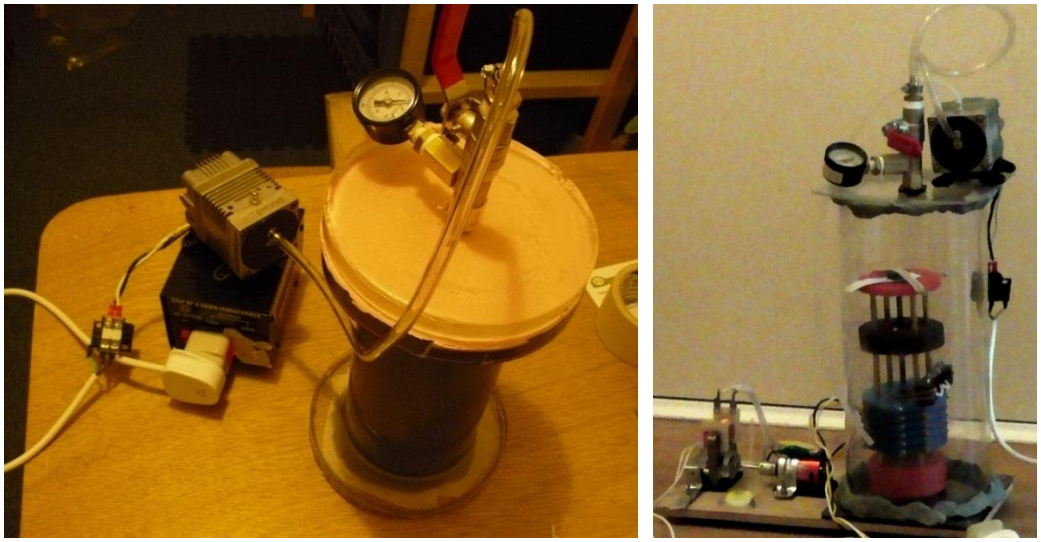

Figure 6-2: Vacuum chamber for the diamagnetic bearing assembly. The bearing fits inside the tube. Typical vacuum pressures used were at low vacuum at around -60 [KPa].

Unfortunately, this approach had many problems. A lack of proper reluctance machine controller and the low power of the three-phase supply meant that the rotor assembly couldn't be driven automatically and produce consistent conditions. To help alleviate this issue, an air blower was used to drive the bearing. Furthermore, the handheld optical approach was accompanied by a large margin of error at lower velocities and could only be used, in some cases, for estimating a general trend – the details of these trends are provided in the results chapter.

A further problem lay in accounting for air friction. As easy access to a vacuum environment was challenging, an attempt was made to construct a vacuum chamber to remove air from the system as shown in Figure 6-2. The top lid of the chamber was transparent to allow for optical measurements in an early version – this was replaced by a clear chamber in a later version. Unfortunately, this approach, without proper rotor control meant that the rotor couldn't be effectively driven without manual intervention. Attempts to pass wiring through the chamber were met with limited success and vacuum preservation proved somewhat difficult. The tachometer apparatus was also found to operate ineffectively through the transparent cylindrical vacuum chamber and so measurements related to power loss proved difficult to make.

6.2 X-Ray Diffraction (XRD)

XRD measurements on synthesized particles were used in this study to provide limited first step characterization to verify composition, crystallite size and density characteristics. The XRD process is most suited to measurements of crystalline materials [238] making this approach less than ideal for amorphous materials generally noted to be produced via the co-precipitation approach. In practice, however, despite suggestions in literature, the co-precipitation routes used to create magnetite samples in this study proved to be sufficiently crystalline for diffraction mechanisms occur.

The process of preparing samples for XRD characterization is diagrammed in Figure 6-3. After synthesis, a calibrant (NaCl) was added and the particles were dispersed in one of three solvents, water, acetone or ethanol. The resulting dispersion was collected via a pipette and deposited onto a glass slide. The slide was then baked in an oven at low temperature (60 [°C]) to evaporate the solvent and leave a powdered material behind. Because of the high frequencies, X-ray penetration depth through the magnetite sample is shallow meaning that a thin powder coating is sufficient for accurate analysis. Sample slides are loaded into powder diffraction machinery in batches of eight for analysis.

The process of analysis involves production of 2θ v.s. count (n_X) plots where the sample is rotated as the emitter-detector combination, likewise, rotates through 2θ. Figure 6-4 demonstrates an example plot from a synthesized nano-particle sample. The XRD emitter-detector combination act as an interferometer. In an earlier, brief discussion of magnetite crystal structure (Chapter 4), we noted a unit cell delineation. A known wavelength (λ) emission is reflected at varying d-spacing from the crystal planes – the result of traveling this distance, d, means that the resulting reflected waves interfere to produce a diffraction pattern at the receiver. The resulting counts provide a measure of the intensity of this pattern. The d-spacing was extracted and fit to existing mineral database patterns to produce an estimate of the lattice parameter indicating the size of the magnetite unit cell and resulting density of the sample.

Equation (6-1) demonstrates this count and angle relationship [238] and is referred to as Bragg's Law with solutions to d giving rise to our lattice parameter (Å). Notice from the counts plot that a background effect is superimposed on our count values. This is a result of the materials present in the XRD mechanism itself – this background must be eliminated prior to analysis.

$$\mathbf{n_x = \frac{2d}{\lambda} \sin \theta} \tag{6-1}$$

Determining the particle size relationship from the plot is somewhat complicated and can be done by parameter fitting of the Scherrer equation [239] shown in the equation below (Equation (6-2)).

$$\mathbf{D} = \frac{\boldsymbol{\mathcal{K}\lambda}}{\boldsymbol{\mathcal{B}\cos\theta}} \tag{6-2}$$

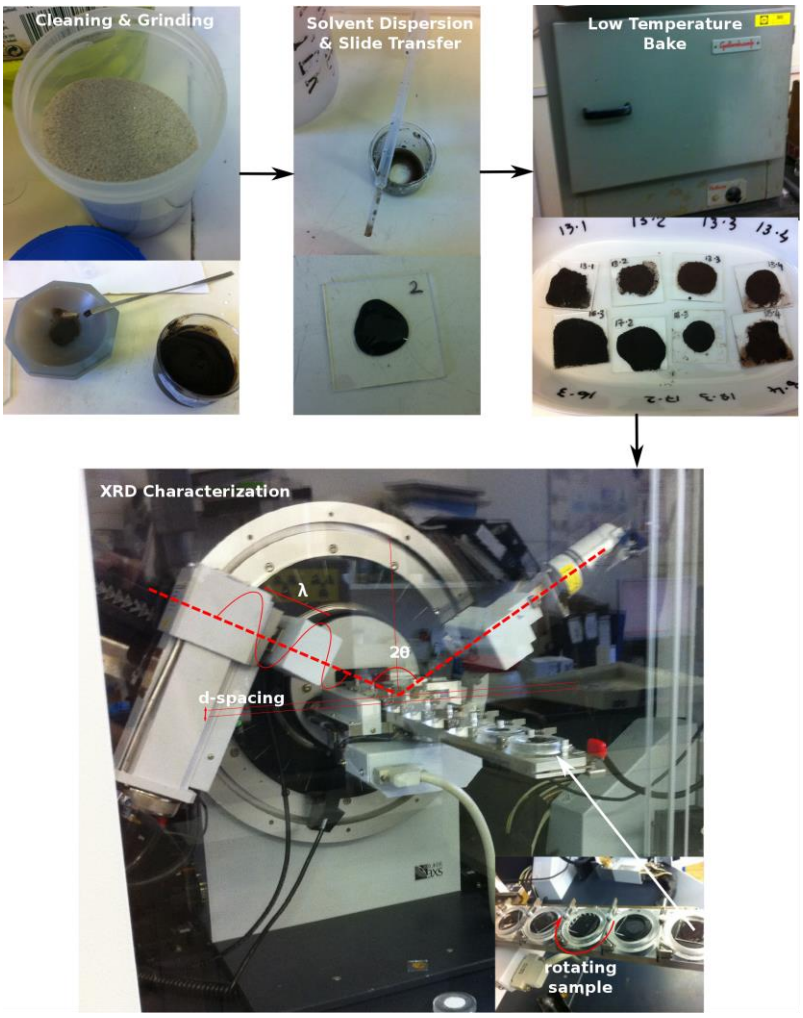

Figure 6-3: Steps in sample preparation for XRD analysis. A mortar is cleaned using sand and a small quantity of magnetite grinded. This grinded magnetite is dispersed in a solvent (e.g. water, ethanol) and using a pipette transferred on to a slide and dried. The dried sample is loaded for XRD analysis.

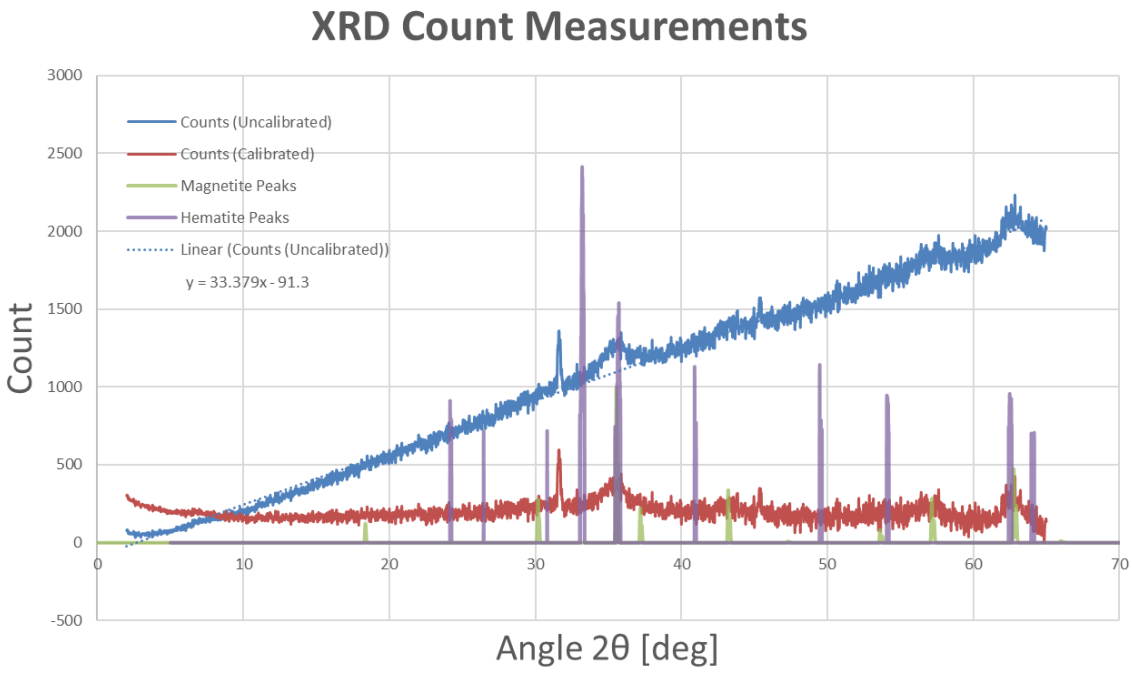

Figure 6-4: XRD measurement for a synthesized magnetite nanoparticles sample from this study. Notice the 10x scaled peaks normally associated with magnetite and hematite. Data from maghemite, while not presented shows peaks in the same region as magnetite.

Here the value $\mathcal{K}$ is a shape factor associated with the crystalline structure of the material, D is the particle diameter and $\mathcal{B}$ is the broadness of the peaks of the XRD counts. As seen in Figure 6-4, determining these parameters can be challenging. The problem becomes a parameter fitting problem – an existing software was used to determine this fit.

One particularly important thing observed through this process was that at the particle diameters (e.g. 10 [nm]) under consideration, peaks in the XRD counts plot tend to widen considerably from the normally narrow peaks. This means that fitting above the not inconsiderable noise in the measurements becomes challenging. Furthermore, given that magnetite and particularly, maghemite, tend to exhibit close characteristic peaks, the broadness of a peak may be a result of the combined contributions of the oxide states. Given these issues, measurements from XRD

analysis alone are insufficient to provide sufficient verification of actual particle diameter. To account for this further characterization is needed by alternate means.

6.3 Scanning Electron Microscopy (SEM)

Electron microscopy is another, somewhat more costly, approach to verifying particle size. Furthermore, such measurements also provided additional data on aspect ratio and size distribution that can be used for more precise estimation of parameters such as blocking temperature – details will follow in a later chapter.

As with earlier XRD measurements, sample preparation occurs by taking powdered material generated during the synthesis process, grinding it and using an adhesive tape to stick it on to a sample holder (Figure 6-5). The sample undergoes sputtering, a process which coats particles with a thin conductive graphite layer. After sputtering, the samples must be carefully stored to prevent moisture absorption until actual measurement can take place.

The electron microscope works by bombarding a sample with a scanning electron beam. The returned scattering of this beam into detectors provides information on the surface profile of the material. Two detectors are shown in Figure 6-5f, the In-Lens (IL) and Secondary Electron (SE) detector. Both these detectors were used and greater reliability found for in lens detection. Initial attempts to perform imaging were done at beam voltages of 20 [KV] and after experimentation were dropped to 10 [KV] and eventually 8 [KV] to reducing imaging artefacts.

Several problems occurred during microscopy early on. Synthesis of sets of samples containing sodium hydroxide and PEG were found to be particularly difficult to put under vacuum. Leftover impurities from insufficient washing prevented sufficient vacuum formation in the SEM column. These impurities boiled off and became deposited on the inner walls of the column. The resultant implications of this process can be drastic. For instance, the author noted a half year delay during which the

microscope column had to be decontaminated. Similarly, contaminants introduced from the drying furnace were found to further make imaging challenging.

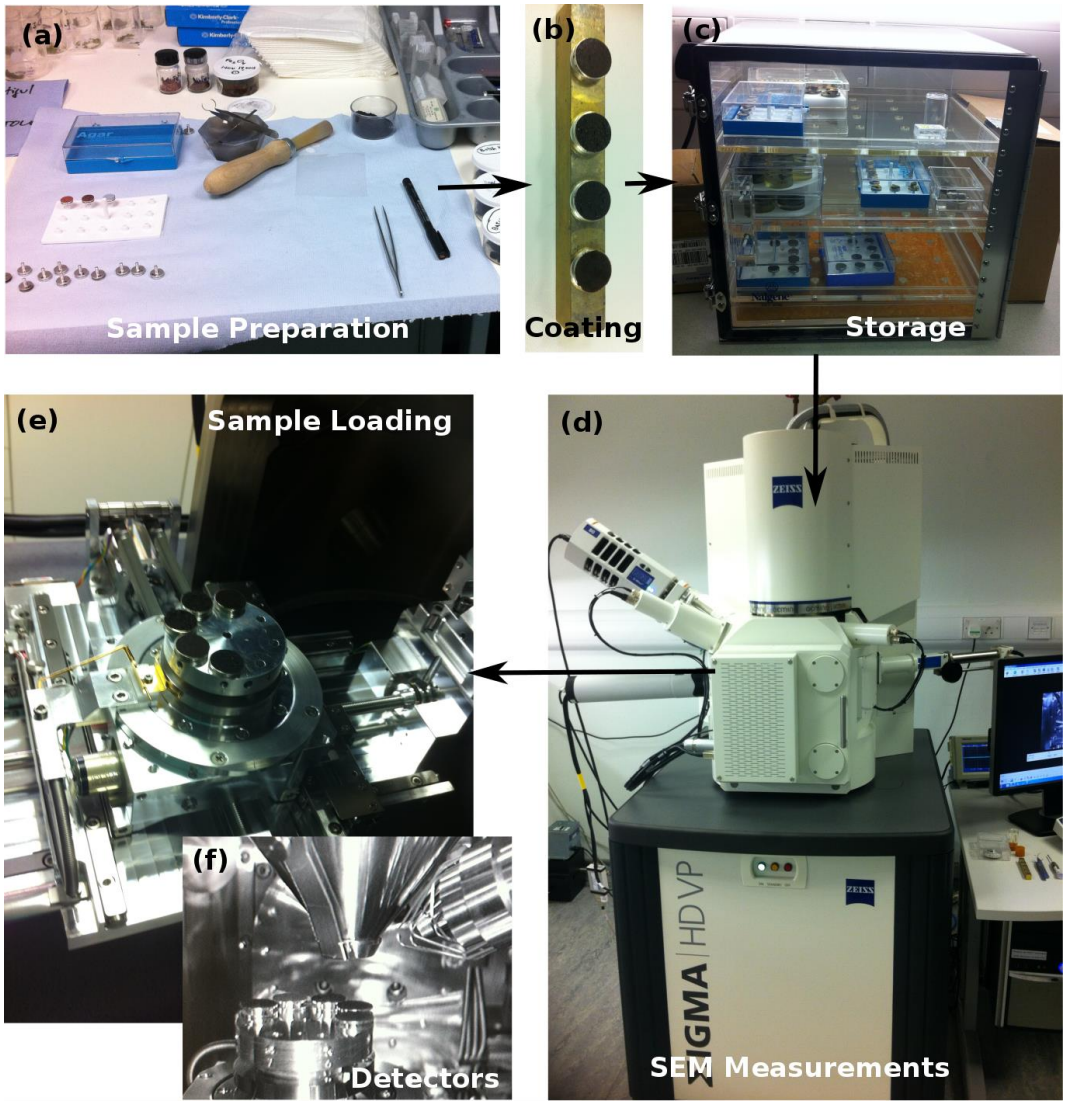

Figure 6-5: Sample preparation and characterization via SEM. (a) Powdered material is ground down and stuck to a sample holder via an adhesive tape. (b, c) Samples are sputter coated with graphite and placed in low moisture storage. (d, e, f) Sample holders are loaded with up to 8 samples for imaging.

The purpose of the sputtered layer was to provide a ground path along which electrons can flow through to the holder and on to ground. This layer is extremely important in that as high energy electrons are fired on to the sample, a charge will build up, this charge will deflect further electron firing leading to significant image artefacts - Figure 6-6 demonstrates some artefacts encountered. In many cases, during measurement, an improper or incomplete coating was found to generate a force that moved powder particles mid-measurement. This was particularly noticeable at the high magnification factors needed to image particles at sufficient resolution to determine diameters and shapes. At these resolutions, the beam ever narrowing scanning field of view was noted to cause added charge build up. Originally, given the ferrimagnetic nature of the particles, it was thought that induced magnetization resulting from electron motion would similarly effect the beam path. However, this did not appear to be the case.

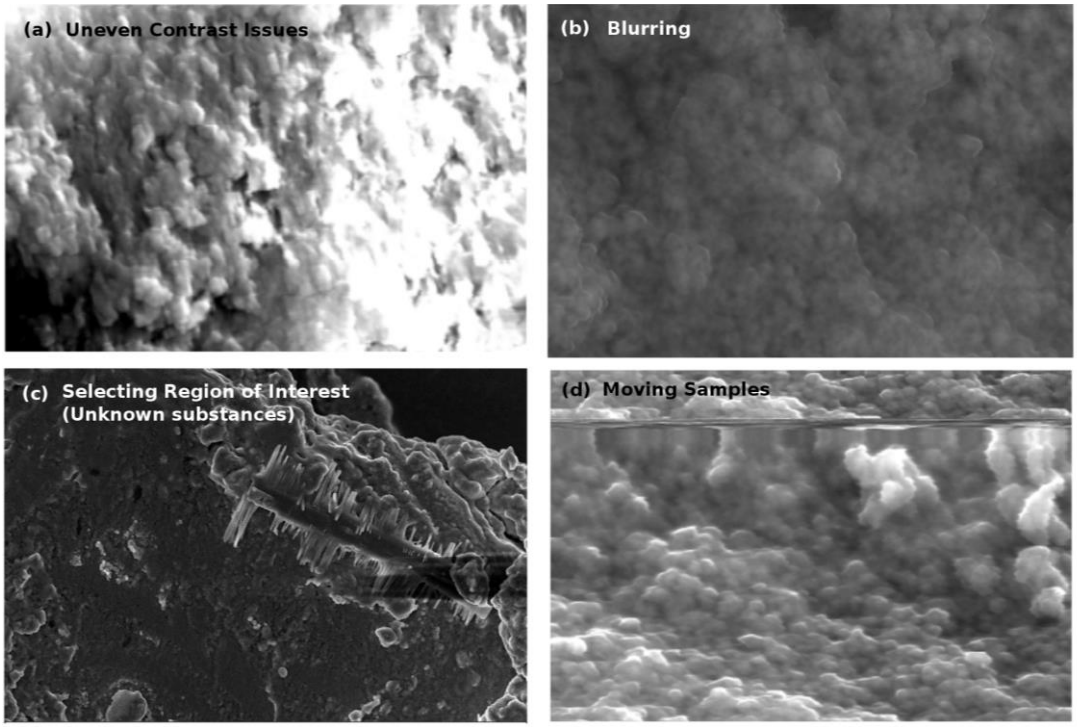

Figure 6-6: Examples of some imaging artefacts during the SEM image acquisition process.

Table 6-1: Examples of some imaging artefacts during the SEM image acquisition process.

	Step	Description	Image
(A)	Image Selection	An appropriate SEM image must be selected and physical and pixel dimensions related to each other. A typical scale might be 1.11 [px/ nm]	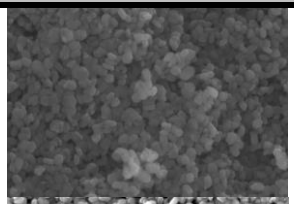
(B)	Fast Fourier Filter	A Fourier bandpass filter is used to remove noise frequency components in the image intensity values that come from pixel features below 3.6 [nm] & above 90 [nm] sizes.	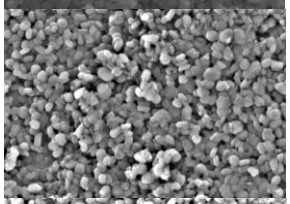
(C)	Window Filter	Intensity values are enhanced further to pull out high contrast regions in the image. These high contrast regions are likely to be a result of individual particles.	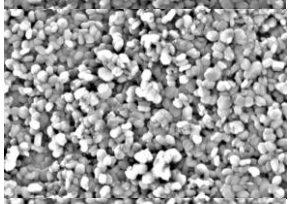
(D)	Gaussian Filter	An additional small window size Gaussian filter (3.6 [nm]) is used to eliminate any further narrow features that may be mistaken for a particle. The filter further softens edge transitions.	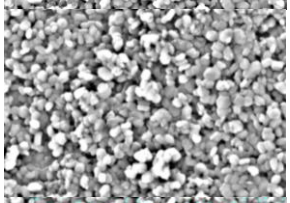
(E)	Identify Maxima	With the softened edge transitions, local maxima in intensities are likely to fall close to the actual particle centre.	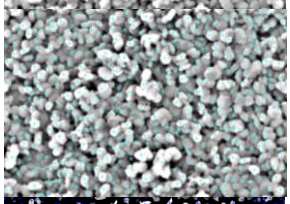
(F)	Locate Foci	The local maxima are further refined to provide better centre of mass locations. Regions where local maxima peak heights & widths that were not sufficiently above the background and within 7% of the identified local maxima were eliminated.	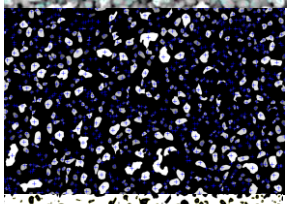
(G)	Binary Threshold	Binary thresholding is used to produce a black and white image for extracting particle statistics via blob detection.	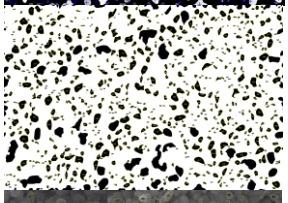
(H)	Particle Statistics	A list of particle centre of mass', aspect ratios and associated diameters are extracted. This is combined with manual selection and algorithm re-runs with slightly varying conditions to compute error estimates on particles sizes.	

As a result of these issues, each electron microscope image can take between 2-4 hours to acquire. The process of imaging is something that requires a certain amount of artistic finesse, however, after images at the appropriate resolution have been acquired, considerably more processing is required to extract useful information associated with particle size distributions, crystalline structure and shape morphologies (aspect ratios). The processing steps can roughly be divided into the steps shown in Table 6-1. To simplify image process somewhat, an existing tool, called ImageJ, commonly used by researchers working in image analysis was used to partially automate extraction of particle statistics.

The particle size distribution resulting from the above image analysis tended to follow a log normal distribution. To verify the semi-automated image analysis, a smaller set of samples was analysed using manual identification as well. Aspect ratios for most samples generally showed that particle sizes were not completely spherical, suggesting that shape related anisotropy exists.

6.4 Magnetometry (SQUID)

Given that many of the samples produced during synthesis showed themselves to be in the superparamagnetic or single domain size range through both XRD and SEM characterization, further characterization of hysteresis loss was undertaken. A Superconducting Quantum Interference Device (SQUID) was used to analyse hysteresis, zero field cooling (ZFC) and field cooling (FC) effects.

As with XRD and SEM characterization, prior to measurement some sample preparation was required – Figure 6-7 demonstrates. This preparation initially involved sample grinding followed by insertion into a small gelatin capsule. Careful measurement of the sample weight is required so that magnetization measurements may be mass normalized – such measurements are typically in the high microgram range and so precision instrumentation is needed.

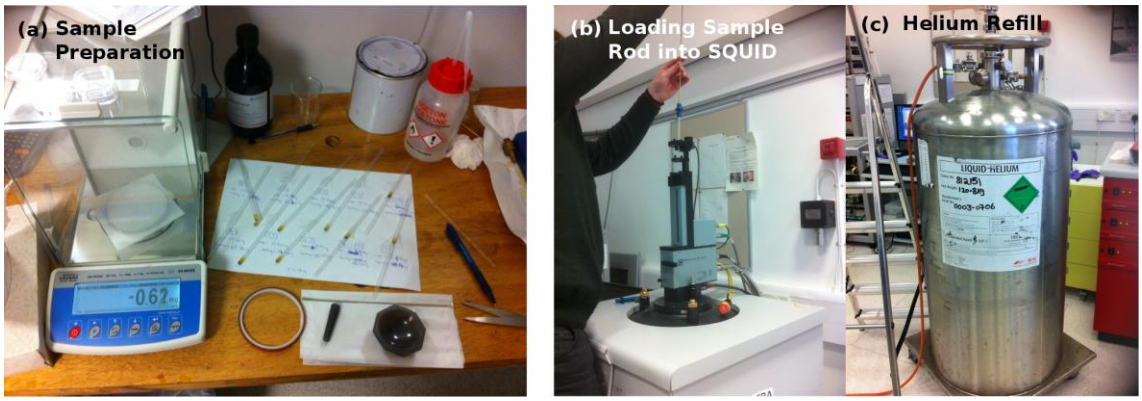

Figure 6-7: Producing samples for the SQUID magnetometer and inserting them for measurement. The SQUID requires super cooled helium to maintain temperature of the internal superconducting coil.

Once inserted into the capsule, the samples are fixed in place by inverting the capsule lid and securing it on with polymide (heat resistant) tape. Early experiments found that this method of securing led to sample movement from the high fields generated by the SQUID. To better affix the sample a low melting point wax known as Eicosane was used to secure the sample with the help of a heat gun. The capsule is inserted into a straw and fixed onto a long rod (sample holder) that is inserted into the magnetometer via an air-lock mechanism.

A liquid helium dewar provides a constant (and expensive) supply of helium to keep the superconductor cool. Most samples prepared took roughly four hours of processing time under DC field. Ideally to obtain better estimates of anisotropy, blocking temperature and other frequency dependant effects via RF field mode of operation and vibrating sample magnetometry. Such processes are costly and time consuming, however, and so were avoided. With the support of modelling work a relatively sparse set of data at low cost and reduced time could be obtained and analysed to extract critical point information and power loss information.

The SQUID magnetometer [4] in DC field mode provides an extremely sensitive magnetic measurement device allowing field measurements as low as 10^{-15} [T].

Given that superparamagnetic behaviour was expected, the use of this device was chosen specifically to provide very precise estimates of the remanent and coercive critical points on our hysteresis curve. Recall that it is these points that characterize the extent to which power is likely to be lost in our synthesized materials when subjected to the changing magnetic field from the diamagnetic bearing motor coils.

The heart of SQUID devices is a superconducting coil divided by two non-superconducting junctions known as the Josephson junctions [240]. When cooled by liquid helium, superconduction takes place via oppositely traveling spin coupled electrons (Cooper pair). A constant bias current is maintained in the superconducting coil. Our magnetite samples are placed one by one in a pickup coil that closely interacts with the superconducting coil – as the sample is moved incrementally through the pickup coil, an induced field causes phase mis-alignment between the electron pairs and a resulting voltage change across the superconductor. This measured voltage change provides an estimate of the magnetization of the original sample based on the applied bias H-field in the superconductor.

Despite the high sensitivity of the magnetometer, precision was limited to $0.33\ [\mathrm{Oe}] = 26.26\ [\mathrm{A/m}]$ for the applied bias H-field. The use of the co-precipitation approach has been extensively reported as consistently being superparamagnetic, however, such reports are unconvincing given that error data is rarely reported. In this study, we noted that of the large number of samples synthesized, only two demonstrated coercivities below the margin of error. This suggests that, perhaps, that attributing superparamagnetic behaviour requires some more considerable attention to error. Looking at the two samples, we note that the two samples fall below the coercivities and remanence of an equivalent silicon steel sample with H_c= 23.07 [A/m] and $B_r = 2.89 \times 10^{-6}$ [T]. By comparison, silicon steel falls at: H_c= 33.51 [A/m] and $B_r = 1.76$ [T] proving a very substantial difference. This significant improvement, however seems to come at a very high cost, the resultant initial permeability of the material drops significantly from a value $\mu_{ri} = 10$ to $\mu_{ri} = 3$. This does not compare favourably to silicon steel ($\mu_{ri} = 1825$) unfortunately. Here we should note that great care must be taken in defining

permeability (or related susceptibility). Much ambiguity exists in literature in relation to susceptibility – in particular susceptibility values can have differing meaning. For instance, the commercial sample of magnetite measured in this study had an initial susceptibility of 10 and a maximum susceptibility of 30. A further distinction should be made with regards to mean susceptibility, high field susceptibility, DC/AC susceptibility as well as differential susceptibility.

Returning to difficulties related to measurement, in addition to the relatively large margin of error, measuring the magnetization at low fields had an additional challenge. Some key calibration problems were noted. Measurement of hysteresis curves consistently yielded non-physical results where by the decreasing and increasing slopes of the hysteresis curve crossed axis incorrectly – Figure 6-8 explains.

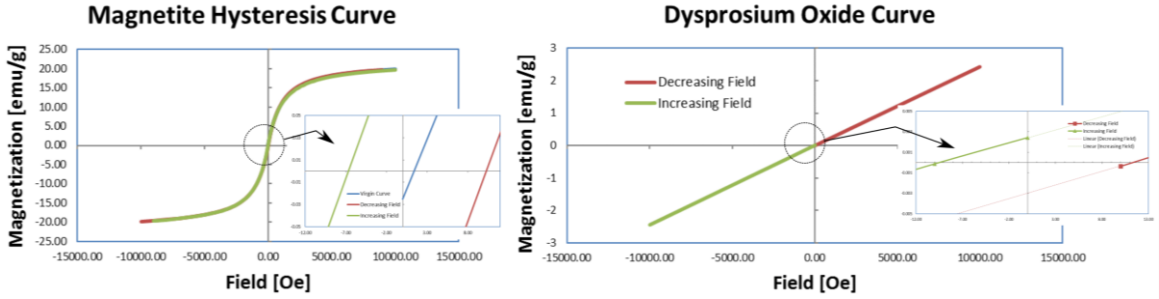

Figure 6-8: Measurement of a sample of magnetite and dysprosium oxide. Notice that the decreasing curve (red) crosses the applied field axis (x) on the positive side rather than the negative. The same appears to be true for the increasing green curve which intersects on the negative rather than positive side. This is a local reversal only in the regions close to the graph origins. A sample of paramagnetic dysprosium oxide can be used to correct for this error.

When transitioning from high to low field, after investigation, was found to result in flux pinning in the superconducting coil. The resultant flux pinning was identified by making use of a sample of high grade dysprosium oxide (Dy_2O_3). Dy_2O_3 is a

paramagnetic material with a clear linear response to an external field. The magnetization curve produced however showed clear signs of local reversal suggesting that flux pinning was likely responsible. The dysprosium sample was used as a calibration to account for this pinning for all magnetite sample measurements. Past papers have pointed out the presence of localized reversals. Such reversals, known as clockwise hysteresis or proteresis is believed to be a real effect [241], [242] often related to core-shell structures such as the ones noted for samples in this study. However, given the general unawareness noted among regular SQUID users of the indicated pinning effect, it is likely that in some cases, at least during high to low field SQUID measurements, localized reversals may be misattributed as proteresis.

Speaking of core-shell structures, we noted in earlier discussions that the FM-AFM structure resulting from magnetite oxidation results in an exchange coupling. This exchange coupling is clearly seen as exchange bias (H_{ex}) in hysteresis curves measured through SQUID magnetometry. In some cases, sample colour itself can provide clear supporting evidence of oxidation as well. If bulk material is to be made from the sintering process, converting the unstable oxides back into stable magnetite is an important step. Noting the physical colour changes between the synthesized base material and the post-sinter product can provide an important indication of whether the conversion happened.

6.5 Camera Colorimetry

While characterization of sintering output could not be completed, some initial colorimetry was attempted. This colorimetry establishes a baseline to easily test and compare synthesized samples to sintered samples as a part future work. The colorimetry was done via a simple controlled lighting setup that made use of a digital SLR camera placed on a fixed position adjustable mount as shown in Figure 6-9.

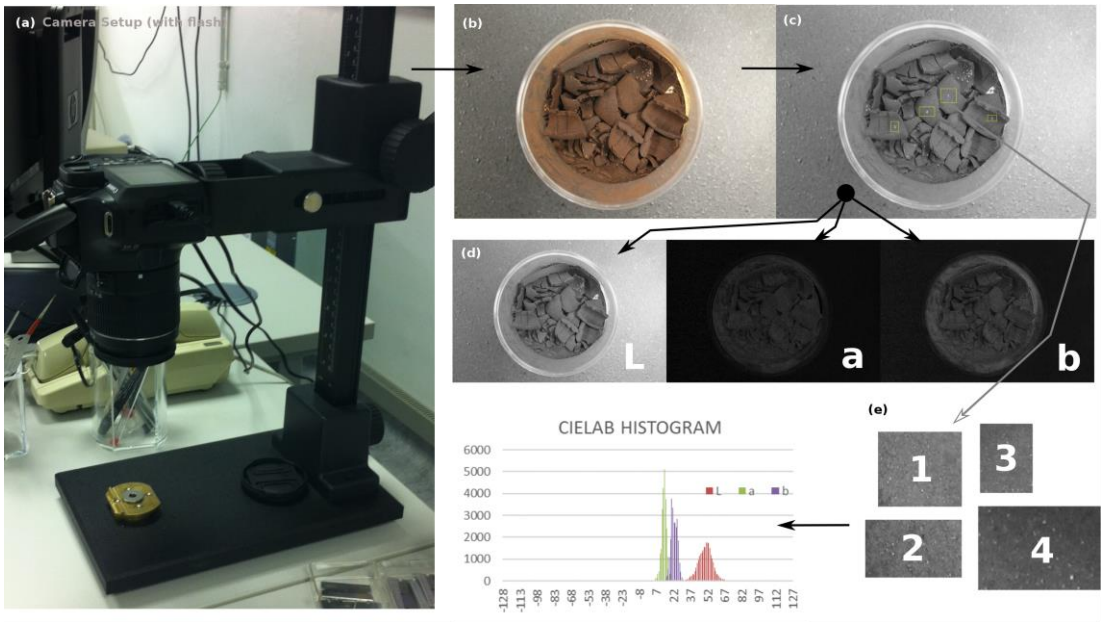

Figure 6-9: Pictures of samples are taken under fixed lighting conditions from a known flash colour profile and then converted to the CIE LAB colour space. Various sample regions are averaged to produce a colour histogram that can be resolved into a distance when comparing to other samples.

Images were taken from a flash with a known colour profile and then converted to the CIE LAB colour space [243]. This colour space is divided into a separate lightness (L) and opponent-colour (a & b) channels. The main advantage of the LAB transform lies in its ability to represent colour in a device independent manner not possible via the traditional RGB and CMYK space. The highest white point in an image is used as a reference in LAB, so it should be noted that some dependence does remain. For instance, if samples imaged via two different devices have differing maximum white points, colour comparisons will be somewhat skewed – however, despite this, significant independence from the illumination is provided. This is particularly important when comparing the oxidation states of samples prior to and after sintering. A valuable effect of LAB transformation is that it additionally provides a more uniform distance measure when compared to perception of colour distance in humans. The transformation process to and from LAB space is a matter of some complexity and will not be discussed here – transformation to this space was

accomplished via a well-regarded, scientific image processing software called ImageJ. Using our commercial magnetite reference sample however, the purity and oxidation of our synthesized samples could be quantified by the relative Euclidean colour distance. This is demonstrated in the Chapter 9 of this study.

6.6 Thermal Measurements

Sintered samples produced through our proof-of-concept microwave furnace, would need to undergo similar colorimetry as the powder synthesis material. Likewise, such samples would also need grinding for analysis via XRD, SEM and SQUID. But prior to this, thermal measurements are necessary. These thermal measurements allow for careful control of sintering related coarsening and densification effects. The resulting analysis of these measurements can be correlated to future XRD, SEM and SQUID characterization to determine which sintering regimes are most conducive to preserving nano-scale structure and resulting superparamagnetism.

The approach taken to observe temperature changes was to use a sheathed metal K-Type thermocouple combined with a PID control box and temperature display. Unfortunately, such approaches can have significant problems in terms of microwave interactions with the thermocouple and skew temperature readings. Further, it is challenging to ensure that the thermocouple is in direct contact with the sample. Thus, characterization for many of the samples tested, represented chamber temperature rather than sample temperature. An alternative approach using a high temperature infrared sensor was also trialled and considered. Unfortunately, while designs were developed, taking this sensor into a high temperature microwave environment required specialized germanium lenses and heat removal that have been left as future work at this juncture.

The initial proof-of-concept build, preparation of the sample was done by producing a metal/ceramic clay and compressing this through a die. The resulting sample formed a rough cylinder of known volume allowing correlation between power loss

by mass and volume. Thin film coatings were also attempted with some characterization. The process of compression and production of samples from the clays, however, often produced poorly formed shapes and extensive experimentation was needed to get clay consistencies suited for die compression and removal. The lack of sufficient existing literature for the characterization data of materials in a microwave furnace meant that selection for hybrid heating considerations was challenging as well.

The measurements made had to be consistently monitored and recorded on a minute by minute basis with the help of a timer, with a single material from clay to characterization taking roughly $3-4$ [hours] to complete. It was hoped that from this resultant heat response, high heating rate susceptor material combinations, needed for hybrid heating to the 800 [°C] sintering temperature, could be selected more readily. Unfortunately, the non-linear response and variations between thin film and bulk materials demonstrated that this was not as simple as indicated by some sources. A strong non-linearity was found to exist based on the permittivity and permeability related losses induced by the magnetron at varying temperatures. Further, placement of the sample in the insulating chamber requires considerable care to ensure that it intersects with anti-nodes of the incoming electromagnetic wave. Noting this during experimentation, to help with alignment, thermal paper was used to assess the wave patterns around the cylindrical chamber and determine sample height.

The high thermal gradient generated by the microwaves, resulted in considerable stress on the insulating material causing cracking and requiring frequent replacement. The high alumina thermal material, itself, absorbed a significant percentage of energy, almost certainly effecting the heating rate negatively. It should be noted, however, that materials with low loss characteristics at low temperatures allowed the cavity to maintain a high Q-factor leading to excessive heating of the magnetron. Ideally the use of a three-way circulator capped with a matched impedance load would allow for energy returning to the magnetron to be dissipated as heat. The cost of such circulators at microwave frequencies is high and perhaps not suited for early

experimentation. As such, a high temperature borosilicate beaker of salt water was used to dissipate this energy at low temperatures where Q-factor tended to be high.

6.7 Electromagnetic Simulations, Analysis and Optimization

At this point it is important to note that measured results were accompanied by extensive simulation and analytical results as well. These simulations were divided into a number of classes, namely:

- Direct computation via analytical means
- MATLAB electromagnetic simulations
- COMSOL electromagnetic simulations and analysis
- Optimization Algorithm outputs

Direct computations were done via analytical means presented in Chapter 3. These computations were used to estimate magnetic fields, forces and energies of the plattered diamagnetic bearing solution presented in Section 2.5. With analytical tools it was possible to evaluate the effects of increasing number of platters on the stability zone and the liftable mass of the bearing. Further to this as will be seen in Chapter 7, bearing loss calculations were also made using a combination of analytical means, simulations and measurement results.

The analytical approach from Chapter 3 was used to build a set of crude test electromagnetic simulations in MATLAB. These established some understanding of the potential energy surfaces. Figure 6-10 demonstrates one such example of a simple two dimensional calculation. This same two dimensional arrangement was used to build more complex arrangements of three dimensional magnetic dipoles as well. A simple example is presented in Figure 6-11. There were a number of challenges to such an approach however. As simulations of two and three dimensional topologies become more advanced and ferromagnetic and diamagnetic materials are incorporated, the need for iterative computation and careful boundary condition propagation becomes more and more important. The introduction of

ferromagnetic material has the effect of changing the magnetic field everywhere in space. Unfortunately, the use of sequential computations of the field over the coordinate space is insufficient to capture such complex field changes without iteration. In order to avoid such complexities, it is prudent to make use of existing commercial packages capable of giving thorough treatment to such complexities.

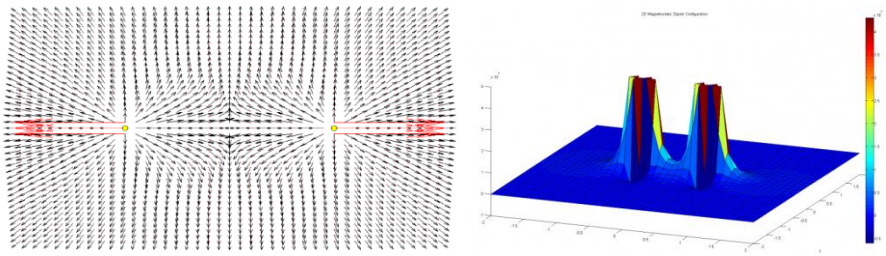

Figure 6-10: An example of the computation of simple topological arrangements of magnets in MATLAB. Two yellow circles in the left image represent dipoles with oppositely pointing moments. In the right image is the potential energy surface from which force and other quantities can be derived. Note that the vertical axis represents the energy and the horizontal axes the position in 2D space.

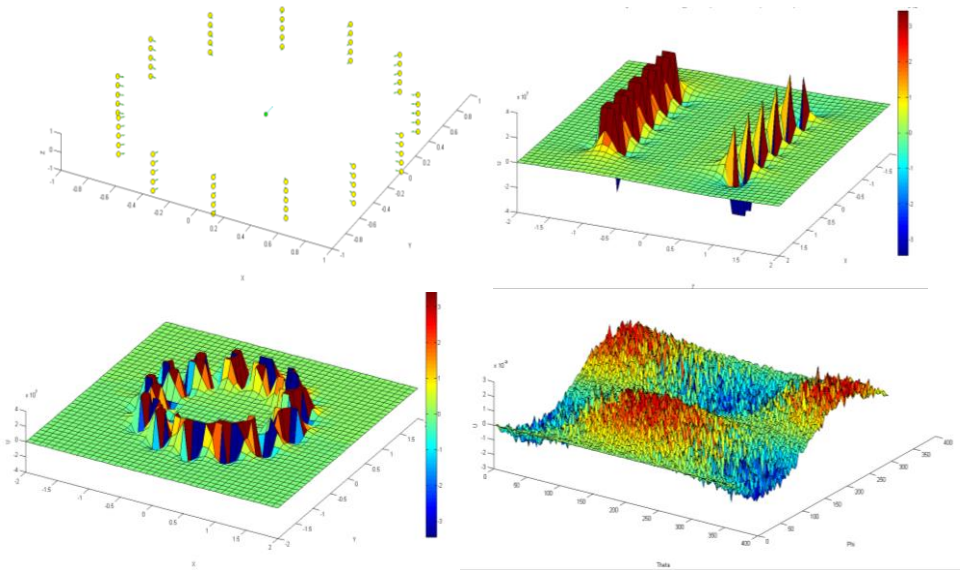

Figure 6-11: An example of a simple three dimensional arrangement of magnetic dipoles as simulated in MATLAB. In the top left image, yellow circles represent dipoles, with green arrows pointing in the direction of the moment. In the top right and bottom images, the energy surface resulting from moving a test dipole through the space and through an angle.

One such finite element package is COMSOL Multiphysics. The use of COMSOL allowed detailed geometry construction, material assignment, mesh structuring and parametric simulation over a wide variety of conditions. The use of COMSOL allowed rapid translation of the bearing geometry and magnetic circuits into a simpler representation as shown in Figure 6-12 and Figure 6-13.

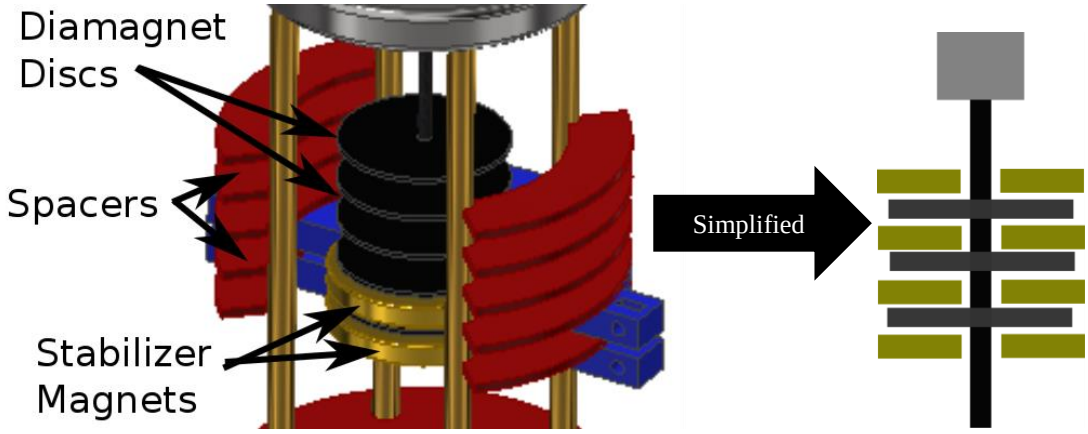

Figure 6-12: An example of how the bearing design was simplified into a 2D axis symmetric problem. Note that in cases of loss computation or computation with a flux path such a 2D simplification was not always possible.

In some cases it was possible to reduce the problem down to an axis symmetric problem and eliminate the need for full three dimensional computations. Taking the simplest case where only one platter existed we see such a COMSOL representation in Figure 6-13. A set of parameters can be used to define the dimensionality of the model and make it easier to make adjustments.

The parameterization process was used as a method of assessing the effect of dimensional changes and the effect of rotor position changes on the overall fields, forces and energies associated with the rotor assembly. An example of the parameterizations is presented in

In order to understand the effect of rotor dynamics and associated field and force effects (where horizontal or a combination of horizontal and vertical motion is occurring) requires full three dimensional modeling. Such modeling is significantly more time consuming (12 hrs plus for simple simulations) from a computational perspective. However, it can be done – an example is shown in Figure 6-14. The more complex 3D representation provides a tool for estimating eddy current losses from off-centric rotation. Because of the time complexity of the problem however, a set of simplifications were needed. The individual platters were modeled separately and simulated independently. Results from these independent calculations were then combined via superposition to arrive at a limited but sufficient understanding of the field, forces, energy and loss behavior of the rotor assembly in our bearing. A similar approach was taken for the lifter magnets and associated electrical machine. To improve the efficiency of the platter magnetic circuit an iron yoke could also be added and tested separately. Examples are shown in Figure 6-15 for three separated simulations of bearing components: platter, floater-lifter and electrical machine.

Table 6-2. Note that, the rotor position parameter used in axis symmetric simulations can only be adjusted vertically.

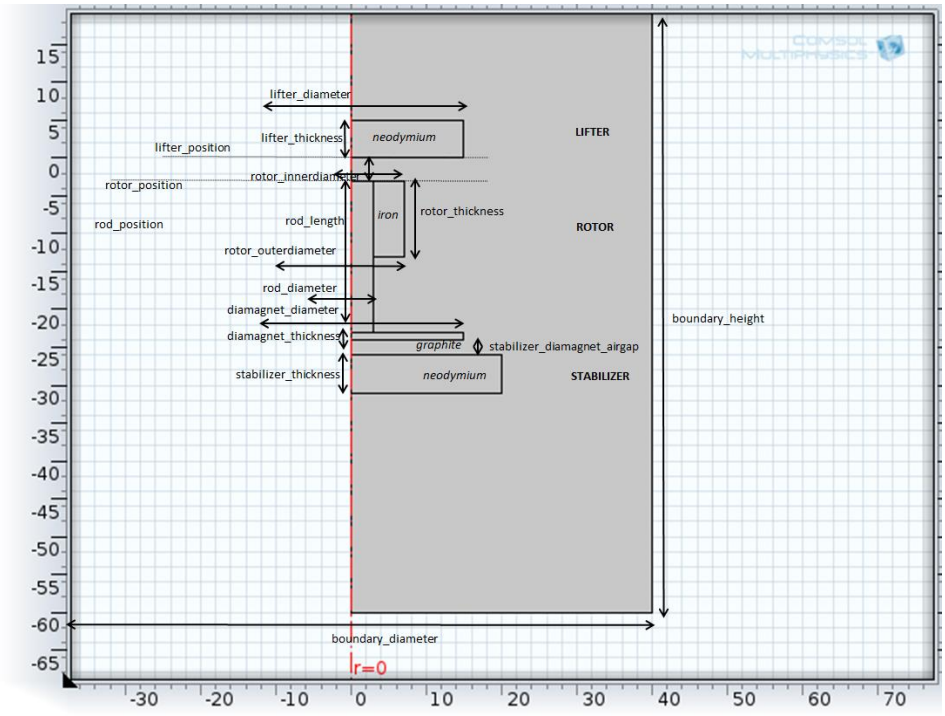

Figure 6-13: An example of a simple case of the bearing design problem imported into COMSOL. This case only involves one platter and consists of an axis symmetric computation.

In order to understand the effect of rotor dynamics and associated field and force effects (where horizontal or a combination of horizontal and vertical motion is occurring) requires full three dimensional modeling. Such modeling is significantly more time consuming (12 hrs plus for simple simulations) from a computational perspective. However, it can be done – an example is shown in Figure 6-14. The more complex 3D representation provides a tool for estimating eddy current losses from off-centric rotation. Because of the time complexity of the problem however, a set of simplifications were needed. The individual platters were modeled separately and simulated independently. Results from these independent calculations were then combined via superposition to arrive at a limited but sufficient understanding of the field, forces, energy and loss behavior of the rotor assembly in our bearing. A similar approach was taken for the lifter magnets and associated electrical machine. To

improve the efficiency of the platter magnetic circuit an iron yoke could also be added and tested separately. Examples are shown in Figure 6-15 for three separated simulations of bearing components: platter, floater-lifter and electrical machine.

Table 6-2: Examples of parameterizations in the COMSOL modeling environment. These parameterizations match the labels shown in Figure 6-13.

Parameters	Value
boundary_diameter	80[mm]
boundary_height	160[mm]
boundary_position	-140[mm]
lifter_diameter	40[mm]
lifter_thickness	5[mm]
lifter_position	0[mm]
lifter_field	0.25[T]
rotor_outerdiameter	10[mm]
rotor_innerdiameter	5[mm]
rotor_thickness	5[mm]
rotor_position	0.25[mm]
airgap_meshsize_lifter_rotor	0.01[mm]
rod_diameter	rotor_innerdiameter
rod_length	40[mm]
rod_position	rotor_position
diamagnet_diameter	30[mm]
diamagnet_thickness	1[mm]
diamagnet_position	rod_position+rod_length
stabilizer_diameter	40[mm]
stabilizer_thickness	5[mm]
stabilizer_position	0.25[mm]+diamagnet_position+diamagnet_thickness
airgap_meshsize_diamagnet_stabilizer	0.01[mm]
stabilizer_field	0.25[T]

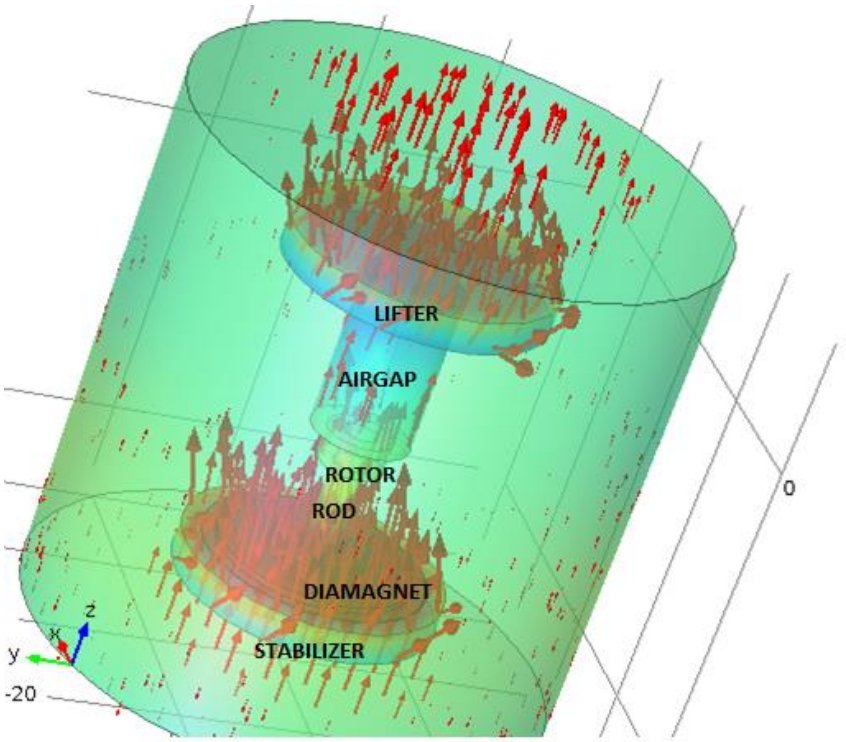

Figure 6-14: A simple simulation that takes the example axis symmetric problem from Figure 6-13 into more time consuming 3D analysis.

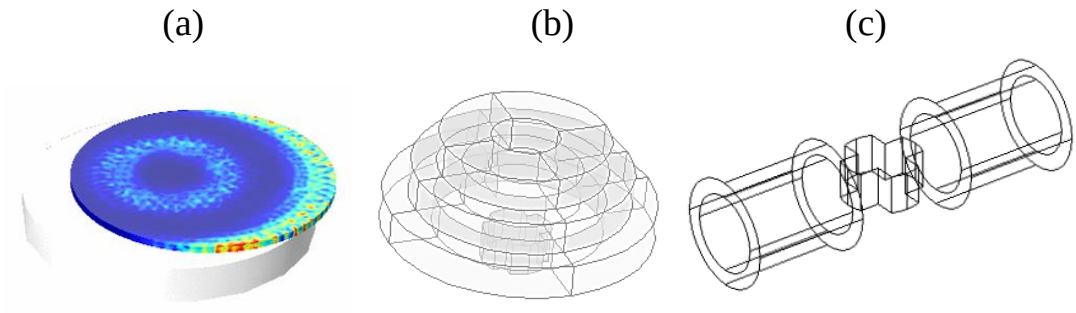

Figure 6-15: From left to right: (a) Simulation of a single diamagnetic platter, (b) Simulation of the floater and lifter assembly, (c) Simulation of a simplified driving electrical machine for the rotor assembly.

One final consideration during COMSOL simulations is the importance of the meshing approach. Diamagnetic platter regions and associated air-gaps were relatively small with forces in the order of [mN] while forces associated with the lifter-floater assembly and electrical machine were several orders of magnitude larger. This meant that several empty air boundary regions had to be created within the air region to help with gradual mesh refinement. One such example mesh, where mesh refinment was needed, is shown in . In some cases the boundary regions of mesh refinement must vary as different rotor positions are simulated and compared.

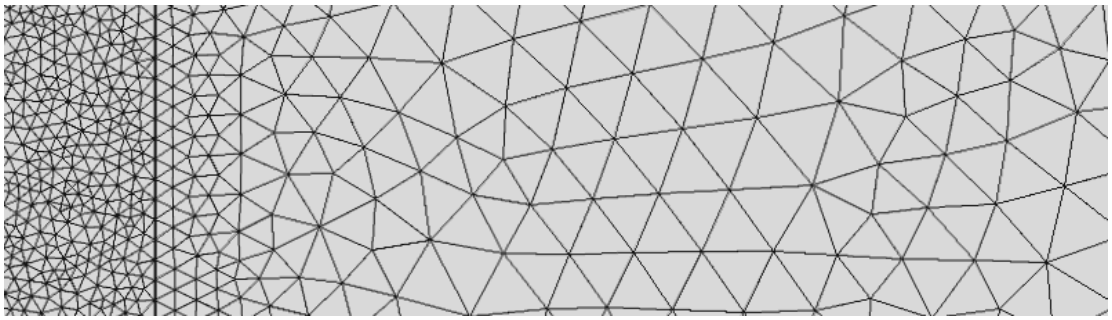

Figure 6-16: Finer mesh structure is needed in regions close to the platters or where magnetic fields increase drastically over small distances – i.e. in air-gaps.

Combined with these macro-scale simulations, sparse hysteresis measurement data from SQUID magnetometry had to be resolved into detailed dense data accompanied by a parameterizable model, namely a modified Jiles-Atherton Model. The approach to this modeling is discussed extensively in Chapter 8. The need for this model was a result of constraints associated with the bearing measurement apparatus. As discussed with reference to the SQUID magnetometer, magnetic hysteresis measurements themselves were insufficient for the a full understanding of both the minor and major loop losses. In order to estimate all losses of the electrical machine assembly, a computable model was required.

6.8 Summary and Final Remarks

To complete the calculations associated with power loss, characterization is a key process. The characterization process involves measurements via SEM, XRD, SQUID, Colorimetry, Thermocouple and non-contact tachometer. Considerable effort is required to prepare samples and run them through the relevant measuring devices. It was found that no one measurement work was sufficient to draw firm conclusions about the superparamagnetic nature of the particles or the associated power loss. Combined, SEM, XRD and SQUID measurements provided some confidence that particles were likely in the superparamagnetic range. Colorimetry provided details of the oxidation state of the particles synthesized. Measurements related to the thermal conditions during sintering had several challenges that put a hold to further characterization via SEM, XRD, SQUID or colorimetry.

Considerably more basic susceptor characterization was found to be needed prior to any significant sintering efforts on actual MNP samples. While one nano-scale sample was sintered, a bulk of sintering and characterization work (by SEM, XRD, SQUID and colorimetry) for the MNPs is left as a future exercise.

More significant problems were noted with regards to measuring power loss during rotation in the diamagnetic bearing. This was because, making such measurements under vacuum conditions proved challenging without a properly functioning motor. Getting this motor to work effectively proved challenging without the added cost and time associated with building a custom motor control unit. Some attempts were made to circumvent the need for such a controller by making use of a high inertia 3-phase motor. However, the resulting output proved to be too low power to establish sufficient torque in the diamagnetic bearing's rotor assembly. As a result, the bearing speed measurements discussed in this chapter must be combined with analytical estimating of air friction, eddy currents, simulations associated with homopolar stabilizing machinery and additional analytical and numerical results related to material hysteresis effects. The details for these added bits of analysis are provided in the next chapter.

Simulations of the electromagnetic system accompanied the physical measurements. These simulations were done via four separate approaches. One approach was purely analytical and supported by crude FEM in MATLAB. While more detailed simulation was completed of individual components of the bearing assembly using COMSOL. In order to substitute and assisted with rotational power loss estimation, hysteresis modelling for both major and minor loops was also used as a simulation tool.

7 Rotational Loss in Bearing Rotor

The primary thesis of this study is that diamagnetic bearings coupled with nano-structured ferrites reduce parasitic losses in FES systems. The measurements and characterization approaches used in the prior chapter can help evaluate the extent of loss in the rotor assembly of our diamagnetic bearing.

At the macro-scale, losses can be a result of air friction as well as a result of electromagnetic losses. Electromagnetic losses come from three main sources: induced currents in stabilizing and lifter-floater machinery, eddy currents in the electrical machine and, likewise, iron losses from material hysteresis in the same machine's rotor and stator assembly. Hysteresis loss can not only occur during power transfer to and from the rotor assembly, but also during idling rotation. This idling rotational loss is a result of remanent magnetization induced cogging drag between the stator and rotor. Alternatively, remagnetization of the rotor and stator may also occur leading to loss as well.

This chapter will provided an expanded analysis of rotational loss in our bearing prototype. Here, simple estimates of air-friction related losses, eddy current losses (including those in the homopolar stabilizing machine) and hysteresis losses will be analytically computed or estimated by way of simulation or numerical methods. These losses will provide a breakdown of the bearing loss measurements done via non-contact tachometry introduced in the previous chapter. A detailed treatment of hysteresis loss associated with our synthesized MNPs will be provided in the next chapter.

7.1 Air Friction Losses

Considering the challenges associated with a vacuum setup, a simple approach to estimating air friction was taken instead. Since the angular velocity (ω) at each point in time is known for our rotor assembly – i.e. values have been measured via a tachometer - it is possible to compute the power lost by the rotor assembly as it deaccelerates. This deceleration occurs at a rate given by $\alpha = \alpha_f + \alpha_m$ as a result of both air friction (α_f) and electromagnetic losses (α_m). This total power loss (P) is shown in Equation (7-1). The torque (τ) is a result of deceleration as well as the moment of inertia (I) of the levitating rotor assembly.

$$P = \tau \cdot \omega = I \cdot \alpha \cdot \omega \tag{7-1}$$

$$\mathbf{P = I \cdot \left(\frac{\omega_n - \omega_{n-1}}{t_n - t_{n-1}}\right) \cdot \omega_n}$$

$$\mathbf{P = [I \cdot (\alpha_f + \alpha_m)] \cdot \omega}$$

This moment of inertia is the combined result of the different rotor elements shown in Figure 7-1. The diamagnetic bearing rotor assembly consists of p diamagnetic discs of mass dm and outer radius dd each. Further to these discs, a rotor of mass rm, diameter rd and thickness rt is also present. A spherical floater of diameter fd and mass fm, along with a thin walled shaft of outer radius shd and mass shm add further to the rotor assembly. The resultant moment of inertia (I) from these elements is shown in Equation (7-2). This moment assumes rotation in the z direction about the axis of symmetry of the rotor assembly. The inertia for the diamagnetic disc (I_d) and the rotor (I_r) is approximated as that of a thin solid disc or cylinder respectively. The shaft (I_{sh}) is considered a thin walled cylinder and the floater (I_f), a sphere.

$$I = p \cdot I_d + I_r + I_f + I_{sh} \tag{7-2}$$

$$\mathbf{I = p \cdot \left(\frac{dm \cdot dd^2}{8}\right) + \left(\frac{rm \cdot rd^2}{8}\right) + \left(\frac{fm \cdot fd^2}{10}\right) + \left(\frac{shm \cdot shd^2}{4}\right)}$$

Since measurement values provide sufficient data to estimate the total power loss on the system, the loss as a result of electromagnetic effects (P_m) can be estimated if a loss term for air friction (P_a) or a deceleration term (α_f) can be arrived upon. This requires an estimation of aerodynamic drag on the rotating rotor assembly. Since a detailed study of drag is out of the scope of this study, a more straight-forward approach is taken. A simplified and semi-empirical approach has been taken by some when estimating this drag [244], [245]. This approach to drag estimation has been used for estimation of power loss in multi-plattered hard disk drives. There is some theoretical grounding for this approach and under particular flow conditions can be derived from the linear representation of frictional/drag force (F_{al}) shown in Equation (7-3). In this equation, ρ_d is the density of air, v the tangential/linear velocity of the moving object, C_d the drag coefficient and A the area of the object with normal in the direction of linear motion (see Figure 7-1b).

$$\mathbf{F_{al} = \frac{1}{2}\rho_d v^2 C_d A} \tag{7-3}$$

We note that the area (A) for the motion of our rotational system would be a result of surface friction on the top, bottom and sides of our diamagnetic platters and as a result of friction on both top and bottom surfaces as well as side walls from our rotor (approximated as a cylinder). Similarly, added friction from the shaft and the floater (on its exposed spherical sides) – again these sides can be approximated as cylindrical. See Figure 7-1c for further details.

The resulting power loss from air friction in a rotating body can utilize the linear drag formulation as shown in Equation (7-4). We note that the power loss (P_a) is the rate of change of work done (E_a) on the disc surfaces as a result of friction at a particular time (t). This can be represented as the drag over some swept arc length, $s = r\,\partial\theta$. This $\partial s/\partial t$ relationship is the tangential velocity, $v = \omega r$. Summing our differential area elements (dA) gives the total area (A) over which air is sweeping to generate resistance and in the case of the top and bottom surface, can be given by A_{tb}. For the disc sides this would be A_s.

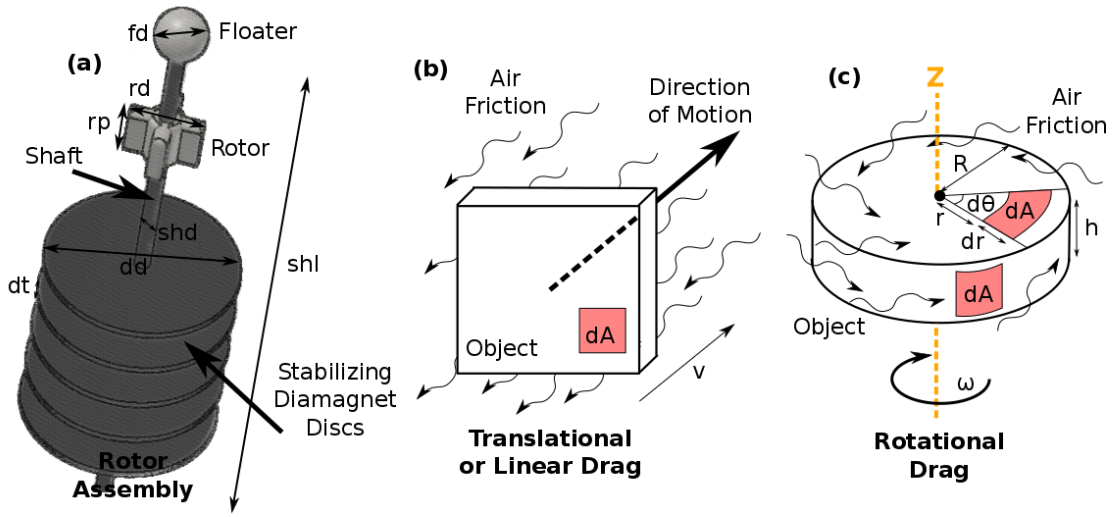

Figure 7-1: (a) The rotor assembly of our diamagnetic bearing. (b) Drag from translating an object. (c) Drag from rotation with area element dA applied to the diamagnetic disc, rotor and floater in our rotor assembly.

$$P_a = \frac{\partial E_f}{\partial t} = F_{fl} \cdot \frac{\partial s}{\partial t} = \left(\frac{1}{2}\rho v^2 C_d A\right) \cdot v = \frac{1}{2}\rho v^3 C_d A \tag{7-4}$$

$$P_a = \frac{1}{2}\rho(\omega r)^3 C_d (A_{tb} + A_s) = \frac{1}{2}\rho\omega^3 C_d (A_{tb} r^3 + A_s r^3)$$

$$P_a = \frac{1}{2}\rho\omega^3 C_d \left(\iint r^3 dA_{tb} + \iint r^3 \, dA_s \right)$$

$$P_a = \frac{1}{2}\rho\omega^3 C_d \left(\iint_{r=0,\theta=0}^{R,2\pi} r^4 \, \partial r \, \partial\theta + \iint_{\theta=0,h=0}^{2\pi,h} R^4 \, \partial\theta \, \partial h \right)$$

$$\mathbf{P_a = \pi\rho\omega^3 C_d R^4 \left(\frac{1}{5} R + h \right)}$$

A more specific expression for power loss can be constructed for the dimensions of our rotor as shown in Equation (7-5). Here the individual power loss from p diamagnetic discs ($p \cdot P_{ad}$), the rotor (P_{ar}), the shaft (P_{ash}) and the floater (P_{af}) are aggregated.

Up to this point no discussion of the coefficient of drag (C_d) has been made [246]. For our purposes we will use the coefficient for flow over a thin cylindrical disc ($C_{dd} = 1.1$) for the diamagnetic disc, the coefficient for flow over a cube ($C_{dr} = 1.05$) for the rotor, the coefficient for a vertical cylinder for the shaft ($C_{dsh} = 0.6$) and the coefficient for a sphere for the floater ($C_{df} = 0.5$). A higher coefficient is chosen for the rotor to provide some accounting for the presence of rotor salient poles. While not necessarily accurate, we believe the assumption of linearly directed laminar flow is sufficient for the purposes of this study.

$$P_a = p \cdot P_{ad} + P_{ar} + P_{ash} + P_{af} \tag{7-5}$$

$$\mathbf{P_a = \frac{\pi\rho\omega^3}{160}\left(p \cdot C_{dd} dd^4 (dd + 10dt) + C_{dr} rd^4 (rd + 10rp) + C_{dsh} shd^4 (shd + 10shl) + 11 C_{df} fd^5 \right)}$$

At this stage we can return to our total power loss (P) from Equation (7-1) and (7-2) and note that this power loss is a result of two components, air friction (P_a) and electromagnetic effects (P_m). Removing the contributions of air friction, the power loss as a result of the effects of eddy currents and iron related losses can be estimated as shown in Equation (7-6). Under vacuum conditions this loss would be the total contributor to parasitic loss in a flywheel system utilizing diamagnetic bearings of the style presented in this study.

$$P = P_a + P_m \tag{7-6}$$

$$P_m = P - P_a$$

$$\mathbf{P_m} = \left[\boldsymbol{\omega}\,(\boldsymbol{\alpha_f} + \boldsymbol{\alpha_m})\left(\mathbf{p}\cdot\left(\frac{\mathbf{dm}\cdot\mathbf{dd^2}}{\mathbf{8}}\right) + \left(\frac{\mathbf{rm}\cdot\mathbf{rd^2}}{\mathbf{8}}\right) + \left(\frac{\mathbf{fm}\cdot\mathbf{fd^2}}{\mathbf{10}}\right) + \left(\frac{\mathbf{shm}\cdot\mathbf{shd^2}}{\mathbf{4}}\right)\right)\right]$$
$$- \left[\frac{\boldsymbol{\pi\rho\omega^3}}{\mathbf{160}}\left(\mathbf{p}\cdot\mathbf{C_{dd}}\mathbf{dd^4}(\mathbf{dd}+\mathbf{10dt}) + \mathbf{C_{dr}}\mathbf{rd^4}(\mathbf{rd}+\mathbf{10rp})\right.\right.$$
$$\left.\left. + \mathbf{C_{dsh}}\mathbf{shd^4}(\mathbf{shd}+\mathbf{10shl}) + \mathbf{11}\mathbf{C_{df}}\mathbf{fd^5}\right)\right]$$

The remainder of parasitic loss can be quantified by the total power dissipated using the above electromagnetic loss expression.

7.2 Stabilization & Stabilizer Losses

The diamagnetic discs, sandwiched between stabilizer permanent magnets, form a homopolar machine. Rotation of an electrically conductive diamagnetic material in the constant field source of our stabilizer magnets generates a potential difference between the centre and edge of the material – see Equation (7-7) [247].

$$\varepsilon_d = \int_C \left(\vec{v} \times \vec{B}_m\right) \cdot \vec{dl} = \int_C \left((\omega \times \vec{r}) \times \vec{B}_m\right) \vec{dr} = \int_0^{dd/2} (\omega r B_{mz})\, dr \qquad (7\text{-}7)$$

$$\boldsymbol{\varepsilon_d = \frac{\omega\, dd^2 B_{mz}}{8}}$$

We take ε_d as the induced voltage across the rotating diamagnetic material of radius, $dd/2$, at some tangential velocity (v) or angular velocity (ω). The field generated by the permanent magnets making up our particular platter is given by B_{mz} and the induced voltage is measured over some closed path C with length element $d\vec{l}$ or $d\vec{r}$. Connecting the inside and outside diameter of the diamagnetic material to produce a closed circuit can result in current flow from this induced voltage.

In a diamagnetic bearing no circuit is present in this region except that produced by the medium (e.g. air) in which the rotating assembly is immersed. The parasitic loss through the medium is unlikely to be significant given that homopolar machines are characterized by low voltages and high currents. However, in regions where there is a change in the field (either a decrease or an increase), particularly where the B-field fringes, losses can result [248], [249]. These losses may be particularly significant where the diamagnet is rotating off-axis in the xy plane. Some authors have correctly indicated that no such losses occur in symmetric configurations of the Faraday disc [247] – this is true as long as the field remains uniform, something that is not the case in fringing regions of our particular design.

Within the uniform field region, electrons experience a force ($F = q\,\vec{v} \times \vec{B}_m$) that generates a charge difference between the outer and inner regions of the spinning diamagnet. As the field drops off in the fringing region towards the edge of the disc (radial distance r increasing), the force applied on the electrons drops away as well. This is because the velocity ($v = \omega r$) increases linearly with radius but the B-field drops away significantly faster. The result is inefficiencies from counter current

flows in the non-uniform field region as shown in Figure 7-2. It is possible (but complicated) to quantify these losses to some extent using analytical means. As a result of complexities, we forego analysis of the homopolar machines, preferring finite element simulation as a means of estimating power loss. Further, we note that given dt ≪ dd, the losses resulting from current counter flows generated as a result of z-directional motion of the diamagnetic material should be several orders of magnitude smaller than those generated by centric and off-centric rotation in the xy plane. This is particularly true given that the graphite diamagnet used in this study has cleavage planes oriented horizontally – the resistivity between planes is relatively high in comparison to resistivity within points in the same plane. This inefficiency can thus be neglected. Likewise, we make the assumption that the system is stationary and that induced wobble (rotation about the radial axis) is zero.

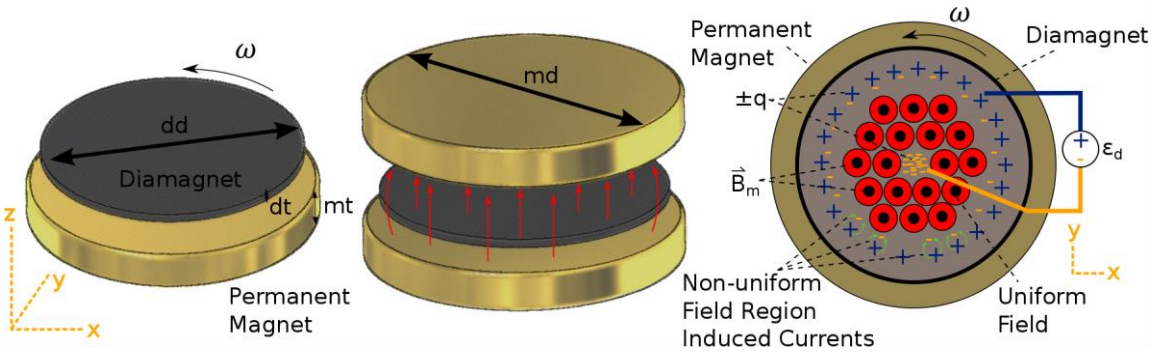

Figure 7-2: Another look at the stabilizing machine. This is a homopolar machine similar to the Faraday disc. A uniform field within a diamagnet sandwiched between two permanent magnets drops away at the outer regions as a result of fringing effects. The result is inefficiencies from counter current flows.

Using a finite element modelling software called COMSOL Multiphysics, a set of simulations were completed to determine homopolar machine loss during rotor assembly rotation. An example image of one such simulation is provided in below in Figure 7-3.

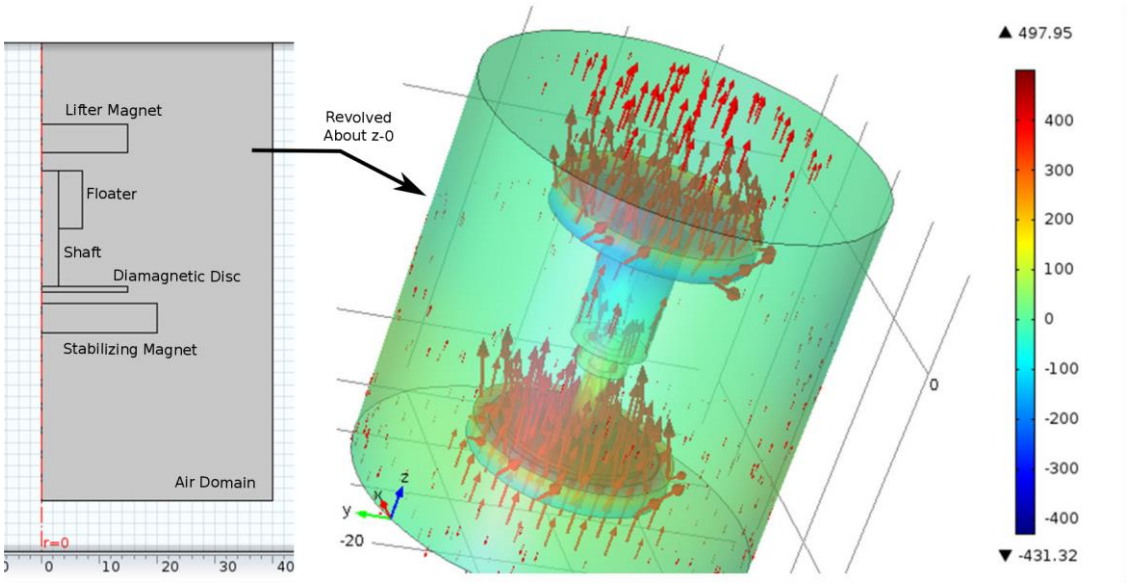

Figure 7-3: An example of geometry superimposed results from one particular COMSOL simulation.

In addition to rotational loss data, variations similar to the simulation shown in Figure 7-3 were used to generate position, force, energy and stiffness data. Effort was given to topological changes in field sources for the stabilizing machine as well as for the lifter. Not only have a number of authors pointed out the benefit of ring shaped topologies, but simulation results to some extent have corroborated an added xy-directional stability from these setups. However, in the real implementation of the bearing assembly, it was found that such a setup could not be achieved. The prototype bearing implementation had a relatively small number of platters ($p = 6$) which meant a relatively small stabilizing zone. Furthermore, the distance between the stabilizing magnets (mg) had to be relatively large to permit construction within the low tolerance of the tools used for part prototyping. The opposite was true for the floater and lifter combination where the distance (fg) between the two was relatively small. The challenge with this setup is that the distance of the lifting magnet has to be such that the rate of change of the B-field resulting from small perturbations in the floater position must be relatively small. A high rate of change can push the floater

out of the stable region more easily. The effect of topological variations will be discussed in Chapter 9 along with homopolar rotational loss related results.

7.3 Reluctance Machine Losses

Losses also exist in the reluctance machine. We noted that losses are a result of two particular sources, namely, hysteresis and induced eddy currents. The hysteresis loss is always present in one form or another in that a magnetic field applied to the rotor during rotation results in a remanent magnetization. This remanent magnetization then introduces cogging torque as a result of the stationary stator of the reluctance machine. Alternatively, this loss may also result from the energy required to change the direction of the remanent field as well – termed remagnetization loss in this study. The remanent field or induced magnetization can also induce eddy currents in the stator/rotor core material during rotor idling as well as power transfer. Power transfer losses are a result of the typical changing magnetic fields applied to the stator phase windings.

7.3.1 Hysteresis Effects

Before continuing, it is worth looking at a sample hysteresis curve. Figure 7-4 demonstrates such an example curve. Here we note the coercivity (H_c) provides a measure of the applied field needed to bring the magnetization (M) down to zero. At zero applied field, the magnetization remaining in the material is given by the remanence (M_r). Commonly, in literature, significant confusion exists in relation to understanding the difference between the M-H curve and B-H curve. The key difference is encapsulated by the relationship $B = u_0(H + M)$. Here B is the B-field, $M = \chi H$ the magnetization of the material due to internal magnetic moments and H is the applied field. The susceptibility of the material is given as $\chi = \mu_r - 1$ and u_0 is the permeability of free space while μ_r is the relative permeability of the material.

At some stage, increases to the applied field, H, do not yield a change in the the magnetization of the material – all magnetic moments in the material are aligned with the external applied field leading to a saturation (M_s). Typically, a source of much confusion, a B-H curve will not have an asymptotic approach towards saturation and so no equivalent value for saturation exists with the B-field. However, we can regard B-field saturation as the value of the field at saturation M_s.

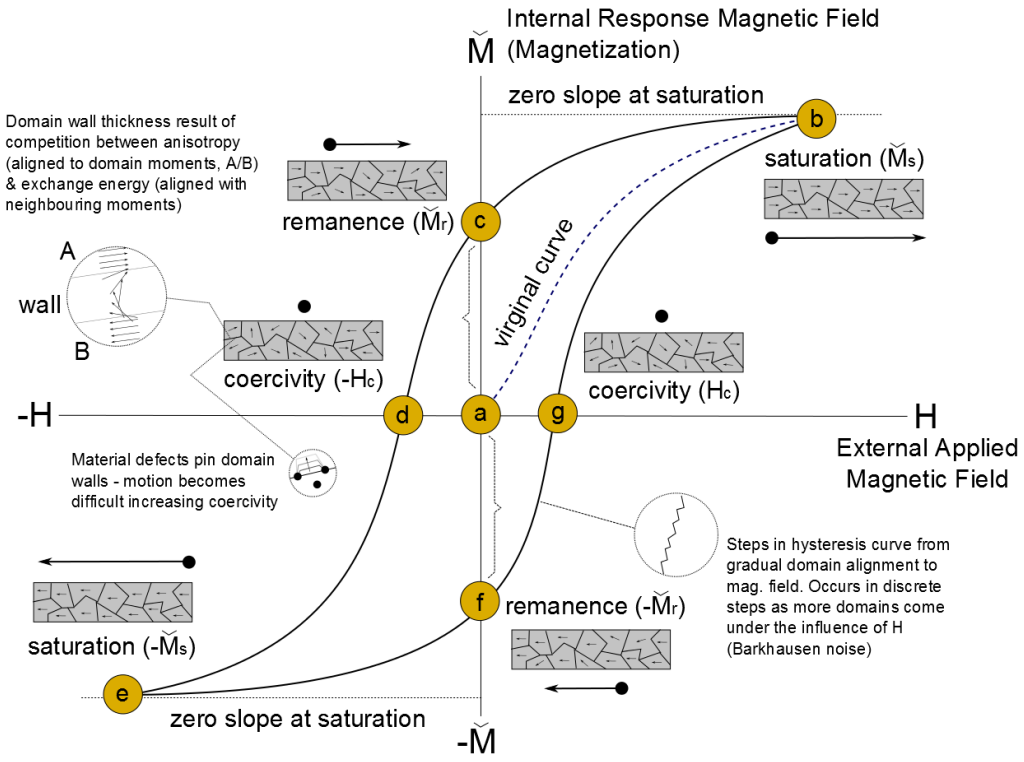

Figure 7-4: The demonstration hysteresis M-H curve. The shape and size of domains and interactions between domains play an important part in the shape of this hysteresis loop and consequently the resulting power loss. As particles shrink to the nano-meter scale domains disappear and losses drop significantly.

The hysteretic nature of a material can generally be attributed to the shape/size of its magnetic domains/particles and associated inter-domain/inter-particle interactions

[5]. These shape, size and interaction properties cause anisotropic responses to applied magnetic fields. The result is variations in the shape and position of the hysteresis curve and changes in the resulting saturation magnetization, remanent magnetization and coercive field strength of the material. Further to this, particular core-shell structures in the nano-scale materials can lead to exchange bias (H_{ex}) whereby the hysteresis curve is shifted horizontally or vertically. Figure 7-5 demonstrates examples of changes in each of these properties.

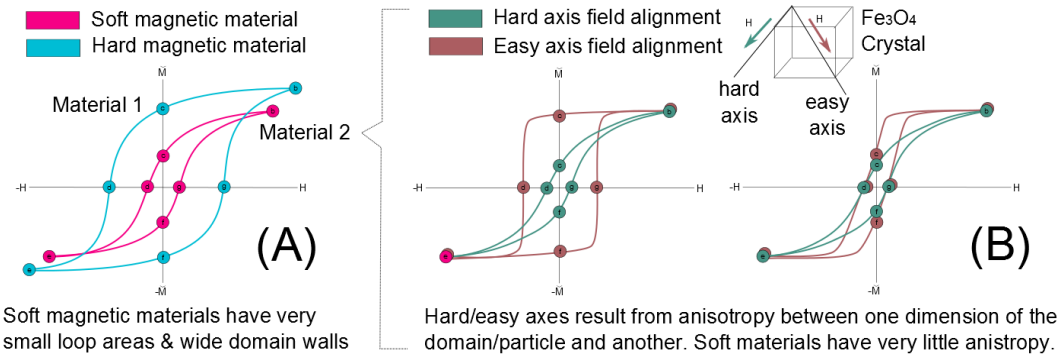

Figure 7-5: A demonstration of various shapes of the hysteresis curve as a result of material anisotropies. Note that the hysteresis loop area shown for hard magnetic materials is not to scale. This area is typically several orders of magnitude bigger than that of soft materials. Anisotropy is an undesirable property in soft materials and leads to a preferred direction of magnetization.

These nano-scale considerations will be put aside for now until we proceed with discussions of hysteresis modelling in greater detail in the next chapter. For now, we note that the area enclosed by the hysteresis curve acts to quantify loss contributions resulting from magnetization changes when an H-field is applied. This could occur as a result of energizing coils in our reluctance machine.

One should note that the frequency of operation of this machine, if high enough, can breakdown the superparamagnetic properties of a machine made from magnetite

nano-particles leading to further hysteretic loss. In the vacuum environment of a flywheel, this can be quite a significant problem leading to overheating.

A part of the losses, in a flywheel system, lead to inefficient power conversion while energy is being added or removed from the rotor. Such losses can be related to a combination of remanence and coercivity in the machine caused by hysteresis. During idling, hysteresis related loss should drop away.

However, this is not necessarily the case. The operational frequency of the machine during power transfer can lead to a higher remanent magnetization since a frequency relationship exists between the applied field and response magnetization. In the superparamagnetic materials considered for our reluctance machine, if the frequency is high enough the result is superparamagnetic breakdown (related to Neel relaxation time) and increased remanence. While it remains a topic of research and the answer is unclear, the continuous rotation of a rotor relative to the stator at these breakdown (non-superparamagnetic) frequencies may self-sustain a higher remanence leading to higher iron losses and greater parasitic loss even during rotor idling. Regardless of this frequency regime, however, the remanent magnetization of the rotor is a potentially significant contribution to total electromagnetic loss. Ultimately, the remanent magnetization of the material making up the reluctance machine, once the particular material has been characterized, can be used to estimate idling losses. Clarification of the nano-scale considerations that lead to breakdown of superparamagnetism will follow later in the next chapter.

7.3.2 Quantifying Losses from Remanence

So how can these losses in our electrical machine be analysed? A variety of methods exist for estimating losses [5], [116], among the most popular are variations of the Steinmetz equation – an equation based on a semi-empirical approach. Variations of this approach have attempted to separate contributions to loss into hysteresis, eddy current and anomalous loss terms. The anomalous loss term being a fudge factor. We will forgo the use of the Steinmetz formulation as it cannot provide for the range of

considerations in our design. We will however make use of a formulation that separates considerations of hysteresis loss (P_{rh}) and eddy current (P_{re}) loss in the rotor-stator assembly.

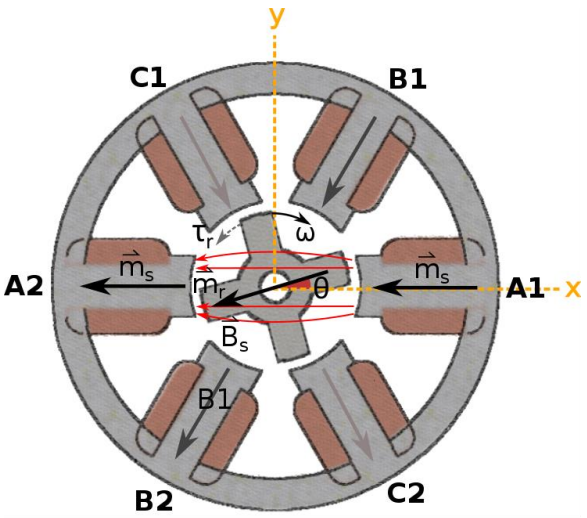

Figure 7-6: Motor motion and source of parasitic loss

Consider Figure 7-6. Suppose that the order in which current (sI) is passed through the stator coils begins with phase A followed by B and C. The energization of coil A induces a magnetic moment $\vec{m}_s$ on the corresponding stator poles and $\vec{m}_r$ on the corresponding rotor poles. As a result of the remanent magnetization (surface field, $\vec{B}_{sr}$) of the stator poles, a B-field ($\vec{B}_s$) is generated through the aligned rotor poles during idling. As the rotor rotates, the combined effect of the iron magnetic moment of the rotor and the added induced remanent magnetization generates a torque in the presence of $\vec{B}_s$. The resultant power lost via this torque can be quantized as the idling parasitic loss of the rotor.

This loss increases with increased rotational frequency ($\omega = \partial\theta/\partial t$) and number of stator poles ($\mathcal{s}$) as well as the number of rotor poles ($\mathfrak{r}$). After the switching needed for rotor power transfer is complete, we can assume that the stator poles all have radially oriented remanent magnetic moments. At this stage, it should be noted that

while considerable discussion exists in literature for reluctance machines operating as motors, their operation as generators is somewhat less discussed [250]. The complexities of control are beyond the present discussion, however, what should be noted is that to operate such machines both as motors and generators requires excitation of the stator coils (though at slightly different rotor positions). This means that regardless of mode of operation, such motors will experience stator/rotor pole remanent magnetization and associated losses.

Quantifying these losses can be done analytically using the earlier discussion of theory associated with reluctance motor stiffness. As we noted earlier the total rotational power loss from electromagnetic contributions (P_m) can be given as shown in Equation (7-8). This loss is divided into contributions from various electromagnetic parts of the bearing system.

$$P_m = p \cdot P_d + P_f + P_r \tag{7-8}$$

$$\mathbf{P_m = p \cdot P_d + P_f + (P_{rh} + P_{re})}$$

Here the contributions include the diamagnetic stabilizer disc loss resulting from induced eddy currents in the homopolar machine ($p \cdot P_d$). Similar contributions occur as a result of the floater induced currents in the permanent magnet field of the lifter (P_f). Both of these two losses are significant only as the field from stabilizing magnets or lifter magnet becomes non-uniform relative to the rotating floater or diamagnet. As a result of the complexity of analysis of the homopolar machine, finite element modelling has been used to estimate loss from both centric and non-centric rotation.

Computation of the power lost as a result of hysteresis in the rotor (P_{rh}) can be subtracted from the electromagnetic loss (P_m) to provide loss estimates for the combined rotating floater and diamagnetic discs. Furthermore, simulation of only the

losses from the diamagnetic discs is needed to complete the picture and compute the individual contribution of the floater-lifter loss as well.

Now analysing rotor loss (P_r) from remanent fields (P_{rh}) in our reluctance machine, we note that $P_{rh} = \partial E_{rh}/\partial t$. Details are presented in Equation (7-9). The energy loss for the rotor (E_{rh}), in this scenario, is a function of the orientation (θ) of the rotor pole relative to the B-field of the particular stator pole and the torque (τ_{rh}). The resultant torque from this stator pole can thus be computed if the magnetic remanence ($M_{rhr} = M_{shr}$) of the core material of the machine is known. The characterization of our nano-materials and commercial samples using SQUID magnetometry is one method of determining this remanent magnetization. The stator remanence after conversion to B-Field form is given by $B_{shr} = \mu_0 M_{shr}$ and, thus, the torque on our machine would be $\tau_{rh} = m_{rh} \cdot B_{sh}$. Here, we note once more, that our magnetization is a volume quantity and further that our magnetic moment is a sum of the internal moment (m_{rhr}) and the externally induced moment (m_{rhs}). We can make a further assumption that the total loss from the stator and rotor pole can be approximated by the maximum loss occurring when the poles are in the fully aligned state (i.e. $\cos\theta = 1$). This is very likely to be an overestimate as it assumes that the energy associated with the torque does not vary as the rotor poles move from one stator pole pair to the next and that the moments and stator field are roughly constant over the rotation.

$$P_{rh} = \frac{\partial E_{rh}}{\partial t} = \frac{\partial(\tau_{rh}\theta)}{\partial t} = \frac{\partial(\theta\, m_{rh} B_{sh}\cos\theta)}{\partial t} \tag{7-9}$$

$$P_{rh} = \frac{\partial}{\partial t}(\theta\,(m_{rhr} + m_{rhs})B_{sh})$$

$$\mathbf{P_{rh} = (m_{rhr} + m_{rhs})B_{sh}\frac{\partial\theta}{\partial t} = (m_{rhr} + m_{rhs})B_{sh}\omega}$$

From here, we can utilize our earlier formulation of the rotor magnetic moment (Equation (3-61)). Recall that derivation of this moment made a spherical assumption for the rotor. We will preserve this spherical assumption for the purposes of this analysis of m_{rhs}. Likewise, we note that the remanent field (M_{rhr}) from previous energization of the rotor will also induce a moment given as $m_{rhr} = M_{rhr}V_r$ with V_r referring to the volume of our assumed spherical rotor. This induced moment will then be subject to a torque resulting from the stator pole field B_{sh} as given in Equation (3-62). A point of note here would be that centric rotation is assumed with position $x = 0$ and further that relative uniformity of the field as it passes through the rotor is assumed. The cogging resulting from the rotation of the rotor will occur as each rotor pole comes into alignment with a stator pole (Figure 7-7). If there are r rotor poles and s stator poles in the machine this occurs $rs/2$ times every rotation and leads to a further addition to our power loss as shown in Equation (7-10). In this equation we assume that that the remanence in the rotor and stator will be the same such that: $M_{rhr} = M_{shr}$

It is important to note that the simplification in Equation (7-10) assumes that the contribution of the two magnetic moments, m_{rhr} and m_{rhs}, are always additive. Clearly, this is not the case, and can be seen in Figure 7-6. For one half of the rotation the relationship is subtractive at each pole combination.

At the low speeds (approx. 180 [rpm]), low relative magnetic permeability (given as $\mu_{ri} = 10$) and small number of stator/rotor poles ($r = 4$, $s = 6$) considered in our prototype diamagnetic bearing system, the contribution from remanent losses for a standard commercial micro-scale sample of magnetite is significant at roughly two orders of magnitude smaller than air friction losses. The losses from remanent magnetization effects for both nano-structured and micro-structured samples are quantified in the results chapter of this study.

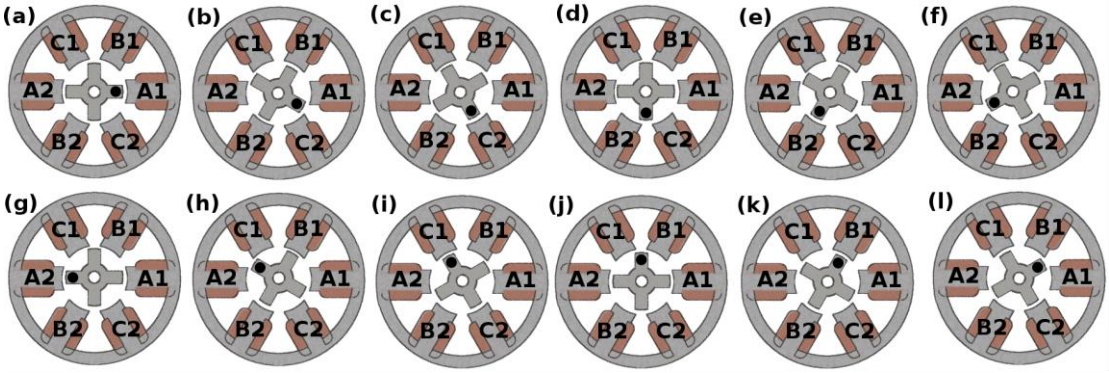

Figure 7-7: Rotation of the rotor in a 6-4 configuration reluctance machine. Note that it takes 12 steps to complete rotation leading to the $\mathbf{r\mathcal{S}/2}$ relation.

$$P_{rh} = \frac{r\mathcal{S}}{2}(m_{rhr} + m_{rhs})B_{sh}\omega \tag{7-10}$$

$$P_{rh} = \frac{r\mathcal{S}}{2}\cdot\left[\left(M_{rhr}V_r + \frac{\pi\, rd^3\chi_r}{\mu_0(\chi_r+3)}B_{sh}\right)B_{sh}\right]\omega$$

$$P_{rh} = \frac{r\mathcal{S}}{2}\cdot\left[\left(M_{rhr}V_r + \frac{\pi\, rd^3\chi_r}{\mu_0(\chi_r+3)}\left(\frac{sd^2st}{sd^3} + \frac{sd^2st}{(sd^2+4sg^2)^{\frac{3}{2}}}\right)B_{shr}\right)\left(\frac{sd^2st}{sd^3} + \frac{sd^2st}{(sd^2+4sg^2)^{\frac{3}{2}}}\right)B_{shr}\right]\omega$$

$$\mathbf{P_{rh} = \frac{r\mathcal{S}}{2}\cdot\left[\left(V_r + \frac{\pi\, rd^3\chi_r}{(\chi_r+3)}\left(\frac{sd^2st}{sd^3} + \frac{sd^2st}{(sd^2+4sg^2)^{\frac{3}{2}}}\right)\right)\left(\frac{sd^2st}{sd^3} + \frac{sd^2st}{(sd^2+4sg^2)^{\frac{3}{2}}}\right)\right]\mu_0 M_{rhr}\omega}$$

A point of note is that the above analysis hasn't taken into consideration coercivity related factors. For instance, if the sum total magnetization of the rotor-stator material is higher than the coercive field, then this magnetization should be sufficient to traverse a minor loop in the hysteresis curve and so the power loss at each pole should require computation of the area under the hysteresis curve for this minor loop – this computation will be discussed in the subsequent chapter related to nano-scale considerations (i.e. Chapter 8). In the case where the coercivity is large, the applied field generated from the remanent magnetization is unlikely to de-magnetize the remanent moments.

We note that for the commercial magnetite sample used to construct the reluctance machine for our bearing system, the coercivity is one order of magnitude higher than the remanence. This means that significant power is not likely to be lost as a result of magnetization reversal in the material and hysteresis computations don't require an area calculation. In the case of our nano-scale samples, this is not true however. For some of these samples, the coercivity is in the same order of magnitude as the remanence and so the minor loop area becomes an added contributor to the power loss in the rotor – estimating this minor loop requires modelling of the hysteresis curve and accounting for nano-scale considerations.

7.3.3 Quantifying Losses from Eddy Currents

During conversations concerning sintering, it was noted that one key advantage of using ferrite material for the rotor and stator assembly is the higher electrical resistance. It is at this stage, worth comparing the difference that the higher resistance can make to electromagnetic losses resulting from induced eddy currents. While these losses definitely exist during power transfer to and from the rotor, do such losses exist during rotor idling?

If remanent magnetization of the rotor and stator are taken into account, the answer is yes, though the contribution is likely to be small. In the case of laminations, we noted earlier in examining existing materials, in Table 4-1, that electrical steel has very high remanence yet low coercivity. It is, thus, possible that rather than eddy current losses, hysteretic considerations of field reversals in a minor hysteresis loop will be the primary consideration. Nevertheless, it is instructive to compare losses.

To estimate losses (P_{re}) in an equivalent machine made from laminations, an existing formulation based on a separated version of the Steinmetz equation is one approach to solving for the losses [116]. This is a common technique and is, thus, shown in Equation (7-11). Here the values $f = \omega/2\pi$ and B_{peak} refer to the frequency of the B-field and to the peak value of this field, respectively. Unfortunately, recall earlier discussions concerning the Steinmetz equation where a simple formulation of power

loss must combine an anomalous loss term (η_{an}) for accuracy in describing some materials such as silicon steel (electrical steel). The equation is also semi-empirical, having some loss coefficient, C. This means that for our purposes, without the appropriate measurement of a physical sample, estimation of this parameter would be difficult. As such, a much simpler analytical approach should more than suffice [116], [251] – this approach is shown in Equation (7-12). Part of the challenge in this approach (derived from Maxwell's equations) lies in the underlying assumptions of homogeneity in permeability, permittivity and resistivity. This uniformity, as we shall see when talking about nano-scale considerations is generally not true for magnetic materials – factors like domain walls, etc. interfere and can lead to significant discrepancy between analytical and real results. For our purposes, however, such accuracy is not required and it is sufficient to speak in terms of orders of magnitude.

$$\mathbf{P_{re}} = \boldsymbol{\eta_{an}} \mathbf{C}\, \mathbf{f^2} \mathbf{B_{peak}^2} \tag{7-11}$$

$$\mathbf{P_{re}} = \frac{\mathbf{d^2} \left(\frac{\partial \mathbf{B}}{\partial \mathbf{t}}\right)^{\mathbf{2}}}{\mathbf{12} \boldsymbol{\rho_r} \boldsymbol{\rho_d}} \tag{7-12}$$

In Equation (7-12), the value d represents the thickness of laminations, ρ_r represents the resistivity of the material and ρ_d the density. Making a few assumptions based on our earlier review of existing materials from Table 4-1, we note that these values for silicon steel are in the order of: $d = 0.35$ [mm], $\rho_r = 2.60\ x\ 10^{-7}$[Ωm] and $\rho_d = 7160$ [Kg/m^3]. Furthermore, considering the case where the field across the rotor is a result of the remanent magnetization, we note that the remanence (B_r) can be represented as some peak value changing in a sinusoidal manner as $B_r = B_{peak}\sin(\omega t)$ as the rotor rotates. This peak remanent value falls at roughly 1.76 [T] for silicon steel, according to literature. Furthermore, the number of poles that the rotor passes through will multiple the induced losses as $\mathfrak{r}\mathfrak{s}/2$, as will the number of

stacked laminations. The number of laminations for the reluctance machine design associated with this study would come to $\ell = 28$ in order to provide a machine pole height (rp). The number of poles will be $\mathfrak{r} = 4$ and $\mathcal{s} = 6$. Given this information a new power loss equation can be constructed via Equation (7-12) as in Equation (7-13).

$$P_{re} = \frac{\ell\, \mathfrak{r}\, \mathcal{s}\, d^2 \left(\frac{\partial}{\partial t}\left(B_{peak}\sin(\omega t)\right)\right)^2}{24\rho_r\rho_d} \tag{7-13}$$

$$P_{re} = \frac{\ell\, \mathfrak{r}\, \mathcal{s}\, d^2 B_{peak}^2 \omega^2 \sin^2(\omega t)}{24\rho_r\rho_d}$$

$$\mathbf{P_{re} = \frac{\ell\, \mathfrak{r}\, \mathcal{s}\, d^2 B_{peak}^2 \omega^2}{24\rho_r\rho_d}\ (under\ peak\ conditions)}$$

Comparing the peak power loss resulting from our earlier diamagnetic bearing reluctance machine constructed from these laminations to one constructed from ferrite material is difficult to do using this formulation. This is particularly true, considering that the number of laminations, ℓ, and the thickness of the laminations, d, aren't relevant quantities in ferrites and have little meaning. We can however, make the somewhat inaccurate assumption that the thickness of our ferrite "laminations" is the diameter of the particles themselves. Furthermore, we can assume that the number of laminations is equal to the number of particles making up the height (rp) of the reluctance machine. Let us assume, using characterized and measured values from the commercial magnetite sample used in this study, that ferrite particles have a diameter, $d = 2340$ [nm], before sintering. From here we can come up with the parameters for a ferrite machine such that: $\ell = 4273504$, $B_{peak} = 0.032$ [T], $\rho_r \approx 1\, x\, 10^{-6}$ [Ωm] and $\rho_d = 5195$ [Kg/m^3]. The resulting eddy current loss is roughly 18 orders of magnitude bigger in the silicon lamination based

approach even at very low speeds of 42 [rpm]. Likewise, the ferrite eddy current loss from the remanent field is also about 9 orders of magnitude smaller than the cogging loss (P_{rh}) resulting from hysteresis effects in the rotor. This suggests it can be neglected as a contributor.

However, here it should be stressed that the likely contribution from idling eddy current losses in the laminated silicon steel isn't expected to be the dominant contributor to loss – rather the minor loop formed by the hysteresis of the silicon steel is likely to be more significant. This is because the remanent magnetization of 1.76 [T] of the material is combined with a low coercivity of, roughly, 33 [A/m]. So the change in magnetization of the rotor from positive remanent to negative remanent field will also have a significant contribution to this loss. The representative loss should have a contribution computed as the area of the minor hysteresis curve. This minor curve area cannot be computed just from the sparse data available from the SQUID hysteresis measurements. The next chapter, Chapter 8, discusses an approach to modelling the hysteresis of the material from the sparse data. This modelling approach allows the regeneration of minor hysteresis loops through parameter estimation.

7.4 Summary and Final Remarks

This chapter noted the challenges of producing estimates of power loss from the prototype diamagnetic bearing presented in this study. Some attempts were made to provide estimates of power loss associated with air friction as well as losses resulting from the rotating rotor material. Putting aside air friction related losses, a few contributors to electromagnetic loss were noted: counter current flows in the stabilizing machinery and lifter-floater assembly, eddy currents in the electrical machine and hysteresis loss.

This chapter avoided analytical approaches or measurement as a method of estimating losses in the stabilizing machinery. Instead simulations via commercial finite element software were used instead.

An analytical formulation for eddy current loss in our electrical machine (made from ferrite material) was presented. A comparison between this magnetite-based ferrite cored machine was noted to have significantly lower eddy current losses than traditional machines constructed from silicon steel laminations.

Electrical machine hysteresis effects were noted to be a contributor to rotational power loss in our bearing as well. These hysteresis effects can be divided into remanent field induced cogging drag and remagnetization related loss. A further analytical expression for computing power loss from remanent related cogging was discussed and noted to be a significant source of loss (about two orders of magnitude smaller than air friction and significantly larger than eddy current loss). Remagnetization related losses can be computed by hysteresis curve area computations. However, such computations require hysteresis modelling considering that only sparse SQUID magnetization data was available in this study. The next chapter will focus on loss from remagnetization of the rotor stator combination in our diamagnetic bearing reluctance machine.

8 Hysteresis Modelling

Now focussing in on the question of hysteresis loops. How can the area and hence remagnetization loss of the M-H curve be computed? If reasonably dense data is available for the entire curve some form of grid-based area counting can be performed. This may be done by dividing the space into a uniform grid of sufficient resolution and counting the individual area contributions.

However, in the case of the experimental data collected for the large number of synthesized magnetite samples in this study, dense data collection was not practical. Time taken and the corresponding cost of helium in the SQUID magnetometer used to make the measurements would have been prohibitive. The sparse magnetization data collected, thus, makes grid counting approaches difficult to do with any reasonable accuracy.

Furthermore, a grid counting approach doesn't allow area computations associated with the minor hysteresis loops. Figure 8-1 demonstrates these minor loops are a result of an H-field applied to induce a magnetization below that of saturation. As long as the coercive field is sufficiently small – in the same order of magnitude as the remanence – as the rotor spins the remanent moment in the rotor and stator will act as the applied field and have sufficient magnitude to significantly alter the original remanent magnetization and cause traversal along a minor loop.

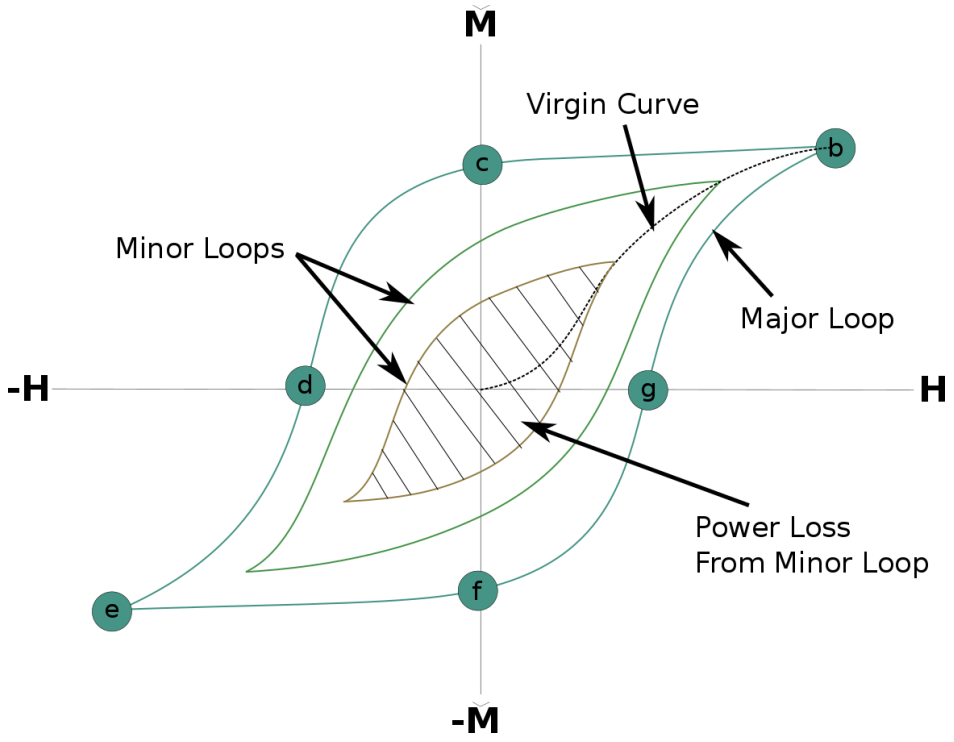

Figure 8-1: An example of major and minor hysteresis loops.

An alternative to grid based area counting is to create a model that takes into consideration nano-scale concerns. Parameters can be estimated from such a fitted model to not only provide a curve along which integration can take place, but to provide a means of generating minor hysteresis loops and computing their power loss contributions. Depending on some heuristic understanding of the data, different models are more or less suited for representation of the hysteresis curve. Two of the most popular of these models are the: Preisach Model [252] and the Jiles-Atherton Model [253]–[259]. The Preisach model is beyond the scope of this study, but the Jiles-Atherton model has applicability in the analysis of the Fe_3O_4 nano-particles and it is this model that will be used for estimating power loss contributions.

8.1 Modified Jiles-Atherton Model

The Jiles-Atherton Model [253], [260], at its most basic, models the magnetization of a material as a separation between a reversible magnetization (M_{rev}) and an irreversible magnetization (M_{irr}) as shown in Equation (8-1).

$$\mathbf{M} = \mathbf{M_{rev}} + \mathbf{M_{irr}} \quad \xrightarrow{\text{diff.form}} \quad \frac{\mathbf{dM}}{\mathbf{dH}} = \frac{\mathbf{dM_{rev}}}{\mathbf{dH}} + \frac{\mathbf{dM_{irr}}}{\mathbf{dH}} \tag{8-1}$$

The basis of this model relies on some foundational, physically-based, hypotheses about the nature of magnetic domains in a material. For instance, the reversible contributions can be thought to be a result of domain wall (e.g. Bloch & Neel walls) motion between (but not across) pinning sites. Such reversibility can also be a result of the rotation of magnetic moments [258], [260]. The irreversible contributions would then be the result of crossing beyond pinning sites within the material.

Despite this, there are a number of non-physical properties that can be attributed to the model as well [255]. Putting aside these non-physical attributions for the time being, the Jiles-Atherton model hypothesizes that ferromagnetic (and ferrimagnetic) materials strive for anhysteretic behaviour. This anhysteretic behaviour is one in which the material operates as an idealized ferromagnet/ferrimagnet [36] or, more practically speaking, a superparamagnet. This is particularly applicable to materials without the presence of dislocations (pinning sites) resulting from inhomogeneities or other impurities.

The anhysteretic magnetization (M_{an}) is needed for computations of M_{rev} and M_{irr} and can be well modelled [91] using a Langevin function ($\mathcal{L}$) as shown in Equation (8-2) (with derivative in Equation (8-3)). Our sample of Fe_3O_4, for instance, in the ideal case would exhibit this behaviour.

$$\mathbf{M_{an}} = \mathbf{M_s}\mathcal{L}(\mathbf{z}) = \mathbf{M_s}\left(\mathbf{coth}(\mathbf{z}) - \frac{\mathbf{1}}{\mathbf{z}}\right) \quad \text{where} \quad (8\text{-}2)$$

$$\xrightarrow{\text{diff.form}} \quad \frac{\mathbf{dM_{an}}}{\mathbf{dH}} = \frac{\mathbf{M_s}}{\mathbf{H}}\left(\mathbf{z} - \mathbf{z}\,\mathbf{coth^2}(\mathbf{z}) + \frac{\mathbf{1}}{\boldsymbol{z}}\right) \qquad z = \frac{m\mu_0 H}{k_b T},\ M_s = n \cdot m \quad (8\text{-}3)$$

Note that this model is only valid when the magnetic anisotropy of the material is considered negligible [5], [261] and when the resulting energy of a single particle is given only by the Zeeman (free) energy, that is, $E_z = -m \cdot \mu_0 H = -m \cdot B$ (where energy is at a minimum when B and m are aligned). This is only true for magnetically isotropic particles.

The value M_s in the equation represents the magnetic saturation of the superparamagnetic material and may also be represented in terms of magnetic moments [91] as was done earlier in Chapter 3 – in such a case, we note that n indicates the number of magnetic moments (m) per unit volume or mass. In this scenario, the parameters: m and n can thus become fitting parameters for our anhysteretic model. If a particle (and associated moment) is sufficiently small, the Zeeman energy (E_z) and anisotropy energy (E_{an}), required to change the orientation of a magnetic moment from one easy axis to another, becomes very small [6], [144]. At such a small size, this decreased energy allows for competition with thermal energy ($E_t = k_b T$) and the resulting Brownian motion of the particles [262] begins to dominate ($z < 1$) leading to anhysteretic behaviour and is responsible for the definition of $z = E_z/E_t$ in our Langevin model in Equation (8-2). A deeper discussion of anisotropy energy will follow later in this study.

Expanding on this, two improvements to the earlier Langevin model can help account for the contributions of localized moment interaction and uneven exchange coupling as shown in Equation (8-4).

$$\mathbf{M_{an}} = \mathbf{M_s}\left(\mathbf{coth(z)} - \frac{\mathbf{1}}{\mathbf{z}}\right) + \boldsymbol{\chi}_{\mathbf{AF}}\mathbf{H_{eff}} \qquad \text{Where:} \qquad (8\text{-}4)$$

$$\xrightarrow{\text{diff.form}} \quad \frac{\mathbf{dM_{an}}}{\mathbf{dH}} = \left(\mathbf{1} + \boldsymbol{\alpha}\frac{\mathbf{dM}}{\mathbf{dH}}\right)\left(\frac{\mathbf{M_s}}{\mathbf{H_{eff}}}\left(\mathbf{z} - \mathbf{z\,coth^2(z)} + \frac{\mathbf{1}}{\mathbf{z}}\right) + \boldsymbol{\chi}_{\mathbf{AF}}\right)$$

$$\begin{cases} z = \frac{m\mu_0 H_{eff}}{k_b T} = aH_{eff} \\ H_{eff} = H + \alpha M \\ M_s = n \cdot m \end{cases} \qquad (8\text{-}5)$$

Our moments (m) are considered uncompensated magnetic moments (m_{uc}) when exchange interactions between ferrimagnetic (FM) and antiferromagnetic (AFM) regions occur in the material [5], [263], [264].

At this point, a departure is needed to discuss exchange interactions. These interactions generally take three forms, of which, iron-iron exchange and oxygen-iron super-exchange interactions are the dominant form that is likely taking place in our magnetite samples. The magnetization of a particular material arises from the unpaired electron spins in an atom. These unpaired spins interact weakly with neighbouring atoms leading to exchange that alters the overall nano-scale behaviour of the material. Figure 8-2 clarifies.

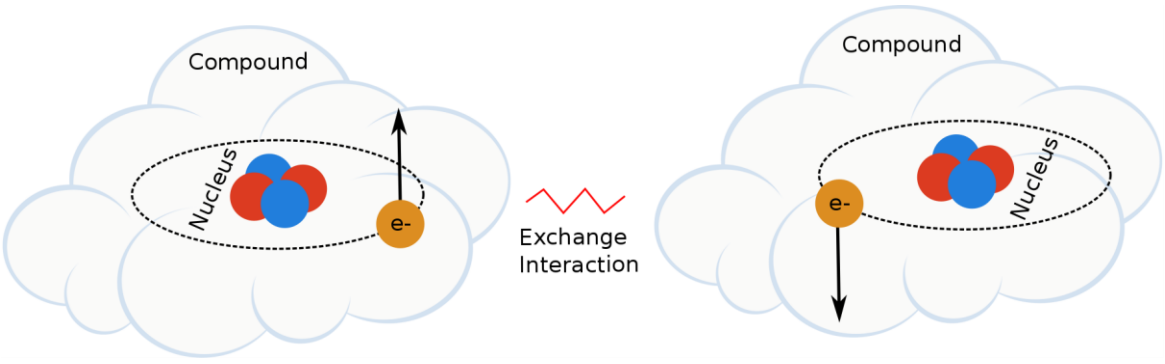

Figure 8-2: A representation of exchange interactions.

In the case of magnetite, to understand super-exchange, some background of the crystal lattice structure is needed as well (Figure 8-3). Magnetite (Fe_3O_4) consists of

a combination of covalent and ionic bonds, with tetrahedral sites in the lattice generally being covalent and octahedral sites being ionic. Tetrahedral sites (A sites) are the empty spaces generated by the stacking of 4 oxygen atoms (O^{2-}) in a 3D triangular (tetrahedral) pattern while octahedral sites (B sites) are a result of the stacking of 6 oxygen atoms. These empty spaces are filled with Fe^{3+} ions for A sites and Fe^{2+} and Fe^{3+} ions for B sites – there are twice as many B sites as A sites in a unit cell. At B sites, electron hopping (and limited delocalization) between our ions results in electric polarization of the material and subsequent propagation of this polarization leads to iron-iron exchange interactions.

With the nano-particles synthesized during this study, the resulting oxidation produces a FM-AFM core-shell structure. The result is uneven exchanging coupling at the boundary regions between such layers. As with our earlier discussion, such uneven exchange coupling is a result of indirect quantum interactions among the layer particles and can cause deviations from our earlier presented Langevin behaviour. Where such coupling occurs more, exchange bias may also occur [5] and results in shifted hysteresis loops. This effect can be represented by the term: $\chi_{AF}H_{eff}$ added to our original Langevin model with the aim of helping to compensate for these antiferromagnetic exchange interactions [261], [265]–[269]. In the case of magnetite (Fe_3O_4), the antiferromagnetic material will typically take the form of hematite (α-Fe_2O_3). Here the susceptibility (χ_{AF}) above the Neel temperature (T_N) is given by a positive number in the same range as that associated with α-Fe_2O_3. According to [260] this would fall roughly at the susceptibility value given by: $\acute{\chi}_{AF}^{si} = (1.44 \pm 0.25) \times 10^{-6}$ [m^3/Kg]. Here, the χ_{AF} value can become an additional model fitting parameter that can help model our exchange bias (H_{ex}).

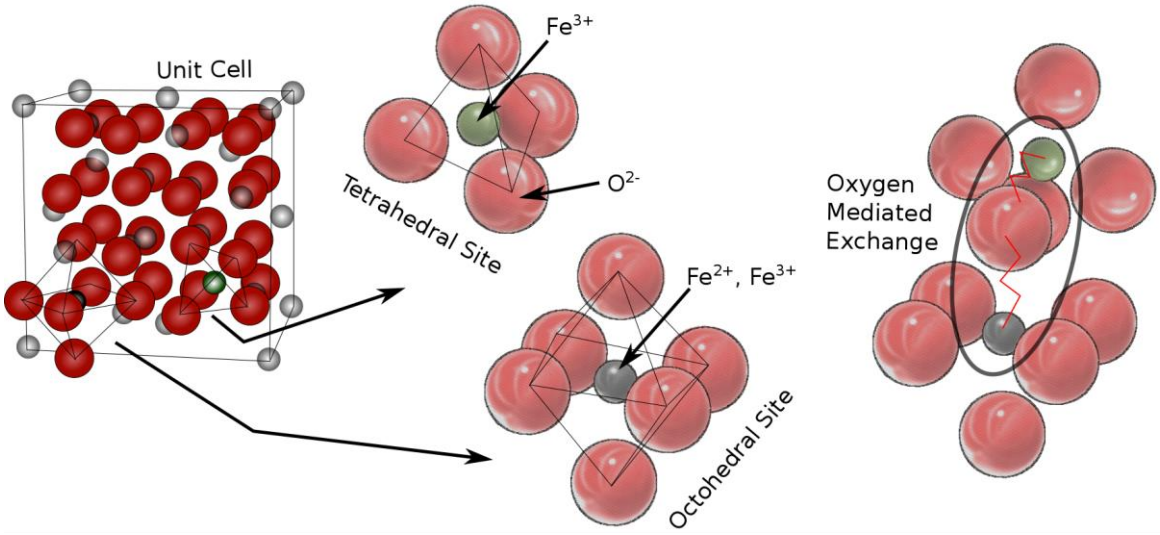

Figure 8-3: Crystal lattice structure for magnetite. Two types of sites exist: Tetrahedral (A) and Octahedral (B). Twice as many B sites as A sites in a unit cell.

The effect of localized moment interactions can also change the effective applied field (H_{eff}) for a particular moment and may cause additional deviations from our Langevin behaviour [5], [253], [259]. We can extend our definition of Zeeman energy for our particle to account for the inter-domain coupling of the bulk magnetization such that: $E_z = -m \cdot \mu_0 H_{eff}$ (expanded: $E_z = -m \cdot \mu_0 (H + \alpha M)$). As we see, the effective field [5], [266] is a result of the addition of the Weiss molecular (mean) field, αM [5], [270], and is defined as $H_{eff} = (H + \alpha M)$. A value α (also known as the Weiss coefficient or mean field parameter) becomes a model fitting parameter that represents the coupling of localized magnetic moments. It should be noted that the resultant Weiss field αM is a purely fictitious average contribution of neighbouring moments and only serves to represent the coupling of these neighbours on a specific unit-cell in our magnetite crystal. The unit-cell is the smallest unit of symmetry that encapsulates our magnetite sample's crystal structure.

Now given the definition of M_{an}, an equation for M_{rev} can be defined [253], [257] as shown in the Equation (8-6) below.

$$\mathbf{M_{rev}} = \mathbf{c}(\mathbf{M_{an}} - \mathbf{M_{irr}}) \xrightarrow{\text{diff.form}} \frac{\mathbf{dM_{rev}}}{\mathbf{dH}} = \mathbf{c}\left(\frac{\mathbf{dM_{an}}}{\mathbf{dH}} - \frac{\mathbf{dM_{irr}}}{\mathbf{dH}}\right) \tag{8-6}$$

The value c represents a unit-less fraction of the anhysteretic and irreversible component difference and thus becomes a model fitting parameter. Likewise, we can define the irreversible magnetization in terms of a differential equation as shown in Equation (8-7). Given the implicit nature of the differential equation, the challenge lies in solving this equation for parameter estimation.

$$\frac{\mathbf{dM_{irr}}}{\mathbf{dH}} = \frac{\overline{\boldsymbol{\delta}}(\mathbf{M_{an}} - \mathbf{M_{irr}})}{\boldsymbol{\kappa\delta} - \boldsymbol{\alpha}(\mathbf{M_{an}} - \mathbf{M_{irr}})} \tag{8-7}$$

In this equation, κ forms an additional model parameter representing the pinning coefficient for the wasted energy resulting from domain walls moving across material pinning sites. These pinning sites are a result of inhomogeneity or impurities in our sample material. In order to change the magnetization direction of the material, this pinning musty be overcome by the external field. The value, κ is associated with this wasted energy, $E_{pin} = \kappa \int dM$ such that $\kappa = \bar{n}\langle\epsilon_\pi\rangle/2m$ and $\bar{n}\langle\epsilon_\pi\rangle$ is the average energy $\langle\epsilon_\pi\rangle$ required to move the moment (m) through 180° over $\bar{n}$ pinning sites [253]. Incidentally, for soft materials this value κ is roughly equal to the coercivity in SI units ($\kappa = H_c$).

The value δ is used to make adjustments to the sign of the denominator depending on whether the decreasing or increasing part of the hysteresis curve is being considered. Correspondingly, $\overline{\delta}$ excludes the contribution of irreversible fields when the material is in a demagnetized (virginal) or saturated state and if invalid or irregular localized loop shapes exists. We note that not all irregular loop shapes are invalid and both

asymmetries, inversions and localized loop reversals have been observed by some researchers [271], [272]. Though as discovered by the author and corroborated by another researcher [273], it is likely such anomalies are artefacts of poorly calibrated SQUID experimental setups. Ultimately, the removal of invalid conditions can be formalized as shown in Equation (8-8).

$$\boldsymbol{\delta} = \begin{cases} +\mathbf{1} & \textbf{if } \dfrac{\mathbf{dH}}{\mathbf{dt}} \geq \mathbf{0} \\ -\mathbf{1} & \textbf{if } \dfrac{\mathbf{dH}}{\mathbf{d}} < \mathbf{0} \end{cases} \qquad \bar{\boldsymbol{\delta}} = \begin{cases} \mathbf{1} & \textbf{if } \dfrac{\mathbf{dH}}{\mathbf{dt}} > \mathbf{0} \textbf{ and } \mathbf{M_{an}} > \mathbf{M_{irr}} \\ \mathbf{1} & \textbf{if } \dfrac{\mathbf{dH}}{\mathbf{dt}} < \mathbf{0} \textbf{ and } \mathbf{M_{an}} < \mathbf{M_{irr}} \\ \mathbf{0} & \textbf{otherwise} \end{cases} \tag{8-8}$$

Putting all equations from Equations (8-1) to (8-8) together we can now produce a single differential equation representing the total magnetization with respect to the applied field shown in Equation (8-9).

$$\begin{aligned} \frac{dM}{dH} &= \frac{dM_{rev}}{dH} + \frac{dM_{irr}}{dH} \\ &= c\left(\frac{dM_{an}}{dH} - \frac{dM_{irr}}{dH}\right) + \frac{dM_{irr}}{dH} \\ &= c\frac{dM_{an}}{dH} + (1-c)\frac{dM_{irr}}{dH} \\ \boxed{\frac{\mathbf{dM}}{\mathbf{dH}} &= \mathbf{c}\frac{\mathbf{dM_{an}}}{\mathbf{dH}} + (\mathbf{1}-\mathbf{c})\frac{\bar{\boldsymbol{\delta}}(\mathbf{M_{an}}-\mathbf{M_{irr}})}{\boldsymbol{\kappa\delta} - \boldsymbol{\alpha}(\mathbf{M_{an}}-\mathbf{M_{irr}})}} \end{aligned} \tag{8-9}$$

At this point, we have a set of fitting parameters $\theta = \{n, m, \alpha, c, \kappa, \chi_{AF}\}$. Noting that an analytical solution to this problem isn't possible, perhaps the most important question that arises is how the Jiles-Atherton model may be combined with numerical approaches and used to estimate our final parameters, $\hat{\theta}$, leading to best fit.

8.2 Numerical Optimization Approach

The solution becomes a least squares minimization problem over some cost function ($C(\theta)$) of the form shown in Equation (8-10). In this function, the value M_j for $j = 1$ to N_M indicates the N_M measured magnetization values for respective, N_M applied H values. For a particular set of estimated parameter values, an estimate for this measured magnetization can be computed as $\widehat{M}_j$. The residual ($r_j = M_j - \widehat{M}_j$) squared provides a measure of the sum-of-squared-difference (SSD) cost (S). This cost is modified by an additional equality penalty function (P_{eq}) and inequality penalty function (P_{neq}) to constrain it within boundary conditions needed to reduce the solution space for faster convergence. Here the values G_{eq_p} and G_{neq_q} are a set of p or q constraint equations with some manually tuned parameters β and ρ introduced to ensure large fixed penalties when deviations outside the boundary conditions occur. The use of this penalty function approach also allows for traditional unconstrained optimization.

$$\hat{\theta} = \underset{\theta}{\operatorname{argmin}}\{C(\theta|M_j \text{ for } j = 1 \,..\, N_M)\} = \underset{\theta}{\operatorname{argmin}}\{S + P_{eq} + P_{neq}\} \tag{8-10}$$

$$\widehat{\boldsymbol{\theta}} = \mathbf{argmin}_{\boldsymbol{\theta}} \left\{ \sum_{\mathbf{j=0}}^{\mathbf{N_M}} \left(\mathbf{M_j} - \widehat{\mathbf{M}}_\mathbf{j}\right)^2 + \frac{\mathbf{1}}{\mathbf{p}} \sum_{\mathbf{p}}^{\mathbf{N_{eq}}} \left(\boldsymbol{\beta}\, \mathbf{G}_{\mathbf{eq_p}}^{\mathbf{2}}\right) + \frac{\mathbf{1}}{\mathbf{q}} \sum_{\mathbf{q}}^{\mathbf{N_{neq}}} \left(\boldsymbol{\rho}\, \mathbf{G}_{\mathbf{neq_q}}^{\mathbf{2}}\right) \right\}$$

The optimization (minimization) is done using a modified unconstrained approach to gradient descent via an existing implementation of the Levenberg Marquardt [274] algorithm. The process involves iterative refinement of our estimate, $\hat{\theta}$, by gradient computations of our cost function with respect to each parameter θ_i in our parameter set of six variables. Equation (8-11) demonstrates.

$$\boldsymbol{\theta_{i_{n+1}} = \theta_{i_n} + \lambda \cdot \frac{\partial C(\theta_{i_n})}{\partial \theta_{i_n}}} \tag{8-11}$$

Here the traditional learning rate (λ) is damped repeatedly to provide the fastest local convergence based on the undershoot or overshoot (in our magnetization estimate) resulting from our gradient step size ($\partial C(\theta_{i_n}) / \partial \theta_{i_n}$). The stopping criteria is reached when the changes in our parameter estimates are sufficiently small.

A further difficulty lies in finding the magnetization estimate, $\widehat{M}_j$, for our iterative computation, however. This is because our original model is a challenging inseparable differential equation (Equation (8-9)). Prior to finding this estimate, therefore, another numerical approximation is needed to estimate the solution for this differential equation as a sub-problem of the parameter estimation/minimization problem. This solution makes use of a pre-existing stiff solver based on an implicit Runge-Kutta approach [275]. Given that the data set available to us for the magnetization values is discrete, an additional level of linear interpolation is needed to estimate step increments in the differential equation solver. Furthermore, solutions to monotonically decreasing and increasing regions of the hysteresis curve must occur separately to ensure correct convergence.

Some method of propagating error from the measured magnetization data to the final parameter values is also needed. This propagation can provide an error in resulting power computations from our minor loop hysteresis curve area. A Monte Carlo approach to generating a set of new measured magnetization datasets was used. Here, under the assumption of normally distributed measurement error, each sample magnetization data set is perturbed by a random normal error to produce N_{mc} datasets over which hysteresis modelling can take place. The resulting mean and standard deviation of the aggregated results of the N_{mc} parameters generated from these N_{mc} data sets then become an estimate for parameter error.

The overall algorithm developed to numerically solve this problem and generate the complete hysteresis curve (including minor loops) and associated power loss can be summarized by the flow chart shown in Figure 8-4.

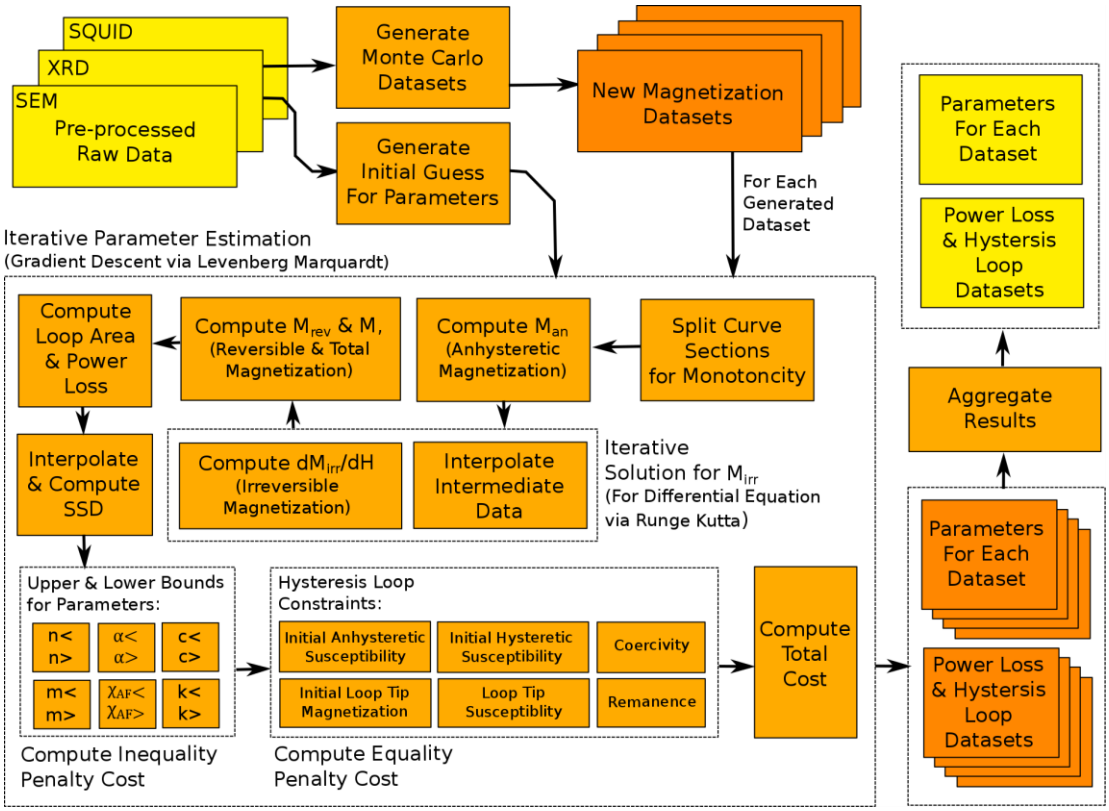

Figure 8-4: Algorithm for power loss estimation from hysteresis loop. Notice that yellow boxes indicates input/output stage data, light orange processing & dark orange generated data. Inputting new applied field data at the output stage can be used to generate minor loops.

Typically, numerical approaches require some initial guess for the parameters, θ_0 as a starting point. Unfortunately, solutions to the earlier equations are known to be extremely sensitive to this starting guess – the guess must already be close to the real value of the parameters to lead to the optimum solution. If this is not the case, convergence to some incorrect local minima, is common. As mentioned earlier, the convergence can be significantly improved with the addition of a set of constraints

(G_{eq} and G_{neq}). Considerable work is required to ensure that inequality and equality constraints are properly constructed. The subsequent section (i.e. Section 8.3) discusses how a good initial guess can be formulated and the specific constrain equations used for providing boundary conditions for our hysteresis curve estimation.

It should be noted that the power losses associated with the changing field across the motor material would also have to be modelled as those losses associated with minor hysteresis loops. These loops are captured directly by the model presented in this section.

8.3 Selecting an Initial Guess for Optimization

An initial guess for some of these parameters is needed. Knowledge of our antiferromagnetic material (hematite) [276] can start us off and provides an initial guess: $\acute{\chi}_{AF}^{si} = 1.44 \times 10^{-6}[m^3/Kg]$. Moving to volumetric SI units this is equivalent to a dimensionless value: $\chi_{AF} = \rho_d^{si}\acute{\chi}_{AF}^{si} = 7.48 \times 10^{-3}$.

An initial guess for n and m requires a deeper look at the underlying chemistry and physics. We can start by writing our magnetic saturation (M_s) in terms of the number of Bohr magnetons (m_B) in our sample as shown in Equation (8-12). Note that N_A represents Avogadro's constant, ρ_d the density of a sample and $\mathcal{M}_W$ the molecular weight per formula unit.

$$\mathbf{M_s} = \mathbf{n} \cdot \mathbf{m} = \frac{\mathbf{N_A \rho_d}}{\boldsymbol{\mathcal{M}_W}}\mathbf{m} = \frac{\mathbf{N_A \rho_d}}{\boldsymbol{\mathcal{M}_W}}\mathbf{g m_B} \qquad \text{where: } \begin{cases} m = g m_B \\ m_B^{si} = \dfrac{e\hbar}{2\mathcal{M}_e} \\ m_B^{cgs} = \dfrac{e\hbar}{2\mathcal{M}_e c} \end{cases} \qquad (8\text{-}12)$$

The value m_B is calculated by looking at the orbital angular momentum (magnetic dipole moment) of an unpaired electron with charge e and mass $\mathcal{M}_e$. Here $\hbar$ is the reduced plank's constant. The g-factor (g) is a dimensionless quantity that can be determined experimentally and is related to the gyromagnetic ratio ($\gamma = (g/\hbar)m_B$). The ratio is a proportionality constant that describes the rate of moment precession at the atomic scale (Larmor frequency, $f_L = \gamma H/2\pi$) in the presence of a magnetic field [5]. More importantly, the g-factor also relates m_B to the specific magnetic moment of our sample. For a sample of magnetite, theoretically the magnetic moment (per formula unit, f.u.) should fall at $m = 14m_B$ (where $g = 14$). This is a result of the 4 unpaired electrons from Fe^{2+} and the 10 unpaired electrons from $2Fe^{3+}$.

In practice, however, things look slightly different. Experimental evidence has shown the value of m to fall at $m = 4m_B$ [277], [278] for typical samples. Of-course, given the nature of ionic and metallic bonding in magnetite, there is likely to be some level of electron sharing (and contributions from direct iron-iron exchange interactions and oxygen-iron superexchange interactions). For instance, the oxygen mediated superexchange interaction between Fe^{2+} and Fe^{3+} is likely to result in a mutually exclusive spin direction in the iron ions causing some of the moment to cancel.

Combining this with a decreasing particle size and increasing pressure on the sample, a greater sharing of electrons and a reduced magnetic moment is likely. While an initial guess for the moment can be taken as $m = 4m_B$, an alternative approach can be used to compute the number of Bohr magnetons from our experimentally obtained magnetic saturation and sample density data.

Consider a typical sample of magnetite. One such sample was measured by the authors and yielded $\acute{M}_s^{cgs} = 85.63$ [emu/g], $\rho_d^{cgs} = 5.195$ [g/cm^3]. With $\mathcal{M}_W^{cgs} = 231.5$ [g/(mol · f. u.)]. Converting to SI units, an initial guess can be made for n such that it is given as $n = N_A\rho_d/\mathcal{M}_W = 1.35 \times 10^{28}$ [dipoles · f. u./m^3]. Furthermore, we also note that, in SI units, $M_s = 10^3\acute{M}_s^{cgs}\rho_d^{cgs} = 4.45 \times 10^5$ [A/m]. This calculation of our magnetic saturation gives us a guess for m such that m =

$M_s/n = 3.29 \times 10^{-23}$[J/T] for a formula unit. This also means $g = 3.55$ showing a relationship $m = 3.55m_B$ for a single formula unit.

We can also go further and estimate the number of formula units per unit cell of magnetite. This could be determined as shown in Equation (8-13) below in which n_{fu} indicates the number of formula units. The value, Å in this equation represents the lattice parameter, a measure of the physical dimensions of a unit cell. This parameter can be estimated from X-ray diffraction (XRD) measurements and, for the magnetite sample nanoparticle samples in this study, falls at around: $Å = 0.840 \times 10^{-9}$ [m]. The resultant number of formula units per unit cell is thus: $n_{fu} = 8$ [f.u./unit cell].

$$\mathbf{n_{fu}} = \frac{\mathbf{Å^3 \rho_d}}{\mathcal{M}_\mathbf{W}} \mathbf{N_A} \tag{8-13}$$

Now moving on to α. The effective field, H_{eff}, has to be very large in order to induce spontaneous magnetization at room temperature [5], [270]. Considering our earlier sample the magnetic saturation was brought to a maximum at saturation of $H_s^{cgs} = 10000$ [Oe]. Converting to SI unit system this yields $H_s = (10^3/4\pi)\, H^{cgs} = 7.96 \times 10^5$ [A/m]. We note that at the loop tips, our anhysteretic field, M_{an} will be in the same order of magnitude as the magnetic saturation M_s. A small contribution from the exchange bias resulting from antiferromagnetic effects is expected as demonstrated by Equation (8-4). For our earlier magnetite sample, this bias is quite small at a measured value of $H_{ex}^{cgs} = 0.67$ [Oe], $H_{ex} = 53.32$ [A/m]. In turn, we can estimate the effective field from this bias as $H_{eff} = H_{ex}/\chi_{AF} = 7.13 \times 10^3$ [A/m]. At saturation the effective field can be written as $H_{eff} = H_s + \alpha M_s$ and can provide us with an initial guess for our Weiss coefficient, α such that $\alpha = (H_{eff} - H_s)/M_s = 823$. This value is within that suggested by some literature [5], [270] for 3d transition type ferromagnetic and ferrimagnetic materials (i.e. $\alpha = 10^3$ [A/m]). A point of

note, however, that some literature tentatively suggests a higher effective field of $H_{eff} = 10^9$ [A/m] suggesting that some discrepancy is present.

As noted, the coercive field, H_c, taken directly from our experimental data can provide a good estimate for parameter $\kappa = H_c$. This, approximation, however, only applies when soft materials are under consideration. Depending on the sample being considered a ballpark figure of 839 [A/m] or less is sufficient. Finally, one final initial estimate is needed for the value c. Since this value provides an indication of the fraction of contribution from anhysteretic and irreversible field contributions it must lie between 0 and 1. Given that the contribution of the anhysteretic component is likely to be dominant for our soft magnetic materials, this value c can be set at $c = 0.75$ to bias in favour M_{an}.

8.4 Producing Optimization Constraints

A number of physical constraints exist on our hysteresis curve. Especially given our sparse data of the magnetization curves, these physical constraints can be more effectively used to limit our parameter solution space to a more plausible range closer to the global (as opposed to local) minima. The first type of penalty function used to do this provides a set of boundary constraints given as G_{neq}. An upper and lower bound constraint for each parameter, θ_i, can be constructed. These are represented in the form: $G_{neq_q} <= 0$ as shown in the Equation (8-14). Here the parameter values with subscripts lb refer to lower bounds and ub refer to upper bounds.

$$G_{neq_1} = n_{lb} - n \leq 0 \qquad G_{neq_2} = n - n_{ub} \leq 0 \qquad (8\text{-}14)$$

$$G_{neq_3} = m_{lb} - m \leq 0 \qquad G_{neq_4} = m - m_{ub} \leq 0$$

$$G_{neq_5} = \alpha_{lb} - \alpha \leq 0 \qquad G_{neq_6} = \alpha - \alpha_{ub} \leq 0$$

$$G_{neq_7} = \chi_{AF_{lb}} - \chi_{AF} \leq 0 \qquad G_{neq_8} = \chi_{AF} - \chi_{AF_{ub}} \leq 0$$

$$G_{neq_9} = \kappa_{lb} - \kappa \leq 0 \qquad G_{neq_{10}} = \kappa - \kappa_{ub} \leq 0$$

$$G_{neq_{11}} = c_{lb} - c \leq 0 \qquad G_{neq_{12}} = c - c_{ub} \leq 0$$

While these inequality constraints are useful, the more critical constraints are the equality constraints denoted by $G_{eq_p} = 0$. Such constraints require a more careful look at the various contributions from our irreversible, reversible and anhysteretic contributions to the total magnetization represented by the hysteresis curve. Below follows a discussion of six possible equality constraints that can be constructed from an understanding of these contributions.

8.4.1 Initial Anhysteretic Susceptibility Constraint

Looking back at our model equations, we note that when our magnetite sample is fully demagnetized (virginal) with no applied field ($H = 0$) or internal magnetization ($M = 0$), the material will experience an initial magnetization path. This initial magnetization, as an H-field is applied, should have the same slope as the anhysteretic magnetization (M_{an}). Knowing this, our equation $\partial M_{an}/\partial H$ as shown in Equation (8-5) can be rearranged as shown in Equation (8-15) where $\partial M_{an}/\partial H = \partial M/\partial H$.

$$\frac{dM_{an}}{dH} = \left(1 + \alpha\frac{dM_{an}}{dH}\right)\left(\frac{M_s}{H_{eff}}\left(z - z\coth^2(z) + \frac{1}{z}\right) + \chi_{AF}\right) \tag{8-15}$$

$$\frac{dM_{an}}{dH} = \frac{\left(\frac{M_s}{H_{eff}}\left(z - z\coth^2(z) + \frac{1}{z}\right) + \chi_{AF}\right)}{1 - \alpha\left(\frac{M_s}{H_{eff}}\left(z - z\coth^2(z) + \frac{1}{z}\right) + \chi_{AF}\right)}$$

$$\hat{\chi}_{an_{init}} = \lim_{H_{eff}=0} \frac{dM_{an}}{dH} = \frac{nm^2 u_0 - 3X_{AF}k_b T}{\alpha nm^2 \mu_0 + 3\alpha X_{AF}k_b T - 3k_b T}$$

$$\mathbf{G_{eq_1}} = \hat{\boldsymbol{\chi}}_{\mathbf{an_{init}}} - \frac{\mathbf{nm^2 u_0 - 3X_{AF}k_b T}}{\boldsymbol{\alpha nm^2 \mu_0 + 3\alpha X_{AF}k_b T - 3k_b T}}$$

We are interested in the case where our magnetization and applied field approach zero, that is, $M \to 0$ and $H \to 0$. This is equivalent to the case where our effective field approaches zero ($H_{eff} \to 0$). For a given estimate of our parameter space, an estimate (represented by the hat notation) of the initial susceptibility is, thus, given as $\hat{X}_{an_{init}} = X_{an_{init}}$ and leads to a constraint G_{eq_1}. Note that here as with *Equation (*8-5) we use the definition: $z = (m\mu_0 H_{eff})/(k_b T)$.

8.4.2 Initial Hysteretic Susceptibility Constraint

Like the anhysteretic curve, our hysteretic magnetization curve has an initial magnetization slope, $\chi_{init} = \partial M/\partial H$ for $(H = 0, M = 0)$. We can solve for this by noting that $M = 0$ and $M_{irr} = 0$ at the origin and substituting into Equation (8-9). Here we note that: $z = (m\mu_0(H + \alpha M))/(k_b T)$. Furthermore, as with our previous constraint computation for the anhysteretic initial susceptibility, the estimator $\hat{\chi}_{init} = \chi_{init}$, requires a calculation of the limit as $M \to 0$, $H \to 0$ and $M_{irr} \to 0$.

$$\frac{dM}{dH} = c\frac{dM_{an}}{dH} + (1-c)\frac{\bar{\delta}(M_{an} - M_{irr})}{\kappa\delta - \alpha(M_{an} - M_{irr})} \tag{8-16}$$

$$\frac{dM}{dH} = c\left[\left(1+\alpha\frac{dM}{dH}\right)\left(\frac{M_s}{H_{eff}}\left(z - z\coth^2(z)+\frac{1}{z}\right)+\chi_{AF}\right)\right] + (1-c)\left[\frac{\bar{\delta}\left(\left(M_s\left(\coth(z)-\frac{1}{z}\right)+\chi_{AF}H_{eff}\right)-M_{irr}\right)}{\kappa\delta-\alpha\left(\left(M_s\left(\coth(z)-\frac{1}{z}\right)+\chi_{AF}H_{eff}\right)-M_{irr}\right)}\right]$$

$$\hat{\chi}_{init} = \lim_{H,M,M_{irr}\to 0}\frac{dM}{dH} = c\left(\chi_{AF}+m^2 n\frac{\mu_0}{3k_b T}\right)$$

$$\mathbf{G_{eq_2} = \hat{\chi}_{init} - c\left(\chi_{AF}+\frac{m^2 n\,\mu_0}{3k_b T}\right) = 0}$$

8.4.3 Loop Tip Susceptibility Constraint

Continuing on, ignoring the virginal curve, we note that the loop tips on either end of the hysteresis curve should converge for both the hysteretic and anhysteretic paths. In order to understand what happens at the loop tips we need to think about the nature of domain wall pinning. The irreversible contribution, M_{irr}, is a contribution resulting from domain wall pinning. As an applied field, H, is placed across the sample and increased from zero, in a perfect material, all magnetic moments will align instantly with the field. In imperfect materials, there are pinning sites – i.e. the presence of other materials or internal stresses.

Around the locale of the pinning site the magnetic moments will not align with the applied field. This will result in a domain wall that defines a boundary between aligned magnetic moments and unaligned magnetic moments. Because of regional coupling between pinning sites and their surrounding area, the fixed and pinned moments will influence surrounding moments to align somewhat with the pinning moment and somewhat with the applied field direction. Increasing the field will cause more of the surrounding moments to couple with the field rather than with the pinning moment causing the wall to bend. This is demonstrated in Figure 8-5.

Removing the applied field will realign these surrounding moments with the dominant field - i.e. that of the pinning moments. This pinning field is the M_{irr} field. The reversible field, M_{rev}, is the field generated by the surrounding (non-pinning site) moments when under the influence of the applied field. As this applied field is removed the contributions of M_{rev} go down to zero. We note, however, that with a sufficiently large field the pinned moments can be made to snap into alignment with the external field. At this point the material experiences the breakdown of the particular pinned domain wall, resulting in the Barkhausen effect (Figure 8-5).

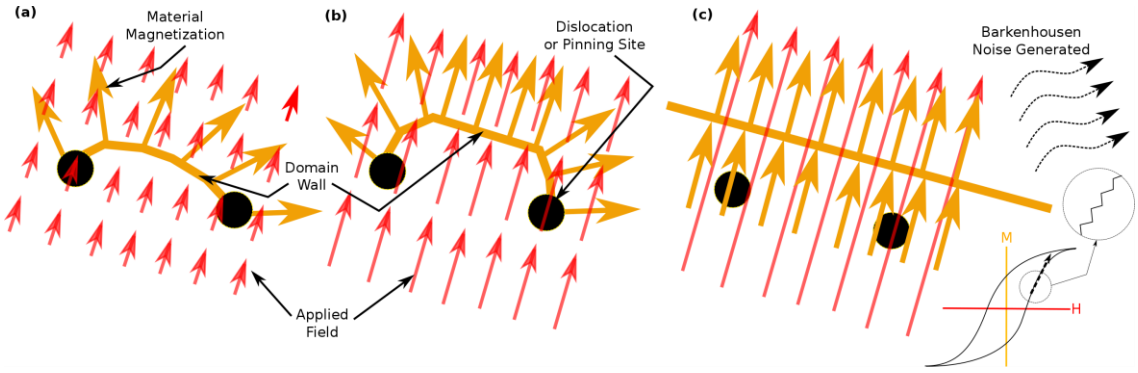

Figure 8-5: Domain wall formation from pinning sites in the material and the resulting Barkenhousen effect. (a) Small applied field, no domain wall change. (b) Larger applied field, domain wall moments begin to align. (c) Very large field, domain wall breaks free of pinning sites and releases energy to produce Barkenhousen noise.

Here a point of observation may be significant – it is likely, if this explanation of the underlying mechanism is correct, that as the material becomes fully superparamagnetic, the Barkhausen effect should become immeasurable and effectively vanish. To meet these conditions, however, would likely require extreme purity and monodisperse nano-particle size distributions. Furthermore, a measurement of this effect may be more cost effective and provide an alternative technique to measuring the extent to which a sample, as a bulk, has achieved superparamagnetic transition.

At the point of saturation, all magnetic domains have been aligned and the resulting irreversible field is now fixed in a single orientation. Relaxing the applied field now will simply cause changes in the reversible field since all the pinned moments are now already in the applied field direction. Relaxation will simply reverse the direction of the surrounding moments to eventually align with the pinned moments. This means that $\partial \mathrm{M_{irr}} / \partial \mathrm{H}$ will not change as the field is relaxed from saturation - so on the decreasing slope of loop tip and on the increasing slope of the loop tip only, will $\partial \mathrm{M_{irr}} / \partial \mathrm{H} = 0$. Note, however, that as soon as the H field reverses direction (crosses the zero value) this condition is no longer valid - at this point the irreversible components will once again begin to change. It is noting these observations that an additional two constraints can be constructed for the two loop tips (via Equation (8-9)) as shown in Equation (8-17). Here the loop tip conditions hold only when $\mathrm{M} \to \mathrm{M_s}$ and $\mathrm{H} \to \mathrm{H_s}$. The estimated susceptibilities for the decreasing and increasing tip portions of the hysteresis curve ($\hat{\chi}_{\mathrm{dec\ tip}}, \hat{\chi}_{\mathrm{inc\ tip}}, \hat{\chi}_{\mathrm{an_{dec\ tip}}}, \hat{\chi}_{\mathrm{an_{inc\ tip}}}$) as generated from our estimated parameters can be used to compute this constraint.

$$\frac{\mathrm{dM}}{\mathrm{dH}} = \mathrm{c}\frac{\mathrm{dM_{an}}}{\mathrm{dH}} + (1-\mathrm{c})\frac{\mathrm{dM_{irr}}}{\mathrm{dH}} \Rightarrow \frac{\mathrm{dM}}{\mathrm{dH}} = \mathrm{c}\frac{\mathrm{dM_{an}}}{\mathrm{dH}} \tag{8-17}$$

$$\lim_{\substack{\mathrm{H}\to\pm\mathrm{H_s} \\ \mathrm{M}\to\pm\mathrm{M_s}}} \left(\frac{\mathrm{dM}}{\mathrm{dH}} - \mathrm{c}\frac{\mathrm{dM_{an}}}{\mathrm{dH}}\right) = 0$$

$$\mathbf{G_{eq_3}} = \hat{\boldsymbol{\chi}}_{\mathbf{dec\ tip}} - \mathbf{c}\,\hat{\boldsymbol{\chi}}_{\mathbf{an_{dec\ tip}}} = \mathbf{0}$$

$$\mathbf{G_{eq_4}} = \hat{\boldsymbol{\chi}}_{\mathbf{inc\ tip}} - \mathbf{c}\,\hat{\boldsymbol{\chi}}_{\mathbf{an_{inc\ tip}}} = \mathbf{0}$$

8.4.4 Initial Loop Tip Magnetization Constraint

We can use the observations from our previous constraint derivation to provide an additional constraint directly on our magnetization as well. In particular, ignoring the

virgin curve, we noted that $\partial M_{irr}/\partial H = 0$ only as the hysteresis curve decreases or increases from positive saturation or negative saturation values. And this, only when near the loop tips. However, in the case of the initial virgin curve this susceptibility closely matches the susceptibility of the irreversible curve such that: $\chi_{irr} = \partial M_{irr}/\partial H = \partial M/\partial H$.

The reason for this is related to the rate of change (χ_{rev}) of the M_{rev} component. For a demagnetized material, during the rise from zero applied field, the reversible moments in the material are oriented randomly with no net force from pinning sites forcing alignment. As the external field increases, the moments experience a peak in the rate of alignment (χ_{rev}) early on. This is followed by a drop in this rate as more and more of the moments come back into alignment. At the same time, the contributions (χ_{irr}) continue at a steady pace matching the virgin curve's susceptibility. Noting this, and starting from our definition of M in Equations (8-1), (8-6) and (8-7) we can construct an additional constraint as shown in Equation (8-18). As with previous constraints, we can estimate our susceptibility for the virgin curve ($\chi_{init\ tip}$) as $\hat{\chi}_{init\ tip} = \partial M/\partial H$ as $M = M_s$ and $H = H_s$. Likewise, we can use the estimates for our loop tip magnetization from the initial curve as well, i.e. $\widehat{M}_{init\ tip}$ and $\widehat{M}_{an_{init\ tip}}$.

$$M = c\,M_{an} + (1-c)M_{irr} \tag{8-18}$$

$$(M_{an} - M_{irr}) = M_{an} - \left(\frac{M - c\,M_{an}}{(1-c)}\right) \Rightarrow (M_{an} - M_{irr}) = \frac{M_{an} - M}{1-c}$$

$$\frac{dM_{irr}}{dH} = \frac{\bar{\delta}(M_{an} - M_{irr})}{\kappa\delta - \alpha(M_{an} - M_{irr})} \Rightarrow \frac{dM}{dH} = \frac{\frac{M_{an} - M}{1-c}}{\kappa - \alpha\left(\frac{M_{an} - M}{1-c}\right)}$$

$$\hat{\chi}_{init\ tip} = \frac{\widehat{M}_{an_{init\ tip}} - \widehat{M}_{init\ tip}}{(1-c)\kappa - \alpha\left(\widehat{M}_{an_{init\ tip}} - \widehat{M}_{init\ tip}\right)}$$

$$\mathbf{G_{eq_5}} = \widehat{\mathbf{M}}_{\mathbf{init\ tip}} - \left(\widehat{\mathbf{M}}_{\mathbf{an}_{\mathbf{init\ tip}}} - \frac{\boldsymbol{\kappa}\, \hat{\boldsymbol{\chi}}_{\mathbf{init\ tip}} (\mathbf{1} - \mathbf{c})}{\mathbf{1} + \boldsymbol{\alpha}\, \hat{\boldsymbol{\chi}}_{\mathbf{init\ tip}}} \right) = \mathbf{0}$$

8.4.5 Coercivity Constraint

The coercivity is another point that can be used to constraint the solution even further. At saturation we have full alignment of all magnetic moments in the material. This means that when the applied field, H, is relaxed to zero the only contributors to the magnetization are from the irreversible field. As the field direction of H is changed to the negative coercive value, our total magnetization goes to zero ($\mathrm{M} = 0$). This means that there is a direct relationship between our irreversible component, $\mathrm{M_{irr}}$ and the anhysteretic component, $\mathrm{M_{an}}$ such that $(\mathrm{M_{an}} - \mathrm{M_{irr}}) = \mathrm{M_{an}}/(1 - \mathrm{c})$. Add to this, that our susceptibility $\chi_{\mathrm{irr}} = \partial \mathrm{Mirr}/\,\partial \mathrm{H}$ falls as the difference between $\partial \mathrm{M}/\,\partial \mathrm{H}$ and $\partial \mathrm{M_{an}}/\,\partial \mathrm{H}$ on any point on our hysteresis curve, we can construct the formulation shown in Equation (8-19) for a coercivity constraint. Two constraints can be constructed, one for each coercive point resulting from either the decreasing portion or the increasing portion of the hysteresis curve as controlled by the sign of δ and $\overline{\delta}$. Given the numerical approach taken, linear interpolation can be used to evaluate the exact coercivity if it is not defined in for $\mathrm{M} = 0$. The values $\mathrm{M_{an_c}}$, $\mathrm{X_c}$ and $\mathrm{X_{an_c}}$ represent the anhysteretic magnetization projection at the coercive applied field, the coercive point susceptibility of the hysteretic curve and the susceptibility of the projection of the coercive point on the anhysteretic curve respectively.

$$\frac{\mathrm{dM_{irr}}}{\mathrm{dH}} = \frac{\overline{\delta}(\mathrm{M_{an}} - \mathrm{M_{irr}})}{\kappa\delta - \alpha(\mathrm{M_{an}} - \mathrm{M_{irr}})} = \frac{1}{1 - \mathrm{c}} \frac{\mathrm{dM}}{\mathrm{dH}} - \frac{\mathrm{c}}{1 - \mathrm{c}} \frac{\mathrm{dM_{an}}}{\mathrm{dH}} \tag{8-19}$$

$$\kappa\delta = \bar{\delta}\left(\frac{\mathrm{M_{an}}}{1-\mathrm{c}}\right)\left(\frac{1}{1-\mathrm{c}}\frac{\mathrm{dM}}{\mathrm{dH}} - \frac{\mathrm{c}}{1-\mathrm{c}}\frac{\mathrm{dM_{an}}}{\mathrm{dH}}\right)^{-1} + \alpha\left(\frac{\mathrm{M_{an}}}{1-c}\right)$$

$$\kappa = \frac{\bar{\delta}}{\delta}\left(\frac{\mathrm{M_{an}}}{1-\mathrm{c}}\right)\left(\alpha + \frac{1}{\left(\frac{1}{1-\mathrm{c}}\frac{\mathrm{dM}}{\mathrm{dH}} - \frac{\mathrm{c}}{1-\mathrm{c}}\frac{\mathrm{dM_{an}}}{\mathrm{dH}}\right)}\right)$$

$$\mathbf{G_{eq_6}} = \boldsymbol{\kappa} \pm \left[\frac{\widehat{\mathbf{M}}_{\mathbf{an_c}}}{\mathbf{1-c}} \cdot \left(\frac{\mathbf{1}}{\frac{\mathbf{1}}{\mathbf{1-c}}\hat{\boldsymbol{\chi}}_{\mathbf{c}} - \frac{\mathbf{c}}{\mathbf{1-c}}\hat{\boldsymbol{\chi}}_{\mathbf{an_c}}}\right)\right] = \mathbf{0}$$

8.4.6 Remanence Constraint

As with the coercive point, the final constraint can be provided by analyzing the remanent point. At this point our applied field is given as $\mathrm{H} = 0$. Now making use of our representation of the hysteretic susceptibility, $\mathrm{dM/dH} = \mathrm{c}\,\mathrm{dM_{an}/dH} + (1-\mathrm{c})\mathrm{dM_{irr}/dH}$, at our zero field position, the constraint shown in Equation (8-20) can be derived. As with prior constraints, the hat accent refers to an estimate computed from a particular iteration value of our parameter set of six variable. Where the estimated magnetization data is not available at $\mathrm{H} = 0$, an estimate for the hysteretic remanence ($\widehat{\mathrm{M}}_{\mathrm{r}}$) and the anhysteretic value at this remanence ($\widehat{\mathrm{M}}_{\mathrm{an_r}}$) is done via linear interpolation.

$$\frac{\mathrm{dM}}{\mathrm{dH}} = \mathrm{c}\frac{\mathrm{dM_{an}}}{\mathrm{dH}} + (1-c)\frac{\bar{\delta}(\mathrm{M_{an}} - \mathrm{M_{irr}})}{\kappa\delta - \alpha(\mathrm{M_{an}} - \mathrm{M_{irr}})} \tag{8-20}$$

$$\frac{1}{\frac{\mathrm{dM}}{\mathrm{dH}} - \mathrm{c}\frac{\mathrm{dM_{an}}}{\mathrm{dH}}} = \frac{\kappa\delta - \alpha(\mathrm{M_{an}} - \mathrm{M_{irr}})}{(1-c)\bar{\delta}(\mathrm{M_{an}} - \mathrm{M_{irr}})}$$

$$M = M_{an} - \kappa\frac{\delta}{\bar{\delta}}\left(\frac{1}{\frac{dM}{dH} - c\frac{dM_{an}}{dH}} + \frac{\alpha}{(1-c)\bar{\delta}}\right)^{-1}$$

$$\mathbf{G_{eq_7}} = \widehat{\mathbf{M}}_{\mathbf{r}} - \left[\widehat{\mathbf{M}}_{\mathbf{an_r}} \pm \left(\frac{\boldsymbol{\kappa}}{\frac{\mathbf{1}}{\left(\hat{\boldsymbol{\chi}}_{\mathbf{r}} - \mathbf{c}\hat{\boldsymbol{\chi}}_{\mathbf{an_r}}\right)} + \frac{\boldsymbol{\alpha}}{\mathbf{1}-\boldsymbol{c}}}\right)\right] = \mathbf{0}$$

8.5 Frequency of Operation and Hysteresis

At this stage, the necessary estimates of our power loss from the hysteresis curve, given our particular sample, can be calculated by first estimating the hysteresis loop parameters using the Jiles-Atherton model, with some initial guess and the introduced constraints. From here, a full hysteresis curve for the family of minor loops can be estimated and the area under the curve computed by summation.

One final concern exists, however. In prior discussions, the possibility of superparamagnetic breakdown was introduced. The high frequency rotation and resulting changes in induced magnetization on the rotor-stator of our reluctance machine was identified as a possible culprit.

A critical particle size is needed to ensure single domain and superparamagnetic properties in our magnetite samples. The superparamagnetic nature of the material is a result of a process called relaxation. A relaxation time, known as the Neel relaxation time (τ_N), quantifies the average time it takes for magnetic moments in our sample to flip magnetization as a result of thermal fluctuations [5], [91]. This is typically presented as shown in Equation (8-21). As particles become smaller and smaller, the combined energy ($E = E_{an} + E_z$) of the magnetic anisotropy energy (E_{an}) and Zeeman energy (E_z) of the particles decreases. That is, the amount of energy needed to flip our magnetization from one easy axis to another begins to

decrease. The Stoner−Wohlfarth model [278] is famously known to describe this energy in single domain monodisperse particles.

$$\tau_N = \tau_0 e^{\frac{E}{E_t}} = \tau_0 e^{\frac{\mathfrak{K}_{eff} V}{k_b T}} \tag{8-21}$$

At some critical size (i.e. blocking radius/diameter), the flipping energy barrier is sufficiently low that thermal energy (E_t) begins to become more dominant. At sufficient time scales, the moments of the particles in the material flip under Brownian conditions resulting in a net zero moment (and magnetization) for the material. For a sufficiently small applied field the value $E = E_{an}$.

The magnetic anisotropy energy ($E_a = \mathfrak{K}V$) is a result of the volume (V) of the particle and the anisotropy constant ($\mathfrak{K}$). The anisotropy constant defines the extent of directional dependence of the materials magnetic properties is a combined result of magnetocrystalline (intrinsic), shape (grain) and stress (exchange) anisotropies. As a result, the combination of the magnetic anisotropy related effects can be combined to produce an effective anisotropy constant ($\mathfrak{K}_{eff}$) [279].

The quantity, τ_0, presented in Equation (8-21) has further significance. This is the attempt time and provides an average timescale between two successive fluctuations resulting from thermal excitation of our particle [280]. Generally, τ_0 is poorly constrained and so can be a challenge to determine – as a result it is common to use values in the range of $\tau_0 = 10^{-13}$ to 10^{-8} [s] in literature [5], [91], [281]–[283]. By some accountings, using such differing values for the anisotropy is not unreasonable considering that the exponential term in our equation would dominate quite significantly as long as the fraction E_a/E_t remains sufficiently above one. While for this study, we will follow suit and use an intermediate time of $\tau_0 = 10^{-12}$ [s], it should be noted that for low anisotropy nano-particles used in this study, such a variable order of magnitude in the attempt time can have drastic impact on the

accuracy of the Neel time and resulting frequency of operation of our bearing motor when our fraction E_a/E_t is closer (within a few orders of magnitude) to 1. As insufficient measurement data was available for parameter estimation of τ_0, the mentioned assumption for its value has been made.

Ultimately, if a Neel relaxation time can be found for our motor material, then a maximum frequency of operation, under which the magnetic remanence and coercivity of the material will remain effectively zero, can be determined. Given scanning electron microscopy (SEM) and x-ray diffractometry (XRD), the crystallite and resulting bulk particles size and volume (V) can be determined. At this point, we make the observation that at high enough frequency or low enough temperature the magnetic moments in our material will cross into a blocking region where the material once again exhibits hysteresis (Figure 8-6a).

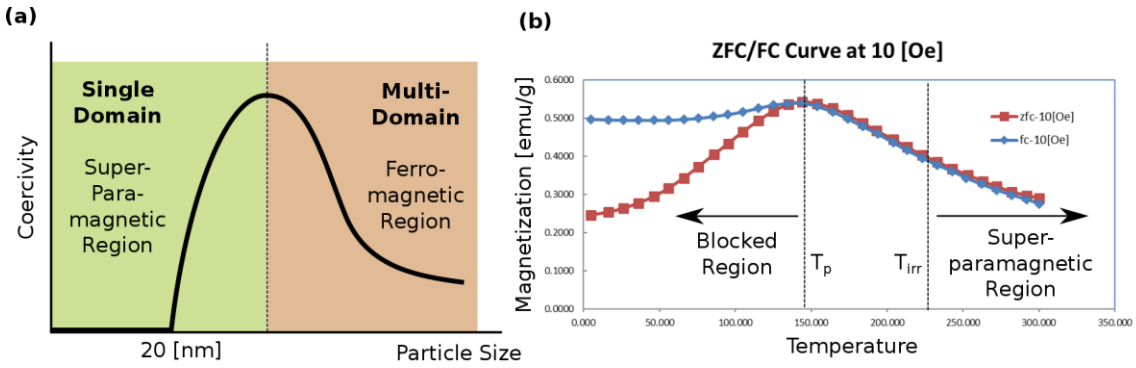

Figure 8-6: (a) Generic relationship between particle size and superparamagnetism. (b) Zero field cooling (ZFC) and field cooling curves (FC) measurements for a synthesized nano-particle sample from this study – as characterized by a SQUID magnetometer.

Figure 8-6b demonstrates two curves sometimes used to characterize the transition point – these are the zero-field cooling (ZFC) and field cooling (FC) curves. In the figure, a particular synthesized magnetite sample has been chosen. The transition to blocked conditions occurs at a blocking temperature T_b. This blocking temperature can be used to represent the net thermal energy in the system as $E_t = k_b T_b$ in our

Neel relaxation time (τ_N) and associated Neel frequency (f_N) calculation. Reducing this frequency by some reasonable margin, the f_N value can be used as a maximum operating frequency of our motor.

Unfortunately, the blocking temperature is dependent on the applied field magnitude, frequency and the particle size. As amplitude of the applied field increases the blocking temperature is known to decrease [284], [285]. This is clear given that the additional energy supplied by the external field pushes higher the energy barrier that needs to be overcome by thermal fluctuations. Likewise, as frequency of the field increases the blocking temperature is known to increase [265], [284]. This frequency dependence can be likened to considerations of measurement time (τ_m). Finally, we note that increasing particle size is accompanied by increasing blocking temperature as well [286].

Various approaches to estimating the blocking temperature exist [283], [284], [287]–[289]. Among the simpler approaches, this temperature is directly ascertained from the peak temperature (T_p) in the ZFC curve. A slightly more complex approach uses the temperature of irreversibility (T_{irr}) whereby the difference in the slopes of the ZFC and FC curve are within 10% of the peak value as shown in Equation (8-22). Here, Newton's method can be used to find the zero crossing (T-intercept) leading to $T_b = T_{irr}$. Note that the equation finds the inflection point for N_t data points in our ZFC data where the difference in the slope at its maximum is used as a reference point.

$$\frac{\partial(\mathbf{M_{zfc}(T)} - \mathbf{M_{fc}(T)})}{\partial \mathbf{T}} \leq \mathbf{0.1} \cdot \max_{\mathbf{i=1\ to\ N_t}} \left(\frac{\partial(\mathbf{M_{zfc}(T_i)} - \mathbf{M_{fc}(T_i)})}{\partial \mathbf{T}} \right) \tag{8-22}$$

While not attempted, an even more complex approach would make use of the actual volume distributions of our synthesized particles and model the ZFC-FC curves as a superposition of equivalently distributed curves produced from this original

distribution [286], [289]. The ZFC curve in a monodisperse sample (one with a narrow size distribution) has a sharp and narrow peak at T_p making the delineation between superparamagnetic and blocked states relatively easy to understand. Unfortunately, with wide distributions, this peak becomes wide as well and is the result of the combined contributions of the individual blocking temperatures of the particle distribution. In such scenarios, an average blocking temperature is considered, though a relationship between blocking temperature and particle size can be constructed [286]. Generally, the distribution of particles during the synthesis process is examined by the analysis of SEM images – in the case of this study, the log-normal probability density function most closely models the actual distribution present in samples. By way of example, Figure 8-7 demonstrates the particle distribution for the ZFC-FC curve presented in Figure 8-6b as extracted from the SEM image shown.

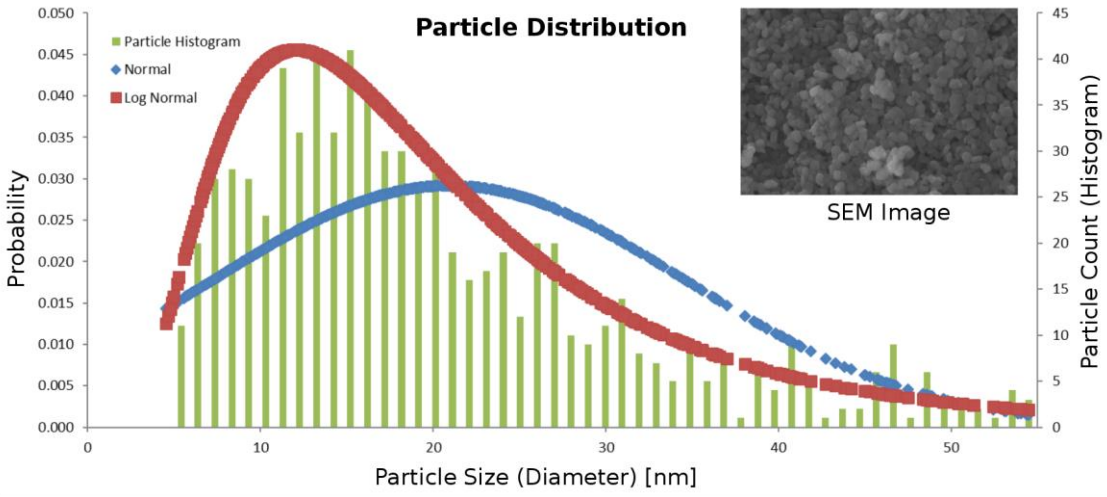

Figure 8-7: The measured distribution of particles from a magnetite nanoparticle sample from this study. This distribution is for the ZFC-FC example shown in Figure 8-6b. Notice the close fit to log-normal v.s. normal probability density function.

For the purposes of this study, this distribution based modelling approach adds significant complexity to the estimation process. As such it has been left as a future exercise in favour of the simpler approach shown in Equation (8-22).

Now note that our anisotropy value, $\mathfrak{K}_{eff}$, is itself dependent on temperature. Before computation of the Neel frequency (f_N) can be completed, a value of $\mathfrak{K}_{eff}$, thus, needs to be computed for our estimated blocking temperature. Unfortunately, insufficient data was available from existing measurements to provide an accurate measure of this anisotropy. Utilizing existing published data [286] an approximation of $\mathfrak{K}_{eff}(5) = 5.9 \times 10^5$ [J/m^3] at 5 [°K] and $\mathfrak{K}_{eff}(280) = 1.1 \times 10^4$ [J/m^3] at 280 [°K] was used instead as a method of approximation for our particular samples of magnetite.

We note, however, that the dominant contribution to this $\mathfrak{K}_{eff}$ value, at nano-scales, is from shape anisotropy rather than magnetocrystalline considerations [290]. This suggests that particle geometric considerations are a factor in computing $\mathfrak{K}_{eff}$. Such particle geometry can be estimated via the aspect ratio of particles in our SEM images and incorporated into a value called the demagnetization factor [291]. As with our particle distribution and specific sample anisotropy calculations, this estimation is left as a future exercise.

An operating assumption that $E_a \approx 25\ E_t$ [281], [286] is often an approach to estimate the anisotropy resulting from the typical SQUID magnetometric measurement times (τ_m). For nanoparticles the resultant anisotropy from this process can be somewhat small (in the order of 10^3 [J/m^3]) and isn't necessarily a good representative of the anisotropy of a superparamagnetic material.

An alternative is to assume a decreasing linear dependence between temperature and our anisotropy as shown in Equation (8-23) [286]. This is, of-course, not completely accurate, but is sufficient. A significant problem arises, however. The anisotropy ($\mathfrak{K}_{eff}(0)$) at 0 [°K] must be known along with the temperature (T_0) at which this anisotropy reaches zero value – neither of these have been characterized for our particular nano-particle samples.

$$\mathfrak{K}_{\mathbf{eff}}(\mathbf{T}) = \mathfrak{K}_{\mathbf{eff}}(\mathbf{0})\left(\mathbf{1} - \frac{\mathbf{T}}{\mathbf{T_0}}\right) \tag{8-23}$$

Brillouin Light Spectroscopy (BLS) and Ferromagnetic Resonance (FMR) are the most common methods of estimating anisotropy from our sample. Unfortunately, such characterization equipment was unavailable.

There is a strong link between $\mathfrak{K}_{\text{eff}}$ and the hysteresis of the material and so, at least in theory, it is possible to should be possible to use critical points in our hysteresis curve to extract two values of $\mathfrak{K}_{\text{eff}}$ for estimation of $\mathfrak{K}_{\text{eff}}(0)$ and T_0. To do so requires measurement of hysteresis and subsequently K_{eff} at two different temperatures and at different frequencies. For the purposes of this study, only a single sample hysteresis was extracted for differing temperature regimes. This estimate was then used as a means of approximating $\mathfrak{K}_{\text{eff}}$ for the remaining samples using existing models presented in literature [290], [292]. Such models made use of the magnetic saturation and coercivity values to help with estimation. Choosing one nano-particle sample from this study, the magnetic saturation of $M_s(50) = 41.79$ [emu/g] and $M_s(300) = 34.99$ [emu/g]) and coercivity of $H_c(50) = 104.70$ [Oe], $H_c(300) = 5.87$ [Oe] was considered as a starting point. Measurements were made at 50 [K] and 300 [K] respectively, with time between measurement as $\tau_m = 136$ [s]. We note that using the simple models, this is sufficient to estimate two $\mathfrak{K}_{\text{eff}}$ values (i.e. $\mathfrak{K}_{\text{eff}}(50)$ and $\mathfrak{K}_{\text{eff}}(100)$ in our case). Unfortunately, these existing model were found to be suspect both and yielded extremely high resultant $\mathfrak{K}_{\text{eff}}$ values leading to the use of existing $K_{\text{eff}}(5)$ and $\mathfrak{K}_{\text{eff}}(280)$ values from literature [286] as an approximation instead. These two values can be used directly with Equations (8-21) to (8-23) to estimate our relaxation time and reciprocal frequency of operation. This frequency varies roughly between values of 40 [KHz] to 1.5 [GHz] for small changes in our test sample blocking temperature.

There are some significant challenges with this approach to estimating anisotropy in that the Neel relaxation time, as a result of the exponential term, is very sensitive to resulting changes in blocking temperature with changes of 5 [°K] leading to a two order of magnitude change in the resulting frequency of operation. It is clear, that precise estimates of anisotropy, blocking temperature and attempt time are needed to predict superparamagnetic operating frequency with any reasonable degree of accuracy.

8.6 Summary and Final Remarks

The sparse SQUID hysteresis data was fitted to a modified formulation of the Jiles-Atherton model. An approach to computing an initial guess was proposed. Furthermore, a set of constraints were derived to improve convergence in the model. In order to propagate measurement error to the estimated fitting parameters, a Monte Carlo approach to dataset generation was used. The resulting estimates of fitting parameters were then used to regenerate dense minor hysteresis loops and to compute power loss resulting from remagnetization of the rotor under idling conditions

At sufficiently high idling frequency superparmagnetic properties may break down. An estimate of the maximum frequency at which this happens can be done through Neel relaxation theory. To do so, blocking temperature and anisotropy estimates were made from a combination of hysteresis data and zero field cooling and field cooling data. Unfortunately, accurate estimation of blocking temperature proved to be difficult, making superparamagnetic breakdown frequency estimates too inaccurate to be useful.

9 Results & Discussion

A range of topics and associated contributions to knowledge have been covered thus far. This chapter will provide numerical and graphical results produced by the individual contributions of knowledge discussed in each of the prior chapters. We will begin by returning to Earnshaw's theorem and introducing examples of various electrostatic monopole and magnetic dipole geometries to demonstrate the validity of the theory. This introduction facilitates a deeper understanding of diamagnetic bearing design. A radial multi-plattered prototype diamagnetic bearing was introduced in this study. The combined results of derived analytical expressions and COMSOL Multiphysics simulations are presented to evaluate the stability of the bearing prototype. Contributions of diamagnetic disc position and thickness along with the number of platters and floater-lifter topologies are taken into account to produce relationships between with liftable rotor mass. This is a key concern as it provides a measure of how viable diamagnetic bearings may be for FES systems.

Considering that the main focus of this study is on the potential of diamagnetic bearings towards reduced parasitic loss in FES systems, the remainder of this chapter focusses on power loss. Measurements of actual rotor power loss are presented. The individual loss contributors are identified and a discussion of air friction losses, stabilizer losses and electrical machine hysteresis losses provided. It was hypothesized that the dominant loss contributor after air friction would be hysteresis loss. This is confirmed in this chapter.

Hysteresis loss was noted as possibly occurring via two avenues: remanence related drag and core remagnetization. In order to reduce contributions from both of these

effects, a significant portion of this study looked at the use of nano-materials in reducing hysteresis loss. A key property of magnetite nano-materials is their superparamagnetic behaviour. True superparamagnetic behaviour holds the promise of eliminating hysteresis loss completely within some operating frequency. A range of experimental results are presented for synthesized magnetite samples. Various synthesis routes are compared in order to evaluate the most effective approach to obtaining superparamagnetic MNPs. By and large, results focus on the effect of surfactant (PEG) quantity and molecular weight, base pH and quantity, cooling, nitrogen shielding and magnetic field effects. While promise is shown by some MNPs towards close-to-superparamagnetic behavior, a great deal of future study with greater controls is required. Power loss associated with each synthesized sample is discussed as are the frequency of operation considerations needed to maintain operation within the superparamagnetic regime.

The chapter concludes with a brief look at microwave sintering related considerations and results. While no final characterization and limited sintering could be performed for MNPs. Thermal absorption results are presented and a first look at characterizing susceptors provided. Such susceptor characterization provides an important step in tuning microwave sintering towards successful production of bulk nano-structured magnetite.

Note that detailed graphs and data for results presented in this section are provided in the Appendix.

9.1 Earnshaw and Stability

We noted at the beginning of our discussions concerning magnetic levitation that Earnshaw's theorem demonstrates that no stable equilibrium condition exists for a static configuration of charge or dipoles. We can consider a variety of static conditions to demonstrate that no energy minima (or stability) exists in static conditions. This is more easily noted with electrostatic systems. Figure 9-1

demonstrates various topologies of electrostatic configurations and their related potential energy surfaces.

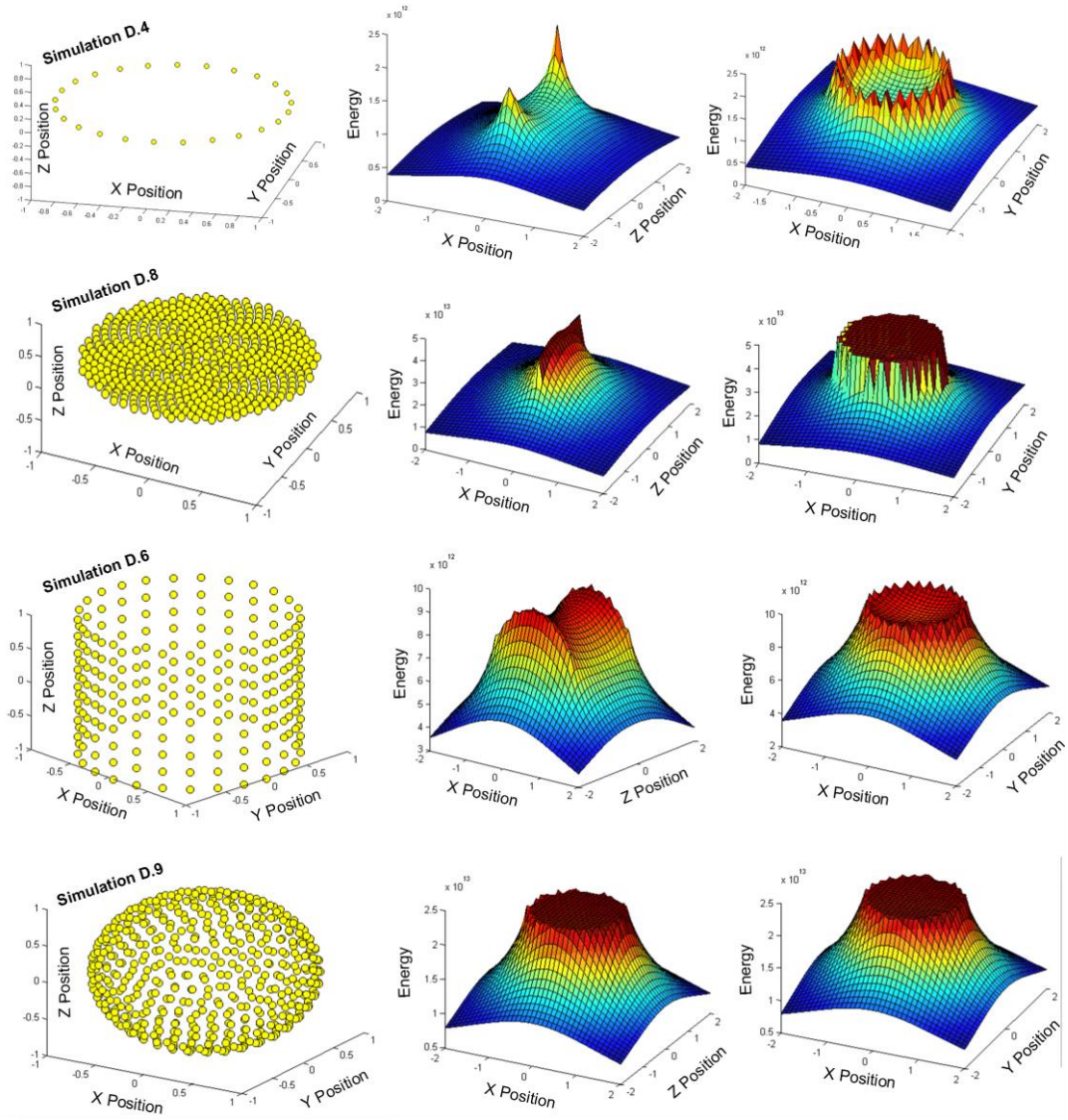

Figure 9-1: Topologies of potential energy surfaces demonstrate a lack of stable levitation in all three dimensions in electrostatic systems. Note that yz-configurations haven't been shown. Position of monopole is centered within the geometry at position (0, 0, 0). These surfaces correspond to virtual experiments D.4, D.6, D.8, D.9. All surfaces computed via simulation.

It's clear that Earnshaw's theorem holds valid for electrostatic systems. Figure 9-1 demonstrates four particular simulations completed as demonstrators of electrostatic potential energy surfaces. It is seen that a variety of topological arrangements can be attempted. Moving a levitating test charge within the yellow charge arrangements can be used to determine experimentally if there is any combination of stationary charges that can actually lead to a potential energy minima for the levitating charge. Moving from simple ring arrangement to discs cylinders and spheres provides an intuitive understanding that the potential energy has no minimum and hence levitation is impossible with a static configuration.

Magnetostatic systems show similar behavior with the added complications of dipoles as opposed to monopoles. The challenge here lies in the added dipole moment associated with the particles in the system. Rotation of the particle through spherical angles as well as translational changes now have an effect.

The resulting potential energy surfaces from both these positional changes are shown in Figure 9-2 for a ring topology system.

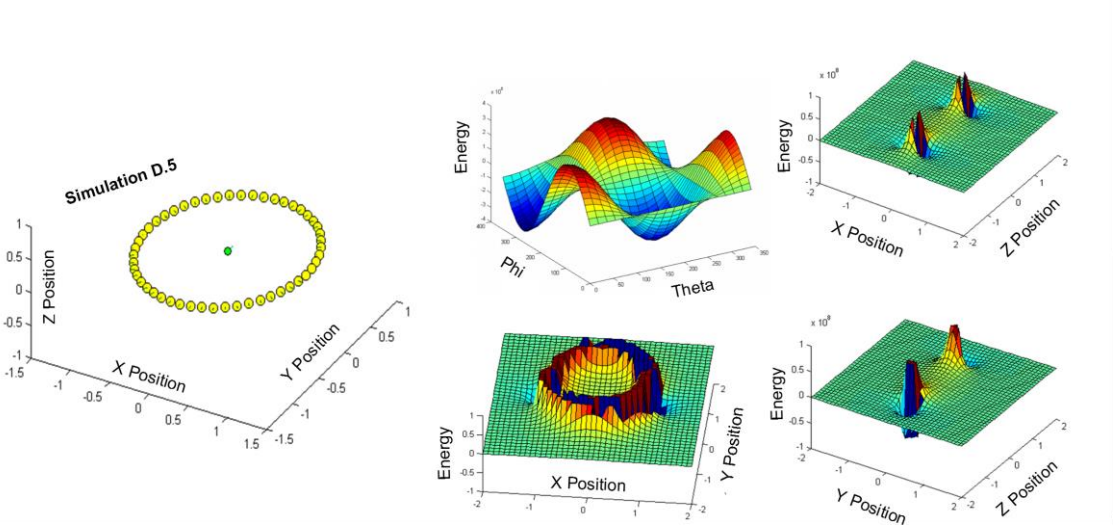

Figure 9-2: Looking at the energies of a magnetic dipole placed in a ring configuration of magnetic dipoles – simulated computations. There are strong similarities with an electrostatic configuration with one notable difference. The singularities resulting from the dipole motion towards the fixed ring moments will switch between a high positive and high negative energy. The surfaces shown correspond to virtual experiment labelled D.5 in this study.

Further exploration was also attempted using a commercial software called COMSOL for a permanent magnet linear machine. Here the machine topology consisted of an extruded x-shaped rotor with north poles of a series of permanent magnets pointed outwards. A similar outward north facing set of magnets on the stator assembly was used to constrain the movement of the rotor. The configuration for this machine is shown in Figure 9-3.

The linear configuration, as was the case with other magnetostatic and electrostatic configurations, showed itself to be unstable as well even with one direction of motion constrained. This instability demonstrates a clear saddle point in the equilibrium position as shown in Figure 9-4. Likewise angle stability (phi angle) also shows instability as well.

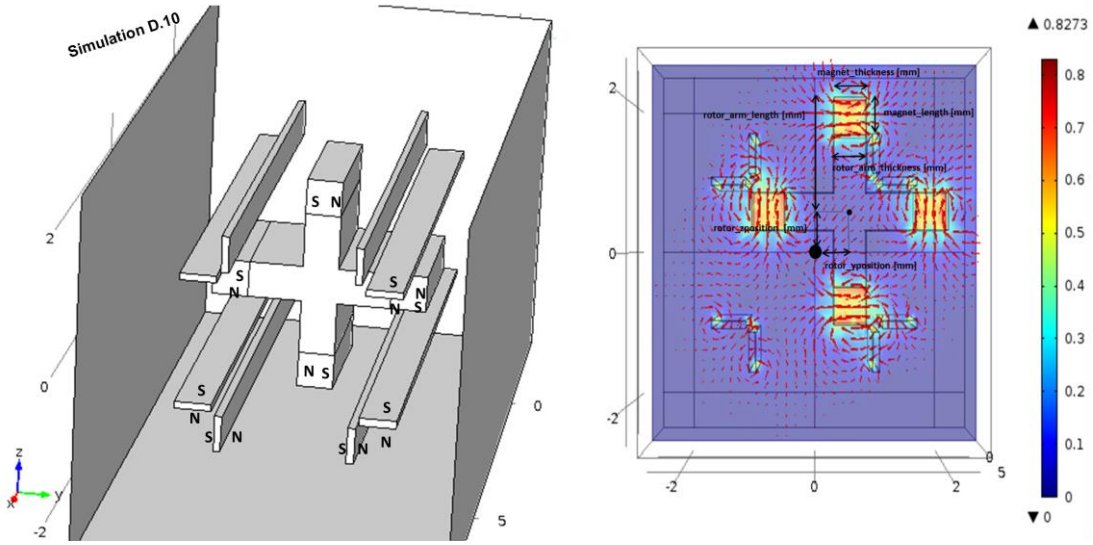

Figure 9-3: Considering a more complex permanent magnet configuration aimed at testing stability with just magnetostatic permanent magnet configurations. This simulation corresponds to the label D.10 introduced in this study.

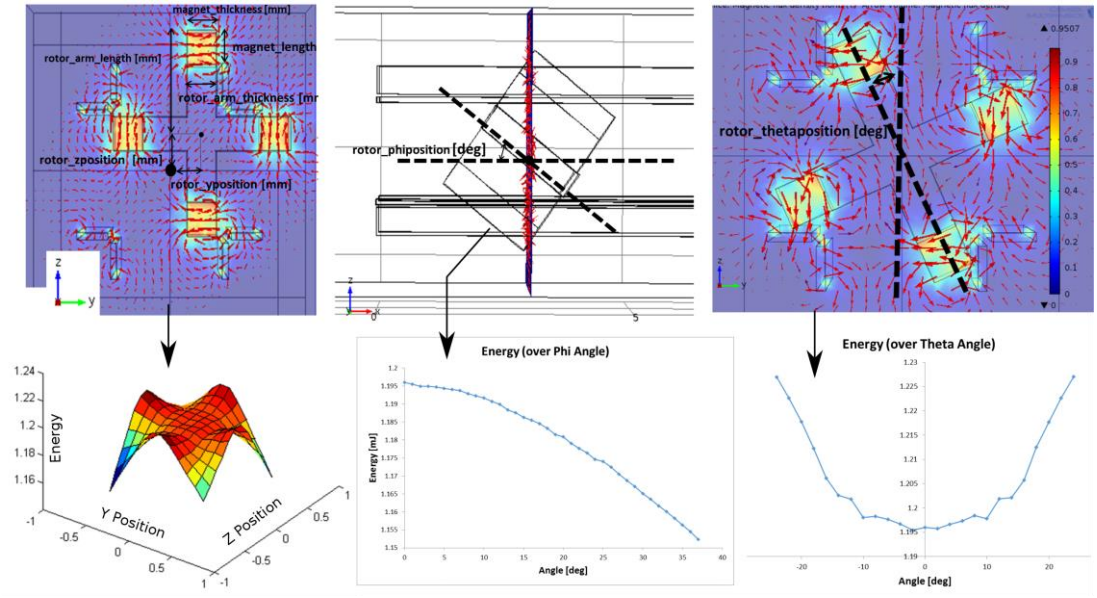

Figure 9-4: Even with one direction completely constrained, a linear machine using just magnetostatic configurations of permanent magnets remains unstable both in positional changes and in some angular positions (phi angle). Simulations in COMSOL.

9.2 Diamagnetic Stabilization and Mass Considerations

Given this understanding of static systems, the presence of a diamagnet can be introduced into the mix. A theoretical derivation of this process was shown in earlier discussions (Chapter 3). The focus of this study was on a particular geometry for a diamagnetic bearing consisting of a diamagnetic disc levitating above or between permanent disc magnets. Making use of the same underlying method of calculating energy we can start to look at the energetics of a levitating diamagnetic disc. Likewise, these can be compared to other simulated approaches to estimating energy and force via commercially available software as well. As with the earlier discussion of a linear permanent magnet machine (Figure 9-3), COMSOL was used for these simulations.

Figure 9-5 below considers a COMSOL simulation of single diamagnet levitating below a permanent disc magnet. The magnetic potential energy of the diamagnet (normalized by volume) is shown.

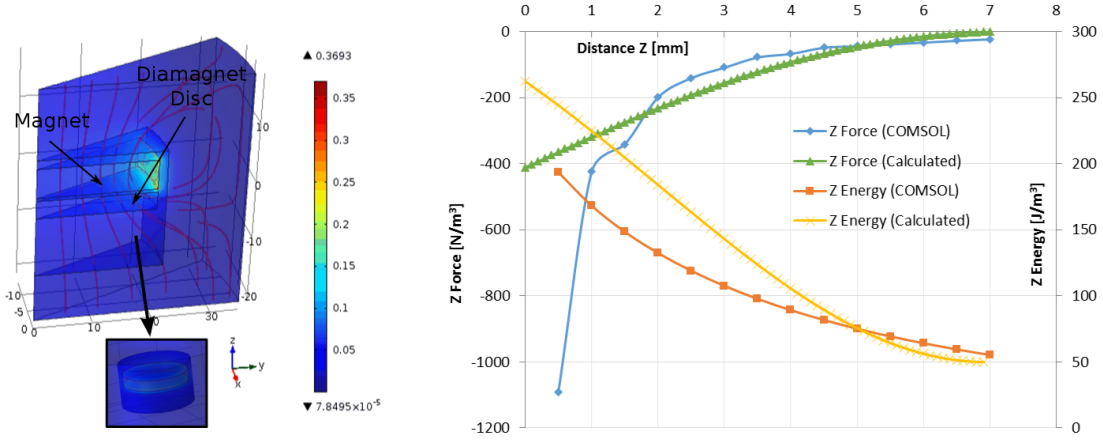

Figure 9-5: Diamagnetic graphite disc levitating below a disc permanent magnet as simulated by COMSOL Multiphysics software and by direct calculation.

There seems to be significant deviation in the theoretical calculations of energy compared to that generated by COMSOL. This discrepancy is likely a result of the numerous simplifications made during the theoretical approach. These results can, however, still be considered as a method of better understanding the behavior of our diamagnetic system.

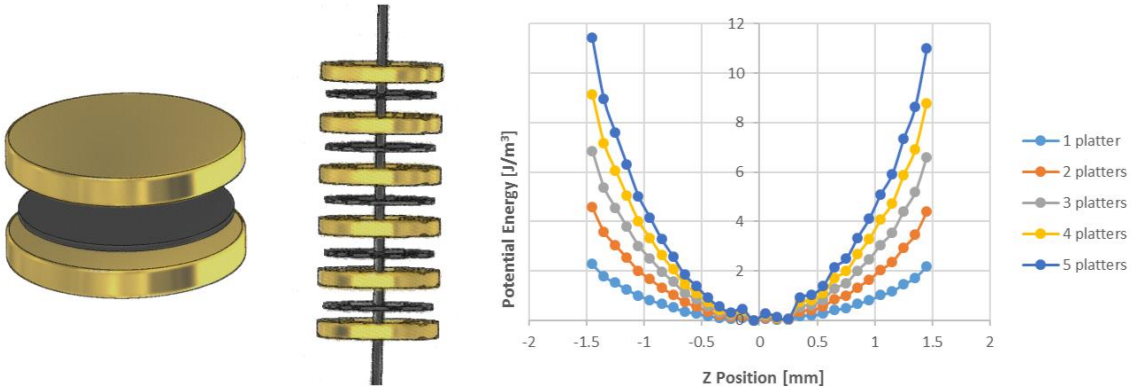

Figure 9-6: Diamagnetic disc sandwiched between two permanent magnets. Multiple platters consist of multiple disc-magnet pairs stacked on top of each other. For aesthetic reasons, the energy has been normalized for each platter such that at equilibrium they all have zero value. Values have been simulated.

Note that the earlier single magnet system ignored the effects of gravity. Continuing along the same lines and adding a second permanent magnet such that the diamagnetic disc is sandwiched between two disc magnets an energy minima exists in the z direction. Noting that a multiple platter system can be constructed by stacking this sandwiched topology, the stiffness (sharpness of the energy curve) increases with the number of platters. Figure 9-6 demonstrates this effect. We can also see similar effects from the thickness of the diamagnetic material as shown in Figure 9-7.

We can take this characterization further by looking at theoretical calculations as well and incorporating the effects of gravity and weight compensation. The weight compensation is a result of the floater-lifter combination. After considering our particular diamagnetic bearing's rotor mass of approximately 30 [g] we can see the effect of the stability resulting from the diamagnetic material – under normal conditions the floater balanced by the lifter would have no local energy minima. The diamagnetic material changes this, however, as shown in Figure 9-8. Note that we are only considering the z-directional force in this case. As the number of platters increases, the stabilizing region sharpens to create a stiffer bearing assembly.

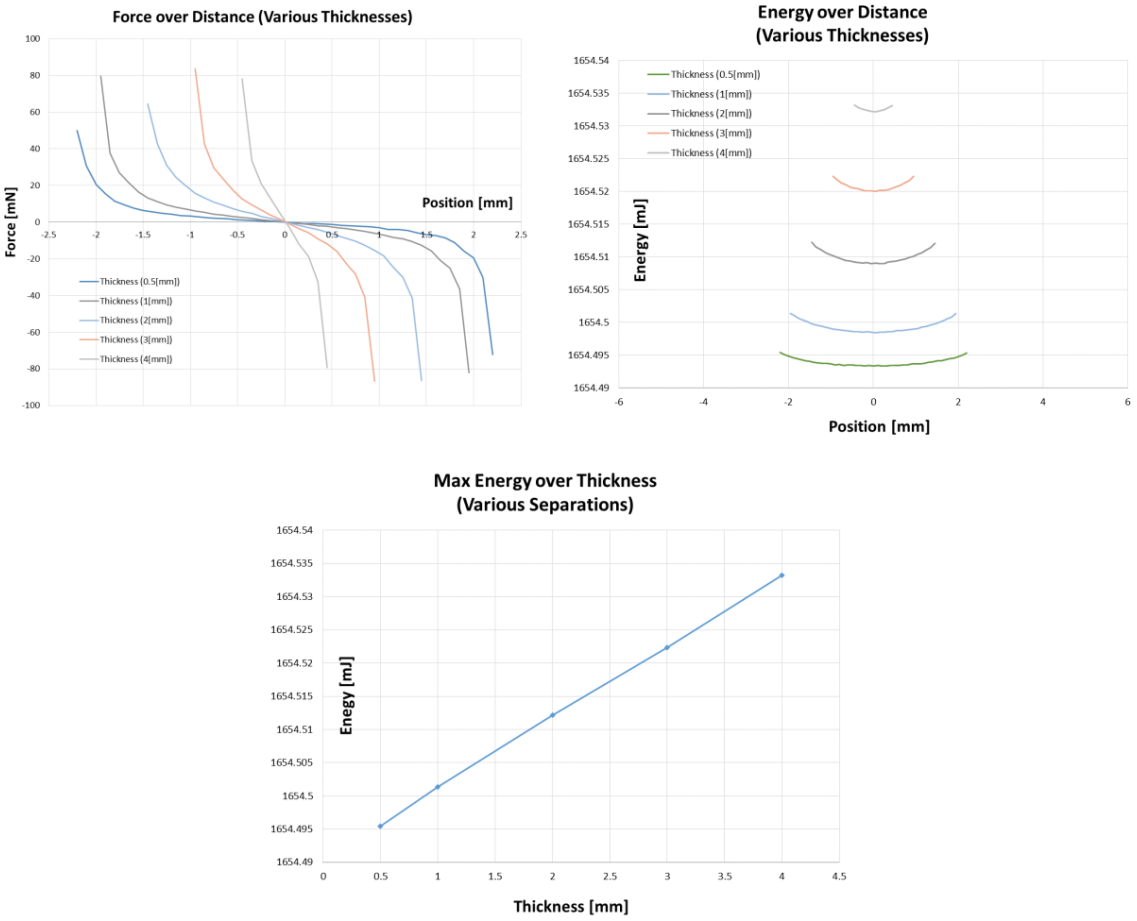

Figure 9-7: The energy relationship with thickness of diamagnetic material. Notice that increasing thickness leads to increases in energy as well as stiffness. The zero position in these graphs represents a diamagnet position centred equidistant from both fixed stabilizer magnets. Results derived directly from simulations in COMSOL and MATLAB.

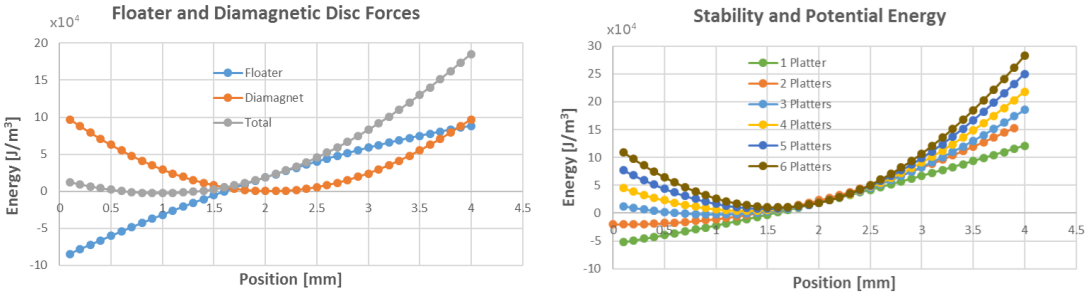

Figure 9-8: Combining the effects of the floater-lifter combination, gravity and diamagnetic forces. Note that we consider only the z directional position and energy here. Simulated results from analytical expressions.

This behavior correlates well with results from COMSOL simulations as well. In-fact, considering that the theoretical model presented in this study only considered z-directional (axial) motion, we can take a closer look at stability in both the axial (z) and radial (xy) directions via COMSOL (see Figure 9-9). From such an approach, we can iterate through a variety of conditions. For instance, our theoretical model did not consider the reduced force resulting from a hole in our stabilizer magnets. In practice, such a hole would be needed for a shaft connecting the various diamagnetic platters together.

Furthermore, additional use for an iron flux path (yoke) can also be considered – though it should be noted that the discounted leakage flux in our model, may indicate a reason for the higher energy estimates produced when compared to COMSOL results. The theoretical model assumed that all flux flowed in the axial direction.

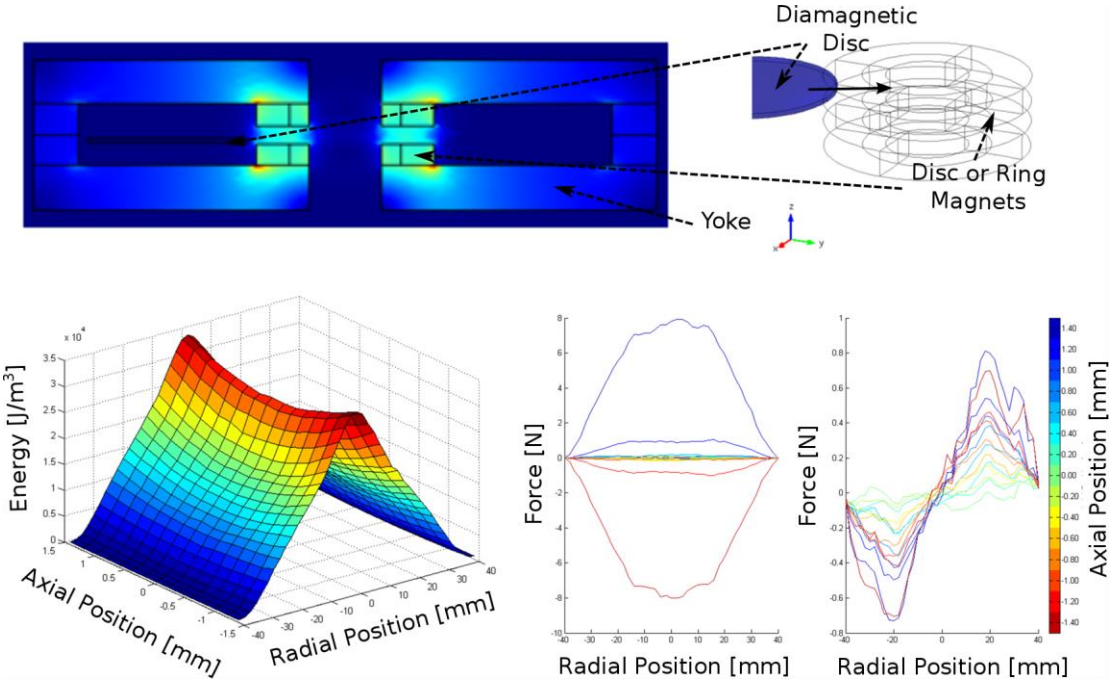

Figure 9-9: Looking at energy and force in both the axial and radial directions via COMSOL simulations. We can consider a situation where a yoke is present to minimize flux leakage as well.

Introduction of a yoke can account for some of the difference between COMSOL results and analytical results. As seen in Figure 9-9, the energy magnitude produced with this core falls into line with that of theoretical results produced via the derived model equations from Chapter 3 in this study.

We can examine the energetics of the system further for a single stabilizer platter under various topological considerations. For instance, changes could include the use of ring versus disc stabilizing magnets, the presence and absence of a yoke, the thickness of our diamagnetic disc. Figure 9-10 encapsulates the effects of these changes under slightly different field conditions than those presented in the previous figure. As is expected the reduced magnetization volume of a ring magnet sees a substantial drop in energy and associated stiffness. An iron flux path (yoke) can compensate for this loss.

While theoretical consideration was given largely to a disc and ring lifter, we can further explore the geometric effects of not only lifter shape, but also floater shape on the energetics of the system. This is shown in Figure 9-11.

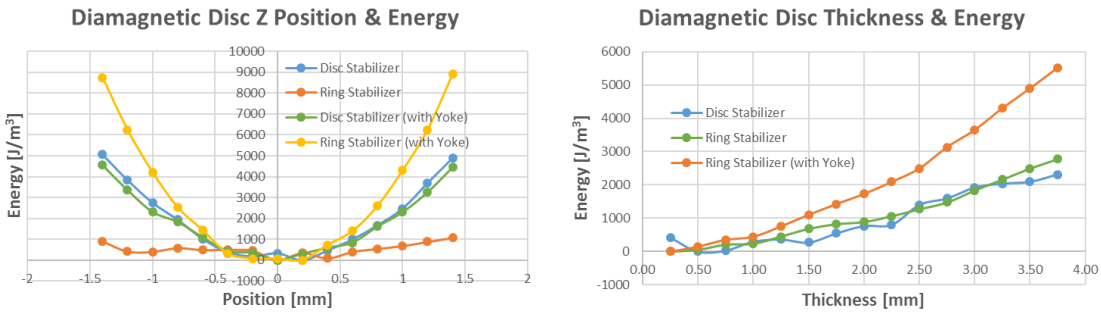

Figure 9-10: Energy of single diamagnetic disc sandwiched between a disc or ring stabilizer magnet pair with and without flux path (yoke). Simulated with the aid of COMSOL.

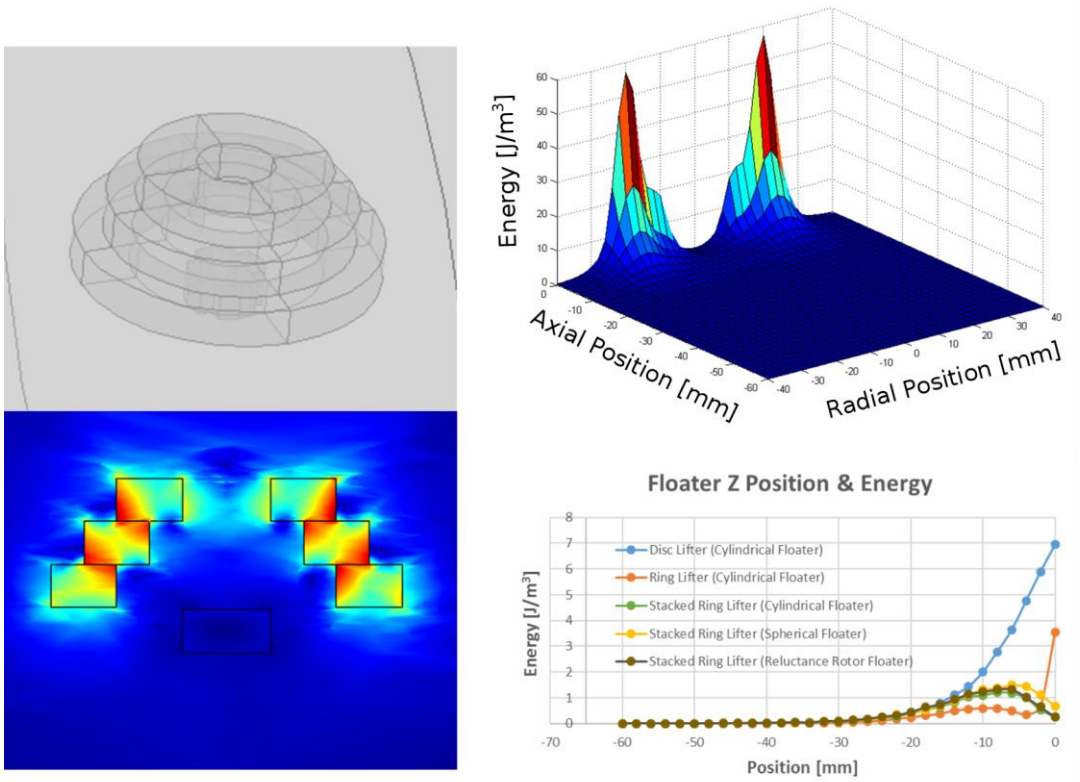

Figure 9-11: Energy of various topologies of floaters (cylindrical, spherical, rotor shaped) under various topologies of lifters (disc, ring, stacked ring). Simulated with the aid of COMSOL.

In the case of the ring lifter configuration, an additional contribution had to be taken into account. Unlike a disc lifter where a position change in the xy-direction will result in a drop in the force on the floater relatively slowly, a ring lifter will experience a relatively rapid increase. As a result, when the floater is close to the ring lifter, a high field gradient will be experienced by the rotor assembly as it moves off-axis. This will also be accompanied by a higher z-directional force. As a result, for ring configurations, a larger gap between the lifter and floater is needed.

There are a number of challenges that should be noted when using both analytically developed expressions and commercial finite element modelling as simulation tools. Despite the simplicity of the final diamagnetic bearing configuration, a complete simulation proved prohibitively difficult to setup. Analytical expressions and finite

element geometries were, thus, broken down into the individual elements of the diamagnetic bearing assembly, namely: the stabilizing machine, the lifter-floater system, and the reluctance machine. Despite this a number of problems and inconsistencies were still observed in the results. For instance, discrepancy was noted between the theoretical and analytical framework and the finite element based results. Changes to simple dimensional parameters within the COMSOL environment itself resulted in discrepancies between even virtually identical simulations.

While it is somewhat unclear what the causes of simulation discrepancies are, some educated guesses can be made. With the analytical framework, a number of assumptions were made. For instance, the magnetic charge model, breaks down as the distance between the dipole and the field source decrease. In addition, this model assumed uniformity in that no variation occurred in the B-field from horizontal displacement. This is clearly not the case. Furthermore, investigating mesh considerations in COMSOL, some variation in results were found to occur simply from sizing and related solver issues (see Figure 9-12).

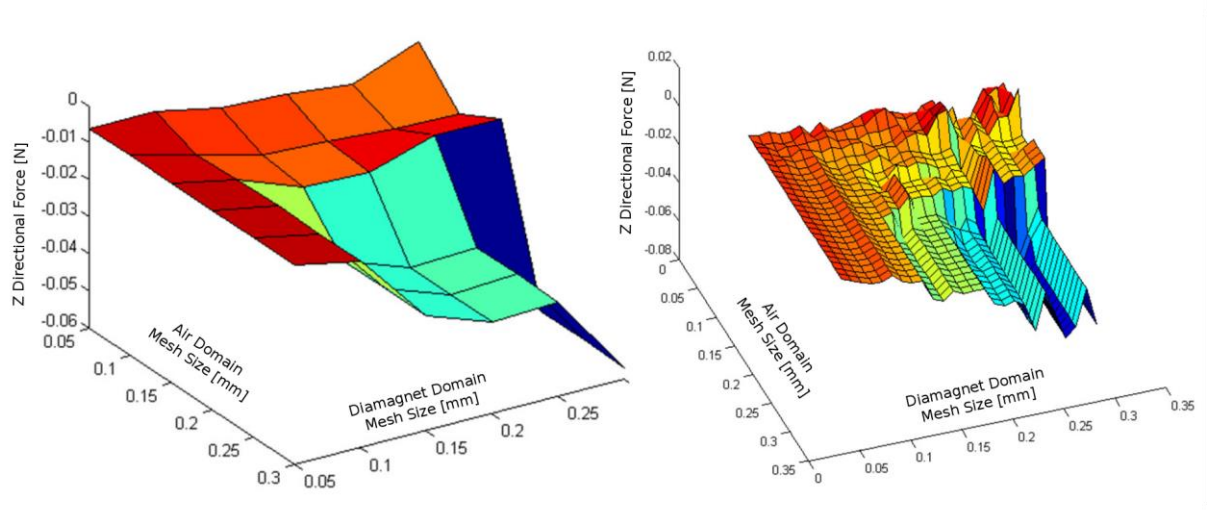

Figure 9-12: Mesh size can have a significant effect on simulation results. Simulations in COMSOL.

Such meshing issues required careful mesh analysis before simulating and completing any of the experiments. Unfortunately, such analysis was often too time consuming to run, especially considering that in some cases simulations could stretch from 2 hours on the low end to up to 21 hours or more on the upper end.

The prototype magnetic bearing built in this study made use of a disc lifter. This lifter was particularly difficult in terms of fine tuning of the air gap between the lifter and the spherical floater. A small change of just around 100 [μm] could shift the equilibrium position significantly. The reason for this becomes clear from Figure 9-11 where the exponential increase in energy is seen as the floater-lifter airgap gets small. In effect, we have a high gradient in the slope of the force close to the magnet. The ring lifter fairs somewhat better, however we note that a stacked ring arrangement reduces the slope significantly, suggesting that force near the airgap remains far more linear.

From the combination of floater-lifter and diamagnetic disc energies, the number of platters needed to achieve a certain levitation mass in our bearing assembly can also be estimated as shown in Figure 9-13. We expected a non-linear relationship between the number of platters and the levitating mass. Interestingly, the actual relationship was found to be linear instead, though the relationship with the lifter B-Field required to maintain levitation of a particular mass and the number of platters is non-linear.

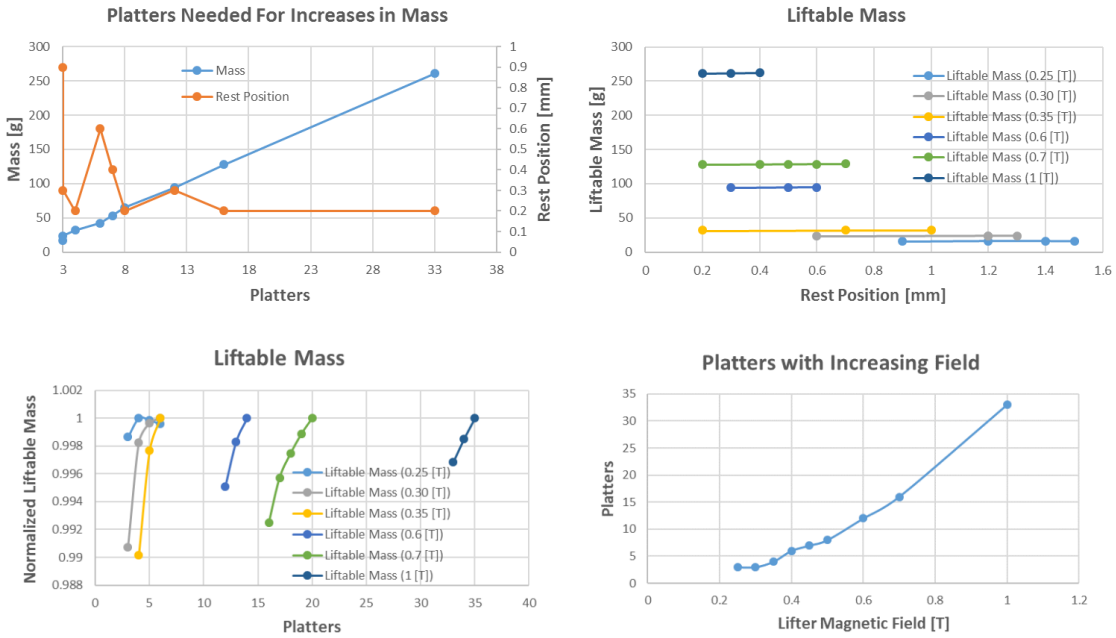

Figure 9-13: Mass, position and magnetic field effects in the prototype multi-plattered diamagnetic bearing assembly. Results are from simulations in COMSOL and MATLAB.

The reason for this difference becomes apparent when we note that the air gap between the lifter and floater is tunable leading to a situation where a higher mass will tend to shift further away from the lifter magnet and the diamagnetic platters shift closer to the stabilizer magnets. As a result, the stabilizing field rises exponentially while the lifter field drops away exponentially. In the prototype, the resting air gap between the diamagnetic platter and the stabilizing magnet was estimated at roughly 0.5 to 1 [mm] using paper inserts and calipers. Unfortunately, this estimate is highly suspect – a more accurate way to make such measurement would be by way of laser interferometry.

However, when looking at the platter and lifter B-field relationship, we note that the minimum number of platters needed for stability grows exponentially with the field. This is because for a given platter position and floater position, the stabilizing force can only grow linearly while the lifter force can grow exponentially. At some point

the field gradient will be so strong that the linear relationship between the number of platters and the mass is also likely to break down with the gap between diamagnet and stabilizer become so small that levitation without collision becomes untenable. As was seen with the floater-lifter configurations presented in Section 2.4.1), the use of a stacked ring lifter magnet topology can greatly reduce this non-linearity.

9.3 Power Loss (Macro-scale)

From here we can start to look at the power loss effects more closely. As we saw, the contributions of power loss in the diamagnetic bearing system can come from three main sources. The first of these is air friction, with homopolar losses from the stabilizer and floater-lifter machinery being the second and reluctance machine losses being the third. There are of-course losses as a result of thermal and radiative effects along with other quantum mechanical effects – however, these are likely to be negligible in comparison.

The total power loss in the real prototype bearing system was found to be 0.244 [W/ m^3] at 158 [rpm]. The largest single contributor to loss is air friction with a value of 0.0759 [W/m^3] for a rotor rotating at 158 [rpm]. While attempts were made to remove the contribution of air friction by pumping the system down by at least -60 [KPa], making measurements under these conditions proved difficult.

Measurements of velocity over time were, thus, done in open air. However, to account for electromagnetic effects COMSOL simulations were used. Figure 9-14 demonstrates some examples of simulated geometries.

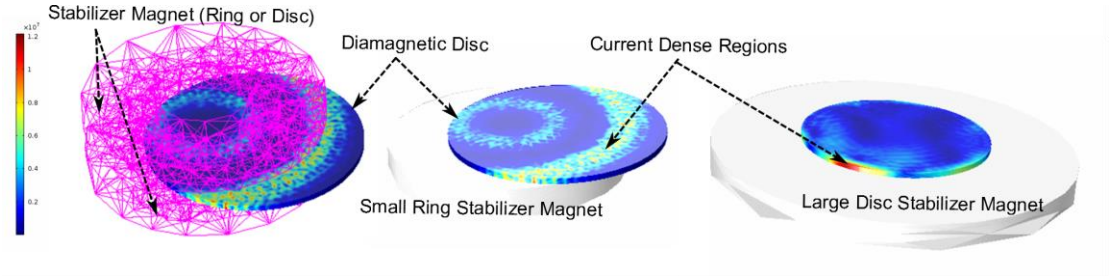

Figure 9-14: Examples of simulated geometries and associated induced currents. Current counter flows are a result of rotation of the diamagnetic disc in the non-uniform field regions. Simulated results from COMSOL.

The overall loss as determined from measurements of the prototype diamagnetic bearing is shown in Figure 9-15a. This loss can be divided into contributions from air friction and a few different forms of electromagnetic loss as shown in Figure 9-15b.

Electromagnetic loss is a result of stabilizer loss and electrical machine loss (e.g. remanent cogging loss and eddy current loss). Figure 9-15c demonstrates loss resulting from different stabilizing machine topologies while Figure 9-15d demonstrates loss resulting from hysteresis related remanent cogging effects and remagnetization effects.

From these figures, it is clear that our earlier assumption that homopolar losses (Chapter 7) are likely to be much less significant than electrical machine losses is correct. Losses in the stabilizing machinery appear to be quite high in magnetic configuration that involve field greater field changes along the diameter of the diamagnetic disc material. For instance, the use of ring magnets over disc magnets sees a significant increase in loss. Further, this loss increases as the rotating diamagnetic disc shifts off axis.

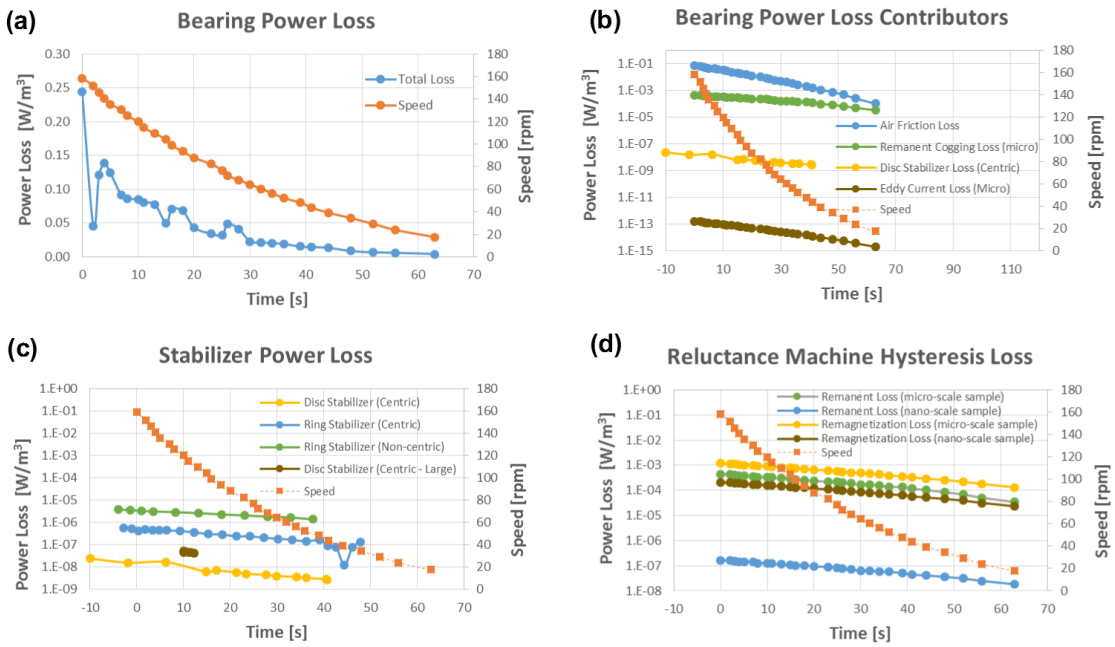

Figure 9-15: Separating sources of loss from measured data for our diamagnet bearing prototype. A combination of measured speed data and loss simulations from COMSOL and MATLAB. (a) The overall loss. (b) The different contributors to loss. (c) The effect of stabilizer machinery on loss.

It was thought that this off-centric loss was a result of non-uniformities in the field and that such losses should vanish as field uniformity improves. Brief simulations of large diameter uniform magnetic field sources did not appear to show this however. It remains unclear why this contradictory result has appeared. There is significant possibility that COMSOL meshing or numerical issues might be a factor in this inaccuracy.

In this study, it was suggested that homopolar losses are likely to be very small compared to loss in the reluctance machine materials. This was a result of noting that homopolar losses should vanish as magnetic field uniformity improves and that material hysteresis and motor eddy current loss would be a greater contributor. This was an accurate estimation in that homopolar losses were found to be very small at 2.41×10^{-8} [W/m^3] for a rotor assembly spinning centrically at 158 [rpm] for

stabilizing magnetic fields from a disc magnet. This loss increases by an order of magnitude at a value of 5.84×10^{-7} [W/m^3] when rotating centrically through a ring magnet stabilizer field. For a ring magnet stabilizer in off-axis or non-centric conditions, the situation is even worse, with losses increasing to a significantly higher value of 3.86×10^{-6} [W/m^3] when off axis by 4.5 [mm] for our 158 [rpm] rotor. As the rotor becomes more and more off axis to 9 [mm] off from the center position, this loss can double to 6.20×10^{-6} [W/m^3].

Using a ferrite material for the reluctance machine rotor, eddy current losses are generally negligible as noted in prior discussions (Section 7.3.3). We see very small losses of around 5.81×10^{-19} [W/m^3] for our 158 [rpm] rotor assembly - almost 18 orders of magnitude smaller than that of silicon steel (1.11×10^{5} [W/m^3]) and 5 to 7 orders of magnitude smaller than that observed for losses from the homopolar machine. A commercial magnetite powder sample has eddy current loss that is 6 orders of magnitude larger at 1.67×10^{-13} [W/m^3]. We note however, as suggested in earlier discussions (i.e. Section 7.3), the losses from cogging related drag, in a rotor produced from commercial micro-structured magnetite ferrite is higher. As such a rotor spins through the reluctance machine stator losses fall at 4.42×10^{-4} [W/m^3] for 158 [rpm] rotational velocity. While significantly smaller than air friction, these losses are a major contributor to loss. As we will see later in this discussion, there is competition between cogging related drag and remagnetization related hysteresis loss. The use of the same commercial micro-structured magnetite ferrite will produce losses of 1.13×10^{-3} [W/m^3] when remagnetization is the dominant loss.

The value of remanence induced cogging drag decreases significantly with the use of nano-structure magnetite as a base material in our machine. Losses in our synthesized MNP material fall at 1.65×10^{-7}[W/m^3] for a select sample with behavior closest to superparamagnetic (remanent magnetization of 8.63 [A/m] or 0.00165 [emu/g]). This loss thus falls in the same order of magnitude as the lowest possible loss from achievable from the homopolar stabilizing machine. Likewise, we

can consider losses from remagnetization of our rotor via traversal of a minor hysteresis loop. In reality, loss will be a competition between either remanent cogging loss or remagnetization loss. This competition depends on the whether the coercive field is low or high in comparison to the generated applied "self" field passing through the stator/rotor pole combination. We note that the remagnetization loss for a synthesized nanoparticle sample falls at 2.11×10^{-4} [W/m^3] for rotor speed of 158 [rpm]. This is a one order of magnitude reduction in loss.

9.4 Synthesis of MNPs

Considering that superparamagnetic properties are key to reducing losses from hysteresis, a number of experimental approaches were taken to produce motor core material (refer to Table 4-2). The experimental routes can be correlated to the following: particle size, density, shape morphology (aspect ratio), colour and composition, remanence, coercivity, saturation, exchange bias, blocking temperature and associated frequency of operation and power loss. These synthesis routes can be grouped into five distinct comparative studies:

- The Effect of PEG Quantity
- The Effect of PEG Molecular Weight
- The Effect of Base pH
- The Effect of Volume & Cooling
- The Effect of Magnetic field & Shielding Gas

A range of 31 experiments were carried out to examine each of the above effects. Where applicable, for comparison a commercial micro-structured magnetite sample, herein called S.-1, was used as a base line for comparing synthesized nanoparticles.

In the next sub-sections, we look at the effects of synthesis routes on the properties of the final MNP product. We note here that the aim was to produce small amorphous particles around the 10 [nm] size range as they are commonly believed to exhibit superparamagnetic behaviour. Earlier in Section 4.2, it was pointed out, that while low oxidation effects were desirable, they were not considered critical. This is because reversal of oxidation states is believed to be possible via sintering. Despite this some attempt was made to analyze oxidation effects via colour, XRD composition analysis and exchange interactions as well. Further to this, the effectiveness of synthesis route in reducing material coercivity and remanence is of particular importance in reducing material losses. These losses can be thought of as a result of the hysteresis loop path taken as the particular magnetic bearing rotates through an externally applied field or through its own internal "self" remanent field. Likewise preserving high saturation magnetization also has implications for reducing leakage flux and increasing power input/output in the electrical machine.

9.4.1 PEG Quantity Effects (Particle Morphology)

We noted earlier, in Section 4.4, that addition of surfactant has been seen, by a number researchers, as being of value in reducing particle agglomeration and limiting particle size. This study makes use of PEG for this purpose and evaluates its effectiveness. A total of 12 synthesized samples involved changes in PEG quantity. These samples have been labeled: S.18.1, S.18.2, S.18.3, S.18.4, S.10, S.10.1, S.10.2, S.10.3, S.7, S.7.2, S.7.3, S.7.4.

Figure 9-16 provides an overview of particle sizes and aspect ratios across all samples as a result of type of base and PEG quantity. It is somewhat challenging to see correlations and relationships with this figure. We can break it down to look specifically at the effect of PEG quantity on each of particle size and aspect ratio independently as shown in Figure 9-17.

As seen with this newer figure, the type of base used during synthesis can have a significant impact on morphology. For instance, the use of NaOH with increasing

quantities of PEG (300 [da] molecular weight) showed clear, but slight reductions in particle size. XRD Particle size varied from 10.57 [nm] to 6.85 [nm] while SEM particle size varied from 14.20 [nm] to 10.87 [nm].

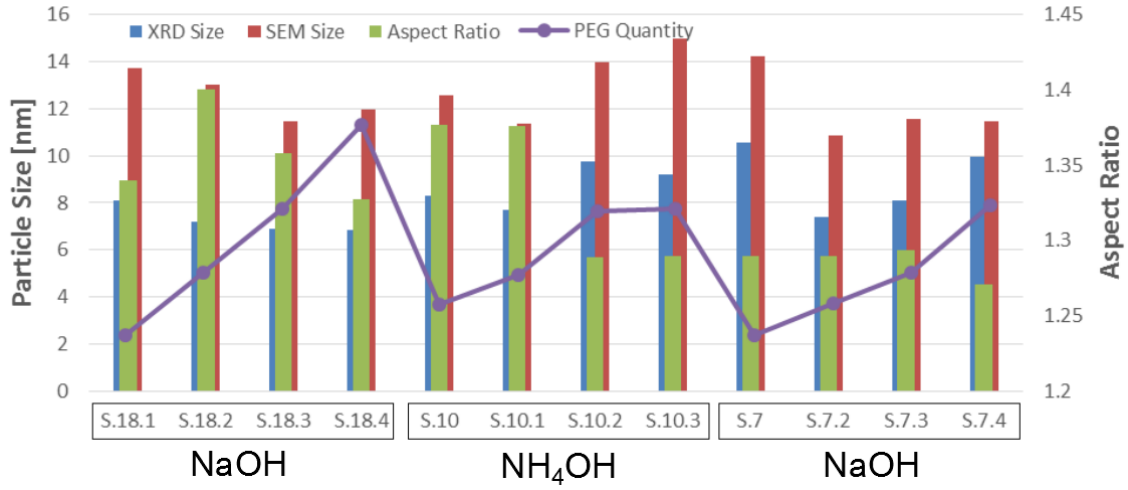

Figure 9-16: An overview of magnetite particle size and shape effects resulting from PEG Quantity changes during synthesis. Measured mass and SEM data for the following samples: S.18.1, S.18.2, S.18.3, S.18.4, S.10, S.10.1, S.10.2, S.10.3, S.7, S.7.2, S.7.3, S.7.4.

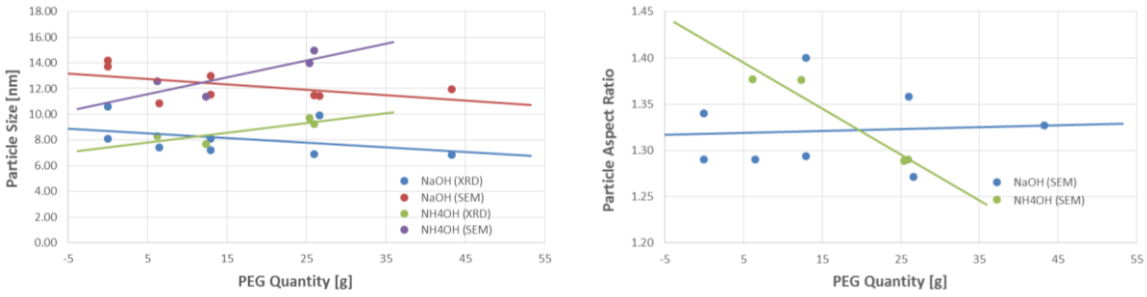

Figure 9-17: Magnetite particle size and shape effects resulting from PEG Quantity changes during synthesis. Results from measured mass and SEM particle data for the following samples: S.18.1, S.18.2, S.18.3, S.18.4, S.10, S.10.1, S.10.2, S.10.3, S.7, S.7.2, S.7.3, S.7.4.

While the consistent trend across both XRD and SEM measurements suggests some real effect here, it should be noted that these reductions are close to the typical XRD margin of error of 0.40 [nm] to 1.4 [nm]. SEM measurements are of far lower quality with margin of errors ranging between 1.83 [nm] and 9.40 [nm] across all synthesized samples. Given the consistency across both SEM and XRD measurements, however, we can tentatively say that there is likely some correlation between increasing PEG quantity and decreasing particle size when NaOH is used as the reaction base.

Before continuing, an added point must be made with regards to particle size estimates via XRD and SEM characterization. XRD estimation provides a bias towards crystallite material and so, alone, does not necessarily provide a good measure of the overall particle sizes of the synthesized material. This is because of the partially amorphous nature of the material. SEM measurements are good supplements and consistently show larger particle size estimates than XRD. However, poorly resolved images and limits of SEM style electron microscopy, especially with regards to magnetic materials, may blur particle boundaries making identifying individual particles challenging and artificially enlarging size estimates.

Interestingly, an opposite trend of increasing particle size was found to be true for increases in PEG with NH_4OH as a reaction medium. Resulting particles varied from 7.69 [nm] to 9.73 [nm] via XRD measurements and 11.35 [nm] to 14.94 [nm] via SEM measurements. One reason for this may be that PEG interactions with the ammonium hydroxide and water could reduce the availability of OH^- that would normally disassociate (in the weak base) as these ions became used up during reaction. Clearly, the presence of PEG does not act favorably with NH_4OH base reactions and causes a net increase in particle size with increasing PEG quantity.

At this stage, let’s move on and consider particle shape. The particle shape can have a significant impact on anisotropy leading to preferred orientations for our particles and potential increases in coercivity and remanence (and power loss) as a result of the higher anisotropy energy. This higher anisotropy energy raises the energy barrier

for Neel relaxation and thermal competition to occur. We note that, for our NaOH base, unlike our look at particle size, added PEG quantity does not appear to have any significant effect on particle aspect ratio – ratios fall between 1.29 and 1.4 and vary without any meaningful pattern. This ratio change is well below the margin of error of 0.190 to 0.290 associated with the imaging estimates as well, indicating that there is no significant difference.

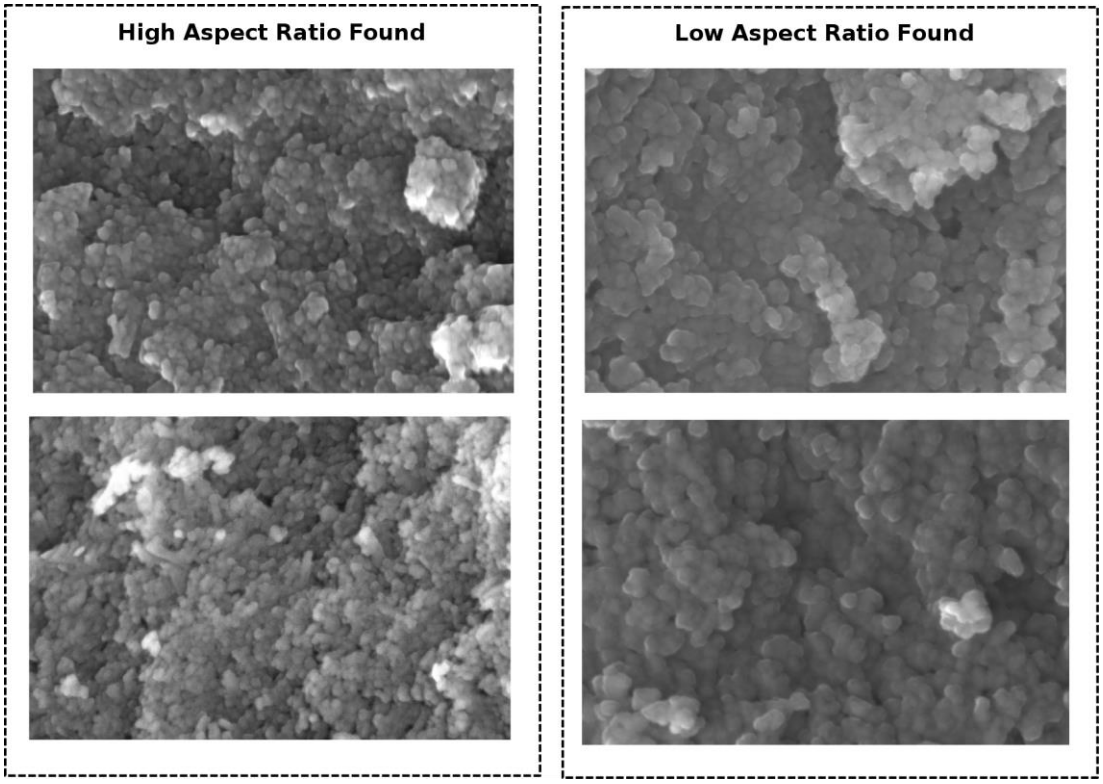

Figure 9-18: More isotropic particles found (aspect ratio close to 1) for NH_4OH synthesis with increasing PEG quantity may be a result of the better resolved SEM images (right).

However, for PEG and NH_4OH, this aspect ratio shows clear (above the margin of error) decline to a more isotropic shape (ratio close to 1) with increasing quantity. Ratios quantitatively vary along a similar range as NaOH from 1.38 to 1.28. This is an interesting effect considering the corresponding increase in particle size.

However, it should be noted that SEM imaging of particles is challenging and some concern remains in terms of resolving shape effectively. One explanation, thus, for the greater isotropy may well be related to challenges in imaging. For instance, consider Figure 9-18. The lower aspect ratios noted for higher PEG quantities were also associated with somewhat better resolved images. It is thus, difficult to make any firm conclusions about anisotropy/shape and associated base type and PEG quantity.

9.4.2 PEG Quantity Effects (Yield, Colour and Density)

We can continue our analysis of changes in PEG quantity on the synthesized particles. For instance, looking across samples at magnetite yield or colour and density we note the results shown in Figure 9-19. Here, a small but known NaCl calibrant quantity, mixed in with XRD magnetite samples, was used to provide better calibration for estimation of not only particles size, but also density and yield.

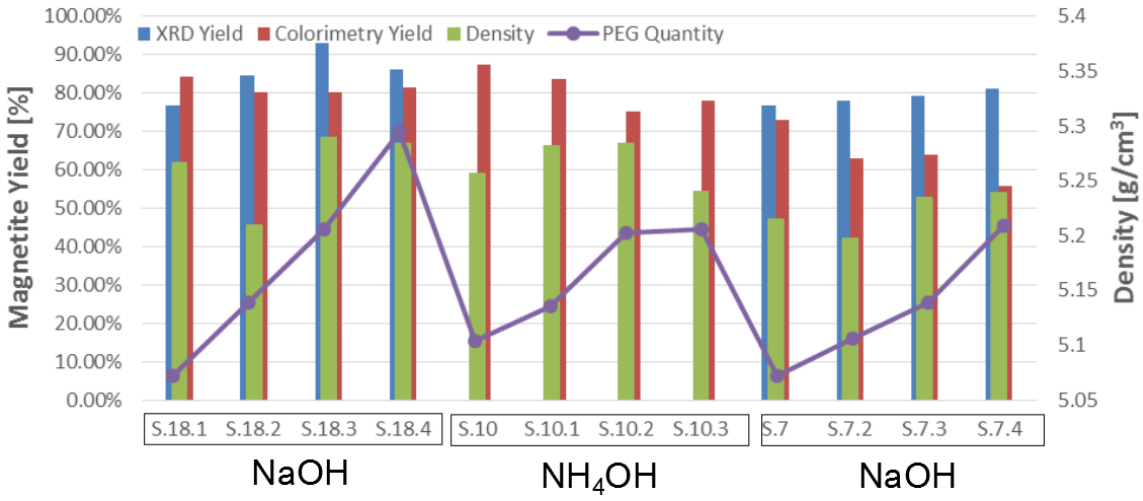

Figure 9-19: An overview of magnetite yield and color effects with differing PEG quantities. Note that colour distance percentage is relative fractional percentage computed from our commercial magnetite sample (S.-1). Measured mass data combined with XRD analysis and camera colorimetry. Samples under consideration: S.18.1, S.18.2, S.18.3, S.18.4, S.10, S.10.1, S.10.2, S.10.3, S.7, S.7.2, S.7.3, S.7.4.

Yield was determined via XRD by making use of a well-mixed sample of magnetite precipitate. XRD peaks were used to assess the potential mineral components present in the measured sample. For instance, a measured sample could contain not only magnetite, but also hematite, maghemite and other impurities. The process of identifying each of these impurities was a partially automated and directed trial and error approach. A series of matched comparisons was attempted with a large database of existing XRD count data for various minerals. Utilizing this data, an approximate relative count of each impurity could be made. With the assumption that the XRD sample was a representative sample of the larger batch it was thus possible to measure yield. Estimating yield from sample colour was somewhat cruder still. Here the LAB colour distance from a known high purity powder magnetite sample was used to assess the relative yield of magnetite over other impurities. However, it should be noted that such an approach relies on colour properties that may or may not change across different impurities and that may also be strongly affected by particle size.

The XRD measurements demonstrate increasing magnetite yield with increasing PEG Quantity. Such yields range from 76.88 [%] to 93.12 [%] for synthesis using NaOH base. The increase is above the margin of error of 0.72 [%] to 4.80 [%]. NH_4OH yields were not measured and have thus not be shown in the figure. The significance of this increase suggests that, PEG quantity does, in-fact, have an effect on reducing oxidation. In the CIE LAB colour space, colour changes relative to a commercial magnetite sample can be used to estimate the purity and the magnetite yield as well. As particle sizes shrink to the range of the visible light spectrum, some diffraction changes were noted between micro-scale and nano-scale particles. Furthermore, consistency of conditions resulting from the various lumping and agglomeration effects of the particles in each sample also caused colour artifacts. As a result, changes in colour can only be regarded as a very approximate (but useful measure) indicative of oxidation. As seen from Figure 9-20, no correlation appears to exist between PEG quantity and such colour based magnetite yield estimates

suggesting that such an approach may not be sufficiently nuanced to evaluate oxidation effects.

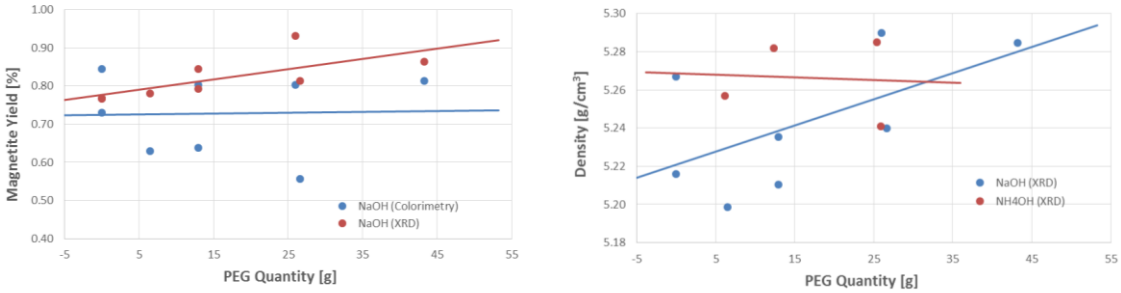

Figure 9-20: Magnetite yield and color effects with differing PEG quantities (left). Further effects on particle density are also visible. Results shown from mass and XRD measurements for samples: S.18.1, S.18.2, S.18.3, S.18.4, S.10, S.10.1, S.10.2, S.10.3, S.7, S.7.2, S.7.3, S.7.4.

This lack of nuance becomes clearer when looking at a pure sample of magnetite in Figure 9-21 and comparing it to Figure 9-22. Figure 9-22 shows some representative samples to demonstrate the range of qualitative changes in colour across the various synthesized samples. These samples demonstrate various surface oxidation states and the resulting CIE LAB colour variation.

Figure 9-21: Sample colour for a pure sample of magnetite. Sample S.-1. The vertical axis represents colour histogram counts while the horizontal the specific colour. Colorimetry produced via camera image.

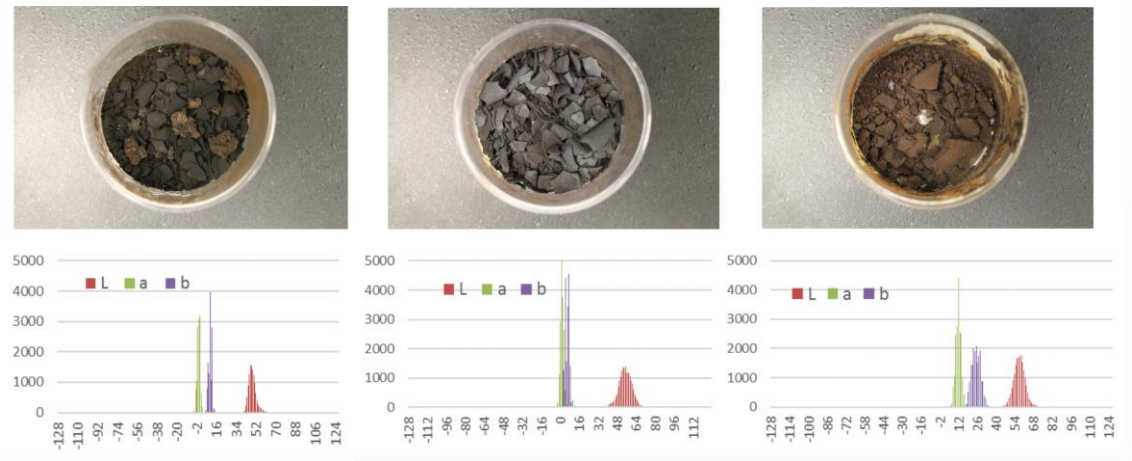

Figure 9-22: Sample colour variations across select synthesized samples and CIE LAB variations. From left to right, samples used were: S.7.2, S.18.1, S.1. Colorimetry produced via camera images and image processing.

Looking at the density of samples, as computed via the lattice parameters from XRD characterization, data shows itself to be distributed with no clear trend. While trend lines are shown in Figure 9-20, given the extent of spread of the actual density values, no firm conclusions can be made about the effects of PEG quantity on the density of the final MNP sample. This is reasonable, considering that unit cell dimensions are more likely to be influenced by high regional pressure and temperature effects than PEG quantity alone. The density values of magnetite samples varied between 5.194 [g/cm^3] and 5.320 [g/cm^3] with margin of error varying between 0.005 [g/cm^3] and 0.072 [g/cm^3]. With one notable exception, these density values, are higher than those of our micro-scale commercial magnetite sample (S.-1) whose value fell at 5.195 [g/cm^3]. Thus, nano-scale samples appear to be connected to increasing material densities. In-fact, it is likely that for genuinely high saturation, something very desirable in our material, high pressure synthesis may prove beneficial and would be a recommendation for future research.

9.4.3 PEG Quantity Effects (Hysteresis curve critical points)

The effect on saturation magnetization can be clearly captured for our sample under conditions where the PEG quantity is varied. Furthermore, exchange bias lends to added understanding of the core-shell structure of the synthesized samples. The exchange bias can provide some additional quantitative information on the nature of oxidation in the produced samples. An overview of the relationship between the different samples with respect to saturation, exchange bias and PEG quantity is provided in Figure 9-23.

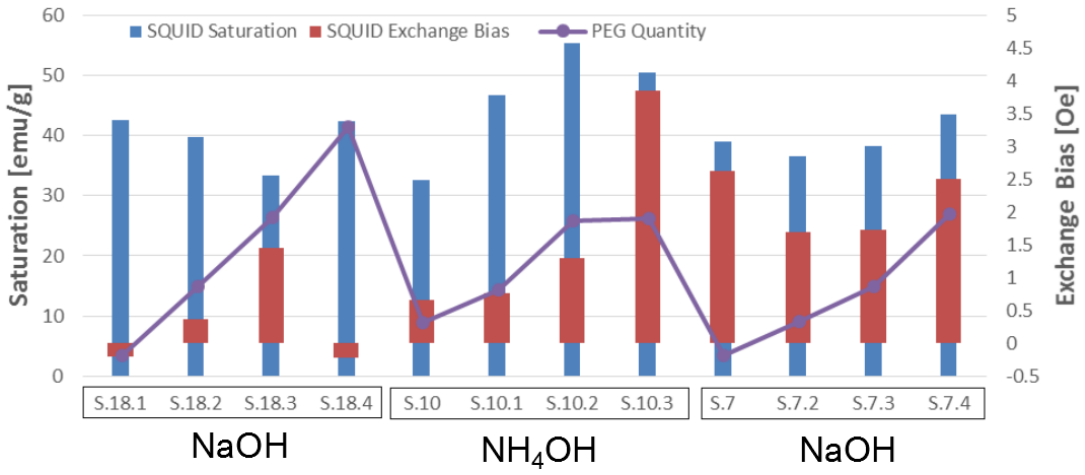

Figure 9-23: Overview of saturation and exchange bias relationships to PEG Quantity and base type across various samples. Magnetic measurements via SQUID for samples: S.18.1, S.18.2, S.18.3, S.18.4, S.10, S.10.1, S.10.2, S.10.3, S.7, S.7.2, S.7.3, S.7.4.

Expanding on this summary in Figure 9-24, we can see saturation varying considerably across samples with values ranging from 27.89 [emu/g] up to 54.96 [emu/g] – with errors ranging between 0.16 [emu/g] to 0.74 [emu/g]. This is considerably lower than the commercial control (S.-1) which demonstrated a saturation value of 85.62 [emu/g]. It is here that we see the potential importance of smaller unit cell dimensions and higher densities.

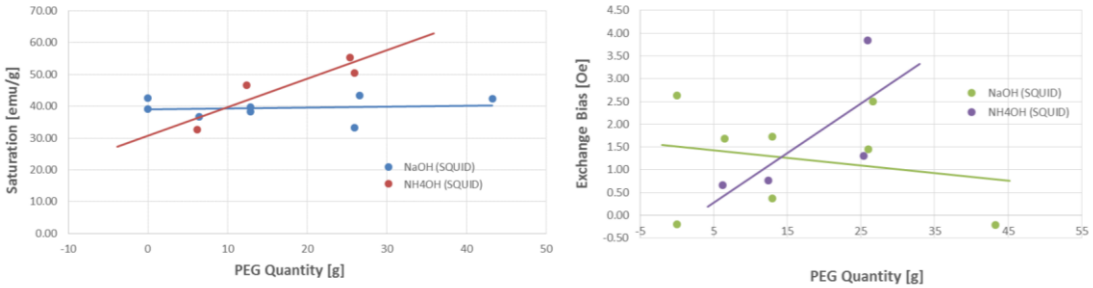

Figure 9-24: Saturation and exchange bias and the effects of differing quantities of PEG during synthesis. SQUID results and data analysis for samples: S.18.1, S.18.2, S.18.3, S.18.4, S.10, S.10.1, S.10.2, S.10.3, S.7, S.7.2, S.7.3, S.7.4.

We note from Figure 9-24, a trend whereby increases in PEG quantity lead to increasing saturation magnetization when NH_4OH is used as the reaction base. This does not appear to be the case both for NaOH however. A similar trend is noted for the exchange bias. This is a curious effect, however, noting our earlier discussion of particle size changes with PEG quantity (Section 9.4.1), this increase becomes understandable. Increases in PEG quantity were found to increase particle size. Such increases in particle size, as indicated previously, have been correlated with increased saturation. The results presented in Figure 9-17 and Figure 9-24 demonstrate the correlation.

We can go further and analyze the effects of PEG quantity on coercivity and remanence as shown in Figure 9-25. As with previous overviews, it is difficult to see clear relationships between the different variables. Figure 9-26 attempts to clarify some of the relationships. Despite the trendline, given the spread of data for synthesis using both NaOH and NH_4OH, we note little or no correlation between coercivity and PEG quantity. However, despite the spread, if considering the coercivity trendline the general directionality is likely correlated to increasing particle size rather than any direct effect from the added PEG. The typical values of sample coercivity range from -0.71 [Oe] to 12.45 [Oe]. Samples S.18.3 and S.10.1 are notable in that the coercivity falls quite low at 0.85 [Oe] and 0.71 [Oe].

Unfortunately this is still above the error of 0.47 [Oe] suggesting that even these samples have not quite reached the superparamagnetic regime. Two samples from among the 31 synthesized samples in this study, if remanence effects are ignored, did exhibit potential superparamagnetic properties with coercivities falling below error at −0.17 [Oe] (S.11.2) and 0.29 [Oe] (S.12.2). We note here that the negative coercivity is a non-physical value. However, given that this value lies within the margin of error, the non-physical nature of the number is easily attributable.

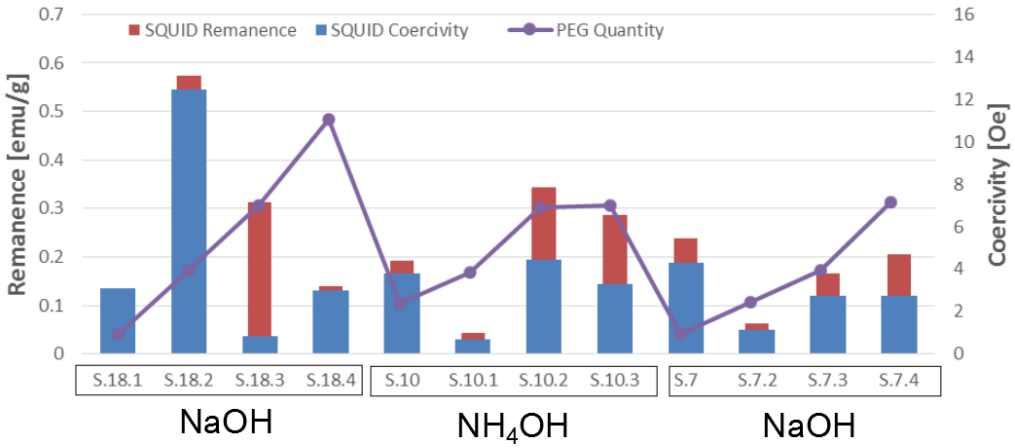

Figure 9-25: Overview of coercivity and remanence and their relationship to PEG quantity across synthesized samples. Results from SQUID measurement and analysis of samples: S.18.1, S.18.2, S.18.3, S.18.4, S.10, S.10.1, S.10.2, S.10.3, S.7, S.7.2, S.7.3, S.7.4.

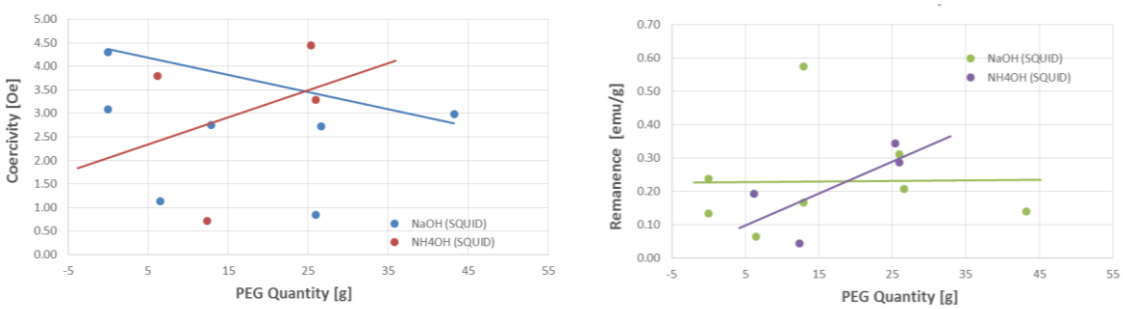

Figure 9-26: Coercivity and remanence and the effects of differing quantities of PEG during synthesis. Results from SQUID measurements and analysis for samples: S.18.1, S.18.2, S.18.3, S.18.4, S.10, S.10.1, S.10.2, S.10.3, S.7, S.7.2, S.7.3, S.7.4.

As with our coercivity, we see that the remanence doesn't appear correlated to changes in PEG quantity for NaOH. An increase in remanence is however seen for NH_4OH. This increase is easily explained by increasing particle size. Looking at the range of remanence values we note that values fall between 0.04398 [emu/g] and 0.57 [emu/g]. Typical errors fall between 0.29×10^{-3} [emu/g] and 0.467 [emu/g] if all synthesized samples are considered. The lowest remanence with reference to PEG quantity is seen by S.10.1 (0.04398 [emu/g]) and S.7.2 (0.064 [emu/g]). This is particularly interesting in that low coercivity and remanence don't always appear to match. For instance in the case of S.18.3 the coercivity is low but remanence is high at 0.31197 [emu/g]. Unlike coercivity, remanence values don't show themselves to fall below the error for any of the samples synthesized in this study. This is a clear indication that no sample is likely to have a zero coercivity. While a number of authors have noted repeatedly the superparamagnetic nature of particles produced by co-precipitation synthesis routes, considering the results, it is believed that such superparamagnetism, in many cases, is likely to be a mis-attribution. We do note that the samples with the lowest coercivities among all synthesized samples have the lowest remanence values of 1.65×10^{-2} [emu/g] and 7.57×10^{-2}[emu/g].

9.4.4 PEG Quantity Effects (Frequency and Power Loss)

The coercivity and remanence together with the saturation can provide some measure of power loss in the synthesized materials. Using these critical points along with sparse SQUID magnetization curves and some tertiary XRD and SEM data (e.g. particle size, density), the Jiles-Atherton model was used to generate a full hysteresis curve. The resultant hysteresis curve model allowed direct computation of power loss (area inside the curves) that would have been challenging using sparse data.
Figure 9-27 demonstrates both, the sparse data collected for one particular sample and the resulting dense model output. We note that during measurements only a part of the decreasing curve (red) and a part of the increasing curve (green) were measured. The dense reconstruction provides the entire virginal (blue), decreasing (red) and increasing (green) parts of the hysteresis curve.

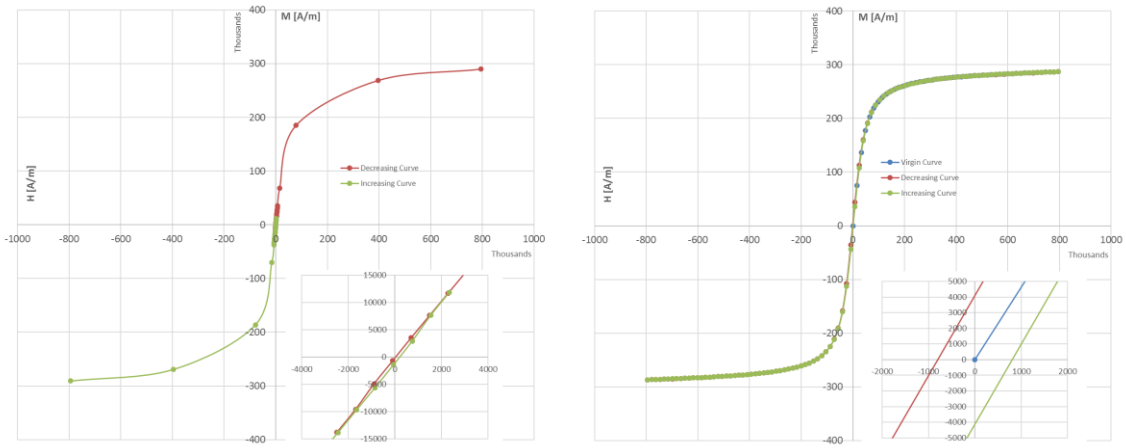

Figure 9-27: Actual data collected from SQUID magnetization measurements v.s. the final hysteresis curve model. Two example curves (real data on the left, model generated data on the right) for sample S.2. Note that a full listing of hysteresis curves measured in this study is provided in the Appendix.

A set of 6 parameters were optimized to provide best fit curves using a sum-of-squared difference (SSD) cost function. Convergence was extremely sensitive to initial conditions meaning that slight variations could lead to non-optimal convergence. Manual tuning combined with calculation were first used to arrive at reasonable initial values. From here, within 40 iterations, convergence was reached as shown in Figure 9-28. We note that in this figure the reducing SSD value and a convergence of our six parameters, namely: $\theta = \{n, m, \alpha, X_{AF}, c, k\}$. To ascertain, somewhat, the error associated with the parameter estimates and the resulting dense hysteresis curve model, 15 Monte Carlo, normally distributed datasets were generated. The results shown, in the figure, are the mean values of the resulting output distributions.

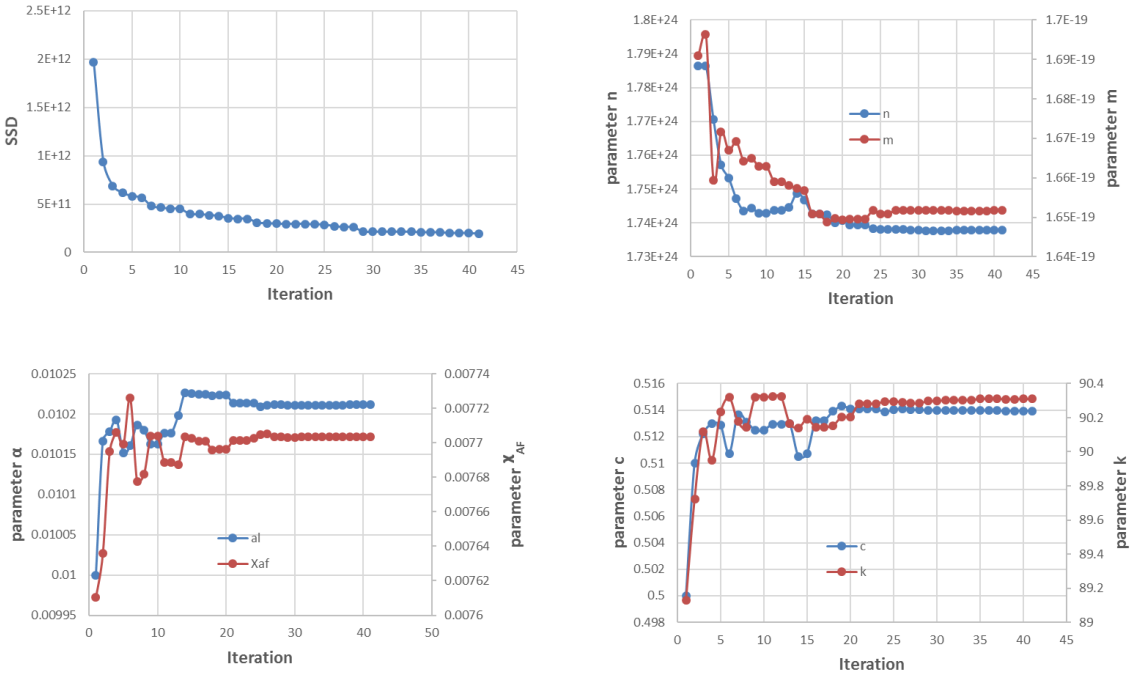

Figure 9-28: Convergence results for the SSD value and associated parameter estimates. Results generated by optimization algorithm with measured hysteresis data. Note that full optimization results can be found in the Appendix of this study.

Complementing the hysteresis data, SQUID was also used to produce ZFC and FC characterizations – some examples are shown in Figure 9-29 for sample set 7 and 18. These were used to produce an estimate of blocking temperature. Blocking temperature, together with XRD particle size and volume data can help estimate operating frequency. As was shown earlier (in Section 8.5), a small change in the particle size or blocking temperature has drastic effects on the Neel frequency. In-fact, this effect is so drastic as to make frequency results obtained from SEM particle size estimates, swing to unreasonably low values. Nevertheless, some frequency estimates can be presented.

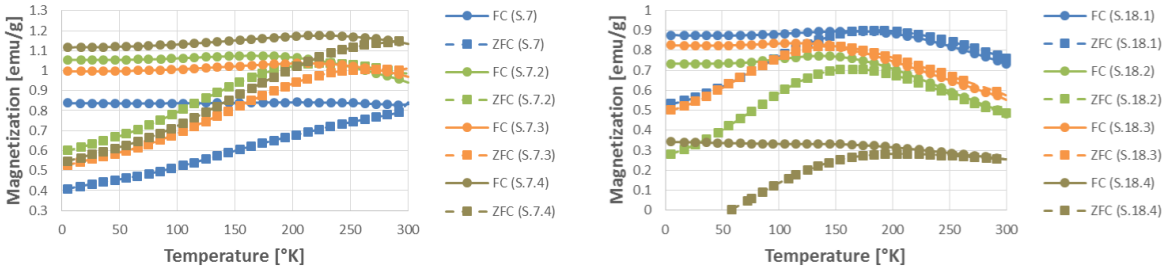

Figure 9-29: Zero field cooling (ZFC) and field cooling (FC) curves can be used to estimate blocking temperature. Example curves for sample set 7 and 18 shown. Results obtained via SQUID measurements for samples: S.18.1, S.18.2, S.18.3, S.18.4, S.10, S.10.1, S.10.2, S.10.3, S.7, S.7.2, S.7.3, S.7.4. Note that full and detailed graphs and results for the ZFC and FC curves is provided in the Appendix of this study.

Figure 9-30 and Figure 9-31 demonstrate the potential range of operating frequencies for synthesized material. The power loss resulting from both major and minor hysteresis loops is also presented. The figures compare synthesis routes with differing quantities of PEG present.

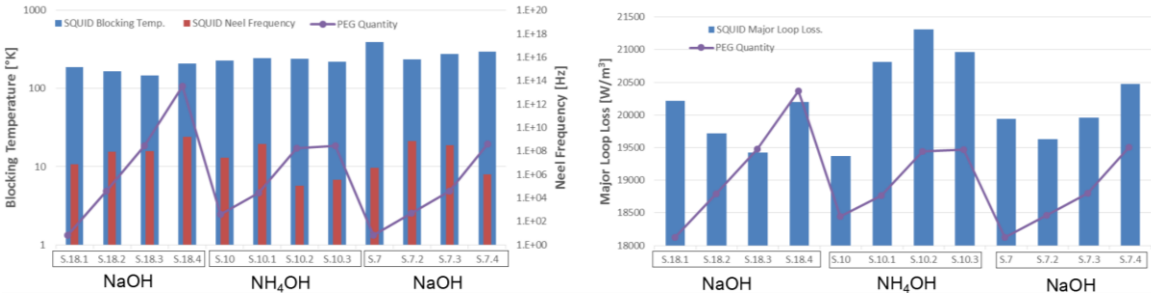

Figure 9-30: Overview of blocking temperature, frequency and power-loss with PEG quantity. Analysis of SQUID FC and ZFC data for samples: S.18.1, S.18.2, S.18.3, S.18.4, S.10, S.10.1, S.10.2, S.10.3, S.7, S.7.2, S.7.3, S.7.4.

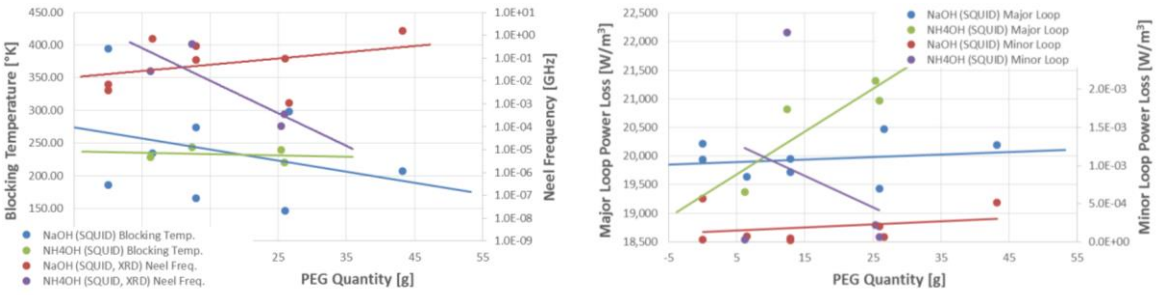

Figure 9-31: Blocking temperature, frequency and power loss for varying amounts of PEG. Results determined from analysis of SQUID measurements combined with hysteresis optimization outputs for samples: S.18.1, S.18.2, S.18.3, S.18.4, S.10, S.10.1, S.10.2, S.10.3, S.7, S.7.2, S.7.3, S.7.4.

No notable correlation can be seen for blocking temperature or Neel frequency with increasing PEG quantity. The exception seems to be a clear decline in frequency under synthesis using NH_4OH as reaction base. Considering that increasing particle size is accompanied by larger relaxation times and lower frequencies, this is not an unexpected result – especially given the notable increase in particle size with increasing PEG content in NH_4OH from Figure 9-17. The frequency range over which various synthesized samples appear to operate falls between 1.92×10^{-38} [Hz] to 108 [GHz]. This range is over variations in blocking temperature between just 146.59 [°K] and 300 [°K] and particle size range between just 4.36 [nm] and 15.75 [nm]. This is a clear indication of how unreliable the Neel relaxation frequency can be with the imprecise anisotropy energy estimate, attempt time estimate, particle size estimate and blocking temperature estimate.

Looking at power loss, the spread of power loss data across synthesis samples is too wide to make any firm determination of how PEG quantity is correlated. The exception appears to be power loss in the major hysteresis loop under NH_4OH reaction base. Here, power loss appears to increase with increasing PEG quantity. This correlates well with existing potential increases in both coercivity and remanence shown for NH_4OH in Figure 9-26.

Recall that the major hysteresis loop power loss occurs when the reluctance machine rotor is either being slowed down or sped up. The range of power loss in our particular synthesized samples ranges from 18760 [W/m^3] on the low end to 21663 [W/m^3] on the high end. The lowest value is linked to the sample with the lowest coercivity and remanence. However, the low coercivity/remanence particles are not all associated with the lower range of power loss. We noted that optimization of the Jiles-Atherton model was extremely challenging – it is with some consternation that the author must note that where initial conditions are not sufficiently close to the real parameter values, convergence has most likely occurred at an insufficiently close fit. In-fact, we note that SSD values for the various sample hysteresis model fits can vary by up to two order of magnitude from each other. Ultimately, we can compare this power loss to the loss from our commercial magnetite sample. This sample demonstrated power loss in the order of 25000 [W/m^3]. In another iron sample (S.0), this loss was noted as high as 40441 [W/m^3]. Both values are higher than losses from the nano-scale powder synthesis indicating that some benefit is obtained from nanoparticles. Minor loop power loss across samples is poorly correlated and falls b/w 9.96×10^{-6} [W/m^3] and 2.74×10^{-3} [W/m^3].

9.4.5 PEG Molecular Weight Effects

We can move on and use similar analysis as used for PEG quantity related effects for other variables as well. As with PEG quantity, PEG molecular weight adjustments were also attempted. Analyzing the effect on variables such as particle size, aspect ratio, yield & colour and density we note the trends shown in Figure 9-32. Samples used for the analysis are: S.13.1, S.13.2, S.13.3 and S.13.4.

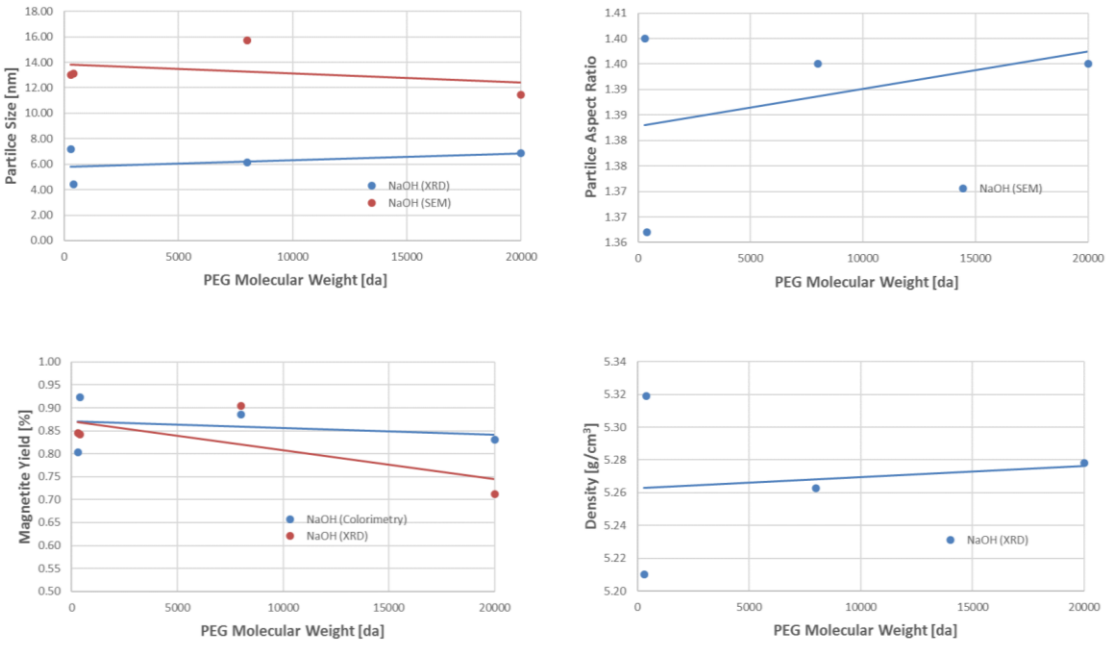

Figure 9-32: Particle morphology, yield and density effects from PEG molecular weight changes during synthesis. Measurements from XRD and SEM results for samples: S.13.1, S.13.2, S.13.3, S.13.4.

Looking at the trends across all these variables, at the spread of data and the associated error, there seems to be very little correlation to changes in PEG molecular weight. The exception seems to be a decrease in magnetite yield with the very high molecular weight of 20000 [da]. This is, of-course, not unreasonable considering that the large molecules associated with high molecular weight are likely to reduce accessibility for iron salts to OH^- ions in solution.

A similar situation is seen when looking at both coercivity and remanence as shown in Figure 9-33. The spread of data prevents any reasonable conclusion being made. It is likely that there is little or no correlation between molecular weight, coercivity and remanence. The same can be said for exchange bias as well. One point of note is that very high molecular weight does seem to have an effect on reducing magnetic saturation.

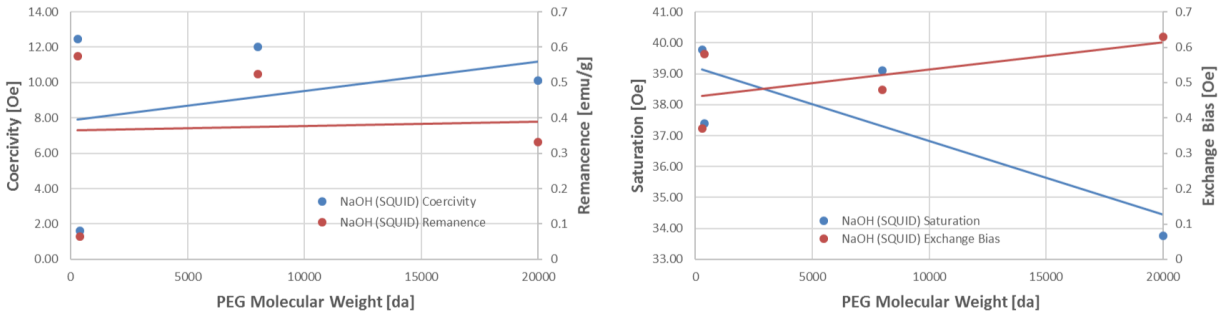

Figure 9-33: Coercivity, Remanence, Saturation, Exchange Bias effects resulting from PEG molecular weight changes during synthesis. Measurements from SQUID for samples: S.13.1, S.13.2, S.13.3, S.13.4.

Looking further at Neel frequency for our material, we see that it has correlation to molecular weight (as does blocking temperature). This is shown in Figure 9-34 below. Likewise, we see correlation between power loss resulting from the major hysteresis loop. From the perspective of the minor hysteresis loop, the real effect relative to molecular weight is somewhat difficult to determine.

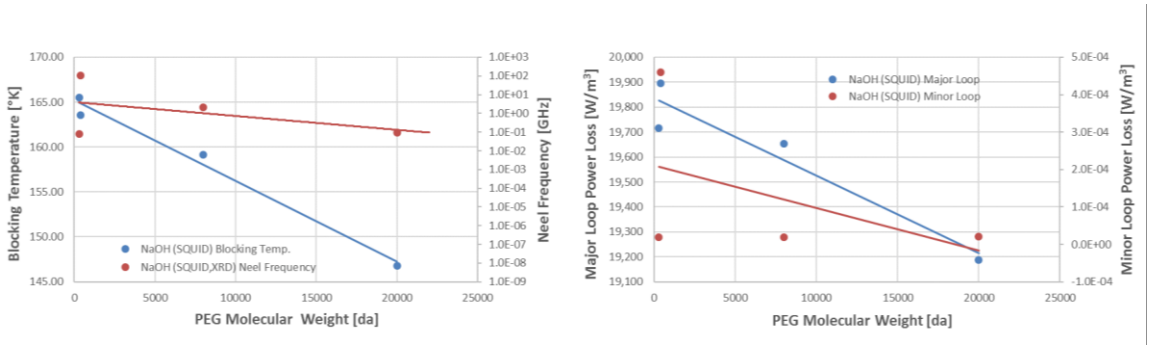

Figure 9-34: Frequency of operation and power loss for particles synthesized under varying amounts of PEG. Measurements from SQUID and hysteresis optimization process for samples: S.13.1, S.13.2, S.13.3, S.13.4.

9.4.6 Effect of Base pH

Switching from a look at our PEG surfactant, to the base pH, we find strong correlation with particle size, aspect ratio, yield and density. Applicable samples are samples: S.11.1, S.11.2, S.11.3 and S.11.4. This is easily seen from Figure 9-35. There are, however, some contradictory results. For instance, looking at particle size, we note that SEM results show increasing particle size with increasing pH while XRD results show decreasing particle size with increasing pH. It is difficult to resolve this issue considering that, unlike previous contradictions, the quality of the SEM images is relatively high. One possible explanation for the discrepancy may lie in the modality of imaging used by XRD characterization approach versus the SEM approach. SEM images form a useful basis for topographical examination of our MNPs, however, given the high degree of magnification, these images can only really be used to image very small fractions of the actual sample material. If focus is given to a particular region that falls on the tail ends of the real particle size distribution, an unrepresentative view of particle size values is likely to be noted.

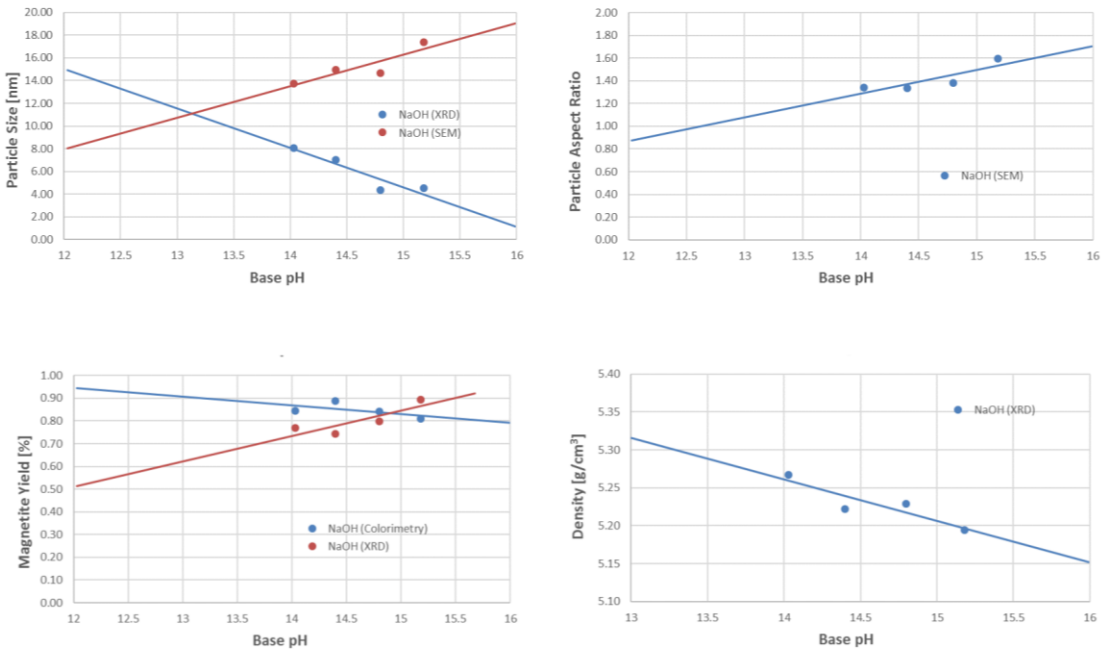

Figure 9-35: Particle morphology, yield and density effects from base pH changes during synthesis. Measurements presented from SEM and XRD for samples: S.11.1, S.11.2, S.11.3, S.11.4.

Likewise, while XRD approaches provide much better overall statistics for the entire sample under examination, they are best suited to crystalline material. Where crystal orientation is not appropriate or long range order lacks periodicity (is amorphous), XRD measurements become challenging. The XRD sample could likewise preferentially show smaller crystals over large amorphous particles visible via SEM.

This explanation, however is a stretch. Therefore, making use of added data from SQUID characterization to come up with a more meaningful answer is a way forward. Looking at Figure 9-36, for instance, we note that both coercivity and remanence drop with increasing base pH. This suggests that a decrease in particle size is likely happening. It is this added information that can help eliminate SEM particle size increases (with pH) as being spurious.

Interestingly we note from Figure 9-35, that increasing pH has the effect of higher yield with less impurities. As with previous discussions of colorimetry, however, we note that the colorimetric results show a slight decrease in magnetite quantity. As discussed, this slight decrease is likely to be less reliable than XRD measurements. One possible reason for the slight variation in colour away from that of our commercial sample of magnetite may have to do with increasing diffraction of light leading to an increasing colour distance in CIE LAB space for smaller particles.

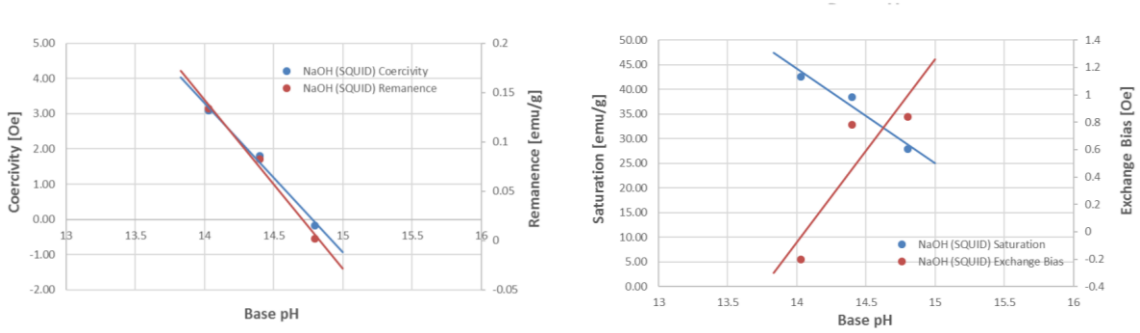

Figure 9-36: Coercivity, Remanence, Saturation, Exchange Bias effects resulting from Base pH changes during synthesis. SQUID magnetometric measurements and analysis for samples: S.11.2, S.11.3, S.11.4.

A further point of note is the increasing aspect ratio and reduction in density with increases in pH. One possible explanation for the increase in aspect ratio may have to do with the method by which iron salts are added to the reaction base. The flow direction of the salts may have an effect on the rate or reaction leading to a preferred growth direction tangential to the motion of the nucleation site. It is unclear why density would decrease however and further investigation is recommended.

From Figure 9-36, there is clear evidence that a higher pH base is more desirable in reducing coercivity and remanence. One point of note should be that increases in base pH can have unintended consequences and side reactions with surfactants. For instance, the addition of PEG to a NaOH base with pH of around 15 or above led to a breakdown of added PEG. A further tradeoff for the lower coercivity appears to be an accompanying lower saturation and an increasing exchange bias. Both these added effects fit well with reductions in particle size observed by other researchers.

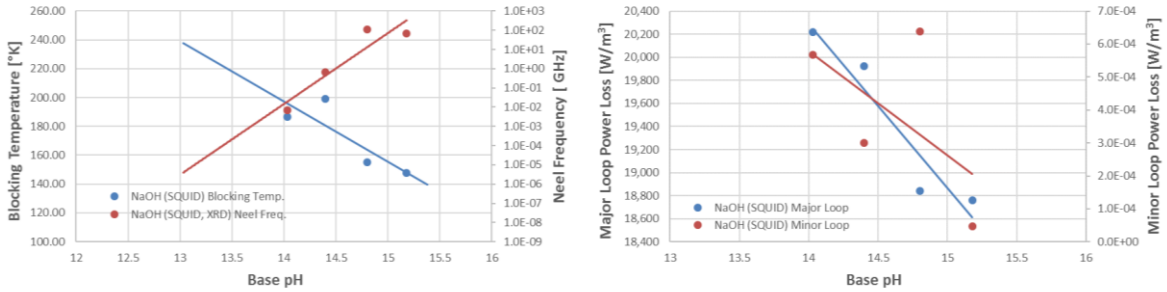

Figure 9-37: Frequency of operation and power loss for particles synthesized under varying amounts of PEG. SQUID measurements and analysis for samples: S.11.1, S.11.2, S.11.3, S.11.4.

Examining blocking temperature, frequency and power loss, there is strong correlation with base pH. For instance, looking at Figure 9-37, a drop in blocking temperature is noted with increasing pH and an increase in Neel frequency. This is interesting to note, as it suggests that small particle size is the driving force rather

than blocking temperature. A consequence of this is that decreases in blocking temperature aren't necessarily directly associated with increases in particle size. A more complex view of variation in blocking temperature is needed.

Looking briefly at minor hysteresis loop power loss, we see a clear decline in loss with increasing base pH. It appears that pH is a significant influencer in reducing power loss as well as other particle morphology.

9.4.7 Base Quantity and Cooling

The co-precipitation reaction used during this study is exothermic. This mean that as the reaction proceeds a significant increase in reaction temperature is likely. This higher temperature can encourage high growth after nucleation and increase the likelihood of chemical sintering (aggregation) as well. Maintaining a relatively consistent and low temperature for the reaction can, therefore, be important.

Keeping a stable temperature of reaction can be achieved via two approaches. The first is to make use of water bath chilling (i.e. samples: S.9 and S.9.5). Given the limited surface area and the insulating qualities of the reaction vessel, such cooling was found to have no clear effect on reaction temperature and resulting particles. With the use of a water bath, some suggestions of greater isotropy in particles and some reduction in aspect ratio have been noted however. Unfortunately, given the errors, and the challenges of water cooling, it is difficult to ascertain whether these effects were a result of a genuine trend or some subtle variation in experimental conditions. Similar issues arise with discussions of density changes, coercivity, remanence, saturation and exchange bias.

An alternative approach to cooling was also attempted. Here excess base quantity of fixed pH was used. Once cooled to a known temperature, making use of large quantities of base were used to provide thermal stability during the reaction. Figure 9-38 examines whether increases in base quantity had any effect on the

resulting particles produced during synthesis. Note that the following samples are used throughout this sub-section: S.11.3, S.12.1, S.12.2, S.12.3, S.1, S.2, S.4.

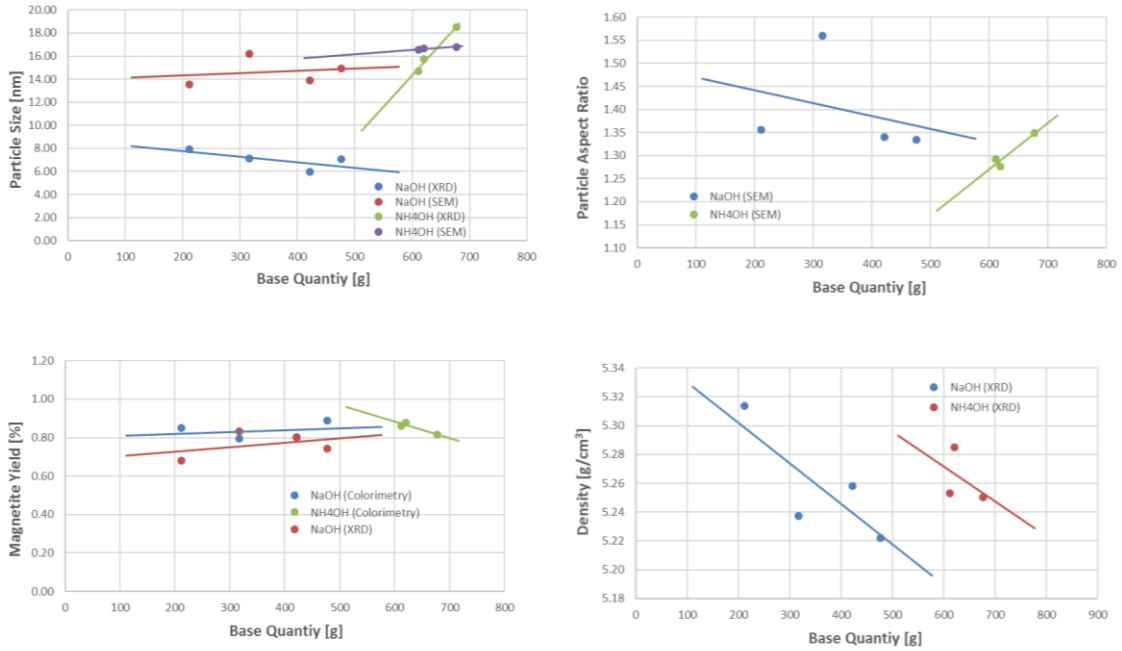

Figure 9-38: Particle morphology, yield and density effects from changes in base quantity. SEM and XRD data used to extract graphical data for samples: S.11.3, S.12.1, S.12.2, S.12.3, S.1, S.2, S.4.

This method of temperature control does appear to have some effect on particle size when making use of the NaOH base. As with prior analysis, we note the contradictory results from SEM and XRD measurements. Taking into consideration Figure 9-39 and the trends of coercivity and remanence it is likely that the decreasing particle size trend shown by XRD measurements is a real effect. Correlation also seems to exist between increasing particle size and base quantity when considering NH_4OH synthesis routes. It is unclear why this should be the case. Given the contradiction in results between SEM and XRD data, combined with large variations in both coercivity and remanence, it is likely that this is a spurious result. Particle aspect ratio also appears to be relatively independent of base quantity – one exception is noted where the ratio increases to 1.56. Looking at density changes,

there appear to be some clear reductions in density with increasing base quantity perhaps as a result of greater numbers of nucleation sites available

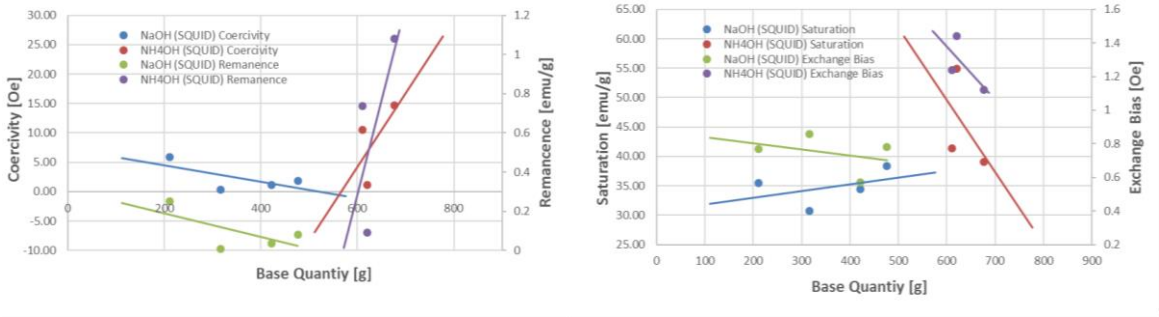

Figure 9-39: Coercivity, Remanence, Saturation, Exchange Bias effects resulting from base quantity changes. Results obtained from SQUID measurements for samples: S.11.3, S.12.1, S.12.2, S.12.3, S.1, S.2, S.4.

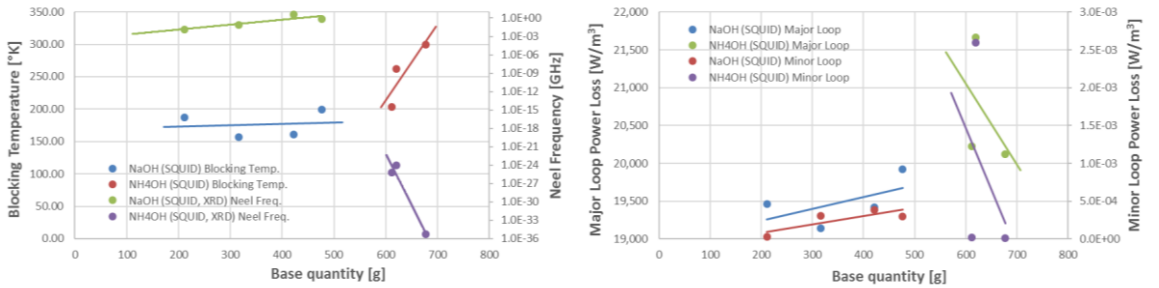

Figure 9-40: Frequency of operation and power loss for particles synthesized under varying amounts of PEG. Results obtained from SQUID measurements and analysis: S.11.3, S.12.1, S.12.2, S.12.3, S.1, S.2, S.4.

As noted earlier, from Figure 9-39, base quantity has a slight impact in reducing coercivity and remanence, when NaOH is the reaction base. However, this is in stark contrast with results using NH_4OH as the reaction base. Both coercivity and remanence vary drastically over a very small range of quantity changes. This suggests that variations in base quantity aren't well correlated and changes in coercivity and remanence are more likely a result of other more significant factors.

We see that saturation and exchange bias values can be similarly explained for NH_4OH base. For NaOH, both these variables are likely independent of base quantity.

Moving on and looking at blocking temperature and Neel frequency, no correlation exists with base quantity changes as shown in Figure 9-40. As with previous cases of NH_4OH, this does not appear to be true with increasing NH_4OH. Here, increasing blocking temperature and decreasing frequency corresponds to increasing base quantity.

9.4.8 Magnetic Field & Nitrogen Shielding

Before moving on we should make note that additional synthesis approaches were attempted in the presence of nitrogen and in the presence of a magnetic field (i.e. samples (S.1, S.2, S.4, S.17.1, S.17.2). In the case of nitrogen environment synthesis, the goal was to reduce oxidation by purging the reactants of oxygen. The complexity of this setup made it quite challenging to synthesize material. Very little gain was seen in terms of particle size reductions as well. The presence of a magnetic field during synthesis, however, yielded larger and more regular anisotropic crystalline material with high magnetic saturation.

9.5 Sintering Thermal Analysis

The next logical step after synthesizing powder material, is to form it into bulk for use as a core material for building our reluctance machine. To do so a metal/ceramic clay was formed. This clay composition was based on existing formulations, however significant refinement was needed to accommodate tests on magnetite and various susceptor materials.

Eventually a rough working formula was found that consisted of 85 [%] magnetite (or susceptor), 4.5 [%] meythl cellulose binder, 1 [%] PEG surfactant, 0.30 [%] light

oil and 9 [%] water. Using this combination focus was given to producing and tuning susceptor material needed to achieve better microwave hybrid heating. Attempts were made with both bulk material and thin film material. Thin films were found to achieve much better heating.

The use of thermal paper to measure the position of the standing wave pattern was particularly important in obtaining optimal heating. A sample placed at a nodal point could experience very slow absorption.

The highest heating rates achieved fell at around $144\ [°C/min]$. This approaches the more desirable rates of $300\ [°C/min]$ useful for ensuring fast sintering of nano-particle samples. Unfortunately, a great deal more experimentation is required to maintain this heating rate consistently all the way up to the sintering temperature of approximately $800\ [°C]$.

Figure 9-41 demonstrates a range of bulk microwave absorption tests for five different material samples labelled as M.3, M.4, M.5, M.8, M.11, M.13 and M.14. Each test was conducted for a known mass object. The refractory material (M.13) formed the insulation material, however, it also acted as a weak susceptor to microwave radiation would heat up. Considering the bulk ceramic clays sintered inside the refractory chamber were of relatively low mass/volume compared to the cavity dimensions, it is likely that steady state temperature is reached at a lower value – a relatively small sample must heat up a large volume of air leading to a lower chamber temperature.

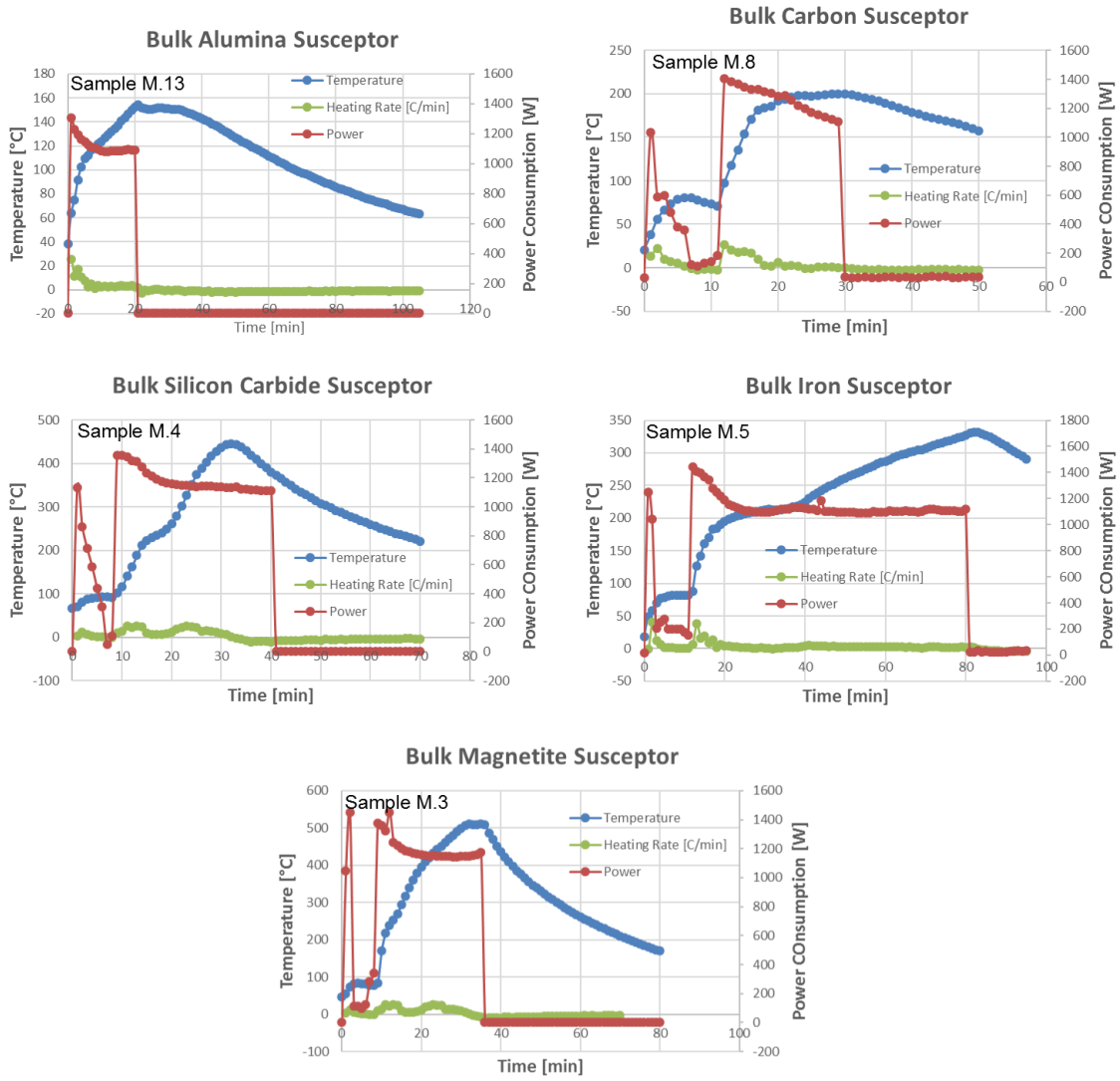

Figure 9-41: Various bulk susceptor heating tests for fixed volume quantities. Measured results obtained from thermocouple and power measurements in furnace control box for samples: M.3, M.4, M.5, M.8, M.13.

Of the five materials tested, magnetite samples showed the highest heating rates and the highest steady state temperature as well. As seen in Figure 9-42, the use of thin film susceptor proved to be the most effective. Temperatures reached the final desired sintering temperature of 800 [°C]. An explanation why an equivalent bulk material couldn't achieve high temperature at the same rate is likely a result of

microwave penetration depth and increased surface eddy currents induced as a result of sintering. Decreasing resistance, here, reduces penetration depth further. A thin film mixture of different conducting and non-conducting materials ensures that resistance of the film remains high and prevents reflection.

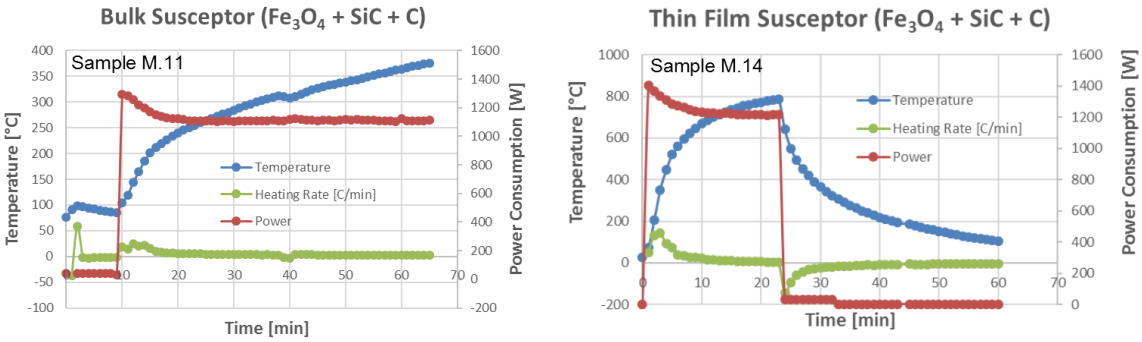

Figure 9-42: Combination susceptor in bulk and thin film form. Results obtained from furnace control box measurements of sample M.11 and M.14.

Certain materials were much more prone to reflection. For instance, silicon carbide with its high conductivity (recall Table 5-1), produced reflected microwaves that quickly caused overheating of the microwave source – this effect disappeared with the addition of magnetite impurities. A similar effect was observed with iron. In the end, a single sample of magnetite nano-particles was sintered using a thin film combination of magnetite, silicon carbide and carbon. Characterization of the sintered product is left as future work.

We note that it is possible to grade the particular susceptor material by looking at its heat capacity under microwave irradiation. For instance, a high specific heat implies that the material requires a great deal of microwave energy to heat up. A material with a low specific heat will heat up quickly. Figure 9-43 demonstrates this for the samples examined in this study. We see from the figure that the lowest specific heat is demonstrated by sample M.14 – this is the thin film susceptor material.

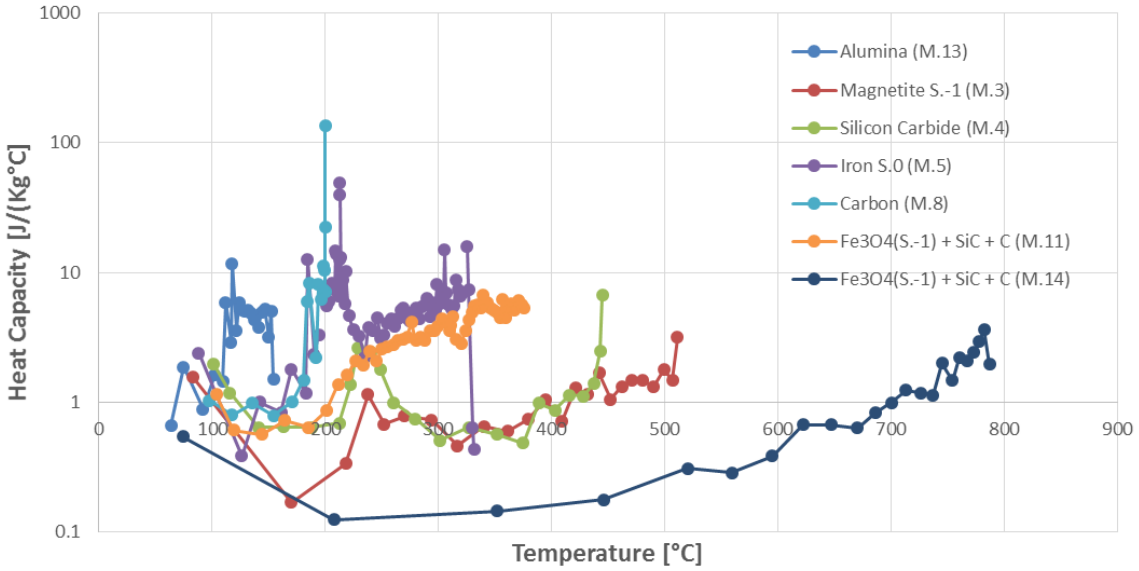

Figure 9-43: Specific heat capacity of a material in the presence of microwave irradiation can be used to rate the quality of a particular material as a heat generating source. Derived results from furnace measurements for samples: M.3, M.4, M.5, M.8, M.11, M.13, M.14.

In the context of our nano-materials we see that clever additions of impurities can potentially improve the heat absorption rate to induce faster sintering. Final characterization of sintered materials via XRD, SEM and SQUID are left as future work.

9.6 Summary and Final Remarks

This chapter began with a series of simulation aimed at understanding permanent magnet bearing system better. It was demonstrated through these simulations that Earnshaw's theorem was indeed valid. Simple geometries of magnetostatic configurations were explored using hand coded modeling. The potential energy surfaces were shown as not possessing a local minima. To gain a better grasp of how

motion might occur in magnetostatic systems, COMSOL Multiphysics was used as a tool to further explore a more complex linear permanent magnet machine.

The model for estimating forces and energy in a diamagnet bearing, developed earlier in Chapter 3, was used in conjunction with more advanced COMSOL simulations to provide quantitative estimates. These estimates quantified equilibrium positions, lift-able rotor mass and associated number of platters. The aiming of this work was to provide a means of computing critical parameters for our prototype diamagnetic bearing design. Not only were forces and energy of levitating diamagnetic discs established, but also the effect of floater-lifter combinations and topologies. Simulations were used to estimate the effect of eddy currents induced on spinning diamagnetic platters as well.

Focus was then shifted to the reluctance drive assembly. Here it was noted that cogging and hysteresis losses should also be estimated. Taking these into consideration attention was given to reducing hysteresis losses through the use of superparamagnetic materials. These materials were synthesized and tested by varying surfactant (PEG) quantity and molecular weight, base pH and quantity. Only two potentially superparamagnetic samples were noted. Some attempt was made to correlate particle size, composition, colour, density, coercivity, remanence, saturation, exchange bias, blocking temperature, Neel frequency and power loss to variations in the synthesis procedure. The strongest correlation found related to increases in base pH. A considerable number of spurious correlations were noted and future work in this area should focus on more careful control of the synthesis process. Some reduced power loss was noted in MNP samples when compared to existing commercial samples however. It was clear from this process that the effect of homopolar losses are likely to be higher than those from the reluctance drive.

The chapter concluded by looking briefly at the next step required for building a reluctance motor from synthesized particles. While a sample was sintered, characterization of the newly made bulk sample is left as future work. A number of avenues for understanding microwave absorption behavior were explored and some

thermal characterization work done so that sintering of relatively precious quantities of nano-particles can be done with greater predictability.

10 Conclusion

Recent trends in renewable energy development have spurred interest into energy storage solutions. Of the vast array of solutions, few viable large scale solutions appear to exist – a detailed and comprehensive review has been separately published by the author on the range of storage solutions. Of these solutions, flywheel storage solutions, offer a number of benefits including large scale applicability, high cycle life, high power capacity, high efficiency, low maintenance needs, wide operating temperatures and low environmental impact. Unfortunately, despite all the advantages, they suffer from two critical problems: High self-discharge and high cost.

This study focused on the self-discharge rate for flywheel systems and proposed an approach to reduce this parasitic loss. Five key sub-systems of the flywheel energy storage system were identified: The containment chamber, the control & power converter, the flywheel, the bearing and the electrical machine. This study confined itself to a detailed study of the bearing and electrical machine assembly – in flywheel systems of low stiffness the bearing and electrical machine need be considered holistically. A wide variety of approaches for loss reduction in the two subsystems exist.

10.1 Diamagnetic Stabilization

Surveying the literature, of the solutions available, electromagnetic bearings showed greater reductions in loss compared to traditional contact bearings. Within the field

of electromagnetic bearings there were found to be a number of options including: active controlled bearings, super-conducting bearings, permanent magnet bearing, ferrofluid stabilized bearings, gyroscopically stabilized bearings, electrodynamically stabilized bearings and diamagnetically stabilized bearings. While most bearings are a hybrid combination of one or more of these bearing types, this study focused primarily on diamagnetic stabilization informed by existing work on permanent magnet bearing variants. A functional diamagnetic bearing was generally found to consist of three main subsystems: The stabilizing machine, the lifter-floater assembly and the electrical machine.

In this study, a multi-plattered approach to diamagnetic levitation was proposed and used to construct the stabilizing machine for the bearing. Here for the first time, a radial machine of this variety has been constructed. Various lifter-floater combinations were assessed as well. An analytical model was produced to describe the combined effect of the number of platters and the floater-lifter on the stability of the levitated rotor assembly. The rest position of the bearing for various rotor masses was assessed and a relationship between mass and the number of stabilizing platters computed.

A prototype diamagnetic bearing was constructed to verify the results of analytical modeling. This prototype showed reasonable correlation with these analytical results. The levitation of an approximate 30 [g] rotor assembly with 6 diamagnetic platters was observed. In order to achieve this a spherical 10 [mm] diameter floater was used with a disc magnetic lifter of field strength of approximately 0.1 [T]. Diamagnetic platters were made from pyrolytic graphite and had a thickness of 1.5 [mm]. For the platters, a resting position of roughly 1.5 [mm] above the stabilizer magnet was measured using paper inserts.

Depending on the lifter and stabilizing magnetic field conditions, analytical results suggest that a mass of 42 [g] can be lifted for 6 platters. Further, a linear rate of increase in liftable mass was seen from calculations. Roughly 7 [g] of mass can theoretically be lifted per pyrolytic graphite platter where no flux path is present

(high flux leakage) in the stabilizing machinery. It would thus take roughly 126 platters to lift a 1 [Kg] mass. For such a large number of platters, a high tolerance manufacturing method is similar to that used in commercial hard disk platters would be ideal.

Definite improvements can be made to stabilizing force and liftable mass by introducing a high permeability flux path and making use of higher flux density stabilizing magnets. It should be noted that as mass increases, higher lifter magnetic flux densities are also required to maintain sufficient clearance between the diamagnetic platters and the stabilizing magnets.

10.2 Electrical Machine and Rotational Losses

In addition to the stabilizing machinery and floater-lifter assembly, the electrical machine was also considered. Ignoring electrostatic machines or variants that require physical contact via brushes or slip rings, three main types of machine are available for use with diamagnetic bearings. These are permanent magnet machines, induction machines and reluctance machines. Of the three choices, reluctance machines offered the greatest convenience, lowest cost and highest simplicity with the lowest cogging related issues and were selected for this study.

Considering the already low loss paradigm of electromagnetic bearings, it was hypothesized that electrical machine core losses would become a significant contributor to further loss if flywheel, containment (vacuum) chamber and controller losses were neglected. An approach to reducing iron (core) losses was considered for the reluctance machine. Reduced eddy current loss, reduced hysteresis loss (remanence induced cogging and remagnetization) related drag were the primary concerns of this study.

It was believed early in this study that once air friction had been accounted for, parasitic losses in the spinning rotor would be affected largely by the hysteresis of

the reluctance machine material. This was confirmed by way of simulation. The hysteresis related losses, themselves, were a result of remanent magnetization induced cogging drag and remagnetization related loss. An additional small contribution was noted from losses in the stabilizing machine and from eddy current losses in the electrical machine as well. Stabilizing machine losses were highly dependent on topological considerations and centric versus off-centric rotation while electrical machine eddy currents were highly dependent on particle size. Figure 10-1 provides a brief summary of the relative loss contribution from each source at 158 [rpm]. These results are combination of modeling work and measured magnetic losses associated with the core material. The use of magnetite core material lowers electrical resistance and virtually eliminates eddy current losses compared to equivalent laminations. Extending this observation to magnetite nanoparticles demonstrated significant drop in eddy currents compared to a commercial magnetite sample as well.

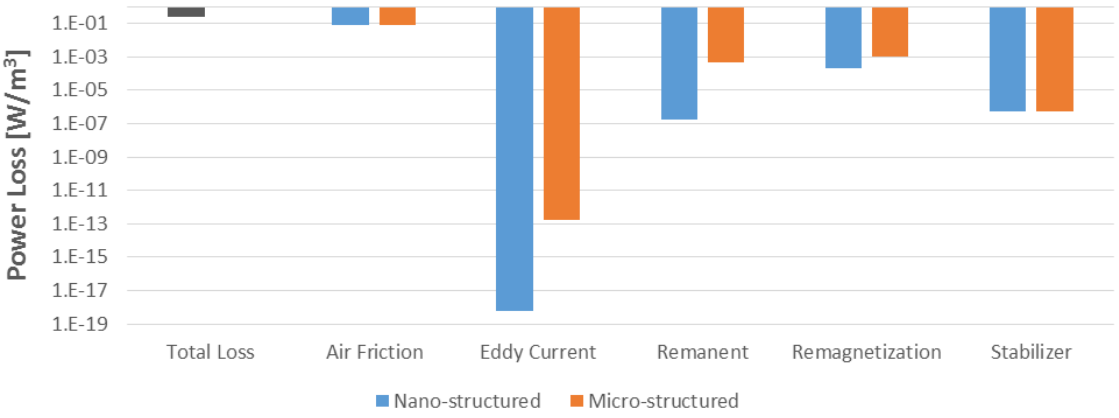

Figure 10-1: Power loss in contributions in the prototype diamagnetic bearing constructed in this study. Note that longer bars indicate lower loss. Eddy current, remanence induced cogging loss and remagnetization loss is smaller for an electrical machine made from nano-particles. Results from a combination of measurement and simulation.

Early in this study we noted that some existing studies have suggested that superconducting bearings experience losses in the order of $0.1 - 2$ [W] at 2500 [rpm]. While it is unclear what the power loss density is for this superconducing bearing, we can say that once air friction has been accounted for, losses in a diamagnetic bearing are likely able to compete. A diamagnetic bearing can have a power loss lower than 0.001 [$\mathrm{W/m^3}$] at 158 [rpm] assuming that we consider remagnetization loss as the greatest source of parasitic loss. If true, superparamagnetic materials can be produced, hysteresis loss can be eliminated, leaving the homopolar machine losses as the primary loss (ignoring air friction) – such losses would be in the order of 1×10^{-6} [$\mathrm{W/m^3}$] for a 158 [rpm] machine.

10.3 Magnetite Nanoparticle Synthesis

Magnetite nano-particles exhibit superparamagnetic properties that can eliminate remagnetization loss and resulting remanence induced cogging drag. Magnetite nano-particles, specifically, were chosen because of their ease of manufacture at the scales required for superparamagnetic behavior. The ceramic nature of magnetite also ensures a high electrical resistance and helps to reduce eddy current related losses. This study investigated a method of synthesizing magnetite nanoparticles and proposed a potential technique for the sintering of these particles to form low loss bulk material for use in our diamagnetic bearing electrical machine.

A well-established co-precipitation technique was used to synthesize magnetite particles by using $FeSO_4$ and $FeCl_3$ iron salt precursors combined with one of two bases: NaOH and NH_4OH. Five main comparative studies were attempted. An additive, polyethylene glycol, was used to limit oxidation effects during reaction. The effects of variations in quantity and molecular weight for PEG were examined. Likewise, base pH (plus type) and volume was varied to help increase the number of particle nucleation sites, stabilize temperature of reaction and reduce resulting

particle size. Some investigation of external cooling and the effect of nitrogen gas purging and externally applied magnetic field was also attempted.

Synthesized particles were evaluated using XRD, SEM and SQUID characterization. Additional crude colorimetry was also used for the characterization process. The data obtained from this process helped to assess particle morphology as shown in Figure 10-2. The figure shows the main properties measured via XRD and SEM characterization.

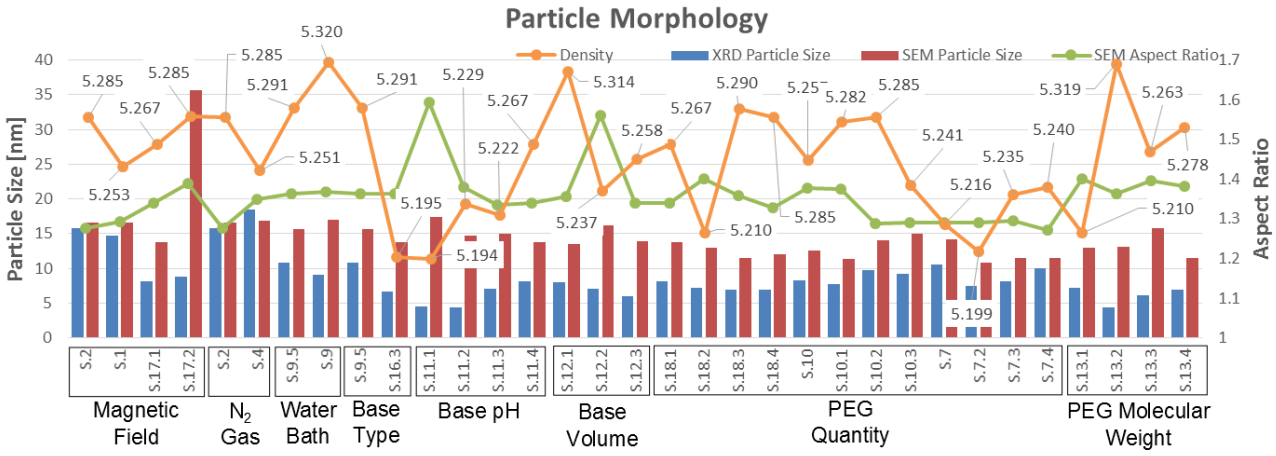

Figure 10-2: An overview of synthesis experiments and resultant characterization of particles. Note that a variety of different conditions were tested and examined. Measured SQUID, SEM and XRD data.

In addition to this characterization, SQUID magnetometry was used to determine and compute critical points of the hysteresis curve of the particular MNP material produced via synthesis. Figure 10-3 provides an overview for the various synthesis experiments attempted.

From here, coercivity, remanence, exchange bias and saturation together with XRD and SEM particle size and density information, were used to produce initial guess for hysteresis modelling. The modeling process made use of a modified version of the

Jiles-Atherton Model. Here an added term was introduced to account for antiferromagnetic exchange interactions. This model was used to generate a dense data set from sparse SQUID measurements by optimizing across six parameters, namely: $\theta = \{n, m, \chi_{AF}, \alpha, c, k\}$. The resulting fitted model was combined with ZFC and FC SQUID measurements and associated blocking temperature data to compute the frequency of operation for the synthesized nanoparticles and to estimate the power loss.

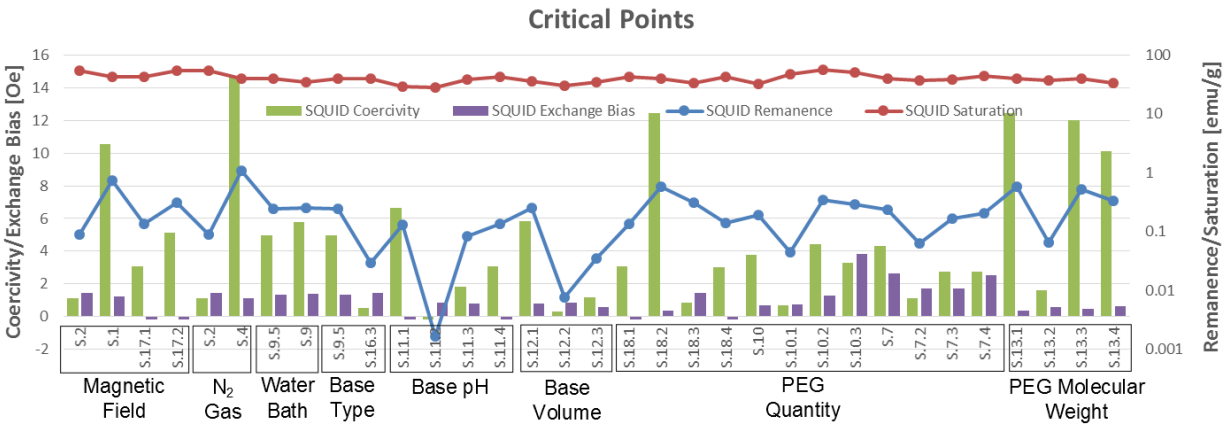

Figure 10-3: An overview of synthesis experiments and resultant extraction of critical parameters from SQUID measurements.

The power loss was divided into four losses. The first of these was a result of eddy currents induced in the reluctance machine as a result of operating frequency. The second of these was the loss occurring during power transfer between the reluctance machine rotor and stator and could mostly be represented by the major hysteresis loop power loss. The third was a result of remanent field cogging drag. The fourth was from idling state remagnetization of the rotor and was represented by minor hysteresis loop power loss. For the bulk reluctance machine, eddy current loss, remanent loss and remagnetization loss were presented in Figure 10-1. The effect of remagnetization related loss was expanded on a sample by sample basis as shown in Figure 10-4.

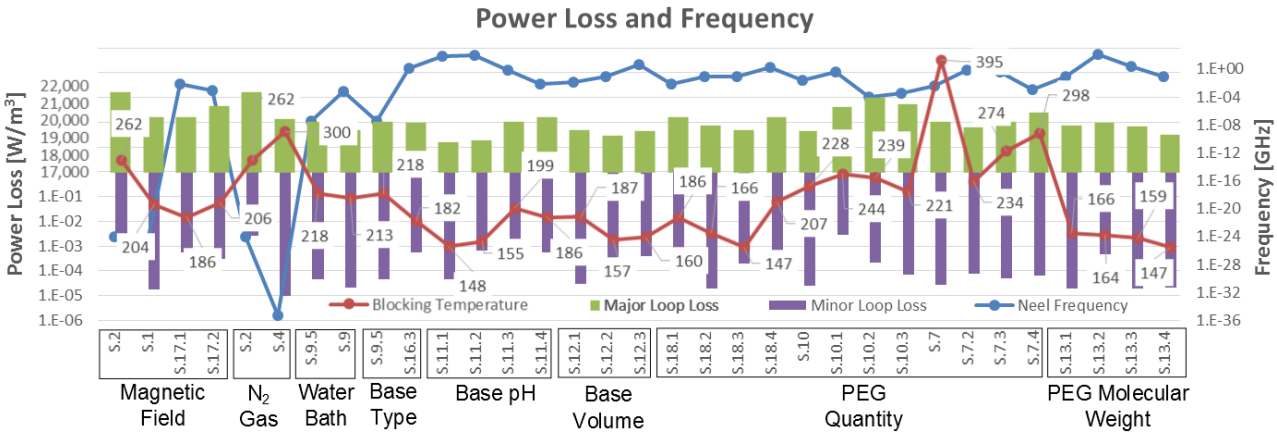

Figure 10-4: An overview of synthesis experiments and computation of power loss and operating frequency on a per sample basis. SQUID data and optimization results.

Of the samples synthesized only two exhibited coercivities that might indicate superparamagnetic behavior. The lowest of these fell at -0.17 ± 0.47 [Oe] and was accompanied by a remanence of 0.00165 ± 0.00070 [emu/g]. This remanence was also the lowest encountered in in any sample and corresponded to the smallest XRD particle size (4.36 [nm]) as well. The sample shown to exhibit this low coercivity and remanence was S.11.2 which made use of a high base pH of 14.80. Unfortunately, the fact that this lowest remanence value is considerably larger than the accompanying error suggests that even this sample has not achieved superparamagnetic behavior.

NaOH was found to be a safer and better base in that it allowed easy tuning of pH and produced smaller particle sizes. Further, unlike NH_4OH, the use of added quantities of PEG (300 [da] molecular weight) notably reduced particle size further when NaOH was used as the base. This added reduction was accompanied by lower oxidation as noted by the sample colorimetry. The same could not be said for

increases in the PEG molecular weight where no significant effect was noted barring a slight decrease in magnetic saturation. A final point of note was that increasing NaOH base quantity (or volume) showed slight decreases in particle size and corresponding remanence and coercivity. Clearly a higher volume and the resulting thermal stability improves synthesis conditions somewhat.

10.4 Magnetite Nanoparticle Sintering

A microwave sintering approach was proposed for converting powder synthesis MNP material to bulk materials. Microwave sintering approaches, while very new in discussions involving nano-particles were noted as having very high heating rates conducive to preserving nano-structure. To facilitate sintering the synthesized powders must be formed into some pre-sinter bulk green body. A die compress was designed and machined for this purpose. This die produced a small cylindrical green compress (14 [mm] x 10 [mm]) from clay material. This clay was formed into with the help of a methyl cellulose binder. These cylinders were used for pelletized bulk heating tests.

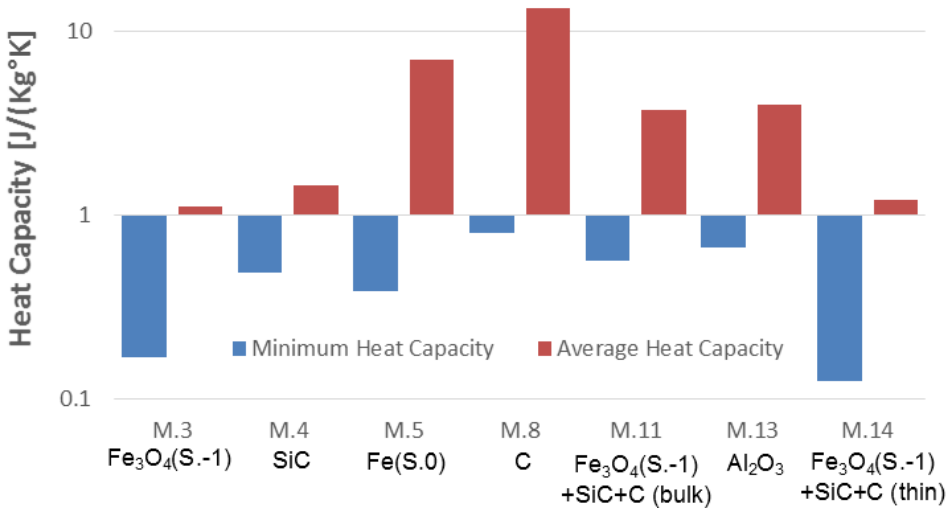

Figure 10-5: The average and minimum heat capacities of each material as it is heated from low temperature to peak temperature. Measured furnace data.

Figure 10-5 demonstrates the microwave response of the various susceptors produced. The peak heating rate was achieved for susceptor material made from a combination of magnetite, silicon carbide and carbon. This material achieved heating rates of up to 144 [℃/min]. It was noted that of the pure materials tested, bulk (pelletized) magnetite response to microwave irradiation was the best of all materials tested. It demonstrated the lowest specific heat capacity and was only exceeded by the combination thin film sample M.14. It has been left as a future exercise to attempt characterization of sintered nano-material samples. It is clear however that magnetite is a good choice for microwave sintering.

10.5 Thesis Statement

This study aimed to answer the question of whether diamagnetic bearings coupled with nano-structured ferrite cored electrical machines hold promise as a method of reducing parasitic loss in FES systems. The thesis of this study proposed that this was indeed the case. Looking at the results produced from this study we find that diamagnetic bearings are workable solutions towards this purpose for applications where high stiffness is not a critical factor. Such bearings are very well suited for flywheel energy storage applications. Furthermore, losses resulting from these bearings are extremely low and have shown that they can compete with existing superconducting solutions.

10.6 Contribution to Knowledge

Nine particular contributions to knowledge were provided by this study. A study of existing literature was used as a basis for the design and implementation of a radial multi-plattered diamagnetic bearing. This bearing is a small innovation on an

existing patent of a linear machine. Analytical expressions were derived for the particular implemented bearing design. These expressions can be used as design tools for engineering these bearings and producing implementations with predictable stabilities/stiffness and predictable rotor masses. A linear relationship between diamagnetic platters and increases in mass was shown for the first time. Further to these predictions, a detailed analysis was done, not only on the power loss in these bearings, but also the resulting improvements that nano-structured superparamagnetic ferrites can achieve relative to their micro-structured and lamination-based cousins. For the first time, the use of co-precipitation route synthesized MNPs has been extended to motor cores. A quantification of rotor idling losses resulting from hysteresis effects in these cores has been provided for the first time – such small loss contributors, relevant here, are not normally so for traditional electrical machines where other bearing losses dominate. Based on prior work, a modified Jiles-Atherton formulation involving an antiferromagnetic term and Monte Carlo parameter error estimation has been proposed for major and minor loop power loss estimation in these cores. The feasibility of a microwave sintering approach to taking synthesized nano-particles to bulk nano-structured material has also been analysed and a technique to implement this sintering trialled. The success of this sintering approach in maintaining nano-structure, however, remains an open question. Future characterization of sintered MNPs will answer this question with greater certainty.

10.7 Limitations and Future Work

It should be noted that there are a number of limitations to this work. The model derived for the diamagnetic bearing prototype built in this study involves a number of simplifications that aren't quite accurate. Furthermore, these models are quite complex for some geometrical arrangements making them difficult to implement without error. Future work should aim to simplify some of the mathematical models and resolve issues of inaccuracies somewhat.

The physical prototype bearing setup itself was noted as a poor testbed for making low error measurements. An improved setup is needed to test the diamagnetic bearing assembly. Better vacuum environments are needed for the bearing and a new motor design is required. A properly designed driver is needed to control the motor used in the setup and additional sensors needed for precise rotor position, velocity and force measurements. It is recommended that future work focus on better experimental controls and more functional prototype builds.

With regards to the synthesis process as well, the limited number trials made correlations difficult to ascertain. In most experimental routes attempted, the nature of the data was insufficient for true statistical relevance to be established. Any future work should aim at controlling experimental precision during synthesis more precisely and generating cross-correlation data. Further effort should be made to develop a more industrialized process where by a large number of trials can be run with greater relative ease. Such a process should also ensure that contamination is kept to a minimum – something that was difficult to do in the poorly controlled laboratory environments considered in this study. The waiting time before characterization and sintering attempts needs to be made more deterministic. Storage methods for samples were also less than ideal in this study. Further effort should be given to ensuring proper storage and timely measurement of synthesized samples in future work.

As was noted, sintering approaches remain in the very early stages. Much more characterization work is required for susceptor materials with regards to microwave sintering. Furthermore, a modified and better controlled furnace design will allow for more consistent and predictable susceptor and heating response. Samples generated in this study should go through a sintering regime and initial characterization with SEM, XRD and SQUID devices to verify that microwave sintering is a feasible and useful approach for the production of nano-structured materials.

This study has provided a promising starting point for assessing and exploring diamagnetic bearings and related nano-structured ferrite cored electrical machines for FES applications. It is hoped that the research community can advance this work towards a more sustainable and functional future for energy storage devices and renewable energy generation.

Appendix

A. Bearing Data (Measured and Simulated)

Bearing data was collected via both measurement and simulation. Simulations covered a range of different types and categories - a sample of these is provided below in Table A1.

Table A1: Measured and calculated results from bearing measurements

Category	Description	Sim	Magnet Br field [T]	Stabilizer/lifter Magnet Diameter (out, in) [mm]	Disc/Lifter/rotor Diameter [mm]	Air gap [mm]	Ang.Velocity [rpm]
Magnets near graphite disc	Centric, No Mag	E8a	0.34	40	36	4	1000
	Centric, Ring	E8b	0.34	40, 16	36	4	1000
	Centric, Disc	E8c	0.34	40	36	4	1000
	Off Center, Ring	E8d	0.34	40, 16	36	4	1000
	Off Center, Ring	E8e	0.34	40, 16	36	4	1000
	Off Center, Ring	E8f	0.34	40, 16	36	4	10000
	Off Center, Ring	E8g	0.34	40, 16	36	4	100000
	Centric, Disc	E8j	1	70	36	4	10000
Plate position changes	Disc, w/ yoke	E0a	1	20	20	0.2 (min)	0
	Disc w/o yoke	E2c	-1	40	36	0.1 (min)	0
	Ring w/o yoke	E2d	-1	40, 16	36	4	0
	Ring ring w/o yoke	E2a	1	40, 16	36	4	0
	Disc disc w/o yoke	E2b	1	40	36	4	0
	Disc disc, w/ yoke	E5	1	40	36	4	0
	Ring ring w/ yoke	E5a	1	40, 16	36	4	0
Plate thickness changes	Disc disc w/o yoke	E0b	1	30	30	10	0
	Ring ring w/o yoke	E6	1	40, 16	36	4	0
	Disc disc w/o yoke	E6b	1	40	36	4	0
	Ring ring w/ yoke	E6a	1	40, 16	36	4	0
Floater and lifter combinations and position changes	cylindrical floater w/ disc lifter	E0c	0.25, 0.32	40	30	0.25 (min)	0
	cylindrical floater w/ disc lifter	E3a	1	40	10 (floater)	0.5 (min)	0
	cylindrical floater w/ ring lifter	E3	1	40	10 (floater)	0.5 (min)	0
	cylindrical floater w/ stacked ring	E3b	1	40, 32.5,25	10 (floater)	0.5 (min)	0

	lifter						
	sphere floater w/ stacked ring lifter	E3c	1	40, 32.5,25	10 (floater)	0.5 (min)	0
	reluctance rotor floater w/ stacked ring lifter	E3d	1	40, 32.5,25	10 (floater), 5 (pole width)	0.5 (min)	0
Reluctance Motor	rotor forces	E4a	0.5 A current, 100 turns	-	10 (floater), 4 (pole width)	-	1000 rpm (coil freq.)

Table A2: A sample of simulation results for simulation set E8 combined with analytical values.

dg [m]	Bm2 (sandwich mag.) [T]	dBm2Dz (sandwich mag) [T/m]	ddBm2Dzz (sandwich mag.) [T/m2]	m_d2 (sandwich mag.) [N.m]	Fdp 5 platters [N]	Kdp 5 platters[N/m]	Diamagnet Force 5 platters [mN]
0	8.46786481	3.399757	-1623.99	-9.76E-06	0.01388	0.00269	13.87957062
0.0001	7.65056146	3.236809	-1634.9	-9.77E-06	0.011939	0.002446	11.93890674
0.0002	6.87352394	3.072795	-1645.29	-9.78E-06	0.010183	0.002212	10.1828013
0.0003	6.13700828	2.907768	-1655.17	-9.80E-06	0.008603	0.001987	8.6034105
0.0004	5.44125774	2.741779	-1664.52	-9.81E-06	0.007193	0.001771	7.19260044
0.0005	4.78650266	2.574881	-1673.34	-9.82E-06	0.005942	0.001567	5.941959924
0.0006	4.17296029	2.407128	-1681.62	-9.83E-06	0.004843	0.001372	4.842813156
0.0007	3.6008346	2.238574	-1689.36	-9.84E-06	0.003886	0.00119	3.886233756
0.0008	3.07031618	2.069274	-1696.55	-9.85E-06	0.003063	0.001019	3.0630588
0.0009	2.58158206	1.899283	-1703.18	-9.85E-06	0.002364	0.00086	2.363903568
0.001	2.13479558	1.728656	-1709.26	-9.86E-06	0.001779	0.000714	1.779176682
0.0011	1.7301063	1.55745	-1714.76	-9.87E-06	0.001299	0.00058	1.299095772
0.0012	1.36764989	1.385722	-1719.7	-9.87E-06	0.000914	0.00046	0.91370346
0.0013	1.04754796	1.213529	-1724.07	-9.88E-06	0.000613	0.000353	0.612883782
0.0014	0.769908084	1.040927	-1727.86	-9.88E-06	0.000386	0.00026	0.386378926
0.0015	0.534823612	0.867976	-1731.07	-9.89E-06	0.000224	0.000181	0.223806283
0.0016	0.34237367	0.694732	-1733.71	-9.89E-06	0.000115	0.000116	0.114675776
0.0017	0.192623074	0.521254	-1735.75	-9.89E-06	4.84E-05	6.54E-05	0.0484074
0.0018	0.085622285	0.3476	-1737.22	-9.89E-06	1.43E-05	2.91E-05	0.014348981
0.0019	0.021407376	0.173829	-1738.1	-9.89E-06	1.79E-06	7.28E-06	0.001794076
0.002	0	0	-1738.39	-9.90E-06	0	0	0
0.0021	0.021407376	-0.17383	-1738.1	-9.89E-06	-1.79E-06	7.28E-06	-0.00179408
0.0022	0.085622285	-0.3476	-1737.22	-9.89E-06	-1.43E-05	2.91E-05	-0.01434898
0.0023	0.192623074	-0.52125	-1735.75	-9.89E-06	-4.84E-05	6.54E-05	-0.0484074
0.0024	0.34237367	-0.69473	-1733.71	-9.89E-06	-0.00011	0.000116	-0.11467578
0.0025	0.534823612	-0.86798	-1731.07	-9.89E-06	-0.00022	0.000181	-0.22380628
0.0026	0.769908084	-1.04093	-1727.86	-9.88E-06	-0.00039	0.00026	-0.38637893
0.0027	1.04754796	-1.21353	-1724.07	-9.88E-06	-0.00061	0.000353	-0.61288378
0.0028	1.36764989	-1.38572	-1719.7	-9.87E-06	-0.00091	0.00046	-0.91370346

0.0029	1.7301063	-1.55745	-1714.76	-9.87E-06	-0.0013	0.00058	-1.29909577
0.003	2.13479558	-1.72866	-1709.26	-9.86E-06	-0.00178	0.000714	-1.77917668
0.0031	2.58158206	-1.89928	-1703.18	-9.85E-06	-0.00236	0.00086	-2.36390357
0.0032	3.07031618	-2.06927	-1696.55	-9.85E-06	-0.00306	0.001019	-3.0630588
0.0033	3.6008346	-2.23857	-1689.36	-9.84E-06	-0.00389	0.00119	-3.88623376
0.0034	4.17296029	-2.40713	-1681.62	-9.83E-06	-0.00484	0.001372	-4.84281316
0.0035	4.78650266	-2.57488	-1673.34	-9.82E-06	-0.00594	0.001567	-5.94195992
0.0036	5.44125774	-2.74178	-1664.52	-9.81E-06	-0.00719	0.001771	-7.19260044
0.0037	6.13700828	-2.90777	-1655.17	-9.80E-06	-0.0086	0.001987	-8.6034105
0.0038	6.87352394	-3.0728	-1645.29	-9.78E-06	-0.01018	0.002212	-10.1828013
0.0039	7.65056146	-3.23681	-1634.9	-9.77E-06	-0.01194	0.002446	-11.9389067
0.004	8.46786481	-3.39976	-1623.99	-9.76E-06	-0.01388	0.00269	-13.8795706

Figure A1 below demonstrates diagrammatic results from simulations of the bearing assembly. Notice that the simulations below are parameterized to display or remove different geometric blocks such as the stabilizer magnets, floater and lifters and the yoke.

Figure A1: Example of various simulations from table A1.

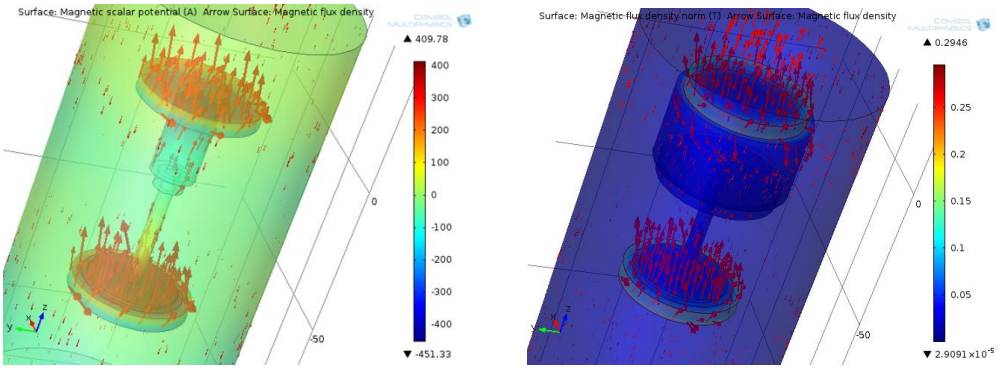

Table A3: Measured and calculated data from actual bearing operation. Measured optically.

Time [s]	Smooth Average Speed [rps]	acceleration [rev/s2]	Smooth Power Loss [W]	Air friction power loss	Magnetic Power Loss [W]	Remanent Loss [W]	Eddy loss (lamination) [W/Kg]	Eddy Loss ferrite [W/Kg]
1	0.646315	-0.05473	7.73666E-08	3.84106E-09	7.35255E-08	3.77E-10	8.74E-01	1.93E-18
2	0.60704	-0.03928	6.47578E-08	3.18251E-09	6.15753E-08	3.54E-10	7.71E-01	1.70E-18
3	0.613223	0.006183	4.59362E-08	3.28075E-09	4.26554E-08	3.59E-10	7.86E-01	1.73E-18
4	0.576594	-0.03663	4.60011E-08	2.72727E-09	4.32739E-08	3.36E-10	6.95E-01	1.53E-18
5	0.53176	-0.04483	4.72303E-08	2.13927E-09	4.5091E-08	3.12E-10	5.91E-01	1.30E-18
6	0.504193	-0.02757	3.78375E-08	1.82351E-09	3.60139E-08	2.95E-10	5.32E-01	1.17E-18
7	0.481984	-0.02221	3.20903E-08	1.593E-09	3.04973E-08	2.83E-10	4.86E-01	1.07E-18
8	0.439313	-0.04267	3.86325E-08	1.20625E-09	3.74262E-08	2.53E-10	4.04E-01	8.90E-19
9	0.445734	0.006422	3.06455E-08	1.25993E-09	2.93856E-08	2.59E-10	4.16E-01	9.16E-19
10	0.426036	-0.0197	2.38873E-08	1.10017E-09	2.27872E-08	2.47E-10	3.80E-01	8.37E-19
11	0.412609	-0.01343	2.02304E-08	9.99391E-10	1.92311E-08	2.42E-10	3.56E-01	7.85E-19
12	0.405057	-0.00755	1.6886E-08	9.45513E-10	1.59405E-08	2.36E-10	3.43E-01	7.57E-19
13	0.403083	-0.00197	9.0333E-09	9.31757E-10	8.10154E-09	2.36E-10	3.40E-01	7.49E-19
14	0.386313	-0.01677	1.06153E-08	8.20228E-10	9.79508E-09	2.24E-10	3.12E-01	6.88E-19
15	0.389552	0.00324	7.49618E-09	8.41036E-10	6.65515E-09	2.24E-10	3.17E-01	7.00E-19
16	0.38976	0.000208	5.1081E-09	8.42387E-10	4.26572E-09	2.24E-10	3.18E-01	7.01E-19
17	0.398313	0.008552	5.26007E-09	8.99063E-10	4.361E-09	2.30E-10	3.32E-01	7.32E-19
17.5	0.368896	-0.05883	1.44064E-08	7.14216E-10	1.36922E-08	2.12E-10	2.85E-01	6.28E-19
18	0.368677	-0.00044	1.16427E-08	7.12946E-10	1.09298E-08	2.12E-10	2.84E-01	6.27E-19
19	0.384854	0.016177	1.38142E-08	8.10974E-10	1.30033E-08	2.24E-10	3.10E-01	6.83E-19
19.5	0.358052	-0.0536	2.2175E-08	6.53066E-10	2.15219E-08	2.06E-10	2.68E-01	5.91E-19
20	0.352542	-0.01102	2.23845E-08	6.23375E-10	2.17611E-08	2.06E-10	2.60E-01	5.73E-19
21	0.374677	0.022135	1.65182E-08	7.48324E-10	1.57699E-08	2.18E-10	2.94E-01	6.47E-19
23	0.377781	0.001552	1.67041E-08	7.67078E-10	1.59371E-08	2.18E-10	2.98E-01	6.58E-19
24	0.334979	-0.0428	2.02528E-08	5.34776E-10	1.97181E-08	1.94E-10	2.35E-01	5.18E-19
25	0.340542	0.005562	1.26853E-08	5.61861E-10	1.21234E-08	2.00E-10	2.43E-01	5.35E-19
26	0.325214	-0.01533	1.31663E-08	4.89355E-10	1.26769E-08	1.89E-10	2.21E-01	4.88E-19
27	0.318974	-0.00624	1.04088E-08	4.61726E-10	9.94708E-09	1.83E-10	2.13E-01	4.69E-19
29	0.31612	-0.00143	1.03497E-08	4.49442E-10	9.90021E-09	1.83E-10	2.09E-01	4.61E-19
30	0.327953	0.011833	5.7751E-09	5.01826E-10	5.27327E-09	1.89E-10	2.25E-01	4.96E-19
31	0.337943	0.00999	6.42326E-09	5.49095E-10	5.87416E-09	1.94E-10	2.39E-01	5.27E-19
32	0.343125	0.005182	5.02043E-09	5.74745E-10	4.44569E-09	2.00E-10	2.46E-01	5.43E-19
33	0.342792	-0.00033	4.19975E-09	5.73072E-10	3.62668E-09	2.00E-10	2.46E-01	5.42E-19
34	0.330302	-0.01249	5.80708E-09	5.12687E-10	5.29439E-09	1.94E-10	2.28E-01	5.03E-19
35	0.328104	-0.0022	4.42486E-09	5.0252E-10	3.92234E-09	1.89E-10	2.25E-01	4.97E-19
36	0.322844	-0.00526	3.69096E-09	4.78735E-10	3.21223E-09	1.89E-10	2.18E-01	4.81E-19
37	0.314125	-0.00872	4.11119E-09	4.40987E-10	3.6702E-09	1.83E-10	2.06E-01	4.55E-19

38	0.301583	-0.01254	5.71585E-09	3.90248E-10	5.3256E-09	1.77E-10	1.90E-01	4.19E-19
39	0.292888	-0.0087	5.02527E-09	3.57456E-10	4.66782E-09	1.71E-10	1.79E-01	3.96E-19
40	0.283971	-0.00892	5.81749E-09	3.25793E-10	5.4917E-09	1.65E-10	1.69E-01	3.72E-19
41	0.275721	-0.00825	6.06965E-09	2.98215E-10	5.77143E-09	1.59E-10	1.59E-01	3.51E-19
42	0.267065	-0.00866	5.88285E-09	2.71E-10	5.61185E-09	1.53E-10	1.49E-01	3.29E-19
43	0.266482	-0.00058	4.29622E-09	2.69228E-10	4.02699E-09	1.53E-10	1.49E-01	3.28E-19
44	0.262979	-0.0035	3.58506E-09	2.58751E-10	3.32631E-09	1.53E-10	1.45E-01	3.19E-19
45	0.257349	-0.00563	3.11122E-09	2.42485E-10	2.86874E-09	1.47E-10	1.39E-01	3.05E-19
46	0.249589	-0.00776	2.96345E-09	2.21204E-10	2.74225E-09	1.41E-10	1.30E-01	2.87E-19
47	0.243177	-0.00641	2.63419E-09	2.04591E-10	2.4296E-09	1.41E-10	1.24E-01	2.73E-19
48	0.23375	-0.00943	3.53017E-09	1.81708E-10	3.34846E-09	1.36E-10	1.14E-01	2.52E-19
49	0.227031	-0.00672	3.79451E-09	1.66485E-10	3.62802E-09	1.30E-10	1.08E-01	2.38E-19
50	0.223443	-0.00359	3.51143E-09	1.58715E-10	3.35271E-09	1.30E-10	1.04E-01	2.30E-19
51	0.223016	-0.00043	2.70577E-09	1.57806E-10	2.54796E-09	1.30E-10	1.04E-01	2.29E-19
52	0.22026	-0.00276	2.28919E-09	1.52029E-10	2.13716E-09	1.30E-10	1.01E-01	2.24E-19
53	0.218417	-0.00184	1.50138E-09	1.48243E-10	1.35313E-09	1.24E-10	9.98E-02	2.20E-19
54	0.216323	-0.00209	1.03223E-09	1.44021E-10	8.88205E-10	1.24E-10	9.79E-02	2.16E-19
55	0.216729	0.000406	7.1997E-10	1.44834E-10	5.75136E-10	1.24E-10	9.82E-02	2.17E-19
56	0.212979	-0.00375	1.02769E-09	1.37445E-10	8.90248E-10	1.24E-10	9.49E-02	2.09E-19
57	0.212323	-0.00066	8.23167E-10	1.36179E-10	6.86989E-10	1.24E-10	9.43E-02	2.08E-19
58	0.207396	-0.00493	1.09402E-09	1.26917E-10	9.67106E-10	1.18E-10	9.00E-02	1.98E-19
59	0.205495	-0.0019	1.06678E-09	1.23458E-10	9.43323E-10	1.18E-10	8.83E-02	1.95E-19
60	0.202432	-0.00306	1.29947E-09	1.18021E-10	1.18145E-09	1.18E-10	8.57E-02	1.89E-19
61	0.202229	-0.0002	9.6805E-10	1.17666E-10	8.50384E-10	1.18E-10	8.55E-02	1.89E-19
62	0.200281	-0.00195	1.07776E-09	1.14298E-10	9.63464E-10	1.18E-10	8.39E-02	1.85E-19
64	0.199974	-0.00015	6.4418E-10	1.13773E-10	5.30407E-10	1.18E-10	8.36E-02	1.84E-19
65	0.194823	-0.00515	9.12295E-10	1.05205E-10	8.07089E-10	1.12E-10	7.94E-02	1.75E-19
66	0.194063	-0.00076	7.05646E-10	1.03978E-10	6.01668E-10	1.12E-10	7.88E-02	1.74E-19
67	0.189672	-0.00439	1.05199E-09	9.70794E-11	9.54906E-10	1.06E-10	7.52E-02	1.66E-19
68	0.183547	-0.00612	1.37312E-09	8.7975E-11	1.28515E-09	1.06E-10	7.05E-02	1.55E-19
69	0.181839	-0.00171	1.49558E-09	8.55413E-11	1.41003E-09	1.06E-10	6.92E-02	1.53E-19
71	0.179885	-0.00098	1.13341E-09	8.28144E-11	1.0506E-09	1.00E-10	6.77E-02	1.49E-19
72	0.17549	-0.0044	1.40633E-09	7.68904E-11	1.32944E-09	1.00E-10	6.44E-02	1.42E-19
74	0.17375	-0.00087	1.10813E-09	7.46264E-11	1.0335E-09	1.00E-10	6.31E-02	1.39E-19
75	0.173021	-0.00073	6.71514E-10	7.36908E-11	5.97823E-10	1.00E-10	6.26E-02	1.38E-19
76	0.167453	-0.00557	9.4348E-10	6.68033E-11	8.76676E-10	9.43E-11	5.86E-02	1.29E-19
77	0.165323	-0.00213	1.02069E-09	6.42861E-11	9.56407E-10	9.43E-11	5.72E-02	1.26E-19
78	0.160396	-0.00493	1.02894E-09	5.8708E-11	9.70236E-10	9.43E-11	5.38E-02	1.19E-19
79	0.155292	-0.0051	1.30958E-09	5.32798E-11	1.2563E-09	8.84E-11	5.04E-02	1.11E-19
80	0.152625	-0.00267	1.43244E-09	5.05819E-11	1.38185E-09	8.84E-11	4.87E-02	1.07E-19
81	0.150292	-0.00233	1.17799E-09	4.82973E-11	1.12969E-09	8.84E-11	4.72E-02	1.04E-19
82	0.147521	-0.00277	1.20274E-09	4.5675E-11	1.15706E-09	8.25E-11	4.55E-02	1.00E-19

83	0.146542	-0.00098	9.19791E-10	4.47715E-11	8.75019E-10	8.25E-11	4.49E-02	9.90E-20
84	0.142688	-0.00385	8.13622E-10	4.1331E-11	7.72291E-10	8.25E-11	4.26E-02	9.39E-20
85	0.139688	-0.003	8.18899E-10	3.87785E-11	7.8012E-10	7.66E-11	4.08E-02	9.00E-20
86	0.139385	-0.0003	6.83909E-10	3.85274E-11	6.45381E-10	7.66E-11	4.06E-02	8.96E-20
88	0.136656	-0.00136	5.86671E-10	3.63084E-11	5.50363E-10	7.66E-11	3.91E-02	8.61E-20

B. X-Ray Diffraction Measurements

XRD measurements were taken using a Bruker D8 Advanced X-Ray Powder Diffraction device. A summary of measured and calculated XRD results for synthesized nano-particles are shown in the table below. These measurements pertain to samples prior to sintering.

Table B: Measured and calculated results from Powder XRD analysis.

Type of Sample	Sample No.	XRD Fe_3O_4 [%]	XRD Fe3O4 [nm]	Lattice Parameter [nm]	Crystal Density [g/cm^3]
Commercial Samples	-1	-	109.9 ± 8.6	0.839687 ± 0.000074	5.1953 ± 0.0014
	0	24 ± 13	75 ± 28	0.286339 ± 0.000053	7.9001 ± 0.0044
NH4OH no peg	1	-	14.7 ± 2.2	0.8366 ± 0.0020	5.253 ± 0.037
	2	-	13.8 ± 1.1, 22.7 ± 4.6, 10.76 ± 0.81	0.8369 ± 0.0030	5.285 ± 0.012
NH4OH w/ PEG & N2	4	-	19.2 ± 1.9, 17.8 ± 1.6	0.83673 ± 0.00048	5.2505 ± 0.0091
NaOH No PEG / Yes PEG	7	76.7 ± 3.7	10.57 ± 0.57	0.83857 ± 0.00028	5.2160 ± 0.0052
	7.1	93.7 ± 1.6	8.08 ± 0.51	0.83879 ± 0.00070	5.212 ± 0.013
	7.2	78.0 ± 4.8	7.42 ± 0.46	0.83951 ± 0.00047	5.1986 ± 0.0087
	7.3	79.2 ± 4.5	8.08 ± 0.57	0.83754 ± 0.00053	5.2353 ± 0.0099
	7.4	81.3 ± 6.7	9.94 ± 0.68	0.83730 ± 0.00041	5.2398 ± 0.0078
NH4OH bath	9	-	9.0 ± 1.4	0.8331 ± 0.0017	5.320 ± 0.032
	9.5	-	10.8 ± 1.4	0.8346 ± 0.0012	5.291 ± 0.022
NH4OH no PEG/ yes peg	10	-	8.32 ± 0.88	0.8364 ± 0.0033	5.257 ± 0.062
	10.1	-	7.69 ± 0.99	0.8350 ± 0.0019	5.282 ± 0.036
	10.2	-	9.73 ± 0.87	0.8349 ± 0.0011	5.285 ± 0.020
	10.3	-	9.22 ± 0.56	0.8372 ± 0.0038	5.241 ± 0.072

NaOH at different pH	11.1	89.23 ± 0.68, 89.43 ± 0.70	4.96 ± 0.28, 4.14 ± 0.27	0.83976 ± 0.00079	5.194 ± 0.015
	11.2	79.71 ± 0.87	4.36 ± 0.26	0.83790 ± 0.00068	5.229 ± 0.013
	11.3	74.3 ± 1.1	7.04 ± 0.50	0.83826 ± 0.00052	5.2219 ± 0.0097
	11.4	76.88 ± 0.93	8.09 ± 0.51	0.83586 ± 0.00043	5.2671 ± 0.0081
NaOh at different volume	12.1	67.9 ± 1.2	7.94 ± 0.64	0.83339 ± 0.00052	5.3139 ± 0.0099
	12.2	83.36 ± 0.72	7.10 ± 0.40	0.83743 ± 0.00040	5.2373 ± 0.0076
	12.3	80.2 ± 1.0	5.94 ± 0.44	0.83632 ± 0.00062	5.258 ± 0.012
NaOH and varying PEG molecular weight	13.1	84.48 ± 0.70	7.20 ± 0.37	0.83888 ± 0.00034	5.2103 ± 0.0064
	13.2	84.2 ± 1.2	4.43 ± 0.39	0.83315 ± 0.00097	5.319 ± 0.019
	13.3	90.48 ± 0.60	6.16 ± 0.36	0.83608 ± 0.00046	5.2627 ± 0.0086
	13.4	71.2 ± 1.6	6.88 ± 0.69	0.83526 ± 0.00074	5.278 ± 0.014
NaOH/NH4OH w&w/o N2	16.3	76.99 ± 0.96	6.63 ± 0.43	0.83971 ± 0.00050	5.1949 ± 0.0093
NaOH w&w/o mag	17.1	76.88 ± 0.93	8.09 ± 0.51	0.83586 ± 0.00043	5.2671 ± 0.0081
	17.2	82.13 ± 0.75	8.83 ± 0.48	0.83490 ± 0.00033	5.2851 ± 0.0063
NaOH w/wo peg	18.1	76.88 ± 0.93	8.09 ± 0.51	0.83586 ± 0.00043	5.2671 ± 0.0081
	18.2	84.48 ± 0.70	7.20 ± 0.37	0.83888 ± 0.00034	5.2103 ± 0.0064
	18.3	93.12 ± 0.70	6.88 ± 0.65	0.83465 ± 0.00092	5.290 ± 0.018
	18.4	86.31 ± 0.74	6.85 ± 0.42	0.83493 ± 0.00047	5.2846 ± 0.0088

C. Scanning Electron Microscope Measurements

SEM measurements were made on a Carl Zeiss SIGMA HD VP Field Emission SEM. Analysis of SEM data is presented in the Table C below.

Table C: Measured and calculated results from SEM and associate image analysis.

Type of Sample	Sample No.	SEM Mean Size +/- Std [nm] (manual)	SEM Hand Select Spread: Max Error [nm] (manual)	SEM Multiple Alg. Mean Size +/- Mean Std [nm] (automatic)	SEM Multiple Alg. Spread: Mean Error +/- error std (automatic)	SEM Mean Aspect Ratio +/- Std (manual) []	SEM Aspect Ratio Hand Select Spread: Max Error (manual) []
Commercial Samples	-1	1222.98 ± 2.62	569.11	1884.92 ± 1.96	917.40 ± 168.49	1.631 ± 0.505	0.448
	0	37.07 ± 13.02, 34.81 ± 14.51	15.03, 10.59	21.87 ± 13.68, 30.73 ± 18.51	1.02 ± 1.61, 0.90 ± 1.52	1.427 ± 0.337, 1.387 ± 0.296	0.397, 0.262
NH4OH no peg	1	24.35 ± 5.24	6.28	16.54 ± 8.79	0.41 ± 0.52	1.292 ± 0.193	0.240
	2	20.90 ± 3.85	5.63	16.64 ± 9.40	1.71 ± 0.87	1.277 ± 0.210	0.462

NH4OH w/ PEG & N2	4	41.38 ± 13.48, 36.22 ± 21.76, 26.77 ± 13.45, 24.77 ± 9.09	12.62, 15.68, 7.51, 4.17	16.30 ± 8.68, 16.72 ± 10.06, 17.39 ± 9.65, 16.80 ± 8.48	1.92 ± 0.62, 1.32 ± 0.78, 0.80 ± 0.80, 1.21 ± 0.60	1.327 ± 0.243, 1.323 ± 0.221, 1.372 ± 0.252, 1.374 ± 0.212	0.316, 0.571, 0.382, 0.420
NaOH No PEG / Yes PEG	7	19.79 ± 4.31	4.80	14.20 ± 7.37	2.95 ± 0.47	1.290 ± 0.190	0.399
	7.1	12.74 ± 2.89	2.76	11.33 ± 5.30	1.18 ± 0.33	1.311 ± 0.200	0.418
	7.2	12.58 ± 2.96	2.48	10.87 ± 5.10	1.54 ± 0.39	1.290 ± 0.211	0.368
	7.3	12.76 ± 2.66	3.37	11.54 ± 5.39	1.93 ± 0.38	1.294 ± 0.208	0.276
	7.4	13.25 ± 2.56	2.35	11.44 ± 5.46	1.24 ± 0.62	1.271 ± 0.229	0.406
NH4OH bath	9	23.41 ± 6.94	2.59	16.98 ± 9.38	2.94 ± 1.64	1.367 ± 0.259	0.328
	9.5	32.84 ± 12.30, 25.01 ± 8.49, 18.26 ± 7.40, 19.80 ± 4.84	7.33, 12.26, 2.91, 3.02	15.89 ± 8.39, 16.82 ± 9.15, 14.94 ± 7.61, 14.94 ± 7.46	1.72 ± 0.56, 4.71 ± 0.70, 3.58 ± 0.47, 3.75 ± 0.48	1.416 ± 0.310, 1.364 ± 0.235, 1.343 ± 0.226, 1.331 ± 0.231	0.197, 0.293, 0.212, 0.340
NH4OH no PEG/ yes peg	10	11.00 ± 2.64	3.19	12.56 ± 6.55	2.98 ± 0.56	1.377 ± 0.269	0.260
	10.1	10.05 ± 2.66	2.85	11.35 ± 5.36	1.97 ± 0.37	1.376 ± 0.239	0.315
	10.2	13.17 ± 3.04	2.16	13.97 ± 6.62	2.43 ± 0.57	1.289 ± 0.190	0.234
	10.3	16.83 ± 3.88	2.53	14.94 ± 7.25	2.10 ± 0.65	1.290 ± 0.205	0.215
NaOH at different pH	11.1	41.15 ± 1.47	3.86	17.38 ± 1.83	0.27 ± 0.69	1.594 ± 0.462	0.163
	11.2	15.34 ± 3.55	2.33	14.68 ± 7.64	1.70 ± 0.44	1.380 ± 0.257	0.240
	11.3	20.26 ± 6.09	1.90	14.92 ± 8.04	2.00 ± 0.77	1.335 ± 0.209	0.150
	11.4	13.19 ± 2.37	3.25	13.72 ± 6.82	3.91 ± 0.39	1.340 ± 0.977	0.434
NaOh at different volume	12.1	12.82 ± 3.23	2.13	13.56 ± 6.88	3.77 ± 0.62	1.356 ± 0.228	0.292
	12.2	29.76 ± 11.70, 29.24 ± 13.21, 26.57 ± 12.95, 29.07 ± 14.42	8.15, 3.38, 3.25, 2.95	16.25 ± 8.38, 17.01 ± 8.71, 15.40 ± 7.73, 16.15 ± 9.45	3.84 ± 0.63, 3.38 ± 0.62, 3.15 ± 0.53, 2.91 ± 0.60	2.171 ± 0.873, 1.424 ± 0.290, 1.368 ± 0.245, 1.279 ± 0.184	0.769, 0.390, 0.440, 0.261
	12.3	15.53 ± 3.47, 13.01 ± 2.61, 12.56 ± 2.64, 11.85 ± 2.55	3.16, 1.43, 3.74, 2.30	17.37 ± 8.97, 13.62 ± 7.20, 12.26 ± 5.53, 12.31 ± 5.66	2.12 ± 0.67, 3.64 ± 0.47, 2.72 ± 0.26, 3.00 ± 0.29	1.449 ± 0.361, 1.318 ± 0.202, 1.305 ± 0.222, 1.291 ± 0.175	0.326, 0.373, 0.342, 0.303
NaOH and varying PEG molecular weight	13.1	10.77 ± 3.04	2.33	13.00 ± 6.56	2.55 ± 0.52	1.400 ± 0.267	0.364
	13.2	11.93 ± 3.41	1.79	13.10 ± 7.29	3.18 ± 0.62	1.362 ± 0.239	0.346
	13.3	19.73 ± 10.77	4.16	15.72 ± 8.08	4.13 ± 0.53	1.395 ± 0.276	0.481
	13.4	10.29 ± 2.82	1.63	11.44 ± 5.24	3.13 ± 0.24	1.383 ± 0.271	0.235
NaOH/NH4OH w&w/o N2	16.3	13.21 ± 3.74	3.16	13.74 ± 6.80	3.41 ± 0.39	1.363 ± 0.251	0.295
NaOH w&w/o mag	17.1	13.19 ± 2.39	3.25	13.72 ± 6.82	3.91 ± 0.39	1.340 ± 0.977	0.434
	17.2	39.31 ± 28.88	5.08	35.69 ± 17.91	1.50 ± 2.79	1.390 ± 0.265	0.056
NaOH w/wo peg	18.1	13.19 ± 2.39	3.25	13.72 ± 6.82	3.91 ± 0.39	1.340 ± 0.977	0.434
	18.2	10.77 ± 3.04	2.33	13.00 ± 6.56	2.55 ± 0.52	1.400 ± 0.267	0.364
	18.3	12.78 ± 3.55	2.37	11.46 ± 5.33	3.65 ± 0.24	1.358 ± 0.232	0.236
	18.4	13.35 ± 3.23	2.31	11.96 ± 6.14	2.67 ± 0.30	1.327 ± 0.248	0.410

Figure C below shows a sample set of SEM images from which the above data was obtained.

Figure C: Measured and calculated results from SEM and associate image analysis. Samples displayed from left to right and top to bottom in the following order: -1, 0, 1, 2, 4, 7, 7.1, 7.2, 7.3, 7.4, 9, 9.5, 10, 10.1, 10.2, 10.3, 11.1, 11.2, 11.3, 11.4, 12.1, 12.2, 12.3, 13.2, 13.3, 13.4, 16.3, 17.2, 18.2, 18.3, 18.4.

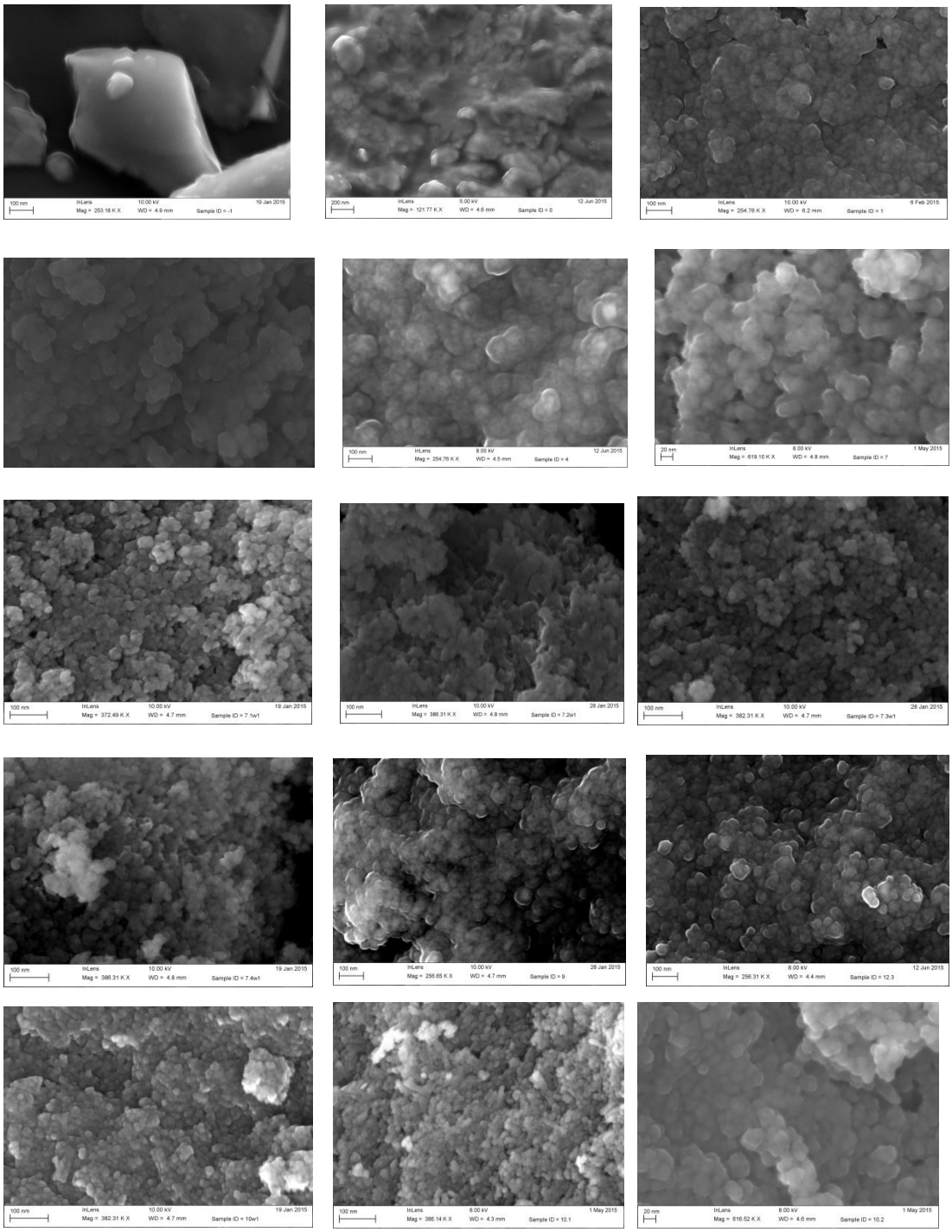

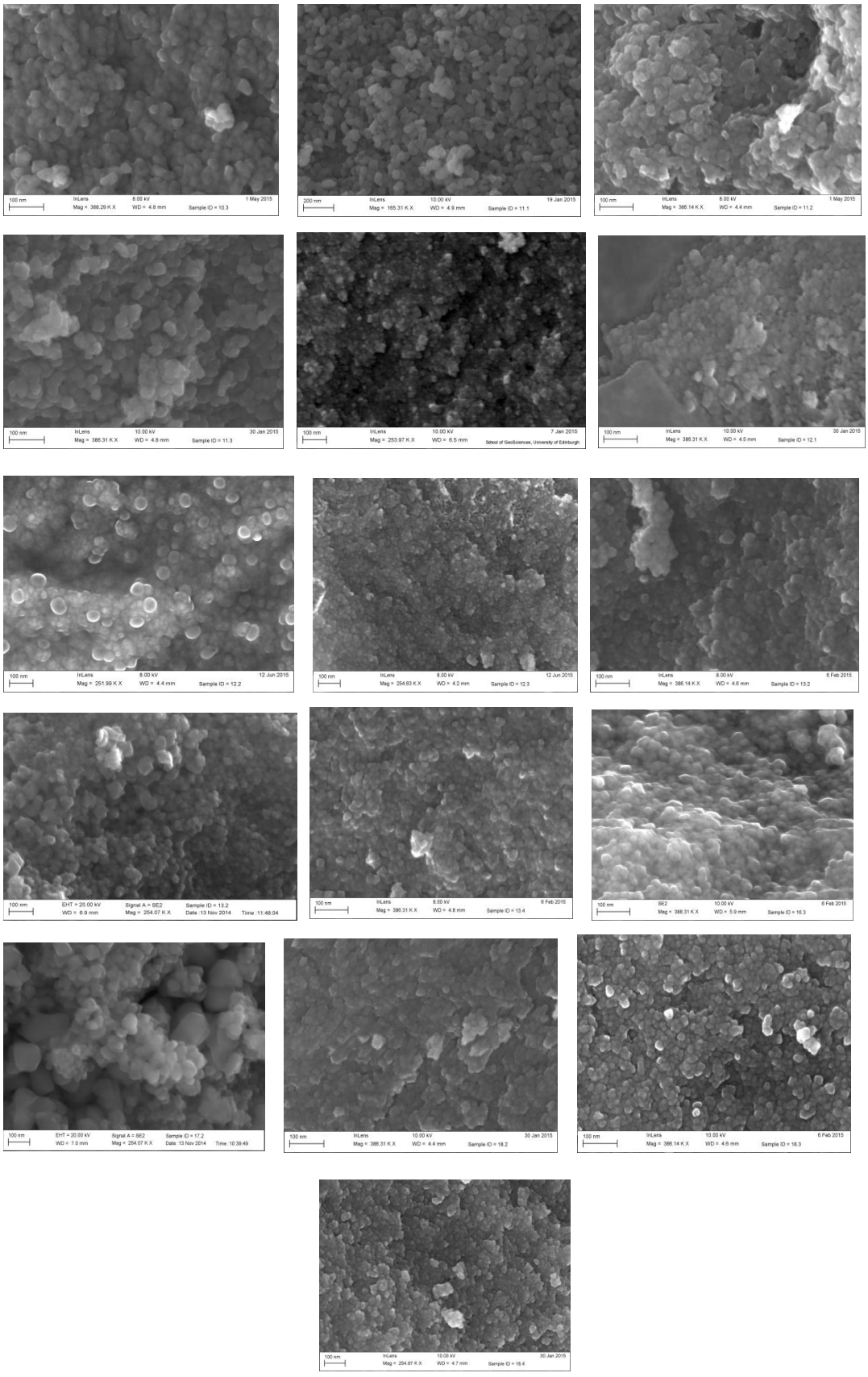

D. SQUID Magnetometer Hysteresis Measurements

Measurements of hysteresis loop data were obtained from a Quantum Design MPMS Superconducting Quantum Interference Device (SQUID). Data collected was sparse in order to cover measurements for a large number of samples. Figure D shows a graphical representation of the data collected from SQUID measurements.

Figure D: Measured results from SQUID magnetometery. Samples displayed from top to bottom in the following order: -1, 0, 1, 2, 4, 7, 7.1, 7.2, 7.3, 7.4, 9, 9.5, 10, 10.1, 10.2, 10.3, 11.1, 11.2, 11.3, 11.4, 12.1, 12.2, 12.3, 13.2, 13.3, 13.4, 16.3, 17.2, 18.2, 18.3, 18.4. Right hand graphs show a close up of the x and y intercept locations of the hysteresis curve. Note that in some cases a cusp is visible in the graphs. This is a result of sparse data in the intermediate regions of the graph not as a result of anomalies in measurement.

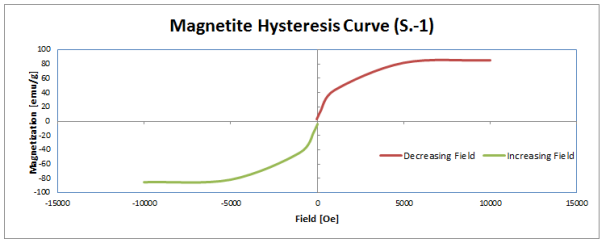

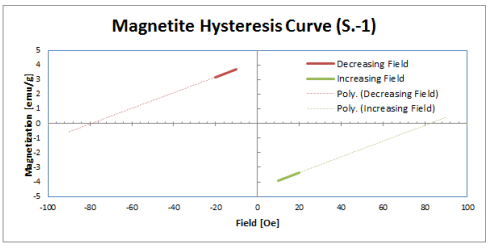

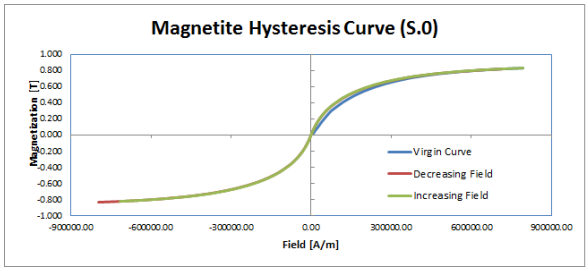

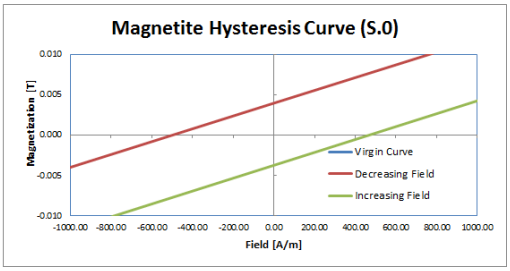

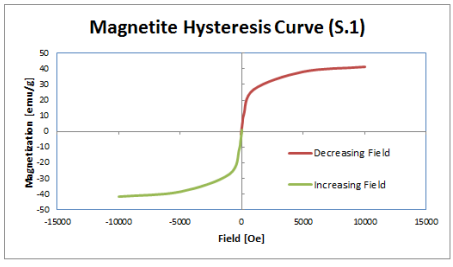

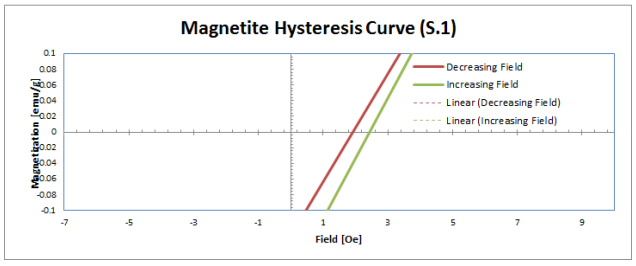

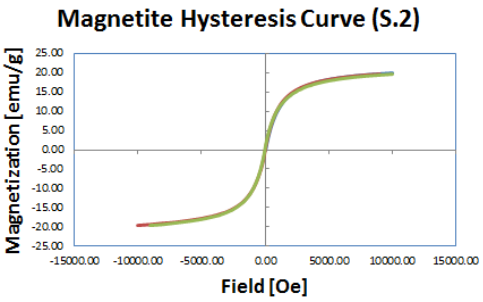
Magnetite Hysteresis Curve (S.2)
Magnetization [emu/g]
Field [Oe]

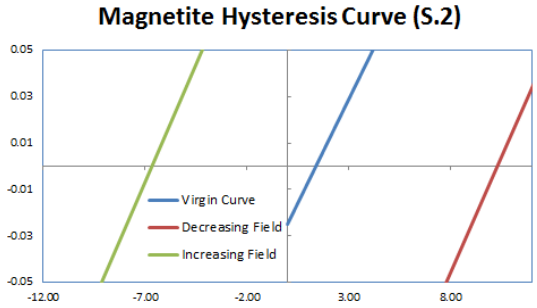
Magnetite Hysteresis Curve (S.2)
Virgin Curve
Decreasing Field
Increasing Field

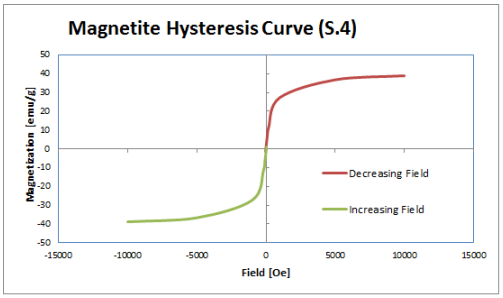
Magnetite Hysteresis Curve (S.4)
Magnetization [emu/g]
Decreasing Field
Increasing Field
Field [Oe]

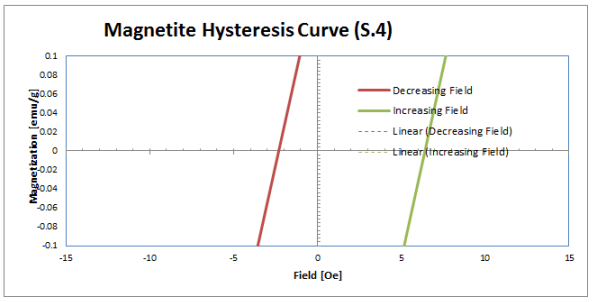
Magnetite Hysteresis Curve (S.4)
Decreasing Field
Increasing Field
Linear (Decreasing Field)
Linear (Increasing Field)
Field [Oe]

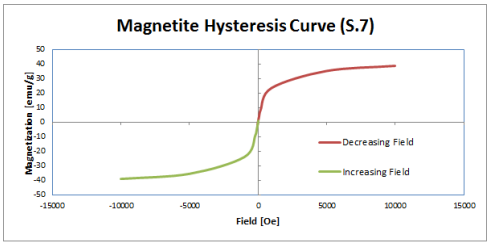
Magnetite Hysteresis Curve (S.7)
Decreasing Field
Increasing Field
Field [Oe]

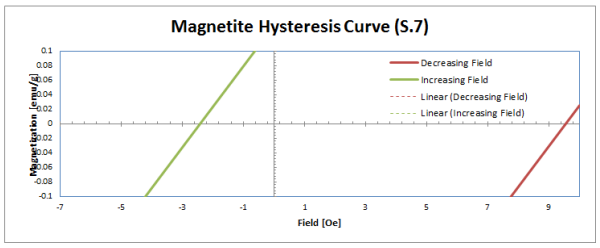
Magnetite Hysteresis Curve (S.7)
Decreasing Field
Increasing Field
Linear (Decreasing Field)
Linear (Increasing Field)
Field [Oe]

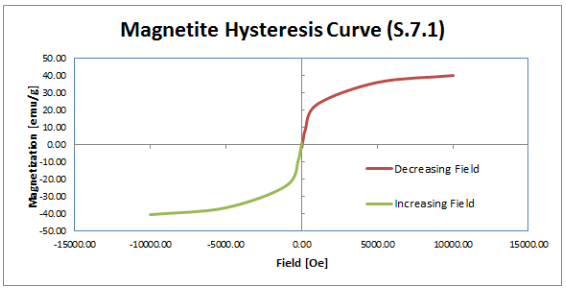
Magnetite Hysteresis Curve (S.7.1)
Magnetization [emu/g]
Decreasing Field
Increasing Field
Field [Oe]

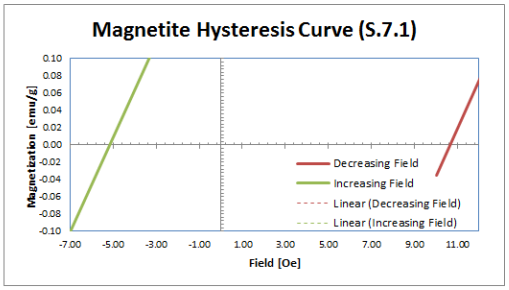
Magnetite Hysteresis Curve (S.7.1)
Decreasing Field
Increasing Field
Linear (Decreasing Field)
Linear (Increasing Field)
Field [Oe]

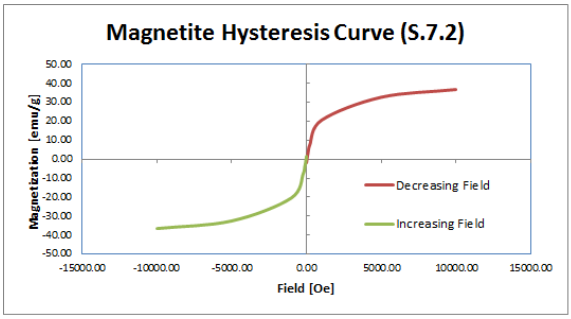
Magnetite Hysteresis Curve (S.7.2)
Magnetization [emu/g]
Decreasing Field
Increasing Field
Field [Oe]

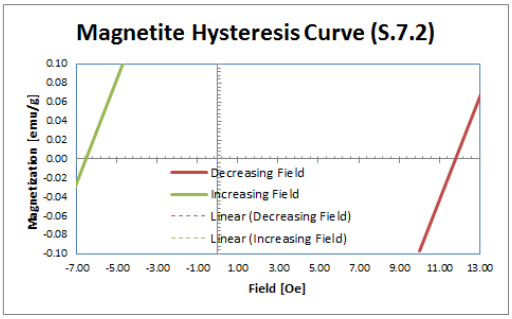
Magnetite Hysteresis Curve (S.7.2)
Decreasing Field
Increasing Field
Linear (Decreasing Field)
Linear (Increasing Field)
Field [Oe]

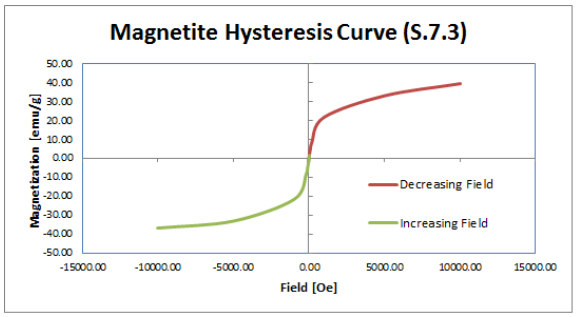
Magnetite Hysteresis Curve (S.7.3)
Magnetization [emu/g]
Field [Oe]
Decreasing Field
Increasing Field

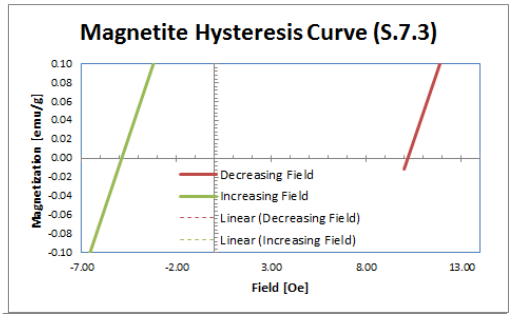
Magnetite Hysteresis Curve (S.7.3)
Magnetization [emu/g]
Field [Oe]
Decreasing Field
Increasing Field
Linear (Decreasing Field)
Linear (Increasing Field)

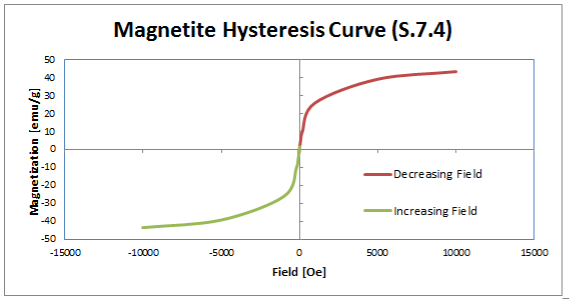
Magnetite Hysteresis Curve (S.7.4)
Magnetization [emu/g]
Field [Oe]
Decreasing Field
Increasing Field

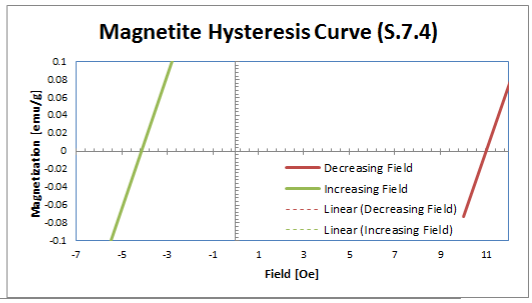
Magnetite Hysteresis Curve (S.7.4)
Magnetization [emu/g]
Field [Oe]
Decreasing Field
Increasing Field
Linear (Decreasing Field)
Linear (Increasing Field)

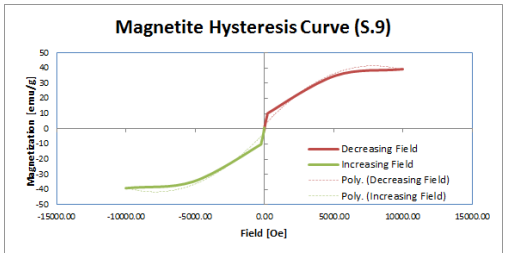
Magnetite Hysteresis Curve (S.9)
Magnetization [emu/g]
Field [Oe]
Decreasing Field
Increasing Field
Poly. (Decreasing Field)
Poly. (Increasing Field)

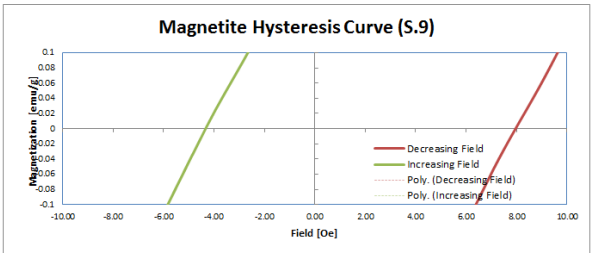
Magnetite Hysteresis Curve (S.9)
Magnetization [emu/g]
Field [Oe]
Decreasing Field
Increasing Field
Poly. (Decreasing Field)
Poly. (Increasing Field)

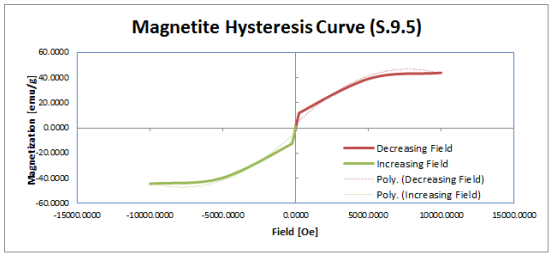
Magnetite Hysteresis Curve (S.9.5)
Magnetization [emu/g]
Field [Oe]
Decreasing Field
Increasing Field
Poly. (Decreasing Field)
Poly. (Increasing Field)

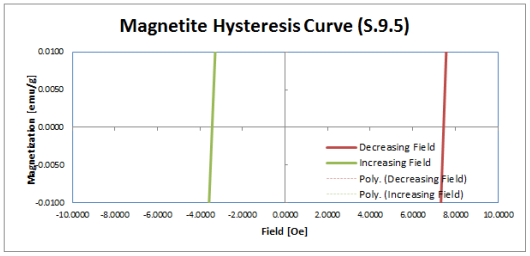
Magnetite Hysteresis Curve (S.9.5)
Magnetization [emu/g]
Field [Oe]
Decreasing Field
Increasing Field
Poly. (Decreasing Field)
Poly. (Increasing Field)

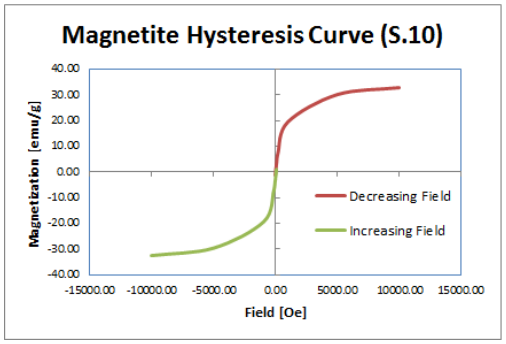
Magnetite Hysteresis Curve (S.10)
Magnetization [emu/g]
Field [Oe]
Decreasing Field
Increasing Field

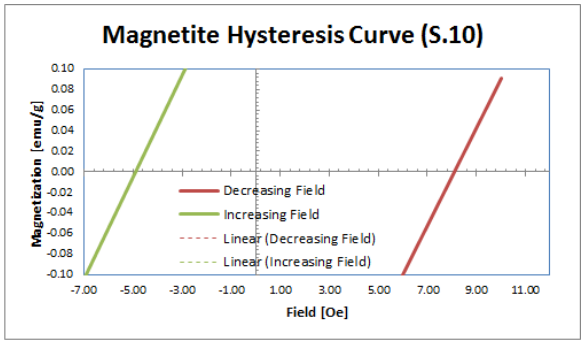
Magnetite Hysteresis Curve (S.10)
Magnetization [emu/g]
Field [Oe]
Decreasing Field
Increasing Field
Linear (Decreasing Field)
Linear (Increasing Field)

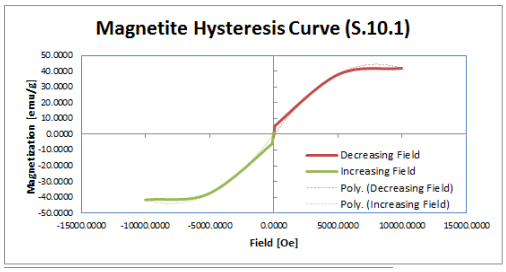
Magnetite Hysteresis Curve (S.10.1)
Magnetization [emu/g]
Field [Oe]
Decreasing Field
Increasing Field
Poly. (Decreasing Field)
Poly. (Increasing Field)

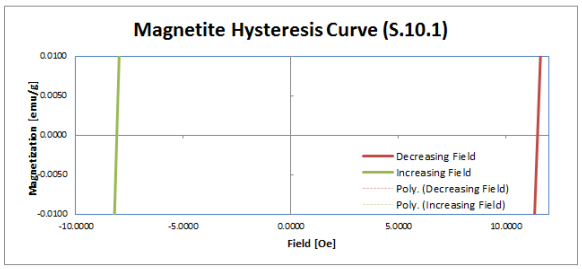
Magnetite Hysteresis Curve (S.10.1)
Magnetization [emu/g]
Field [Oe]
Decreasing Field
Increasing Field
Poly. (Decreasing Field)
Poly. (Increasing Field)

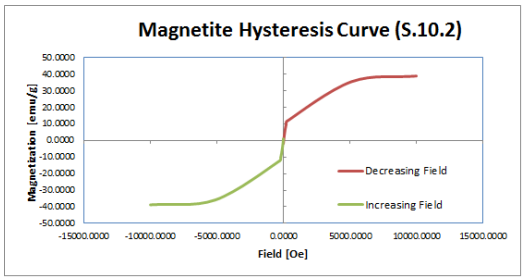
Magnetite Hysteresis Curve (S.10.2)
Magnetization [emu/g]
Field [Oe]
Decreasing Field
Increasing Field

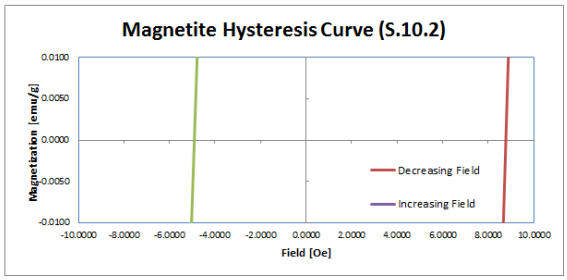
Magnetite Hysteresis Curve (S.10.2)
Magnetization [emu/g]
Field [Oe]
Decreasing Field
Increasing Field

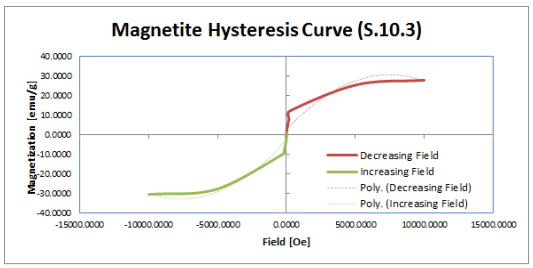
Magnetite Hysteresis Curve (S.10.3)
Magnetization [emu/g]
Field [Oe]
Decreasing Field
Increasing Field
Poly. (Decreasing Field)
Poly. (Increasing Field)

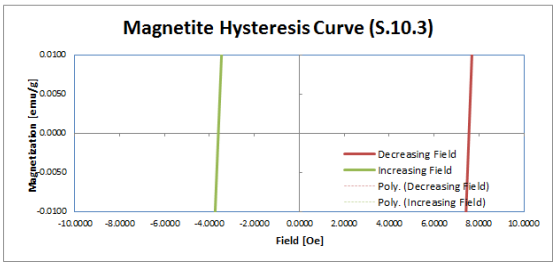
Magnetite Hysteresis Curve (S.10.3)
Magnetization [emu/g]
Field [Oe]
Decreasing Field
Increasing Field
Poly. (Decreasing Field)
Poly. (Increasing Field)

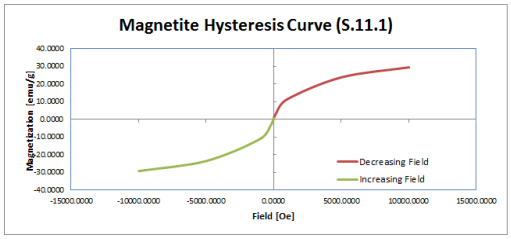
Magnetite Hysteresis Curve (S.11.1)
Magnetization [emu/g]
Field [Oe]
Decreasing Field
Increasing Field

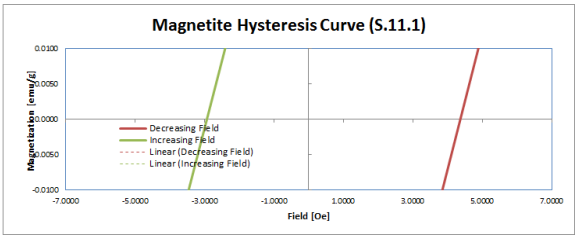
Magnetite Hysteresis Curve (S.11.1)
Magnetization [emu/g]
Field [Oe]
Decreasing Field
Increasing Field
Linear (Decreasing Field)
Linear (Increasing Field)

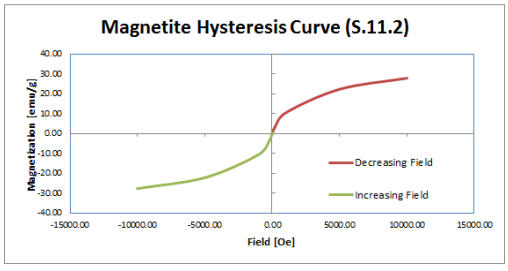
Magnetite Hysteresis Curve (S.11.2)
Magnetization [emu/g]
Field [Oe]
Decreasing Field
Increasing Field

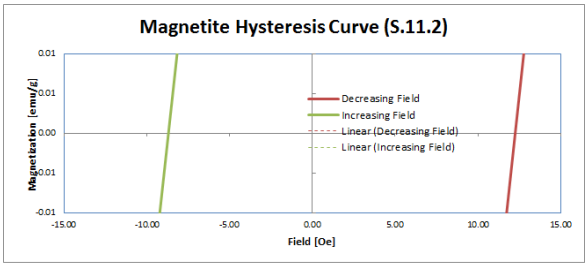
Magnetite Hysteresis Curve (S.11.2)
Magnetization [emu/g]
Field [Oe]
Decreasing Field
Increasing Field
Linear (Decreasing Field)
Linear (Increasing Field)

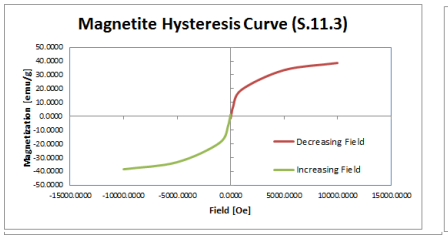
Magnetite Hysteresis Curve (S.11.3)
Magnetization [emu/g]
Field [Oe]
Decreasing Field
Increasing Field

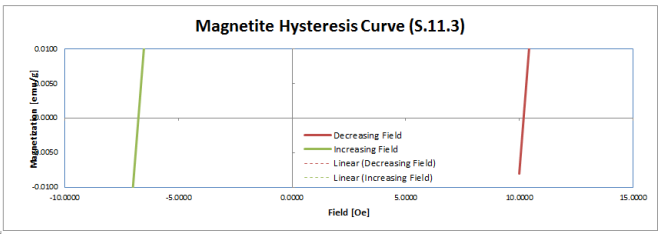
Magnetite Hysteresis Curve (S.11.3)
Magnetization [emu/g]
Field [Oe]
Decreasing Field
Increasing Field
Linear (Decreasing Field)
Linear (Increasing Field)

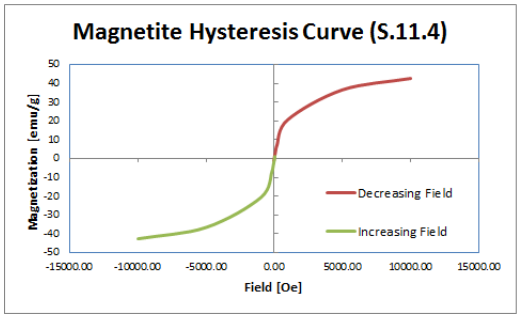
Magnetite Hysteresis Curve (S.11.4)
Magnetization [emu/g]
Field [Oe]
Decreasing Field
Increasing Field

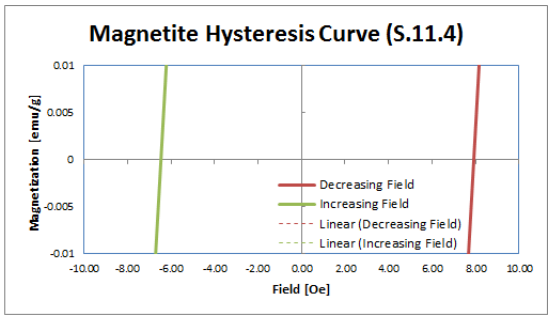
Magnetite Hysteresis Curve (S.11.4)
Magnetization [emu/g]
Field [Oe]
Decreasing Field
Increasing Field
Linear (Decreasing Field)
Linear (Increasing Field)

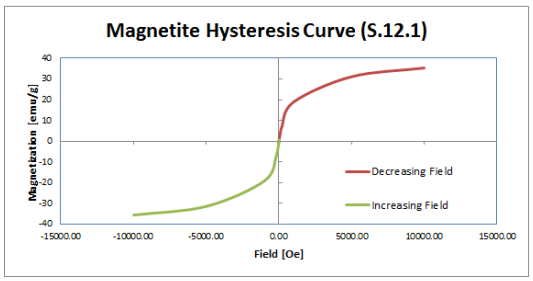
Magnetite Hysteresis Curve (S.12.1)
Magnetization [emu/g]
Field [Oe]
Decreasing Field
Increasing Field

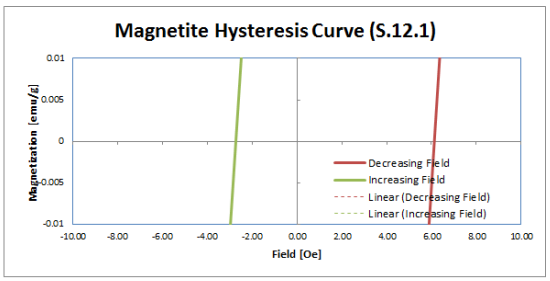
Magnetite Hysteresis Curve (S.12.1)
Magnetization [emu/g]
Field [Oe]
Decreasing Field
Increasing Field
Linear (Decreasing Field)
Linear (Increasing Field)

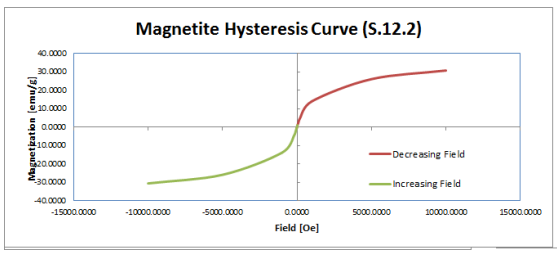
Magnetite Hysteresis Curve (S.12.2)
Magnetization [emu/g]
Field [Oe]
Decreasing Field
Increasing Field

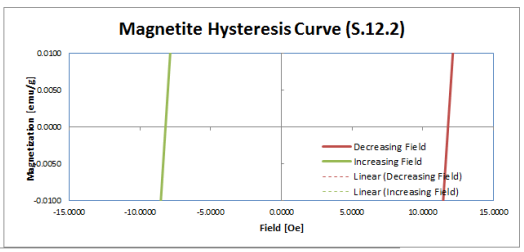
Magnetite Hysteresis Curve (S.12.2)
Magnetization [emu/g]
Field [Oe]
Decreasing Field
Increasing Field
Linear (Decreasing Field)
Linear (Increasing Field)

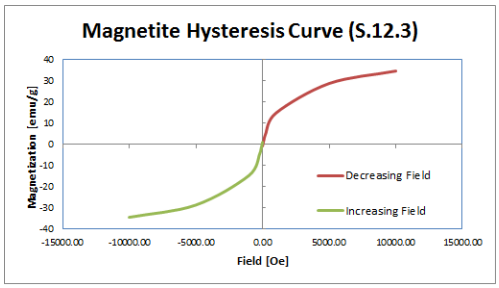
Magnetite Hysteresis Curve (S.12.3)
Magnetization [emu/g]
Field [Oe]
Decreasing Field
Increasing Field

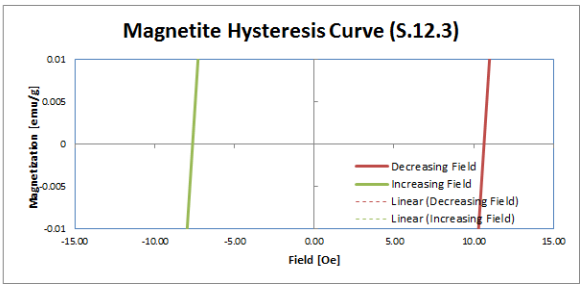
Magnetite Hysteresis Curve (S.12.3)
Magnetization [emu/g]
Field [Oe]
Decreasing Field
Increasing Field
Linear (Decreasing Field)
Linear (Increasing Field)

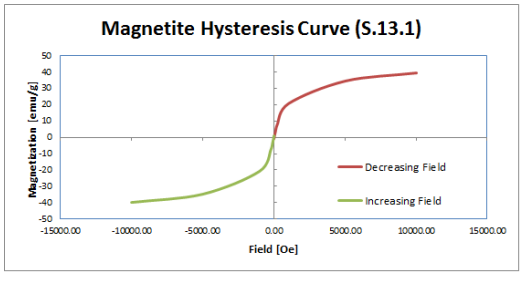
Magnetite Hysteresis Curve (S.13.1)
Magnetization [emu/g]
Field [Oe]
Decreasing Field
Increasing Field

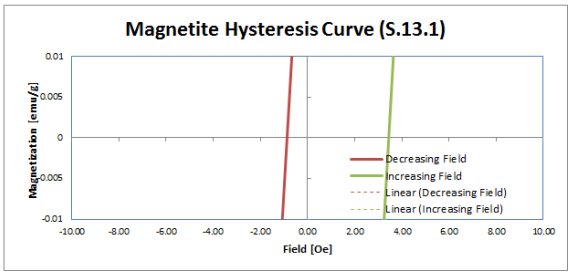
Magnetite Hysteresis Curve (S.13.1)
Magnetization [emu/g]
Field [Oe]
Decreasing Field
Increasing Field
Linear (Decreasing Field)
Linear (Increasing Field)

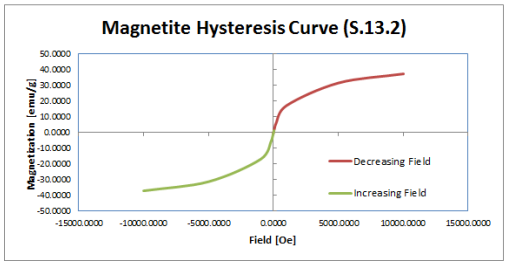
Magnetite Hysteresis Curve (S.13.2)
Magnetization [emu/g]
Field [Oe]
Decreasing Field
Increasing Field

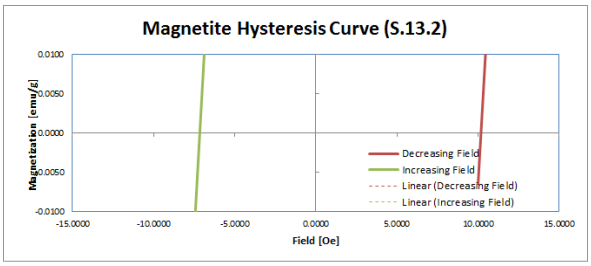
Magnetite Hysteresis Curve (S.13.2)
Magnetization [emu/g]
Field [Oe]
Decreasing Field
Increasing Field
Linear (Decreasing Field)
Linear (Increasing Field)

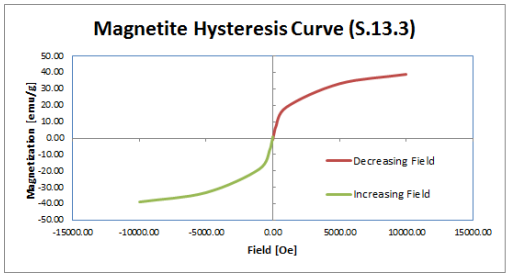
Magnetite Hysteresis Curve (S.13.3)
Magnetization [emu/g]
Field [Oe]
Decreasing Field
Increasing Field

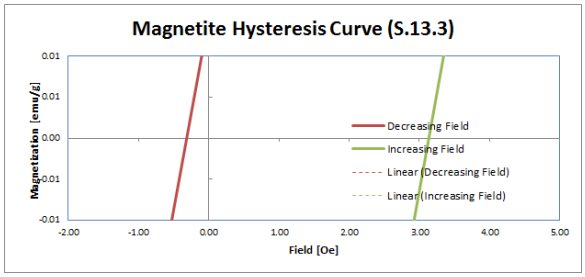
Magnetite Hysteresis Curve (S.13.3)
Magnetization [emu/g]
Field [Oe]
Decreasing Field
Increasing Field
Linear (Decreasing Field)
Linear (Increasing Field)

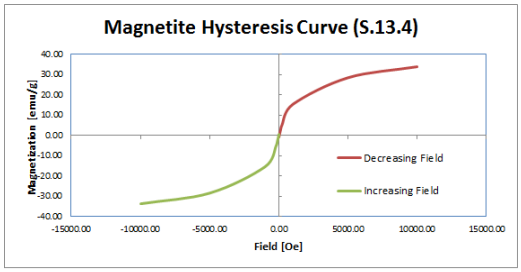
Magnetite Hysteresis Curve (S.13.4)
Magnetization [emu/g]
Field [Oe]
Decreasing Field
Increasing Field

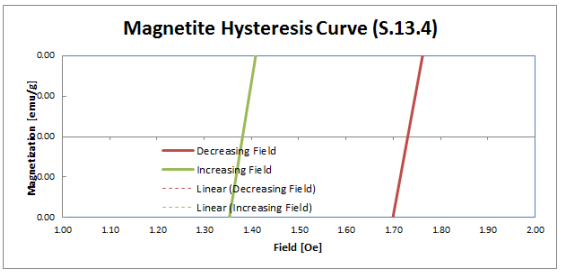
Magnetite Hysteresis Curve (S.13.4)
Magnetization [emu/g]
Field [Oe]
Decreasing Field
Increasing Field
Linear (Decreasing Field)
Linear (Increasing Field)

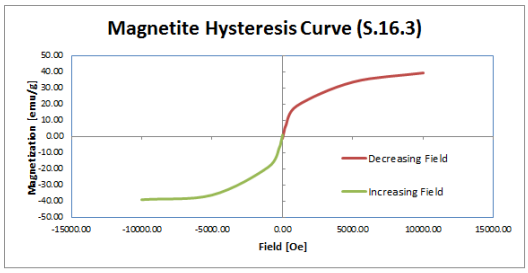
Magnetite Hysteresis Curve (S.16.3)
Magnetization [emu/g]
Field [Oe]
Decreasing Field
Increasing Field

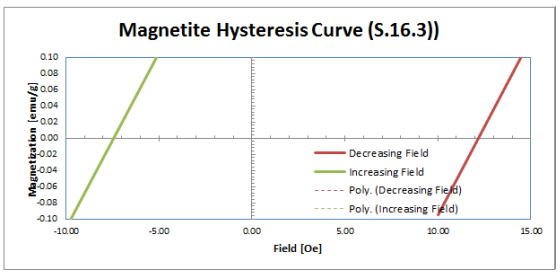
Magnetite Hysteresis Curve (S.16.3))
Magnetization [emu/g]
Field [Oe]
Decreasing Field
Increasing Field
Poly. (Decreasing Field)
Poly. (Increasing Field)

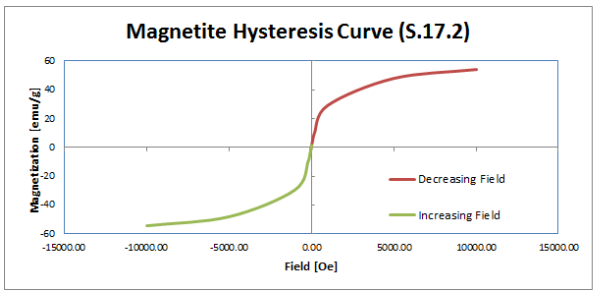
Magnetite Hysteresis Curve (S.17.2)
Magnetization [emu/g]
Field [Oe]
Decreasing Field
Increasing Field

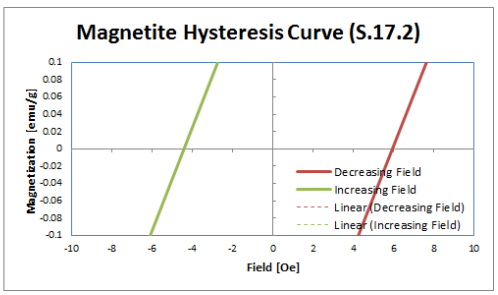
Magnetite Hysteresis Curve (S.17.2)
Magnetization [emu/g]
Field [Oe]
Decreasing Field
Increasing Field
Linear (Decreasing Field)
Linear (Increasing Field)

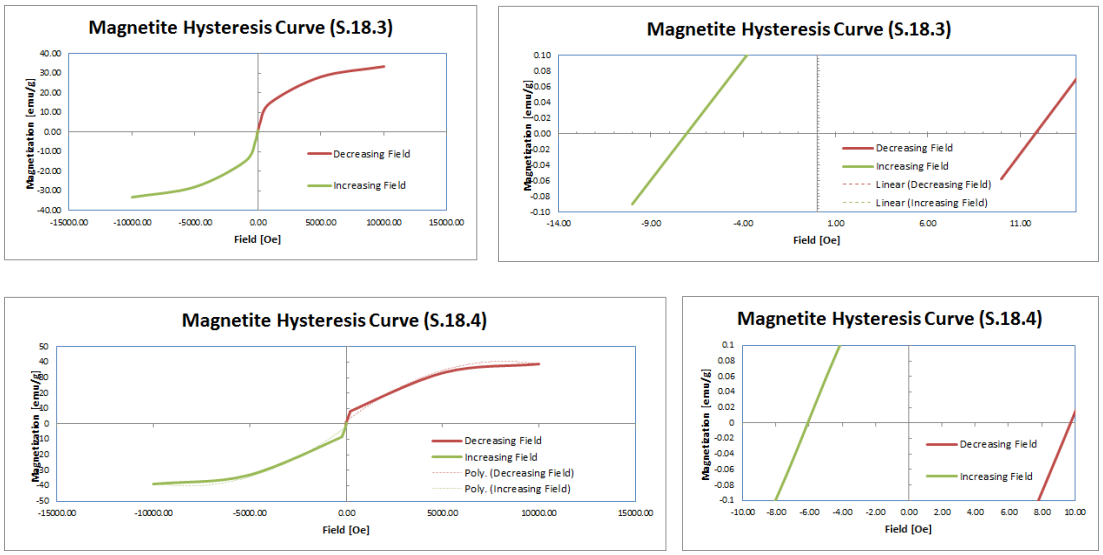

E. SQUID Magnetometer ZFC-FC Measurements

Measurements of zero field and field cooling curves were obtained from a Quantum Design MPMS Superconducting Quantum Interference Device (SQUID). Data collected was sparse in order to cover measurements for a large number of samples. Figure E shows a graphical representation of this data as collected from SQUID measurements.

Figure E: Measured results from SQUID magnetometery. Samples displayed from top to bottom and left to right in the following order: -1, 0, 1, 2, 4, 7, 7.1, 7.2, 7.3, 7.4, 9, 9.5, 10, 10.1, 10.2, 10.3, 11.1, 11.2, 11.3, 11.4, 12.1, 12.2, 12.3, 13.2, 13.3, 13.4, 16.3, 17.2, 18.2, 18.3, 18.4. Right hand graphs show a close up of the x and y intercept locations of the hysteresis curve. Note that in some cases a cusp is visible in the graphs. This is a result of sparse data in the intermediate regions of the graph not as a result of anomalies in measurement.

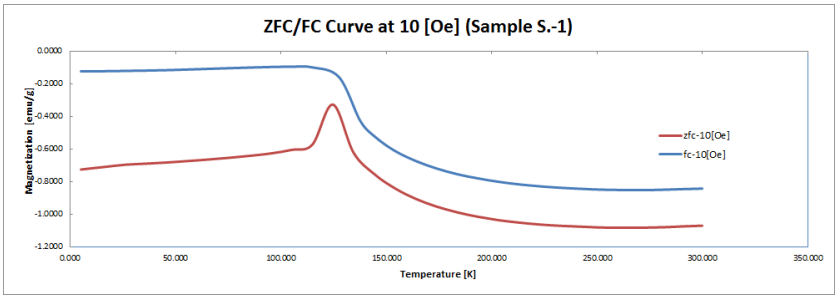

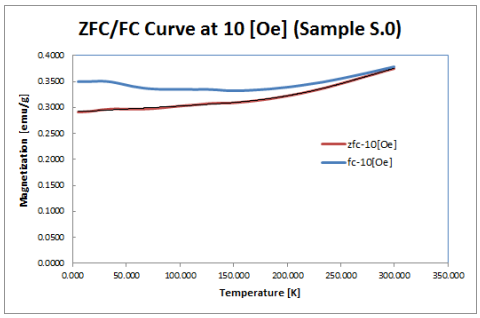
ZFC/FC Curve at 10 [Oe] (Sample S.0)
Magnetization [emu/g]
Temperature [K]
zfc-10[Oe]
fc-10[Oe]

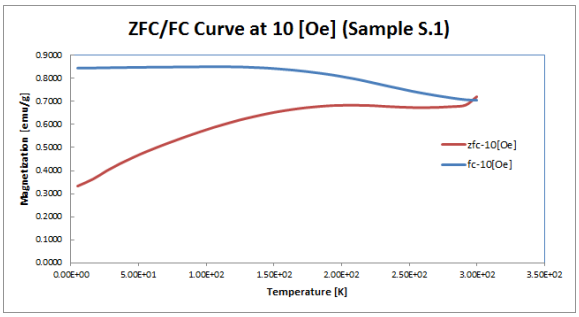
ZFC/FC Curve at 10 [Oe] (Sample S.1)
Magnetization [emu/g]
Temperature [K]
zfc-10[Oe]
fc-10[Oe]

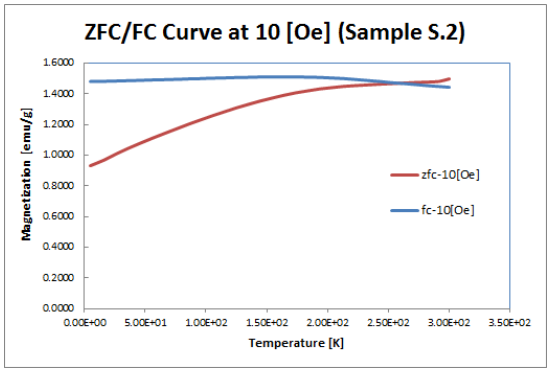
ZFC/FC Curve at 10 [Oe] (Sample S.2)
Magnetization [emu/g]
Temperature [K]
zfc-10[Oe]
fc-10[Oe]

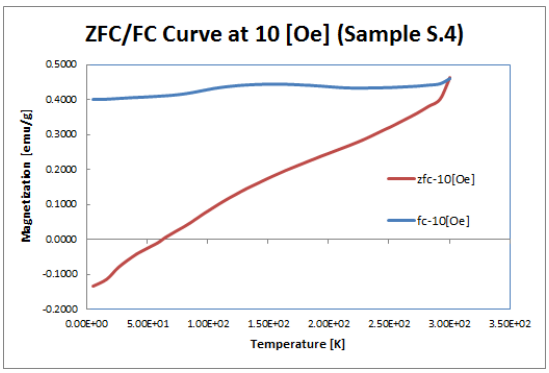
ZFC/FC Curve at 10 [Oe] (Sample S.4)
Magnetization [emu/g]
Temperature [K]
zfc-10[Oe]
fc-10[Oe]

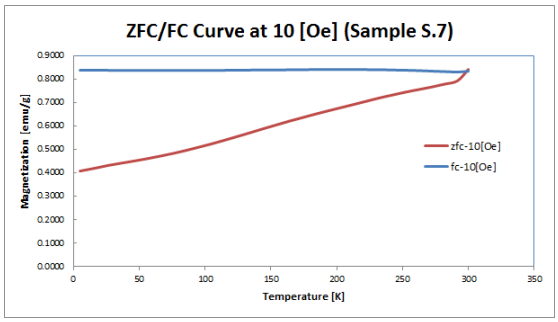
ZFC/FC Curve at 10 [Oe] (Sample S.7)
Magnetization [emu/g]
Temperature [K]
zfc-10[Oe]
fc-10[Oe]

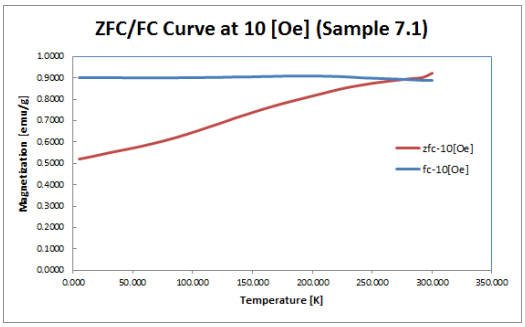
ZFC/FC Curve at 10 [Oe] (Sample 7.1)
Magnetization [emu/g]
Temperature [K]
zfc-10[Oe]
fc-10[Oe]

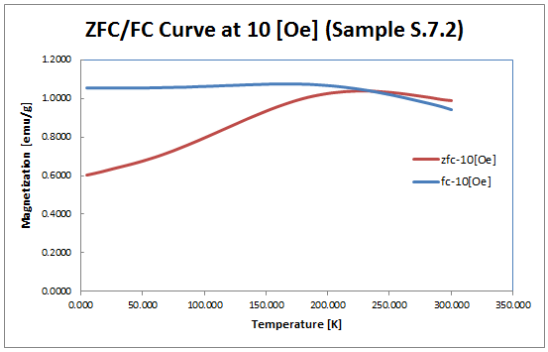
ZFC/FC Curve at 10 [Oe] (Sample S.7.2)
Magnetization [emu/g]
Temperature [K]
zfc-10[Oe]
fc-10[Oe]

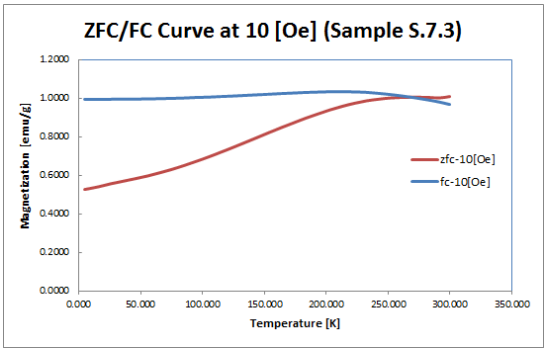
ZFC/FC Curve at 10 [Oe] (Sample S.7.3)
Magnetization [emu/g]
Temperature [K]
zfc-10[Oe]
fc-10[Oe]

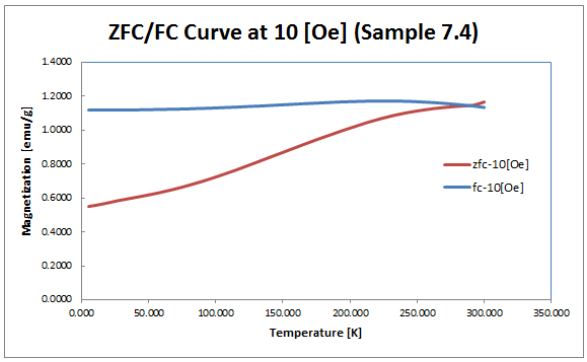
ZFC/FC Curve at 10 [Oe] (Sample 7.4)
Magnetization [emu/g]
Temperature [K]
zfc-10[Oe]
fc-10[Oe]

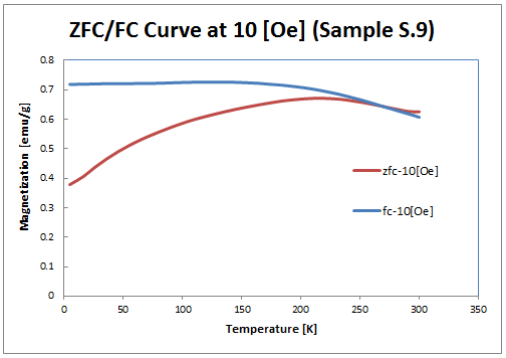
ZFC/FC Curve at 10 [Oe] (Sample S.9)
Magnetization [emu/g]
Temperature [K]
zfc-10[Oe]
fc-10[Oe]

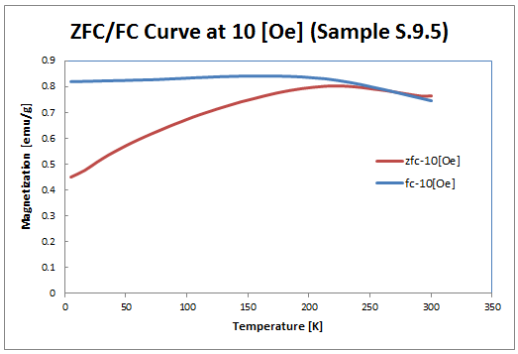
ZFC/FC Curve at 10 [Oe] (Sample S.9.5)
Magnetization [emu/g]
Temperature [K]
zfc-10[Oe]
fc-10[Oe]

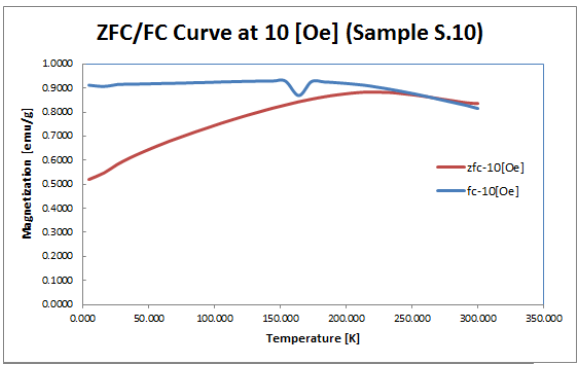
ZFC/FC Curve at 10 [Oe] (Sample S.10)
Magnetization [emu/g]
Temperature [K]
zfc-10[Oe]
fc-10[Oe]

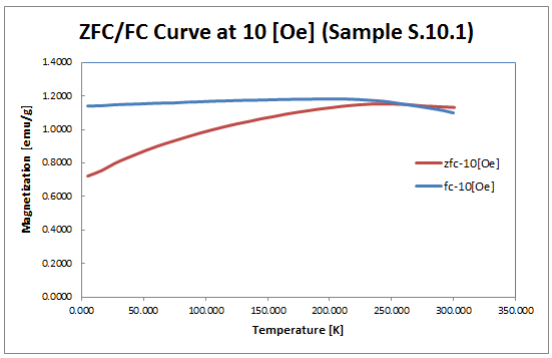
ZFC/FC Curve at 10 [Oe] (Sample S.10.1)
Magnetization [emu/g]
Temperature [K]
zfc-10[Oe]
fc-10[Oe]

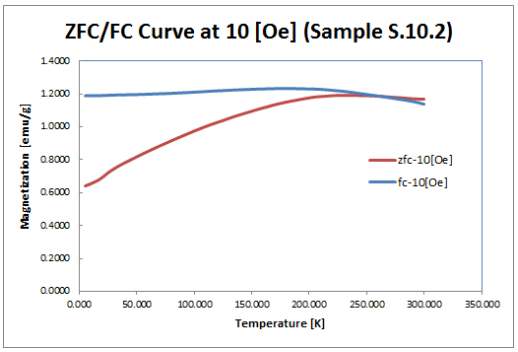
ZFC/FC Curve at 10 [Oe] (Sample S.10.2)
Magnetization [emu/g]
Temperature [K]
zfc-10[Oe]
fc-10[Oe]

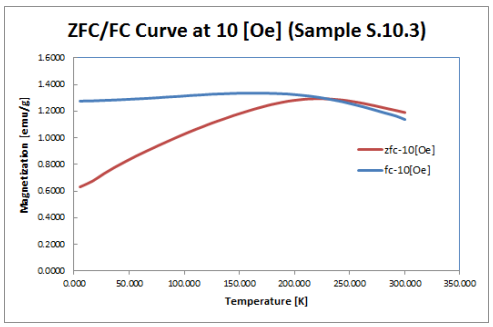
ZFC/FC Curve at 10 [Oe] (Sample S.10.3)
Magnetization [emu/g]
Temperature [K]
zfc-10[Oe]
fc-10[Oe]

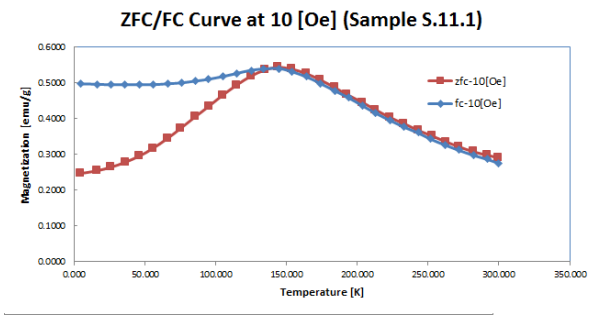
ZFC/FC Curve at 10 [Oe] (Sample S.11.1)
Magnetization [emu/g]
Temperature [K]
zfc-10[Oe]
fc-10[Oe]

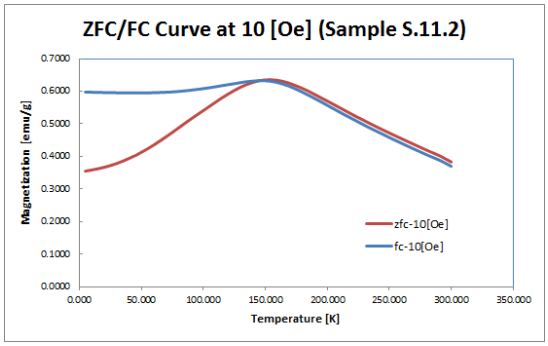
ZFC/FC Curve at 10 [Oe] (Sample S.11.2)
Magnetization [emu/g]
Temperature [K]
zfc-10[Oe]
fc-10[Oe]

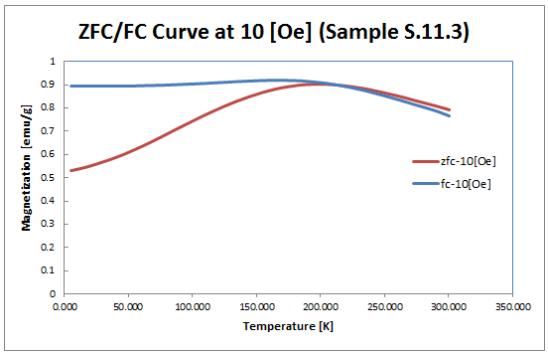
ZFC/FC Curve at 10 [Oe] (Sample S.11.3)
Magnetization [emu/g]
Temperature [K]
zfc-10[Oe]
fc-10[Oe]

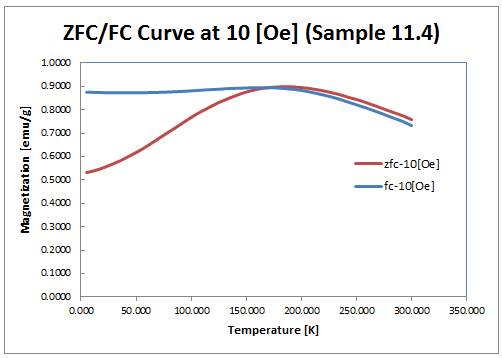
ZFC/FC Curve at 10 [Oe] (Sample 11.4)
Magnetization [emu/g]
Temperature [K]
zfc-10[Oe]
fc-10[Oe]

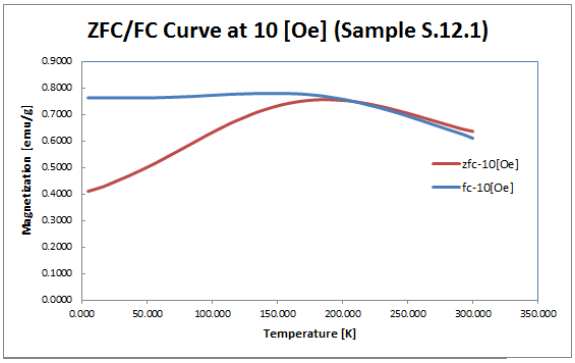
ZFC/FC Curve at 10 [Oe] (Sample S.12.1)
Magnetization [emu/g]
Temperature [K]
zfc-10[Oe]
fc-10[Oe]

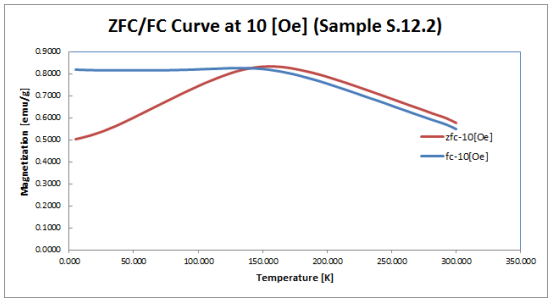
ZFC/FC Curve at 10 [Oe] (Sample S.12.2)
Magnetization [emu/g]
Temperature [K]
zfc-10[Oe]
fc-10[Oe]

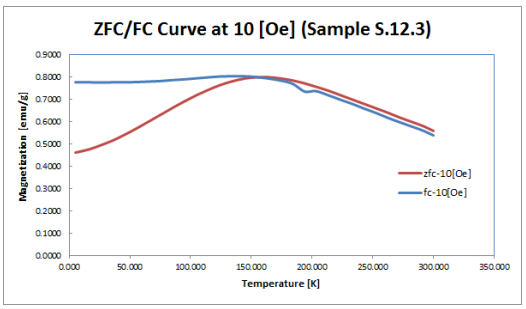
ZFC/FC Curve at 10 [Oe] (Sample S.12.3)
Magnetization [emu/g]
Temperature [K]
zfc-10[Oe]
fc-10[Oe]

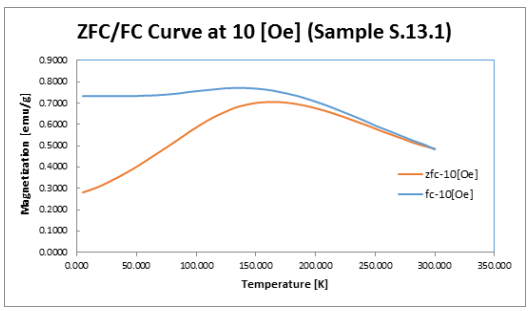
ZFC/FC Curve at 10 [Oe] (Sample S.13.1)
Magnetization [emu/g]
Temperature [K]
zfc-10[Oe]
fc-10[Oe]

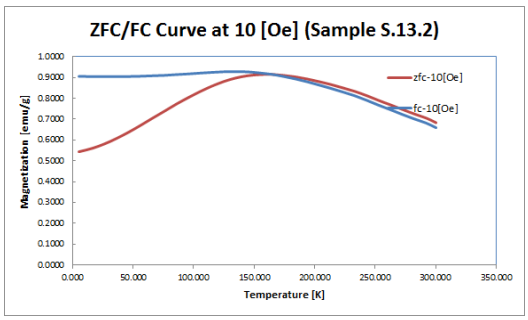
ZFC/FC Curve at 10 [Oe] (Sample S.13.2)
Magnetization [emu/g]
Temperature [K]
zfc-10[Oe]
fc-10[Oe]

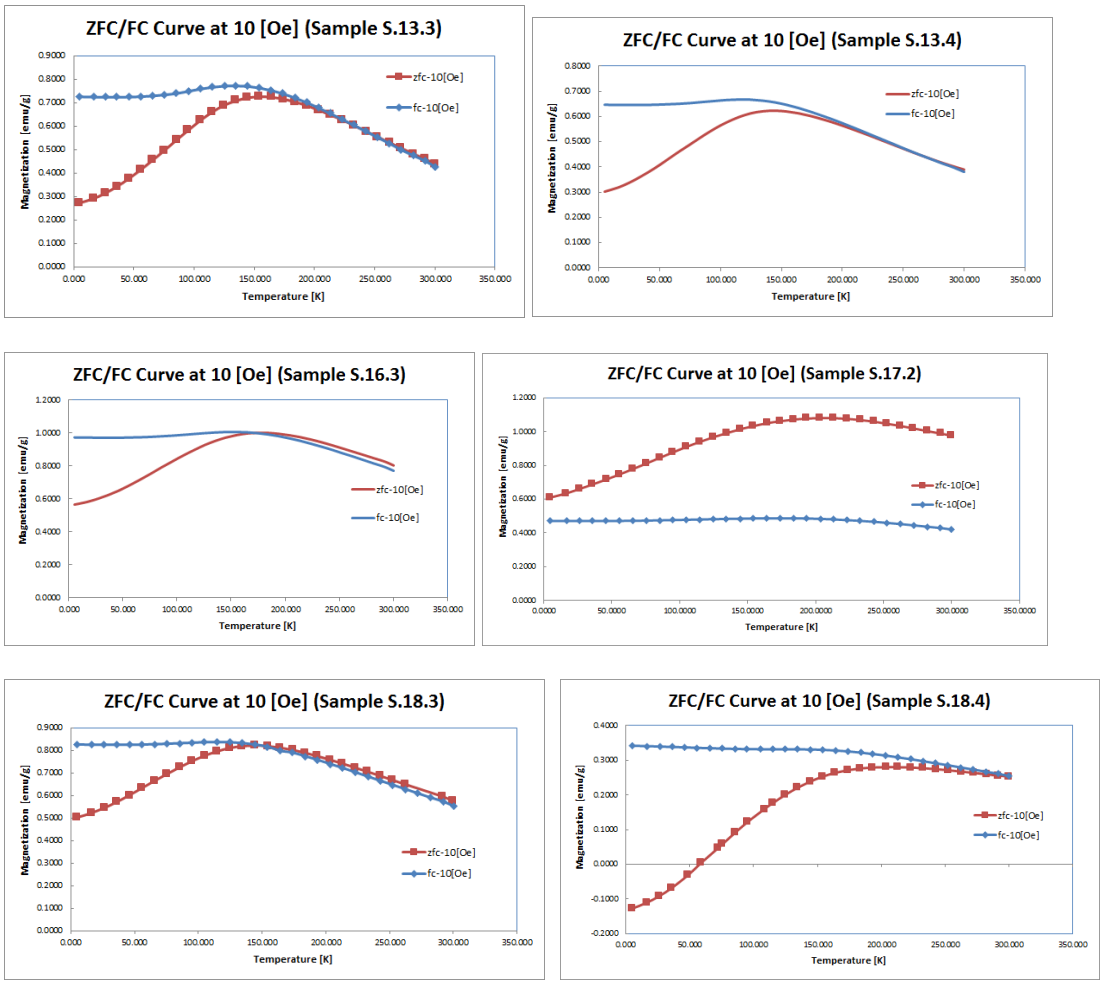

F. Model Fitting and Hysteresis Loop Data

Hysteresis measurements obtained from SQUID are sparse. In order to obtain dense data for analysis of power loss characteristics for both minor and major loop data, a modelling approach must be taken. This modelling involves the optimization and estimation of a number of model parameters, namely, $\theta = \{n, m, \alpha, c, \kappa, \chi_{AF}\}$.

Figure F: Taking measured data from SQUID hysteresis analysis and producing a fitted model. The model parameters $\theta = \{n, m, \alpha, c, \kappa, \chi_{AF}\}$ are shown as: n, m, al, c, k, Xaf respectively. These are minimized using a sum of squared difference cost function (SSD). A power loss estimate is also provided. Samples are listed consecutively in the following order from the first figure to the last: -1, 0, 1, 2, 4, 7, 7.1, 7.2, 7.3, 7.4, 9, 9.5, 10, 10.1, 10.2, 10.3, 11.1, 11.2, 11.3, 11.4, 12.1, 12.2, 12.3, 13.2, 13.3, 13.4, 16.3, 17.2, 18.2, 18.3, 18.4.

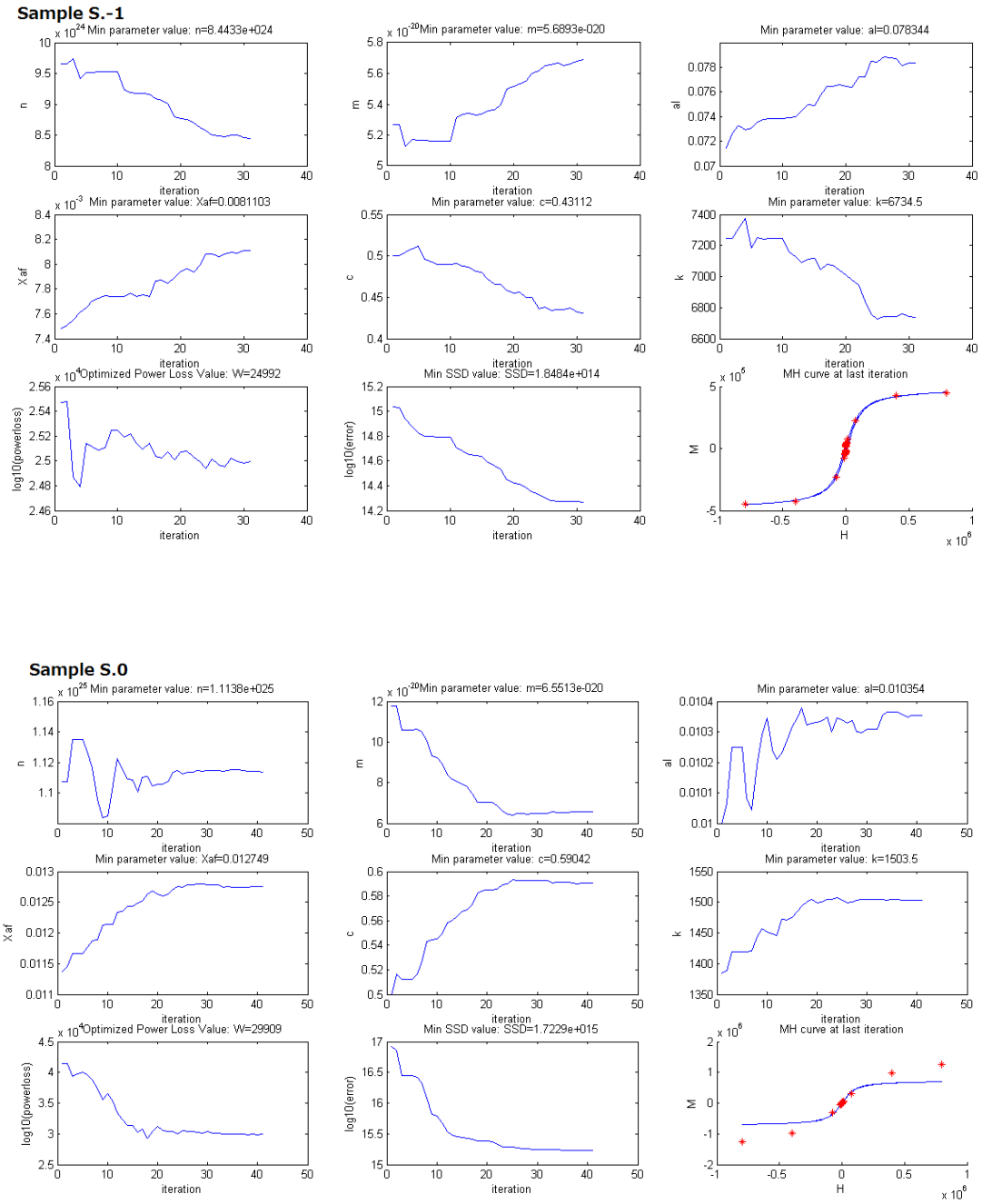

Sample S.1

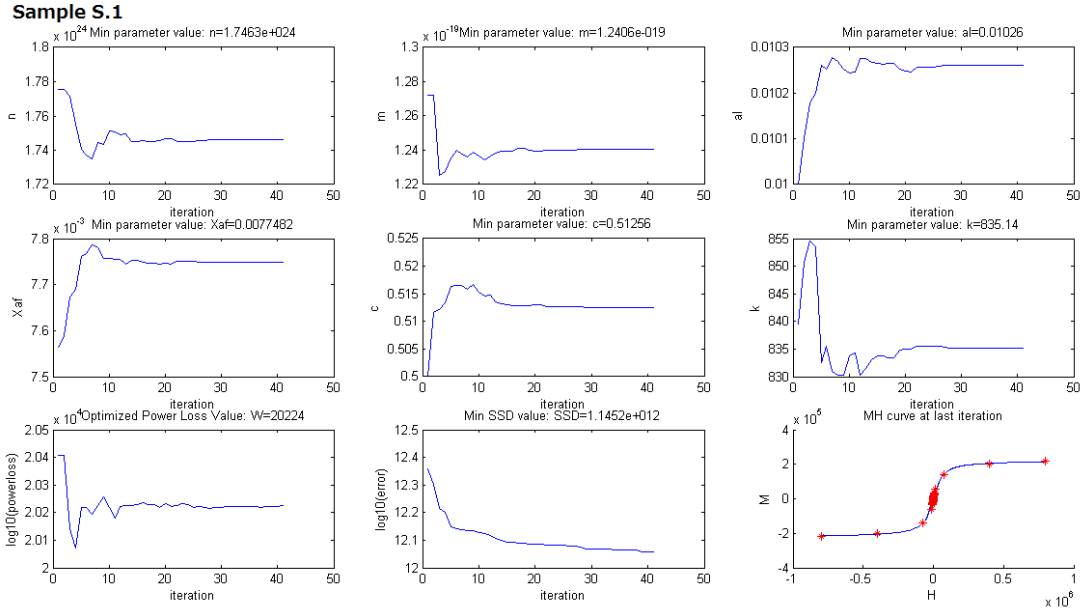

Sample S.2

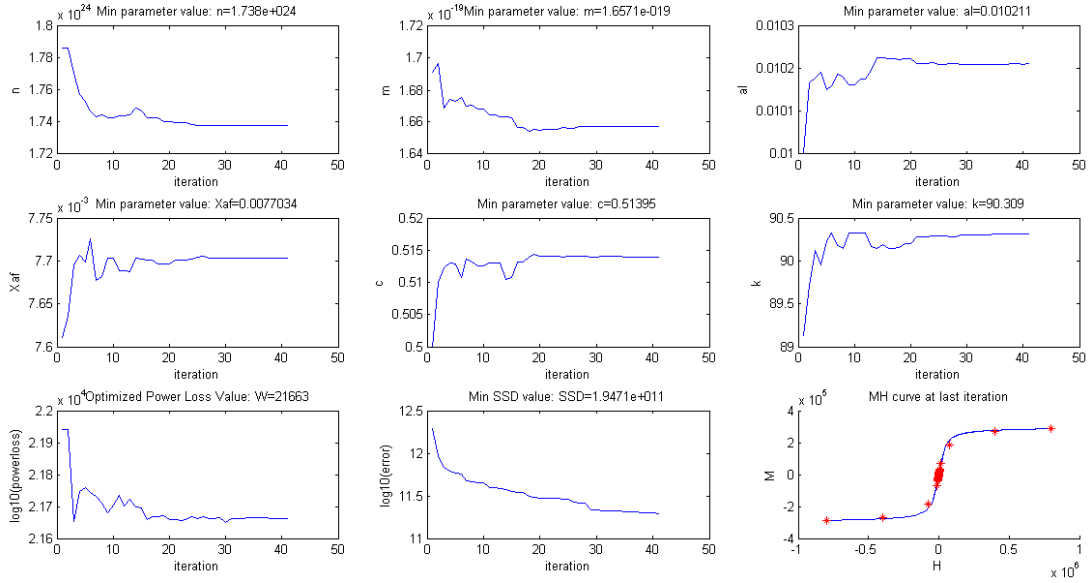

Sample S.4

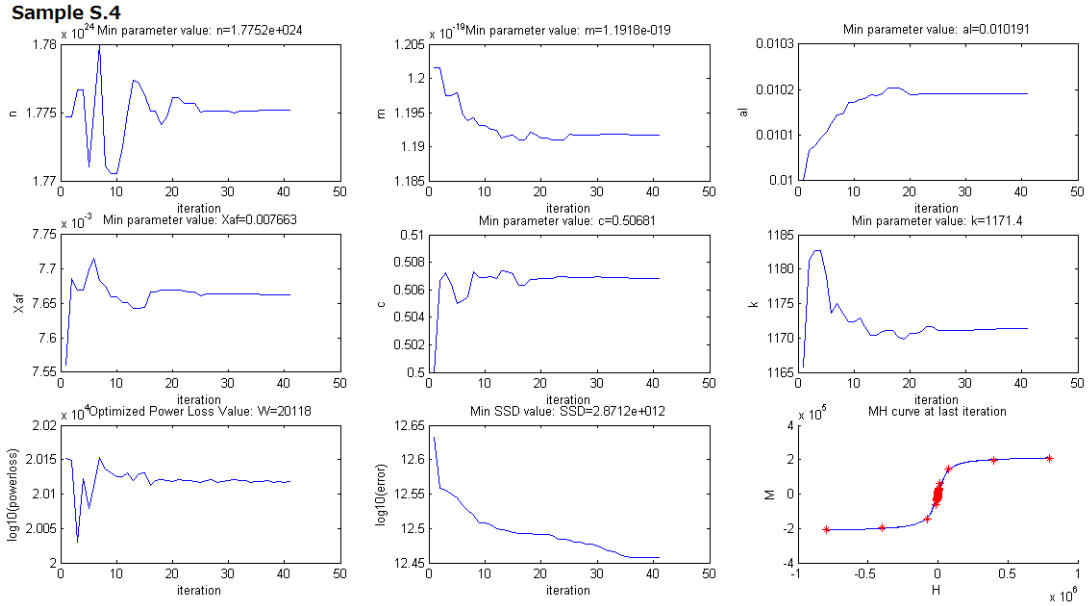

Sample S.7

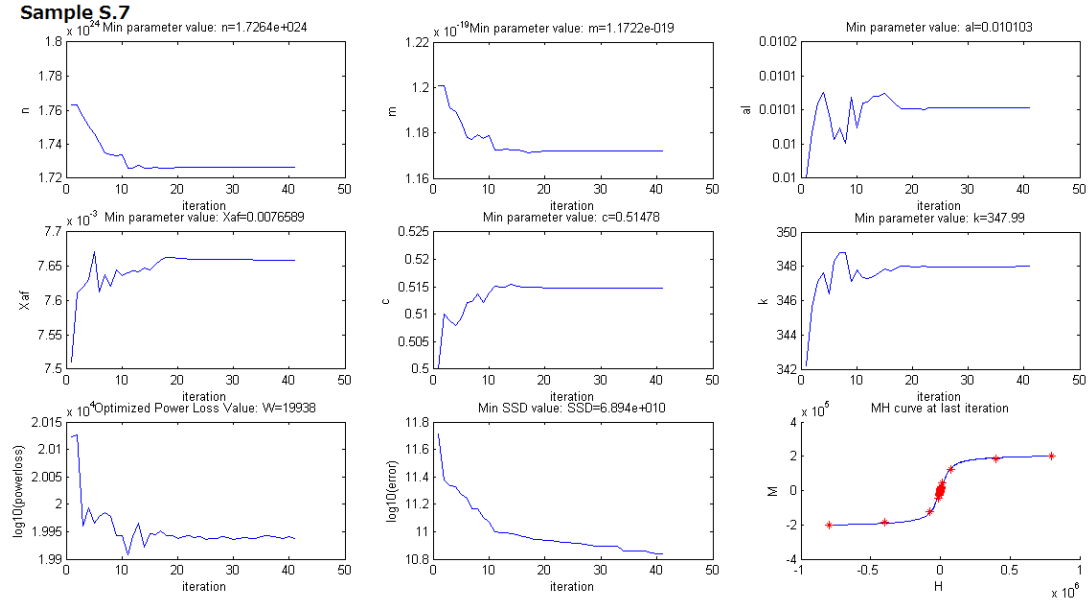

Sample S.7.1

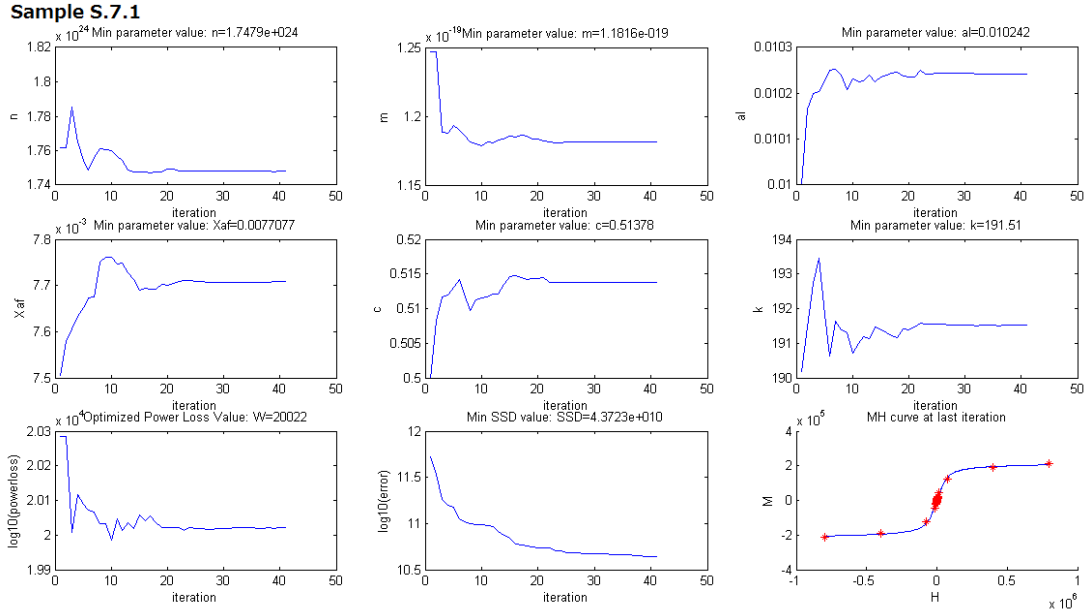

Sample S.7.2

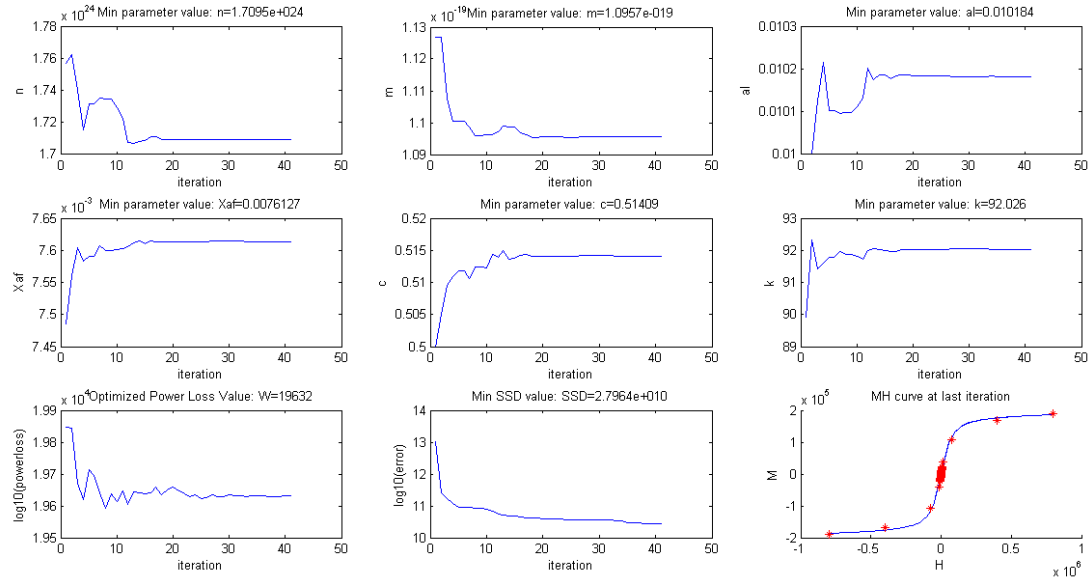

Sample S.7.3

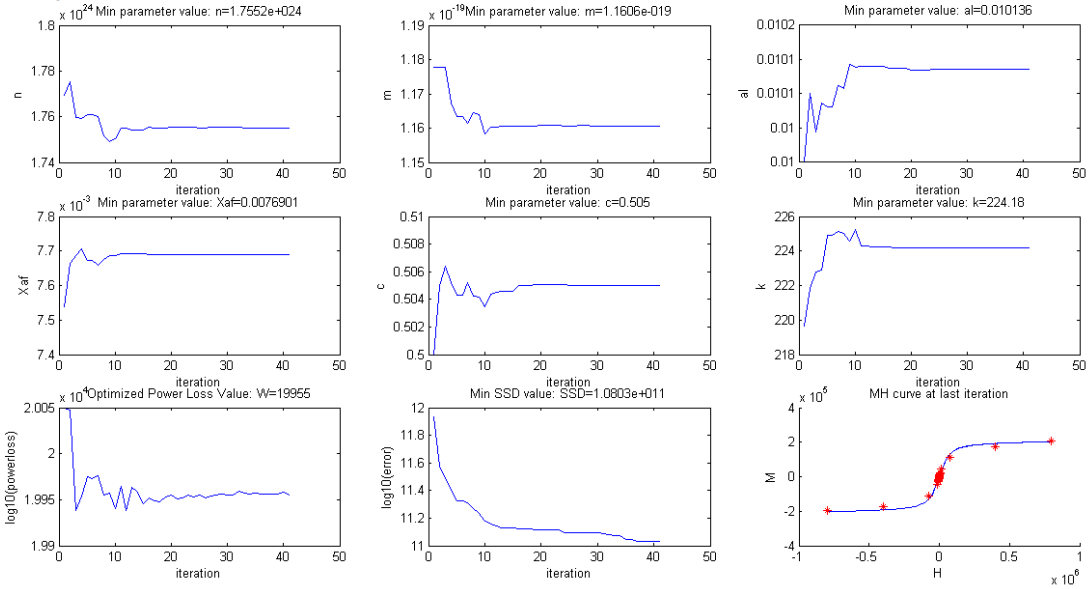

Sample S.7.4

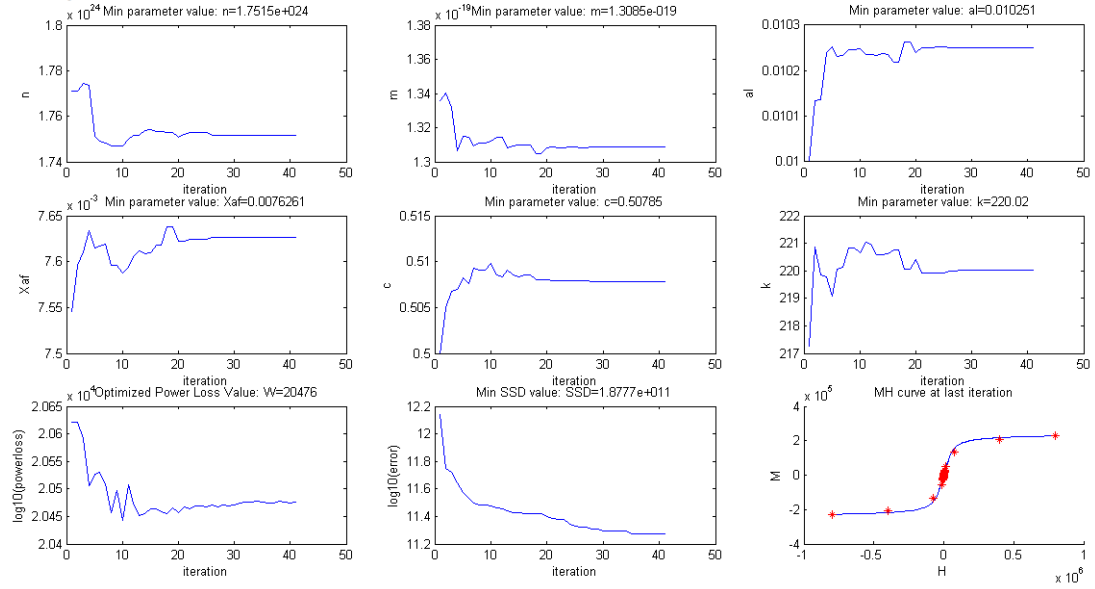

Sample S.9

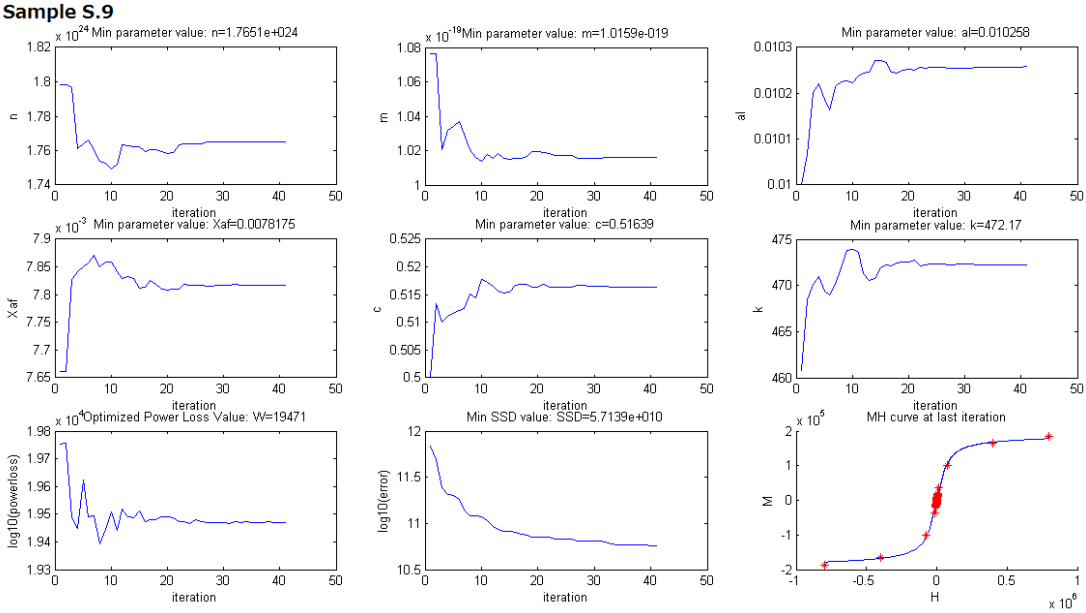

Sample S.9.5

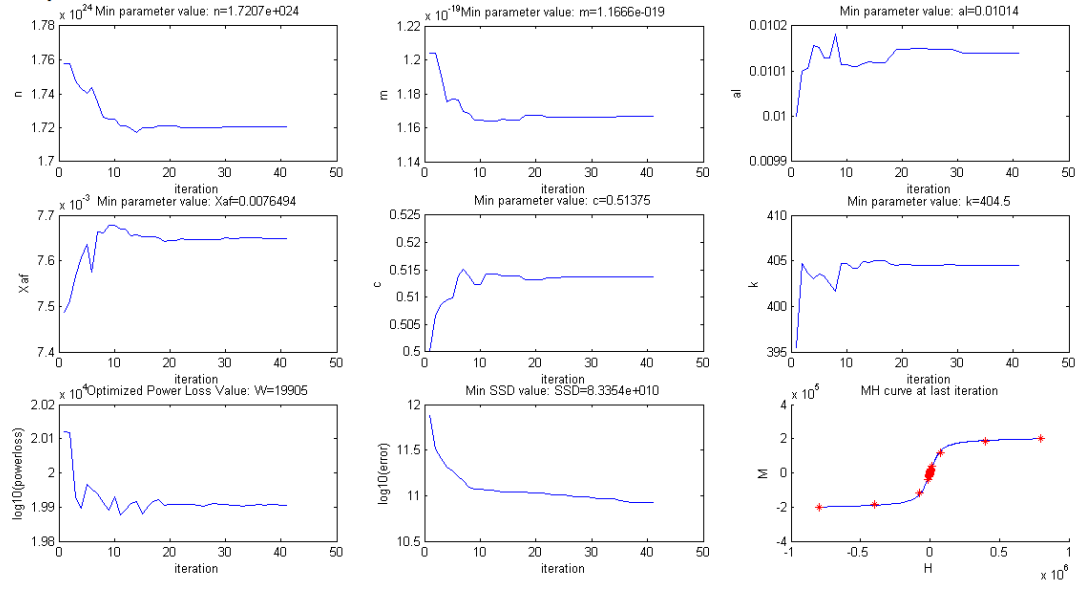

Sample S.10

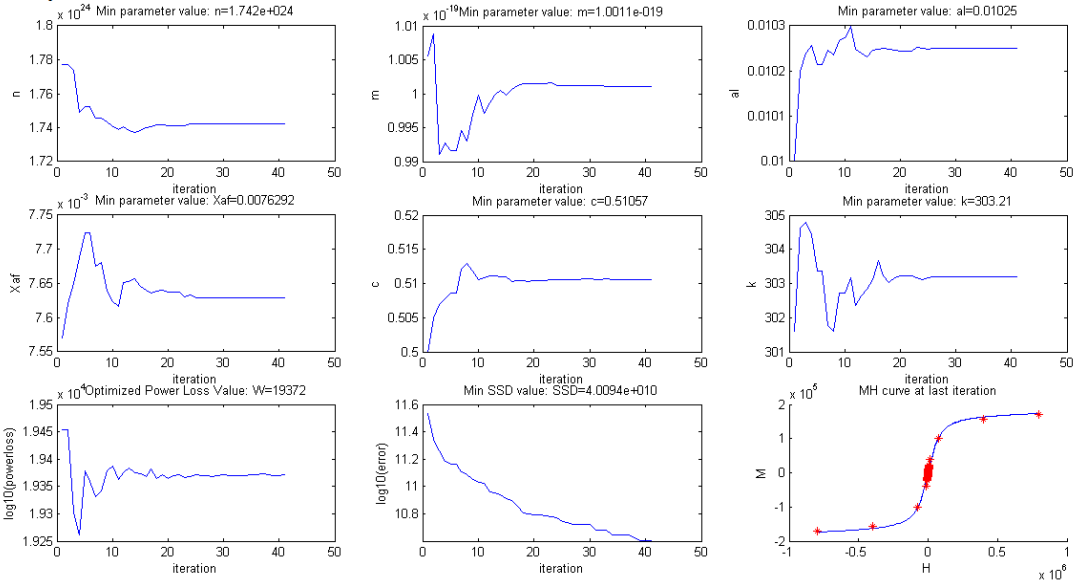

Sample S.10.1

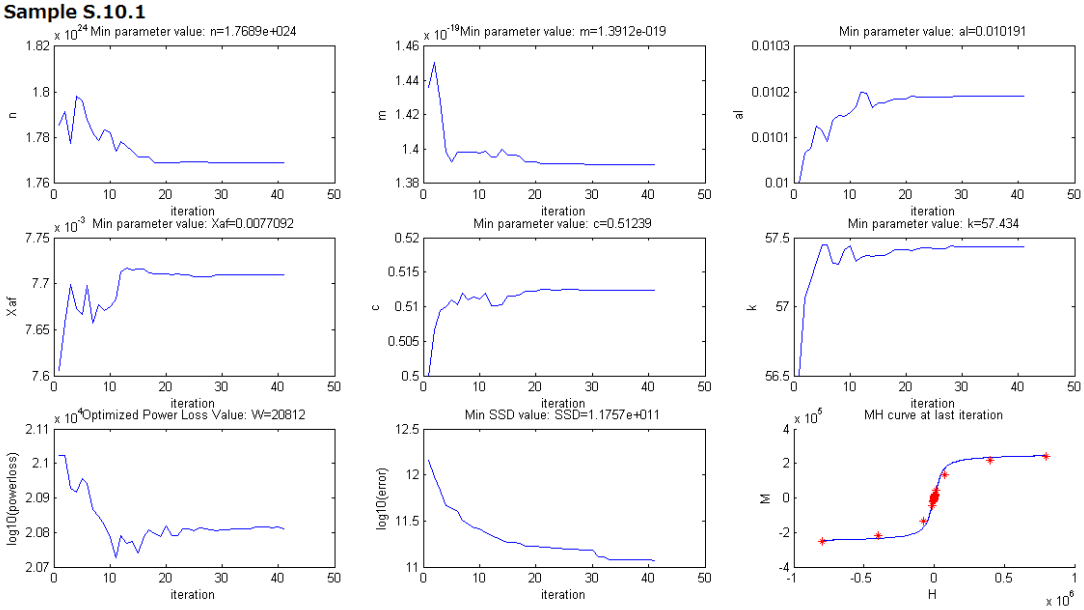

Sample S.10.2

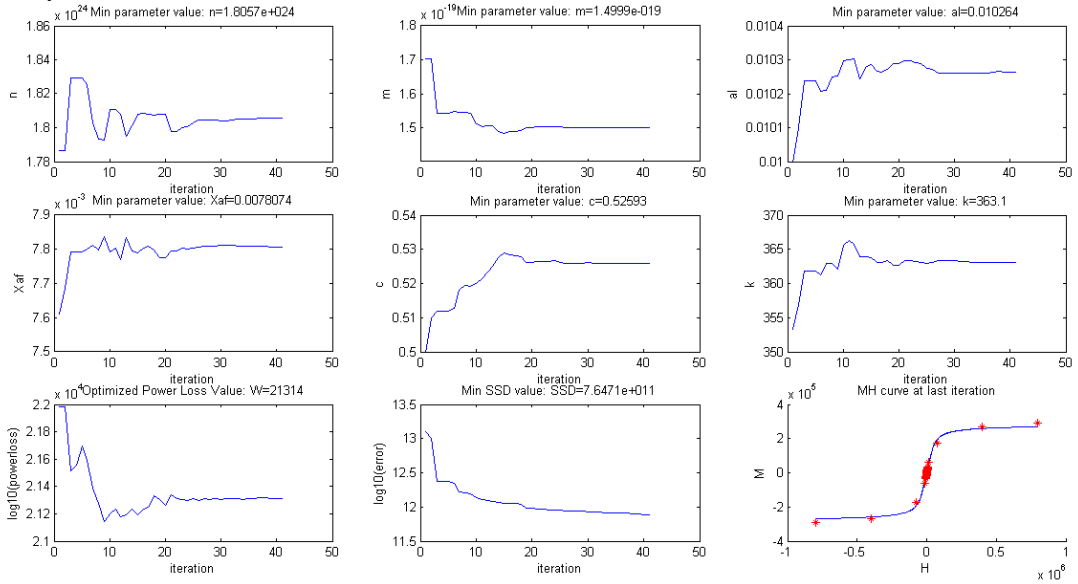

Sample S.10.3

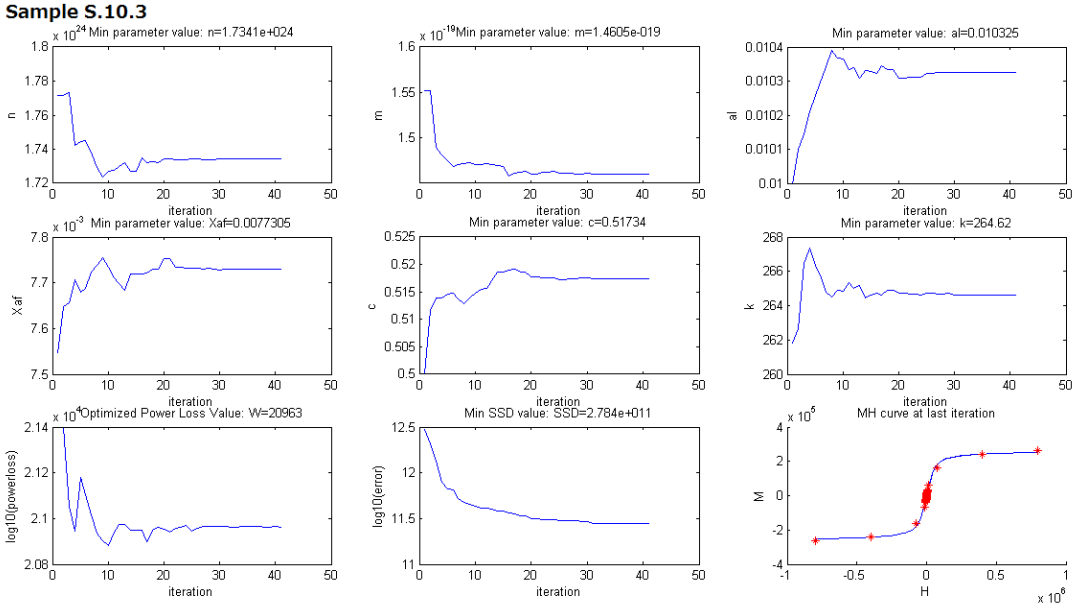

Sample S.11.1

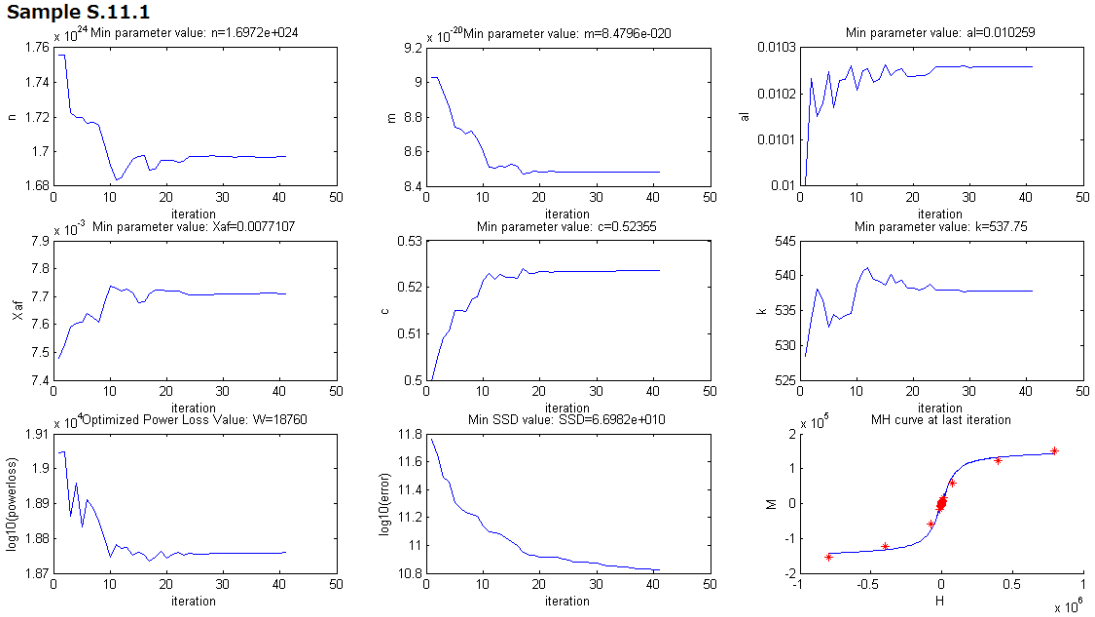

Sample S.11.2

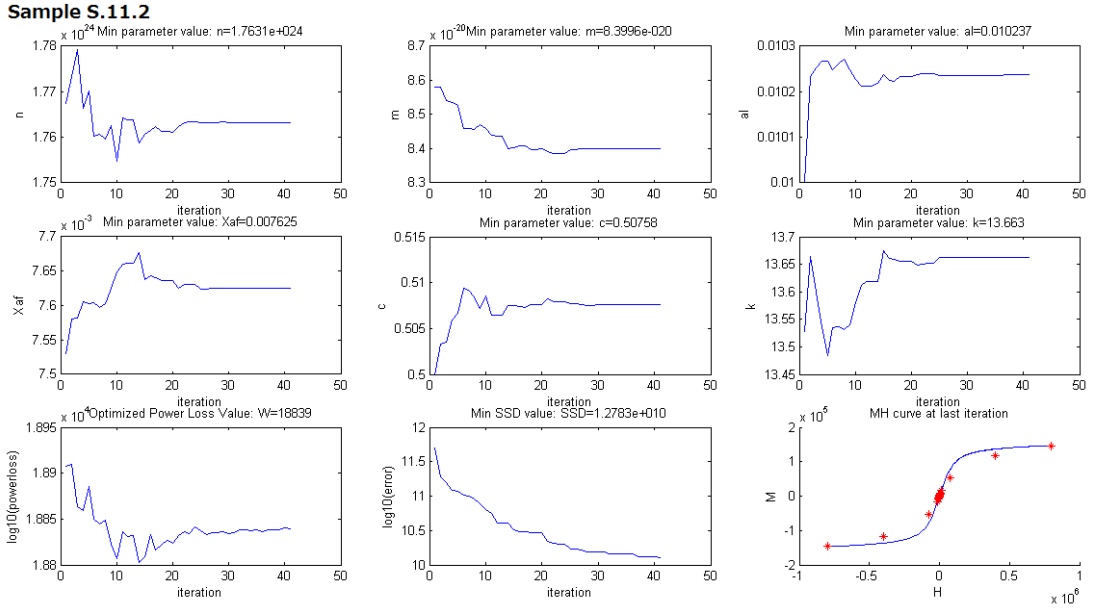

Sample S.11.3

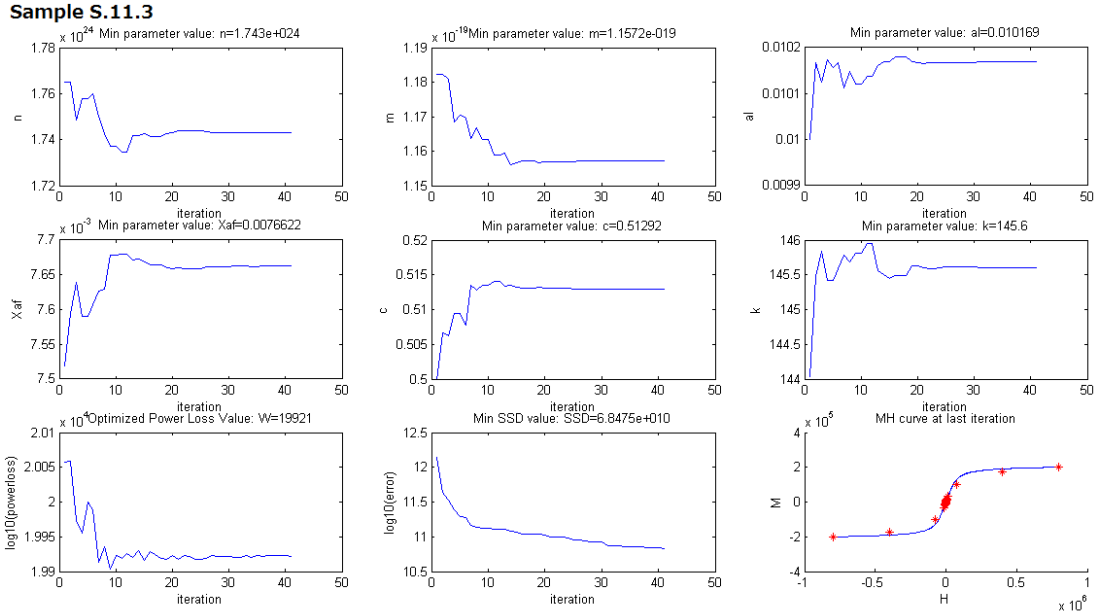

Sample S.11.4

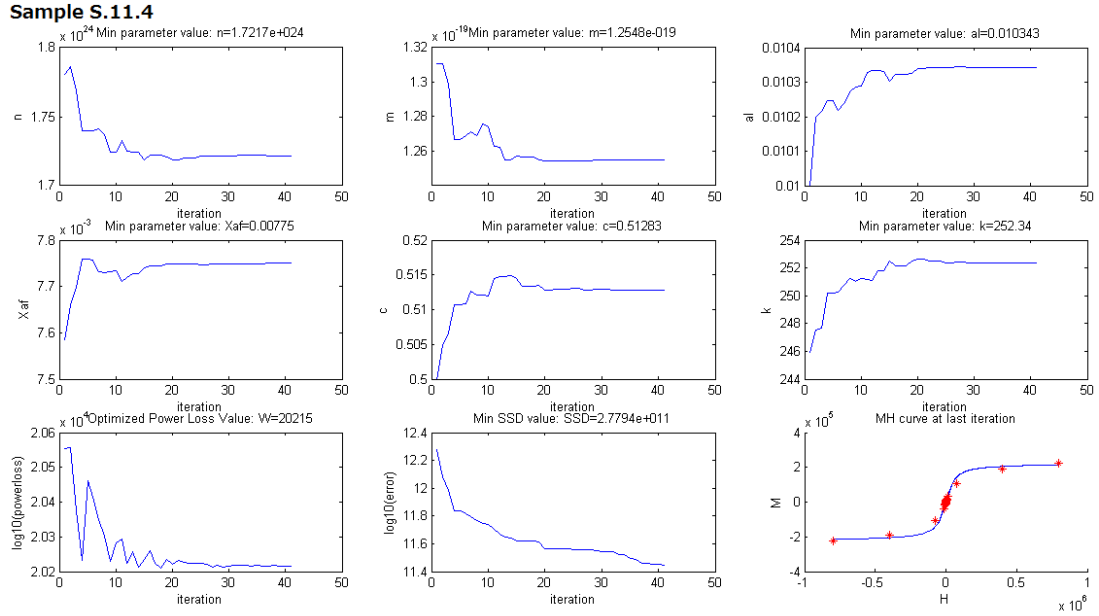

Sample S.12.1

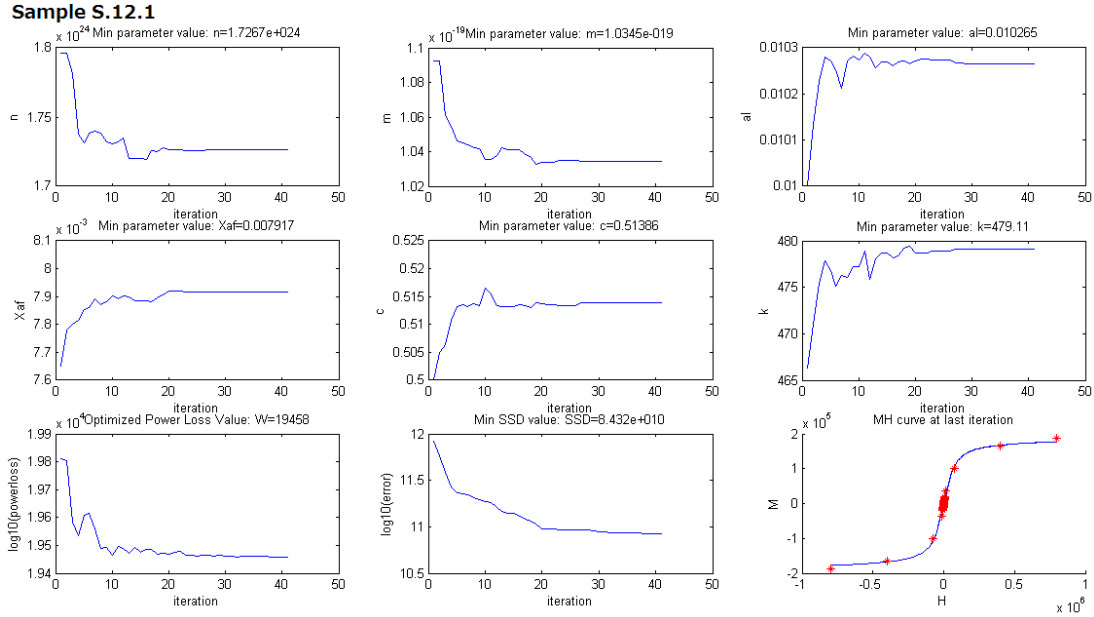

Sample S.12.2

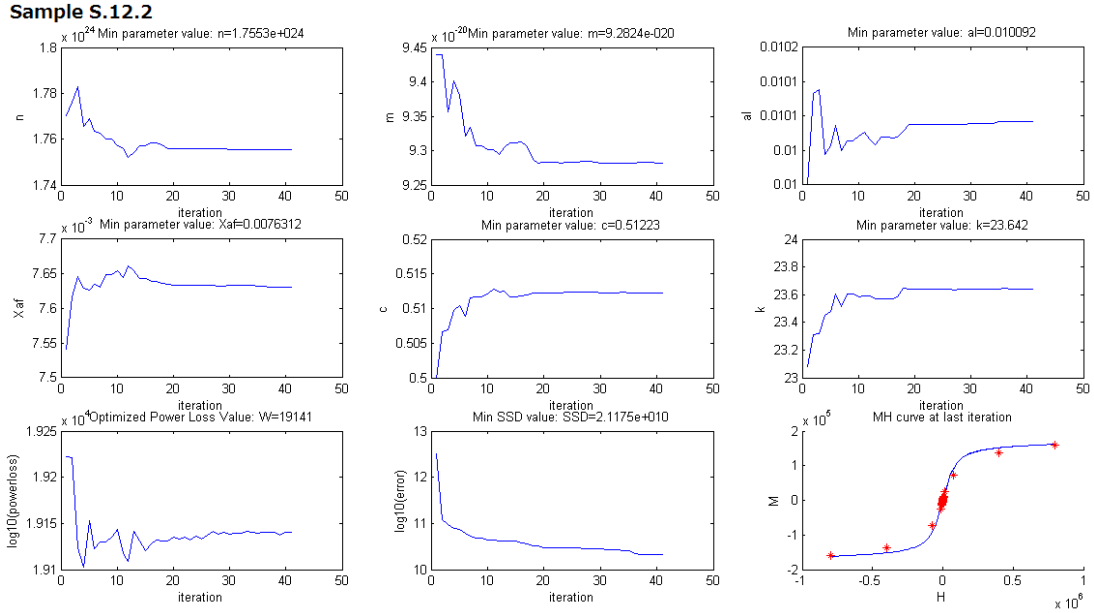

Sample S.12.3

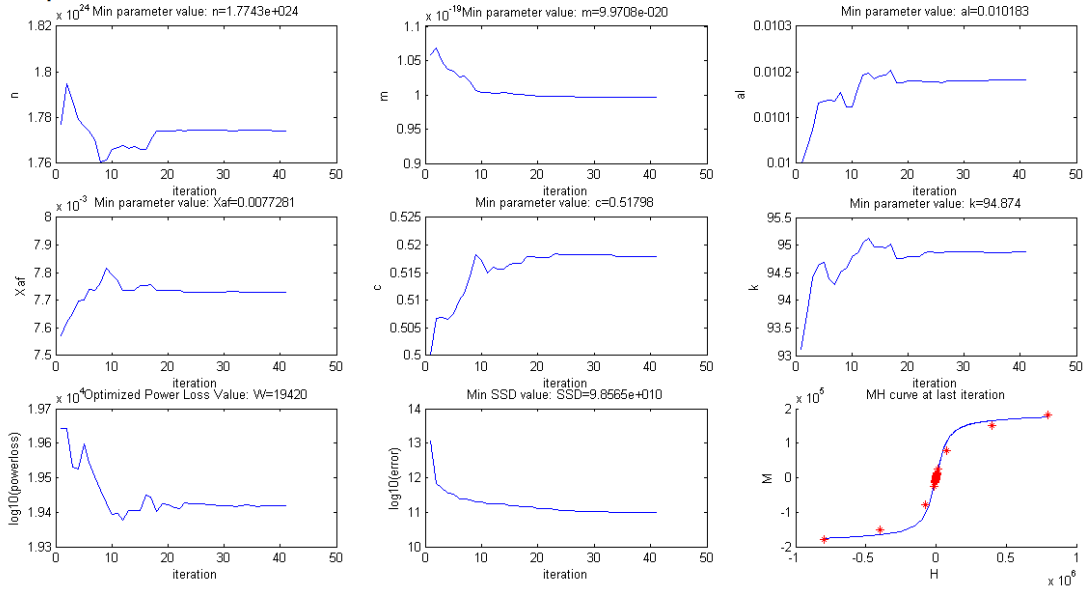

Sample S.13.1

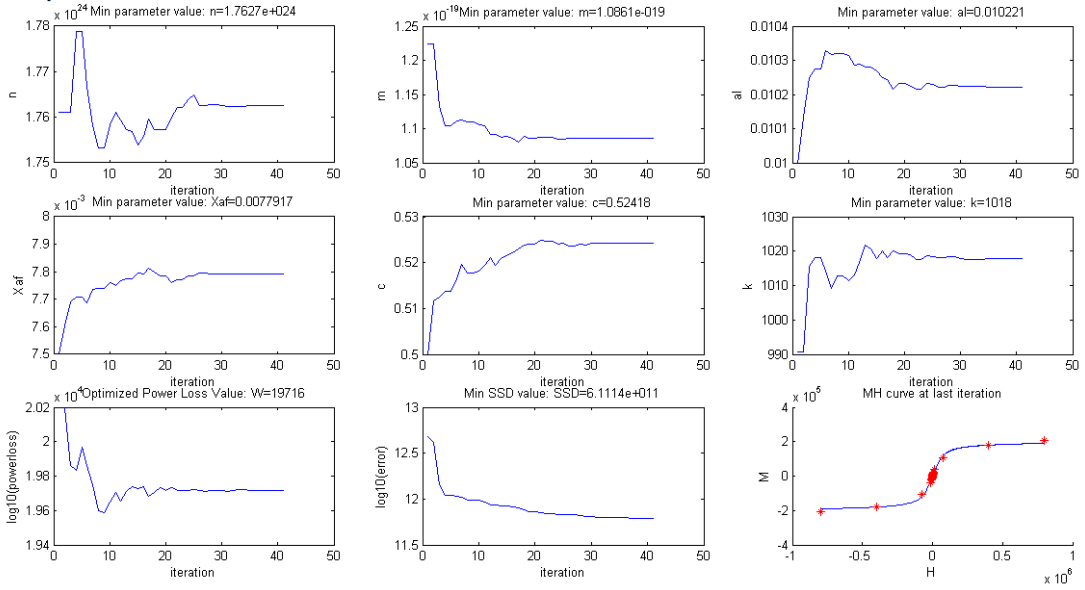

Sample S.13.2

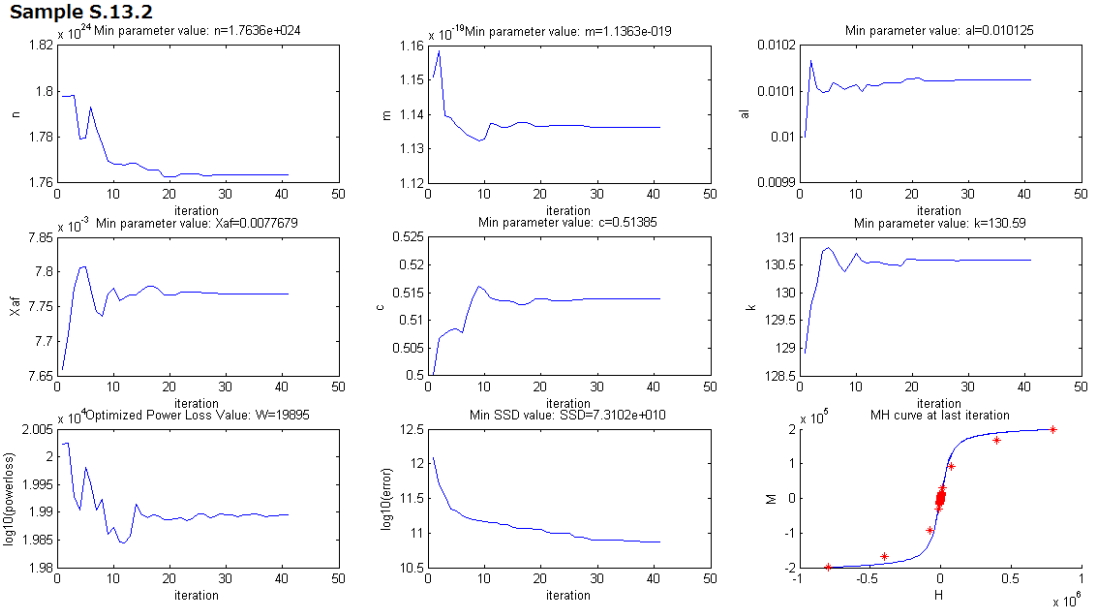

Sample S.13.3

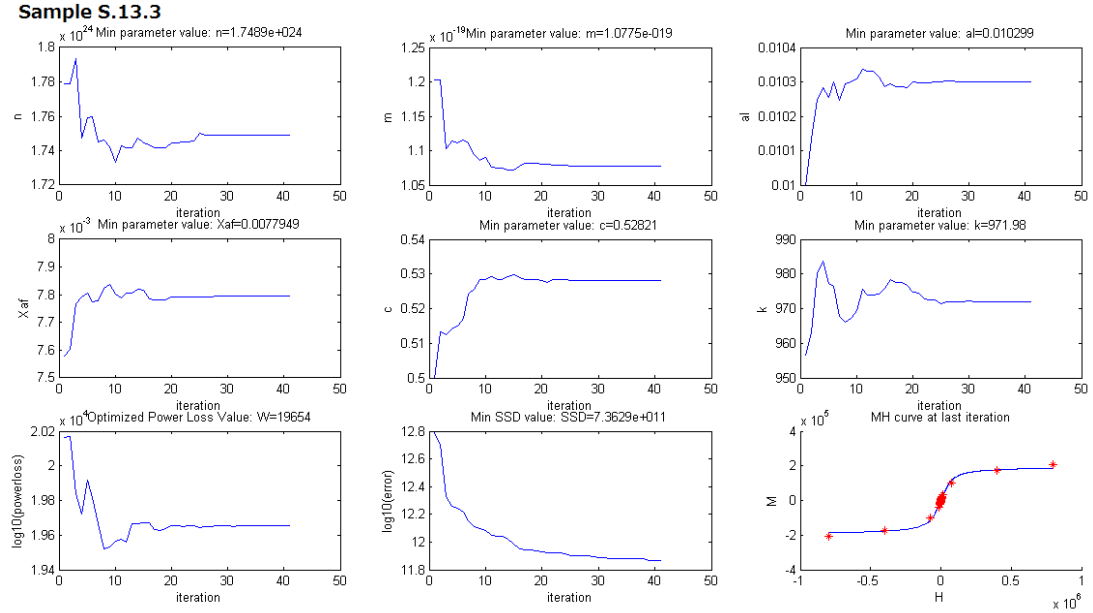

Sample S.13.4

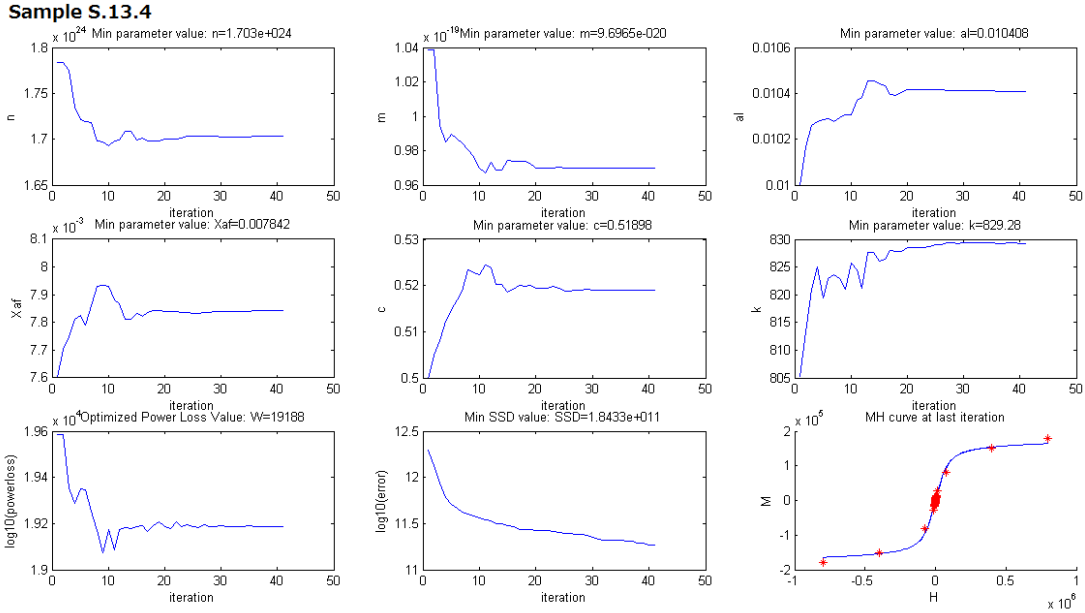

Sample S.16.3

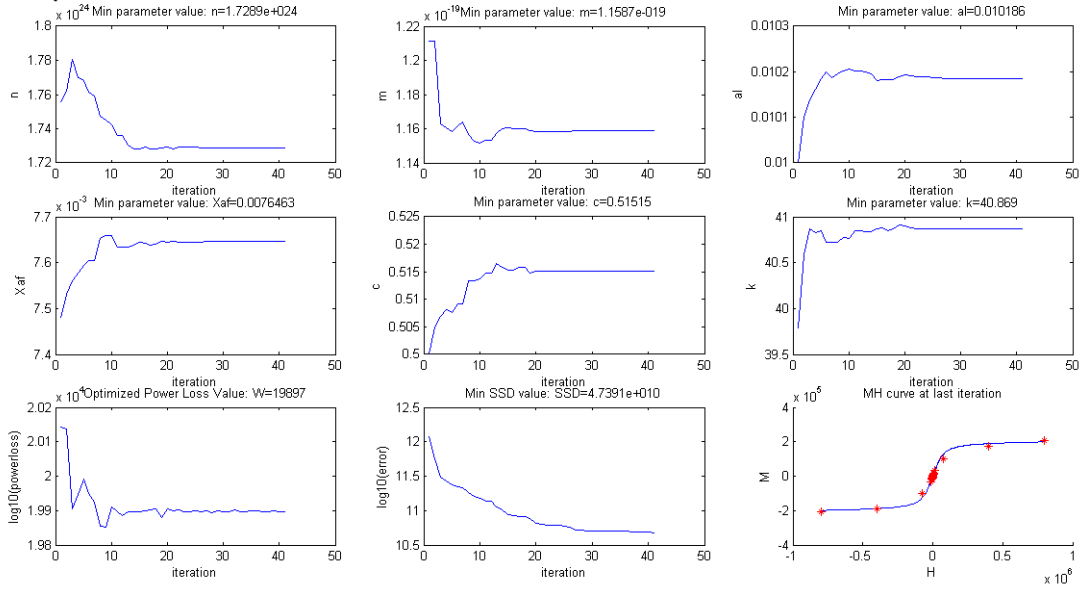

Sample S.17.2

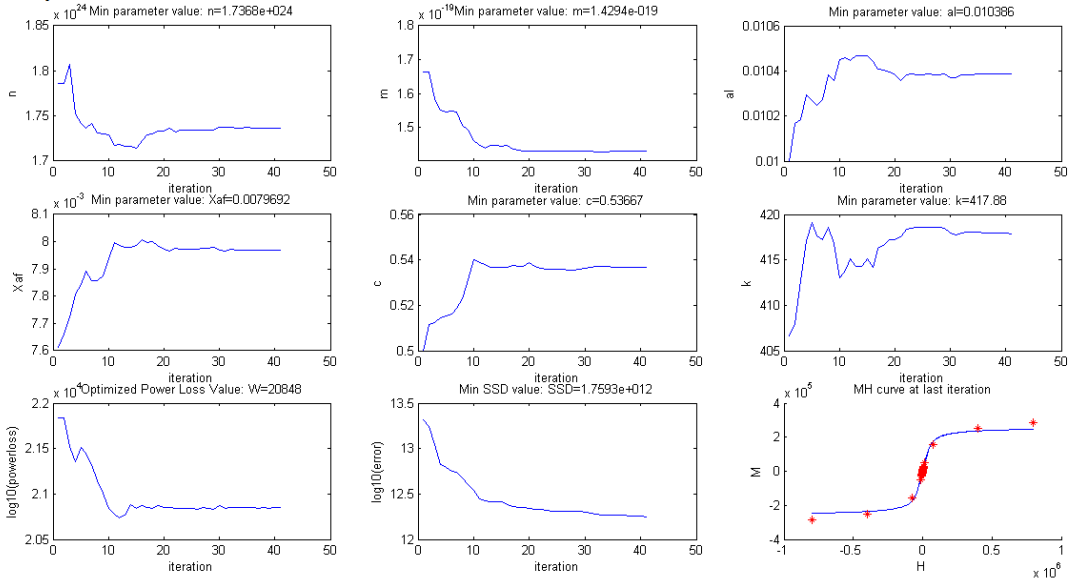

Sample S.18.3

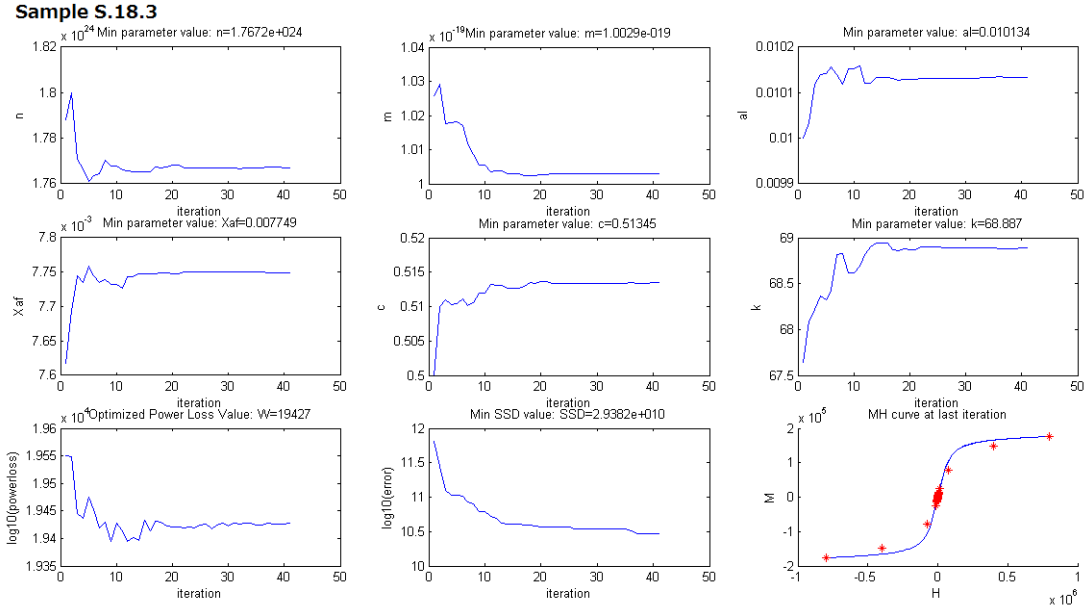

Sample S.18.4

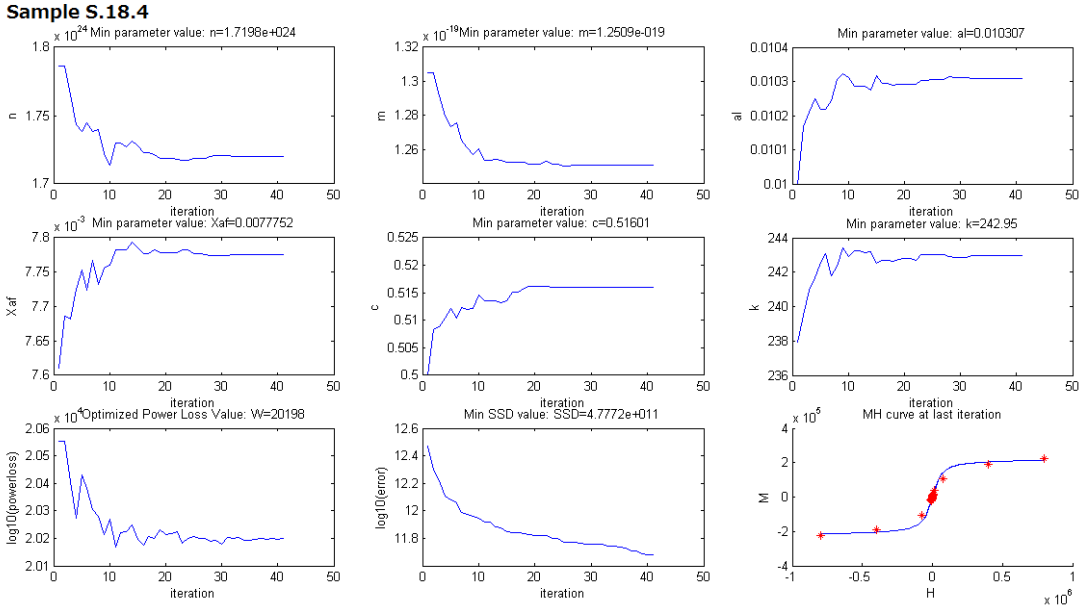
x 10^-24 Min parameter value: n=1.7198e+024
n
iteration
x 10^-19 Min parameter value: m=1.2509e-019
m
iteration
Min parameter value: al=0.010307
al
iteration
x 10^-3 Min parameter value: Xaf=0.0077752
Xaf
iteration
Min parameter value: c=0.51601
c
iteration
Min parameter value: k=242.95
k
iteration
x 10^4 Optimized Power Loss Value: W=20198
log10(powerloss)
iteration
Min SSD value: SSD=4.7772e+011
log10(error)
iteration
x 10^5 MH curve at last iteration
M
H
x 10^6

Bibliography

[1] H. W. F. Sung and C. Rudowicz, “A closer look at the hysteresis loop for ferromagnets - A survey of misconceptions and misinterpretations in textbooks,” no. 1985, p. 24, 2002.

[2] H. W. F. Sung and C. Rudowicz, “Physics behind the magnetic hysteresis loop - A survey of misconceptions in magnetism literature,” *J. Magn. Magn. Mater.*, vol. 260, no. 1–2, pp. 250–260, 2003.

[3] S. Blundell, “Units in magnetism,” *Oxford Univ. Press*, p. 1962005, 2005.

[4] S. Tumanski, *Handbook of Magnetic Measurements*, vol. 96, no. 2395. 2011.

[5] Coey, *Magnetism and Magnetic Materials*. 2009.

[6] Lisa Tauxe, “Essentials of Paleomagnetism,” 2016. [Online]. Available: http://earthref.org/MAGIC/books/Tauxe/Essentials/.

[7] IEEE, “Units for Magnetic Properties.” IEEE, 2015.

[8] B. M. Moskowitz, “Hitchhiker’s Guide to Magnetism,” *Environ. Magn. Work.*, vol. 279, no. 1, p. 48, 1991.

[9] R. Clarke, “Unit Systems in Electromagnetism,” *University of Surrey*, 2016. [Online]. Available: info.ee.surrey.ac.uk/Workshop/advice/coils/unit_systems/.

[10] S. Shafiee and E. Topal, “When will fossil fuel reserves be diminished?,” *Energy Policy*, vol. 37, no. 1, pp. 181–189, 2009.

[11] S. Sabihuddin, A. E. Kiprakis, and M. Mueller, “A numerical and graphical review of energy storage technologies,” *Energies*, vol. 8, no. 1, pp. 172–216, 2015.

[12] Iea, “Worldwide Trends in Energy Use and Efficiency,” *Iea.Org*, p. 93, 2008.

[13] U.S. Energy Information Agency, “International Energy Outlook 2013,” *Outlook 2013*, p. 312, 2013.

[14] B. Bolund, H. Bernhoff, and M. Leijon, “Flywheel energy and power storage systems,” *Renew. Sustain. Energy Rev.*, vol. 11, no. 2, pp. 235–258, 2007.

[15] R. E. Pelrine, “Room temperature, open-loop levitation of microdevices using\ndiamagnetic materials,” *IEEE Proc. Micro Electro Mech. Syst. An Investig. Micro Struct. Sensors, Actuators, Mach. Robot.*, pp. 1–4, 1990.

[16] R. E. Pelrine, “Magnetic Field Levitation,” U.S. Patent Office: US5396136A, 1995.

[17] R. E. Pelrine and J. R. Heim, “Frictionless Transport Apparatus and Method,” U.S. Patent Office: US6483222B2, 2002.

[18] R. E. Pelrine, “Diamagnetic Levitation,” *American Scientist*, American Scientist, 2004.

[19] M. V Berry and A. K. Geim, “Of flying frogs and levitrons,” *Eur. J. Phys.*, vol. 18, no. 4, pp. 307–313, 1999.

[20] A. K. Geim, M. D. Simon, M. I. Boamfa, and L. O. Heflinger, “Magnet levitation at your fingertips,” *Nature*, vol. 400, no. 6742, pp. 323–324, 1999.

[21] M. D. Simon and A. K. Geim, “Diamagnetic levitation: Flying frogs and floating magnets (invited),” *J. Appl. Phys.*, vol. 87, no. 9, pp. 6200–6204, 2000.

[22] M. D. Simon, L. O. Heflinger, and A. K. Geim, “Diamagnetically stabilized magnet levitation,” *Am. J. Phys.*, vol. 69, no. 6, p. 702, 2001.

[23] E. Cazacu and I. V. Nemoianu, “Diamagnetic Levitation Setting with Enlargement Of the Stability Area,” *Rom. J. Tech. Sci.*, vol. 53, no. 1, pp. 23–

29, 2008.

[24] E. Cazacu and I. V. Nemoianu, “A Novel Configuration for Static Permanent Magnet Levitation,” *Rom. J. Tech. Sci.*, vol. 55, no. 2, pp. 153–160, 2010.

[25] E. Cazacu and A. Nicolae, “The influence of the diamagnetic plate thickness on the stability zone in vertical static magnetic levitation,” *11th Int. Conf. Optim. Electr. Electron. Equipment, OPTIM 2008*, vol. 0, no. 4, pp. 15–20, 2008.

[26] G. Kustler, “Diamagnetic levitation - Historical milestones,” *Rev. Roum. Des Sci. Tech. Electrotech. Energ.*, vol. 52, no. 3, pp. 265–282, 2007.

[27] G. Küstler, “Diamagnetically stabilised levitation over copper,” *Electron. Lett.*, vol. 48, no. 2, p. 95, 2012.

[28] G. Küstler, “Extraordinary levitation height in a weight compensated diamagnetic levitation system with permanent magnets,” *IEEE Trans. Magn.*, vol. 48, no. 6, pp. 2044–2048, 2012.

[29] H. Bleuler and J. Sandtner, “Passive magnetic bearings for flywheels,” *Solid Mech. its …*, pp. 2–6, 2005.

[30] R. Pena-Alzola, R. Sebastián, J. Quesada, and A. Colmenar, “Review of Flywheel based Energy Storage Systems,” *Int. Conf. Power Eng. Energy Electr. Drives*, no. May, pp. 1–6, 2011.

[31] H. Liu and J. Jiang, “Flywheel energy storage-An upswing technology for energy sustainability,” *Energy Build.*, vol. 39, no. 5, pp. 599–604, 2007.

[32] M. Ragheb, “Kinetic energy flywheel energy storage ©,” no. 1, 2013.

[33] J. Koyanagi, “Durability of filament-wound composite flywheel rotors,” *Mech. Time-Dependent Mater.*, vol. 16, no. 1, pp. 71–83, 2012.

[34] J. R. Hull, “Superconducting bearings,” *Supercond. Sci. Technol.*, vol. 13, no.

2, pp. R1–R15, 2000.

[35] V. Scholar, “Low-Cost Flywheel Energy Storage for Mitigating the Variability of Renewable Power Generation,” *Ieee*, vol. 22, pp. 1–22, 2012.

[36] J. Hansen, *An Assessment of Flywheel High Power Energy Storage Technology for Hybrid Vehicles [Thesis]*, no. December. 2011.

[37] S. Earnshaw, “On the Nature of the Molecular Forces which Regulate the Constitution of the Luminiferous Ether,” *Trans. Camb. Phil. Soc.*, vol. 7, no. 97, 1839.

[38] M. a. Pichot, J. P. Kajs, B. R. Murphy, A. Ouroua, B. M. Rech, R. J. Hayes, J. H. Beno, G. D. Buckner, and A. B. Palazzolo, “Active magnetic bearings for energy storage systems for combat vehicles,” *IEEE Trans. Magn.*, vol. 37, no. 1, pp. 318–323, 2001.

[39] B. Polajzer, D. Dolinar, and G. Stumberger, “Design of horizontal shaft acive magnetic bearing system,” *Int. Semin. Vib. Acoust. noise Electr. Mach.*, pp. 51–55, 2000.

[40] M. Antila, *Electromechanical Properties of Radial Active Magnetic Bearings*. 1998.

[41] M. Strasik, P. E. Johnson, A. C. Day, J. Mittleider, M. D. Higgins, J. Edwards, J. R. Schindler, K. E. McCrary, C. R. McIver, D. Carlson, J. F. Gonder, and J. R. Hull, “Design, fabrication, and test of a 5-kWh/100-kW flywheel energy storage utilizing a high-temperature superconducting bearing,” *IEEE Trans. Appl. Supercond.*, vol. 17, no. 2, pp. 2133–2137, 2007.

[42] a V Filatov and E. H. Maslen, “Passive magnetic bearing for flywheel energy storage systems,” *IEEE Trans. Magn.*, vol. 37, no. 6, pp. 203–3924, 2001.

[43] Ohji, “Permanent Magnet Bearing for horizontal and vertical shaft machines: A comparative study,” *J. Appl. Phys.*, 1999.

[44] R. Bassani, E. Ciulli, F. DI Puccio, and A. Musolino, “Study of conic permanent magnet bearings,” *Meccanica*, vol. 36, no. 6, pp. 745–754, 2001.

[45] H. W. Lee, K. C. Kim, and J. Lee, “Review of Maglev train technologies,” *IEEE Trans. Magn.*, vol. 42, no. 7, pp. 1917–1925, 2006.

[46] T. Azukizawa, S. Yamamoto, and N. Matsuo, “Feasibility Study of a Passive Magnetic Bearing Using the Ring Shaped Permanent Magnets,” *IEEE Trans. Magn.*, vol. 44, no. 11, pp. 4277–4280, 2008.

[47] Y. M. Choi, M. G. Lee, D. G. Gweon, and J. Jeong, “A new magnetic bearing using Halbach magnet arrays for a magnetic levitation stage,” *Rev. Sci. Instrum.*, vol. 80, no. 4, pp. 1–10, 2009.

[48] S. Y. Yoo, W. Y. Kim, S. J. Kim, W. R. Lee, Y. C. Bae, and M. Noh, “Optimal design of non-contact thrust bearing using permanent magnet rings,” *Int. J. Precis. Eng. Manuf.*, vol. 12, no. 6, pp. 1009–1014, 2011.

[49] J. Sandtner and H. Bleuler, “Electrodynamic Passive Magnetic Bearing with Planar Halbach Array,” *Int. Symp. Magn. Bear.*, pp. 1–6, 2004.

[50] J. Detoni, “Progress on electrodynamic passive magnetic bearings for rotor levitation,” *Proc. Inst. Mech. Eng. Part C J. Mech. Eng. Sci.*, vol. 228, no. 10, pp. 1829–1844, 2013.

[51] T. a. Lembke, *Electrodynamic Bearing*. 2005.

[52] F. J. Muller, “Unipolar induction revisited: New experiments and the ‘edge effect’ theory,” *IEEE Trans. Magn.*, vol. 50, no. 1, 2014.

[53] M. Siebert, B. Ebihara, R. Jansen, R. L. Fusaro, W. Morales, A. Kascak, and A. Kenny, “Magnetic Bearing Flywheel,” no. February, 2002.

[54] R. Jansen and Ei. DiRusso, “Passive Magnetic Bearing Ferrofluid Stabilization,” no. February 1996, 1996.

[55] R. M. Harrigan, “Levitation Device,” 1983.

[56] T. B. Jones, M. Washizu, and R. Gans, “Simple theory for the Levitron®,” *J. Appl. Phys.*, vol. 82, no. 2, p. 883, 1997.

[57] H. R. Dullin and R. W. Easton, “Stability of Levitrons,” *Phys. D*, vol. 126, pp. 1–17, 1999.

[58] M. V. Berry, “The Levitron™- An adiabatic trap for spins.pdf,” *Proceedings of The Royal Society A*. pp. 1207–1220, 1996.

[59] M. D. Simon, “Spin stabilized magnetic levitation,” *Am. J. Phys.*, vol. 65, no. April, p. 286, 1997.

[60] M. M. Michaelis, “Horizontal axis Levitron ∗ — a physics demonstration,” vol. 67.

[61] S. Sabihuddin, A. Kiprakis, and M. Mueller, “A diamagnetically stabilized magnetically levitated flywheel battery,” *2013 8th Int. Conf. Exhib. Ecol. Veh. Renew. Energies, EVER 2013*, no. C, pp. 1–3, 2013.

[62] L. Rolim and A. Ferreira, “Flywheel generator with switched reluctance machine,” *... Electr. Mach.*, 2002.

[63] R. Bassani, “Earnshaw (1805–1888) and Passive Magnetic Levitation,” *Meccanica*, vol. 41, no. 4, pp. 375–389, Aug. 2006.

[64] T. C. S. Chow, P. L. Wong, and K. P. Liu, “Shape effect of magnetic source on stabilizing range of vertical diamagnetic levitation,” *IEEE Trans. Magn.*, vol. 48, no. 1, pp. 26–30, 2012.

[65] T. C. S. Chow, P. L. Wong, and K. P. Liu, “Experimental study on stabilizing range extension of diamagnetic levitation under modulated magnetic field,” *J. Phys. Conf. Ser.*, vol. 200, no. 3, p. 32013, 2010.

[66] K. D. Bachovchin, J. F. Hoburg, and R. F. Post, “Stable levitation of a passive

magnetic bearing," *IEEE Trans. Magn.*, vol. 49, no. 1, pp. 609–617, 2013.

[67] K. D. Bachovchin, J. F. Hoburg, and R. F. Post, "Magnetic fields and forces in permanent magnet levitated bearings," *IEEE Trans. Magn.*, vol. 48, no. 7, pp. 2112–2120, 2012.

[68] M. Boukallel, J. Abadie, E. Piat, and A. Savary, "Levitated micro-nano force sensor using diamagnetic materials magnetic materials," *Proc. IEEE Int. Conf. Robot. Autom.*, pp. 3219–3224, 2003.

[69] R. Moser and H. Bleuler, "Precise positioning using electrostatic glass motor with diamagnetically suspended rotor," *IEEE Trans. Appl. Supercond.*, vol. 12, no. 1, pp. 937–939, 2002.

[70] R. D. Waldron, "Diamagnetic levitation using pyrolytic graphite," *Rev. Sci. Instrum.*, vol. 37, no. 1, pp. 29–35, 1966.

[71] G. T. Gillies, "Levitation of ordinary diamagnets at room temperature," vol. 54, 1991.

[72] R. D. Waldron, "Diamagnetic Levitation And/Or Stabilizing Devices." pp. 1–12, 1969.

[73] Emslie, "Magnetic Support Systems," 1970.

[74] H. Chetouani, C. Jeandey, V. Haguet, H. Rostaing, G. Reyne, and C. Dieppedale, "Diamagnetic levitation with permanent magnet microarrays for precise contactless guiding and trapping of micro-droplets and bioparticles in fluids," *INTERMAG 2006 - IEEE Int. Magn. Conf.*, vol. 42, no. 10, p. 106, 2006.

[75] C. Pigot, H. Chetouani, G. Poulin, and G. Reyne, "Diamagnetic levitation of solids at microscale," *IEEE Trans. Magn.*, vol. 44, no. 11 PART 2, pp. 4521–4524, 2008.

[76] R. H. Austin and K. T. Mcdonald, "Diamagnetic Levitation The Magnetic

Field On the Axis of the Disk," vol. 8544, no. 2, pp. 1–6, 2001.

[77] E. Cazacu and I. Nemoianu, "Estimation of the influence terms involved in static diamagnetic levitation," *Rev. Roum. Des Sci. ...*, pp. 283–290, 2007.

[78] C. Emil, "Permanent magnet levitation stabilized by Diamagnetic materials: a case study," *Int. Conf. Comput. Electromagn.*, pp. 1–2, 2006.

[79] M. Boukallel, E. Piat, and J. Abadie, "Passive diamagnetic levitation: theoretical foundations and application to the design of a micro-nano force sensor," *Proc. 2003 IEEE/RSJ Int. Conf. Intell. Robot. Syst. (IROS 2003) (Cat. No.03CH37453)*, vol. 2, no. October, 2003.

[80] J. N. Ho and W. Wang, "Diamagnetic Levitating Rotor," *Prog. Electromagn. Res.*, pp. 246–250, 2005.

[81] J. N. Ho and W. C. Wang, "Electric generator using a triangular diamagnetic levitating rotor system," *Rev. Sci. Instrum.*, vol. 80, no. 2, pp. 1–9, 2009.

[82] E. N. Economou, T. Koschny, and C. M. Soukoulis, "Strong diamagnetic response in split-ring-resonator metamaterials: Numerical study and two-loop model," *Phys. Rev. B - Condens. Matter Mater. Phys.*, vol. 77, no. 9, pp. 5–8, 2008.

[83] K. Liu, W. Zhang, W. Liu, W. Chen, K. Li, F. Cui, and S. Li, "An innovative micro-diamagnetic levitation system with coils applied in micro-gyroscope," *Microsyst. Technol.*, vol. 16, no. 3, pp. 431–439, 2010.

[84] R. Moser, J. Sandtner, and H. Bleuler, "Diamagnetic Suspension Assisted by Active Electrostatic Actuators," *6th Int. Symp. Magn. Suspens. Technol.*, no. 4, pp. 4–8, 2001.

[85] R. Moser, F. Barrot, J. Sandtner, and H. Bleuler, "Optimization of Two-Dimensional Permanent Magnet Arrays for Diamagnetic Levitation," *Int. Conf. Magn. Levitated Syst. Linear Drives*, pp. 1–5, 2002.

[86] R. Moser, Y. Regamey, J. Sandtner, and H. Bleuler, “Passive diamagnetic levitation for flywheels.” pp. 599–604, 2002.

[87] H. Suzuki, M. Kanke, T. Sato, J. Sekine, and A. Ito, “Extremely Energy-Saving Linear Drive Technique by using Diamagnetic Graphite Plate,” *Int. Conf. Magn. Levitated Syst. Linear Drives*, no. 87, 2008.

[88] H. Suzuki, A. Suzuki, S. Sasaki, and A. Ito, “Preliminary experimental study on new contact-free linear drive system using diamagnetic material,” *... Syst. Linear ...*, pp. 1–5, 2006.

[89] Liu, “Variable Capacitance motor with Levitated Diamagnetic rotor,” 2008.

[90] Griffiths, *Introduction to Electrodynamics 3rd edition*. 1999.

[91] M. Benz, “Superparamagnetism : Theory and Applications,” *Superparamagnetism Theory Appl.*, pp. 1–27, 2012.

[92] “Quotation Q-11471.” Harriet Wooding, 2013.

[93] “Quotation Q63300.” Photofabrication, 2013.

[94] Q. a. Pankhurst, N. T. K. Thanh, S. K. Jones, and J. Dobson, “Progress in applications of magnetic nanoparticles in biomedicine.,” *J. Phys. D. Appl. Phys.*, vol. 42, p. 224001, 2009.

[95] Koch, “Nanostructured Materials: Processing, Properties, and Applications.” 2007.

[96] C. Scherer and A. M. F. Neto, “Ferrofluids — Properties and applications,” *Brazillian J. Phys.*, vol. 35, no. 3, pp. 718–727, 2005.

[97] J. Philip and J. M. Laskar, “Optical Properties and Applications of,” vol. 1, no. 1, pp. 3–20, 2012.

[98] O. Gutfleisch, M. A. Willard, E. Brück, C. H. Chen, S. G. Sankar, and J. P. Liu, “Magnetic materials and devices for the 21st century: Stronger, lighter,

and more energy efficient," *Adv. Mater.*, vol. 23, no. 7, pp. 821–842, 2011.

[99] H. Zeng, J. Li, J. P. Liu, Z. L. Wang, and S. Sun, "Exchange-coupled nanocomposite magnets by nanoparticle self-assembly.," *Nature*, vol. 420, no. 6914, pp. 395–398, 2002.

[100] G. Arnold, "Soft Magnetics Application Guide," *Group*, no. February, pp. 1–37, 2000.

[101] M. E. McHenry, M. A. Willard, and D. E. Laughlin, *Amorphous and nanocrystalline materials for applications as soft magnets*, vol. 44, no. 4. 1999.

[102] "Finemet EMC Components Catalog," 2005.

[103] "Nanoperm Datasheet." Magnetec: Magnet Technologie, 2015.

[104] "Nanocrystalline Vitroperm." EMC Products, 2010.

[105] D. S. Mathew and R. S. Juang, "An overview of the structure and magnetism of spinel ferrite nanoparticles and their synthesis in microemulsions," *Chem. Eng. J.*, vol. 129, no. 1–3, pp. 51–65, 2007.

[106] R. Valenzuela, "Novel applications of ferrites," *Phys. Res. Int.*, vol. 2012, 2012.

[107] S. Sgobba, "Physics and measurements of magnetic materials," *Cern*, vol. 4, p. 25, 2011.

[108] "Coercivity," *Wikipedia*, 2014. [Online]. Available: http://en.wikipedia.org/wiki/Coercivity.

[109] Magnetics Division of Spang & Company, "A Critical Comparison of Ferrites with Other Magnetic Materials," p. 11, 2000.

[110] "Non-oriented Silicon Steel," *Cogent*, 2015. [Online]. Available: http://cogent-power.com/cms-data/downloads/Non oriented electrical

steel.pdf.

[111] “Non-grain Oriented Electrical Steel (NGOES0),” *Arnold Magnetic Technologies*, 2015. [Online]. Available: http://www.arnoldmagnetics.com/Precision-Thin-Metals/Materials/Silicon-Steel/Non-Grain-Oriented-Electrical-Steel.aspx.

[112] “Data Sheet: Metglas 2605,” *Hitachi Metals*, 2011. [Online]. Available: http://www.metglas.com/assets/pdf/2605sa1.pdf.

[113] J. Cox, “Iron Powder Cores for High Q Inductors,” 2015.

[114] “PC Series: Power Conversion & Line Filter Applications,” 2007.

[115] “Magnetite,” *Wikipedia*, 2015. [Online]. Available: https://en.wikipedia.org/wiki/Magnetite.

[116] A. Krings, S. Nategh, and A. Stening, “Measurement and modeling of iron losses in electrical machines,” *Proc. 5th …*, 2012.

[117] “Magnetic materials: Ferrites,” 2001.

[118] “Types of Ferrite Material,” 2015.

[119] Matsuo, “Magnetic Properties and Mechanical Strength of MnZn Ferrite,” 2015. [Online]. Available: http://www.fdk.com/cyber-e/technical/pi_technical04.html.

[120] K. Kawano, M. Hachiya, Y. Iijima, N. Sato, and Y. Mizuno, “The grain size effect on the magnetic properties in NiZn ferrite and the quality factor of the inductor,” *J. Magn. Magn. Mater.*, vol. 321, no. 16, pp. 2488–2493, 2009.

[121] A. Bieńkowski, R. Szewczyk, and A. Wiśniewska, “Magnetostrictive properties and magnetoelastic Villari effect in the high-permeability Mn-Zn ferrites,” *Czechoslov. J. Phys.*, vol. 54, no. SUPPL. 4, pp. 12–15, 2004.

[122] M. Javorski, J. Slavic, and M. Boltezar, “Frequency characteristics of

magnetostriction in electrical steel related to the structural vibrations," *IEEE Trans. Magn.*, vol. 48, no. 12, pp. 4727–4734, 2012.

[123] J. L. Mattei, E. Le Guen, A. Chevalier, and A. C. Tarot, "Experimental determination of magnetocrystalline anisotropy constants and saturation magnetostriction constants of NiZn and NiZnCo ferrites intended to be used for antennas miniaturization," *J. Magn. Magn. Mater.*, vol. 374, no. C, pp. 762–768, 2015.

[124] "Summary of Typical Ferrite Properties," 2015.

[125] V. Zaspalis, V. Tsakaloudi, E. Papazoglou, M. Kolenbrander, R. Guenther, and P. V. a N. D. E. R. Valk, "Development of a New MnZn-Ferrite Soft Magnetic Material for High Temperature Power Applications," pp. 585–591, 2004.

[126] L. Zegadi, J. J. Rousseau, B. Allard, P. Tenant, and D. Renault, "Model of power soft MnZn ferrites, including temperature effects," *IEEE Trans. Magn.*, vol. 36, no. 4 PART 2, pp. 2022–2032, 2000.

[127] M. P. Reddy, "Characterization and Electromagnetic Studies on NiZn and NiCuZn Ferrites Prepared by Microwave Sintering Technique," *Mater. Sci. Appl.*, vol. 3, no. 9, pp. 628–632, 2012.

[128] He, Li, and Sun, "Microstructure and magnetic properties of high silicon electrical steel produced by electron beam PVD," *J. Magn. Magn. Mater.*, vol. 320, pp. 217–221, 2008.

[129] "How to choose Iron Powder, Sendust, Koolmu, High Flux and MPP Cores as output inductor and chokes," *CWS ByteMark*, 2015. [Online]. Available: https://www.coilws.com/index.php?main_page=page&id=41.

[130] J. Cox, "Iron Powder Core Selection For RF Power Applications."

[131] "Soft Magnetic Cobalt-Iron Alloys," 2013.

[132] F. Díaz-González, A. Sumper, O. Gomis-Bellmunt, and R. Villafáfila-Robles, "A review of energy storage technologies for wind power applications," *Renew. Sustain. Energy Rev.*, vol. 16, no. 4, pp. 2154–2171, 2012.

[133] "SMA 48, 50 High Permeability Alloys," *JLC Electromet*, 2015. [Online]. Available: http://www.jlcelectromet.com/sma50.htm.

[134] "Permalloy 80," *ESPI Metal*, 2015. [Online]. Available: http://www.espimetals.com/index.php/technical-data/175-permalloy-80.

[135] "Grain-Oriented Electrical Steel Technical Data Sheet," 2012.

[136] "Carlite Grain Oriented Electrical Steels," 2012.

[137] "Hiperco 50A Alloy (datasheet)," *Carpenter*, 2015. [Online]. Available: http://cartech.ides.com/datasheet.aspx?i=103&e=199&c=TechArt.

[138] "Tape Wound Cores: Round Permalloy 80 Datasheet," *Magnetics*, 2015. [Online]. Available: http://www.mag-inc.com/products/tape-wound-cores/round-permalloy-80.

[139] "MnZn Ferrite Core Datasheet," *Yuxiang*, 2015. [Online]. Available: http://www.magnet-tech.com/core/MnZn/characteristics.htm.

[140] "Saturation curves for soft magnetic materials," *Field Precision LLC*, 2015. [Online]. Available: http://www.fieldp.com/magneticproperties.html.

[141] M. Dekker and A. R. Reserved, "Chapter 2 Magnetic Materials and Their Characteristics," p. 2, 2004.

[142] "Magnetic Properties of materials," *NPL*, 2015. [Online]. Available: http://www.kayelaby.npl.co.uk/general_physics/2_6/2_6_6.html.

[143] "Magnetic properties of Ferromagnetic Materials," *Hyperphysics*, 2015. [Online]. Available: http://hyperphysics.phy-astr.gsu.edu/hbase/tables/magprop.html.

[144] W. Callister and D. Rethwisch, *Materials science and engineering: an introduction*, vol. 94. 2007.

[145] N. Cowlam, M. Sakata, and H. a Davies, "Metallic Glass," *J. Phys. F Met. Phys.*, vol. 9, no. 11, pp. L203–L208, 2001.

[146] A. Lakshmanan, *Sintering of Ceramics - New Emerging Techniques*. InTech, 2012.

[147] S. Grundas, *Advances in Induction and Microwave heating of Mineral and Organic Materials*. InTech, 2011.

[148] S. Takayama, J. Fukushima, J. Nishijo, M. Saito, S. Sano, and M. Sato, "Sintering of soft magnetic material under microwave magnetic field," *Phys. Res. Int.*, vol. 2012, 2012.

[149] W. Wu, Q. He, and C. Jiang, "Magnetic iron oxide nanoparticles: Synthesis and surface functionalization strategies," *Nanoscale Res. Lett.*, vol. 3, no. 11, pp. 397–415, 2008.

[150] S. Laurent, D. Forge, M. Port, A. Roch, C. Robic, L. V Elst, and R. N. Muller, "Magnetic Iron Oxide Nanoparticles: Synthesis, Stabilization, Vectorization, Physicochemical Characterizations, and Biological Applications," *Chem. Rev.*, vol. 108, no. 6, pp. 2064–2110, 2008.

[151] M. Mohapatra and S. Anand, "Synthesis and applications of nano-structured iron oxides / hydroxides – a review," *Int. J. Eng. Sci. Technol.*, vol. 2, no. 8, pp. 127–146, 2010.

[152] R. F. Butler and S. K. Banerjee, "Theoretical single-domain grain size range in magnetite and titanomagnetite," *J. Geophys. Res.*, vol. 80, no. 29, p. 4049, 1975.

[153] M. Winklhofer, K. Fabian, and F. Heider, "Magnetic blocking temperatures of magnetite calculated with a three-dimensional micromagnetic model," *J.*

Geophys. Res., vol. 102, no. B10, pp. 22695–22709, 1997.

[154] H. Kobori, T. Asahi, A. Yamasaki, A. Sugimura, T. Taniguchi, A. Ando, H. Kawanaka, Y. Naitoh, and T. Shimizu, "Electrical- and magneto-resistance control for magnetite nanoparticle sinter by regulation of heat treatment temperature," *J. Magn. Magn. Mater.*, vol. 323, no. 6, pp. 686–690, 2011.

[155] L. J. Kecskes, R. H. Woodman, S. F. Trevino, B. R. Klotz, and S. G. Hirsch, "The sintering and densification behaviour of an iron nanopowder characterized by comparative methods," *Army Res. lab*, no. February, 2003.

[156] M. C. Mascolo, Y. Pei, and T. A. Ring, "Room Temperature Co-Precipitation Synthesis of Magnetite Nanoparticles in a Large ph Window with Different Bases," *Materials (Basel).*, vol. 6, no. 12, pp. 5549–5567, 2013.

[157] M. Fang, V. Ström, R. T. Olsson, L. Belova, and K. V Rao, "Particle size and magnetic properties dependence on growth temperature for rapid mixed co-precipitated magnetite nanoparticles," *Nanotechnology*, vol. 23, p. 145601, 2012.

[158] A. G. Roca, M. P. Morales, and C. J. Serna, "Synthesis of Monodispersed Magnetite Particles From Different Organometallic Precursors," *IEEE Trans. Magn.*, vol. 42, no. 10, pp. 3025–3029, 2006.

[159] J. Xu, H. Yang, W. Fu, K. Du, Y. Sui, J. Chen, Y. Zeng, M. Li, and G. Zou, "Preparation and magnetic properties of magnetite nanoparticles by sol-gel method," *J. Magn. Magn. Mater.*, vol. 309, no. 2, pp. 307–311, 2007.

[160] J. Wang, J. Wan, and K. Chen, "Facile synthesis of superparamagnetic Fe-doped ZnO nanoparticles in liquid polyols," *Mater. Lett.*, vol. 64, no. 21, pp. 2373–2375, 2010.

[161] Y. Hou, J. Yu, and S. Gao, "Solvothermal reduction synthesis and characterization of superparamagnetic magnetite nanoparticles," *J. Mater. Chem.*, vol. 13, no. 8, pp. 1983–1987, 2003.

[162] D. Maity, S. N. Kale, R. Kaul-Ghanekar, J. M. Xue, and J. Ding, “Studies of magnetite nanoparticles synthesized by thermal decomposition of iron (III) acetylacetonate in tri(ethylene glycol),” *J. Magn. Magn. Mater.*, vol. 321, no. 19, pp. 3093–3098, 2009.

[163] R. Alexandrescu, V. Bello, V. Bouzas, R. Costo, and F. Dumitrache, “Iron Oxide Materials Produced by Laser Pyrolysis,” *AIP Conf. Proc.*, vol. 1275, no. 22, pp. 22–25, 2010.

[164] S. A. Kahani and Z. Yagini, “A comparison between chemical synthesis magnetite nanoparticles and biosynthesis magnetite,” *Bioinorg. Chem. Appl.*, p. 7, 2014.

[165] T. H. Ngo, D. L. Tran, H. M. Do, V. H. Tran, V. H. Le, and X. P. Nguyen, “Facile and solvent-free routes for the synthesis of size-controllable Fe_3O_4 nanoparticles,” *Adv. Nat. Sci. Nanosci. Nanotechnol.*, vol. 1, no. 3, p. 35001, 2010.

[166] T. Ahn, J. H. Kim, H. M. Yang, J. W. Lee, and J. D. Kim, “Formation pathways of magnetite nanoparticles by coprecipitation method,” *J. Phys. Chem. C*, vol. 116, no. 10, pp. 6069–6076, 2012.

[167] Y. Wang, I. Nkurikiyimfura, and Z. Pan, “Sonochemical Synthesis of Magnetic Nanoparticles,” *Chem. Eng. Commun.*, vol. 6445, pp. 616–621, 2014.

[168] G. Salazar-Alvarez, M. Muhammed, and A. A. Zagorodni, “Novel flow injection synthesis of iron oxide nanoparticles with narrow size distribution,” *Chem. Eng. Sci.*, vol. 61, no. 14, pp. 4625–4633, 2006.

[169] Z. R. Marand, M. Helmi, R. Farimani, and N. Shahtahmasebi, “Study of magnetic and structural and optical properties of Zn doped Fe 3 O 4 nanoparticles synthesized by co-precipitation method for biomedical application Properties of Zn doped Fe 3 O 4 nanoparticles,” *Nanomed J*, vol.

1, no. 4, pp. 238–247, 2014.

[170] L. Blaney, “Magnetite (Fe3O4): Properties, sinthesis, and applications,” *Lehigh Rev.*, vol. 15, pp. 32–81, 2007.

[171] Y. S. Lim, “A study on growth formation of nano-sized magnetite Fe3O4 via co-precipitation,” *Mater. Res. Innov.*, vol. 18, no. 6, pp. S6-457-S6-461, 2014.

[172] G. Gnanaprakash, S. Mahadevan, T. Jayakumar, P. Kalyanasundaram, J. Philip, and B. Raj, “Effect of initial pH and temperature of iron salt solutions on formation of magnetite nanoparticles,” *Mater. Chem. Phys.*, vol. 103, no. 1, pp. 168–175, 2007.

[173] H. Kazemzadeh, A. Ataie, and F. Rashchi, “Synthesis of Magnetite Nano-Particles By Reverse Co-Precipitation,” *Int. J. Mod. Phys. Conf. Ser.*, vol. 5, pp. 160–167, 2012.

[174] A. Mukhopadhyay, N. Joshi, K. Chattopadhyay, and G. De, “A facile synthesis of PEG-coated magnetite (Fe 3O 4) nanoparticles and their prevention of the reduction of cytochrome C,” *ACS Appl. Mater. Interfaces*, vol. 4, no. 1, pp. 142–149, 2012.

[175] N. Griffete, M. J. D. Clift, A. Lamouri, R. G. Digigow, A. M. Mihut, A. Fink, B. Rothen-Rutishauser, and H. Dietsch, “Amino covalent binding approach on iron oxide nanoparticle surface: Toward biological applications,” *Colloids Surfaces A Physicochem. Eng. Asp.*, vol. 415, pp. 98–104, 2012.

[176] J. Sun, “Synthesis and characterization of biocompatible Fe3O4 nanoparticles,” *J. Biomed. Mater. Res. Part A*, vol. 80, no. 2, pp. 333–41, 2007.

[177] B. Wang, Q. Wei, and S. Qu, “Synthesis and characterization of uniform and crystalline magnetite nanoparticles via oxidation-precipitation and modified co-precipitation methods,” *Int. J. Electrochem. Sci.*, vol. 8, no. 3, pp. 3786–3793, 2013.

[178] N. Mizutani, T. Iwasaki, S. Watano, T. Yanagida, H. Tanaka, and T. Kawai, "Effect of ferrous / ferric ions molar ratio on reaction mechanism for hydrothermal synthesis of magnetite nanoparticles," *Bull. Mater. Sci.*, vol. 31, no. 5, pp. 713–717, 2008.

[179] M. A. Verges, R. Costo, A. G. Roca, J. F. Marco, G. F. Goya, C. J. Serna, and M. P. Morales, "Uniform and water stable magnetite nanoparticles with diameters around the monodomain-multidomain limit," *J. Phys. D-Applied Phys.*, vol. 41, p. 134003, 2008.

[180] R. Valenzuela, M. C. Fuentes, C. Parra, J. Baeza, N. Duran, S. K. Sharma, M. Knobel, and J. Freer, "Influence of stirring velocity on the synthesis of magnetite nanoparticles (Fe3O4) by the co-precipitation method," *J. Alloys Compd.*, vol. 488, no. 1, pp. 227–231, 2009.

[181] D. Hu, Y. Wang, and Q. Song, "Weakly magnetic field-assisted synthesis of magnetite nano-particles in oxidative co-precipitation," *Particuology*, vol. 7, no. 5, pp. 363–367, 2009.

[182] E. K. U. Larsen, T. Nielsen, T. Wittenborn, L. M. Rydtoft, A. R. Lokanathan, L. Hansen, L. Østergaard, P. Kingshott, K. a. Howard, F. Besenbacher, N. C. Nielsen, and J. Kjems, "Accumulation of magnetic iron oxide nanoparticles coated with variably sized polyethylene glycol in murine tumors," *Nanoscale*, vol. 4, no. 7, p. 2352, 2012.

[183] R. Weisslede, *Molecular Imaging Principles and Practice*. Peoples Medical Publishing House of China, 2010.

[184] S. A. Jayanthi, D. Sukanya, A. J. A. Pragasam, and P. Sagayaraj, "The influence of PEG 20 , 000 concentration on the size control and magnetic properties of functionalized bio-compatible magnetic nanoparticles," vol. 5, no. 1, pp. 90–102, 2013.

[185] G. Nabiyouni, A. Barati, and M. Saadat, "Surface Adsorption of Polyethylene

Glycol and Polyvinyl Alcohol with Variable Molecular Weights on Zinc Oxide Nanoparticles," *Iran. J. Chem. Eng.*, vol. 8, no. 1, pp. 20–30, 2011.

[186] A. K. Gupta and M. Gupta, "Synthesis and surface engineering of iron oxide nanoparticles for biomedical applications," *Biomaterials*, vol. 26, no. 18, pp. 3995–4021, 2005.

[187] M. Günay, A. Baykal, and H. Sözeri, "Structural and magnetic properties of triethylene glycol stabilized monodisperse Fe3O4 nanoparticles," *J. Supercond. Nov. Magn.*, vol. 25, no. 7, pp. 2415–2420, 2012.

[188] L. Zhang, R. He, and H. C. Gu, "Oleic acid coating on the monodisperse magnetite nanoparticles," *Appl. Surf. Sci.*, vol. 253, no. 5, pp. 2611–2617, 2006.

[189] A. Kolate, D. Baradia, S. Patil, I. Vhora, G. Kore, and A. Misra, "PEG - A versatile conjugating ligand for drugs and drug delivery systems," *J. Control. Release*, vol. 192, pp. 67–81, 2014.

[190] E. Tombácz, A. Majzik, Z. S. Horvát, E. Ellés, and E. Illés, "Magnetite in Aqueous Medium: Coating Its Surface and Surface Coated With It," *Rom. Reports Phys.*, vol. 58, no. 3, pp. 281–286, 2006.

[191] Puji Loekitowati Hariani, M. Faizal, Ridwan, Marsi, and D. Setiabudidaya, "Synthesis and Propeties of Fe3O4 Nanoparticles by Co-precipitation method to Removal Procion Dye," *Int. J. Environ. Sci. Dev.*, vol. 4, no. 3, pp. 336–340, 2013.

[192] A. H. Lu, E. L. Salabas, and F. Schüth, "Magnetic nanoparticles: Synthesis, protection, functionalization, and application," *Angew. Chemie - Int. Ed.*, vol. 46, no. 8, pp. 1222–1244, 2007.

[193] Schwertmann, *Iron Oxides in the Laboratory*. WILEY-VCH Verlag GmbH, 2007.

[194] U. Scheinost, A.C. Schwertmann, “Color identification of iron oxides and hydroxysulfates: use and limitations,” *Soil Sci. Soc. Am.*, vol. 63, no. 5, pp. 1463–1471, 1999.

[195] J. Torrent and V. Barron, “Iron Oxides in Relation To the Colour of Mediterrranean Soils.” Universidad de Cordoba, pp. 377–386, 2003.

[196] “A Guide to Colorimetry,” *Sherwood Scientific Ltd*. .

[197] P. Sanmartín, E. Chorro, D. Vázquez-Nion, F. M. Martínez-Verdú, and B. Prieto, “Conversion of a digital camera into a non-contact colorimeter for use in stone cultural heritage: The application case to Spanish granites,” *Meas. J. Int. Meas. Confed.*, vol. 56, pp. 194–202, 2014.

[198] Nagano, “The use of color to quantify the effects of ph and temperature on the crystalline kinetics of goethite,” *Clay Miner.*, vol. 42, no. 2, pp. 226–234, 1994.

[199] R. H. R. Castro, “Sintering: Mechanisms of Conventional, Nanodensification and Field Assisted Processes,” vol. 35, 2013.

[200] S.-J. L. Kang, *Sintering Densification, Grain Growth and Microstructure*. 2005.

[201] J. D. Katz, “Microwave Sintering,” *Annu. Rev. Mater. Sci.*, vol. 22, pp. 153–170, 1992.

[202] D. (Material R. I. Agrawal, “Microwave Sintering , Brazing and Melting of Metallic Materials,” *Non-Ferrous Mater. Extr. Process.*, vol. 4, pp. 183–192, 2006.

[203] D. Agarwal and M. Engineering, “Microwave sintering of aluminum alloys,” pp. 153–158.

[204] D. Agrawal, “Microwave sintering of metallic materials,” *Proceedings of 2000 Powder Metllurgy World Congress*. pp. 797–800, 2000.

[205] R. Raman Mishra and A. Sharma, “Microwave Sintering of Pure Metal Powders – A Review,” *Int. J. Adv. Mech. Eng.*, vol. 4, no. 3, pp. 2250–3234, 2014.

[206] J. L. Rosenholtz and D. T. Smith, “The Dielectric Constant of Mineral Powders,” *Am. Mineral.*, vol. 21, pp. 115–120, 1936.

[207] C. L. He, S. J. Ma, X. J. Su, Q. H. Mo, and J. L. Yang, “Comparison of the Microwave Absorption Characteristics of Hematite , Magnetite and Pyrite,” vol. 49, no. 3, pp. 131–146, 2015.

[208] S. M. Bradshaw, E. J. Van Wyk, and J. B. De Swardt, “Microwave heating principles and the application to the regeneration of granular activated carbon,” *J. South African Inst. Min. Metall.*, pp. 201–212, 1998.

[209] *Handbook of Refractory Practice*. Harbison-Walker Refractories, 2005.

[210] Y. Takeuchi, T. Abe, T. Kageyama, and H. Sakai, “RF dielectric properties of SiC ceramics and their application to design of HOM absorbers,” *Proc. IEEE Part. Accel. Conf.*, vol. 2005, no. 1, pp. 1195–1197, 2005.

[211] A. K. Harman, S. Ninomiya, and S. Adachi, “Optical constants of sapphire (α-Al2O3) single crystals,” *J. Appl. Phys.*, vol. 76, no. 12, pp. 8032–8036, 1994.

[212] Fang, “Dielectric Constant for Cr2O3 Crystals,” 1963.

[213] D. R. Lide, “CRC Handbook of Chemistry and Physics, 84th Edition, 2003-2004,” *Handb. Chem. Phys.*, vol. 53, p. 2616, 2003.

[214] K. Kukli, K. Forsgren, M. Ritala, M. Leskelä, J. Aarik, and A. Hårsta, “Dielectric Properties of Zirconium Oxide Grown by Atomic Layer Deposition from Iodide Precursor,” *J. Electrochem. Soc.*, vol. 148, no. 12, p. F227, 2001.

[215] S. S. Shinde, R. a Bansode, C. H. Bhosale, and K. Y. Rajpure, “Physical properties of hematite α-Fe 2 O 3 thin films: application to

photoelectrochemical solar cells," *J. Semicond.*, vol. 32, no. 1, p. 13001, 2011.

[216] I. Kong, S. Hj Ahmad, M. Hj Abdullah, D. Hui, A. Nazlim Yusoff, and D. Puryanti, "Magnetic and microwave absorbing properties of magnetitethermoplastic natural rubber nanocomposites," *J. Magn. Magn. Mater.*, vol. 322, no. 21, pp. 3401–3409, 2010.

[217] T. a Baeraky, "Microwave Measurements of the Dielectric Properties of Silicon Carbide at High Temperature," *Physics (College. Park. Md).*, vol. 25, no. 25, pp. 263–273, 2002.

[218] J. Mølgaard and W. W. Smeltzer, "Thermal conductivity of magnetite and hematite," *J. Appl. Phys.*, vol. 42, no. 9, pp. 3644–3647, 1971.

[219] S. Ito, Y. Yui, and J. Mizuguchi, "Electrical properties of semiconductive α-Fe2O3 and its use as the catalyst for decomposition of volatile organic compounds," *Mater. Trans.*, vol. 51, no. 6, pp. 1163–1167, 2010.

[220] "Relative Permittivity," *Wikipedia*, 2016. [Online]. Available: https://en.wikipedia.org/wiki/Relative_permittivity#cite_note-Gray.26Meyer-3.

[221] D. a. Clark and D. W. Emerson, "Notes on rock magnetization characteristics in applied geophysical studies," *Explor. Geophys.*, vol. 22, no. JANUARY 1991, p. 547, 1991.

[222] "Silicon Carbide Material Properties," 2016.

[223] "Magnetic Susceptibilities of Paramagnetic and Diamagnetic Materials at 20°C," *Hyperphysics*, 2016. [Online]. Available: http://hyperphysics.phy-astr.gsu.edu/hbase/tables/magprop.html.

[224] "Permeability (Electromagnetism)," *Wikipedia*, 2016. [Online]. Available: https://en.wikipedia.org/wiki/Permeability_(electromagnetism).

[225] "Silica - Silicon Dioxide (SiO2)," *AZO Materials*, 2016. [Online]. Available:

http://www.azom.com/article.aspx?ArticleID=1114.

[226] "Material: Chromium Oxide (Cr2O3), bulk," *MEMS-net*, 2016. [Online]. Available: https://www.memsnet.org/material/chromiumoxidecr2o3bulk/.

[227] "Resistivity and Temperature Coefficient at 20 C," *Hyperphysics*, 2016. [Online]. Available: http://hyperphysics.phy-astr.gsu.edu/hbase/tables/rstiv.html.

[228] "Graphite (C) - Classifications, Properties and Applications of Graphite," *AZO Materials*, 2016. [Online]. Available: http://www.azom.com/article.aspx?ArticleID=1630.

[229] "Alumina - Aluminium Oxide - Al2O3 - A Refractory Ceramic Oxide," *AZO Materials*, 2016. [Online]. Available: http://www.azom.com/properties.aspx?ArticleID=52.

[230] M. Takeda, T. Onishi, S. Nakakubo, and S. Fujimoto, "Physical Properties of Iron-Oxide Scales on Si-Containing Steels at High Temperature," *Mater. Trans.*, vol. 50, no. 9, pp. 2242–2246, 2009.

[231] M. A. Khilla and A. A. Hanna, "Elzci'rical," 1981.

[232] "Zirconia - ZrO2, Zirconium Dioxide," *AZO Materials*, 2016. [Online]. Available: http://www.azom.com/article.aspx?ArticleID=133.

[233] Dynamic-Ceramic Ltd, "Dynamic Ceramic Material Properties," *[Online]*.

[234] "Waveguide Components: Isolator," *Muegge*, 2016. [Online]. Available: http://www.muegge.de/en/products/waveguide-components/active-component-isolator/.

[235] A. Thakur, P. Mathur, and M. Singh, "Study of dielectric behaviour of Mn-Zn nano ferrites," *J. Phys. Chem. Solids*, vol. 68, no. 3, pp. 378–381, 2007.

[236] H. M. Zaki, "Temperature dependence of dielectric properties for copper

doped magnetite," *J. Alloys Compd.*, vol. 439, no. 1–2, pp. 1–8, 2007.

[237] Hirasawa, "Silver Powder for Silver Clay and Silver Clay Containing this Silver Powder," 2006.

[238] H. Stanjek and W. Häusler, "Introduction To Powder/ Polycrystalline Diffraction," *Hyperfine Interact.*, vol. 154, pp. 107–119, 2004.

[239] A. L. Patterson, "The scherrer formula for X-ray particle size determination," *Phys. Rev.*, vol. 56, no. 10, pp. 978–982, 1939.

[240] J. Clarke and A. I. Braginski, *The SQUID Handbook: Vol 2 Applications of SQUIDs and SQUID Systems*. 2006.

[241] P. Girard and J.-P. Boissel, "Clockwise Hysteresis or Proteresis," *J. Pharmacokinet. Biopharm.*, vol. 17, no. 3, pp. 401–402, 1989.

[242] S. Y. Wu, J. Ji, P. Shih, and A. C. Gandhi, "Proteresis of Cu2O / CuO core-shell nanoparticles : Experimental observations and Proteresis of Cu 2 O / CuO core-shell nanoparticles : Experimental observations and theoretical considerations," vol. 193906, pp. 1–9, 2014.

[243] P. J. Baldevbhai and R. S. Anand, "Color Image Segmentation for Medical Images using L * a * b * Color Space," *J. Electron. Commun. Eng.*, vol. 1, no. 2, pp. 24–45, 2012.

[244] Al-Shemmeri, *Engineering Fluid Mechanics*. 2012.

[245] N. J. Gunther, "A Note on Disk Drag Dynamics," pp. 1–5, 2012.

[246] M. Sadraey, *Aircraft Performance*. 2007.

[247] G. S. Smith, "Faraday's first dynamo: A retrospective," *Am. J. Phys.*, vol. 81, no. 12, p. 907, 2013.

[248] M. I. Gonzalez, "Experiments with eddy currents: the eddy current brake," *Eur. J. Phys.*, vol. 25, no. 4, pp. 463–468, 2004.

[249] H. Montgomery, “Current flow patterns in a Faraday disc,” *Eur. J. Phys.*, vol. 25, no. 2, pp. 171–183, 2003.

[250] A. Arifin, “State of the Art of Switched Reluctance Generator,” *Energy Power Eng.*, vol. 4, no. 6, pp. 447–458, 2012.

[251] W. a Pluta, “Core loss models in electrical steel sheets with different orientation,” no. 9, pp. 37–42, 2011.

[252] Mayergoyz, “Mathematical models of hysteresis and their applications,” 2003.

[253] D. C. Jiles and D. L. Atherton, “Theory of ferromagnetic hysteresis,” *J. Magn. Magn. Mater.*, vol. 61, no. 1–2, pp. 48–60, 1986.

[254] N. C. Pop and O. F. Caltun, “The fitting of magnetic hysteresis curves using the Jiles -Atherton model(II),” *J. Optoelectron. Adv. Mater.*, vol. 12, no. 4, pp. 885–891, 2010.

[255] S. E. Zirka, Y. I. Moroz, R. G. Harrison, and K. Chwastek, “On physical aspects of the Jiles-Atherton hysteresis models,” *J. Appl. Phys.*, vol. 112, no. 4, 2012.

[256] R. Du and P. Robertson, “Dynamic Jiles–Atherton Model for Determining the Magnetic Power Loss at High Frequency in Permanent Magnet Machines,” *IEEE Trans. Magn.*, vol. 51, no. 6, pp. 1–10, 2015.

[257] X. Wang, D. W. P. Thomas, M. Sumner, J. Paul, and S. H. L. Cabral, “Numerical determination of Jiles-Atherton model parameters,” *COMPEL - Int. J. Comput. Math. Electr. Electron. Eng.*, vol. 28, no. 2, pp. 493–503, 2009.

[258] N. C. Pop and O. F. Caltun, “Jiles – Atherton Magnetic Hysteresis Parameters Identification,” *Acta Phys. Pol. A*, vol. 120, no. 3, p. 491, 2011.

[259] P. Petrovic, N. Mitrovic, M. Stevanovic, and P. Pejovic, “Hysteresis model for magnetic materials using the Jiles-Atherton model,” no. 1.

[260] D. C. Jiles, J. B. Thoelke, and M. K. Devine, "Numerical determination of hysteresis parameters for the modeling of magnetic properties using the theory of ferromagnetic hysteresis," *IEEE Trans. Magn.*, vol. 28, no. 1, pp. 27–35, 1992.

[261] D. E. Madsen, S. Mørup, and M. F. Hansen, "On the interpretation of magnetization data for antiferromagnetic nanoparticles," *J. Magn. Magn. Mater.*, vol. 305, no. 1, pp. 95–99, 2006.

[262] W. F. Brown, "Thermal Fluctuations of a Single-Domain Particle," *Phys. Rev.*, vol. 130, no. 5, pp. 1677–1686, 1963.

[263] "Exchange Interaction." BGU.

[264] "X-Rays Unravel the Puzzle of Exchange Bias," *Stanford University*. [Online]. Available: https://www-ssrl.slac.stanford.edu/stohr/magneticexchange.htm. [Accessed: 01-Jan-2016].

[265] S. H. Kilcoyne and R. Cywinski, "Ferritin: a model superparamagnet," *J. Magn. Magn. Mater.*, vol. 140–144, no. PART 2, pp. 1466–1467, 1995.

[266] C. Gilles, P. Bonville, K. K. W. Wong, and S. Mann, "Non-Langevin behaviour of the uncompensated magnetisation in nanoparticles of artificial ferritin," *arXiv:cond-mat*, vol. 7087, p. 11, 2000.

[267] M. Seehra, V. Babu, a. Manivannan, and J. Lynn, "Neutron scattering and magnetic studies of ferrihydrite nanoparticles," *Phys. Rev. B*, vol. 61, no. 5, pp. 3513–3518, 2000.

[268] J. Nogués, J. Sort, V. Langlais, V. Skumryev, S. Suriñach, J. S. Muñoz, and M. D. Baró, "Exchange bias in nanostructures," *Phys. Rep.*, vol. 422, no. 3, pp. 65–117, 2005.

[269] M. Bañobre-López, C. Vázquez-Vázquez, J. Rivas, and M. A. López-Quintela, "Magnetic properties of chromium (III) oxide nanoparticles,"

Nanotechnology, vol. 14, no. 2, pp. 318–322, 2003.

[270] T. Miyazaki, *The Physics of Ferromagnetism*. 2012.

[271] J. Mejía-López, P. Soto, and D. Altbir, "Asymmetric reversal of the hysteresis loop in exchange-biased nanodots," *Phys. Rev. B - Condens. Matter Mater. Phys.*, vol. 71, no. 10, pp. 2–5, 2005.

[272] A. Berger, C. Binek, D. T. Margulies, A. Moser, and E. E. Fullerton, "Reversible hysteresis loop tuning," *Phys. B Condens. Matter*, vol. 372, no. 1–2, pp. 168–172, 2006.

[273] Jin Hanmin, S. Dongsheng, G. Cunxu, and H. Kim, "Inverted hysteresis loops: Experimental artifacts arising from inappropriate or asymmetric sample positioning and the misinterpretation of experimental data," *J. Magn. Magn. Mater.*, vol. 308, no. 1, pp. 56–60, 2007.

[274] H. P. Gavin, "The Levenberg-Marquardt method for nonlinear least squares curve-fitting problems," *Dep. Civ. Environ. Eng. Duke Univ.*, pp. 1–17, 2013.

[275] J. C. Butcher, "Implicit runge-kutta processes," *Math. Comput.*, vol. 18, no. 85, pp. 50–64, 1964.

[276] Atekwana, "High Resolution Magnetic susceptibility measurements for investigating magnetic mineral formation," *J. Geophys. Res. Biogeosciences*, 2014.

[277] Y. Liu, *Handbook of Advanced Magnetic Materials*, vol. II. 2006.

[278] C. Tannous and J. Gieraltowski, "The Stoner–Wohlfarth model of ferromagnetism," *Eur. J. Phys.*, vol. 29, no. 3, pp. 475–487, 2008.

[279] D. Serantes and D. Baldomir, "Superparamagnetism and Monte Carlo simulations," *Open Surf. Sci. J.*, vol. 4, p. 71, 2012.

[280] T. Berndt, A. R. Muxworthy, and G. A. Paterson, "Determining the magnetic

attempt time τ0, its temperature dependence, and the grain size distribution from magnetic viscosity measurements," *J. Geophys. Res. B Solid Earth*, vol. 120, no. 11, pp. 7322–7336, 2015.

[281] D. Srikala, V. N. Singh, A. Banerjee, and B. R. Mehta, "Effect of induced shape anisotropy on magnetic properties of ferromagnetic cobalt nanocubes.," *J. Nanosci. Nanotechnol.*, vol. 10, no. 12, pp. 8088–8094, 2010.

[282] G. F. Goya, F. C. Fonseca, R. F. Jardim, R. Muccillo, N. L. V Carreño, E. Longo, and E. R. Leite, "Magnetic dynamics of single-domain Ni nanoparticles," *J. Appl. Phys.*, vol. 93, no. 10 2, pp. 6531–6533, 2003.

[283] M. F. Hansen and S. Mørup, "Estimation of blocking temperatures from ZFC/FC curves," *J. Magn. Magn. Mater.*, vol. 203, no. 1–3, pp. 214–216, 1999.

[284] G. F. Goya and M. P. Morales, "Field Dependence of Blocking Temperature in Magnetite Nanoparticles," *J. Metastable Nanocrystalline Mater.*, vol. 20–21, pp. 673–678, 2004.

[285] U. Voskoboynik, "Anomalous field dependence of blocking temperature of natural horse-spleen ferritin," *Acta Phys. Pol. A*, vol. 92, no. SUPPL., 1997.

[286] S. Yoon, "Determination of the Temperature Dependence of the Magnetic Anisotropy Constant in Magnetite Nanoparticles," *J. Korean Phys. Soc.*, vol. 59, no. 5, pp. 3069–3073, 2011.

[287] A. A. Timopheev, V. M. Kalita, and S. M. Ryabchenko, "Simulation of the magnetization reversal of an ensemble of single-domain particles in measurements with a continuous sweep of the magnetic field or temperature," *Low Temp. Phys.*, vol. 34, no. 6, pp. 446–457, 2008.

[288] C. Schmitz-Antoniak, "X-ray absorption spectroscopy on magnetic nanoscale systems for modern applications," *Reports Prog. Phys.*, vol. 78, no. 6, p. 62501, 2015.

[289] I. J. Bruvera, P. Mendoza Zélis, M. Pilar Calatayud, G. F. Goya, and F. H. Sánchez, "Determination of the blocking temperature of magnetic nanoparticles: The good, the bad, and the ugly," *J. Appl. Phys.*, vol. 118, no. 18, pp. 1–8, 2015.

[290] L. He and C. Chen, "Effect of temperature-dependent shape anisotropy on coercivity for aligned Stoner-Wohlfarth soft ferromagnets," *Phys. Rev. B - Condens. Matter Mater. Phys.*, vol. 75, no. 18, pp. 1–22, 2007.

[291] R. C. O'Handley, *Modern Soft Magnetic Materials*, vol. 414–415. 2000.

[292] E. L. Jr, A. L. Brandl, A. D. Arelaro, and G. F. Goya, "Spin Disorder and Magnetic Anisotropy in F e 3 O 4 Nanoparticles," pp. 1–35, 2005.